University of Strathclyde

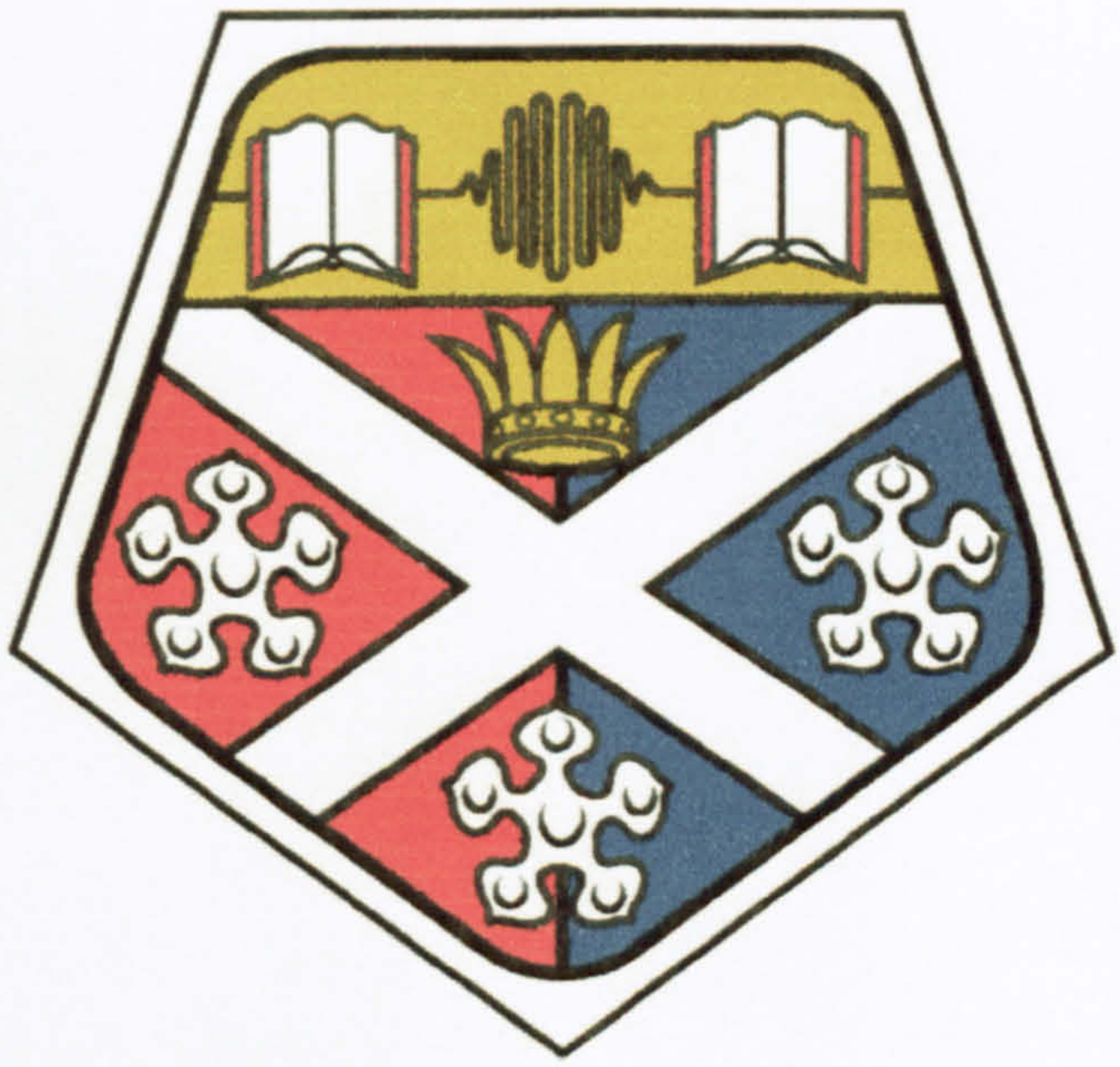

Department of Mechanical Engineering

Measurement and Finite Element Modelling of Temperatures in welding processes

A thesis presented in fulfilment of the requirements for the degree of

Doctor of Philosophy

by

Cheng Peng Henry Tan

2005

Acknowledgements

Firstly, I would like to express my deepest gratitude to Dr C.K. Lee for his endless patience and the invaluable advice, supervision and guidance throughout this project. His strictness and criticism occasionally make me feel even unfair, particular during the process of thesis writing. With no doubt, such process is painful, but it is most worthwhile. I fully understand that it will benefit me throughout my life after this tough training. I am also thankful to Professor T.G.F. Gray for educating me on the concept of welding out-of-plane distortion and Professor Neville Baker for giving me the lesson on the formation of microstructure in the weld and its hardness. In addition, I also want to say many thanks to Mr Alex Galloway for supervising me on the welding experimental work and Mr James Kelly for his guidance on photo taking of the weld macrostructures.

Thanks also to Mr Duncan Camilleri, Mr Chris Cameron, Mr Eric Duncan, Mr Jim Docherty, Mr Pat McGinness, Mr Steven Black, Mr Gerry Johnston and other laboratory technicians for their help and support during experimental work.

I also want to say thank you to Professor James Rhodes, Professor Bill Paton, Dr A. Gilchrist, Dr David Nash, Dr William Demspter, Dr Norrie McPherson and Ms Janet Harbidge for their encouragement and support.

Finally, I would like to thank the Engineering and Physical Sciences Research Council (EPSRC) and BAE systems for their financial support on this research.

Abstract

Out-of-plane welding distortion has been a persistent problem in welding industries. In order to find solutions for such a problem, substantial experimental and computer modelling work on residual stresses and out-of-plane distortion analysis need to be carried out. Such computer modelling requires the temperature fields or histories during welding as pre-requisite input which can be obtained either from actual measurement or computer simulation. The object of this thesis is to develop computational techniques which can be used to compute these temperatures.

Experimental work on temperature measurement has also been carried out to provide data for the purposes of validating the computer models. A data acquisition system was successfully calibrated and used to record temperature histories of the plate during the welding process. Four experiments were carried out by joining rectangular plates of size 500 mm by 250 mm together with "V" weld-preparation configuration at various thicknesses. Thermocouples were affixed to the top and bottom surfaces of the specimen at locations just within or very near to the heat affected zone and at locations remote from the heat affected zone to record the temperature history during welding and cooling.

Related analytical theories were studied and used to validate the finite element models. The method of superposing the effects of a number of instantaneous plane heat sources to the plates has been investigated and used successfully for the evaluation of the temperature history of the plates where the heat input varies with time. Finally, a computational technique to simulate the temperature history near to and remote from the heat source was successfully developed using ANSYS 8.0 finite element software and applied to three-dimensional transient models, three-dimensional steady state models and two-dimensional transient sectional models. All the simulated results were in good agreement with experimental measurements.

Contents

Nomenclature

U	welding speed
Q_{net}	net heat input to the plate in W
V	welding voltage
I	welding current
P	welding power which is VI
η	welding heat input efficiency factor
T_o	ambient temperature
θ	relative temperature after subtracted the ambient temperature
δ	thickness of the plates,
x	co-ordinate in line with the travelling velocity and
y	co-ordinate perpendicular to δ and x.
Q_{net}"	net heat-flux input in J/m^2
t	time in seconds
α	thermal diffusivity
ρ	density
C	specific heat
Q"	heat-flux input in J/m^2
Q_c	heat loss through convection
h	convection heat transfer coefficients
A	surface area
T_s	surface temperature of the conducting solid
T_f	fluid temperature

Nu	Nusselt Number
Gr	Grashof number
Pr	Prandtl number
Ra	Rayleigh number which is the product of Grashof and Prandtl numbers
Q_r	heat transfer through radiation
σ	Stefan Boltzmann constant (5.67×10^{-8} W/m^{2}K^4)
ε	emissivity of the surface
T_a	large enclose temperature
K	thermal conductivity
Q_v	volumetric heat source
Q_{prep}	heat due to the liquid metal in W
A_{prep}	cross-sectional area of the weld-prep
h_{fb}	enthalpy of liquid metal at boiling point
h_{ia}	enthalpy of solid metal at ambient temperature
Q_{arc}	amount of heat due to welding arc in W
$q(r)$	heat flux distribution as a function of radius
r_H	radius of the heat source
r	variable radius ranging from 0 to r_H

Chapter 1 – Introduction

Welding is the most predominant metal fabrication process. Some modern processes such as gas metal arc welding and hybrid laser welding are capable of high levels of automation. Fusion welding involves the application of heat to the materials being joined and the addition of filler metal to the weld-preparation in order to fuse the materials together. Distortions of the welded components arise, among other factors, as a result of non-uniform temperature distribution in the materials during the welding process. Due to the high temperatures involved, thermal stresses in parts of the component exceed the elastic limit during heating and permanent strains and residual stresses are left behind when the temperatures return to the ambient value. Such distortion is difficult to predict and this poses a significant problem to industry.

In order to find solutions for such a problem, substantial experimental and computer modelling work on residual stresses and out-of-plane distortion analysis need to be carried out. Such computer modelling requires temperature fields or histories during welding to be obtained as pre-requisite input. This may be achieved either from actual measurement or computer simulation. It is the object of this thesis to develop computational techniques which can be used to predict these temperatures. The same techniques can also be used for studies of weld microstructure formation, grain structure of the weld, hardness of the weld, weld end cracking, hot cracking and cold cracking.

In the past, a key to modelling the temperature histories or distribution of the welding plate was provided by the analytical moving heat source theory which was first published in 1904 by Wilson [1]. Later, in 1938 Rosenthal [2] published with his own analytical expressions and applied them to the usages of welding. After Rosenthal, significant further contributions were made by several other investigators notably Wells [4], Barry et al [7], Eagar et al [13] and Adrian Bejan [20]. In general, the analytical theory cannot predict an accurate temperature field or history of a welded component because physical factors such as the non-linearity of the thermal physical properties have been neglected and the welding plate surfaces are assumed to be adiabatic.

In recent years, due to advances in computational technology, the finite element approach is capable of solving complex transient non-linear heat flow problems. It can also account for surface heat loss via natural convection and radiation and the effects of latent heat during phase transformation. Convection loss can account for approximate 10% of the net heat input, while the radiation effect is more critical in the high temperature region close to the welding heat source and can account for about 9% of the heat input. Phase transformation occurs during melting and solidification of the weld pool. It also occurs during transformation of ferrite to austenite or austenite to ferrite at around 700°C for steel.

Most studies in the past have been concentrated more on simulating the temperature histories or distributions in a plate where a weld is being deposited on the surface. This is not quite the same as joining two metal plates together. Since industrial metal

welding is mostly performed with a weld-preparation, it is essential to take the weld-preparation into account during the computer simulation.

This project aims at developing computational techniques that can model the temperature fields near to the heat source and provide results which are as close as possible to experimentally measured temperatures by taking into account the actual weld-preparation. Therefore, it is necessary to carry out experiments to make temperature measurements at strategic locations in the welded plates in order to validate the computer simulation models.

Since most of the serious out-of-plane distortions occur in thin plates, this project will focus on single pass welding of thin steel plates. Thin steel plates usually need a weld-preparation and the most common weld-preparation for a single pass welding is the 'V' weld-preparation. This kind of weld-preparation normally has a gap of 1 to 2 mm in between the plates in order to obtain a fully penetrated weld. The root thickness of this type of weld-preparation is usually between 1 to 2.5 mm to preventing burn-through during the arc welding. The angle of the 'V' weld-preparation is usually 30° to 40° so that it can produce a good fusion between the two plates. In addition, single pass welding of steel plates is usually possible up to a maximum thickness of 8 mm for gas metal arc welding. The above considerations have been kept in mind during the design of the experiments.

The present thesis is structured in the following manner. Chapter 2 presents a review of relevant published literature. Chapter 3 gives an account of the experimental work

that has been carried out to provide data for the purposes of validating the computer models. Chapter 4 describes the analytical, moving heat source theory, neglecting factors such as non-linear thermal physical properties and surface heat loss and shows how this can be implemented in finite element analysis. The techniques in Chapter 4 are then implemented in Chapter 5 to perform simulation where the factors neglected in the analytical theory are being taken into account. The inability of the simulation techniques in Chapter 5 to predict the top and bottom weld width is addressed in Chapter 6 where a distributed welding arc heat source is used and the weld-preparation is taken into account. Chapter 7 gives an overall discussion of the studies and Chapter 8 concludes the findings and gives suggestions for future development.

Chapter 2 – Review of Literature Survey

2.1 Introduction

As mentioned in Chapter 1, out-of-plane welding distortion has been a persistent problem in welding industries. In order to analyse the residual stresses and out-of-plane distortion occur after welding, the temperature fields or histories during welding are needed as pre-requisite input for calculation purpose. An accurate modelling of the temperature fields or histories as pre-requisite input will provide to a better solution of the residual stresses or out-of-plane distortion which is useful in finding answers for such problems.

This Chapter presents an account on the development of modelling welding temperature fields or histories. In section 2.2, a brief description on the development of analytical moving heat source theory is presented. This is then followed by a more detailed description on the development of computation techniques to simulate the temperature fields or histories during welding of plates in section 2.3.

In the next section, an account of the experimental work on the measurement of welding thermal efficiency, weld pool shape, heat flux distribution during arc welding and weld pool surface temperature are presented.

Section 2.5 gives an overall discussion on the literatures survey. Lastly, section 2.6 provides a summary on the overall view of current analytical theory and computer simulation.

2.2 Analytical theory development

The analytical theory of a moving heat source was first published in 1904 by Wilson [1]. This theory assumes either a point, a line or a plane heat source applied to a moving media where the moving media can be either a solid or a fluid and all the surfaces are adiabatic. In 1938 Rosenthal [2] provided analytical expressions and applied them to the usages of welding. After Rosenthal, significant further contributions were made by several other investigators. Mahla et al [3] developed a moving circular even heat flux heat source mathematical expression to predict the temperature history but the prediction gave too high maximum temperatures and excessive cooling rates. Wells [4] simplified Rosenthal's solution to an approximate expression to predict the net heat input to the weld metal during welding in terms of the average fusion zone width of a full penetration welding plate. Adams [6] also simplified the solution of line and point sources for the prediction of the peak temperature distribution and temperature history of a plate during welding. Barry et al [7] discovered that the heat flow along the welding direction is negligible and can be ignored for a welding speed as low as 10 inches/min through experiments in steel welding. Therefore, they proposed an instantaneous line source expression for the prediction of the temperature history and derived an expression to predict the peak

temperature at different locations. Eagar et al [13] modified Rosenthal's solution of a moving point heat source to a more realistic moving Gaussian heat source. Adrian Bejan [20] derived expressions for the moving point source and a line source with the heat flow along the welding direction neglected. Kasuya et al [21] derived comprehensive expressions by taking into account the surface convection due to a moving point source inside a welding plate. They also derived an expression for an instantaneous line heat source by taking into account the surface convection and neglecting the heat flow in welding direction. They also proposed an expression to calculate the temperature history of a preheated plate by taking into account surface convection. Kang et al [29] derived an instantaneous Gaussian distributed heat source expression to predict the fusion zone and heat affected zone sizes of welds deposited without a weld-preparation.

2.3 Computer simulation development

In recent years, due to advances in computational technology, the finite element approach has become capable of solving complex transient non-linear heat flow problems. It also can account for surface heat loss and the effects of latent heat due to phase transformation.

In 1969, Pavelic et al [9] proposed a Gaussian heat source that takes the shape of normal distribution function according to measured heat flux distribution [32], the heat flux distribution of a welding arc took the shape of Gaussian. They also

proposed an in-plane shape function to predict the shape of a deposited weld pool in gas tungsten-arc (GTA) welding. They compared their 2D in-plane finite element adiabatic surface model results with experimental results and showed that the computed results agreed fairly well the experimentally measured temperatures.

In 1975, Friedman [10] developed 2D transient sectional models for calculating temperature histories, with the heat flow in the welding direction neglected. In his model, a reference plane was established at some arbitrary position in the work piece. The Gaussian heat source was then moved through the reference plane using the relationship of time equal to travelled distance divided by velocity. The thermal physical properties of the models were extrapolated linearly to the melting temperature and no latent heat of phase transformation was included in the models. No heat loss to surrounding via convection and radiation was considered in the model and there were experimental results were provided to validate the models. Paley et al [11] developed 3D transient models for calculating temperature histories and distribution of the actual weld and used Gaussian heat source for the models. They accounted for the non-linearity of the thermal physical properties and latent heat but left all surfaces in adiabatic condition. The actual deposited weld sectional profiles were compared with the simulation results and showed good agreement between them. However, no temperature measurements were given to verify the models.

In 1978, Krutz et al [12] constructed 3D transient models for calculating temperature histories and used Gaussian heat source for the models. They accounted for the non-

linearity of the thermal physical properties, latent heat of phase transformation and heat loss to the surrounding via constant values of convection and radiation in the models. They also used a conductivity enhancement of 0.4 cal/sec-cm-K (167 W/mK) to simulate the weld pool stirring effect. They used other researchers' experimental temperature measurement to verify the model. They noted that the non-linear model was close to the actual welding conditions but should be used cautiously because the results were sensitive to arc radius and the thermal conductivity enhancement in the molten pool.

In 1984, Goldak et al [15] proposed an arbitrary distributed heat source, namely a double ellipsoidal heat source, where the weld pool shape and size must be known beforehand. This heat source was distributed all over the known weld pool size and shape in order to simulate the weld pool size and shape. This source can only model the pool shape and heat affected zone correctly for thick plates with a weld just deposited on the surface of the plate (shallow penetration). Their simulation results of a thick plate finger penetration weld (deep penetration, shaped like a finger) did not compare well with their experimental results.

In 1985, Moore et al [16] adopted the 'double ellipsoid' heat source for the deposited pool models with the thermal conductivity enhancement of 121 W/mK to simulate the weld pool stirring effect. They compared the analytically calculated cooling time of four different types of mathematical expressions with the computer simulated cooling time and experimental cooling time and showed that none of the analytical solutions could accurately predict the cooling time between 800°C and 500°C, and

cooling time between 1500°C and 100°C. However, the finite element method of computing for cooling times were in reasonable agreement with measured cooling times.

In 1988, Tekriwal et al [17] modelled the gas metal arc welding of a V prep-groove with no gap between the plates and no root face using a 3D transient approach. They simulated the filling up the V prep-groove with electrode metal during welding by adding elements at each time step correspond to filler metal action and used a Gaussian heat source for their model. They claimed that the predicted heat affected zone (HAZ) and fusion zone (FZ) were in close agreement with the experimental data. However, no experimental weld sectional profile was shown in the paper.

In 1989, Pardo et al [19] used Rosenthal's equation to estimate the weld reinforcement width of the gas metal arc welding process and adopted a double ellipsoidal heat source for their 3D steady state computer simulation. They accounted for the weld pool stirring effect by applying a conductivity enhancement of 400 W/m K to the weld pool. They simulated the finger penetration profile of a depositing pool with no weld-preparation by varying the thermal conductivity in the weld pool in an anisotropic manner. Good agreement was obtained between the simulation results and experimental measurement.

In 1993, Kamala et al [22] compared the temperature fields of a simplified 2D transient finite element sectional model with a 3D transient finite element model using a double ellipsoidal heat source and concluded that the error of the 2D transient

sectional model is negligible at a rate of 0.5 cm/s welding speed for a depositing weld.

In 1994, Dighde et al [23] prescribed Gaussian temperature distribution to the weld pool of their 3D transient model to simulate the whole process of Tekken welding and used a conductivity enhancement of 121 W/mK to simulate the effect of convective weld pool. However, no experimental measurement was provided to validate their model.

In 1998, Wahab et al [26] developed a new numerical approach, namely a 'split heat source model'. They adopted the approach of 'double ellipsoidal' heat source with an additional spherical volume below the ellipsoidal heat source to represent the impingement of the metal droplets in order to simulate the finger penetration profile of a depositing pool with no weld-preparation. Their heat source dimensions were not known beforehand and were simply chosen to give the best fit to experimental results. They concluded that the simple 2D sectional and 3D steady state conductive heat-transfer models are adequate to simulate the gas metal arc welding process if a suitable representation of the welding heat source input is used. However, the weld pool lengths were under-predicted due to the failure of adequate compensation of convective flow, even though an artificial enhancement of thermal conductivity 5-10 times normal level was applied to the molten material.

In 1999, Murugan et al [27] computed the 3D steady state models of 6 different manual metal arc welding conditions to predict the temperature histories by applying

square surface heat flux on top of the weld and a conductivity enhancement of 160 W/mK was used to simulate the effect of weld pool stirring for depositing weld models. Their predicted and experimental temperature histories were reported to be in a good match of within 10% error.

In 2000, Bonifaz [30] compared the Gaussian distribution heat source with the double ellipsoid heat source using simplified 2D transient finite element sectional model and observed that the double ellipsoid model is less sensitive than the Gaussian model for an application used to simulate substrate shock responses, in this case, the filler metal is deposited on the substrate in the weld interface direction. The heat from the electrode was suddenly applied to a small spot on a structure which produced an immediate shock response consisting of a very steep temperature profile in the immediate vicinity of the load. Therefore, he recommended simulation of the arc welding processes using Gaussian heat source. The conductivity enhancement used in his model to simulate the effect of weld pool stirring for a depositing weld was 175 W/mK.

In 2002, Annedi et al [31] developed a 3D transient model, using double ellipsoidal heat source with heat input varying with time, to investigate pulsing current gas tungsten arc welding of depositing weld. No thermal conductivity enhancement to simulate the effect of weld pool stirring was reported. The simulated fusion zone was in good agreement with the experimental result.

In 2003, Wang et al [33] recognised that the double ellipsoidal heat source model depended very much on prior knowledge of the weld pool size and shape in order to account for its shape and size correctly in the models. They developed an algorithm to calculate the weld pool shape and size for a high energy beam welding model. This algorithm was developed from the simulation results of ten different welding parameters using 2D transient sectional models. However, no experiment was carried out to verify the developed algorithm.

2.4 Experimental work

2.4.1 Welding net heat input efficiency

Christensen et al [8] measured the welding net heat input to the weld experimentally for solid wire gas metal arc welding and reported that the efficiency was from 66-69% for depositing weld. However, Easterling [14], reported that the net heat input efficiency of gas metal arc welding was in the range of 66 – 75%.

Recently, DuPONT et al [24] measured the welding net heat input to the weld experimentally for gas metal arc welding and reported that the arc efficiency was within 80 – 88% in a random manner.

2.4.2 Weld pool heat flux distribution, shape and temperature

Wu et al [32] measured the heat flux distribution of tungsten inert gas arc welding experimentally. Their measured results showed that the heat flux distributions were Gaussians distributed.

Krans [18] measured the stationary weld pool surface temperature of GTA and reported the peak temperatures from 1950 °C to 2708 °C. He concluded that the peak temperatures of the pool generally increase with welding current up to 150A (2708 °C) but decrease when the welding current is further increase to 200A (2215 °C).

Apps et al [5] investigated the heat flow in Argon Arc Welding for aluminium, lead, nickel, copper, and Armco iron and examined the theoretical predictions of weld-pool shape showing the shapes are narrower and more elongated than would be expected from theoretical predictions using Wells's [4] relationship.

2.5 Discussions

2.5.1 Analytical theory

In general, these theories do not consider the latent heat of phase transformation, surface heat loss and the non-linearity of thermal physical properties. Therefore, the accuracy of the calculated results is not good enough for most industrial applications.

This is the reason for switching to computer simulation, using finite element method that can account of these neglected factors (i.e. latent heat, surface heat loss and non-linearity of thermal physical properties).

2.5.2 Verification of the models

In most of the papers [9, 12, 15, 16 & 27], the models were verified using experimentally measured temperature histories or distributions. Thermocouples were affixed to the specimen at the locations of interest to measure the temperature history or distribution during welding and cooling. In some of the papers [11, 17, 19, 26 & 31] the models were verified by photographs of macrostructure on the weld sectional profiles where the heat affected zone (HAZ) and fusion zone (FZ) were visible. This is not a quite exact way of verifying the models since the FZ and HAZ lines vary quite significantly with the chemical composition of the steel and sometime the lines can hardly be seen. However, some papers [22, 23, 30 & 33] do not have experimental verification.

2.5.3 Welding net heat input efficiency

No references have been found where the welding net heat input efficiency has been determined experimentally for the purpose of computer modelling. Mostly, measured temperature histories or distributions are used as a reference to find a matching value of welding net heat input efficiency and make sure that this value is within the reported range of efficiency for that particular type of welding.

2.5.4 Gaussian heat source

Due to lack of information on the heat flux distribution of other welding processes apart from tungsten inert gas welding, most of the papers [9, 10, 11, 12, 13, 17, 29 & 30] assumed that the heat source for their models would be the same as in the tungsten inert gas welding process.

In most of the papers [9, 10, 11, 12, 13, 17, 29 & 30], the radius of the Gaussian heat source was roughly adjusted in their models to produce top weld widths that matches the experimental weld top widths. This is not a quite exact way of adjusting the radius of the Gaussian heat source because the size of weld pool top width may be correct but the temperature fields near to the weld pool may not be as actual.

2.6 Summary

In general, the analytical theories of moving heat source predicted temperature histories and distributions are not accurate enough for most applications. This is the reason for switching to computer simulation as this provides more accurate results than the analytical prediction.

In section 2.2 on computer simulation, most of the researches were found concentrated mainly on the simulation of depositing weld onto the surface of the plate. This is not quite the same as joining two metal plates together. Since

industrial metal welding is mostly performed with a weld-preparation, it is essential to take the weld-preparation into account during the computer simulation.

Many papers [12, 16, 19, 23, 27 & 30] used an artificial conductivity enhancement ranging from 121 W/mK to 400 W/mK to simulate the weld pool stirring effect without any physical justification. It is therefore necessary to study the effects of these assumptions.

Most of the authors verified their models using experimentally measured temperature histories or distribution. They used the measured temperature histories or distributions to find the fit values of the welding net heat input efficiency in order to produce similar temperature histories or distribution as the experimental measured temperature histories or distribution.

In computer modelling [9, 10, 11, 12, 13, 17, 29 & 30], the radius of the Gaussian heat source was roughly adjusted to produce top weld width that matches the experimental top weld width. The way of adjusting the radius of the Gaussian heat source needs to be improved in order to produce more accurate temperature histories and distribution simulation.

Chapter 3 – Experimental Work

3.1 Introduction

The main purpose of these experiments was to validate the computer simulation models. As reviewed in previous chapter, most of the papers [9, 12, 15, 16 & 27] verified their models using the experimentally measured temperature histories or distribution. Thermocouples were affixed to the specimen at locations of interest to measure the temperature histories or distributions during welding and cooling. Some of the papers [11, 17, 19, 26 & 31] verified their models by photographs of macrostructure on the weld sectional profiled where the heat affected zone (HAZ) and fusion zone (FZ) were visible. As discussed in Chapter 2, this is not a quite exact way of verifying the models since the HAZ and FZ widths vary quite significantly with the chemical composition of the steel and sometimes the lines in the HAZ can hardly be seen. In usual circumstances, the carbon content of the purchased mild steel plate can vary within the range of 0.06% to 0.25% and it is not feasible to check the carbon content of every purchased mild steel plate. Therefore, the method of measuring temperature histories at strategic locations was chosen to carry out this experimental work. Photographs of macrostructure on the weld sectional profile were also taken to compare with the computer simulation results in the later chapter.

In order to capture the transient temperature histories of the welding plates to a reasonably accuracy, the data acquisition logger and the thermocouples were calibrated within the temperature range required to perform these temperature measurement experiments. The thermocouple response was also checked to ensure that it would be able to respond to the kind of transients produced during the welding process. All these essential preparations prior to the actual experiments are presented in section 3.2.

The experiments were carried out using flux-core wire Gas Metal Arc (GMA) welding process with $ArCO_2$ shielding. Four experiments were carried out by joining 2 rectangular plates of the same size, 500 mm by 250 mm together with the same "V" weld-preparation configuration at various thicknesses, 3 mm, 4 mm, 6 mm and 8 mm. The fifth experiment was performed using an unusual weld-preparation, namely by depositing weld along a 3 mm radius semi-circular cross-section slot located at the centre of a rectangular plate of size 160 mm by 125 mm and 6 mm thick. The thermocouples were affixed to the specimen at the locations just within or very near to the heat affected zone (HAZ) to record the top and bottom temperature history and also at a distance from the heat affected zone to record the bottom temperature history during welding and cooling. Photographs of macrostructure on the weld sectional profile were also taken for the purpose of comparison with the computer simulation weld profile. Details on the experimental procedures were carried out and the experimental results are presented in section 3.3.

3.2 Setting up for experiments

3.2.1 The temperature recording unit

The measurement of temperature histories was done by placing type K thermocouples at the locations of interest and recording outputs using a data acquisition unit (From National Instruments Corp.). This data acquisition unit is made up of a terminal block (SCXI-1300) where thermocouple wires are fixed and the rear end of the block is connected to a multiplexer that can multiplex up to 32 thermocouple channels with the signals amplified. This multiplexer is then connected to a signal isolator (SCXI-1100 Chassis) with built in cold-junction compensation, isothermal connections, open-thermocouple detection and differential voltage measurement. The signal isolator is wired to a data acquisition board that is connected to one of the computer ports. The software used to control the acquisition was LabVIEW™ that allows the user to program a Virtual Instrument (VI), so called because the appearance and operation can imitate an actual instrument. The VI in use was modified from an existing VI in that computer to make it suitable for the use in this experiment with specific application that automatically records temperature on a Microsoft Excel spreadsheet. The full set up of the data acquisition unit is shown in Figure 3.1.

Figure 3.1

Data Acquisition Unit

3.2.2 Calibration of the data acquisition logger

The logger was calibrated by sending a number of different voltages to both the data acquisition unit and a calibrated digital thermometer at the same time using a voltage generator. Several temperature points were covered to obtain the temperature range required for the experiment. The results have been plotted into graph in order to obtain an approximate equation of the graph as shown in Figure 3.2. This equation was then used in the LabVIEW™ program as a function to correct the errors of the data logger. Figure 3.3 shows the block diagram of the VI and the places to input the equation.

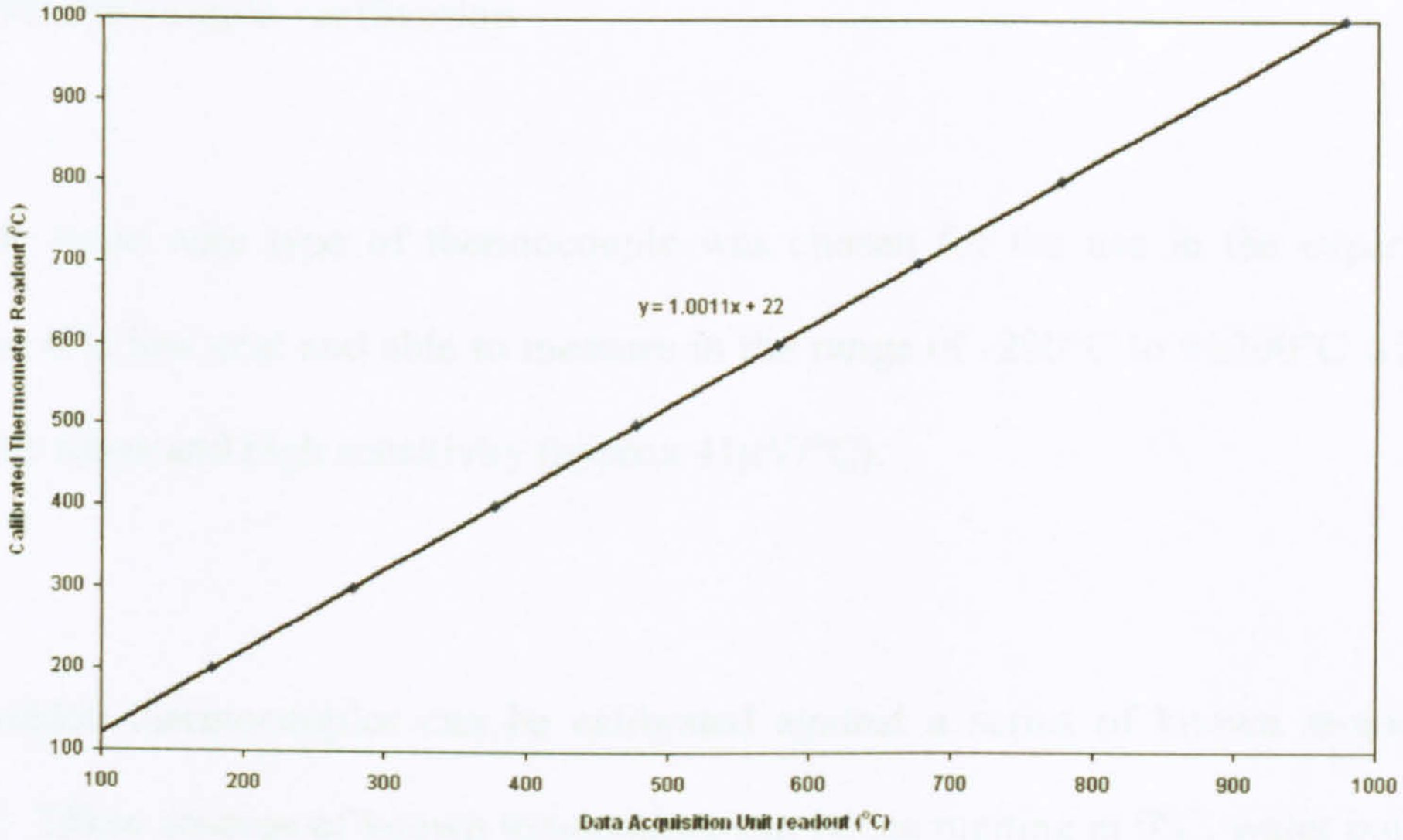

Figure 3.2

A function to correct the errors of the data logger

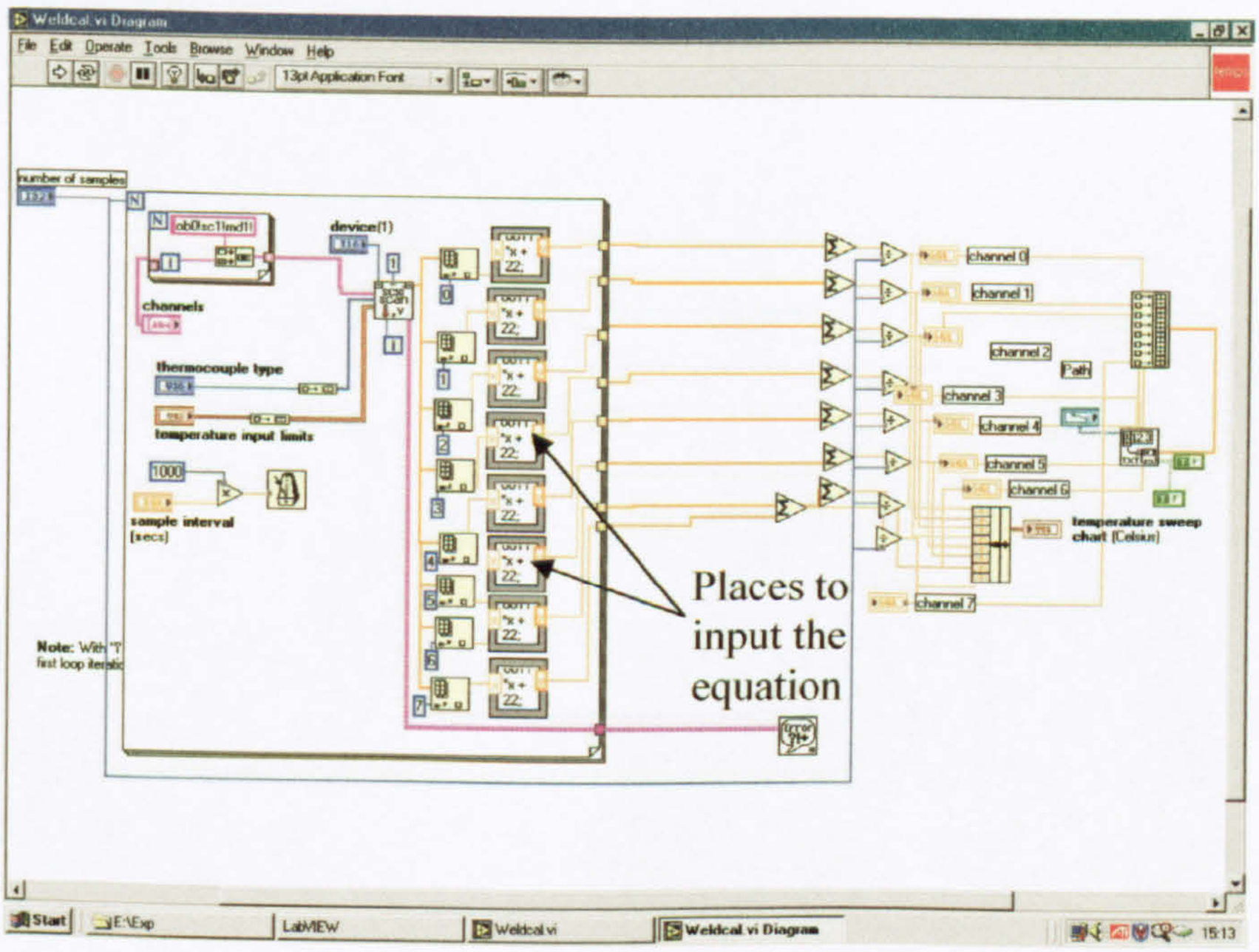

Figure 3.3

The block diagram of the VI

3.2.3 Thermocouple verification

Type K loose wire type of thermocouple was chosen for the use in the experiments because it is low cost and able to measure in the range of -200°C to +1200°C with fast response times and high sensitivity (approx 41μV/°C).

The welded thermocouples can be calibrated against a series of known temperature values. These sources of known temperature can be ice melting at 0°C, water boiling at 100°C. Table 3.1 shows fixed points defining ITS-90 over the range -200 to 1100°C.

Table 3.1

FIXED POINTS DEFINING ITS-90 OVER THE RANGE -200 °C TO 1100 °C

FIXED POINT	PHYSICAL PROPERTY	TEMPERATURE (°C)
Argon	Triple Point	-189.3442
Mercury	Triple Point	-38.8344
Water	Triple Point	0.010
Gallium	Melt Point	29.7646
Indium	Freeze Point	156.5985
Tin	Freeze Point	231.928
Zinc	Freeze Point	419.527
Aluminium	Freeze Point	660.323
Silver	Freeze Point	961.78
Gold	Freeze Point	1064.18

The temperature range need to verify in order to run the experiments is from 100°C to 800°C. Therefore, the boiling point of water at 100°C, the freeze point of tin at 231.928°C, the freeze point of zinc at 419.527°C, the freeze point of aluminium at 660.323°C and the freeze point of silver at 961.78°C were chosen.

3.2.3.1 Measurement of temperature at water boiling point

The water in an electric kettle with a thermocouple dipped in it was heated up to the boiling point for a while before letting it cool. This thermocouple was connected to the data acquisition unit to record the temperature of the water boiling point. The recorded temperature of the water boiling point is shown in Figure 3.4.

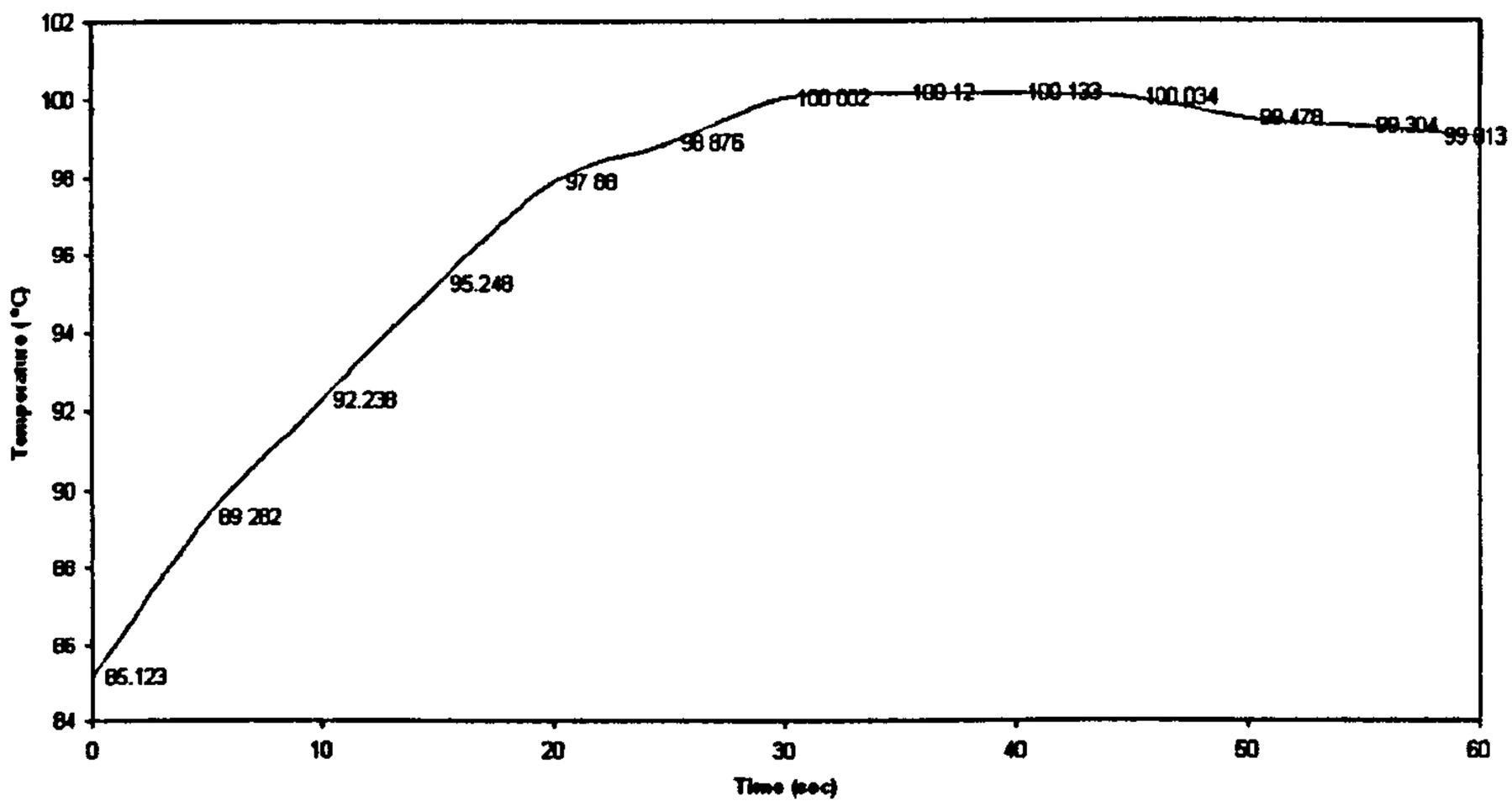

Figure 3.4

Water boil at 100 °C

3.2.3.2 Measurement of temperature at metal freezing point

The metal to be measured was heated up to its molten form in a closed furnace. A thermocouple was then dipped into the molten metal and the metal was allowed to freeze

by keeping the furnace door open. The measured freezing points of tin, zinc, aluminium and silver were shown in Figures 3.5, 3.6, 3.7 and 3.8 respectively.

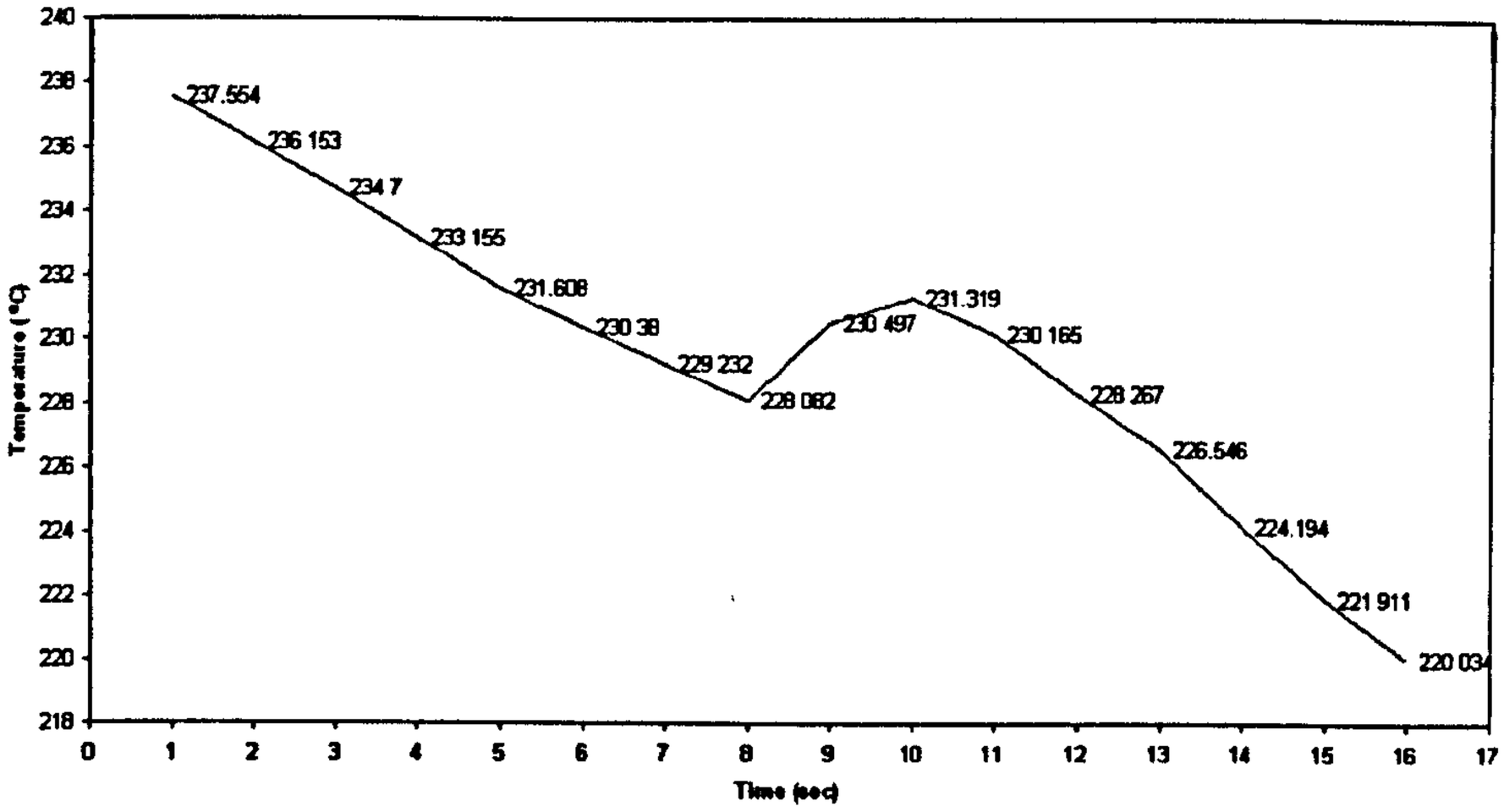

Figure 3.5

Tin Freeze at 230 °C

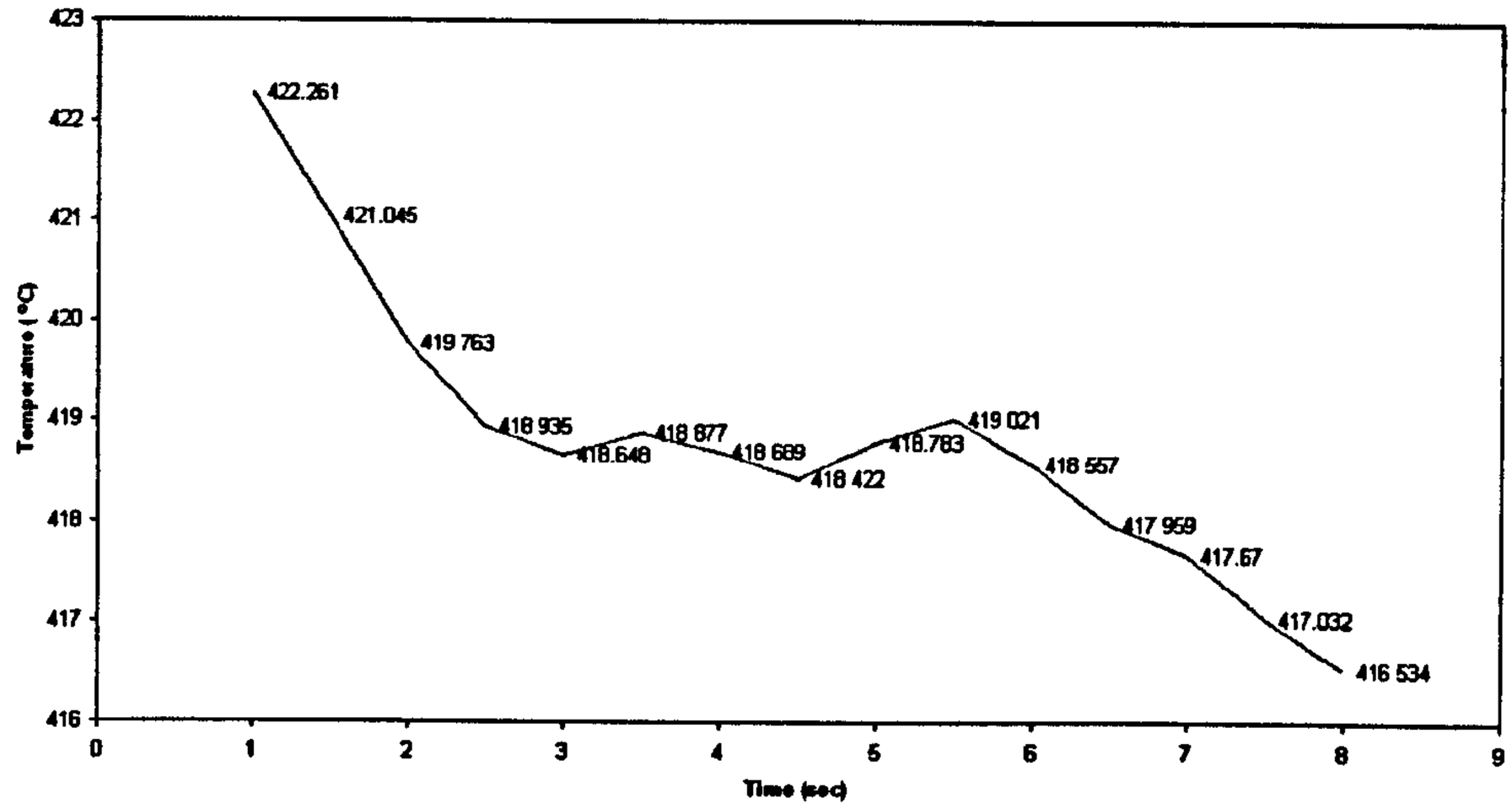

Figure 3.6

Zinc Freeze at 419 °C

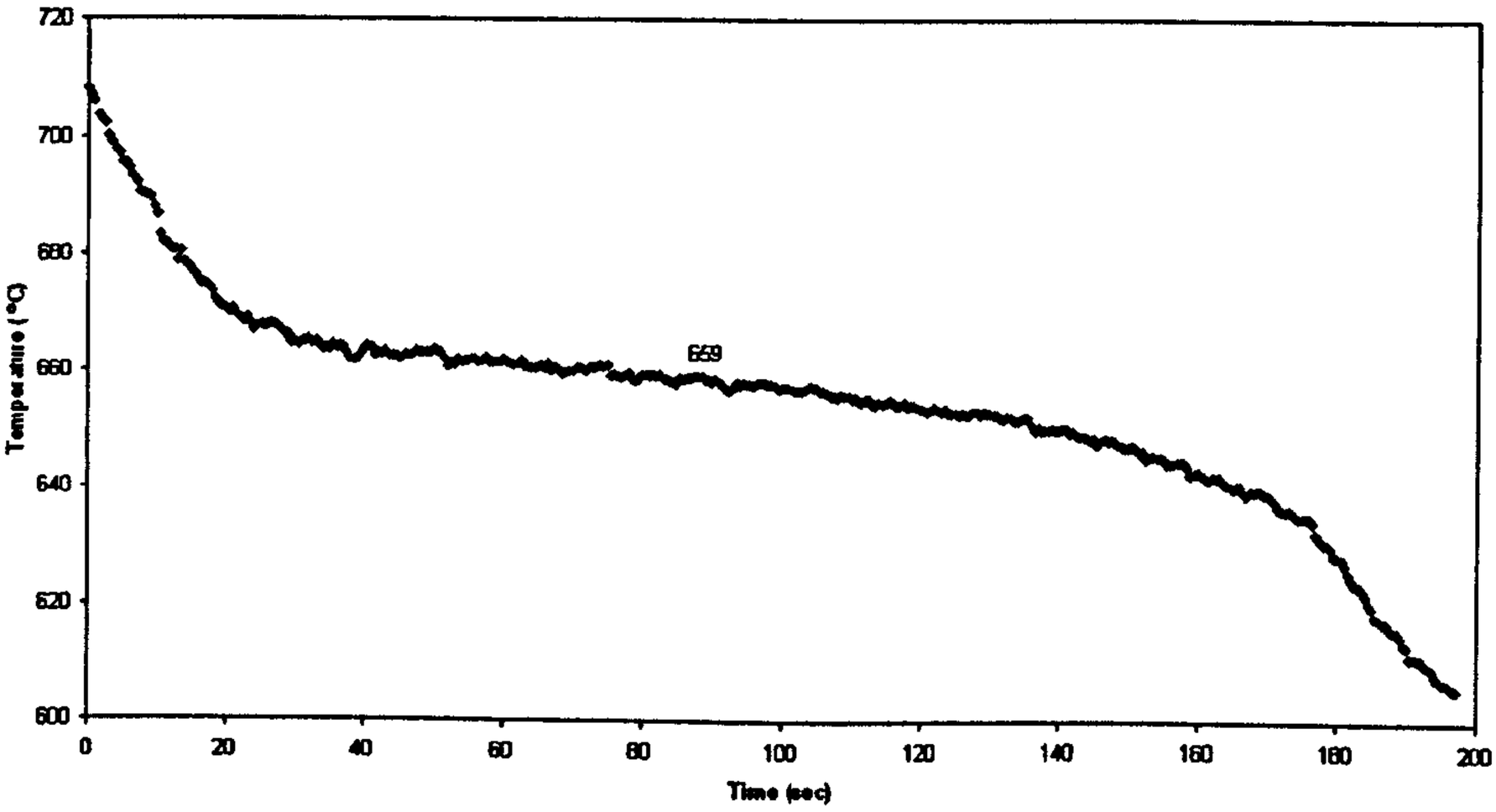

Figure 3.7

Aluminium freeze at 659 °C

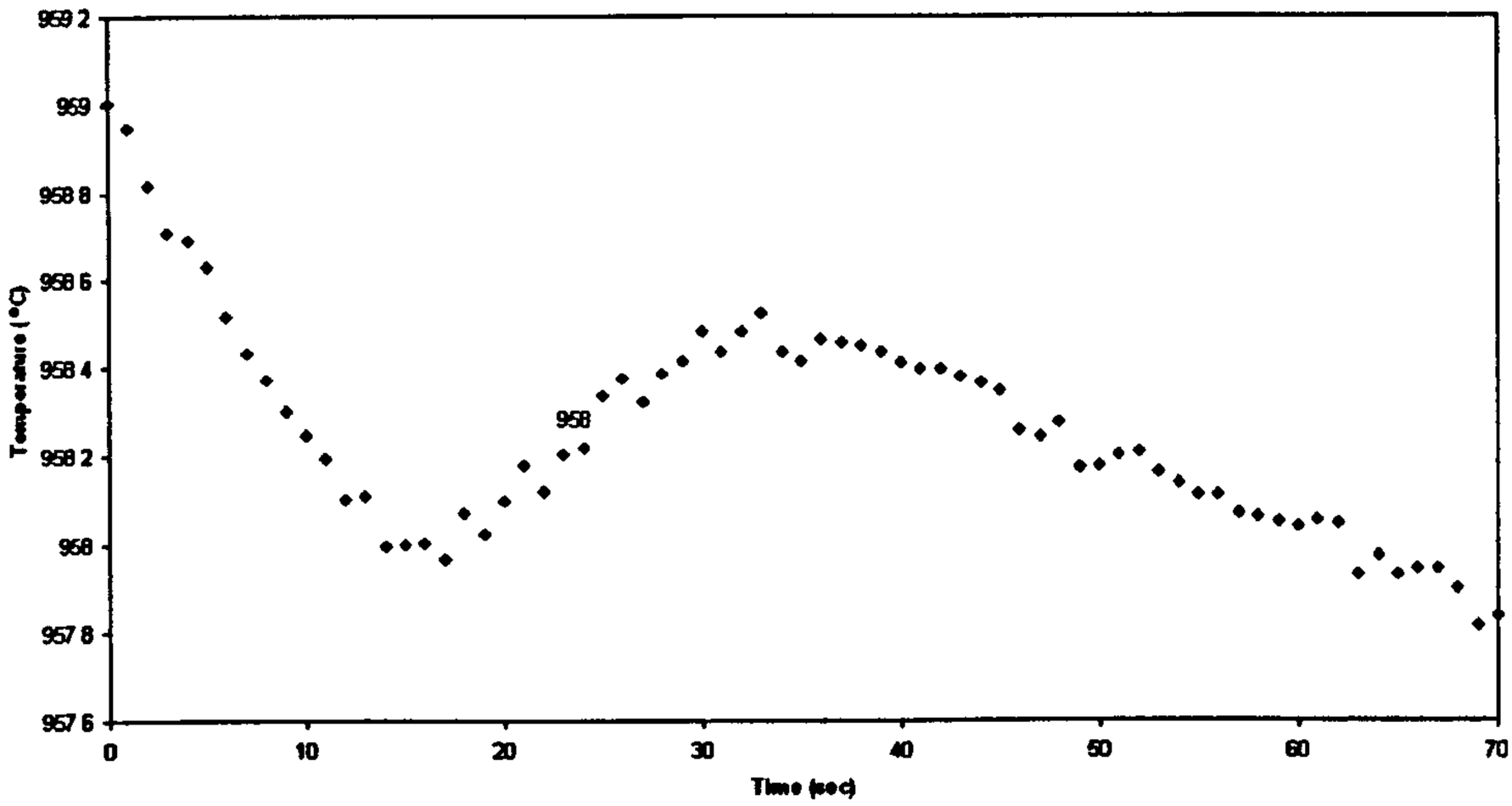

Figure 3.8

Silver freeze at 958 °C

Table 3.2

The errors of thermocouple

Materials	Standard Fixed points (°C)	Measured Fixed points (°C)	Errors (°C)
Water	100	100	0
Tin	231.928	230	-2
Zinc	419.527	419	-0.5
Aluminium	660.323	659	-1
Silver	961.78	958	-4

Table 3.2 shows that the largest error of the thermocouple is -2 °C at 231.928 °C which is still considered as accurate enough for conducting the welding temperature measurement experiments as it is less than 1% in error.

3.2.3.3 Measurement of the response time of thermocouple

The thermocouple response time was measured by jabbing a thermocouple with a head approximately 1.2 mm in diameter into a red hot fire rated brick which had just been taken out from a red hot furnace. This thermocouple was connected to the data acquisition unit to record the response time at intervals of 0.01 sec. The recorded response time is shown in Figure 3.9. Considering the thermocouple as a first order system, the time constant can be obtained as an elapsed time when the output is 63.2% of the step input and it is found to be 0.1 second. This ensures that similar thermocouples will be able to respond to the kind of transients produced in this work during the welding process carried out.

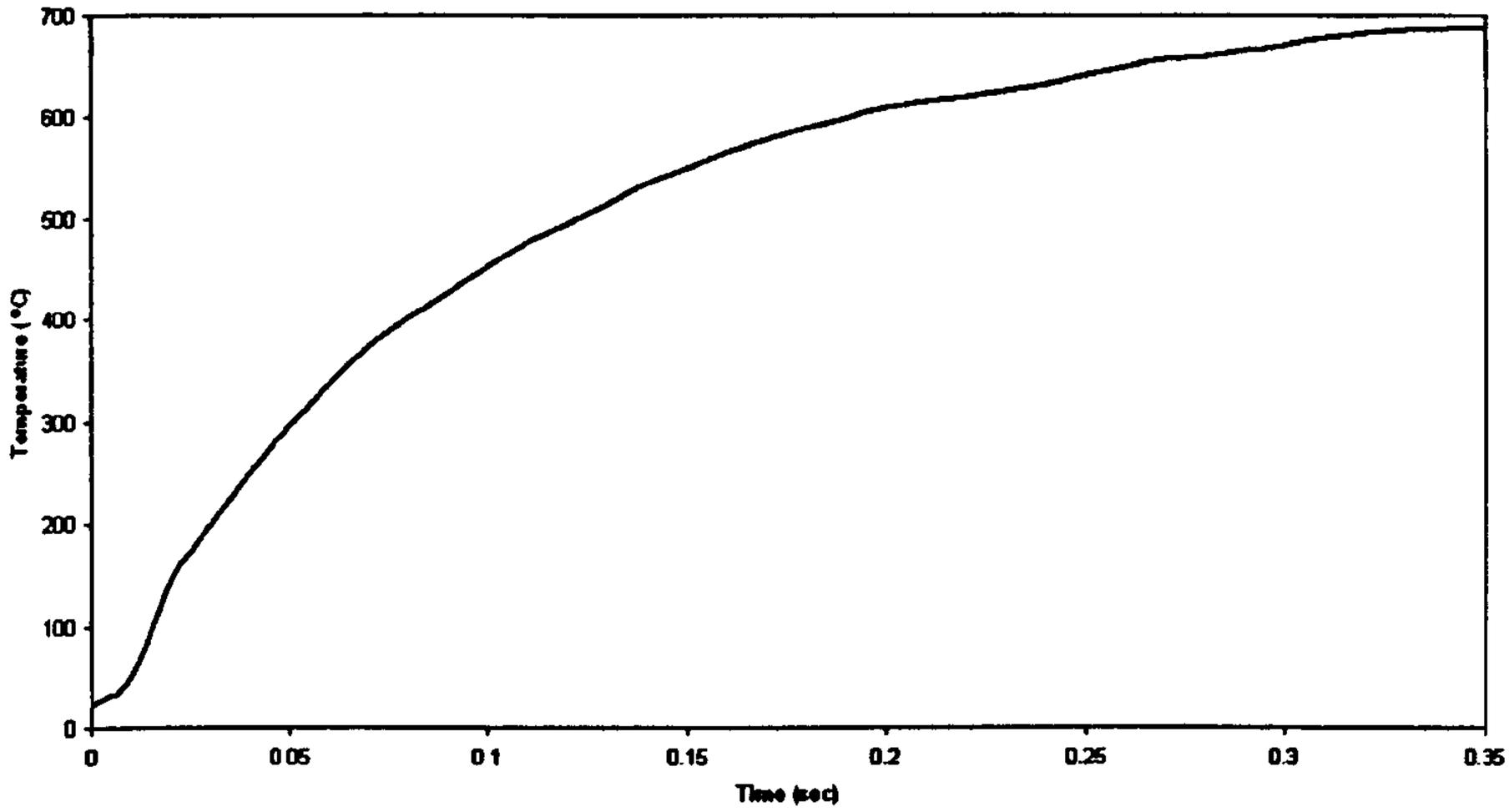

Figure 3.9

Measured temperature response curve to a step input

3.2.4 The Test Specimen

The material used for the experiments was EN 10025 S275 low carbon steel in the form of plates of 3 mm, 4 mm, 6 mm and 8 mm thickness. The plates were cut to the desired size and the weld-preps were machined. The run-on and run-off plates were then welded onto each end of the specimens. Figure 3.10 shows a completed specimen of 4 mm thick plate, is ready for welding. The detailed dimensions of the weld-preparation and the width of the root gap are presented in section 3.3.1 onwards.

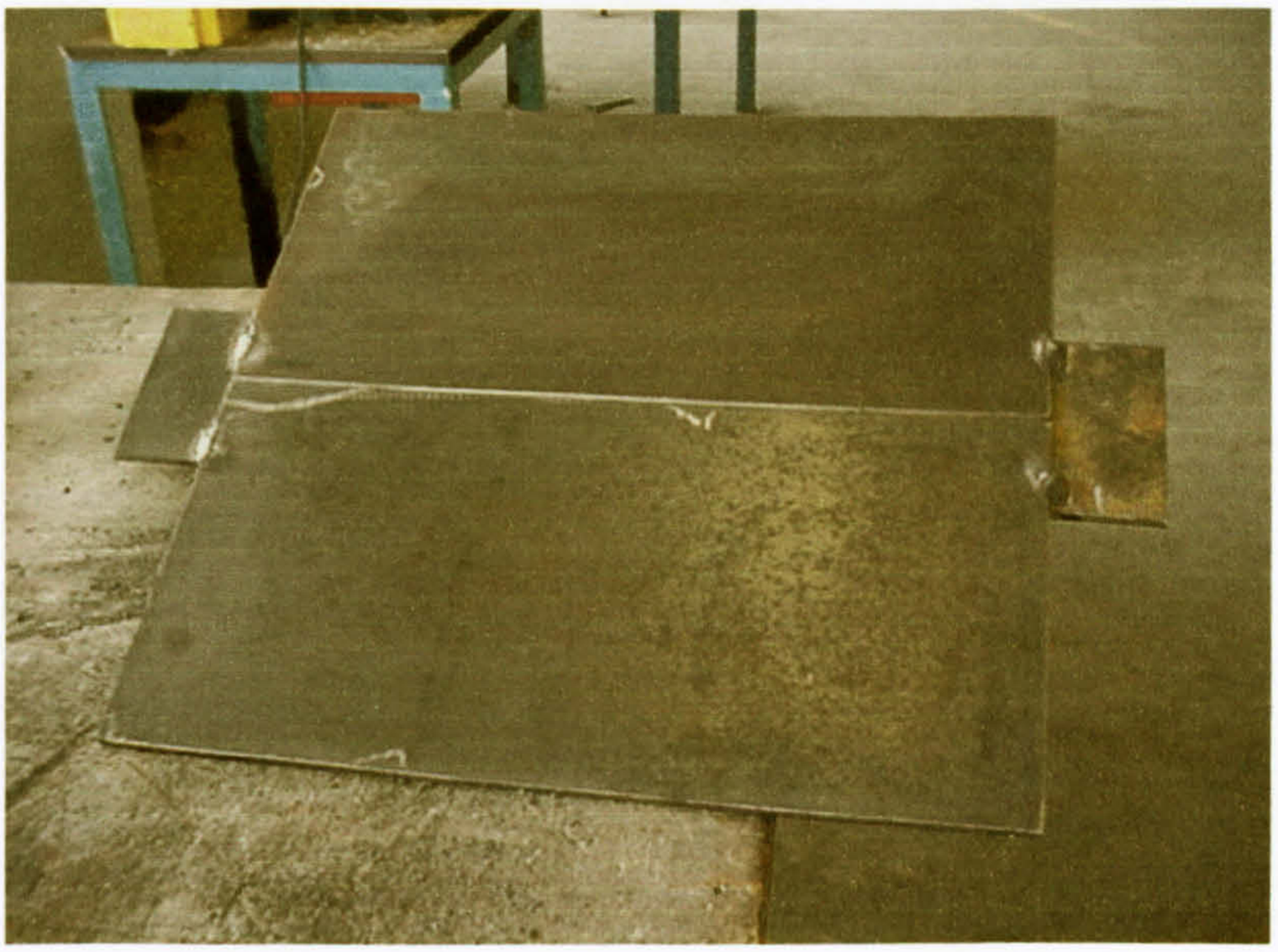

Figure 3.10

The completed specimen

3.2.5 Fixing of thermocouples

The thermocouples used to record the temperature histories of the specimen on the top surface near the heat source were attached by drilling holes from the bottom of the plate to a depth of almost right through leaving 0.3 to 0.4 mm of material and tack welding thermocouples into the drilled holes. This was done to avoid the arc high radiation and spatter from damaging the thermocouples during the welding process. The thermocouples that were used to record the bottom surface temperature histories of the specimen were attached by just tack welding them on the surface of the plate. Figure 3.11 shows a picture of the thermocouples in position.

Figure 3.11

The fixed up thermocouples

The soundness of thermocouple attachments was then checked by testing the continuity of the welded junctions with a multi-meter. Further verification was made by heating up the thermocouples with a lighter flame to a high temperature and displaying the reading using a digital thermometer.

3.3 Welding Experiments

The tests were carried out using the Gas Metal Arc (GMA) welding process, in this case using an electrode made of consumable 1.2 mm diameter flux-cored filler wire, is fed continuously (NITTETSU SF-1A from Nippon Steel Welding Products & Engineering Co., Ltd). The shielding gas used for the process was a mixture of carbon dioxide (20%) and argon. The weld-head was fixed at the centre of the machine and the bench-traverse was used to move the specimen at a constant velocity during the welding process. The specimen was supported using four small metal posts under each corner. In this way, both the top and bottom surfaces of the specimen were exposed to the laboratory ambient conditions and only negligible heat was conducted from the specimen by the support posts. The full set up of the welding equipment is shown in Figure 3.12. The GMA welding machine was supplied by BAE Systems and the welding test rig was modified from a milling machine existing in the workshop.

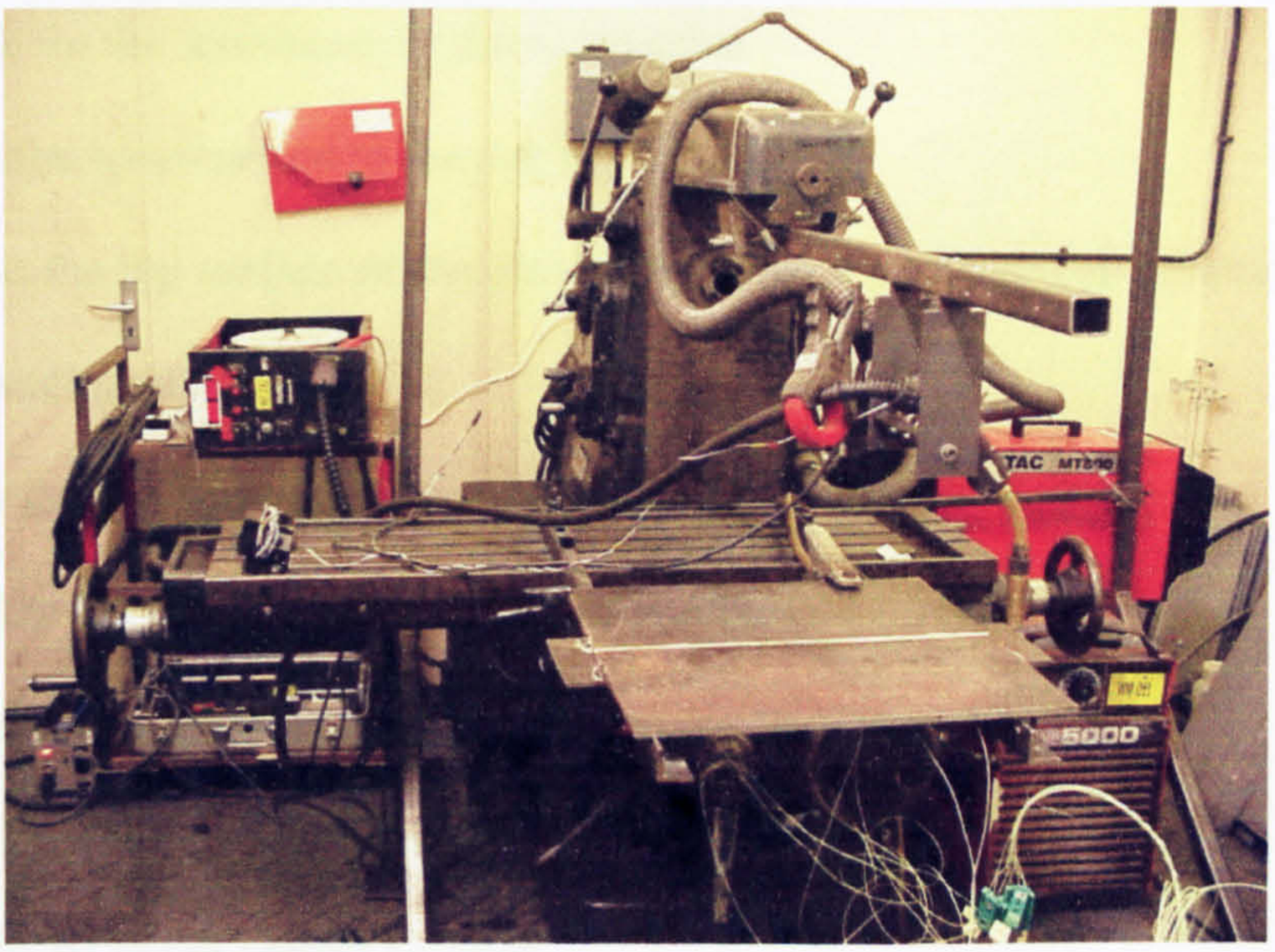

Figure 3.12

Welding experiment set- up

The optimum welding parameter settings were determined by welding a selection of test specimens with a variety of settings including voltage, current, travelling speed, and weld-preparation sizes. The final welding parameters were then used for the actual experiments.

The experiments were conducted via the following procedure:

1. Cut the plates to required size
2. Tack-weld the run-on and run-off plates onto the specimen
3. Mark the thermocouple positions
4. Drill holes for the top thermocouple positions
5. Tack-weld the thermocouples onto the plates

6. Check for the soundness of thermocouples
7. Place the specimen on to the test rig
8. Adjust the top surface of the plate to produce a constant gap of 6mm away from the welding head
9. Align the weld-prep with the travelling path of the welding head
10. Position the welding head at the run-in plate
11. Connect the thermocouples to the data acquisition unit
12. Check for the soundness of thermocouples a second time
13. Set the VI to the correct settings
14. Switch on the welding machine and start welding
15. When the welding head reaches the main plates, start the temperature recording
16. Stop welding when the welding head reaches the run-off plate
17. Leave the specimen to cool to about 100°C and stop temperature recording
18. Check the recorded temperature history for defects
19. If not satisfied with the results, repeat test with a new specimen again and again until satisfactory results are met

3.3.1 Welding parameters and configurations

Table 3.3 shows a summary of the welding parameters use for Experiment 1 to 5. The plate thicknesses were shown in the second column. In the third column, the configuration of weld-preparation for Experiment 1, 2, 3 and 4 was "V" weld-preparation of 1 mm gap, 1 mm root and 30° inclined angle. The weld-preparation for

Experiment 5 was a 3 mm radius semi-circle cross-sectional slot. The detail configuration of the weld-preparation for Experiment 1, 2, 3, 4 and 5 were shown in Figure 3.13, 3.15, 3.17, 3.19 and 3.21 respectively. The fourth, fifth and sixth columns show the welding voltage, current and speed respectively. The last column shows the calculated gross energy input to the plates for one millimetre length.

Table 3.3
A summary of the welding parameters of various experiments

Experiment	Plate thickness (mm)	Weld-preparation	Voltage (V)	Current (A)	Speed (mm/s)	Gross energy input (J/mm)
1	4	V	16.5	160	5	528
2	6	V	23.7	212	5	1005
3	8	V	22.7	236	3.33	1623
4	3	V	15	130	5	390
5	6	∪	16	150	5	480

The dimensions of the specimen and thermocouples positions for Experiment 1, 2, 3, 4 and 5 were shown in Figure 3.14, 3.16, 3.18, 3.20 and 3.22 respectively where T1 and T2 are the top thermocouples positions and the rest are bottom thermocouples positions. It should be noted the thermocouple position, T1 of Experiment 5 is nearer to the weld than other experiments. It should also be noted that Experiment 4 and 5 were additional experiments. Experiment 4 was done to consolidate the range of plate thickness used in the experiments and also to be sure that the overflow of the weld would not affect the

temperature modelling of the plate. Experiment 5 was done to see the differences in computer modelling between two different types of weld-preparation.

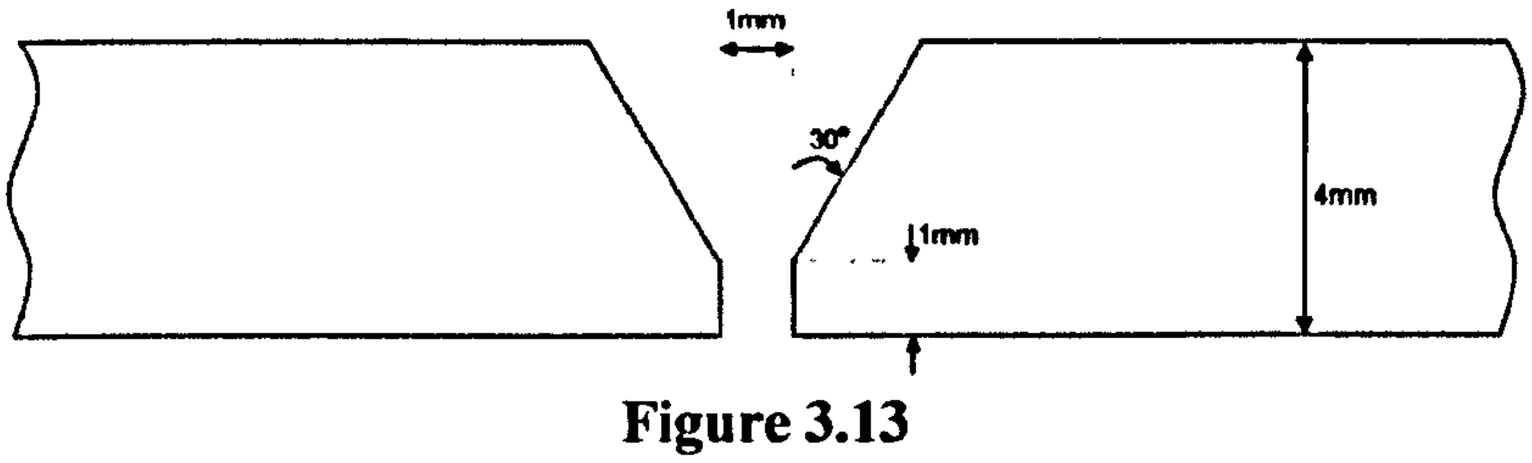

Figure 3.13

Configuration of the "V" weld-preparation for 4 mm thick plate

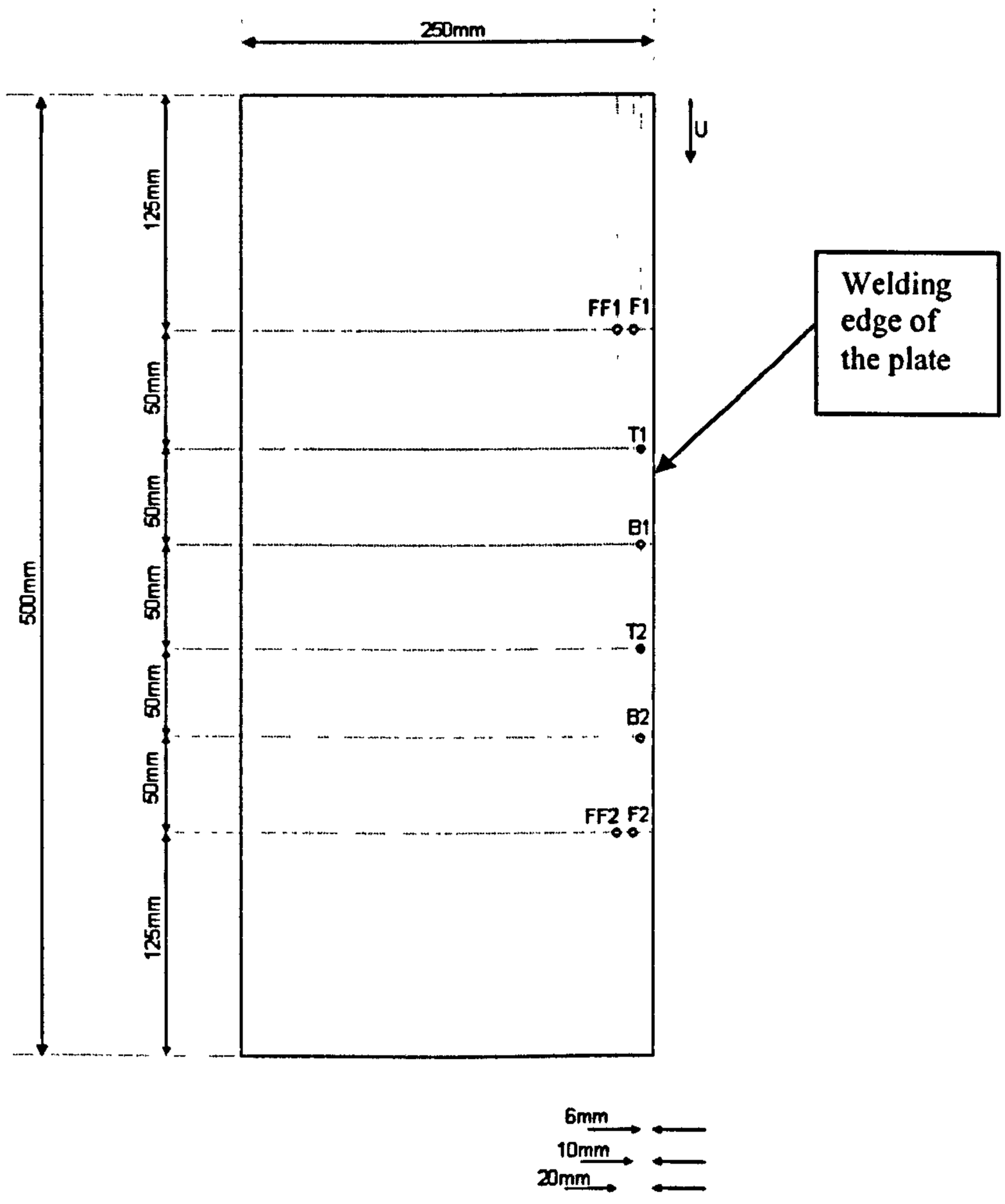

Figure 3.14

Dimensions of the weld specimen and thermocouple positions for 4 mm thick plate

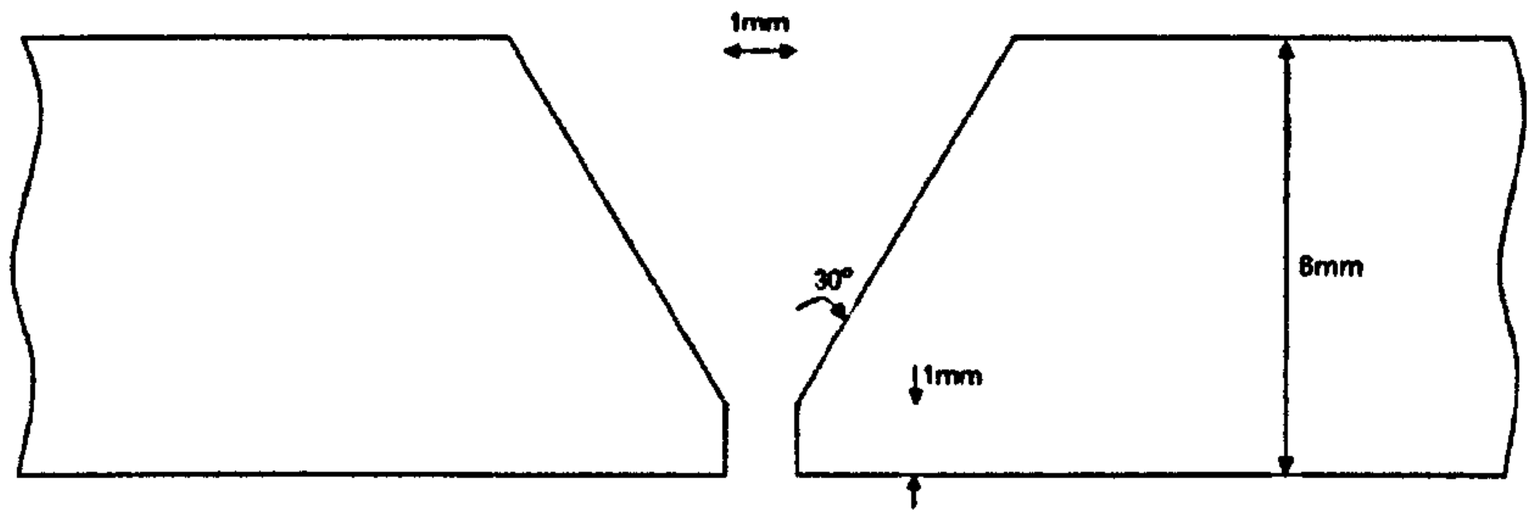

Figure 3.15

Configuration of the "V" weld-preparation for 6 mm thick plate

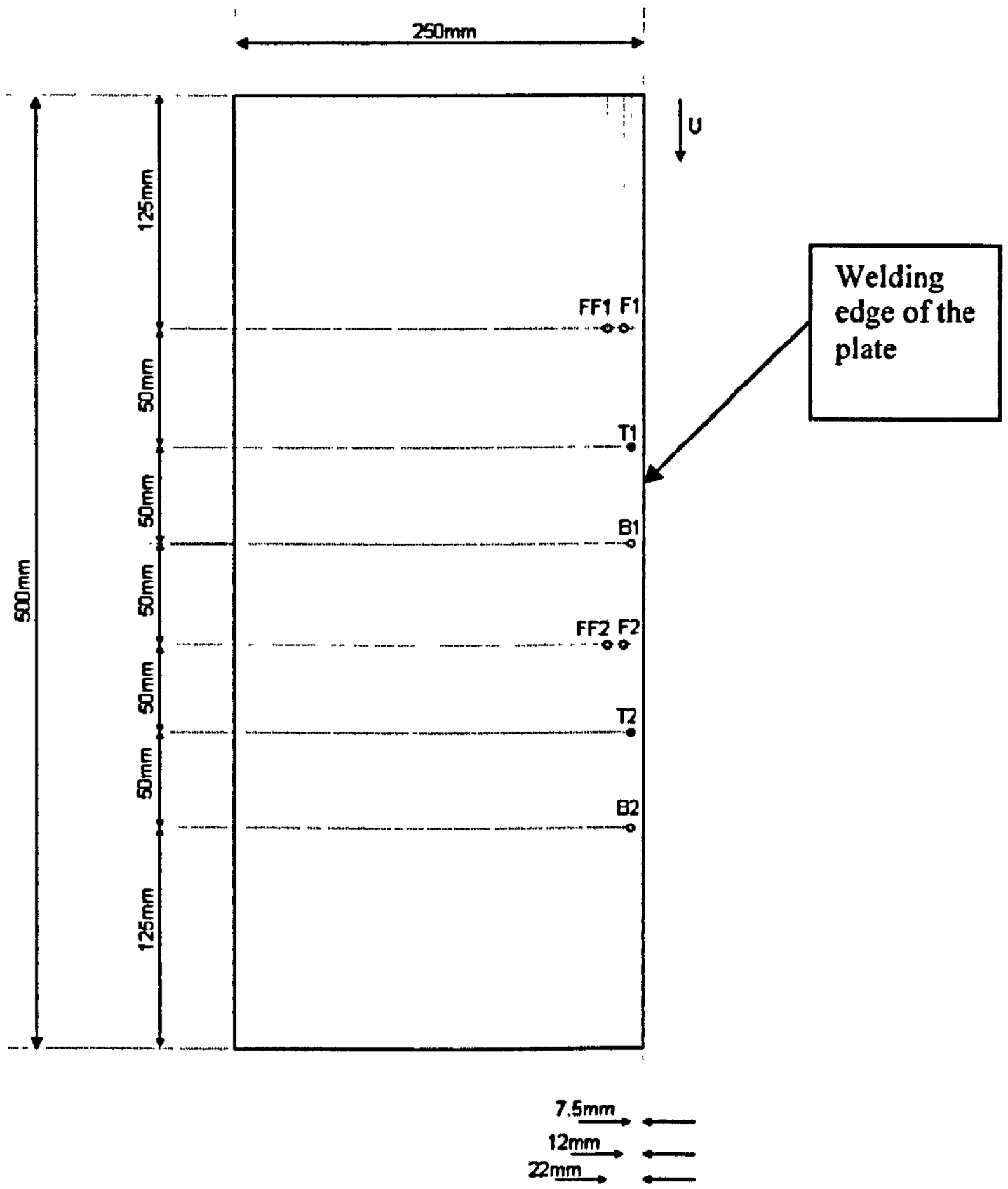

Figure 3.16

Dimensions of the weld specimen and thermocouples positions for 6 mm thick plate

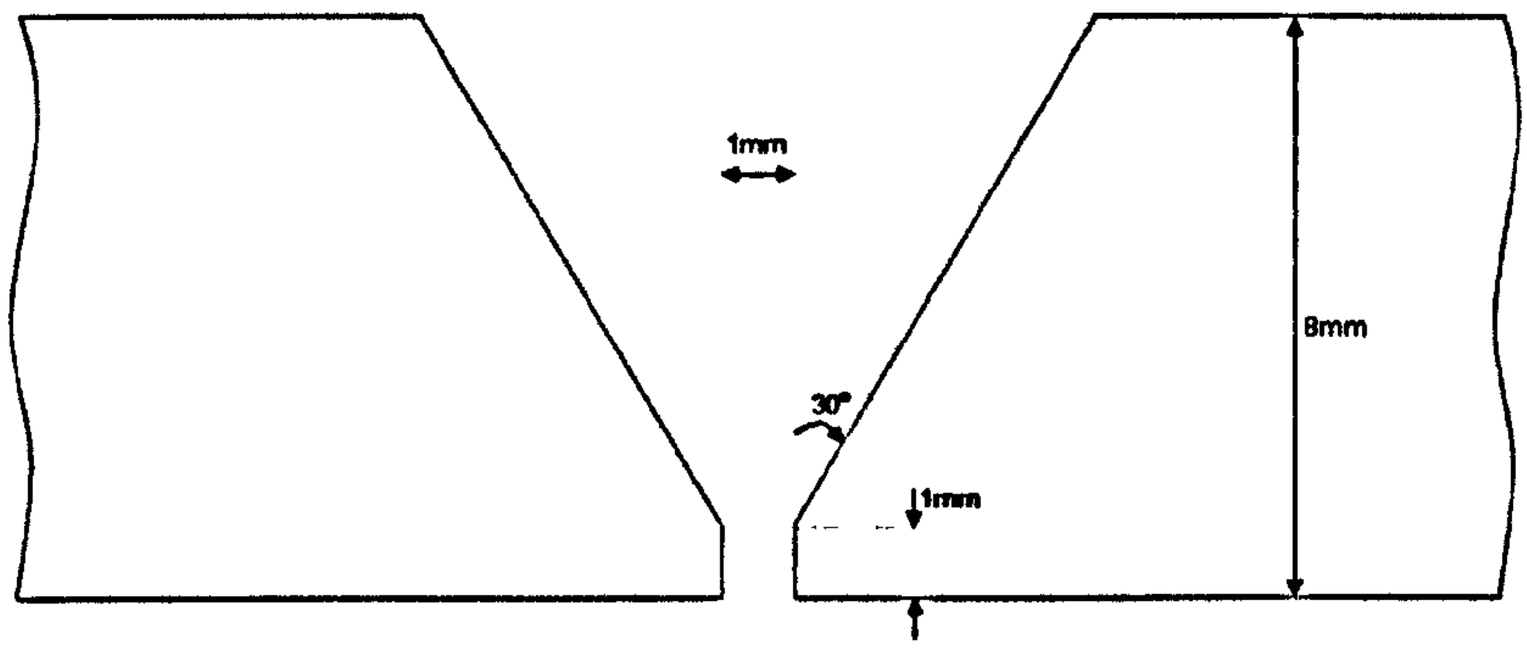

Figure 3.17
Configuration of the "V" weld-preparation for 8 mm thick plate

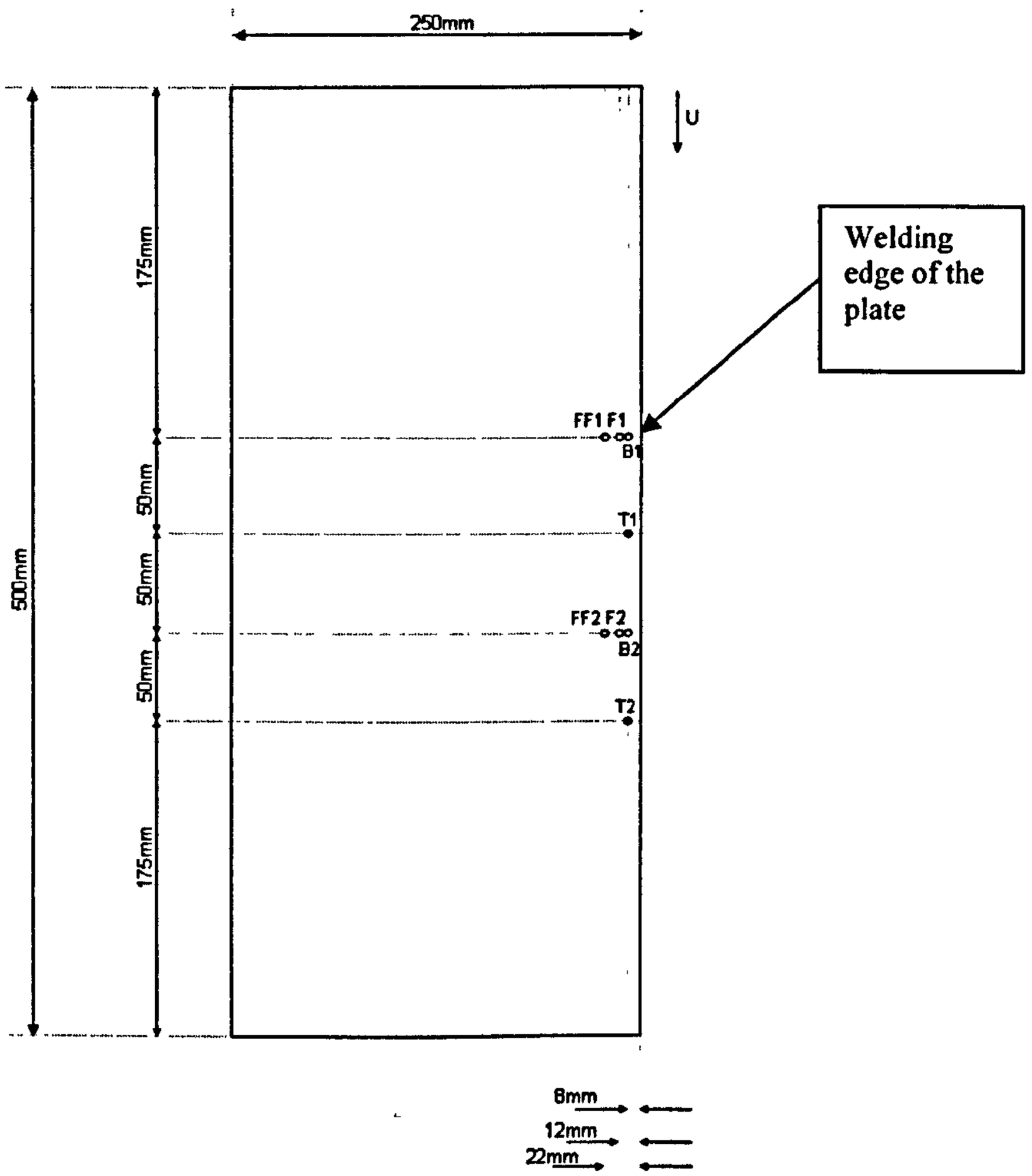

Figure 3.18
Dimensions of the weld specimen and thermocouples positions for 8 mm thick plate

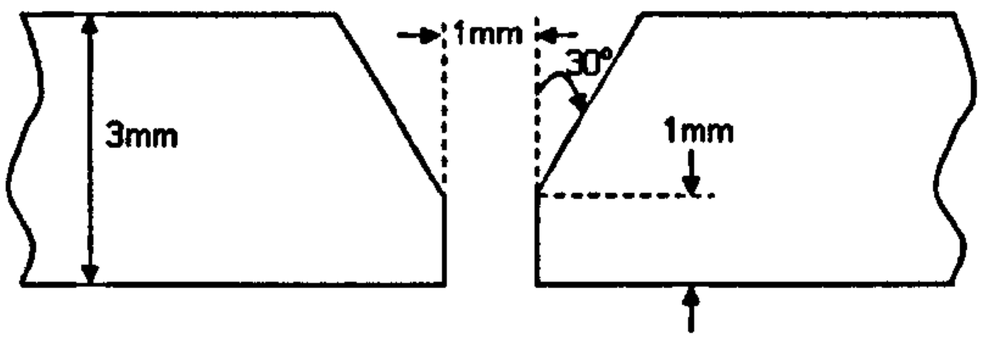

Figure 3.19

Configuration of the "V" weld-preparation for 3 mm thick plate

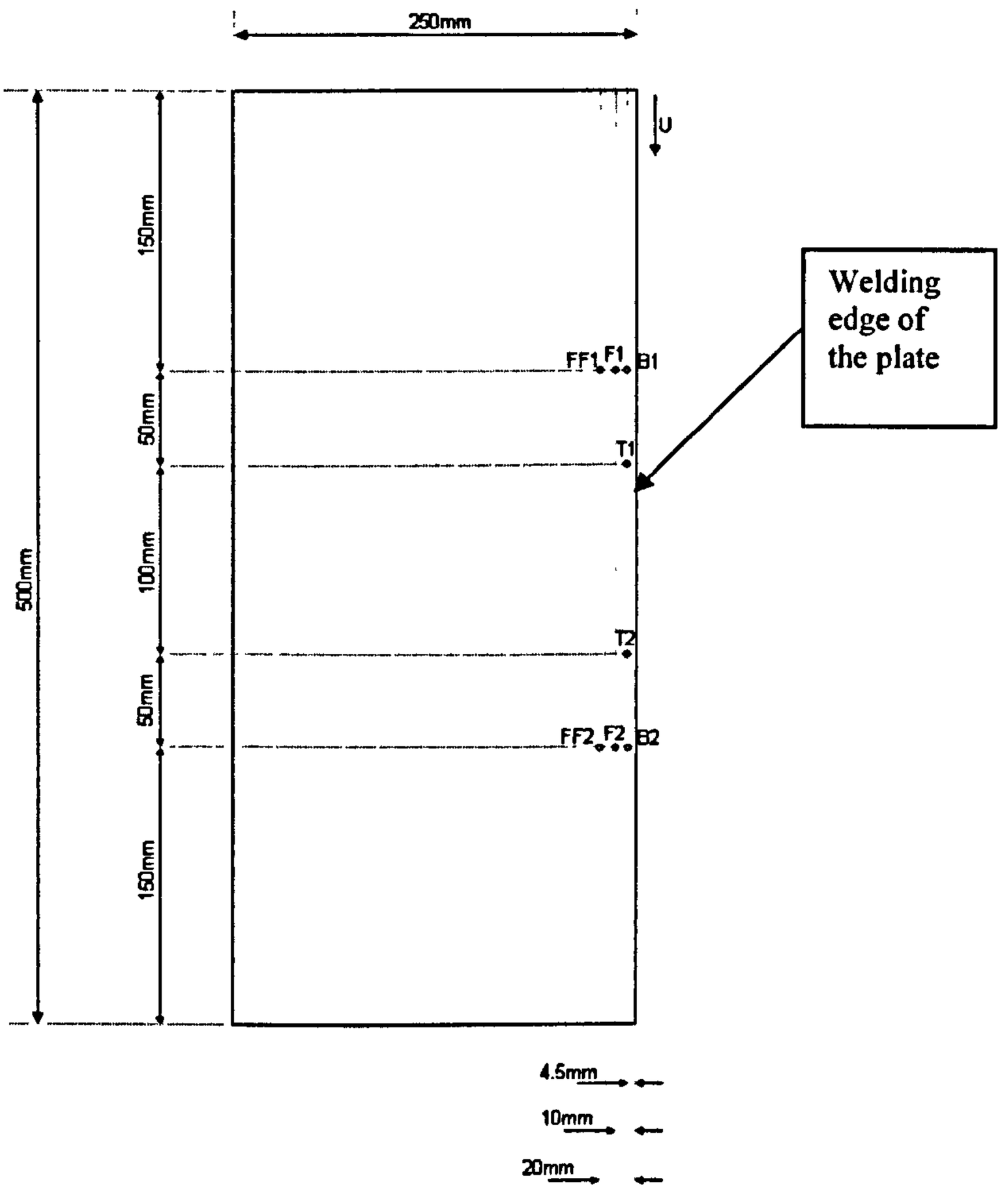

Figure 3.20

Dimensions of the weld specimen and thermocouples positions for 3 mm thick plate

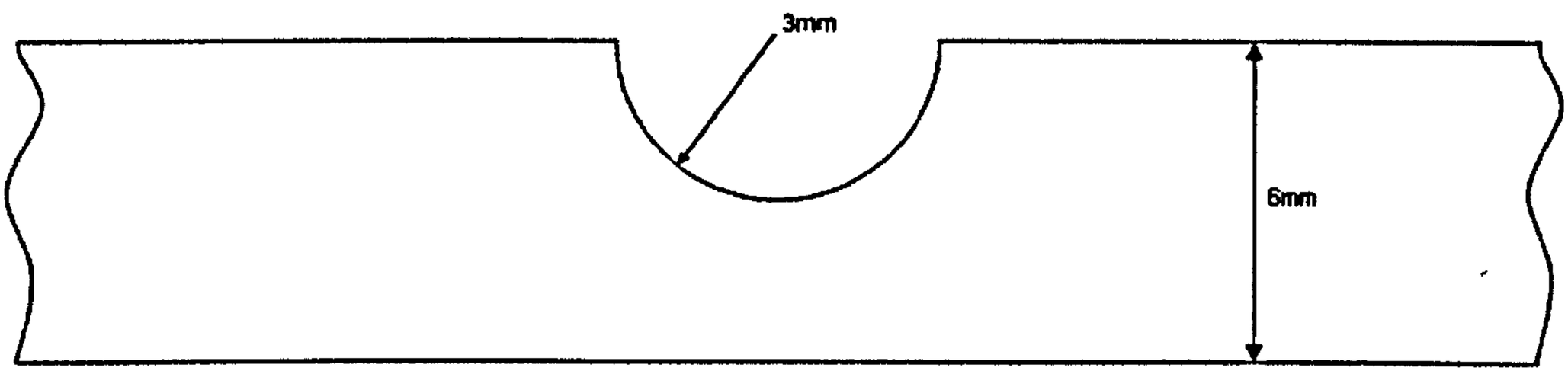

Figure 3.21

Configuration of the semi-circle cross-sectional weld-preparation for 6 mm thick plate

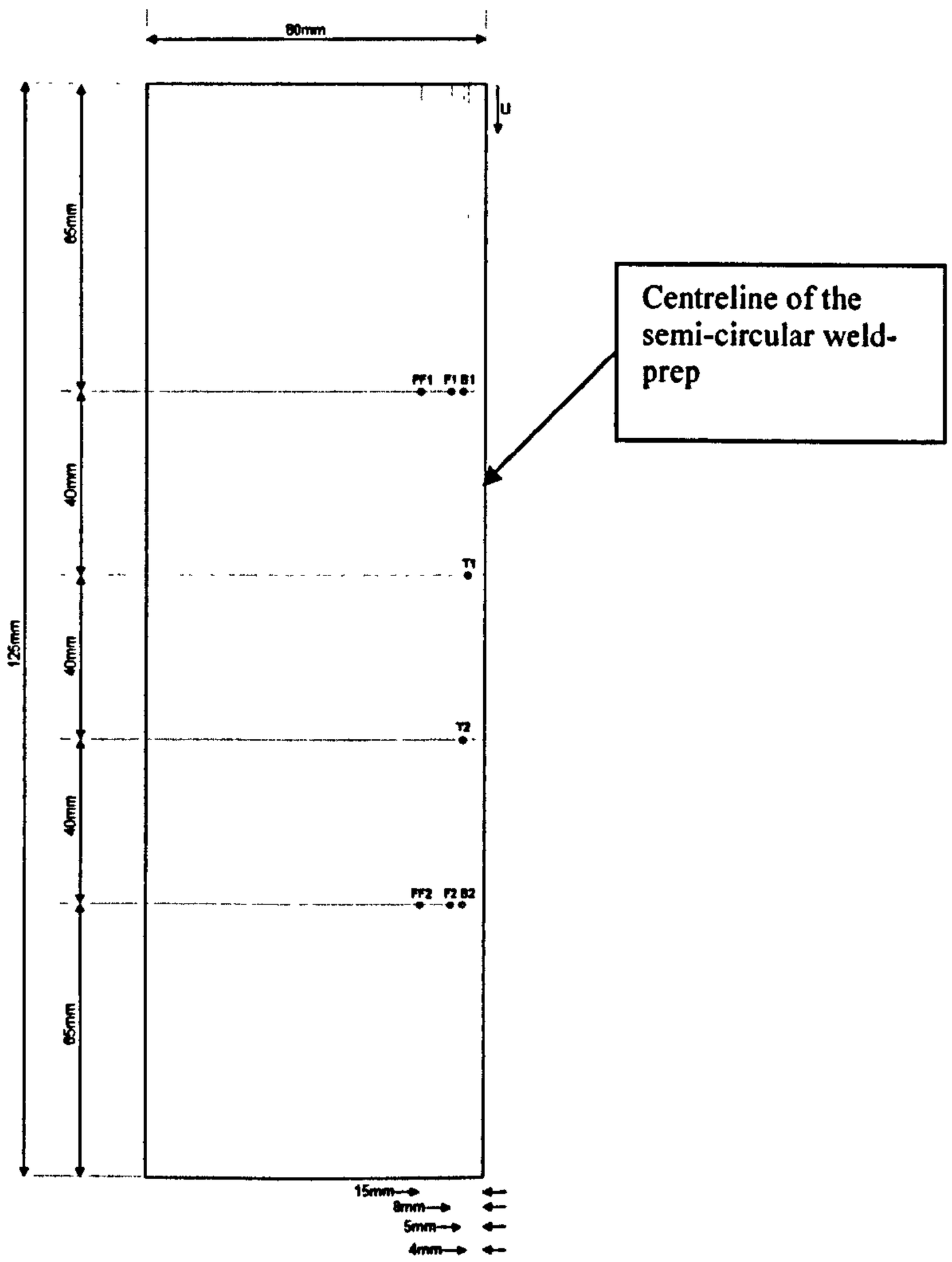

Figure 3.22

Dimensions of the weld specimen and thermocouples positions of the semi-circular cross-section weld-preparation

3.3.2 Experimental measurements and results

Table 3.4
A summary of the experimental measurements and results

Experiment	Ambient temperature (°C)	Duration of recording (sec)	Recording Intervals per data (sec)	Distance from weld centreline (mm)	Top peak temperature, T1 & T2 (°C)	Bottom peak temperature, B1 & B2 (°C)
1	24	400	1	6.5	713 & 733	647 & 654
2	19.4	400	1	8	781 & 748	720 & 680
3	18.2	400	1	8.5	814 & 812	712 & 724
4	20	300	1	5	895 & 916	791 & 812
5	23	150	0.5	4 or 5	1096 & 686	498 & 496

Table 3.4 shows a summary of the experimental measurements and results. The second column of this table provides a list of the measured ambient temperatures. The duration of recording for each experiment was presented in the third column. The forth column shows the temperatures were recorded at intervals of 1 second for Experiment 1, 2, 3 and 4 except Experiment 5 was recorded at intervals of 0.5 second in order to capture the fast rising and cooling temperatures at location T1 which is 4 mm from the weld centreline. The fifth column provides a list of positions where the peak temperatures of T1, T2, B1 and B2 were measured. The sixth column presents the experimentally measured top peak temperatures. It should be noted the measured peak temperatures at location T1 of Experiment 5 is higher because the location T1 is only 4 mm from the weld centreline. The last column shows the experimentally measured bottom peak temperatures. All the measured peak temperatures are within the thermocouple verification range except the peak temperatures at location T1 of Experiment 5 was out of the thermocouple verification range. However, the accuracy of this out of range measurement may be verified when it is compared with the computer generated results.

The recorded temperature histories and the photographs of macrostructure for experiment 1, 2, 3, 4 and 5 were shown in Figure 3.23, 3.24, 3.25, 3.26 and 3.27 respectively. It should be noted that for low carbon steel, the full transformation to austenite occurs roughly at temperatures above 800°C but below melting temperature and the full transformation to ferrite occurs approximately at temperatures below 700°C. Partial recrystallization occurs between these two temperatures during which both austenite and ferrite are present. These photographs of the weld macrostructure show the dimensions of the weld widths. They also show the top and bottom width of the approximate 800°C peak temperature lines in the heat affected zone except Figure 3.27 of experiment 5. The ~800°C peak temperature lines are not obvious in Figure 3.27 instead the ~700°C peak temperature lines are visible. It should be noted that the measurements of the top and bottom width of the heat affected zone were only rough measurements because the lines in the heat affected zone may sometimes be unable to be seen or very unclear. The little lime coloured dots in the photograph of the macrostructure were to indicate the thermocouples positions of T1, T2, B1 and B2 where T1 and T2 were top thermocouples positions and B1 and B2 were bottom thermocouples positions.

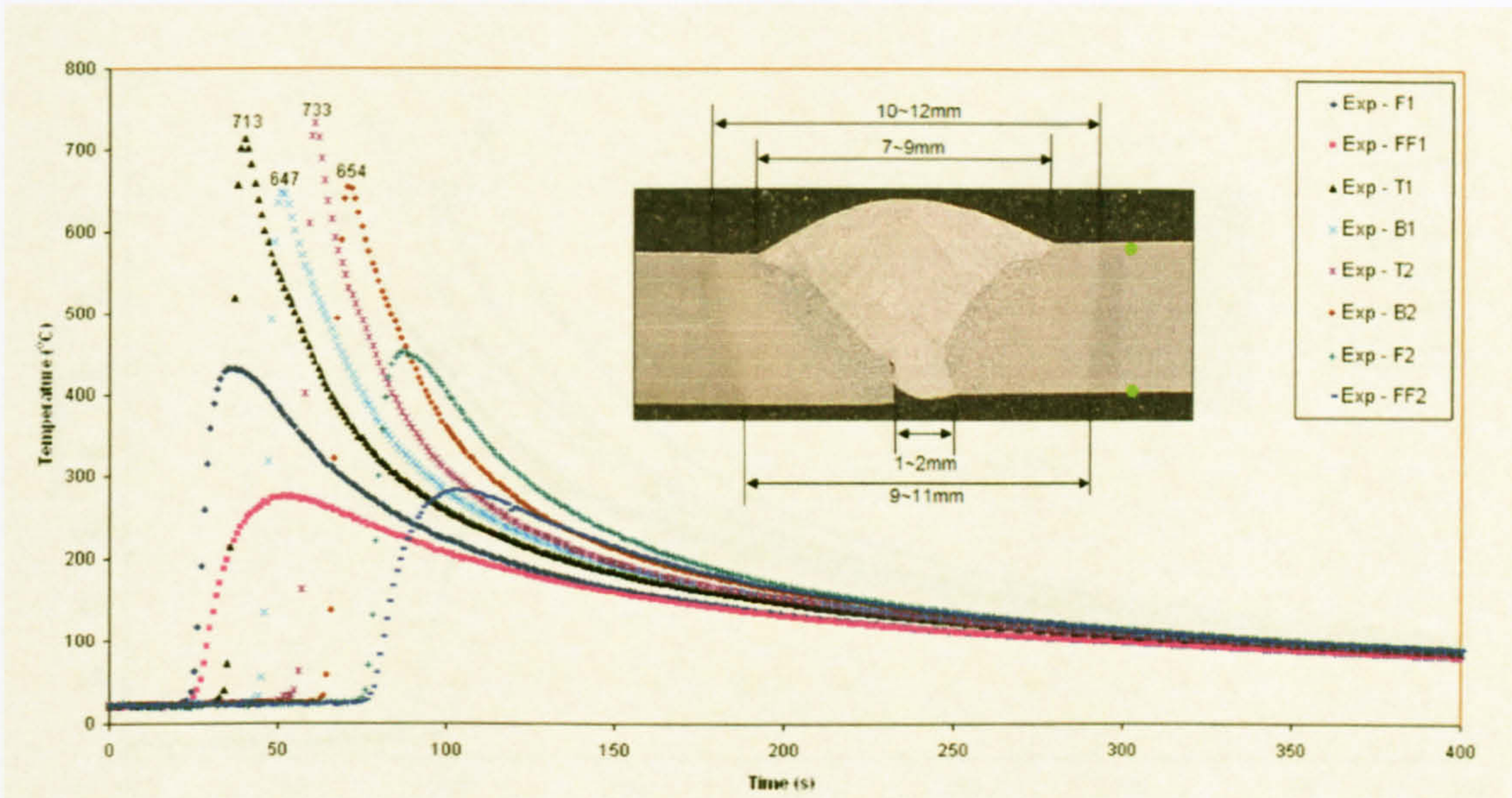

Figure 3.23

Experimental results of 4 mm thick plate with a "V" weld-preparation

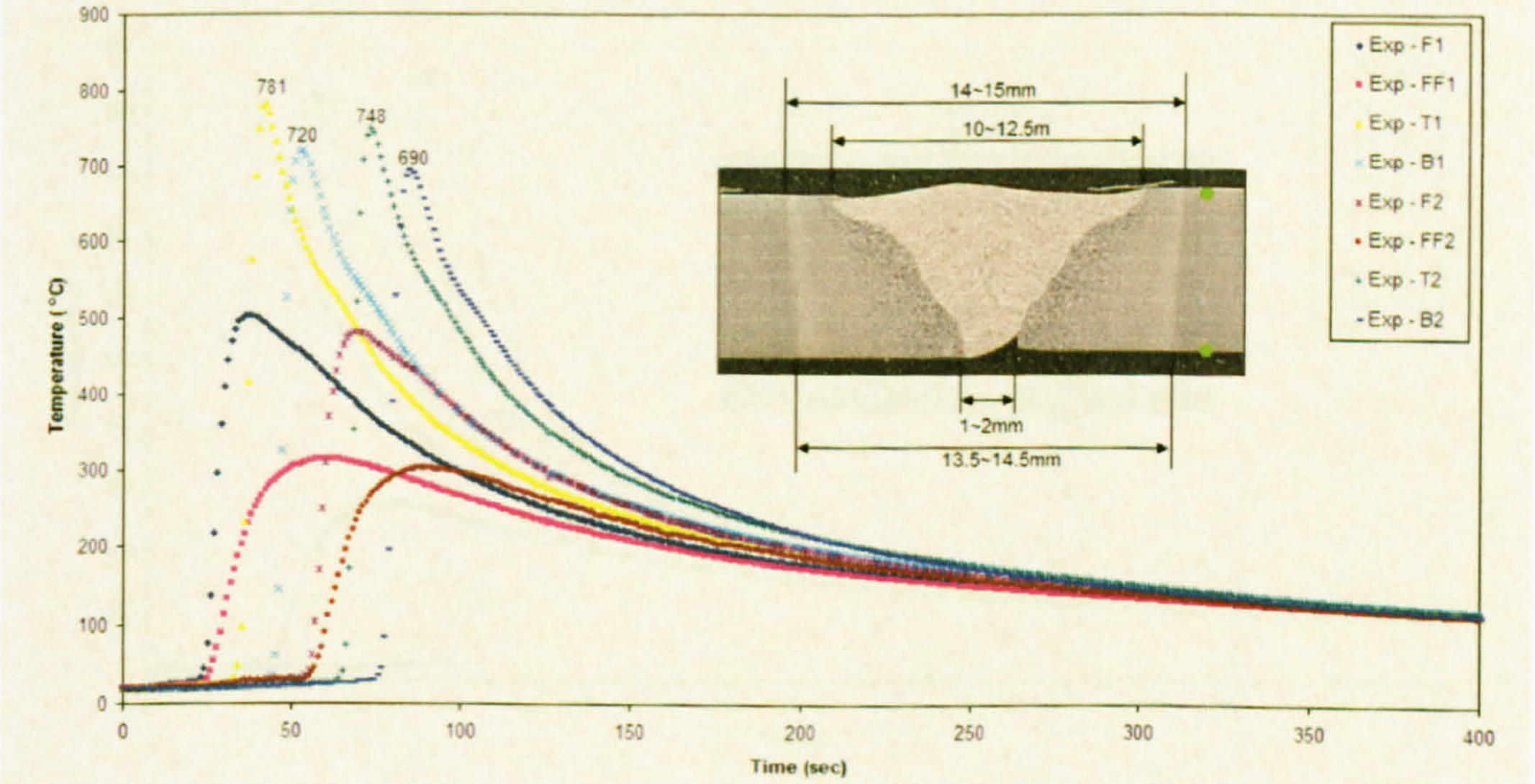

Figure 3.24

The experimental results of 6 mm thick plate with a "V" weld-preparation

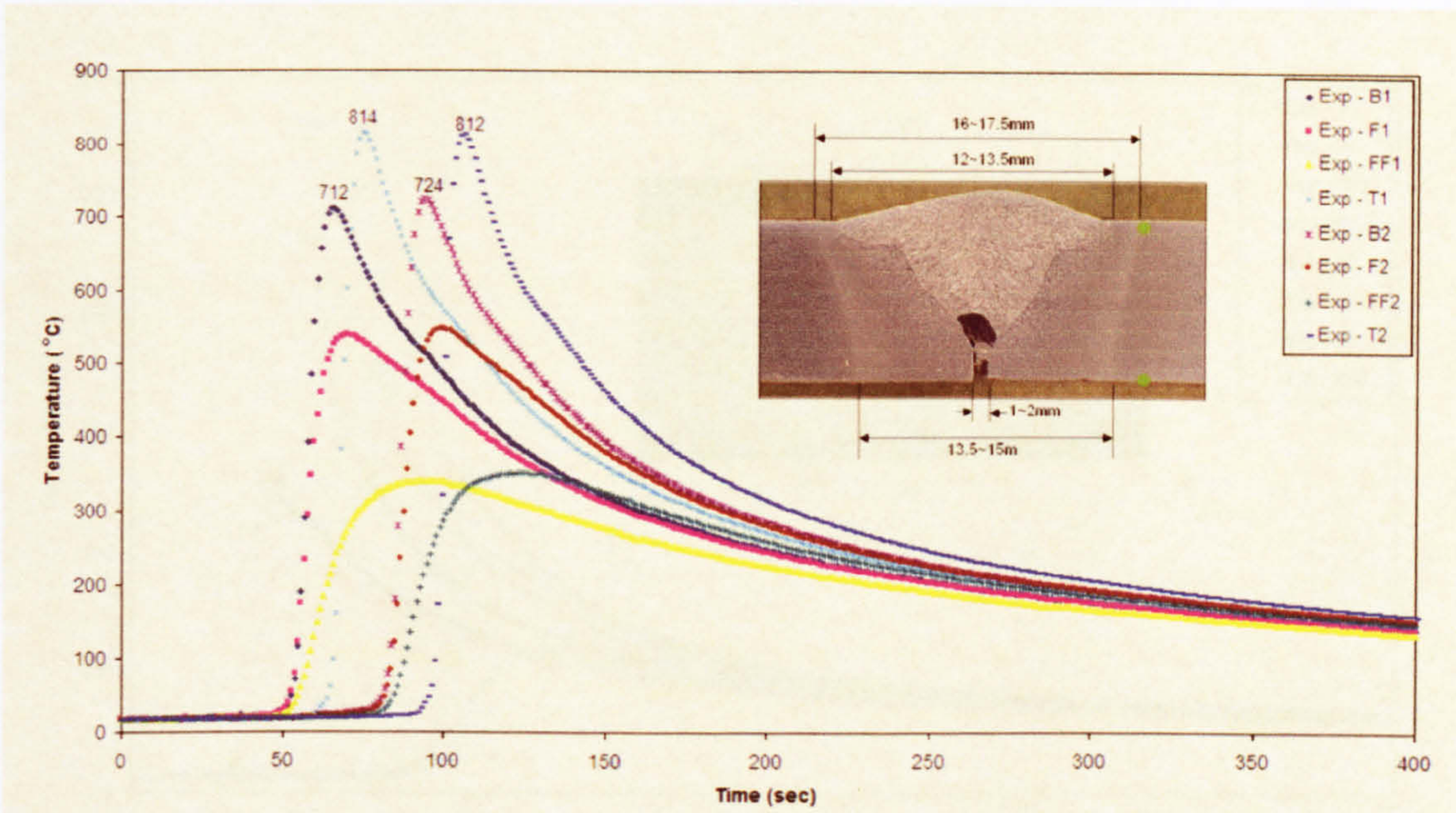

Figure 3.25

The experimental results of 8 mm thick plate with a "V" weld-preparation

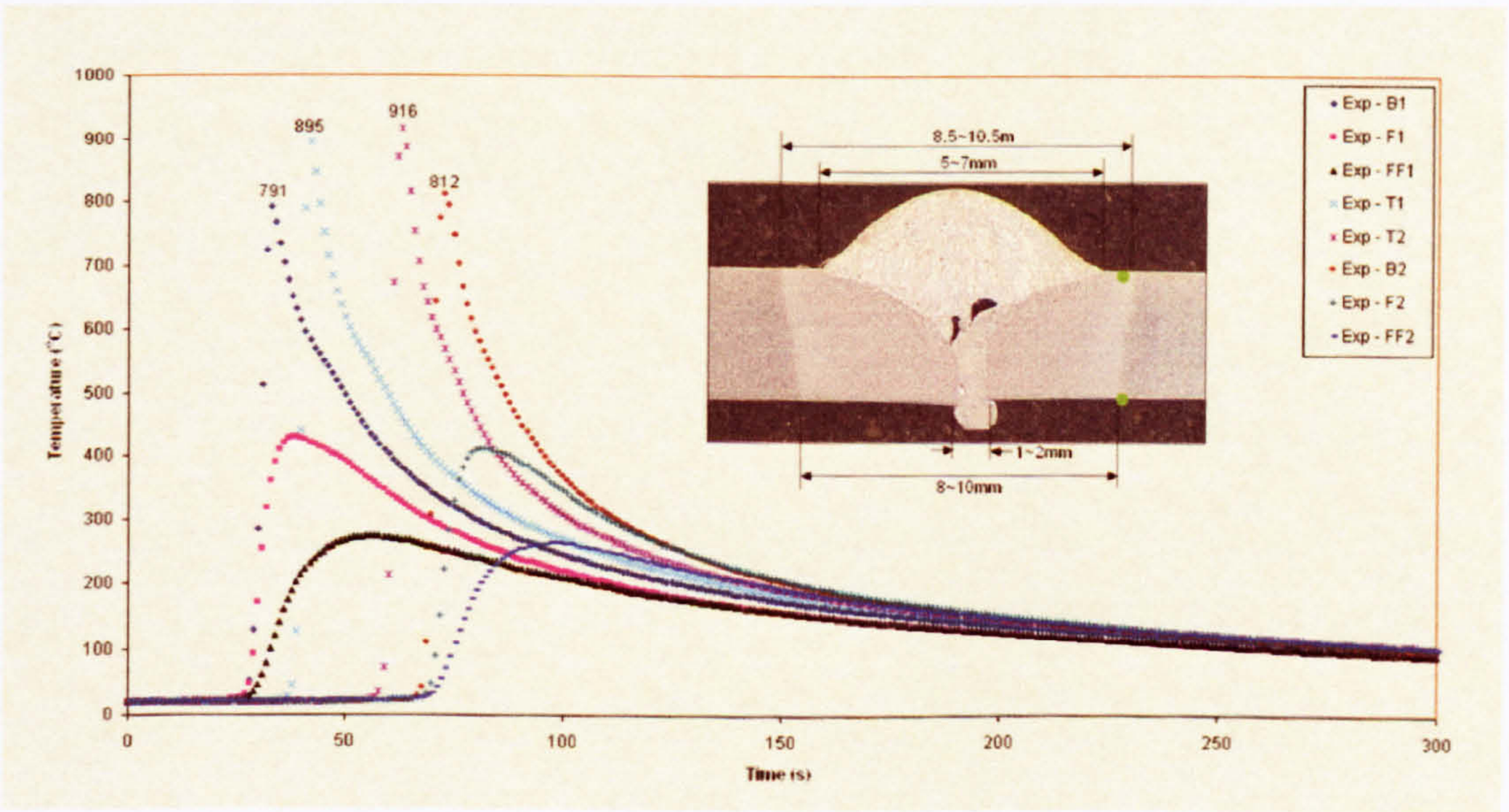

Figure 3.26

The experimental results of 3 mm thick plate with a "V" weld-prep

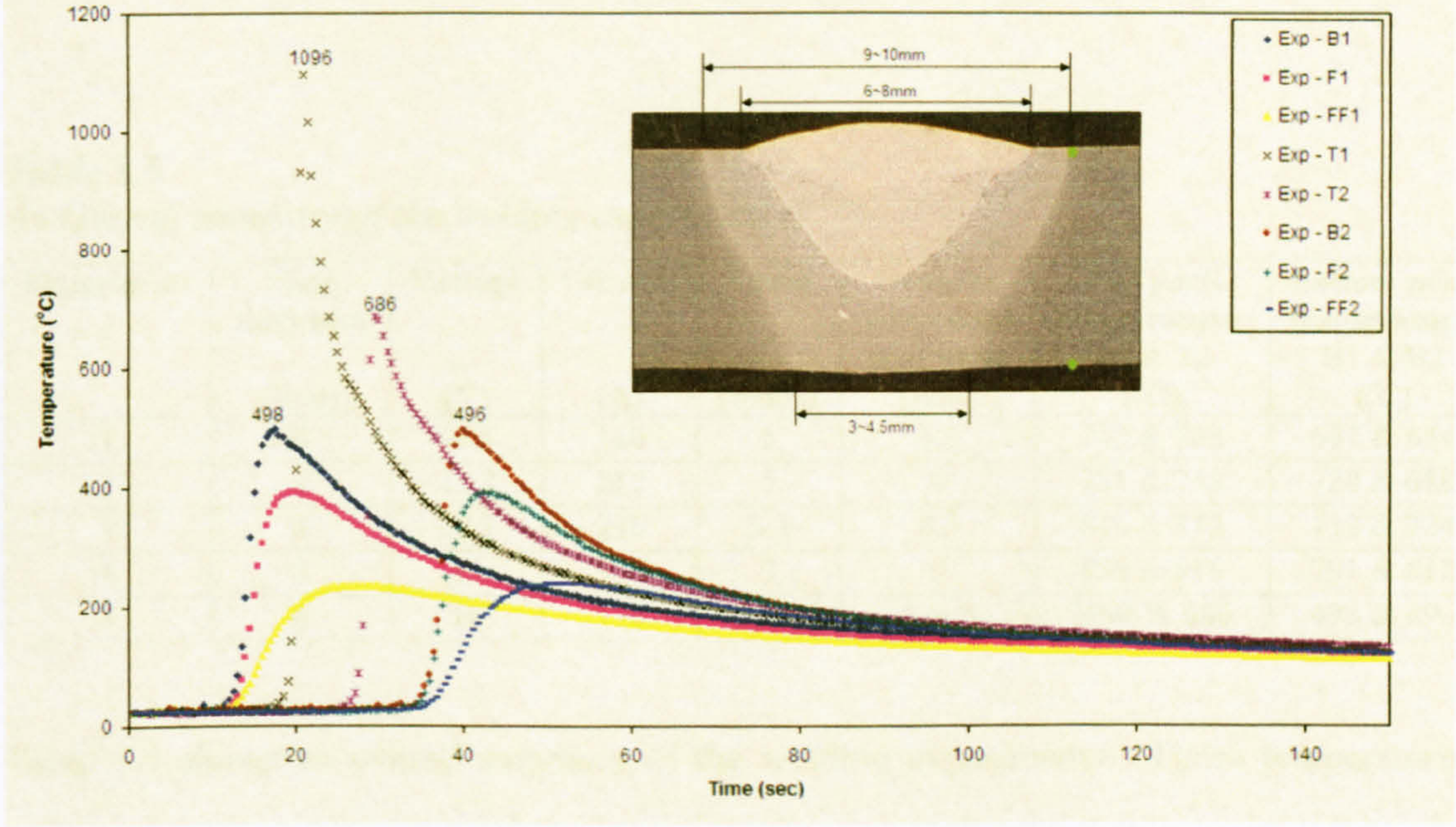

Figure 3.27

The experimental results of 6 mm thick plate with a semi-circle cross-sectional weld-prep

3.4 Conclusion

Table 3.5
An Overall summary of the welding experiments

Experiment	Plate thickness (mm)	Voltage (V)	Current (A)	Speed (mm/s)	Distance away weld centreline (mm)	Top peak temperature, T1 & T2 (°C)	Bottom peak temperature, B1 & B2 (°C)
1	4	16.5	160	5	6.5	713 & 733	647 & 654
2	6	23.7	212	5	8	781 & 748	720 & 680
3	8	22.7	236	3.3	8.5	814 & 812	712 & 724
4	3	15	130	5	5	895 & 916	791 & 812
5	6	16	150	5	4 & 5	1096 & 686	498 & 496

Table 3.5 shows an overall summary of the welding experiments. These temperature measurements possibly incurred errors which are very difficult to avoid or unavoidable. For examples, fixing the thermocouple onto the plate require extra care in the thermocouples positioning as very little mispositioning will result in a large error in the peak temperature measurement. The welding head travelling path alignment with the weld-preparation is equally important as fixing of thermocouple; very slight misalignment may result in a large error. The adjustments for the top surface of the plate to produce a constant gap of 6 mm away from the welding head are not as important as the above because most of the time the plate is not flat but still produce quite good experimental results. Errors such as the built-in errors of K type thermocouple, the built-in backlash of the milling machine resulted in a non-constant travelling speed, noisy environment contributing noise to the temperatures reading, as well as heat conducting away from the thermocouples, the run in and run off plates, the four supporting posts and the metal clip clamp seem to be not significant because these

are all small errors compare to errors committed by thermocouples mispositioning and welding path misalignment.

In spite of these possible errors, in overall, all the experimental results are realistic enough to be used for verifying the computer models. The accuracy of the out of calibration range measurement in Experiment 5 can only be verified when it is compared with the computer generated results.

Chapter 4 – Analytical Moving Heat Source Theory and Validation of Finite Element modelling

4.1 Introduction

As mention previously in section 2.2, analytical methods for prediction of temperature distribution due to the welding process have been examined in considerable detail in the past. The moving heat source analytical theory was first published in 1904 by Wilson [1]. This theory assumes either a point, a line or a plane heat source in a moving media which can be either a solid or fluid. In 1938 Rosenthal [2] provided analytical expressions and applied them to the usages of welding. After Rosenthal, significant further contributions were made by several other investigators notably Wells [4], Barry et al [7], Eagar et al [13] and Adrian Bejan [20]. In general, the analytical theories of moving heat source assume that the heat losses from the surface by convection and radiation are negligible. These methods also generally neglect the effects of latent heat (or enthalpy of fusion) due to phase transformation and non-linearity of the thermal physical properties. Most of the expressions in these theories were derived analytically from the general conduction equation.

The determination of the temperature field of a welding plate during the welding process is generally a three-dimensional (3D) transient problem involving surface heat losses and non-linear thermal physical properties. To this end, there is still no analytical solution for such a complicated problem. Therefore, assumptions are

needed to be made in order to simplify the problem into one that can be solved analytically.

Section 4.2 explains how a three-dimensional heat flow transient problem of welding plates can be simplified to a three-dimensional heat flow steady-state problem. Section 4.3 shows the way of simplifying a three-dimensional heat flow steady-state problem to a two-dimensional (2D) heat flow steady-state problem for full-penetration welds by neglecting several factors. Section 4.4 explains how a two-dimensional heat flow steady state problem for full-penetration welds can be converted into a one-dimensional transient problem by adding a further assumption.

A finite element model was developed and the results were compared with the analytically calculated results for an instantaneous plane heat source [20]. Since an instantaneous plane heat source is not realistic in actual situation, section 4.5 explains how to cater for a heat source that takes a certain time to release energy to the plate at a constant rate. The analytical solution was compared with the finite element solution. In an actual situation the heat input rate is not constant, and section 4.5 also demonstrates the evaluation for the case of a ramp heat input and compares the analytically calculated solution with the finite element solution. Good agreement between analytical and numerical solutions will serve as a positive verification of the finite element implementation techniques.

4.2 Simplification from a three-dimensional transient heat flow problem to a three-dimensional steady state heat flow problem

When a plate is heated by a source of heat moving along its surface, the temperature at any particular location in the plate varies with time and the determination of the temperature field is generally a three-dimensional transient problem. However, if the heat source is moving at a constant speed in a straight line, a temperature distribution pattern is developed in the plate material. The generated pattern, like a 'footprint', becomes established and moves with the heat source. This 'footprint' is shown in Figure 4.1 and appears to be stationary and remains constant to an observer moving with the heat source. Thus by considering the heat source to be stationary with the plate moving at a constant speed, the problem can be converted into a steady state one. There are analytical solutions for the determination of the temperature field for such a problem. These methods mainly rely on the steady state condition where temperature does not vary with time but may vary in the X, Y and Z directions. In the analytical theory, the heat source is often treated as a point moving along the plate surface and the temperature is not uniform across the thickness of the plate. In welding practice, non-full penetration welds (see Figure 4.2) produce temperature patterns similar to that shown in Figure 4.1. Thus this type of welding can be modelled by a moving point heat source.

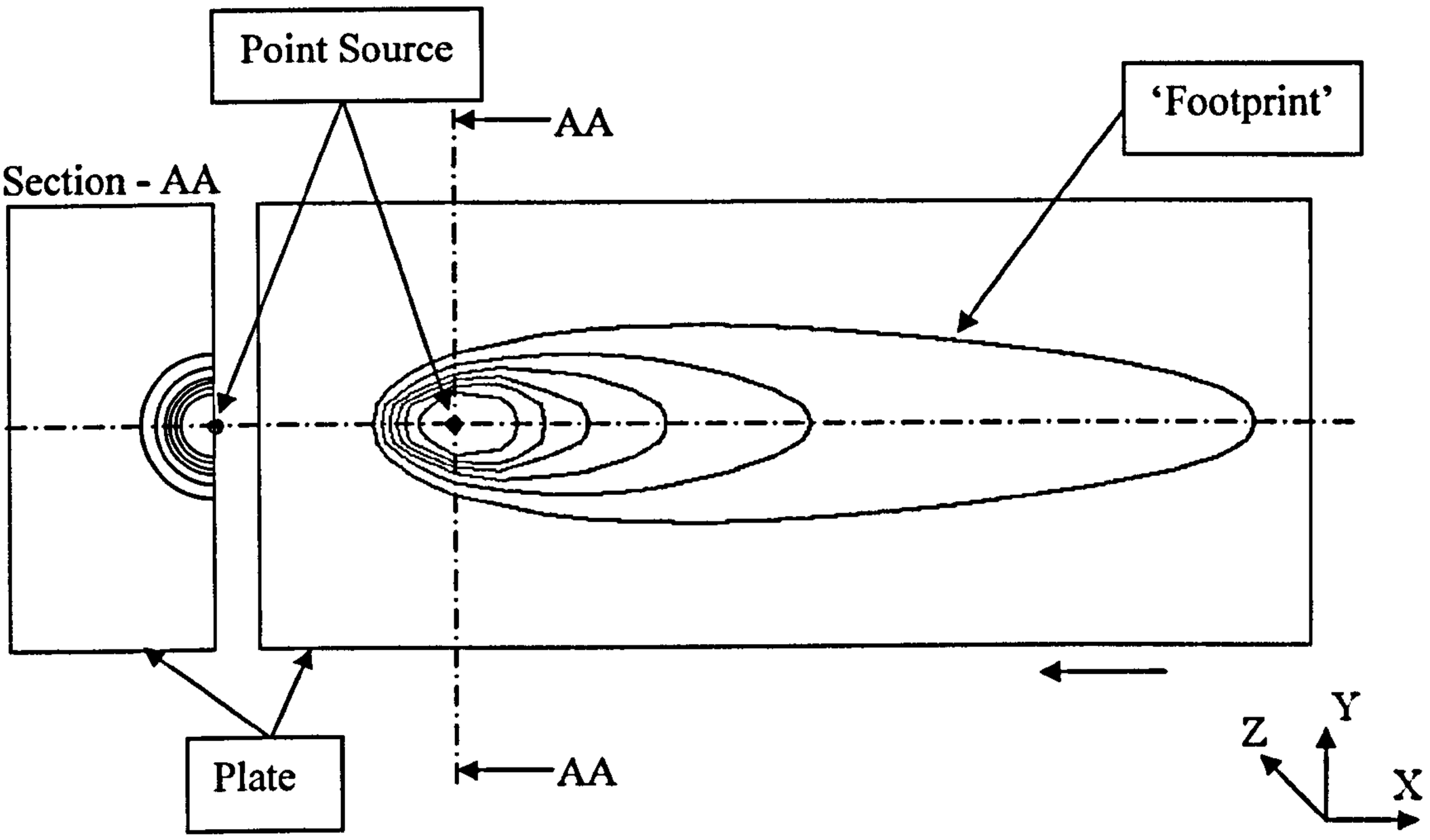

Figure 4.1

A steady state temperature contour of a moving point heat source

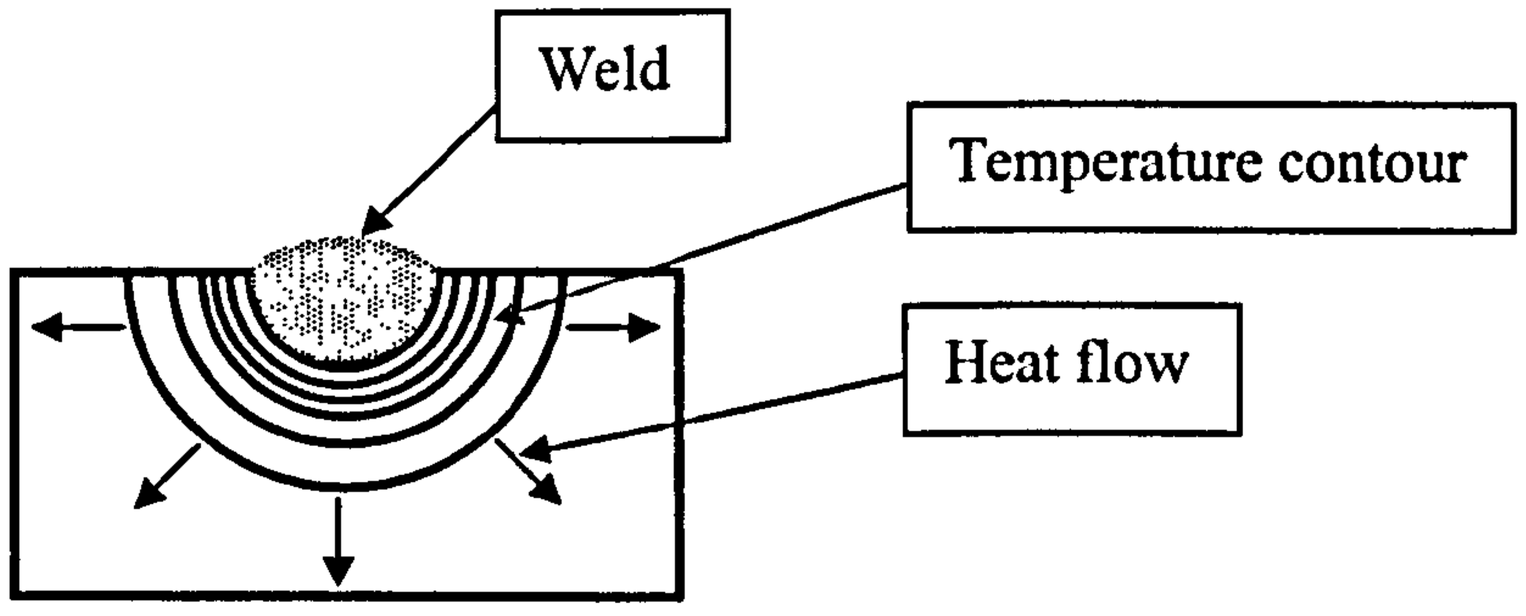

Figure 4.2

A non-full penetration weld where temperature is not uniform across the thickness

4.3 Simplification from a three-dimensional steady state heat flow problem to a two-dimensional steady state heat flow problem

For joining thin plates together by welding, it is often desired to have a full penetration weld so that the joint will be stronger. In such cases, as illustrated in Figure 4.4 the temperature distributions at the top surface, at the bottom surface and in the plate are almost identical during the welding process and the three-dimensional heat flow steady state problem can be further simplified to a two-dimensional steady state heat flow one. Thin plates with full penetration weld can therefore be modelled by a moving line source which produces a temperature pattern similar to the one shown in Figure 4.3 where the temperature varies only along the X and Y directions.

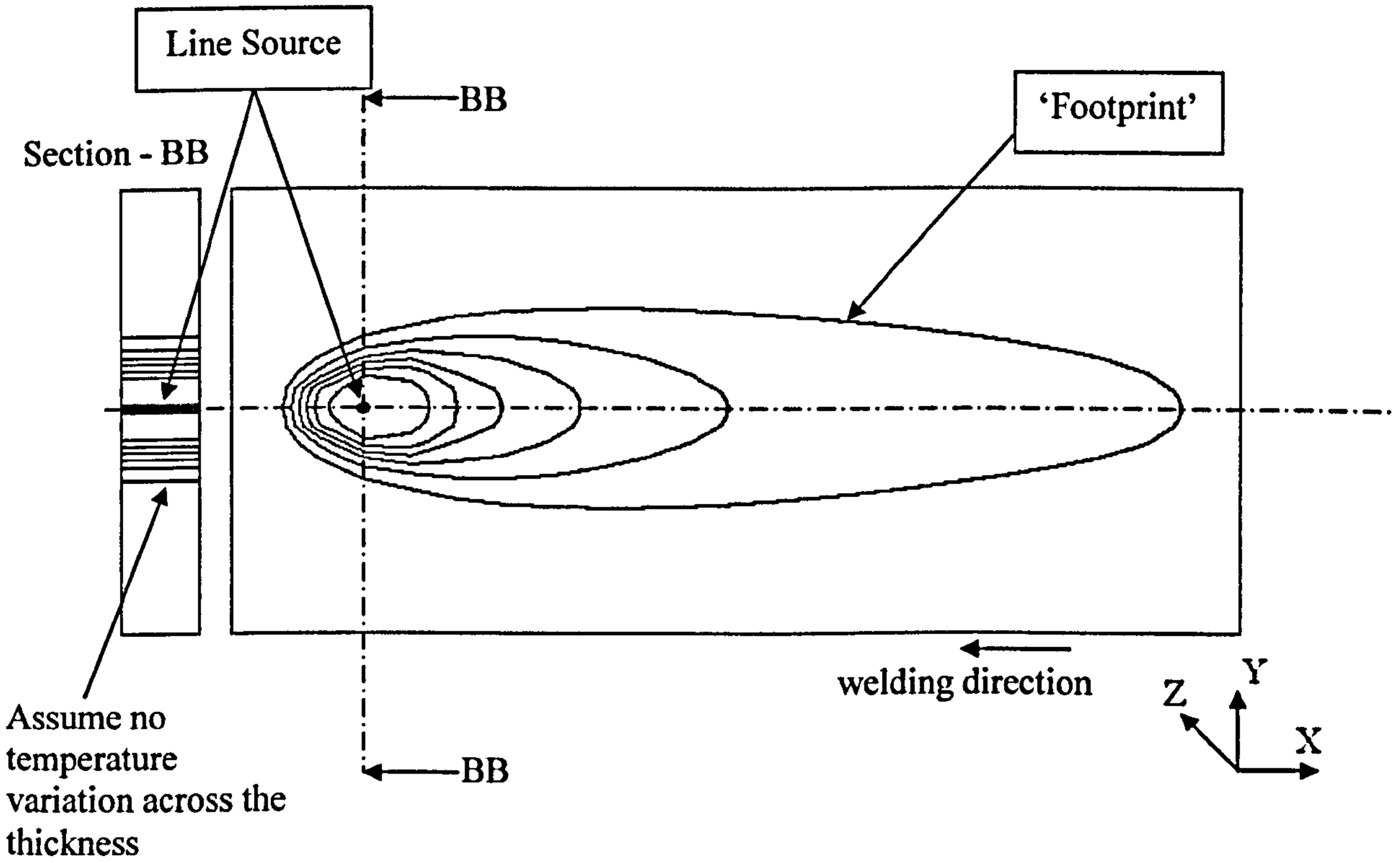

Figure 4.3

A steady state temperature contour of a moving line heat source

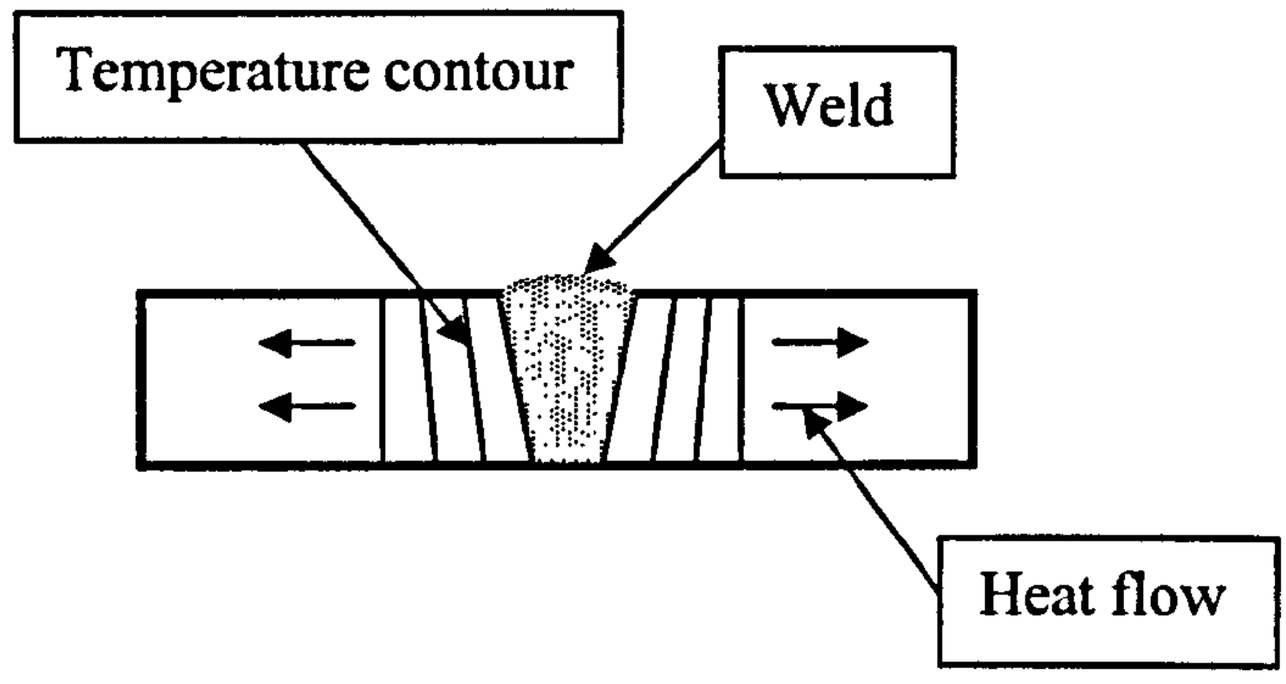

Figure 4.4

A full penetration weld where the temperature is almost uniform across the thickness

4.4 Simplification from a two-dimensional steady state heat flow problem to a one-dimensional transient heat flow problem

If the heat source is moving at a sufficiently high speed, heat conduction in the longitudinal direction can be neglected according to [7, 20 & 10]. The thin plate with full penetration welding can then be modelled analytically in terms of a moving line source using equation 4.1 which has been derived by assuming no heat conduction in the longitudinal direction. Figure 4.5 illustrates the temperature contour of this type of model which produces no temperature contour up-stream of the moving heat source.

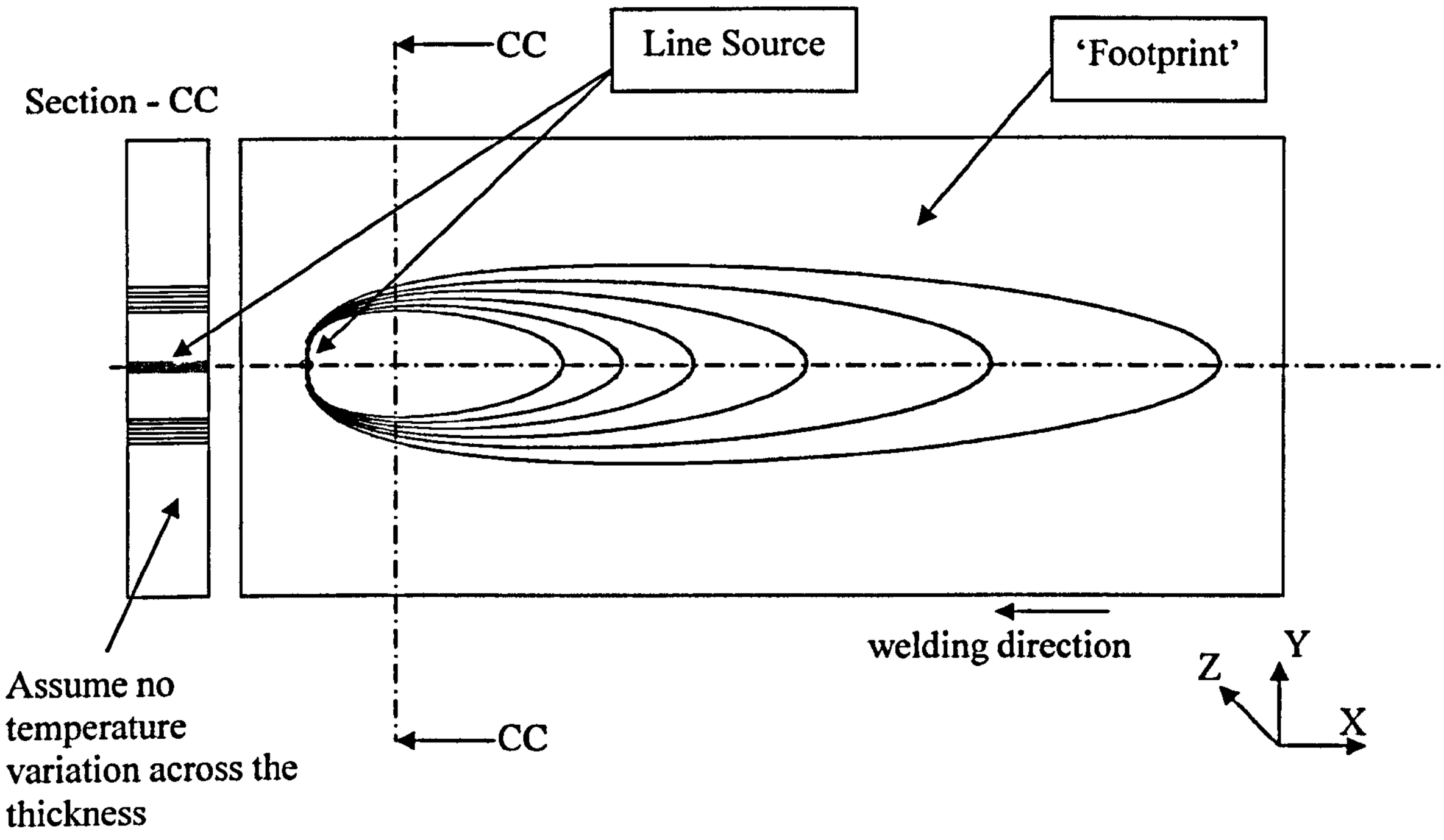

Figure 4.5

A temperature contour of the moving line source with no heat flow in X direction

The relative temperature distribution for a moving line source in between the edges of two plates is [20]:

$$\theta(x,y) = \frac{Q_{net}/\delta}{2\rho C(\pi U \alpha x)^{1/2}} \exp\left(-\frac{Uy^2}{4\alpha x}\right) \text{----------} (4.1)$$

where θ is $T - T_o$ and T_o is the ambient temperature, Q_{net} is the net heat power input, α is thermal diffusivity, U is the travelling velocity of the line source, δ is the thickness of the plates, x is co-ordinate in line with the travelling velocity and y is co-ordinate perpendicular to δ and x.

Substituting $x/U = t$ and $Q_{net}/U\delta = Q_{net}$" into equation (4.1) gives:

$$\theta(y,t) = \frac{Q_{net}"}{2\rho C(\pi\alpha t)^{1/2}} exp\left(-\frac{y^2}{4\alpha t}\right) \text{----------} (4.2)$$

where Q_{net}" is the heat-flux input in J/m^2 and t is time in seconds. In terms of welding, Q_{net}" is equal to the welding net power input per unit plate thickness divided by the welding speed.

This expression of equation 4.2 is often referred to as an instantaneous plane heat source in the analytical theory where all the heat is released at time = 0 into the edges between two plates of a unit length as illustrated in Figure 4.6. The equation gives the temperature history in a cross-section of the plate normal to the plane source.

The above discussion shows that the temperatures for a 2D steady-state analysis due to a moving line source can be obtained from the results of a 1D transient calculation due to an instantaneous plane source by making use of some simple relationships between distance and time, and between energy and heat power. This has the obvious advantage of computational efficiency as if is a one-dimensional rather than a two-dimensional analysis. In practice, the above technique of transforming results from one form to another can be applied to convert the temperature distribution along the weld of the 3D steady state model into the temperature history at any location normal to the weld and vice versa, as will be demonstrated in the next chapter.

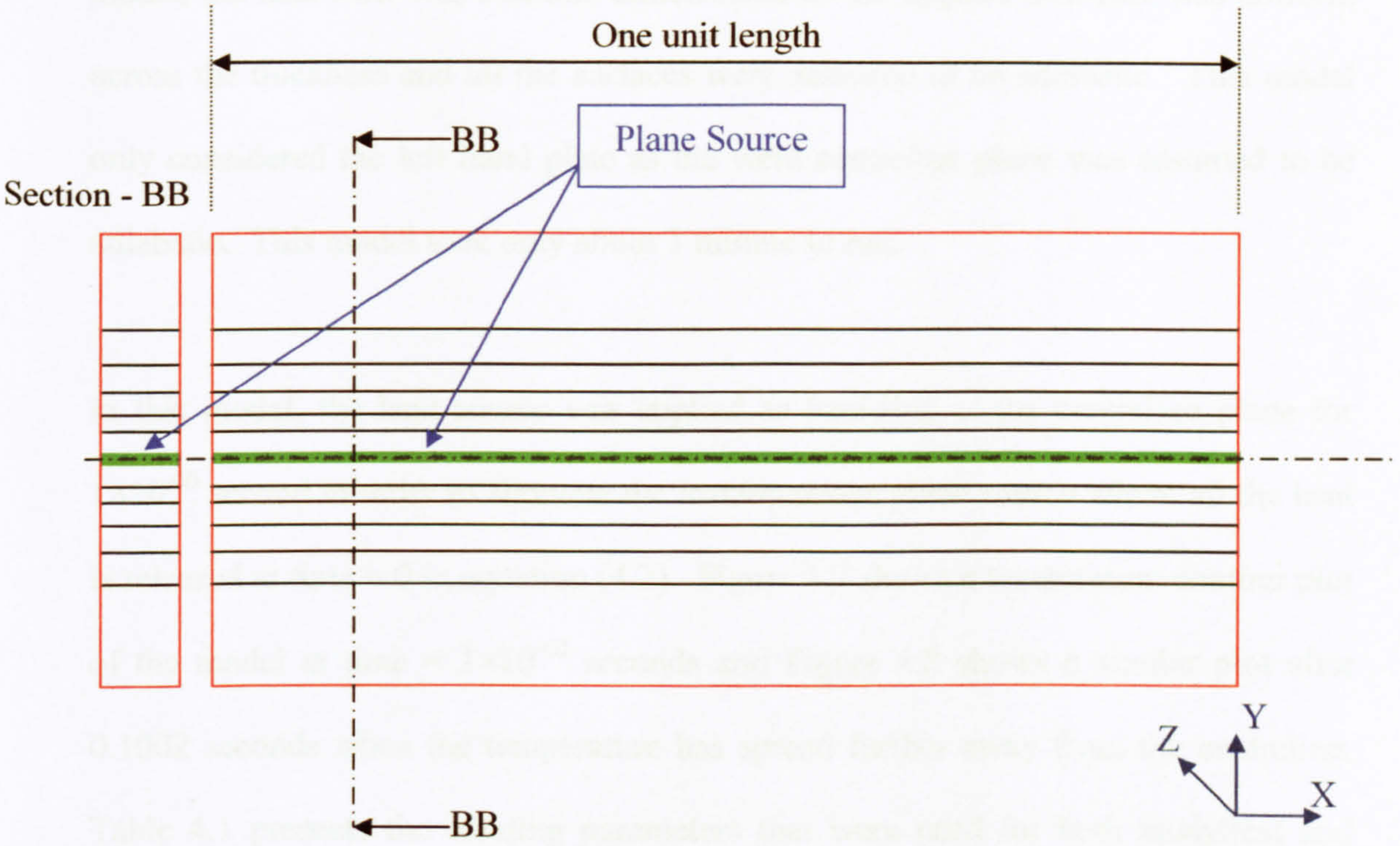

Figure 4.6

A temperature contour of the instantaneous plane heat source

4.4.1 Comparison with finite element model

A two-dimensional transient finite element model was developed using ANSYS software for verification against the results obtained from the analytical instantaneous plane source equation (4.2). The element type chosen to perform the 2D transient simulations is 'PLANE55'. PLANE55 has a 2D thermal conduction capability and has four nodes with a single degree of freedom, namely temperature, at each node. The element is applicable to 2D transient thermal analysis.

Although the modelling was done using a two-dimensional transient finite element model, the heat flow was still one-dimensional as the applied heat-flux was uniform across the thickness and all the surfaces were assumed to be adiabatic. This model only considered the left hand plate as the weld centreline plane was assumed to be adiabatic. This model took only about 1 minute to run.

In this model, the heat source was applied as heat-flux at the centreline plane for 1×10^{-60} second in order to simulate the instantaneous plane source where all the heat is released at time = 0 in equation (4.2). Figure 4.7 shows a temperature contour plot of the model at time = 1×10^{-60} seconds and Figure 4.8 shows a similar plot after 0.1002 seconds when the temperature has spread further away from the centreline. Table 4.1 presents the welding parameters that were used for both analytical and finite element calculations. The thermal physical properties were assumed to be constant.

Figure 4.9 shows a comparison of temperature histories between analytical and finite element solutions. The computer simulated temperature histories matched very well the analytical calculated temperature histories, and the finite element model can be regarded as being validated.

Table 4.1

Input parameters for both analytical and finite element calculations

T_o	25	°C
U	4.444	mm/s
α	9.1×10^{-6}	m^2/s
ρC	4.5×10^{6}	J/m^3
Q_{net}	2368	W

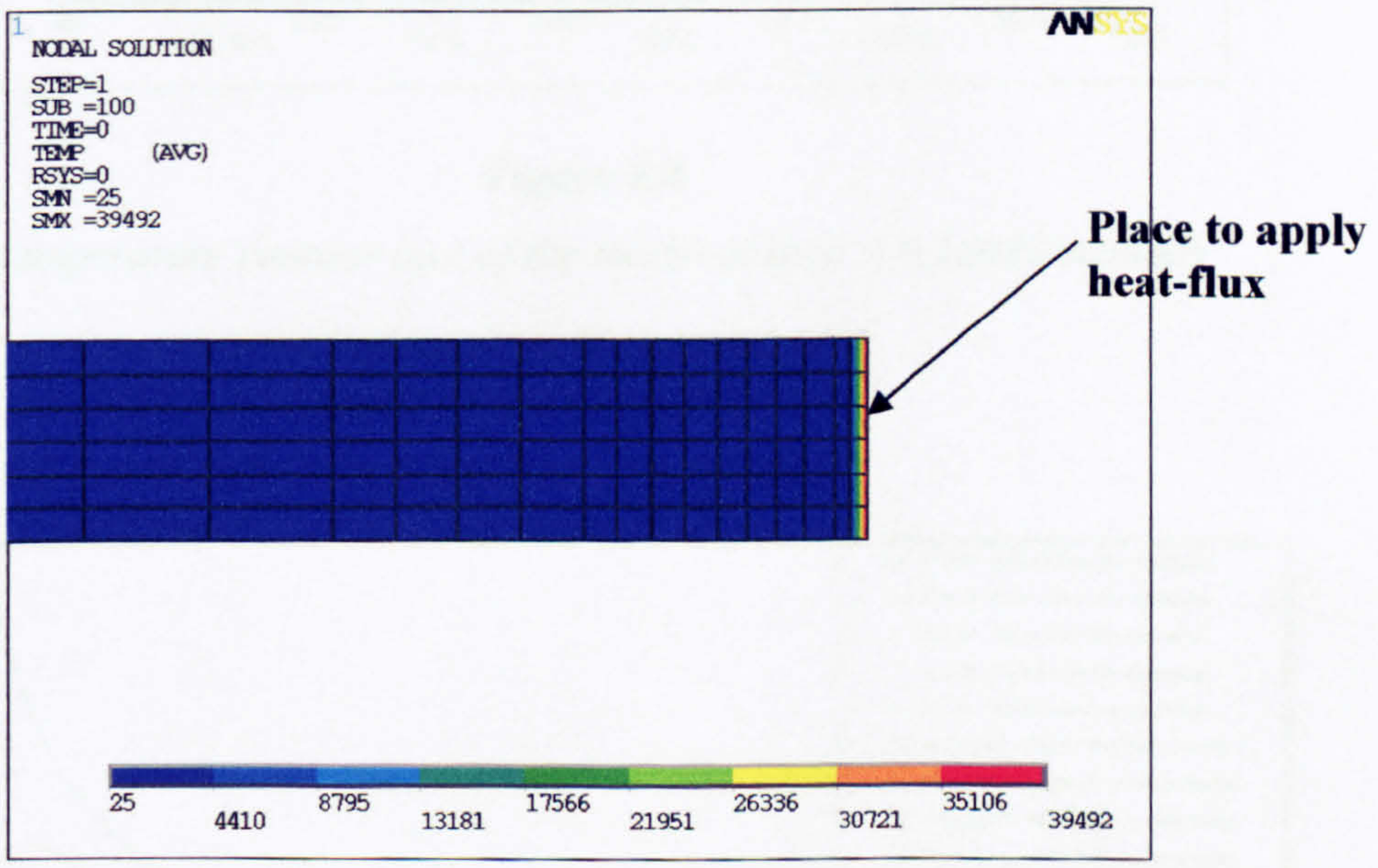

Figure 4.7

A temperature contour plot of the model at time = 1×10^{-60} seconds

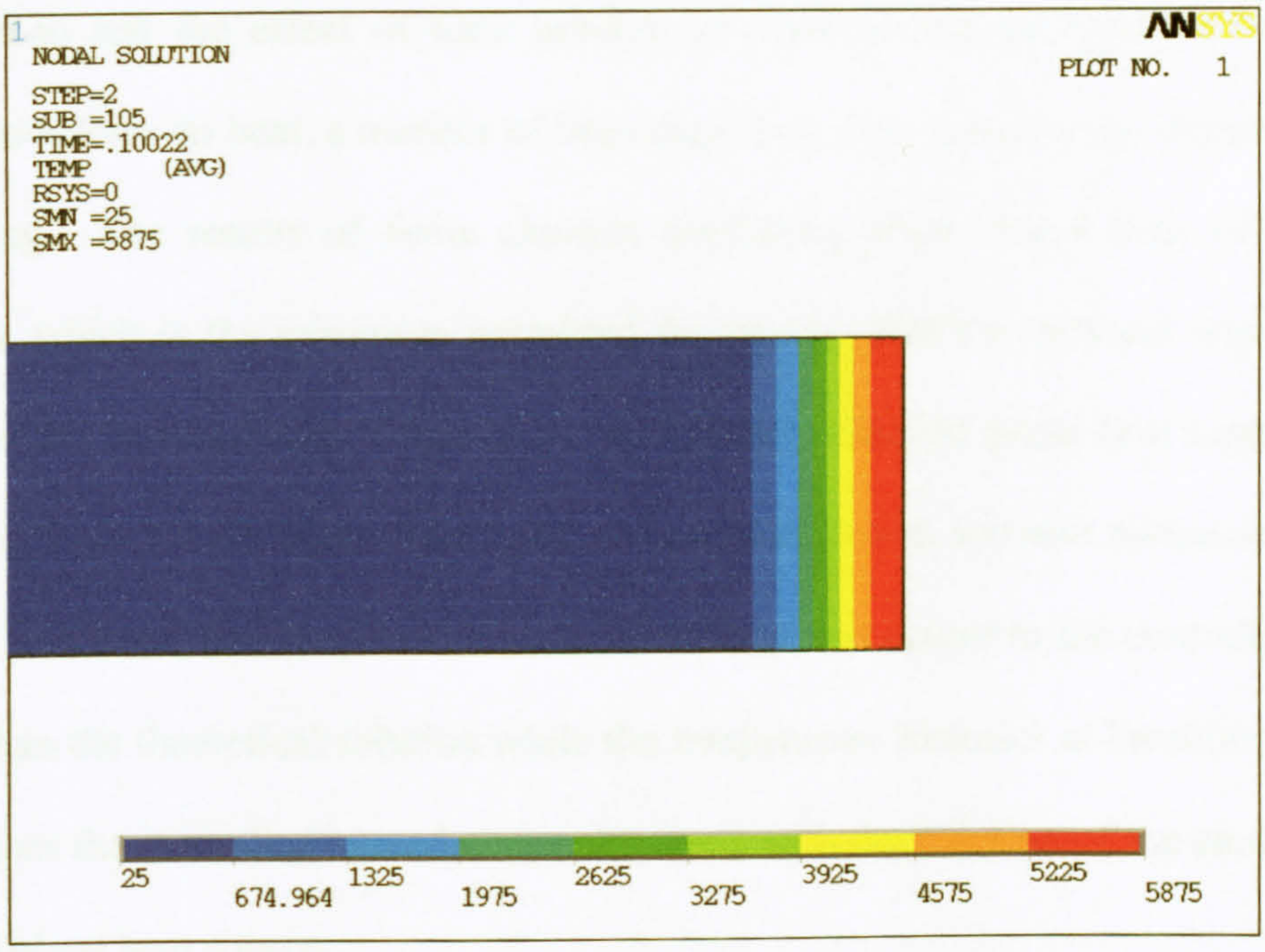

Figure 4.8

A temperature contour plot of the model at time = 0.10022 seconds

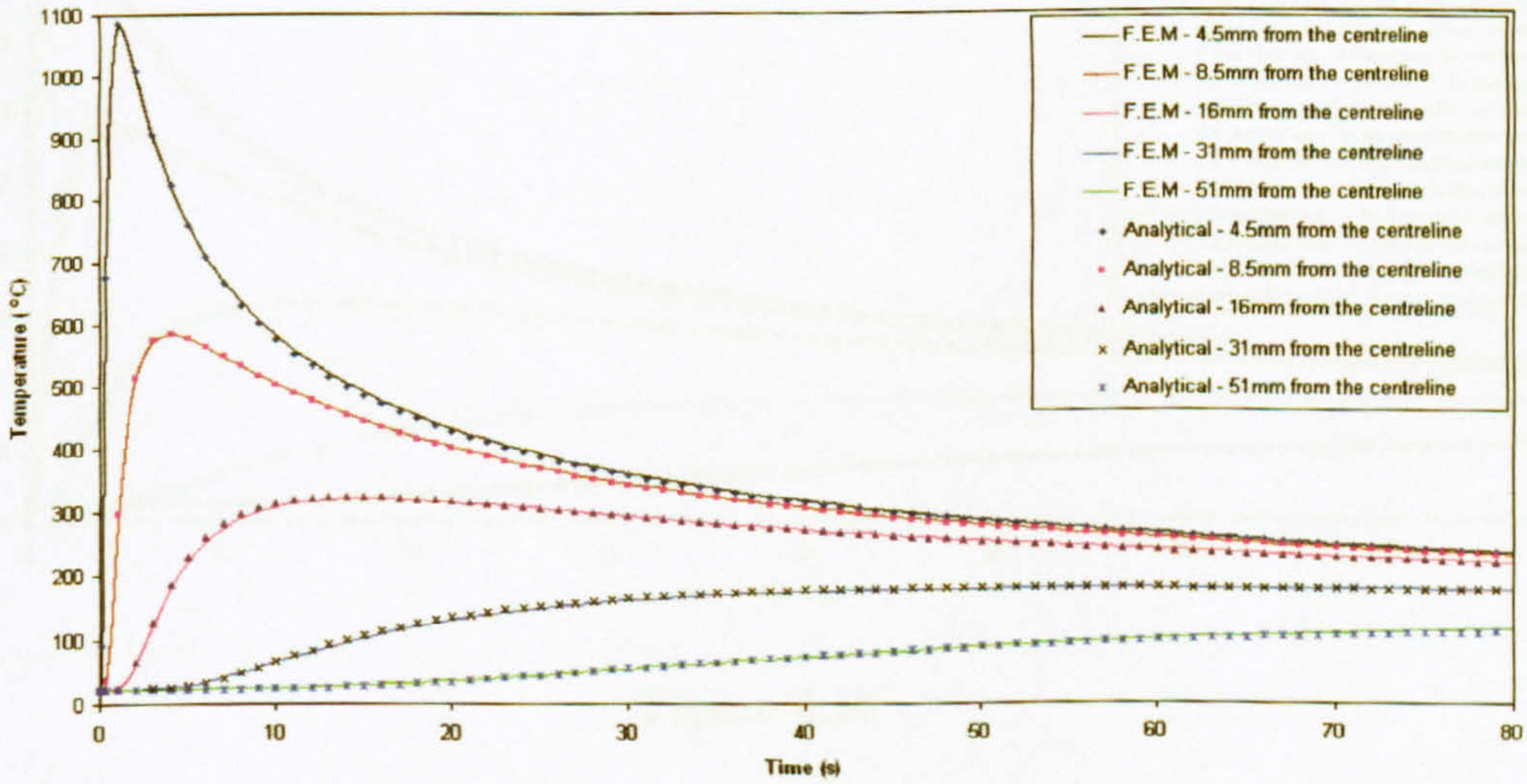

Figure 4.9

A comparison between analytical and finite element calculated temperature histories

In order to test the effect of time needed for representing an instantaneous heat source to release its heat, a number of time durations were tested using finite element modelling. The results of finite element modelling show that a time of 1×10^{-60} seconds, which is the minimum permitted for use in ANSYS software was able to simulate the instantaneous effect of the analytically derived plane heat source. As shown in Figure 4.10, using time equal to one millisecond and one microsecond for its heat to release, the temperature histories at locations nearer to the centreline were lower than the theoretical solution while the temperature histories at locations further away from the centreline agreed reasonably well with the solution of the analytically derived plane heat source.

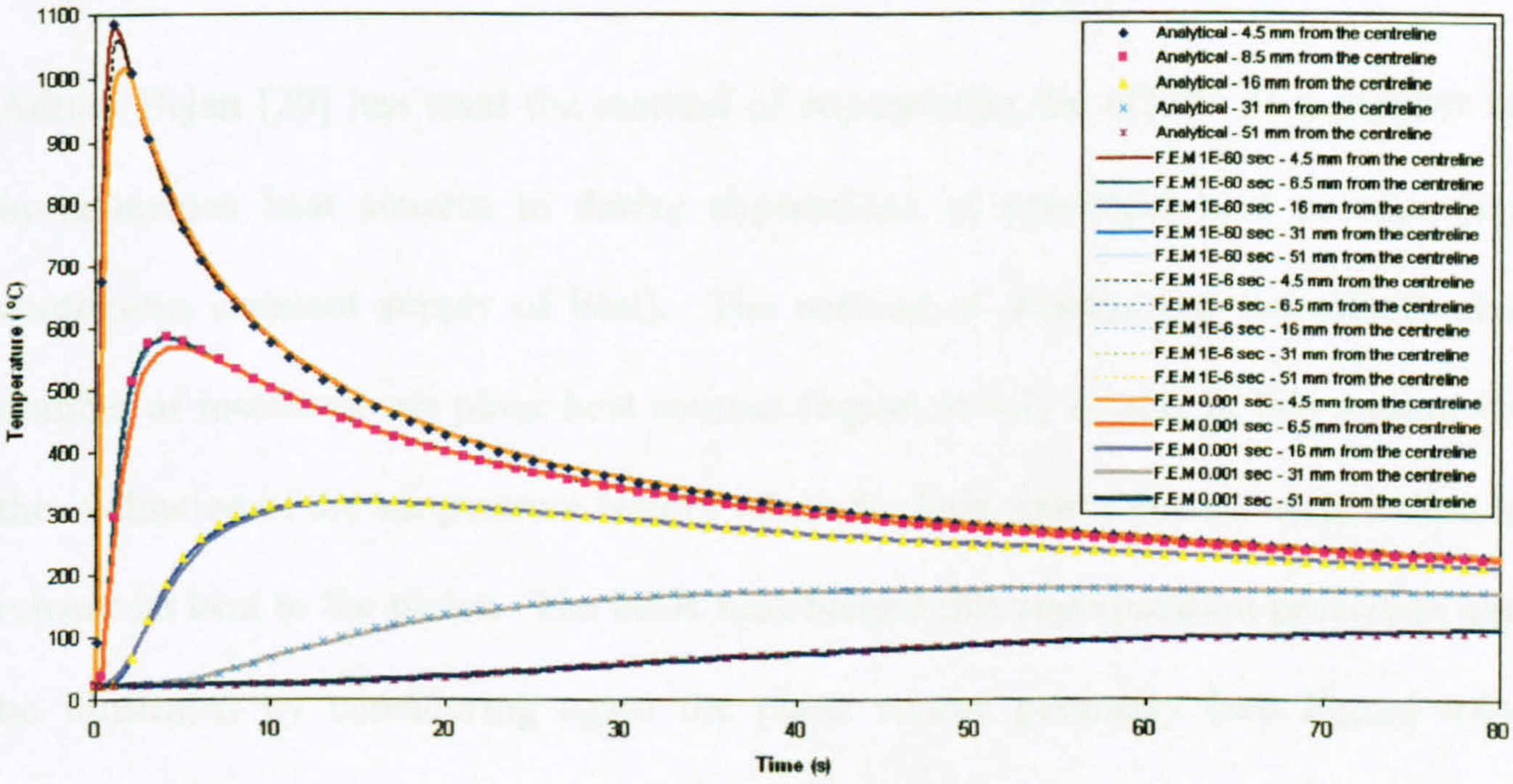

Figure 4.10

A comparison between analytical and finite element temperature histories

4.5 Effect of finite time to release the heat to the plates on a one-dimensional transient problem

In actual welding situations, the heat source takes a finite time to release its heat to the plates and the heat input rate may also vary with time. In order to be sure that the finite element model is capable of modelling such cases correctly, two cases were considered to verify the model. In the first case, the heat source was considered to take one second to release its heat to the model at a constant rate. In the second case, the time taken for the heat source to release the same amount of heat was the same as the first case but the heat input to the plate was applied as a straight line ramp starting from zero time.

Adrian Bejan [20] has used the method of superposing the effects of a number of instantaneous heat sources to derive expressions of persistent heat sources (i.e. continuous constant supply of heat). The method of superposing the effects of a number of instantaneous plane heat sources (equation 4.2) is used in this section for the evaluation of the temperature history where the heat source takes a certain time to release its heat to the plates. The basic idea behind this superposition procedure can be illustrated by considering again the plane source geometry (see Figure 4.6). Assume that at time $t = 0$, the plane $y = 0$ receives the per-unit-area (J/m^2) heat input Q_0"; at a subsequent time when $t = t'$, the plane $y = 0$ receives another per-unit-area heat input Q_1"; at a subsequent time when $t = t''$ the plane $y = 0$ receives another per-unit-area heat input Q_2" and so on until all the heat is released.

4.5.1 First case – constant heat input rate

Assume that the heat source takes one second to release the same amount of heat (Q_{net}") to the plates as the instantaneous heat source model and let the release of heat begin at time t = 0 second and ends at time t = 1 second at intervals of 0.1 second. The heat input to the plate at every 0.1 second is constant, that is $Q_0" = Q_1" = Q_2" = Q_3" = Q_4" = Q_5" = Q_6" = Q_7" = Q_8" = Q_9" = Q_{10}" = Q" \div 11$. The temperature history due to each instantaneous heat input is shown in Figure 4.11. The resultant temperature at any time due to multiple heat inputs is obtained by adding the temperatures at that time due to these heat inputs. For example at time = 0 s, $\theta = \theta_{00}$; at time = 0.1 s, $\theta = \theta_{10} + \theta_{11}$; at time = 0.2 s, $\theta = \theta_{20} + \theta_{21} + \theta_{22}$; at time = 0.3 s, $\theta = \theta_{30} + \theta_{31} + \theta_{32} + \theta_{33}$ and so on. After evaluating it for 10 seconds, the relative temperature history (θ) was obtained as shown in Figure 4.12.

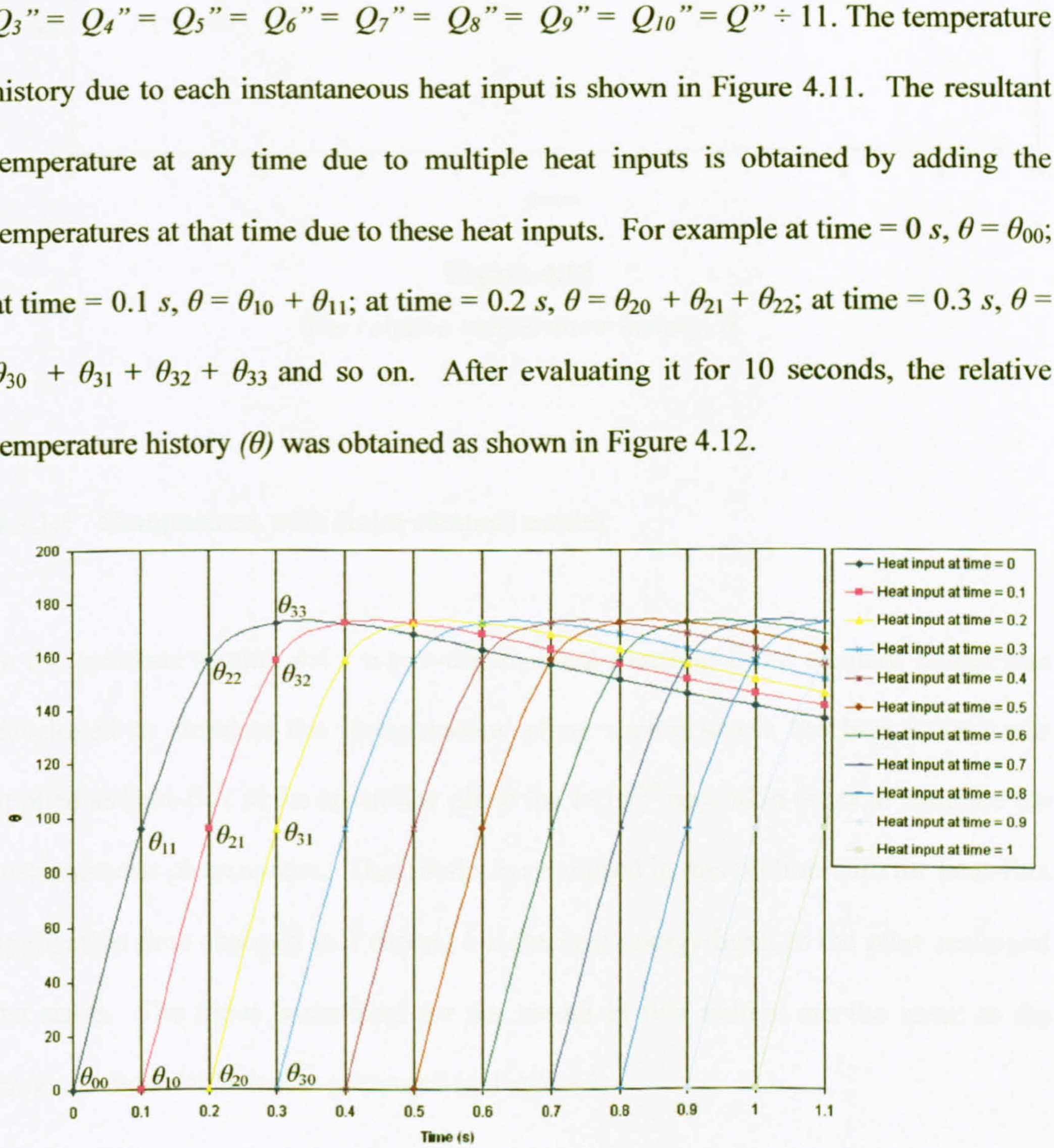

Figure 4.11

An illustration of superposition procedure of the multiple instantaneous heat sources

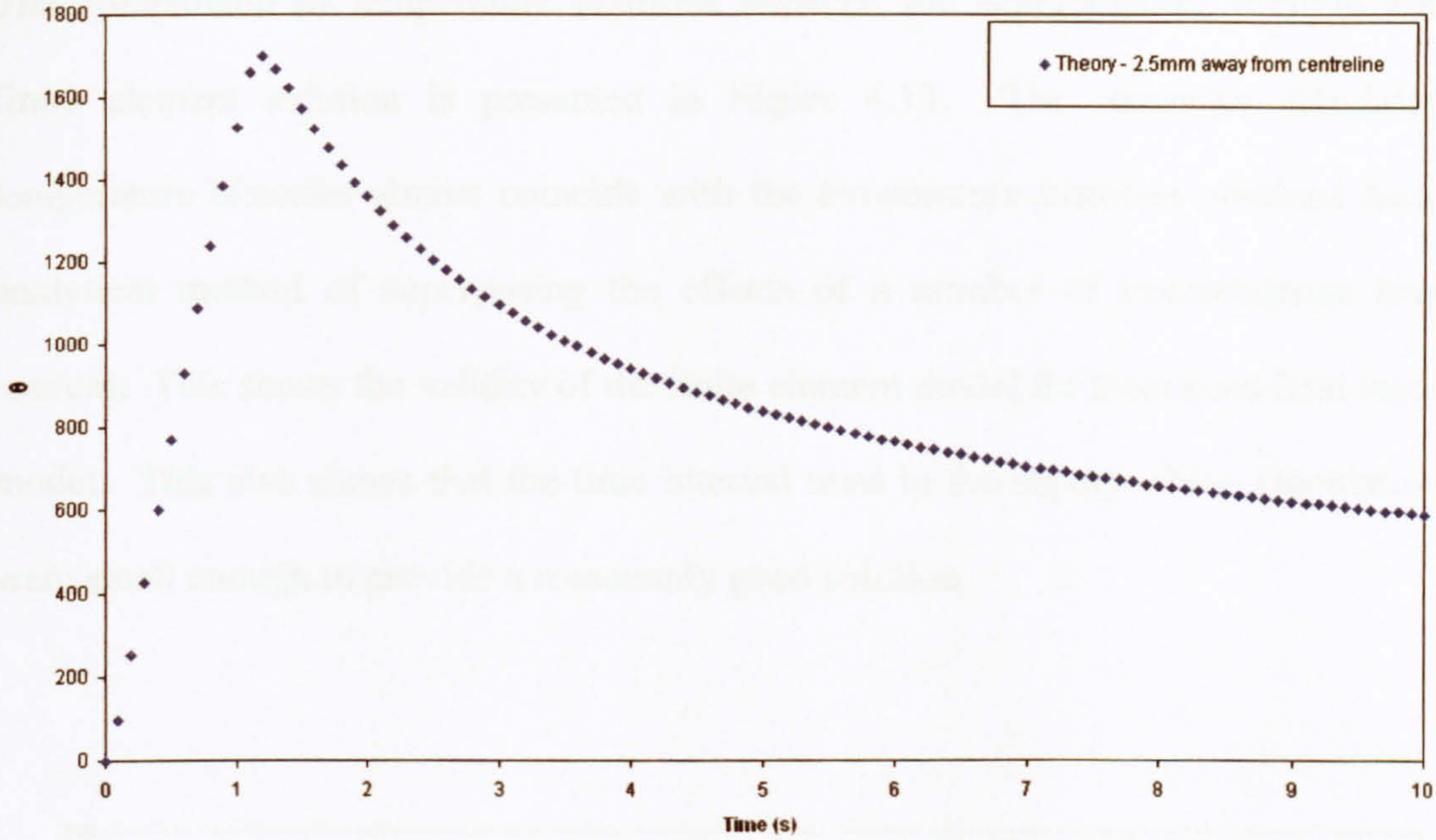

Figure 4.12

The relative temperature history, θ

4.5.1.1 Comparison with finite element model

In the previous section 4.4.1 a two-dimensional transient finite element model was developed to simulate the instantaneous plane source where the heat source was applied as heat-flux at the centreline plane for 1×10^{-60} second in order to simulate the instantaneous plane source. That model is now used in this section with the heat-flux application time changed to 1 second but the heat energy input to the plate remained the same. The input parameters for the model in this section are the same as the previous model which was presented in Table 4.1.

The comparison of temperature histories between the superposition solution and finite element solution is presented in Figure 4.13. The computer simulated temperature histories almost coincide with the temperature histories obtained from analytical method of superposing the effects of a number of instantaneous heat sources. This shows the validity of the finite element model for a constant heat input model. This also shows that the time interval used in the superposition calculation were small enough to provide a reasonably good solution.

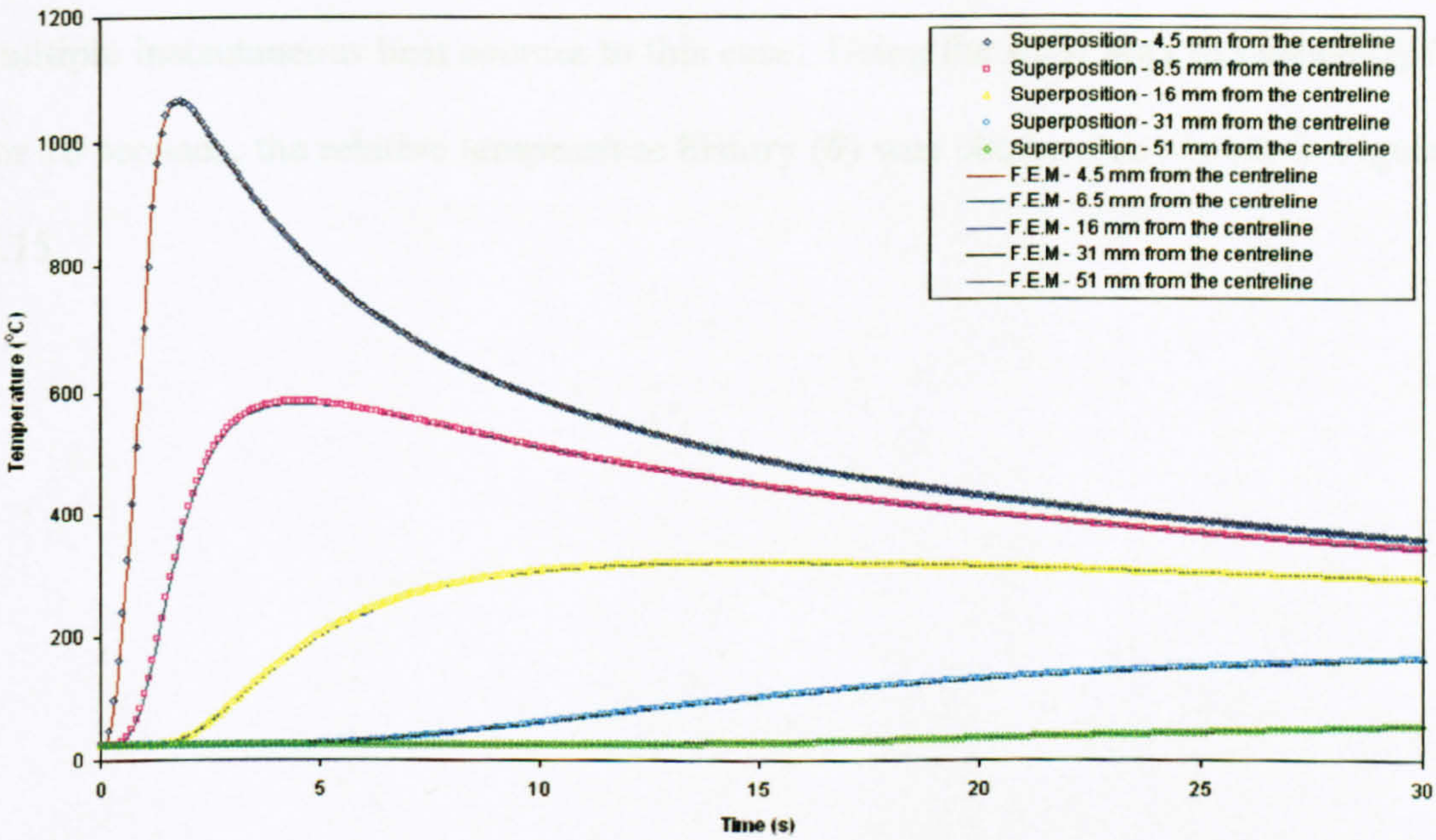

Figure 4.13

Comparing the analytical superposition with finite element temperature histories

4.5.2 Second case – Straight line ramp heat input rate

In this case, the heat source is assumed to take one second to release the same amount of heat (Q_{net}") to the plates in a straight line ramp manner, i.e. it ramp up from time t = 0 sec to time t = 1 sec in intervals of 0.1 sec. The heat input to the plate at every 0.1 seconds keep on increasing that is Q_0" = 0, Q_1" = 1/55Q", Q_2" = 2/55Q", Q_3" = 3/55Q", Q_4" = 4/55Q", Q_5" = 5/55Q", Q_6" = 6/55Q", Q_7" = 7/55Q", Q_8" = 8/55Q", Q_9" = 9/55Q", Q_{10}" = 10/55Q". Figure 4.14 shows the relative temperature history chart after applying the superposition procedure of the multiple instantaneous heat sources to this case. Using the same way in evaluating θ for 10 seconds, the relative temperature history (θ) was obtained as shown in Figure 4.15.

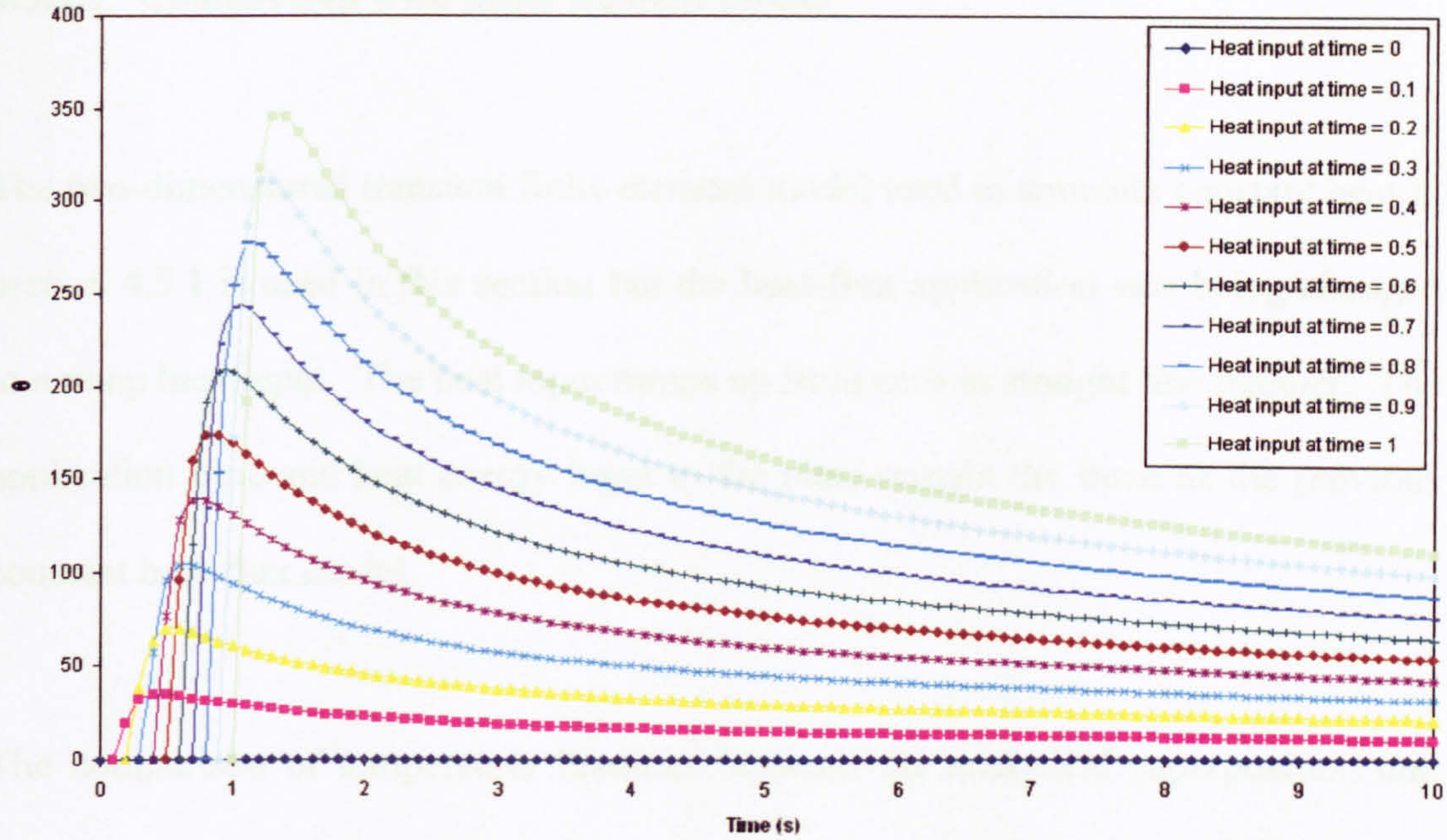

Figure 4.14

An illustration of superposition procedure of the multiple instantaneous heat sources

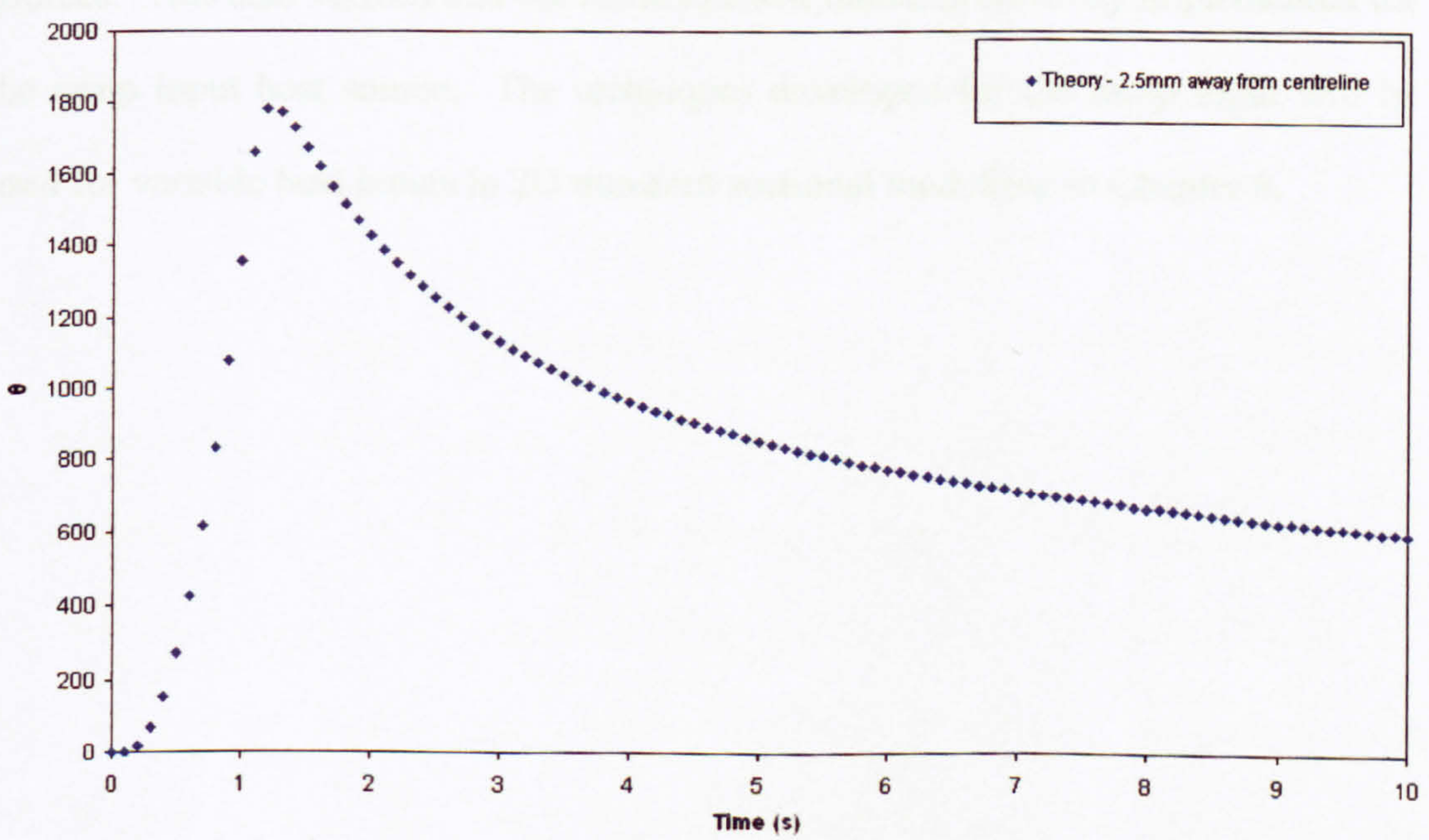

Figure 4.15

The relative temperature history, θ

4.5.2.1 Comparison with finite element model

The two-dimensional transient finite element model used to simulate constant heat in section 4.5.1 is used in this section but the heat-flux application was being changed to a ramp heat input. The heat input ramps up from zero in straight line manner. The application time and heat energy input to the plate remain the same as the previous constant heat-flux model.

The comparison of temperature histories between the analytical superposition and finite element model of ramp heat input is shown in Figure 4.16. The computer simulated temperature histories agree very well with those obtained from the analytical method of superposing the effects of a number of instantaneous heat sources. This also verifies that the finite element model is correctly implemented for the ramp input heat source. The techniques developed for the ramp input will be used for variable heat inputs in 2D transient sectional modelling in Chapter 6.

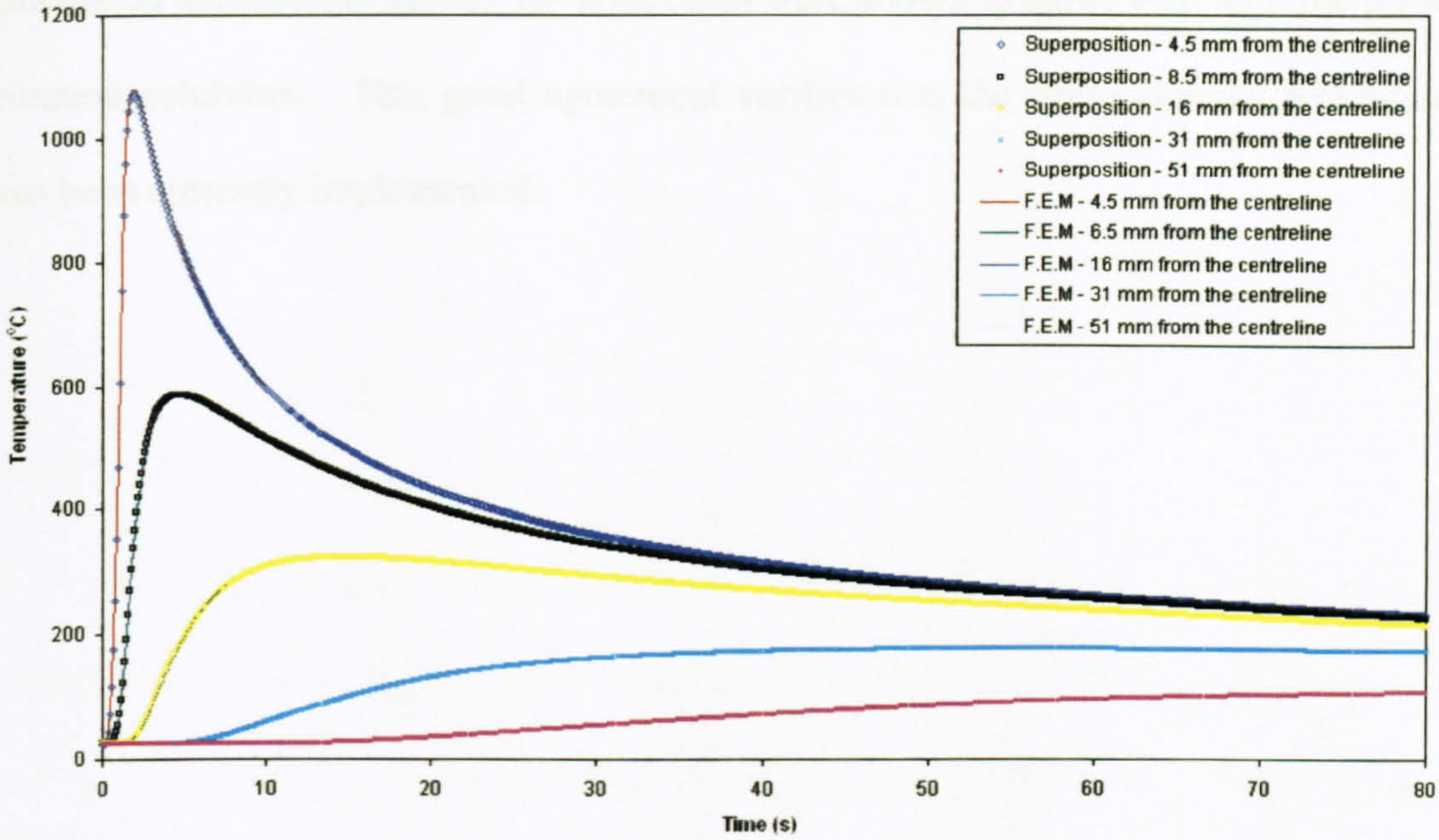

Figure 4.16

Comparing the analytical superposition with finite element temperature histories

4.6 Conclusion

This chapter has demonstrated how a three-dimensional transient heat flow problem of welding plates can be simplified to a three-dimensional steady-state one and then further simplified to a two-dimensional steady state one for full-penetration welds. The two-dimensional steady state heat flow problem for full-penetration welds can then be simplified to a one-dimensional transient heat flow one by assuming no heat flow in the welding direction. It has also demonstrated that the method of superposing the effects of a number of instantaneous plane heat sources (equation 4.2) can be used to calculate the temperature history of the plates. This method has been applied for both the constant heat input and a ramp heat input, and the

calculated temperature history for both cases were shown to agree well with the finite element solutions. This good agreement verifies that the finite element technique has been correctly implemented.

Chapter 5 – Preliminary Finite Element Simulation of the Welding Process

5.1 Introduction

It was noted in previous chapter that the analytically calculated temperatures are not sufficiently accurate due to neglect of heat losses from the surfaces of the plates, the effects of latent heat due to phase transformations and non-linearity of the thermal physical properties. In addition, it was observed that there is no analytical solution for the determination of a three-dimensional transient temperature field in a plate during welding. The finite element method is on the other hand capable of treating such complexities and take account of other neglected factors. For full penetration welds in thin plate, where the temperature is almost uniform across the thickness during the welding process a moving line heat source may be assumed. With finite element simulation, it is possible to apply volumetric heat generation instead of using a non realistic line heat source.

A three-dimensional transient finite element simulation was carried out to study the temperature distribution and history during the welding process and the results are presented in Section 5.4.

In Section 5.5, a three-dimensional steady state finite element simulation is described. In addition, the steady state model was extended to three times of its original length to provide a longer temperature history.

A two-dimensional transient simulation was carried out to study the temperature history during the welding process. This simulation was performed by assuming that heat conduction only occurs normal to the heat source as mention in previous chapter. The results of this model are presented in Section 5.6.

The experimental temperature histories published by Lee *et al* [35] are also use in this chapter. For the sake of completeness, the details of the experiment are described in Section 5.2.

5.2 Experiment

The size of each plate used for this experiment was 200mm × 75mm × 6mm thick. The gap between the plates was 2mm. The welding parameters used were: Voltage = 20 volts, Current = 160 amps, welding speed = 266 mm/min. The weld run took 45 seconds and the ambient temperature was measured as 25°C. The specimens were supported with insulation blocks under each corner. In this way, both the top and bottom surfaces of the specimen were exposed to the laboratory ambient conditions. 15 K-type thermocouples were force-fitted into one of the specimens, halfway through the thickness. The thermocouple positions are shown in Figure 5.1.

Temperatures from the thermocouples were recorded using a computer with Data Acquisition (DAQ) hardware.

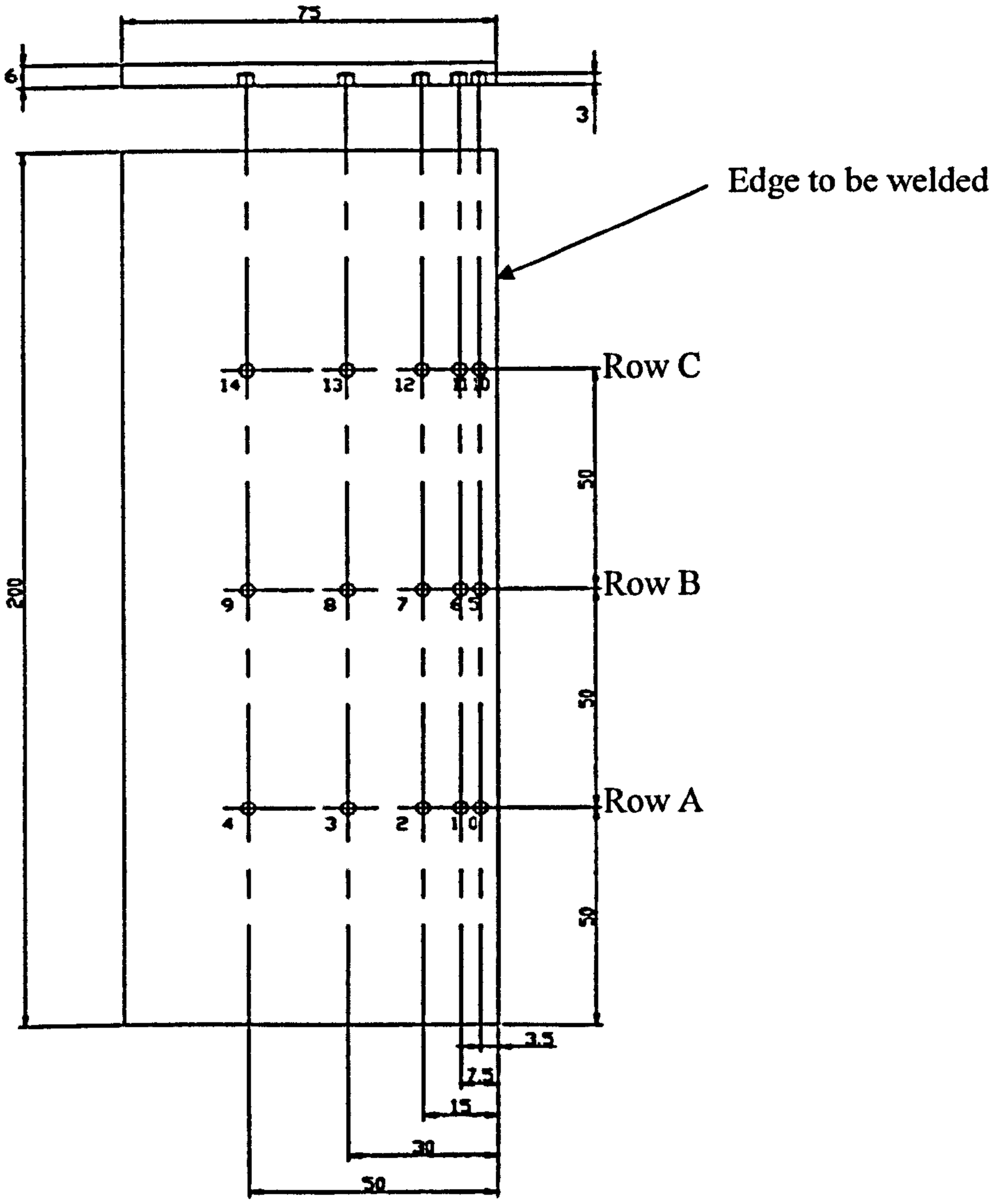

Figure 5.1

Dimensions (in mm) of weld specimen and thermocouples locations

5.3 Boundary conditions and properties used for the models

5.3.1 Heat Input Efficiency factor

The energy losses from the heat source are usually taken into account by an efficiency factor η, defined as, $\eta = Q_{net}/P$, where Q_{net} is the net power received by the weld and P is the welding electrical power.

Easterling [43] reported Metal Inert Gas welding net heat input efficiency factor was reported to be in the range of 0.66 to 0.75. The appropriate net heat input efficiency factor for all the models in this chapter was found to be 0.74 which is within the reported range. Therefore, the useful power supplied to the weld was 74% of 3200W, namely to 2368 W.

5.3.2 Surface heat loss by Natural Convection

During the welding process, there is heat loss to the surrounding from surfaces by natural convection and radiation. Natural convection describes heat loss to the surrounding fluid when warm, less dense fluid rises and cold, more dense fluid sinks under the influence of gravity. A convection coefficient h can be defined by Newton's law of cooling as:

$$Q_c = hA\,(T_s - T_f)$$

where Q_c is the heat loss through convection, h is the convection heat transfer coefficient, A is the surface area, T_s is the surface temperature of the conducting solid and T_f is the fluid temperature.

5.3.2.1 Evaluation of Heat Transfer Coefficients

Convective heat transfer is difficult to approach analytically and such a problem is more readily solved by dimensional analysis and experiment. Velocity is not listed as a variable in this case, as the fluid motion is due to the buoyancy forces acting within the fluid.

According to Lloyd and Moran [37], for flat surfaces facing upward, the Nusselt Number is given as:

$$Nu = 0.54Ra^{0.25}$$

For surfaces facing downward, the Nusselt Number is given as:

$$Nu = 0.27Ra^{0.25}$$

Where:

$$Ra = Pr\ Gr$$

$$\text{Grashof number } (Gr) = \frac{\beta g(T_s - T_f)l'\rho^2}{\mu^2}$$

Prandtl number (Pr) = $\mu C/k$

Nusselt number (Nu) = hl/k

β is the coefficient of cubical expansion, ρ is the density of the fluid, g is gravitational acceleration, μ is viscosity of the fluid, l is the characteristic length for the calculation of flat surfaces (equal to the surface area divided by its perimeter, k is the conductivity of the fluid and C is the specific heat capacity of the fluid.

From the above correlations, it can be seen that the heat transfer coefficient varies with temperature and thus varies with time and location as the plate temperature changes during the welding process. However, assuming an overall average plate temperature of 200°C, the heat transfer coefficient was found to be 10 W/m^{2}K for the top surface and 5 W/m^{2}K for the bottom surface. These values were used in the simulation. For the vertical side surfaces, an approximate value was deemed adequate due to the small surface area and low temperature for the edges. A value of 12 W/m^{2}K was therefore used.

5.3.3 Surface heat loss by Radiation

When the plate is thermally excited, heat loss by radiation transmitted via emitted electromagnetic waves (infrared heat rays) into the surrounding from the surfaces of the plate. This electromagnetic radiation emits in all directions from the welding plate during the welding process. The plate is assumed to be a grey body and the heat transfer by radiation from a small convex to a large enclosure Q_r is given by

$$Q_r = \sigma A \varepsilon (T_s^4 - T_a^4)$$

where σ is the Stefan-Boltzmann constant (5.67×10^{-8} W/m^{2}K^4), A is the surface area, T_s is the hot surface temperature of the plate, T_a is the temperature of the large enclosure and ε is the emissivity of the surface.

Above 200°C, radiation heat loss becomes increasingly important and is particularly significant in the high temperature regions close to the weld. The radiative heat transfer may be expressed in terms of a radiation heat transfer coefficient, $h_r = \sigma\varepsilon(T_s+T_a)\ (T_s^2+T_a^2)$ with $Q_r'' = h_r(T_s - T_a)$. The emissivity depends strongly on the wall temperature and the surface conditions. Values for ε were obtained from [38] and the radiation coefficient h_r can be calculated. This is then coupled with the convection coefficient h_c to give a combined heat transfer coefficient which can be applied to the simulation model. The emissivity and the combined coefficient for the top surface are shown in Figure 5.2.

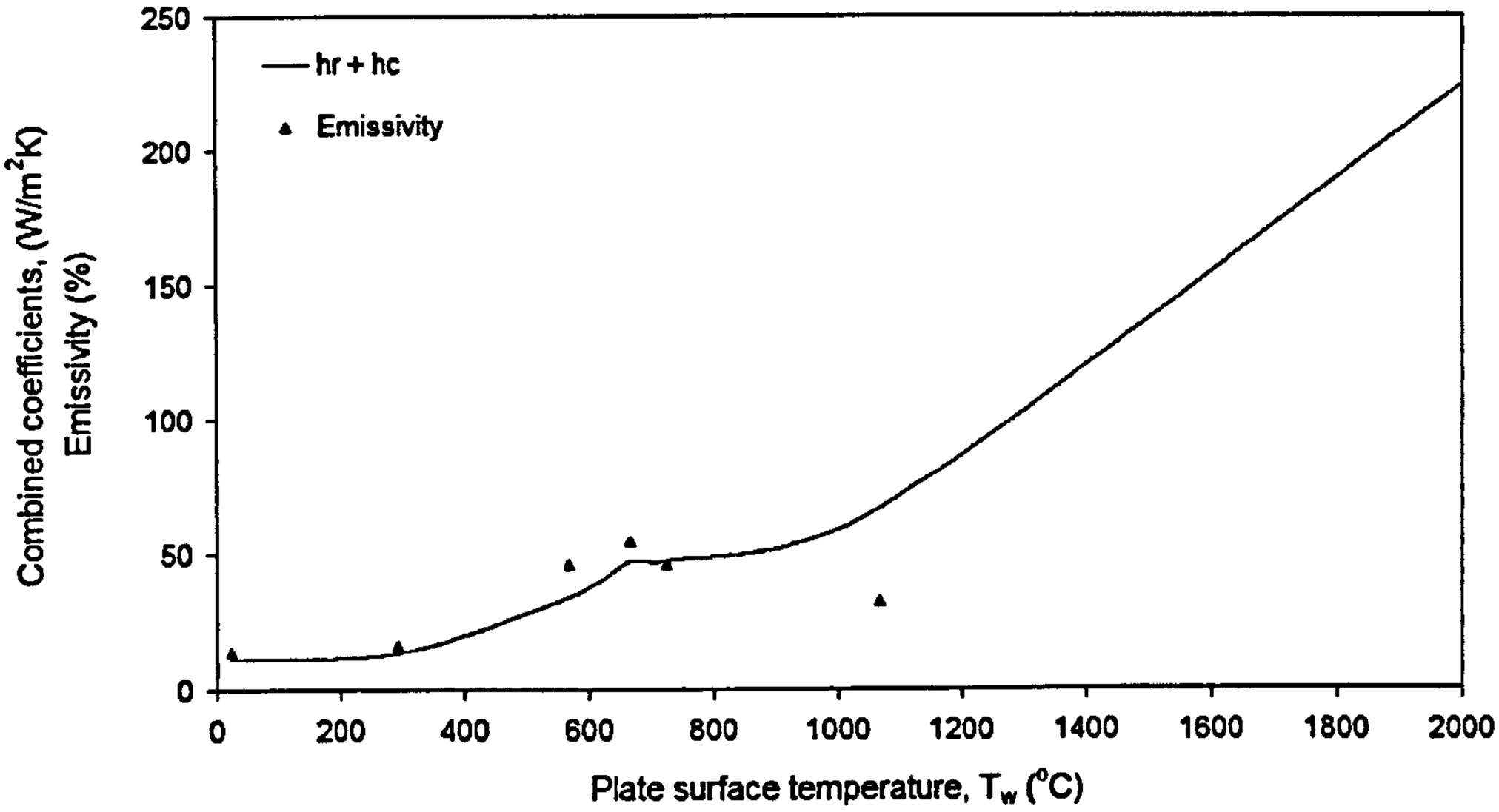

Figure 5.2

Emissivity and Combined heat transfer coefficient

5.3.4 Thermal Physical Properties

The thermal properties are clearly non-linear and vary significantly with temperature. The thermo-physical properties of low carbon steel (0.13%C) used in this study are referenced from [35]. Figure 5.3 shows the variation of the thermal conductivity with temperature. It can be seen that a high conductivity (121 W/m K) is applied to the weld pool to simulate heat transfer by arc impingement and weld pool-stirring effects during the welding process. The effect of applying an artificial conductivity enhancement to the weld pool will be discussed in a later chapter. (also see [38-42] for other types of material)

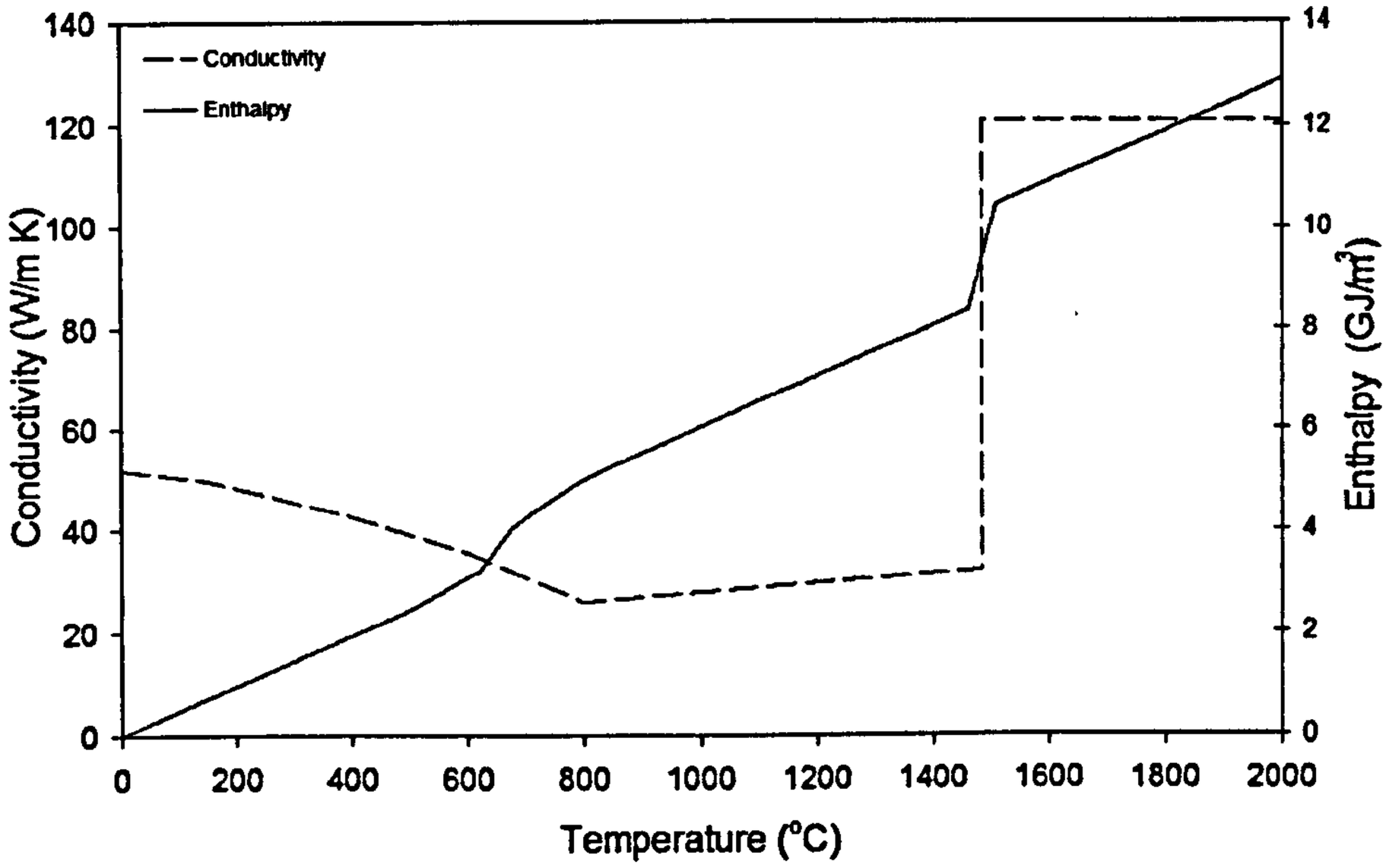

Figure 5.3

Thermal conductivity and Enthalpy

Figure 5.3 also shows the enthalpy per unit volume, being the product of density and specific heat. The use of enthalpy instead of specific heat is recommended for finite element analysis involving phase changes, since it circumvents the need for artificially high specific heats to account for latent heat effects during phase changes. In this model, the latent heat of fusion (2.1 GJ/m^3) is distributed over the melting range from 1486°C to 1510°C. It should also be noted that there are also phase changes in the solid phase when ferrite transforms to austenite or austenite to ferrite approximately over the range of 600°C to 800°C.

5.4 Three-dimensional transient analysis

This simulation was performed as a transient thermal analysis. The actual welding operation was simulated by applying heat generation corresponding to the net power supplied by the electric arc to a set of elements in the gap between the plates. This was applied for a time interval corresponding to the time for passage of the arc over the elements, before removing the load and moving on to the next set of elements. The operation was carried out for the entire length of the weld.

The element type chosen to perform the 3D transient simulations was 'SOLID70'. SOLID70 has a 3D thermal conduction capability and has eight nodes with a single degree of freedom, namely temperature, at each node. The element is therefore applicable to 3D transient thermal analysis.

Since the plates to be welded are symmetric along the weld centreline, the computer model needs to include only one plate plus half the gap for the weld. The thermal gradients are steeper near the heat source and the model requires a finer mesh in that region. Further away from the weld, the thermal gradients are less steep, and hence a coarser mesh is adequate. Along the direction of the weld, the model was divided into forty equal sets of two elements, to correspond with 40 equal time steps at a constant welding speed of 4.44 mm/sec. The mesh pattern of the resulting model is shown in Figure 5.4.

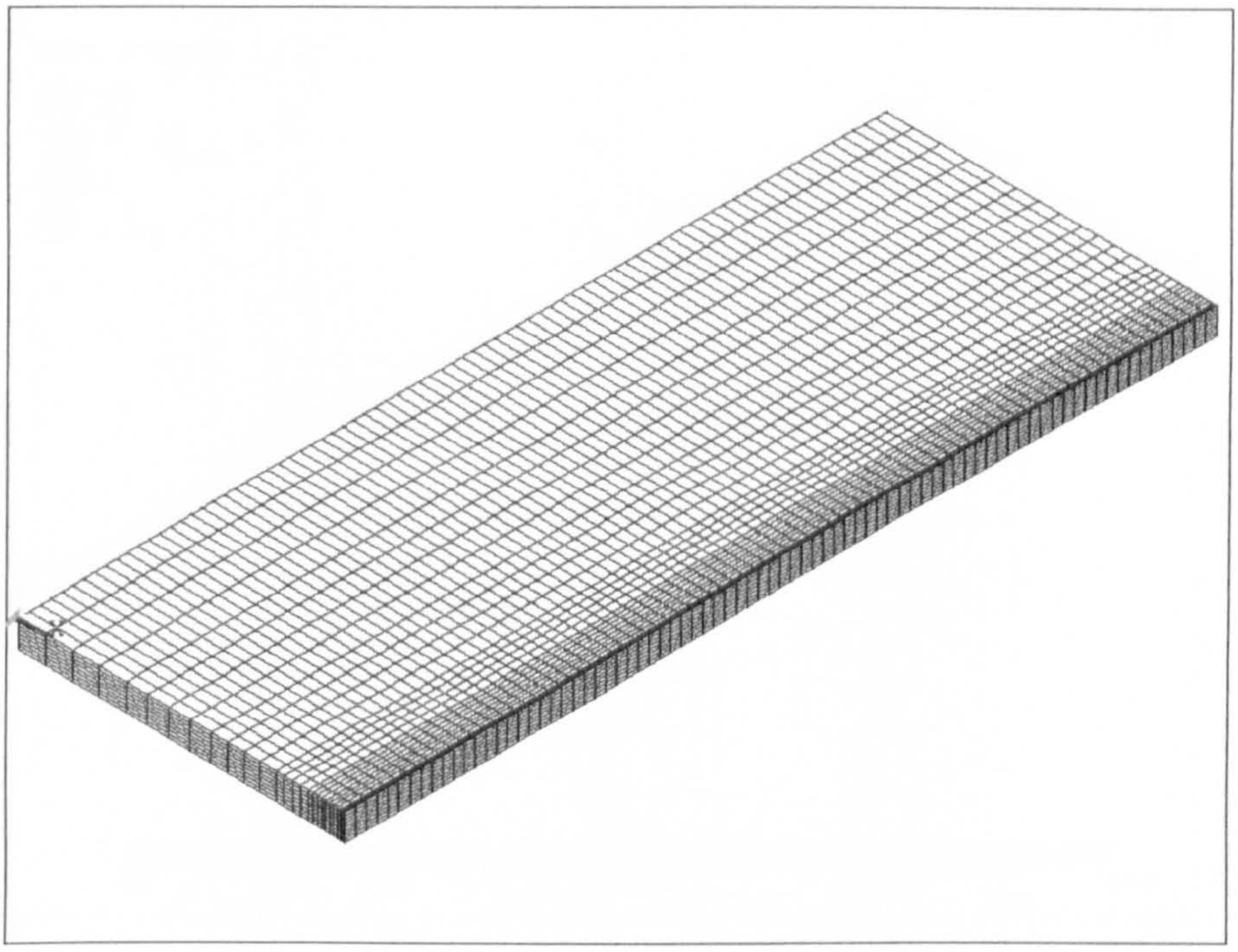

Figure 5.4

Finite element mesh pattern

5.4.1 Discussion of Results

An overall view of the temperature contours in the model at a time of 39.4 seconds from the commencement of welding is shown in Figure 5.5. The maximum temperature of the weld pool was in the region of 2000°C throughout the simulated welding process. This is in good agreement with the experimentally measured stationary weld pool where the peak temperature ranged from 1950°C to 2708°C [18].

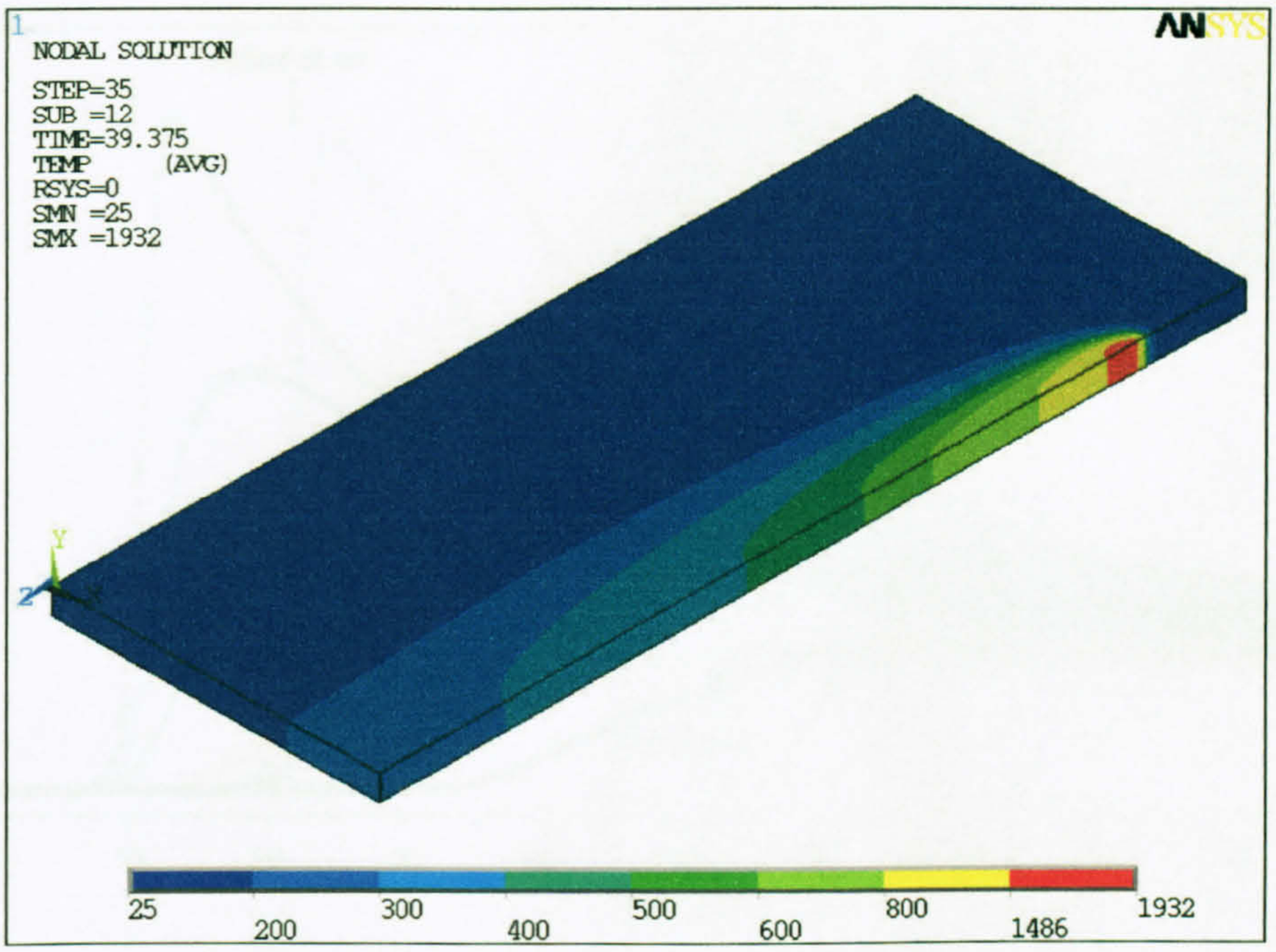

Figure 5.5

Temperature contour at 39.4 seconds

Figure 5.6 shows the temperature histories of measurements at locations 3.5, 7.5, 15 and 30 mm from the edge of the plate (4.5, 8.5, 16 and 31 mm from the weld line respectively). The results are almost identical for the three rows of thermocouples, separated from one another by a time corresponding to the spacing between the rows of thermocouples. The results show the temperatures rising abruptly to a peak as the weld pool passes the measurement points and then falling away after the arc has passed. The instant at which the arc passes the various rows of thermocouples are also shown. The figure highlights the fact that there is a progressively bigger time lag between arc passage and the instant when the peak temperatures are sensed by the thermocouples the farther they are from the weld centreline.

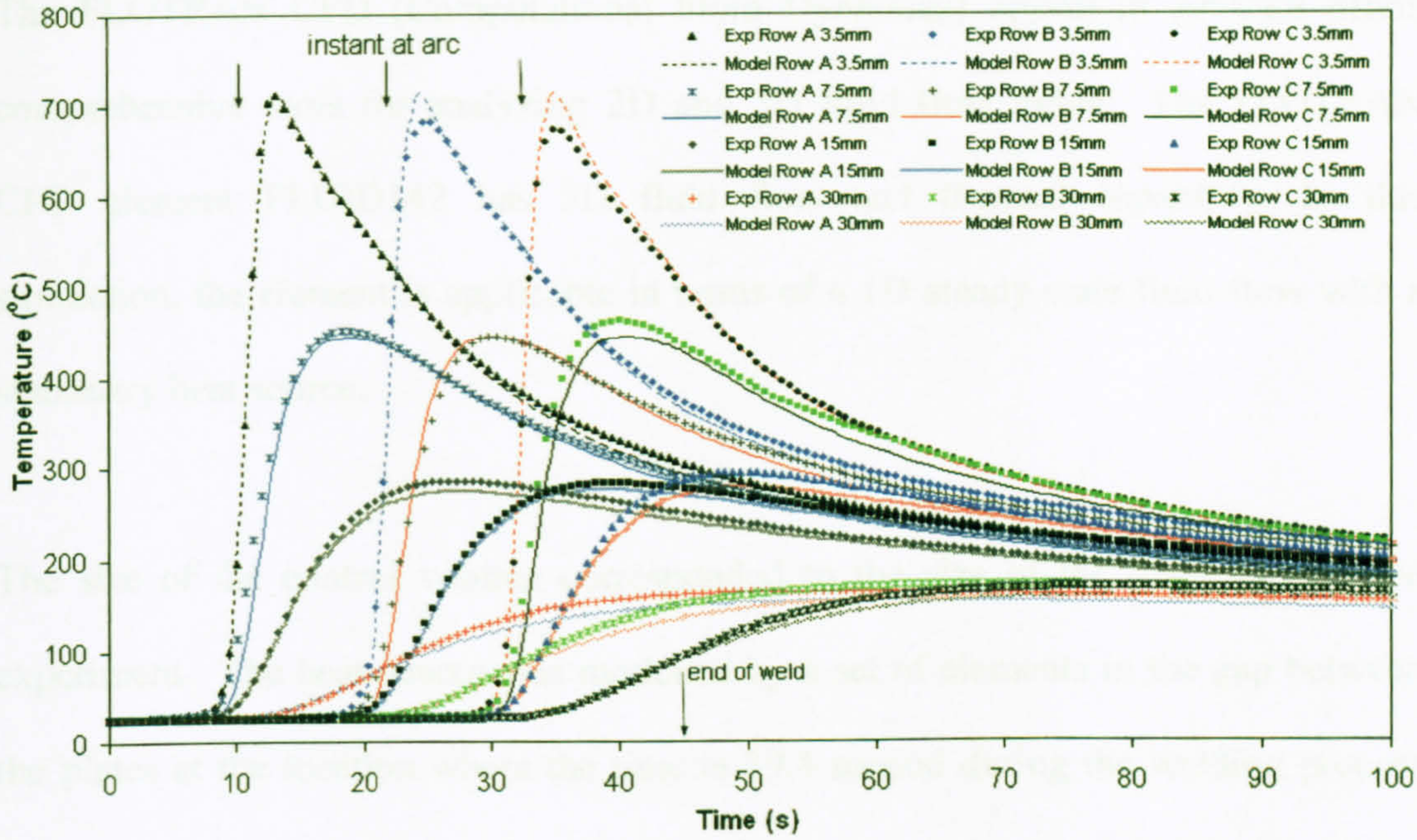

Figure 5.6

A comparison between the experimental and 3D transient model temperature histories

5.5 Three dimensional steady state analyses

The previous chapter noted that when the heat source is moving at a constant speed in a straight line, a temperature distribution pattern appears to remain constant to an observer moving with the heat source. Thus by considering the heat source to be stationary with the plate moving at a constant speed, the problem can be converted into a steady state model. Such a model was computed according to Section 4.3 of the previous chapter assuming a heat source in a moving media, where the moving media is a pseudo-fluid that having the properties of the steel plate. This fluid moves through a control volume.

The FLOTRAN CFD (Computational Fluid Dynamics) option in ANSYS offers comprehensive tools for analyzing 2D and 3D fluid flow fields. The FLOTRAN CFD element FLUID142 has 3D fluid flow and thermal capability. In this simulation, the element is applicable in terms of a 1D steady state fluid flow with a stationary heat source.

The size of the control volume corresponded to the size of the plate used in the experiment. The heat source was modelled by a set of elements in the gap between the plates at the location where the time is 39.4 second during the welding process (as in Figure 5.5). The actual welding operation was simulated by applying heat generation corresponding to the net power supplied by the electric arc to these elements. The simulation was done using specific heat instead of enthalpy because the ANSYS FLOTRAN package does not permit the use of enthalpy. The specific heat used in this model was converted from the enthalpy used in the 3D transient model previously, using the relationship:

$$\Delta H(T) = \int \rho C(T)\, dT$$

The converted specific heat is shown in Figure 5.7.

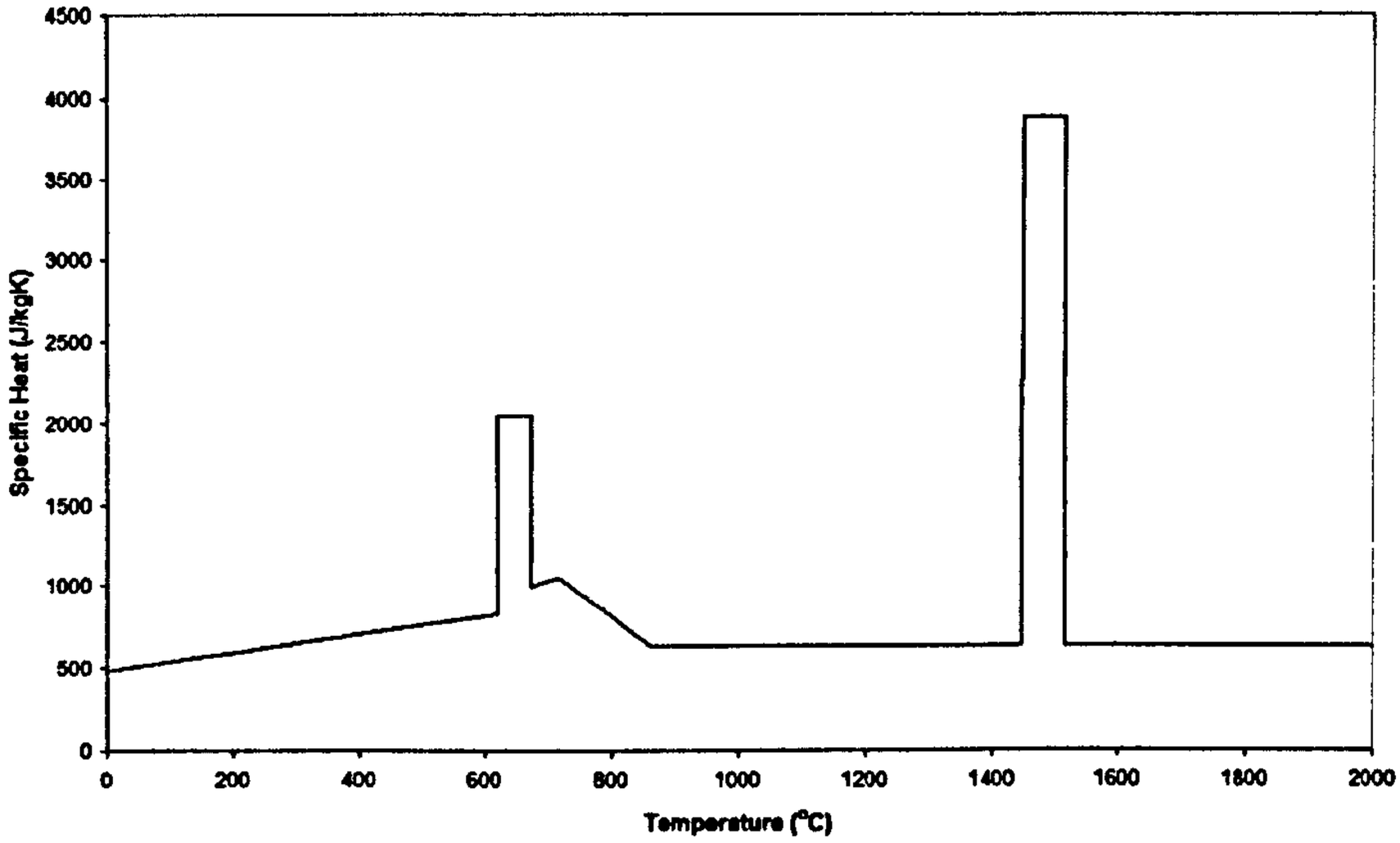

Figure 5.7

Specific Heat

Since there was symmetry along the weld centreline during welding, again only one plate plus half the gap for the weld was modelled. The thermal gradients are steeper near the heat source and the model requires a finer mesh in that region. The mesh pattern of the resulting model is shown in Figure 5.8.

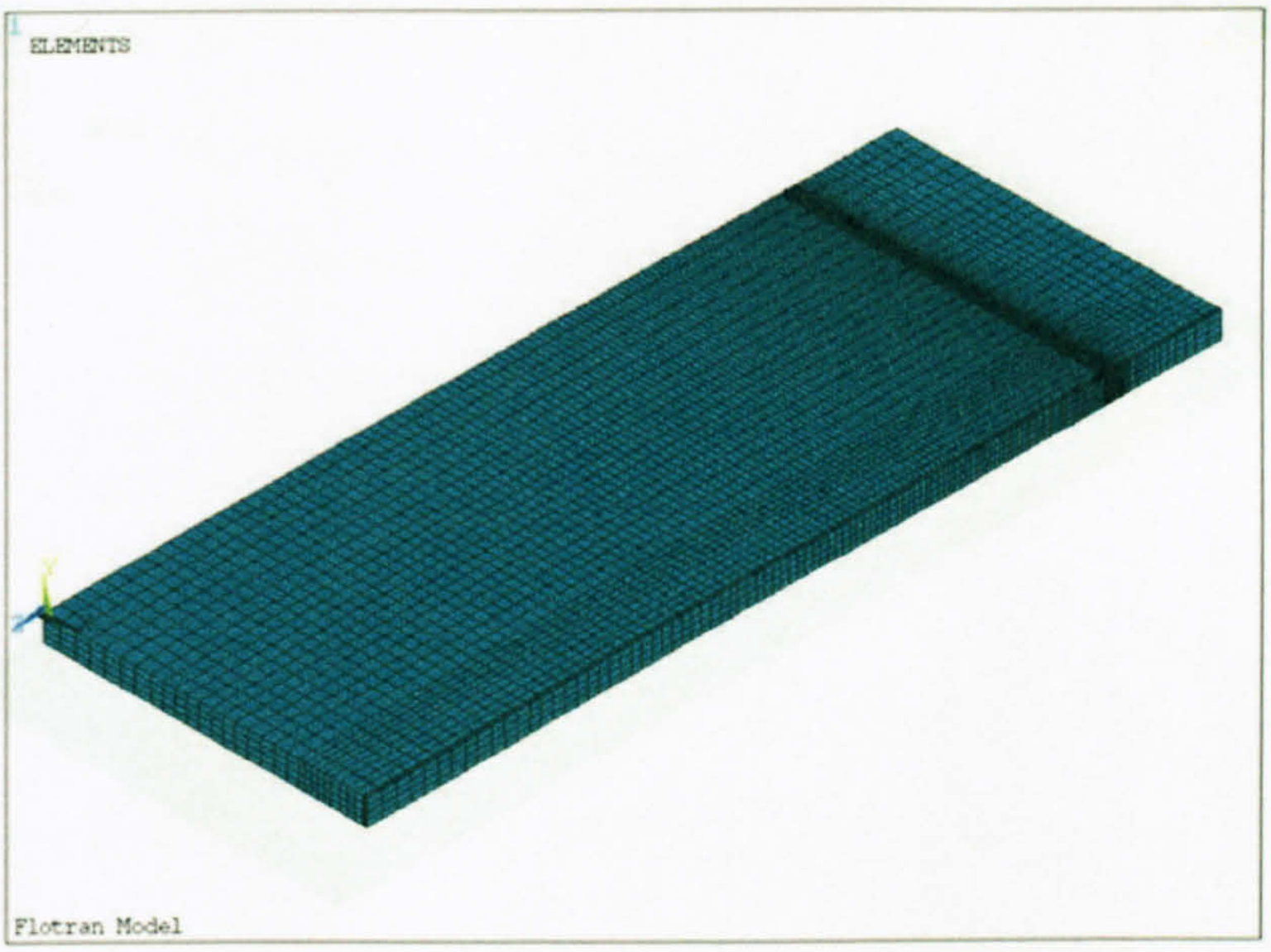

Figure 5.8

Finite element mesh pattern

5.5.1 Discussion of the 3D steady state model results

Overall temperature contours at time 39.4 seconds during the welding process is shown in Figure 5.9. The maximum temperature of the weld pool was around 1805°C. This is not in good agreement with the experimentally measured stationary weld pool where the peak temperature of weld pool ranges from 1950°C to 2708°C [18]. However, this did not greatly affect the temperature fields some distance away from the weld.

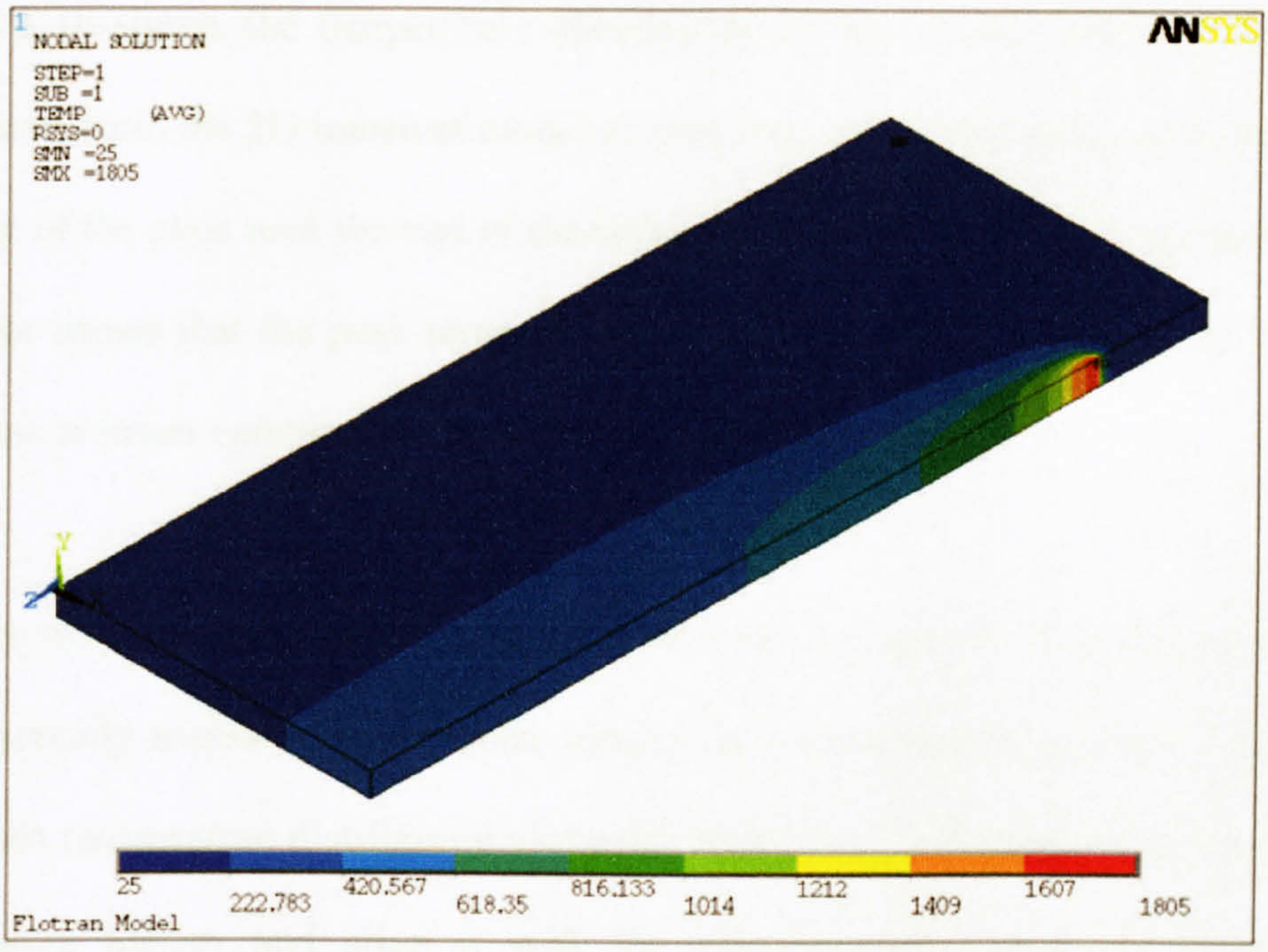

Figure 5.9

Temperature contour at 39.4 seconds

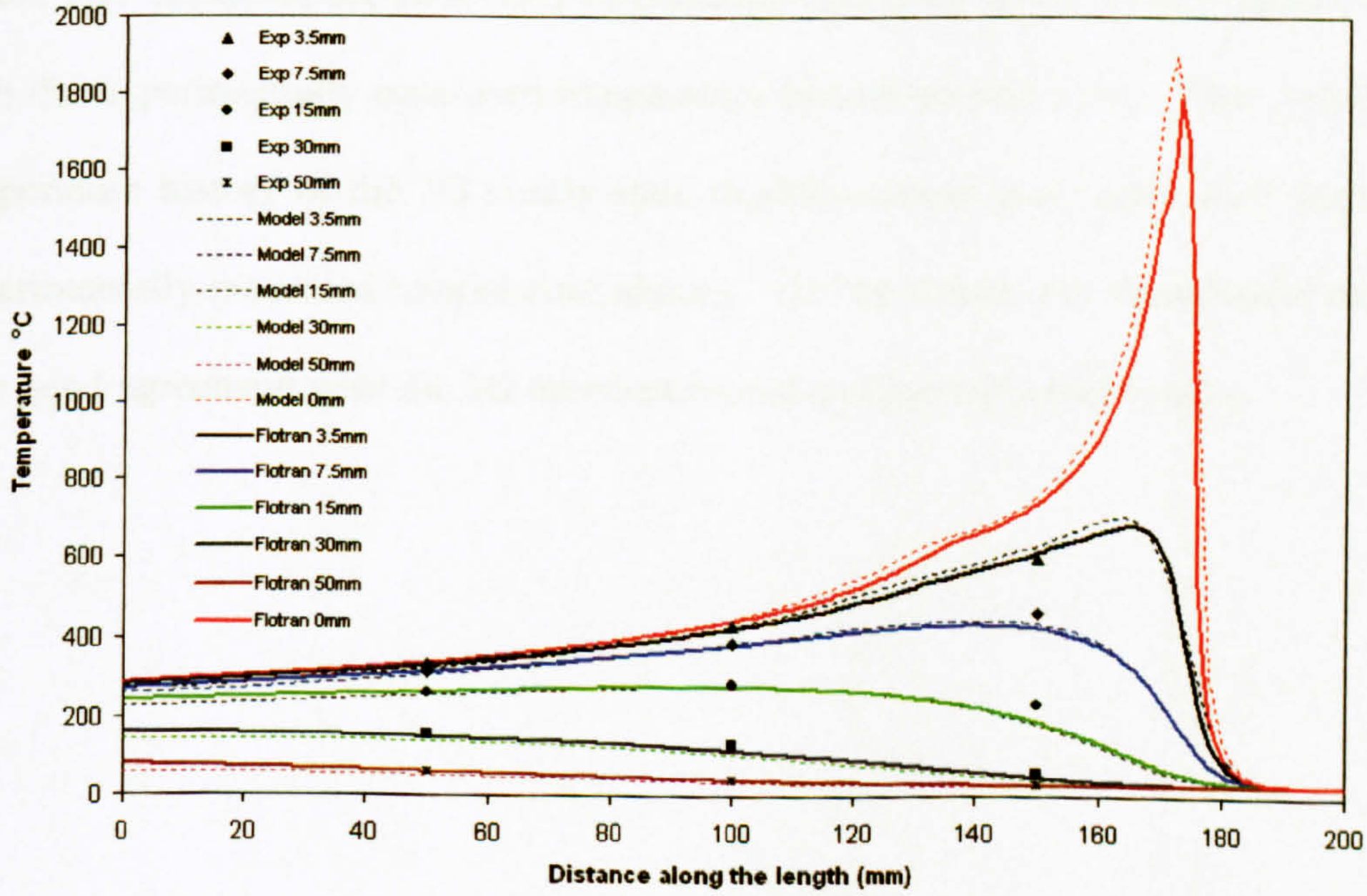

Figure 5.10

Temperature distribution in direction of weld

Figure 5.10 shows the temperature distribution of the current steady state model. The results from the 3D transient model of previous section at various distances from the edge of the plate near the end of the weld run (time 39.4 seconds) are also shown. This plot shows that the peak temperature of the steady state model along the weld centreline is lower compared to the 3D transient model.

In order to make comparison of results between the steady state model and the experimentally measured temperature history, it is necessary to develop a technique to convert temperature distribution along the weld of the 3D steady-state model into temperature history and align it with the experimentally measured temperature history. This technique has been developed and placed in Appendix E.

Figure 5.11 compares the converted temperature history of the 3D steady-state model with the experimentally measured temperature history (centre row). The converted temperature history of the 3D steady-state model matches reasonable well with the experimentally measured temperature history. On the whole, the steady state model is in good agreement with the 3D transient model and experimental results.

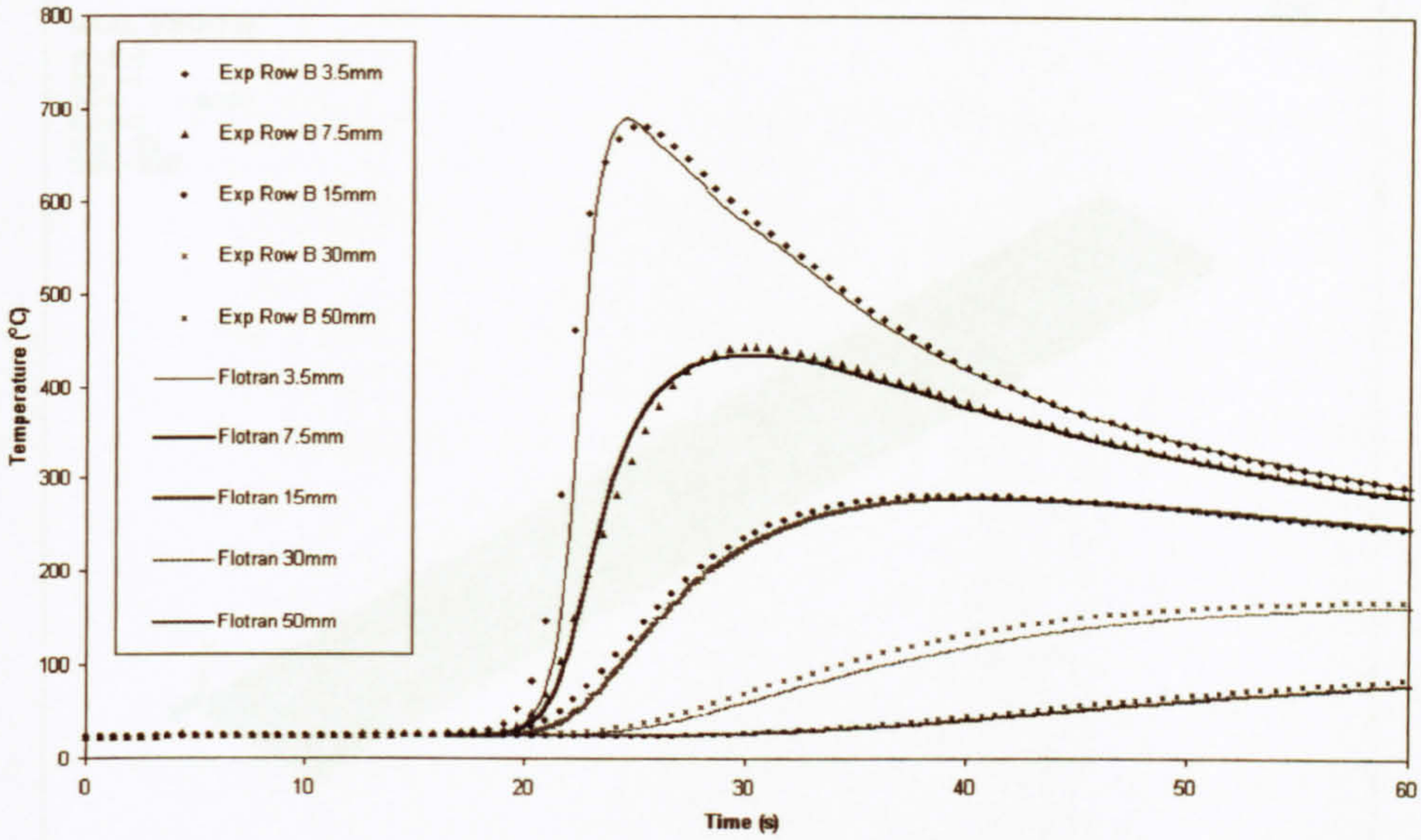

Figure 5.11

Comparison between converted temperature histories of the steady state model and experimentally measured (centre row)

5.5.2 The extended 3D steady state model

In this section, length of the steady state model was extended by a factor of three times in an attempt to obtain a larger temperature history range. Figure 5.12 shows an overall temperature contour plot of the extended model. This model took about 45 minutes for the solution. The weld pool peak temperature dropped a few degrees in the extended model. This plate is acting like a fin. In general, a longer plate will result in more heat loss from the surface.

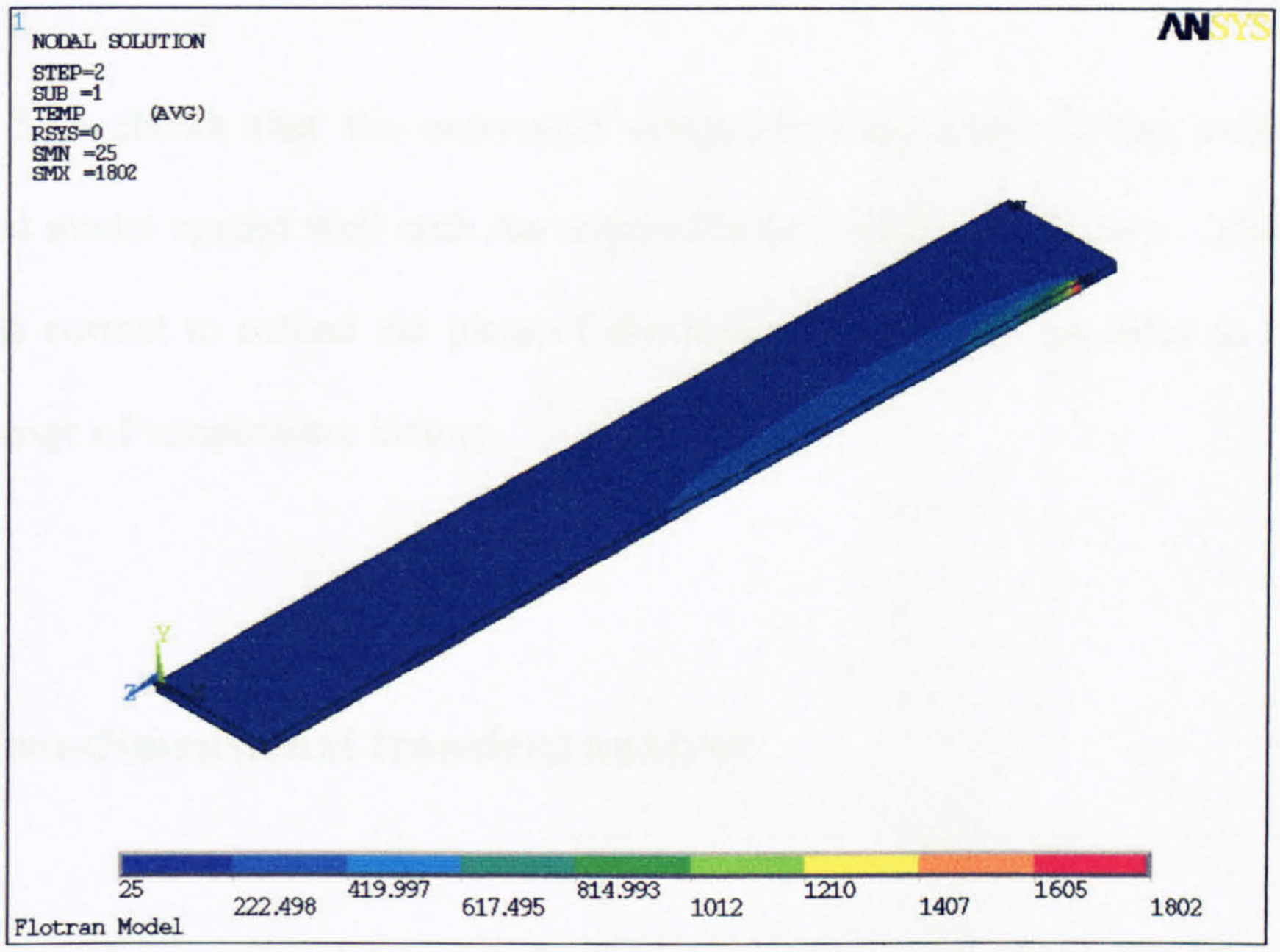

Figure 5.12

Temperature contour the extended model

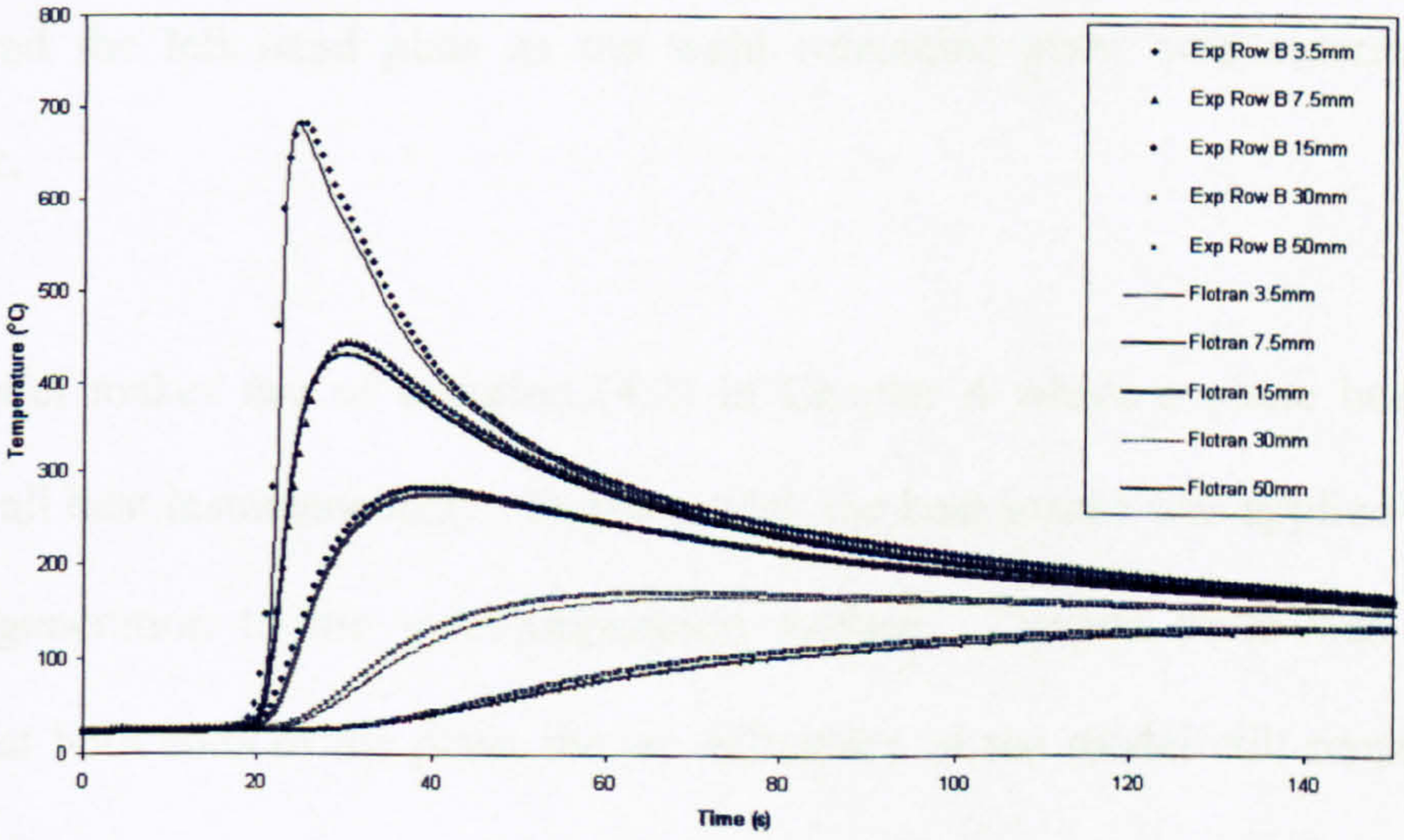

Figure 5.13

Comparison between the converted temperature histories of the steady state extended model and experimentally measured (centre row)

Figure 5.13 shows that the converted temperature histories of the steady state extended model agreed well with the experimental temperature history. This shows that it is correct to extend the plate of the steady state model in order to obtain a larger range of temperature history.

5.6 Two-dimensional transient analysis

As mentioned in section 4.4.1, the element type chosen to perform the 2D transient simulations is 'PLANE55'. PLANE55 has a 2D thermal conduction capability and has four nodes with a single degree of freedom, namely temperature, at each node. The element is applicable to 2D transient thermal analysis. This model only considered the left hand plate as the weld centreline plane was assumed to be adiabatic.

This model makes use of equation (4.2) in Chapter 4 where a plane heat source releases all heat instantaneously. In this model, the heat source was applied for 1 ms as heat-generation to the weld-preparation surface. Despite there was no heat transfer at both ends of the plate, the arc efficiency of the model still remained the same, 74%.

Figure 5.14 shows a comparison of temperature histories 2D transient and experimentally measured. The computer simulated temperature histories of 2D

transient sectional model agreed reasonably well with experimentally measured temperature histories.

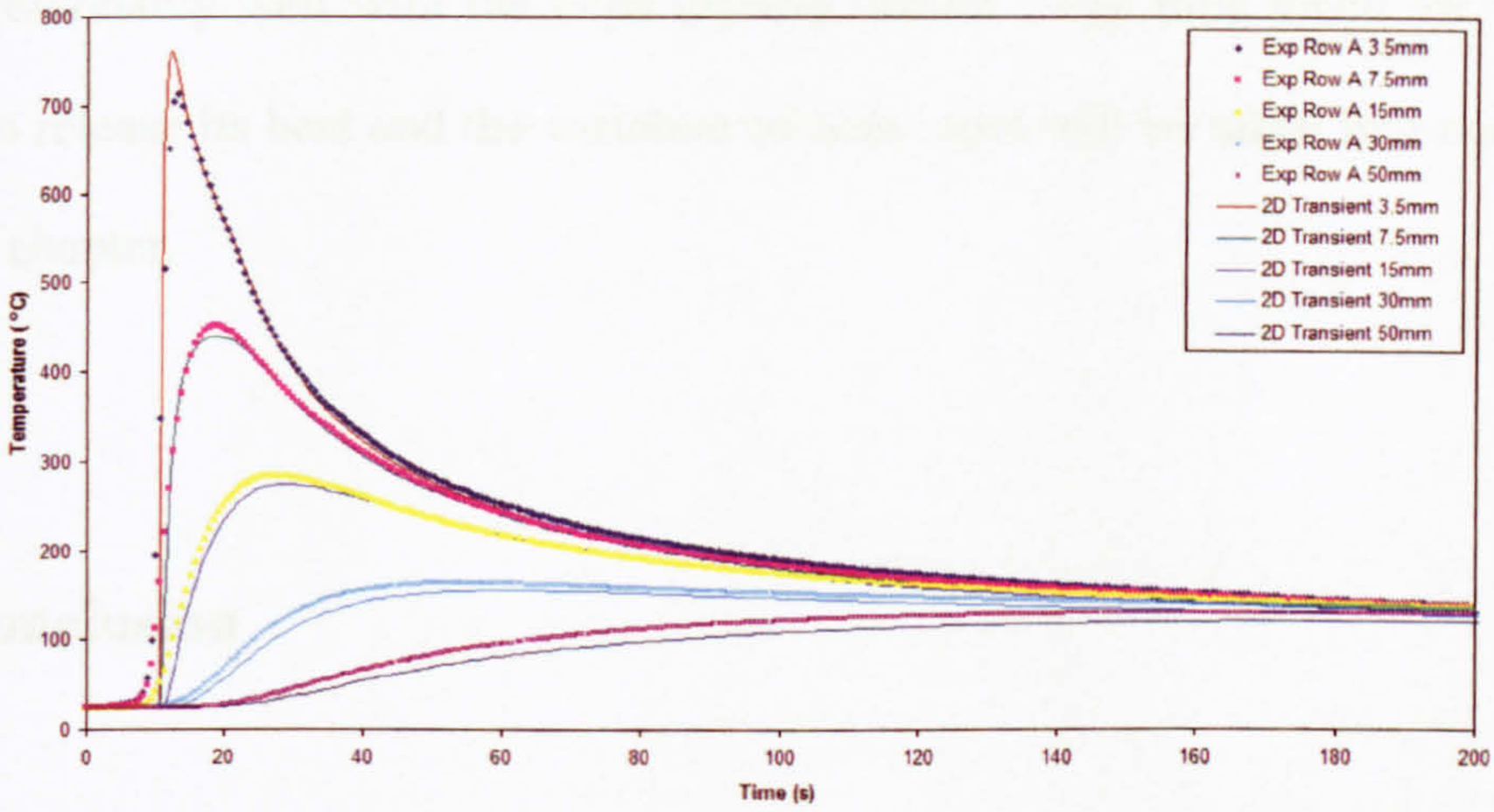

Figure 5.14

A comparison between the experimental and 2D transient model temperature histories

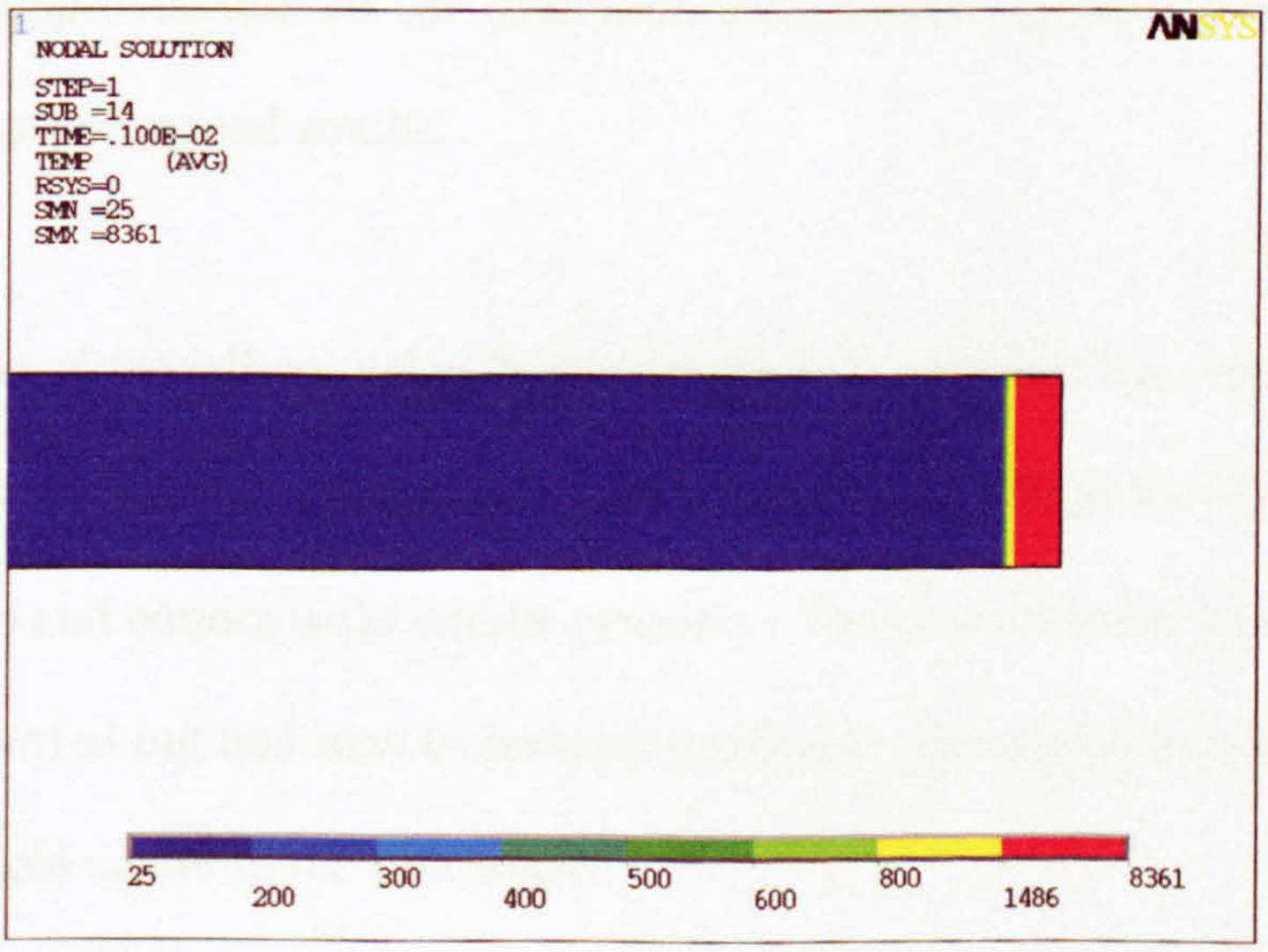

Figure 5.15

Temperature Contour of 2D transient sectional Model

Figure 5.15 shows a temperature contour plot of the model. The peak temperature of the weld pool was unreasonably high (8361°C). This obviously was due to the assumption of heat release over one millisecond. Otherwise, the simulated results agreed reasonably well with the experimental results. The time taken for the heat source to release its heat and the variation of heat input will be taken into account in the next chapter.

5.7 Conclusion

Moving heat source theory has been successfully applied to the finite element models with convection and radiation applied to the outer surfaces of the models and the non-linearity of thermo-physical properties applied to the conduction elements. The accuracy of the predicted temperature field at a distance from the heat source has been greatly improved and all the simulated temperature history curves agree very well with the experimental results.

This technique of modelling, using heat generation to simulate the welding process, cannot predict the top and bottom temperature near to or within the HAZ nor can it predict the top and bottom weld widths properly. Therefore, further simulation work needs to be carried out and new techniques need to be developed in order to predict temperature field nearer to the heat source.

The main outcome of this study is that the input data for the thermo-physical properties of the material are appropriate, together with the method used to model surface heat losses. These data and techniques will be used in the development of an improved model in the next chapter.

Chapter 6 - Finite Element modelling of the temperature fields near the welding heat source

6.1 Introduction

The object of this Chapter is to present the computational techniques which can be used to calculate the temperature fields near the heat source and capture the top and bottom widths of the weld.

During the welding process, the amount of heat received by the welding plate can be considered to be made up of two components: the heat from the welding arc and the heat from the molten filler metal. Both of these components are produced from the electric power supplied after accounting for the losses of heat to the surroundings.

C. S. Wu and J. Q. Gas [32] measured the heat flux distribution of a stationary welding arc and found it to be distributed in a Gaussian manner. Therefore, the simulations presented in this chapter will use the same assumption regarding the heat flux distribution.

The amount of heat from the molten filler metal could be estimated if the temperature of the molten droplets was known, but, as far as the author is aware the temperature of molten droplets has not been measured. However, Kran [18] measured the stationary weld pool surface temperature and reported the peak

temperature as 2708°C for a welding current of 150A. Based on Kran's [18] measurement, the droplets temperature would be higher than 2708°C because there must be some heat lost during metal transfer. Also if the current was higher than 150A, these droplets temperature could be even higher than 2708°C. In any case, the droplet temperature cannot be higher than the boiling point of the liquid metal, which is about 3000°C for impure iron. Therefore, for the purpose of calculating the amount of heat due to the molten filler metal, the temperature of the droplets was assumed to be 3000°C for simplicity. A preliminary calculation shows that the amount of heat attributable to the molten filler metal can therefore only account for approximately 40% of the net heat input to the plate. Therefore, almost 60% of the net heat input to the plate is attributable to the welding arc. The sensitivity of the droplet temperature to the simulation results will be discussed in the next chapter.

Dynamic weld pool stirring during the weld process causes enhancement in heat transfer and also evens up heat distribution in the weld pool. Many authors [12, 16, 19, 23, 27 & 30] use an artificial conductivity enhancement ranging from 121 W/mK to 400 W/mK to simulate the weld pool stirring effect, but without physical justification. This is because, as far as the author is aware, there are no publications on experiments which capture the weld pool stirring motion and study the enhancement of heat transfer during welding. A conductivity enhancement of 121 W/mK was adopted for all the 3D transient models and 3D steady state models in this chapter.

The remainder of the current chapter is presented in the following manner. Section 6.2 shows the development of the finite element heat source to represent the actual welding heat source for simulating the temperature fields of a single pass plate welding. Section 6.3 describes the methodology on the derivation of parameters such as efficiency factor and radius of the Gaussian heat source for simulation. Section 6.4 describes on the boundary conditions of the models. Section 6.5 explains the operation of applying the finite element heat source to three-dimension (3D) transient modelling and discusses the simulation results while Section 6.6 shows 3D steady-state modelling. Section 6.7 describes how the 3D finite element heat source can be applied to the two-dimension (2D) transient sectional models and the simulation results are discussed. Finally, the last section comments on the accuracy of the simulation results and states experience for simulation.

6.2 Heat sources applied to finite element models

6.2.1 Heat source due to filler metal

As the molten filler metal will take the shape of the weld- preparation once the weld-preparation has been filled, the heat due to the molten filler metal can be calculated from the energy rise from ambient temperature to boiling point (an assumption) of the volume of metal in the weld-preparation. Thus, on a per unit time basis, the heat due to the liquid metal is:

$$Q_{prep} = U \times A_{prep} \times (h_{fb} - h_{ia}) \text{ ---------- (6.1)}$$

where Q_{prep} is the heat due to the liquid metal; U is the welding speed; A_{prep} is the cross-sectional area of the weld-preparation; h_{fb} is enthalpy of liquid metal at boiling point (18 GJ/m^3) and h_{ia} is enthalpy of solid metal at ambient temperature (98 MJ/m^3).

6.2.2 Heat source due to welding arc

The net heat input is obtained from:

$$Q_{net} = V \times I \times \eta \text{ ---------- (6.2)}$$

where Q_{net} is the net heat input to the plate; V is the welding voltage; I is the welding current and η is the welding heat input efficiency factor.

The amount of heat due to the welding arc can be obtained by subtracting the heat due to liquid metal from the net heat input to the plate as follows:

$$Q_{arc} = Q_{net} - Q_{prep} \text{ ---------- (6.3)}$$

where Q_{arc} is the amount of heat due to welding arc.

As mentioned in the section 6.1, the heat flux due to the welding arc is approximately Gaussian distributed and has been applied here as a Gaussian distribution to the

models. The Gaussian heat flux being used for these simulations was proposed by Pavelic et al. [9] that takes the shape of a normal distribution function. The derived function for the heat flux is given by:

$$q(r) = \frac{-\ln 0.01 \times Q_{arc}}{\pi r_H^{\,2}} e^{\frac{\ln 0.01}{r_H^{\,2}} r^2} \quad \text{---------- (6.4)}$$

where $q(r)$ is the heat flux distribution as a function of radius; r_H is the radius of the heat source and r is the variable radius ranging from 0 to r_H. It should be noted that the value of 0.01 in the above function is to take into account 99% coverage of heat (Q_{arc}) due to welding arc. Detail derivation of the above function can be found in appendix D.

6.2.3 Combining the two heat sources

The heat from the welding arc was applied as a Gaussian distributed surface heat flux on the top surface of the model and the heat from the filler molten metal was applied as heat generation to a weld-preparation volume of 2 mm in length containing a number of elements in the welding direction. Section 6.5 will explain why the length of this weld-preparation volume is being kept to a size of 2 mm. Figure 6.1 shows the left-hand half of the combined heat source which was used in the finite element model. It should be noted that, for simplicity, the weld bead due to the overfill of filler material during the welding process was not taken into account in these models.

This should not present a problem as the energy in the overfilled material is accounted for as part of the surface heat flux.

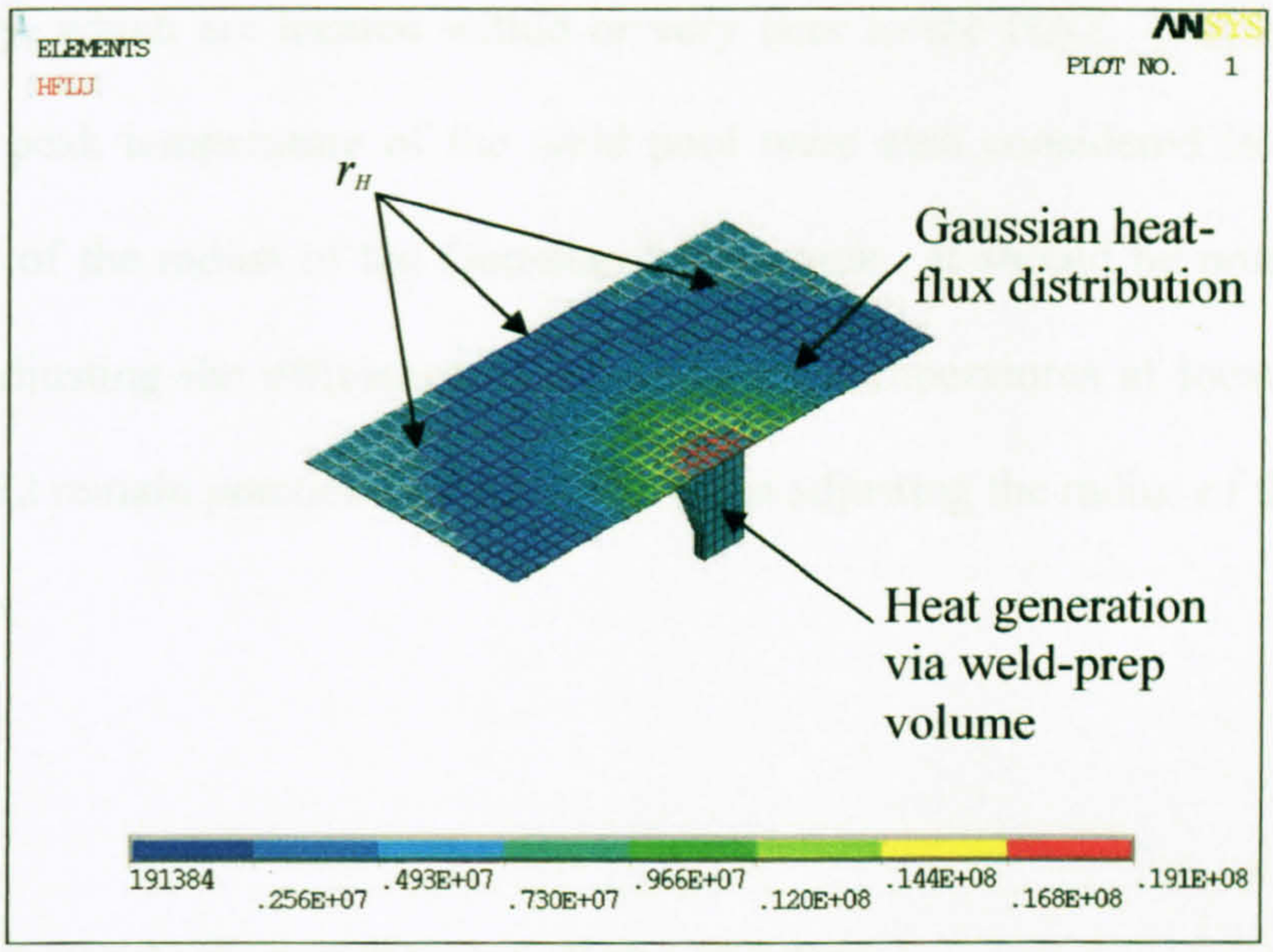

Figure 6.1

Combined heat source

6.3 Methodology

The efficiency factors and radius of the Gaussian heat source (r_H) were not known at the start of the simulation. The efficiency factor was initially assumed to be 0.9 and the radius of the Gaussian heat source to be 10 mm to start the calculations. Then the efficiency factor was adjusted by trial and error to the nearest two decimal places in order to obtain the cooling paths which matched the recorded valves at locations T1/T2 and B1/B2 which located within or very near to the HAZ and the peak temperatures to be close to the measured ones at location F1/F2 and FF1/FF2 which

are located remote from the HAZ of the welding plate. After adjusting the efficiency factor, the radius of the Gaussian heat source was then adjusted by trial and error to the nearest millimetre until top and bottom peak temperatures were obtained which were close to the measured peak temperatures at location T1/T2 and B1/B2 respectively, which are located within or very near to the HAZ. The bottom weld width and peak temperature of the weld pool were also considered in making the adjustment of the radius of the Gaussian heat source. It should be noted that after finishing adjusting the efficiency factor, the peak temperatures at location F1, F2, FF1 and FF2 remain practically unchanged when adjusting the radius of the Gaussian heat source.

6.4 The boundary conditions of the models

Surface heat losses were taken into account by applying combined convection and radiation heat transfer coefficients with the same values as used in the models in Chapter 5. The thermal physical properties used in the models are also the same as those used in Chapter 5. According to [36], a Gas Metal Arc welding heat input efficiency factor was reported in the range 0.66 to 0.93. The appropriate efficiency factors for these models have been found (as described in section 6.3) to be within the reported range and are shown in the second column of table 6.1. The net heat inputs to the weld are shown in the third column of table 6.1. The Gaussian radii used in modelling are shown in the last column. The computer models in this

Chapter also include only the left-hand half of welding specimen by assuming the weld centreline to be adiabatic.

Table 6.1
Input welding parameters to the models

Models	Efficiency factor η	Net heat input Q_{net} (W)	Q_{prep} as % of Q_{net}	Gaussian radius r_H (mm)
1A, 1B, 1C	0.88	2323.2	35	11
2A, 2B, 2C	0.89	4471.7	40.5	14
3A, 3B, 3C	0.86	4607.2	46	14
4A, 4B, 4C	0.87	1696.5	28	10
5A, 5B, 5C	0.89	2136	59	7

"1" refers to experiment 1: 4 mm thick welding plate with a 'V' weld-preparation
"2" refers to experiment 2: 6 mm thick welding plate with a 'V' weld-preparation
"3" refers to experiment 3: 8 mm thick welding plate with a 'V' weld-preparation
"4" refers to experiment 4: 3 mm thick welding plate with a 'V' weld-preparation
"5" refers to experiment 5: 6 mm thick welding plate with a semi-circular cross-section weld-preparation
"A" refers to 3D transient models
"B" refers to 3D steady state models
"C" refers to 2D transient sectional models

6.5 3D transient models – Model A

The simulation was performed as a transient thermal analysis. The weld pool was modelled by moving the combined heat source along the welding path at intervals of 2 mm per load step. The operation began with the vertical centre axis of the combined heat source aligned with the starting edge of the welding path and moved throughout the entire length of the weld. The time interval for each load step was calculated using the relationship of time equal to distance travelled divided by

welding speed. The meshed size of the elements along the welding path was approximately 1 mm.

The length of this weld-preparation volumetric heat source was obtained through trial and error using the computer model. If the length of the weld-preparation volume was too long, the whole volume did not reach melting temperature and thus a portion of the weld-preparation volume was missed as the heat source moved along. Figure 6.2 plots the traced weld pools of two consecutive load steps showing the missed portion due to moving the combined heat source along the welding path at an interval of 4 mm per load step. This missed portion may result in the model being inadequate enough for subsequent applications such as weld cracking analysis, residual stress analysis and out-of-plane distortion analysis. Therefore, the load step length of the weld-preparation was reduced to 2 mm.

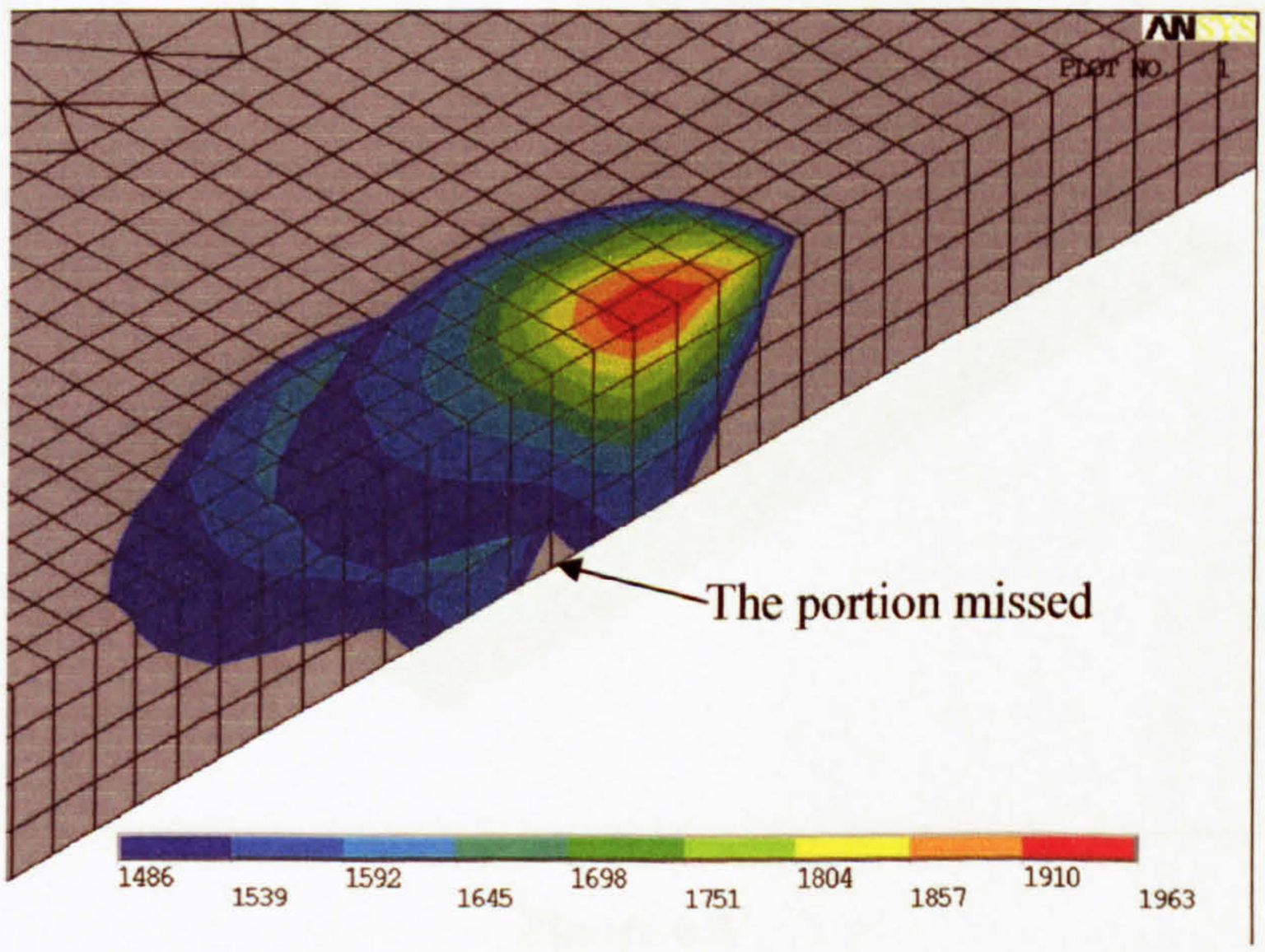

Figure 6.2

The traced weld pools of two consecutive load steps

The element type chosen to perform the 3D transient simulations is 'SOLID70'. SOLID70 has a 3D thermal conduction capability and has eight nodes with a single degree of freedom, temperature, at each node. The element is applicable to 3D transient thermal analysis.

The thermal gradients are steeper near to the heat source and the model requires a finer mesh in that region. Further away from the weld, the thermal gradients are less steep, and hence a coarser mesh is adequate. The regions near to the weld or at the location of the weld were meshed with hexahedral-shaped elements corresponding to element sizes of approximately 1mm. The regions far away from the weld were meshed with coarser tetrahedral-shaped elements. A sample of the mesh patterns is shown in Figure 6.3.

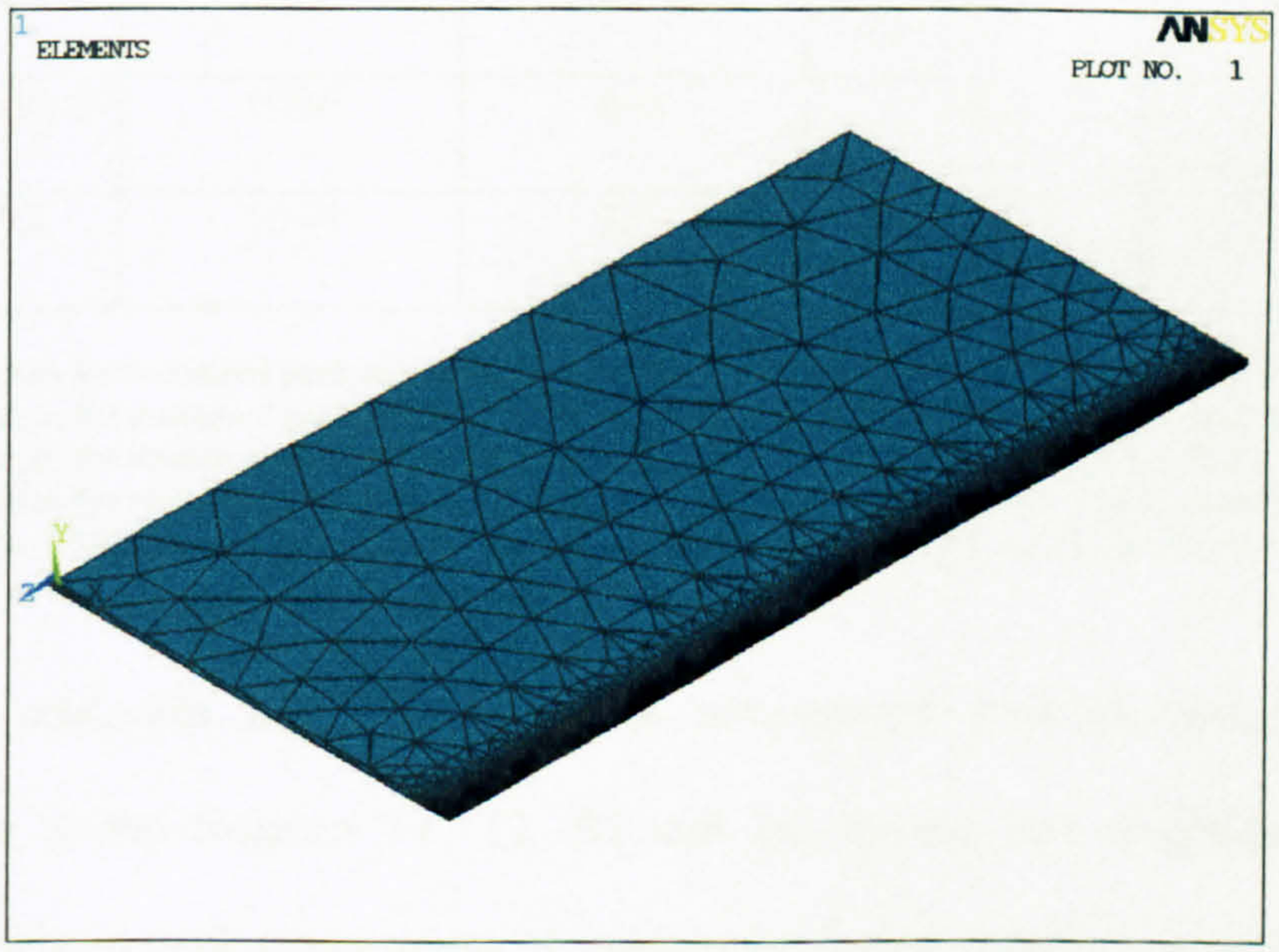

Figure 6.3

Finite element mesh pattern of model 1A

6.5.1 Discussion of results

Table 6.2

Comparison of the simulated peak temperature with the experimental measured peak temperature

	T1 peak (^{o}C)	B1 peak (^{o}C)	T2 peak (^{o}C)	B2 peak (^{o}C)
Experiment 1	713	647	733	654
Model 1A	705	668	705	668
Experiment 2	781	720	748	690
Model 2A	730	695	730	695
Experiment 3	814	712	812	724
Model 3A	827	722	828	722
Experiment 4	895	791	916	812
Model 4A	889	834	889	834
Experiment 5	1096	498	686	496
Model 5A	1099	529	666	529

'T1 peak' refers to the measured peak temperature at location T1, the top thermocouples positions
'B1 peak' refers to the measured peak temperature at location B1, the bottom thermocouples positions
'T2 peak' refers to the measured peak temperature at location T2, the top thermocouples positions
'B2 peak' refers to the measured peak temperature at location B2 the bottom thermocouples positions
See figures 3.14, 3.16, 3.18, 3.20 and 3.22 for the detail locations of T1, B1, T2 and B2 in Chapter 3

Table 6.2 compares the simulated peak temperature with the measured peak temperature at the location T1, T2, B1 and B2 for the five experiments. The simulated bottom peak temperature of experiment 5 was observed to be higher than the measured peak temperature by around 6%. This could be due to errors made during the temperature measurement. Aside from that, all the simulated peak

temperatures in table 6.2 were within a variation of ±5%. In Table 6.2, the simulated top peak temperature of experiment 5 at the location T1 was 1099°C which was almost identical to the experimental measured peak temperature at 1096°C. This verified that the out-of-calibration range experimental measurement was still valid. Overall, all the simulated peak temperatures are in very good agreement with the experimental peak temperatures.

Table 6.3 compares the experimental weld pool widths with simulated weld pool widths and experimental heat affected zone (HAZ) with simulated HAZ. The second column of Table 6.3 compares the experimental weld pool top widths (Figures 3.23, 3.24, 3.25, 3.26 and 3.27) with the modelled weld pool top widths. The modelled weld pool top widths are observed to fall on the low side of the measured values. The third column of Table 6.3 compares the experimental and modelled weld pool bottom widths. The modelled weld pool bottom widths again are on the low side of the experimental weld pool bottom widths. Overall, the simulated weld pool widths agreed well with the experimental weld pool widths. It should be noted that the weld pool widths are important factor to be taken into account for welding out-of-plane distortion calculations. In Chapter 2, it has been mentioned that the melting temperature of carbon steel varies quite significantly with the carbon content. However, for computer simulations, the melting temperature has been assumed to be 1486°C for a carbon content of 0.13%. The carbon content of the test plate weld metal could have been higher resulted in larger weld pool widths.

The fourth and fifth column of Table 6.3 compare the experimental HAZ top and bottom widths with the modelled HAZ top and bottom widths. All the modelled HAZ top and bottom widths are observed to fall within the experimental measured ranges. On the whole, the simulated HAZ widths agree well with the experimental HAZ widths.

Table 6.3
Comparison of the simulated results with the experimental measured results

	Weld top width (mm)	Weld bottom width (mm)	HAZ top width (mm)	HAZ bottom width (mm)
Experiment 1	7~9	1~2	10~12	9~11
Model 1A	7	1	11.6	9.6
Experiment 2	10~12.5	1~2	14~15	13.5~14.5
Model 2A	10.8	1.2	14.4	13.6
Experiment 3	12~13.5	1~2	16~17.5	13.5~15
Model 3A	12.4	1.16	17.4	13.8
Experiment 4	5~7	1~2	8.5~10.5	8~10
Model 4A	5.8	1.2	10.4	9.8
Experiment 5	7~8	NA	9~10	3.5~4.5
Model 5A	7	NA	9.8	4

See also Figures 1A-TW, 2A-TW, 3A-TW, 4A-TW and 5A-TW for the top weld width of model 1A, 2A, 3A, 4A and 5A respectively in Appendix A for the graphical plots. See also Figures 1A-BW, 2A-BW, 3A-BW and 4A-BW for the bottom weld width of model 1A, 2A, 3A and 4A respectively in Appendix A. See also Figures 1A-H, 2A-H, 3A-H, 4A-H and 5A-HT & 5A-HB for HAZ of model 1A, 2A, 3A, 4A and 5A respectively in Appendix A.

An overall view of the temperature contours of model 1A at a time of 96 seconds from the commencement of welding is shown in Figure 6.4. The maximum temperature of the weld pool was around 2013 °C throughout the simulated welding process. The remainder of the similar temperature contour plots of the models are presented in Appendix A. The maximum temperatures of the weld pool of all models were between 1905°C and 2316°C. They are in good agreement with the experimentally measured stationary weld pool where the peak temperature of weld pool ranges from 1950°C to 2708°C [18]. (See also Figures 1A-O, 2A-O, 3A-O, 4A-O and 5A-O for the overall view of the temperature contours of models 1A, 2A, 3A, 4A and 5A respectively in Appendix A)

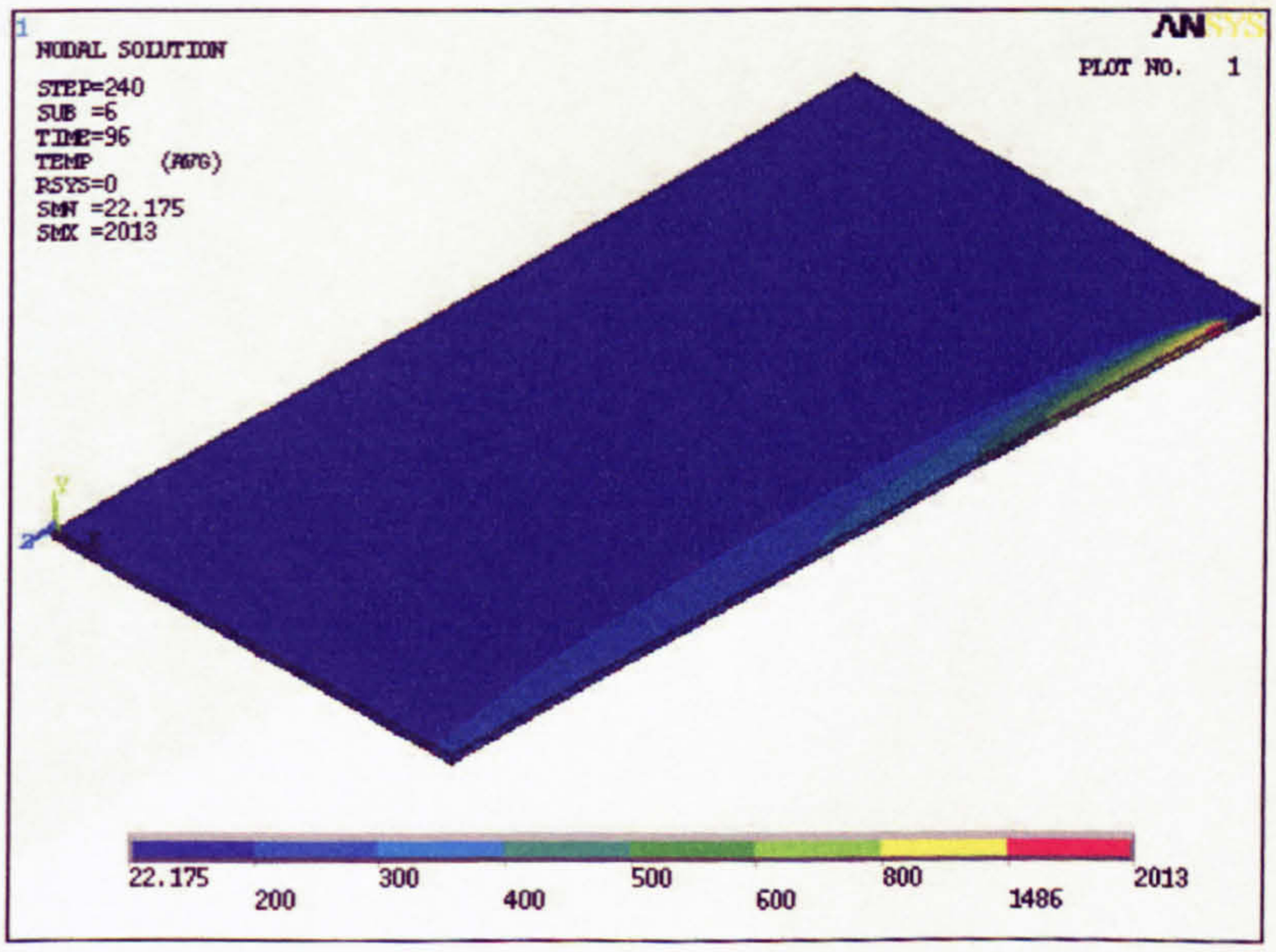

Figure 6.4

Temperature contour at 96 seconds of model 1A

It should be noted that the peak temperature of the weld pool depends on the value of artificial conductivity enhancement assumed. The effect of this conductivity

enhancement on the peak temperature of the weld pool will be discussed in the next chapter.

Figures 6.4 shows an overall view of the simulated weld pool of model 1A at a time of 60 seconds from the commencement of welding. The shapes of the simulated weld pool are seen to be similar to the experimentally captured weld pool shape [9] which is ellipsoidal. It should be noted that, as mentioned previously, the melting temperature for all the models has been assumed to be 1486°C. (See also Figures 1A-P, 2A-P, 3A-P, 4A-P and 5A-P for the overall view of the simulated weld pool of models 1A, 2A, 3A, 4A and 5A respectively in Appendix A)

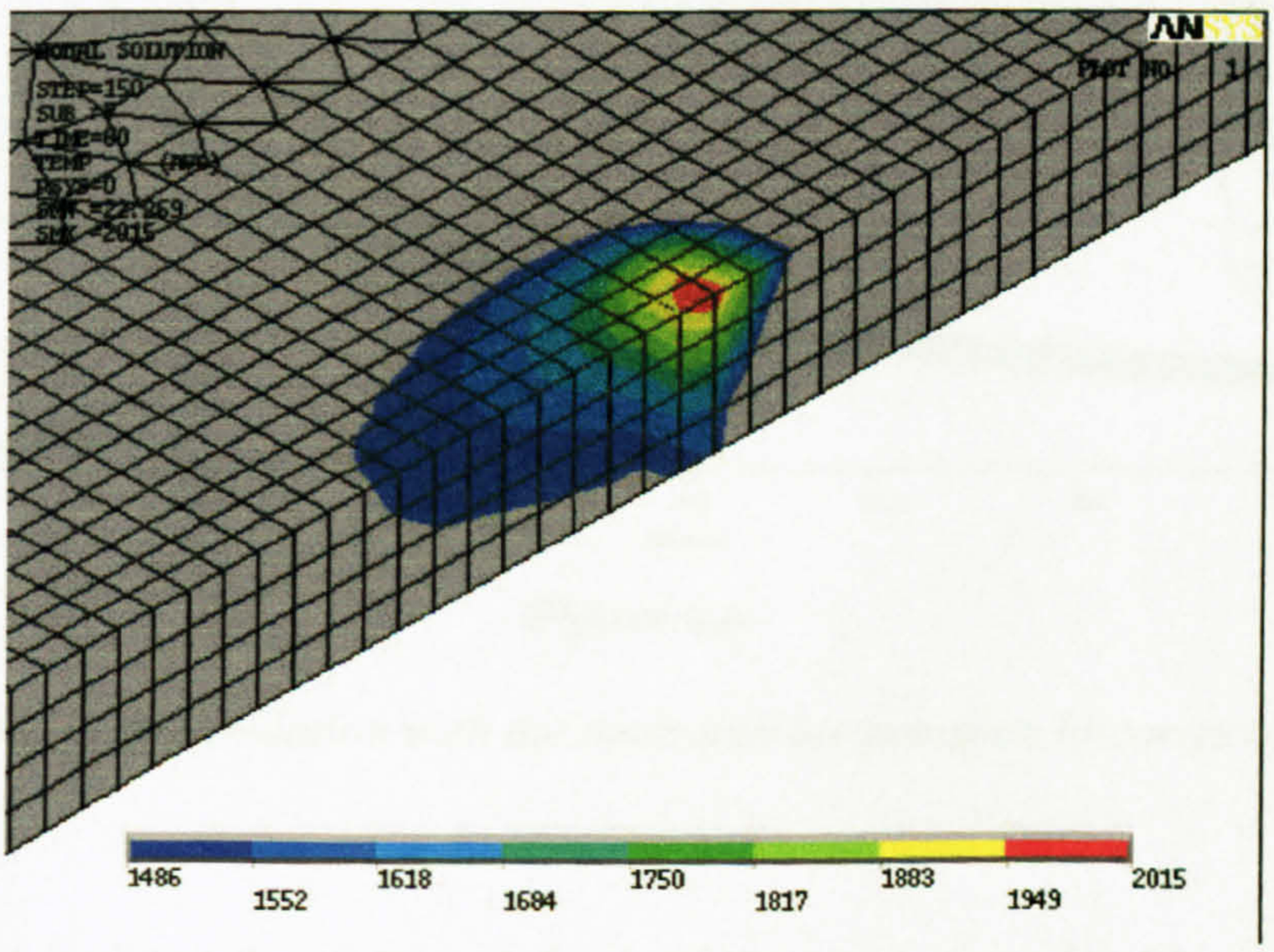

Figure 6.5

Temperature contour of the weld pool of model 1A

Comparison between experimentally measured temperature histories of Experiment 1 and computed temperature histories of models 1A can be observed in Figure 6.6.

The remainder of the modelled temperature histories compared similarly well with the experimentally measured temperature histories as Model 1A. In overall, the simulated temperature histories of all Models A agreed reasonably well with the experimentally measured temperature histories. (See also Figures 1A-TH, 2A-TH, 3A-TH, 4A-TH and 5A-TH for the comparison between the experimentally measured temperature histories and the simulated temperature histories of models 1A, 2A, 3A, 4A and 5A respectively in Appendix A)

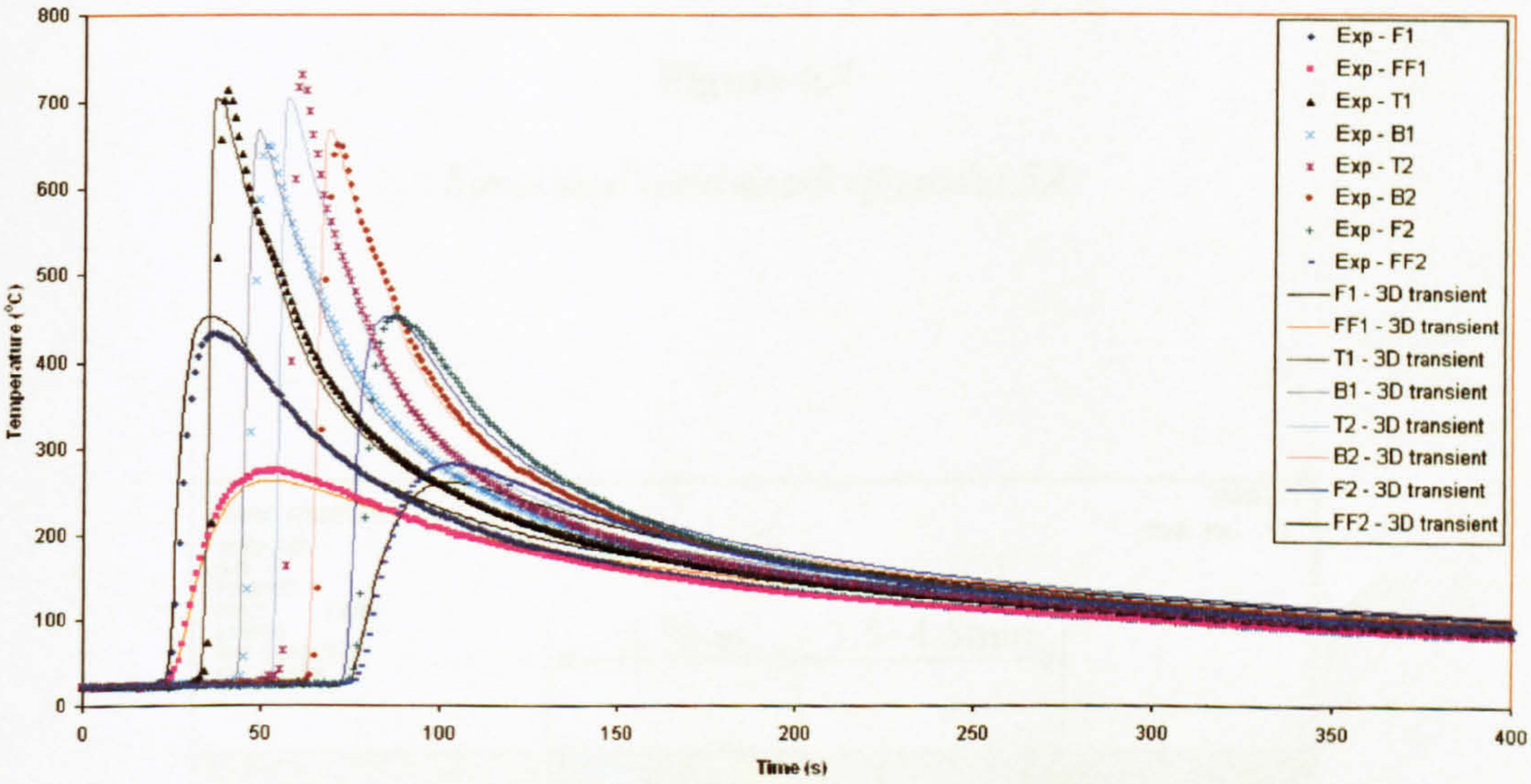

Figure 6.6

Comparison of the simulation with the measured temperature histories of model 1A

Figure 6.7 shows that the simulated depth of the weld of model 5A was shallower than the actual weld depth. This probably was due to the fact that no actual weld pool stirring motion was taken into account in the simulation.

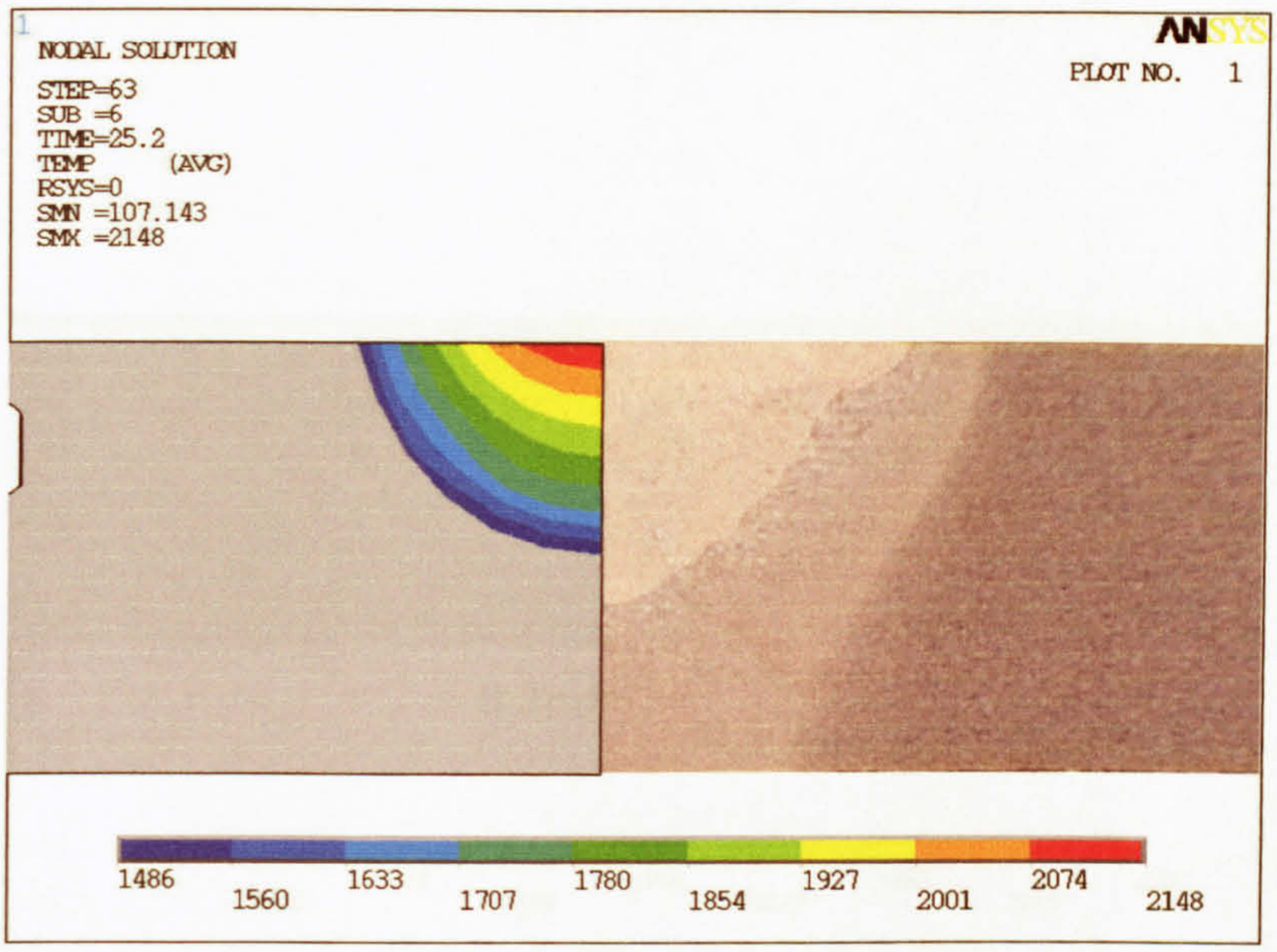

Figure 6.7

Simulated weld depth of model 5A

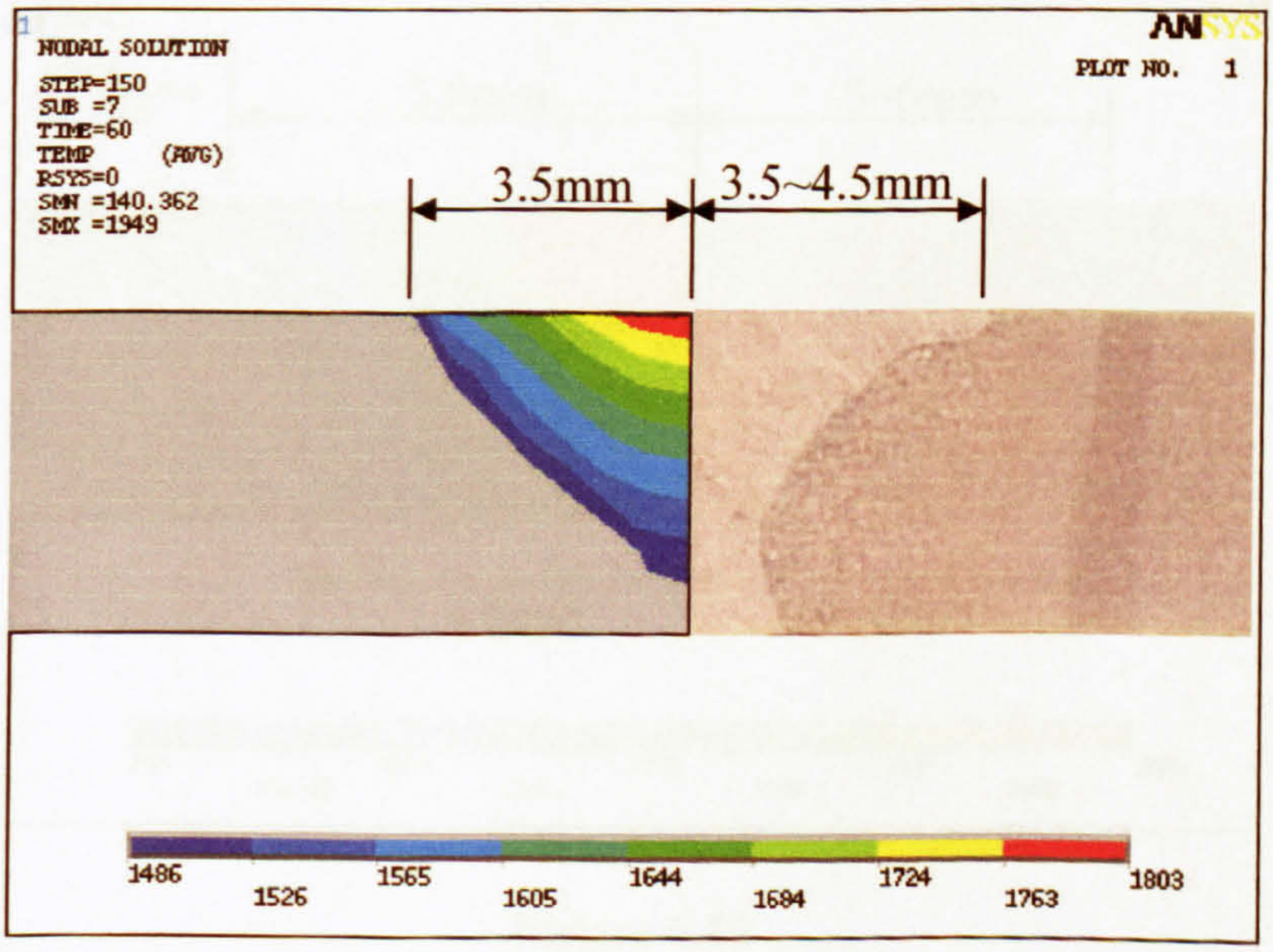

Figure 6.8

Simulated top weld width of model 1A

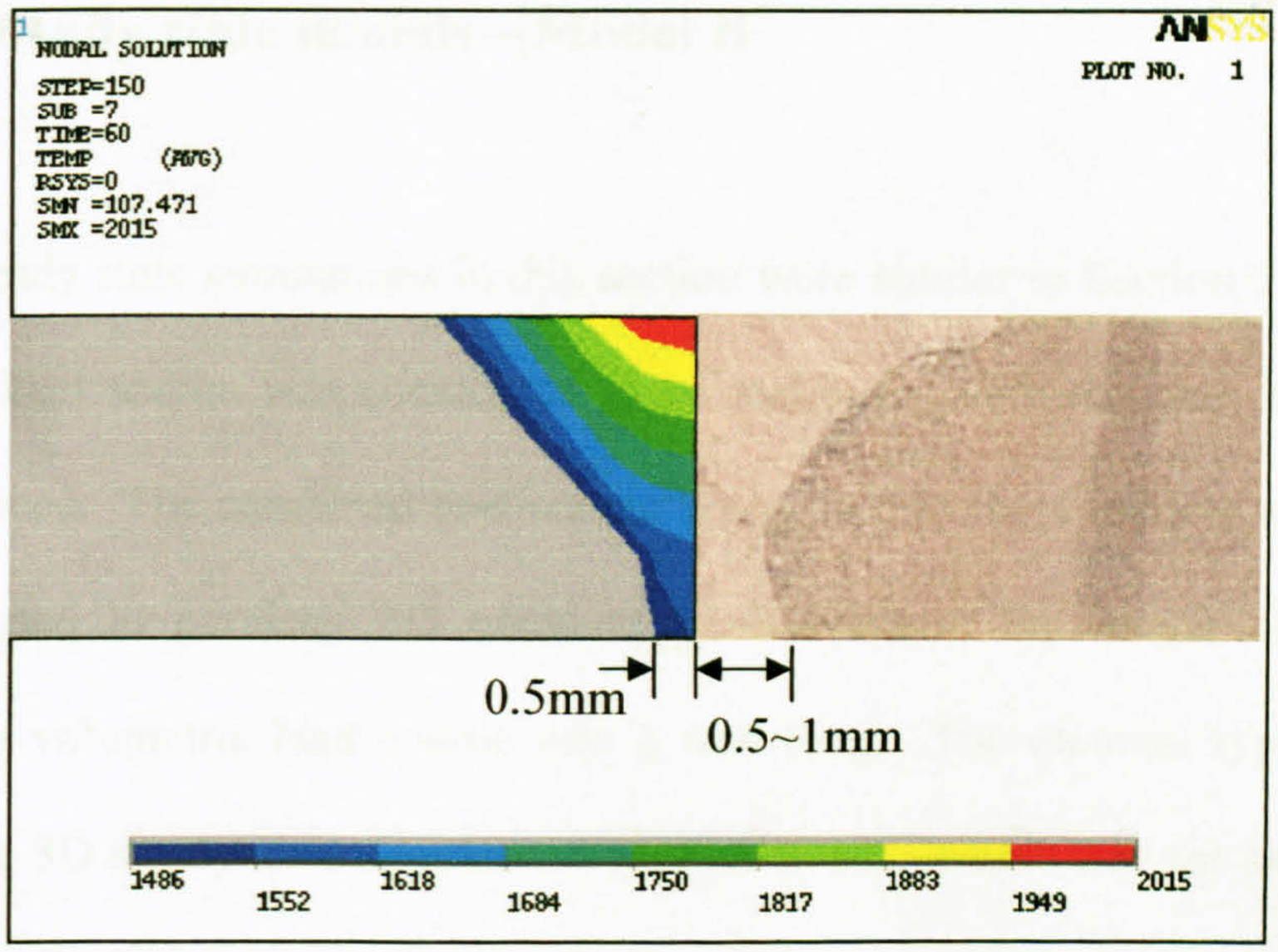

Figure 6.9

Simulated bottom weld width of model 1A

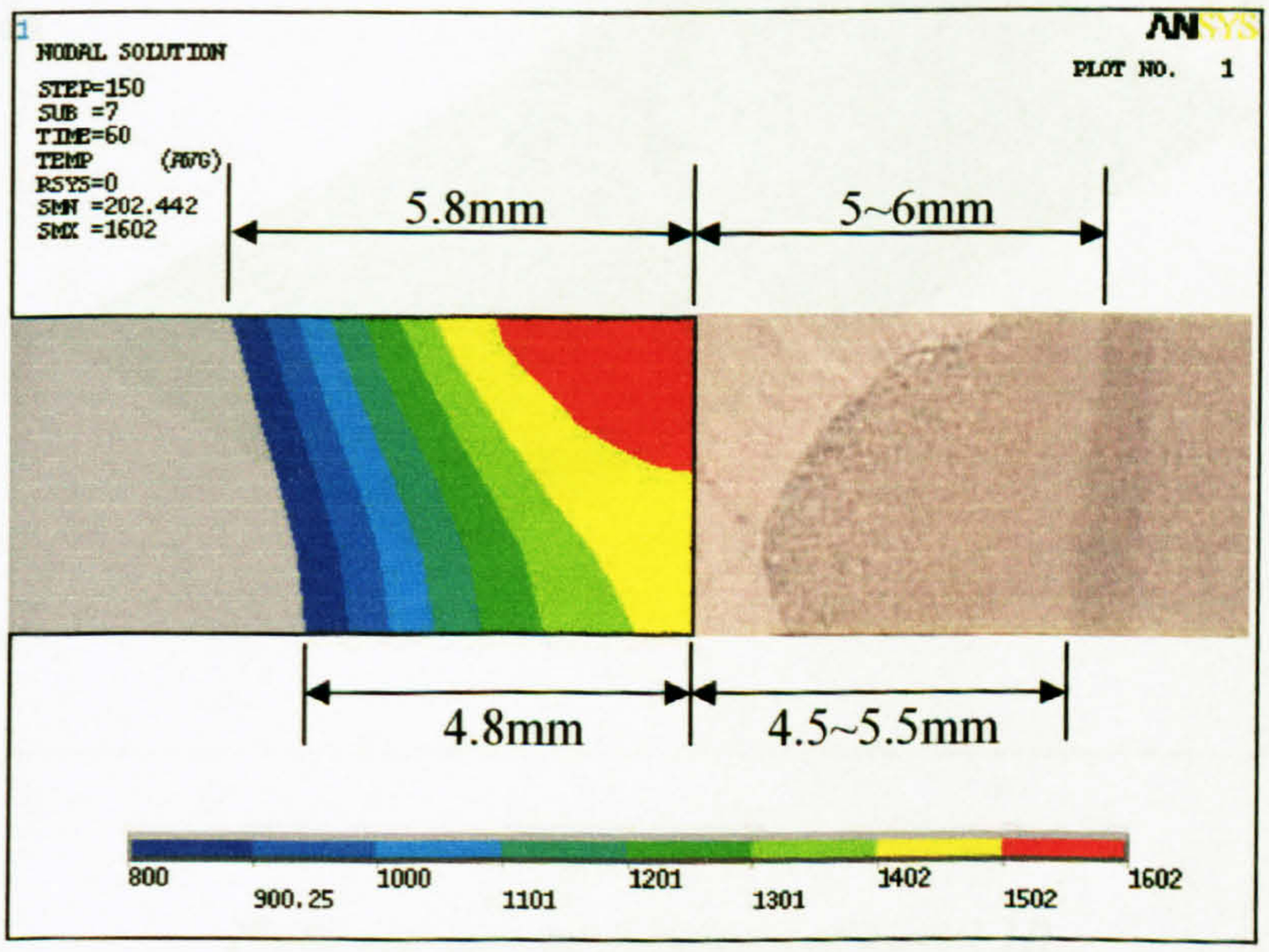

Figure 6.10

Simulated heat affected zone of model 1A

6.6 3D steady state models – Model B

The 3D steady state simulations in this section were similar to Section 5.5 where the combined heat source was considered to be stationary with the plate moving at a constant speed. The combined heat source being used in these models was the same as those used in previous 3D transient models where the length of the weld-preparation volumetric heat source was 2 mm long. The element type chosen to perform the 3D steady state simulations is 'FLUID142' which was the same element type as described in previous Chapter, Section 5.5.

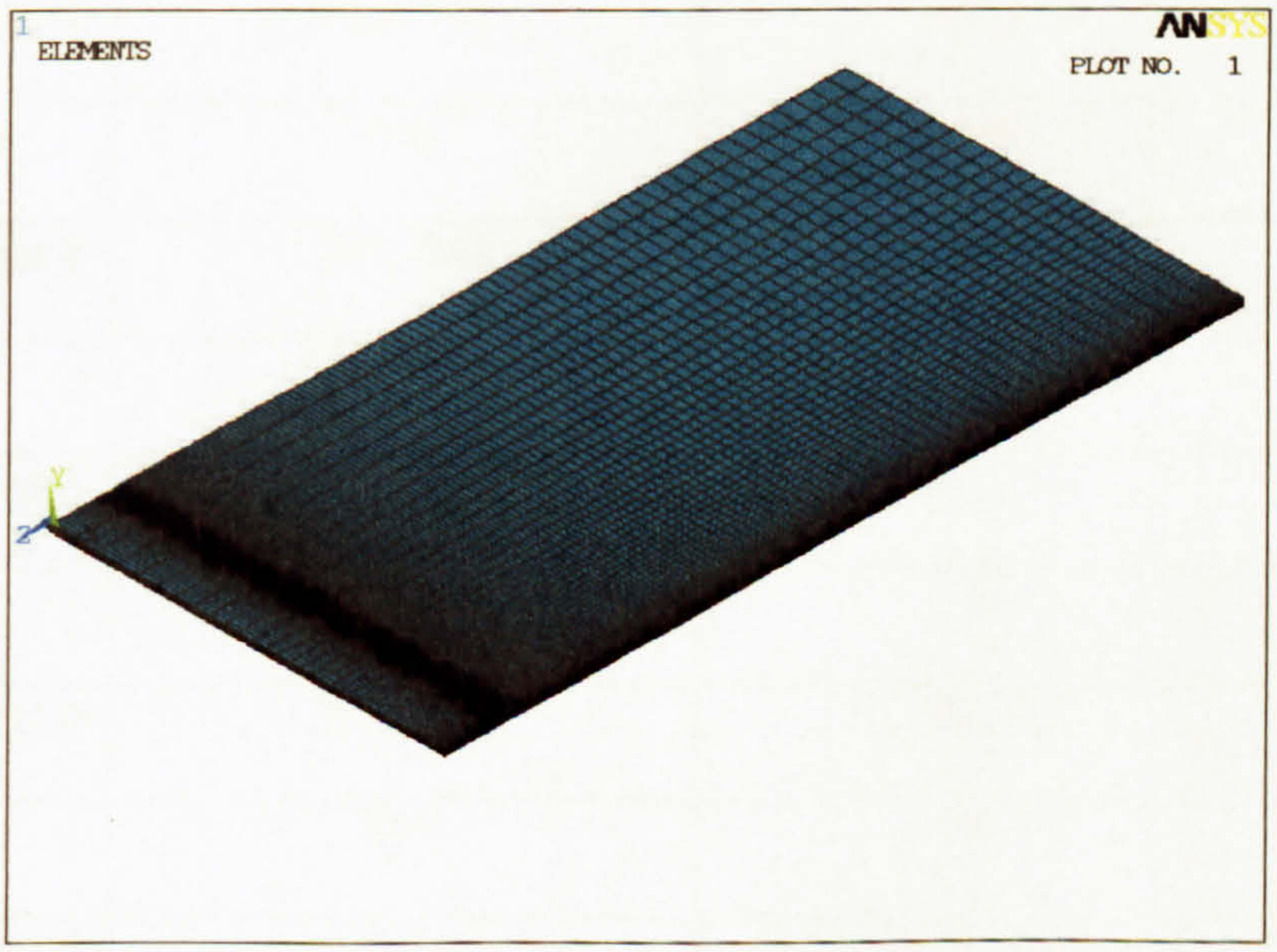

Figure 6.11

Finite element mesh pattern of model 1B

A sample of the mesh patterns is shown in Figure 6.11. The thermal gradients are steeper near the heat source and the model requires a finer mesh in that region. Further away from the weld, the thermal gradients are less steep, and hence a coarser

mesh is adequate. The regions near to the weld pool or at the location of the weld pool were meshed with hexahedral-shaped elements with element size of approximately 0.5 mm. The regions further away from the weld pool were meshed with coarser hexahedral-shaped elements.

6.6.1 Discussion of Results

Table 6.4
Comparison of the simulated peak temperatures with the experimental measured peak temperatures

	T1 peak, T2 peak (°C)	B1 peak, B2 peak (°C)
Experiment 1	713, 733	647, 654
Model 1B	696	656
Experiment 2	781, 748	720, 690
Model 2B	744	694
Experiment 3	814, 812	712, 724
Model 3B	814	727
Experiment 4	895, 916	791, 812
Model 4B	849	807
Experiment 5	1096, 686	498, 496
Model 5B	1101, 673	518

'T1 peak' refers to the measured peak temperature at location T1, the top thermocouples positions
'B1 peak' refers to the measured peak temperature at location B1, the bottom thermocouples positions
'T2 peak' refers to the measured peak temperature at location T2, the top thermocouples positions
'B2 peak' refers to the measured peak temperature at location B2 the bottom thermocouples positions
See figures 3.14, 3.16, 3.18, 3.20 and 3.22 for the detail locations of T1, B1, T2 and B2 in Chapter 3

Table 6.4 compares the simulated peak temperature with the experimentally measured peak temperature. The simulated bottom peak temperature of experiment 4 was observed to be higher than the measured peak temperatures by around 6.4 %. These could be due to errors made during the temperatures measurement and errors made by the ANSYS FLOTRAN solution. Aside from that, all the simulated peak temperatures in table 6.4 were within the variation of ±5.1%.

Table 6.5
Comparison of the simulated results with the experimental measured results

	Weld top width (mm)	Weld bottom width (mm)	HAZ top width (mm)	HAZ bottom width (mm)
Experiment 1	7~9	1~2	10~12	9~11
Model 1B	6.8	1	11	10.2
Experiment 2	10~12.5	1~2	14~15	13.5~14.5
Model 2B	10.2	1	14.6	13.6
Experiment 3	12~13.5	1~2	16~17.5	13.5~15
Model 3B	12	1	17	14.6
Experiment 4	5~7	1~2	8.5~10.5	8~10
Model 4B	5.6	1	10	9.8
Experiment 5	7~8	NA	9~10	3.5~4.5
Model 5B	6.8	NA	10	4

See also Figures 1B-TW, 2B-TW, 3B-TW, 4B-TW and 5B-TW for the top weld width of model 1B, 2B, 3B, 4B and 5B respectively in Appendix B for the graphical plots. See also Figures 1B-BW, 2B-BW, 3B-BW and 4B-BW for the bottom weld width of model 1B, 2B, 3B and 4B respectively in Appendix B. See also Figures 1B-H, 2B-H, 3B-H, 4B-H and 5B-HT & 5B-HB for HAZ of model 1B, 2B, 3B, 4B and 5B respectively in Appendix B.

Table 6.5 compares the experimental weld pool widths with simulated weld pool widths. The second column of Table 6.5 compares the experimental with the modelled weld pool top widths. The modelled weld pool top widths are observed to be on the low side of the experimental weld pool top widths and weld pool top widths Models 1B and 5B are smaller than the experimental weld pool widths by 0.2 mm. Overall, the simulated weld pool widths agreed fairly well with the experimental weld pool widths.

The fourth and fifth columns of Table 6.5 compare the experimental HAZ top and bottom widths with the modelled HAZ top and bottom widths. All the modelled HAZ top and bottom widths fell almost at the centre of the experimental measured ranges. Therefore, the simulated HAZ widths agreed well with the experimental HAZ widths.

Figure 6.12 shows an overall view of the temperature contours of models 1B. The maximum temperature of the weld pool was 2005°C. The rest of the similar temperature contour plots of the models have been placed in Appendix B. The maximum temperatures of the weld pool of all Models B were between 2005°C and 2226°C except Model 4B. The maximum temperature of the weld pool of Model 4B is 1824°C which is slightly lower than expected. On the whole, the maximum temperatures of the weld pool of all 3D steady state models were slightly lower than the 3D transient models. In general, they were in fairly good agreement with the experimentally measured stationary weld pool where the peak temperature of weld pool ranges from 1950°C to 2708°C [18]. (See also Figures 1B-O, 2B-O, 3B-O, 4B-

O and 5B-O for the overall view of the temperature contours of models 1B, 2B, 3B, 4B and 5B respectively in Appendix B for the rest of the models)

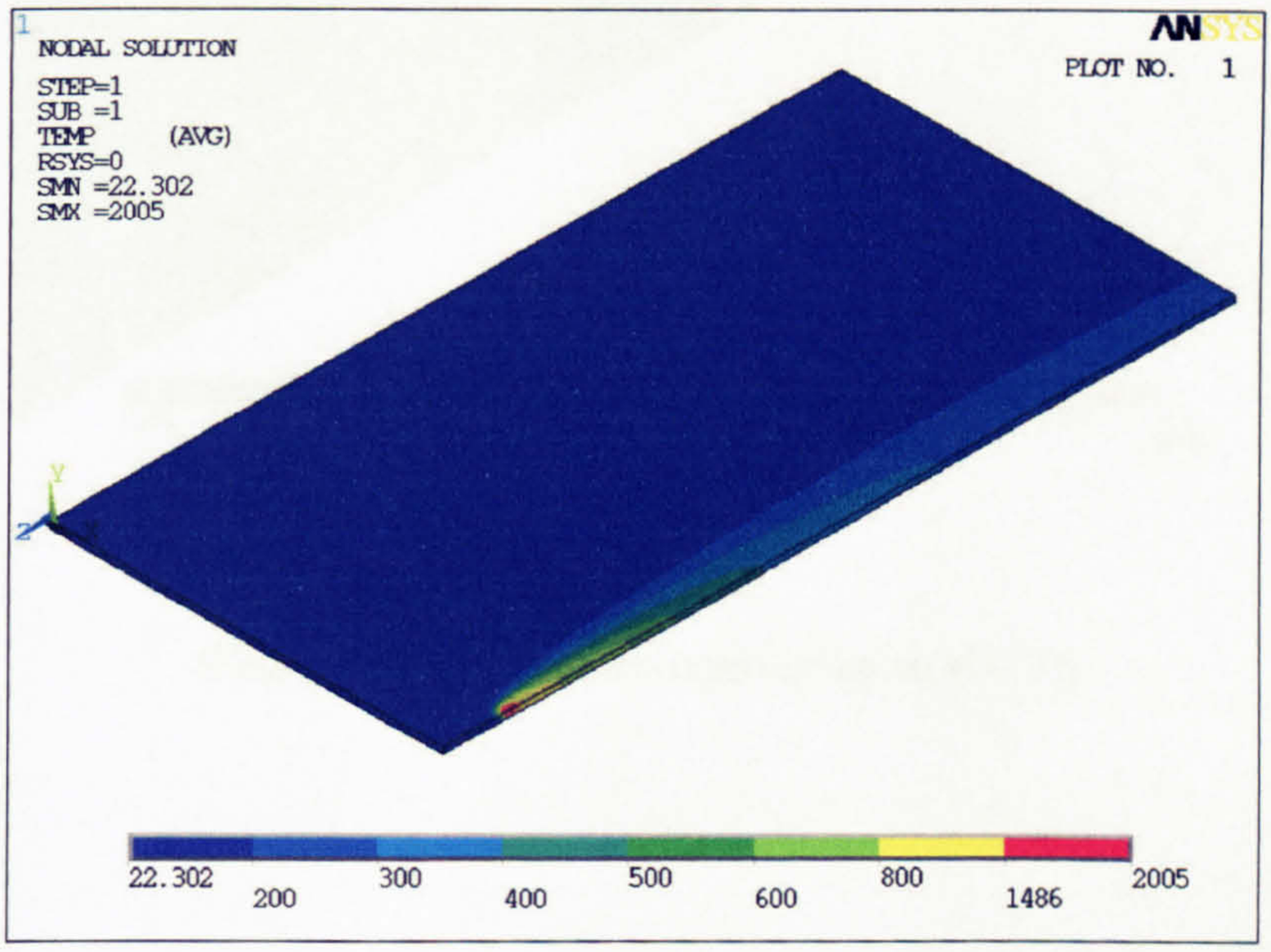

Figure 6.12

Temperature contour of model 1B

An overall view of the simulated weld pool temperature contours of model 1B were shown in Figures 6.13. The length of weld pool of all models B were slightly longer than the previous 3D transient models but the shapes of the simulated weld pool were seen to be in good agreement with the experimentally captured weld pool shape[9]. (See also Figures 1B-P, 2B-P, 3B-P, 4B-P and 5B-P for the overall view of the simulated weld pool of models 1B, 2B, 3B, 4B and 5B respectively in Appendix B)

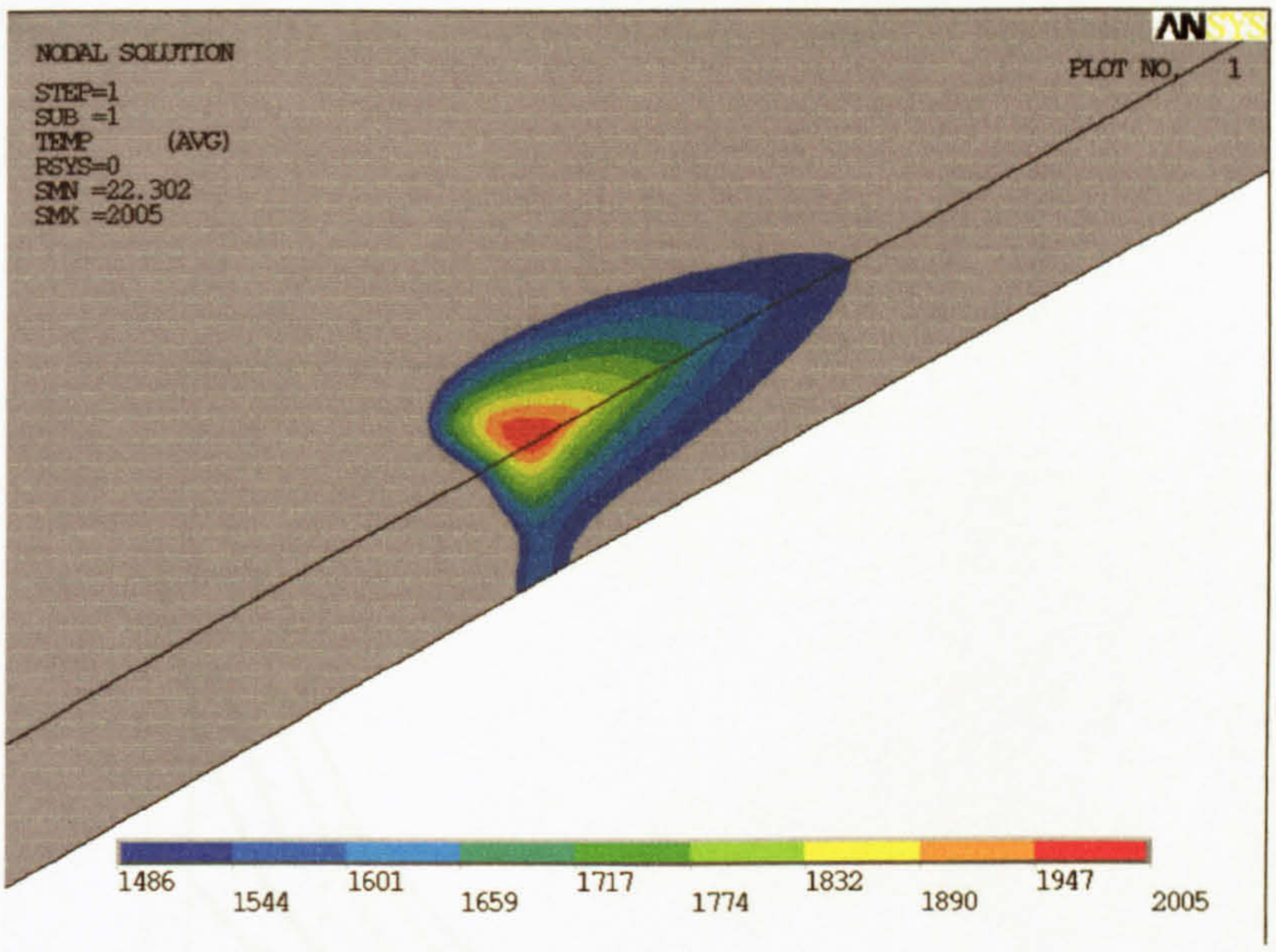

Figure 6.13

Weld pool temperature contour of model 1B

As demonstrated in Appendix E the temperature distribution along the weld can be converted into temperature history and shifted to align with the experimentally measured temperature history. The converted simulation temperature histories of Model 1B were compared with the experimentally measured temperature histories of Experiment 1 as shown in Figure 6.14. Most of the simulated temperature histories compare similarly well with the experimental temperature histories at region near the peak temperatures but not quite well at the temperature falling end. The modelled temperatures were higher than the experimental temperature histories at the temperature falling end as shown in Figure 6.14. In overall, the converted simulation temperature histories agreed fairly well with the experimental measurements. (See also Figures 1B-TH, 2B-TH, 3B-TH, 4B-TH and 5B-TH for the comparison between the experimentally measured temperature histories and the converted temperature

histories of models 1B, 2B, 3B, 4B and 5B respectively in Appendix B for the rest of the models)

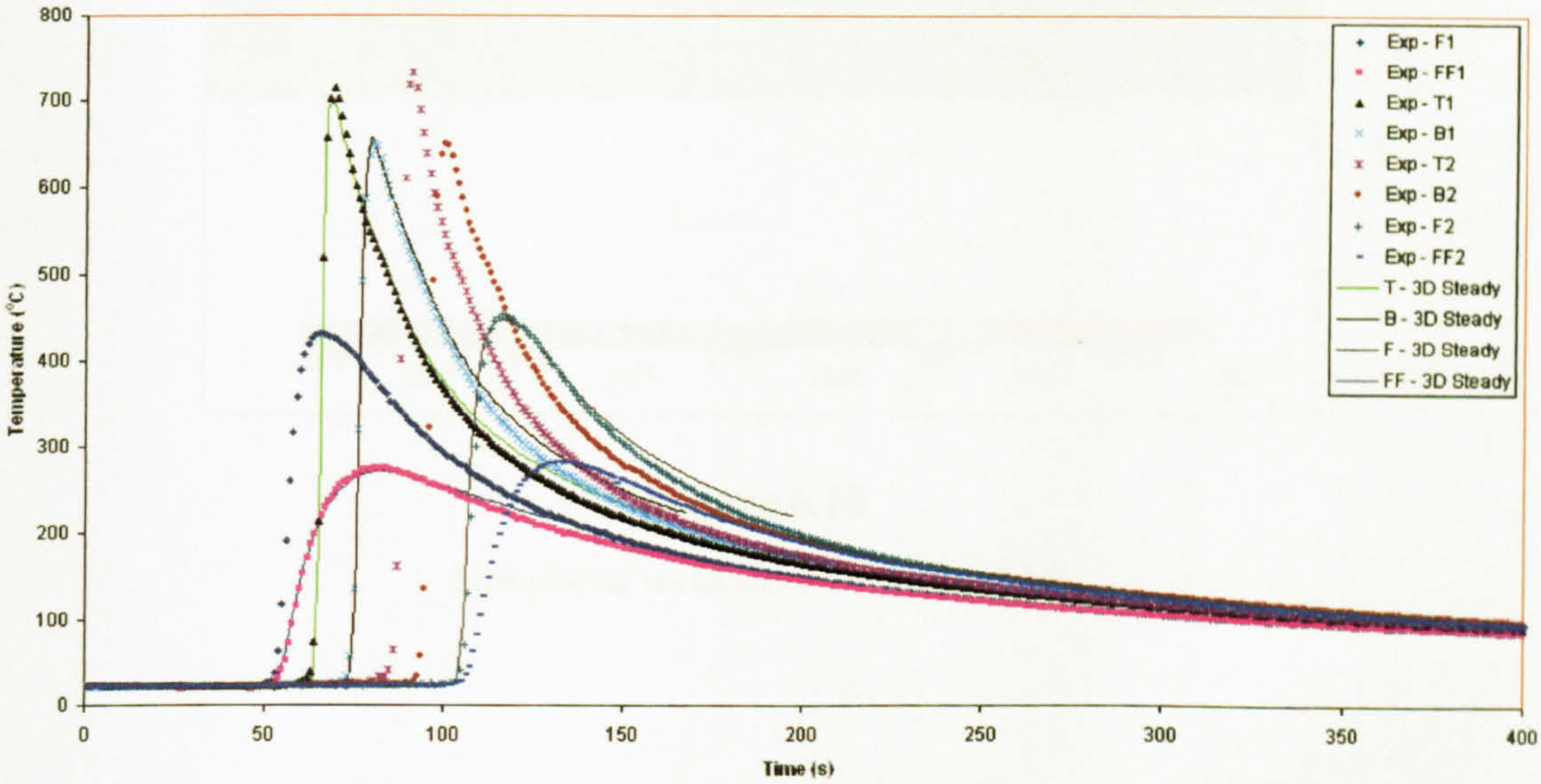

Figure 6.14

Comparison of temperature histories of the measured with the model 1B

The simulated depth of the weld of Experiment 5 again was shallower than actual weld depth as shown in Figure 6.15.

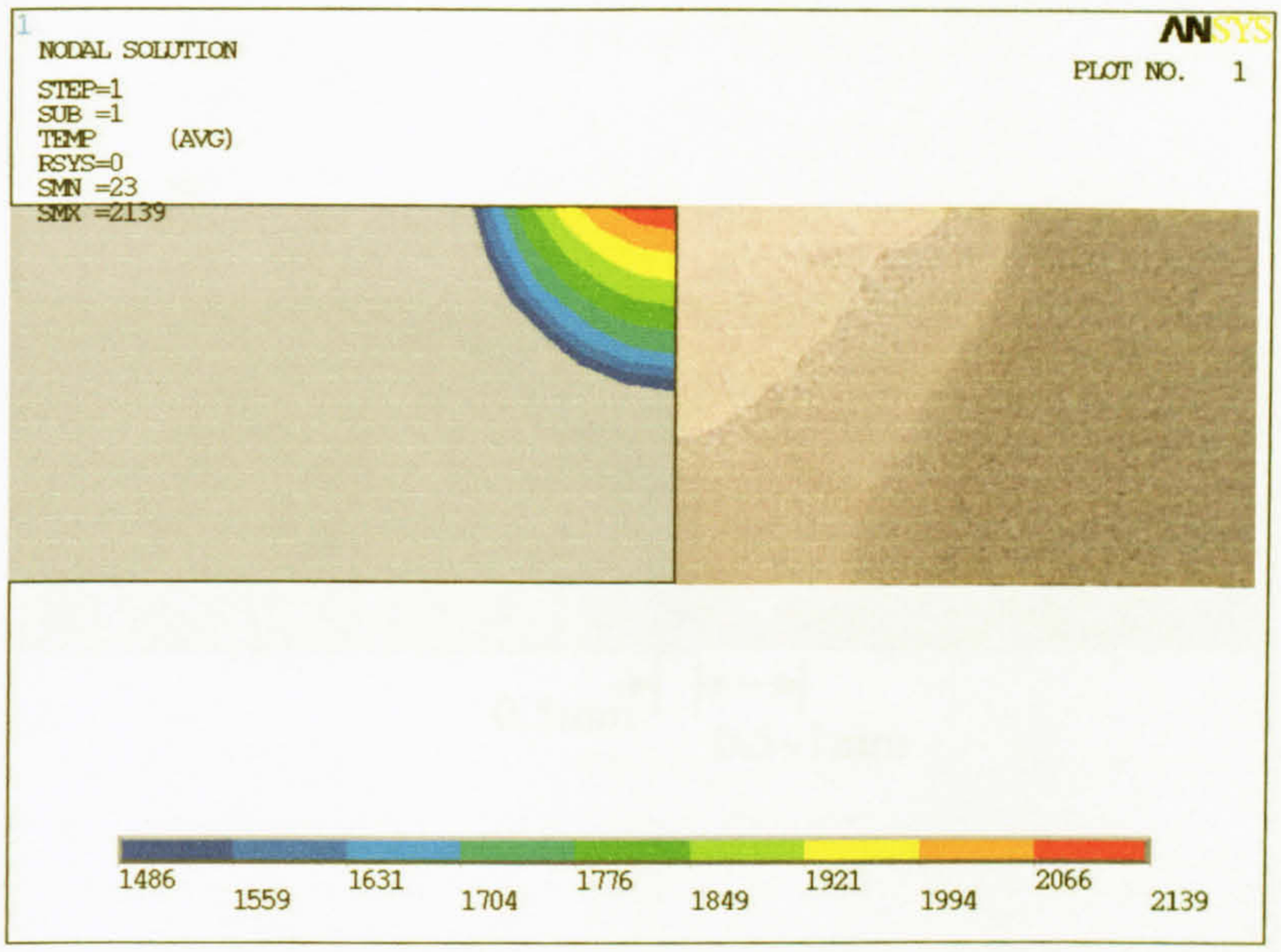

Figure 6.15

Simulated weld depth of model 5B

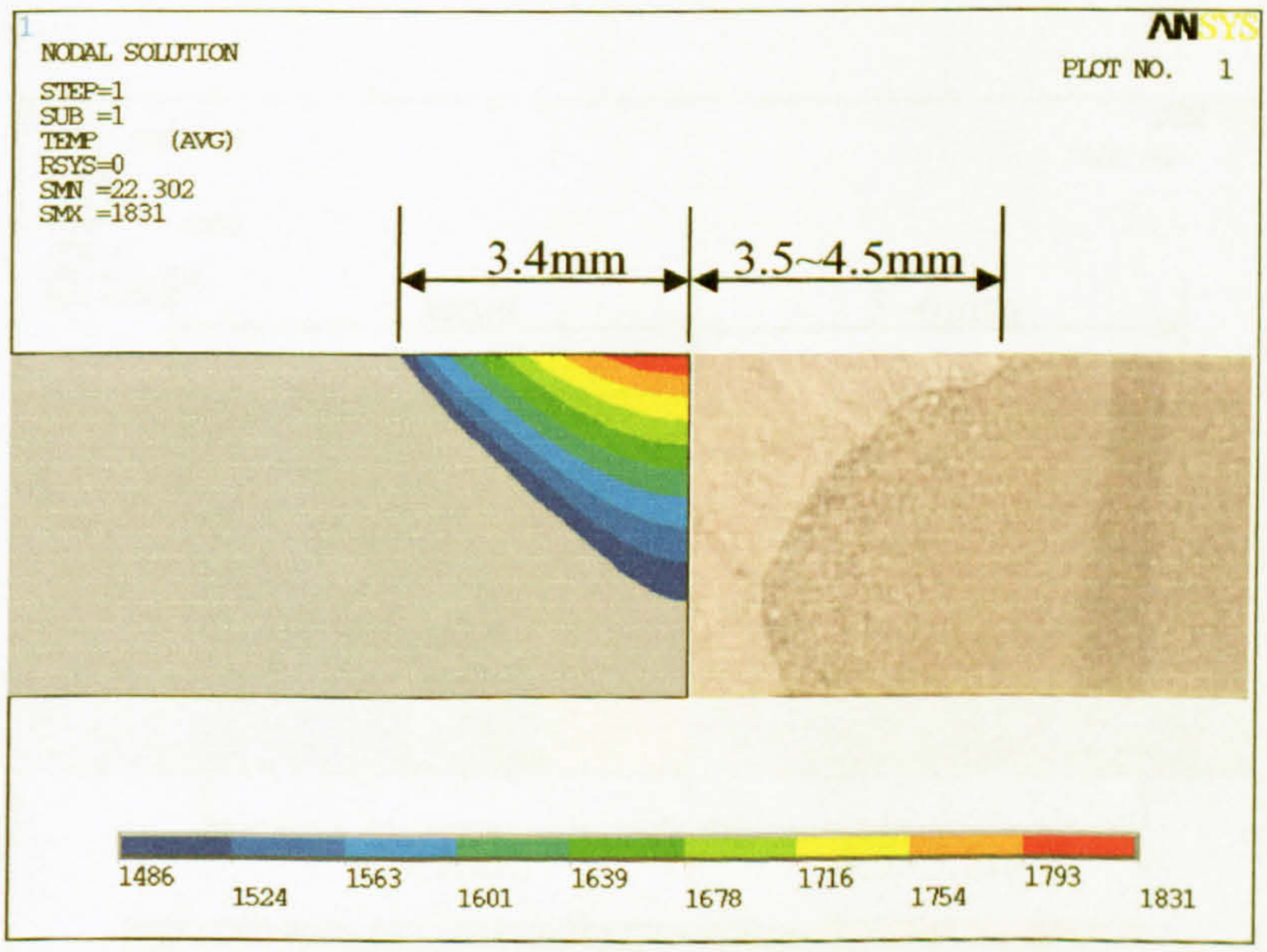

Figure 6.16

Simulated top weld width of model 1B

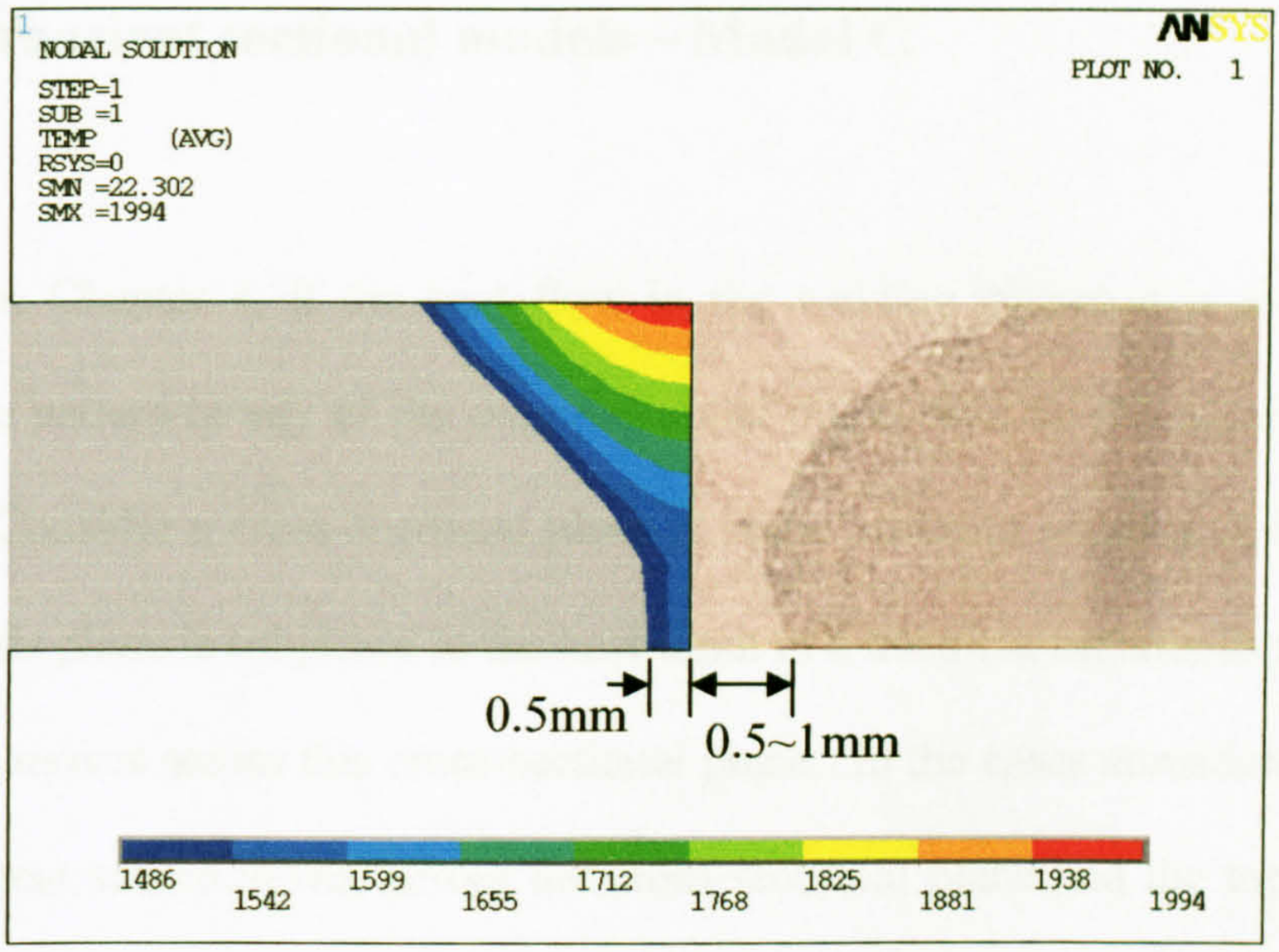

Figure 6.17

Simulated bottom weld width of model 1B

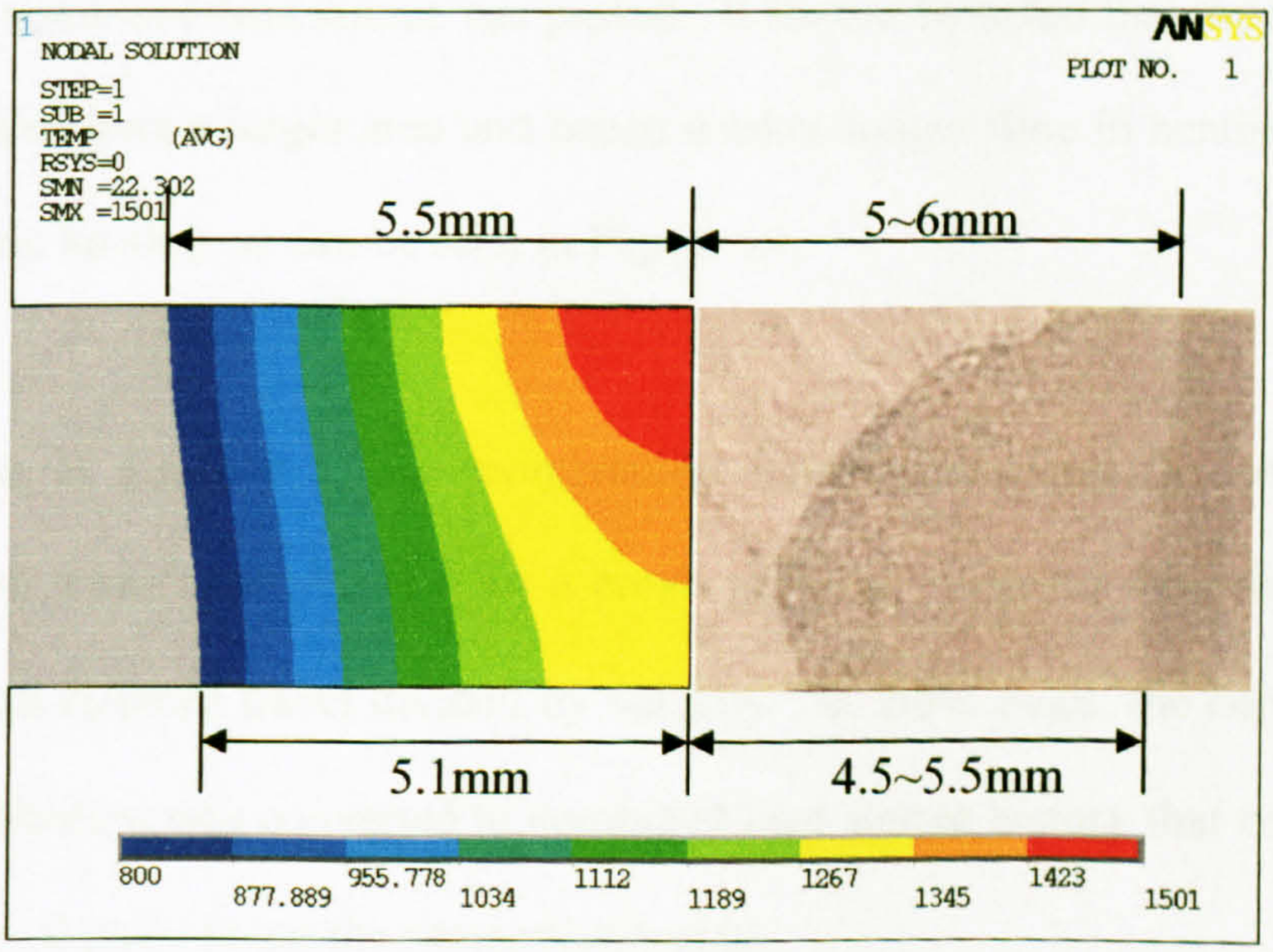

Figure 6.18

Simulated heat affected zone of model 1B

6.7 2D transient sectional models – Model C

As noted in Chapter 4, if the heat flow in the welding direction is neglected the temperature pattern in any of the cross-sectional planes will be the same throughout the plate. Consider a cross-sectional plane at some arbitrary position in the welding plate and this plane is subjected to the heat input in a transient manner as the welding heat source moves across this cross-sectional plane. In the cases considered here, the combined heat source moves across the cross-sectional plane and the top surface of the weld of this cross-sectional plane is subjected to different sections of the Gaussian heat flux at different times. The weld-preparation in this cross-sectional plane will only be subjected to volumetric heating when the heat generation part of the combined heat source reaches and heating terminates when the heat generation part of the combined heat source has passed. It should be noted that the surface heat flux is applied over a larger area and hence it takes longer time in heating compared to volumetric heating, as can be seen in Figure 6.1.

As mention in Chapter 5, the temperature distribution along the weld can be converted to temperature history for a cross-sectional plane via the relationship of time equal to distance travel divided by velocity. In these cases, the combined heat source distribution was converted to combined heat source history that occurred in a cross-sectional plane using the same relationship.

Due to the constraint of zero heat flow in the welding direction, more heat flows in directions normal to the weld path and thickness direction. In the previous models,

an artificial conductivity enhancement was applied to the weld pool to simulate the weld pool stirring effect. However, in these cases, weld pool stirring in the welding direction was not included. This could have generated a wider bottom weld width as shown in Figure 6.19. However, this could be eliminated by omitting the weld pool stirring effect in the thickness direction. This omission has been applied to all the 'V' weld-preparation models in this section.

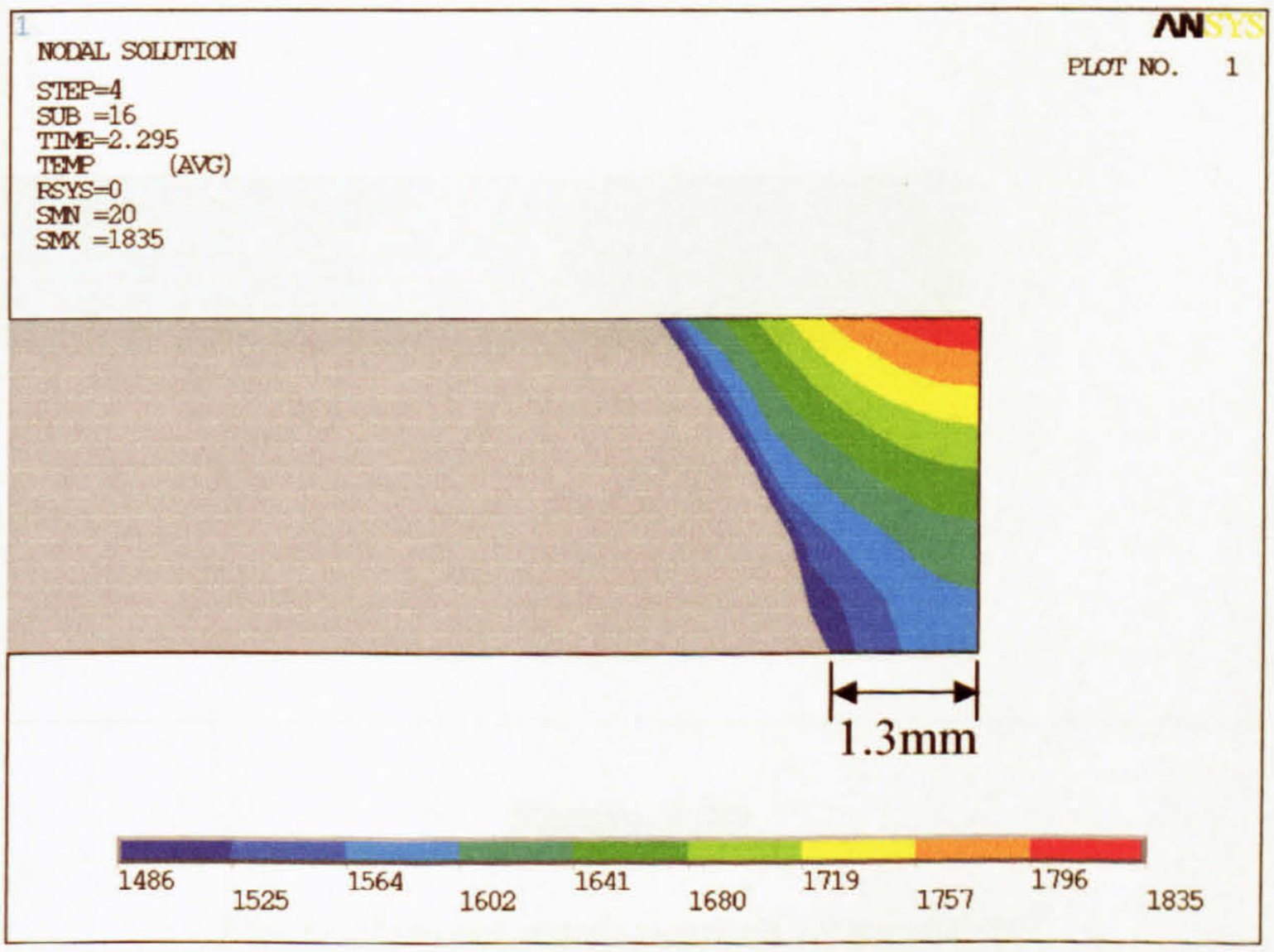

Figure 6.19

An example of wider bottom weld width

The element type chosen to perform the 2D transient simulations was 'PLANE55', which has a 2D thermal conduction capability and has four nodes with a single degree of freedom, temperature, at each node. The element is applicable to 2D transient thermal analysis.

This model only considered the left hand plate as the weld centreline plane was assumed to be adiabatic. Regions near the heat source were meshed with mixed elements corresponding to 0.5 mm per element approximately. A coarser mesh is adequate for the regions further away from the heat source as thermal gradients are less steep. Figure 6.20 shows a sample of the mesh patterns.

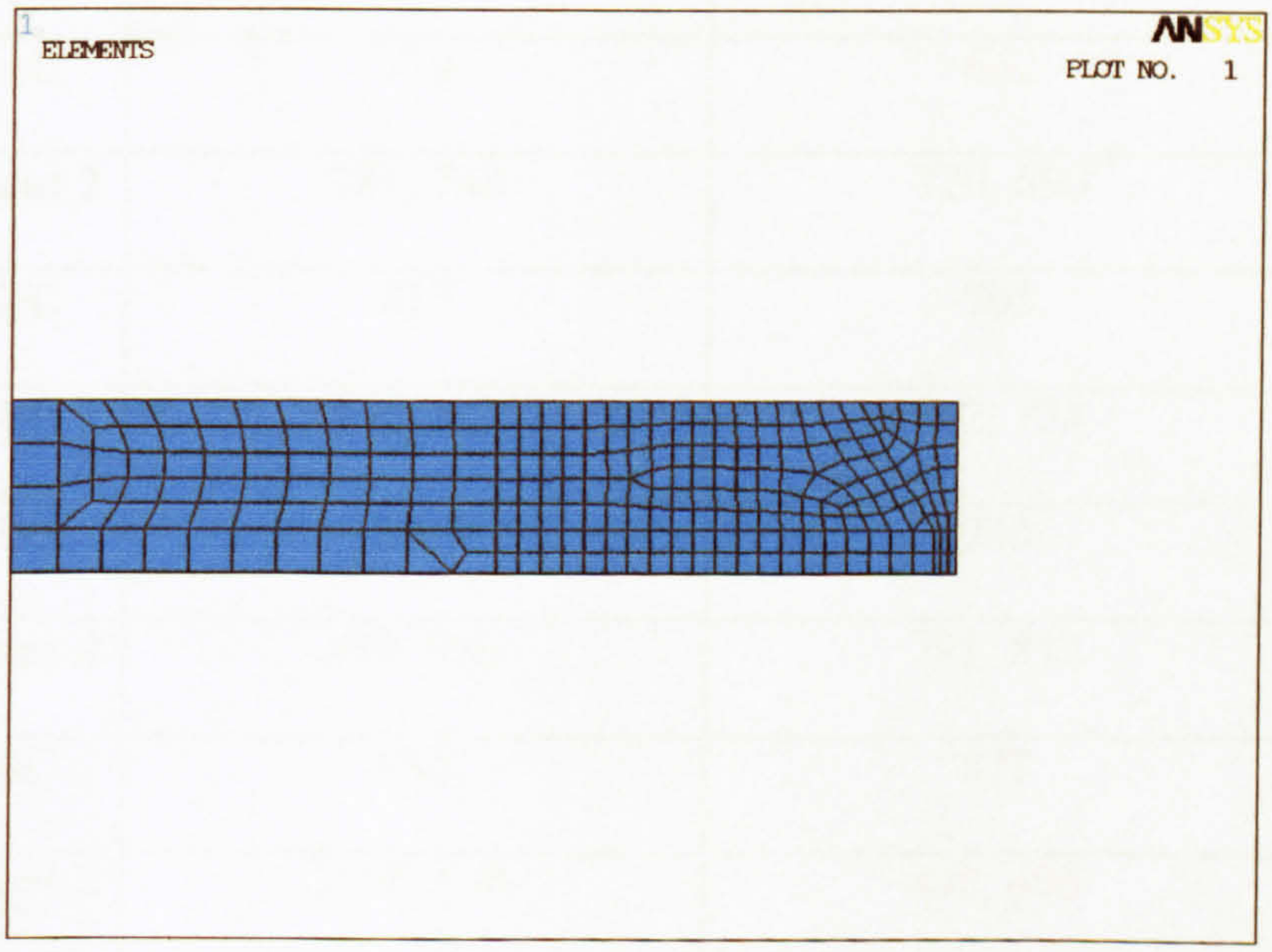

Figure 6.20

Finite element mesh pattern of model 1C

6.7.1 Discussion of Results

Table 6.6

Comparison of the simulated peak temperatures with the experimental measured peak temperatures

	T1 peak, T2 peak (°C)	B1 peak, B2 peak (°C)
Experiment 1	713, 733	647, 651
Model 1C	719	662
Experiment 2	781, 748	720, 690
Model 2C	817	705
Experiment 3	814, 812	712, 724
Model 3C	1084	745
Experiment 4	895, 916	791, 812
Model 4C	930	877
Experiment 5	1096, 686	498, 496
Model 5C	1266, 721	536

'T1 peak' refers to the measured peak temperature at location T1, the top thermocouples positions
'B1 peak' refers to the measured peak temperature at location B1, the bottom thermocouples positions
'T2 peak' refers to the measured peak temperature at location T2, the top thermocouples positions
'B2 peak' refers to the measured peak temperature at location B2 the bottom thermocouples positions
See figures 3.14, 3.16, 3.18, 3.20 and 3.22 for the detail locations of T1, B1, T2 and B2 in Chapter 3

Table 6.6 compares the simulated peak temperature with the measured peak temperature at the locations T1, T2, B1 and B2. The simulated top peak temperature of experiment 3 at locations T1/T2 was 1084°C which was higher than the experimentally measured peak temperature by 33%. This could be due to the fact that the welding speed (3.3 mm/s) of this experiment is not high enough to make the assumption of no heat flow in the welding direction. The simulated bottom peak

temperature of experiment 4 at location B1/B2 was higher than the experimental measured peak temperature by 9%. The simulated top peak temperature of experiment 5 at the location T1, T2 and B1/B2 were higher than the experimental measured peak temperature by 15.5%, 5% and 7.9% respectively. These could be the errors made due to the negligence of heat flow in the welding direction. Apart from that, all the simulated peak temperatures in table 6.6 were within the variation of ±5%. In general, the simulation results agreed fairly well with the experimental measurements.

Table 6.7

Comparison of the simulated results with the experimental measured results

	Weld top	Weld bottom	HAZ top	HAZ bottom
Experiment 1	7~9	1~2	10~12	9~11
Model 1C	8	1.2	11.8	11
Experiment 2	10~12.5	1~2	14~15	13.5~14.5
Model 2C	12.6	1.2	15	14
Experiment 3	12~13.5	1~2	16~17.5	13.5~15
Model 3C	15	1.4	19.2	16.2
Experiment 4	5~7	1~2	8.5~10.5	8~10
Model 4C	7	1.2	11	10.6
Experiment 5	7~8	NA	9~10	3.5~4.5
Model 5C	7.4	NA	10	4.8

See also Figures 1C-TW, 2C-TW, 3C-TW, 4C-TW and 5C-TW for the top weld width of model 1C, 2C, 3C, 4C and 5C respectively in Appendix C for the graphical plots. See also Figures 1C-BW, 2C-BW, 3C-BW and 4C-BW for the bottom weld width of model 1C, 2C, 3C and 4C respectively in Appendix C. See also Figures 1C-H, 2C-H, 3C-HT & 3C-HB, 4C-H and 5C-HT & 5C-HB for HAZ of model 1C, 2C, 3C, 4C and 5C respectively in Appendix C.

Table 6.7 compares the experimental weld pool widths with simulated weld pool widths and experimental heat affected zone (HAZ) with simulated HAZ. The second and third column of table 6.7 compares the experimental with the modelled weld pool top and bottom widths respectively. The simulated top weld pool width of experiment 3 was around 11% bigger than the experimental measured top weld width. This again could be due to the fact that the welding speed (3.3 mm/s) of this experiment is not high enough to make the assumption of no the heat flow in the welding direction. Aside from that, the modelled weld pool top widths were observed to be on the high side of the experimental weld pool top widths ranges or slightly bigger than the experimental top weld widths. The modelled weld pool bottom widths were on the low side of the experimental bottom weld widths.

The forth and last column of table 6.7 compares the experimental HAZ top and bottom widths with the modelled HAZ top and bottom widths. The simulated top and bottom HAZ widths of experiment 3 were around 10% and 8% larger than the experimental measured HAZ widths. This again could be due to the fact that the welding speed (3.3 mm/s) of this experiment is not high enough to make the assumption of no the heat flow in the welding direction. Apart from that, all the modelled HAZ top and bottom widths were observed to be either falls on the high side of the experimentally measured ranges or slightly bigger than the experimental measurements. In overall, the simulation results agreed fairly well with the experimental results.

As demonstrated in Chapter 5, the temperature distribution along the weld of the 3D steady state model can be converted into the temperature history at location normal to the weld. Therefore, the temperature history of the 2D transient sectional model can also be converted into the temperature distribution along the weld using the same relationship. In order to present the simulated 2D sectional weld pools in 3D form, the temperature histories of the 2D sectional weld pool have been converted to temperature distributions along the weld to produce an overall view of the temperature contours of the weld pool as shown in Figure 6.21.

The converted 3D form of weld pool of Model 1C was presented in Figure 6.21. (See also Figures 1C-P, 2C-P, 3C-P, 4C-P and 5C-P for the overall view of the converted weld pool of models 1C, 2C, 3C, 4C and 5C respectively in Appendix C) The maximum temperature of the weld pool for all 2D sectional transient models are higher than Krans's [18] experimental measurement range of stationary weld pools from 1950°C to 2708°C. The peak temperature of the weld pool for Models 2C and 3C were 3690°C and 3875°C respectively. These temperatures were higher than the boiling point of the impure steel (3000°C). These probably were the errors made due to the negligence of heat flow in the welding direction. However, the shapes of the simulated weld pool were similar 3D steady state model where the weld pool length is slightly longer than 3D transient model.

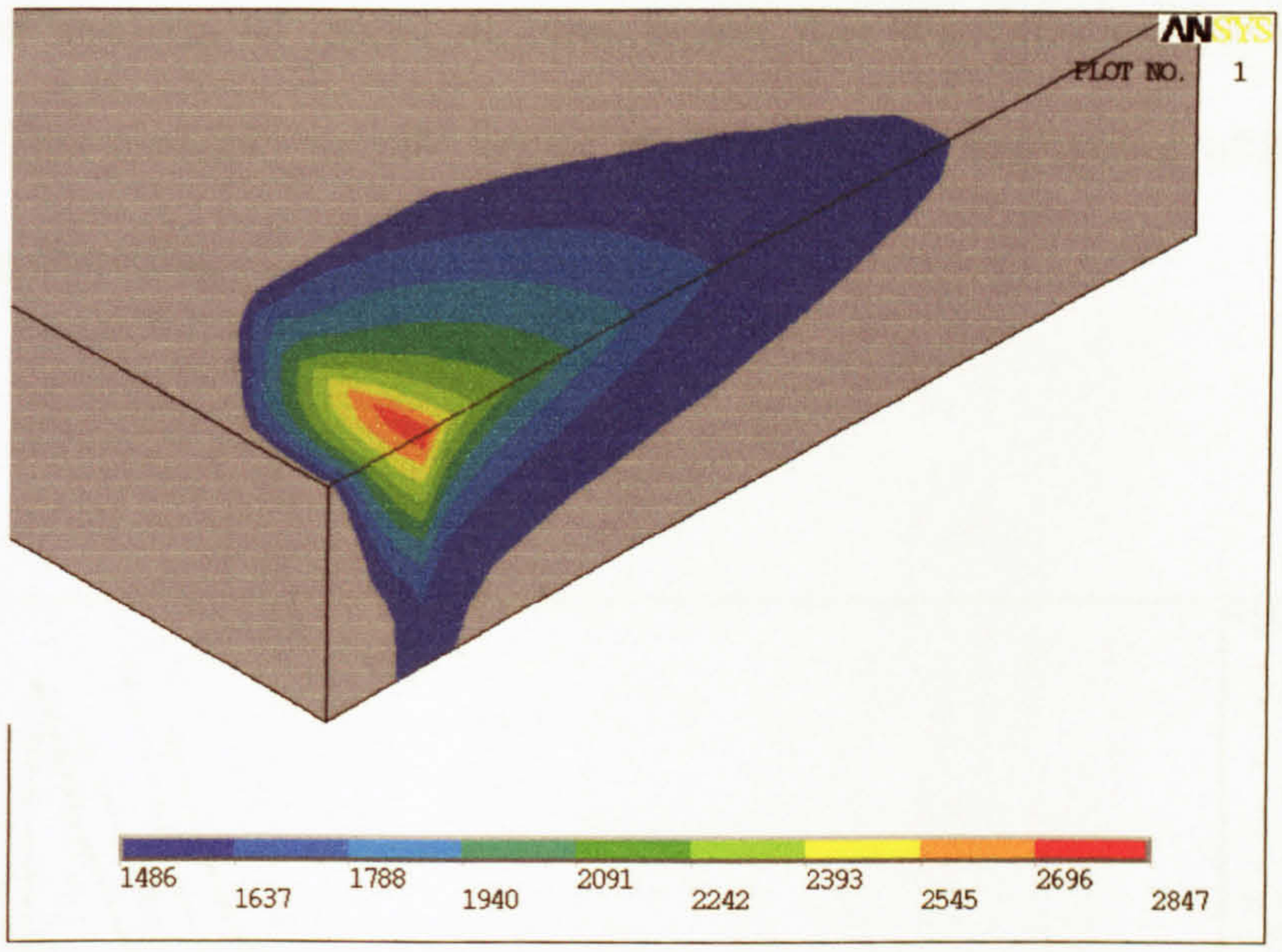

Figure 6.21

The converted temperature contour of the weld pool of model 1C

Figure 6.22 compares the experimentally measured temperature histories with the simulated temperature histories of models 1C. The simulated temperature histories of model 1C were in good agreement with the experimentally measured temperature histories. The rest of the modelled temperature histories compared with similarly well the experimentally measured temperature histories as Model 1C except Model 3C and 4C. (See also Figures 1C-TH, 2C-TH, 3C-TH, 4C-TH and 5C-TH for the comparison between the experimentally measured temperature histories and the converted temperature histories of models 1C, 2C, 3C, 4B and 5B respectively in Appendix C for the rest of the models) The computed top temperature histories of Model 3C was higher that the experimental temperature histories. As mentioned previously, this could be due to the fact that the welding speed is not high enough to make the assumption of no the heat flow in the welding direction. The bottom

temperature histories of model 4C was higher that the experimental temperature histories. This probably was the errors made due to the negligence of heat flow in the welding direction.

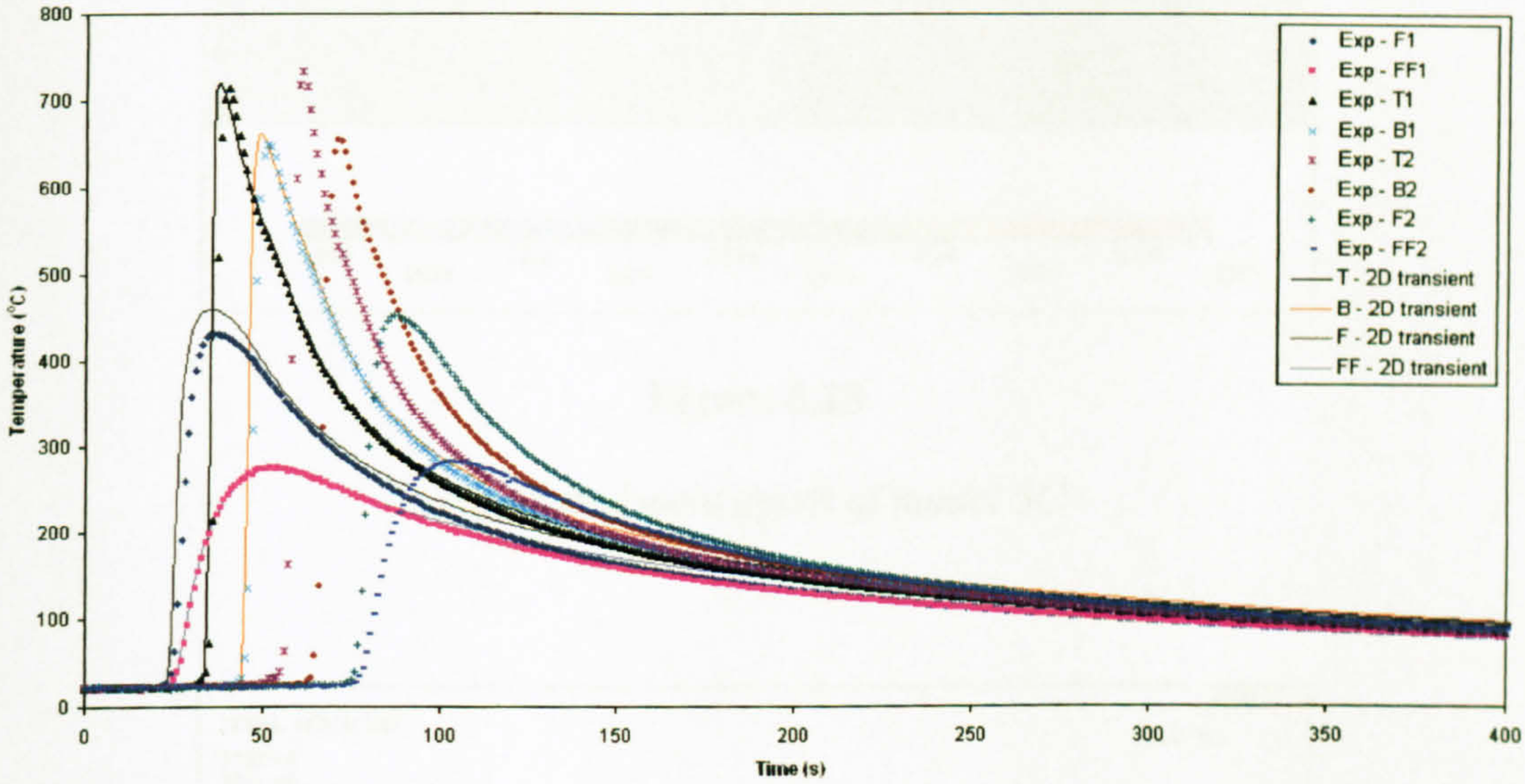

Figure 6.22

Comparison of the simulation temperature histories of model 1C with the measured

Figure 6.23 shows that the simulated depth of the weld of model 5C was shallower than actual weld depth. However, the simulated weld depth of this model was slightly deeper than the previous models. This could be due to the negligence of the heat flow in the welding direction that resulted to more heat flow in the vertical downward direction and thus caused the simulated weld depth to be slightly better than the previous models. In any case, the simulated depth of this model was still shallower than actual weld depth.

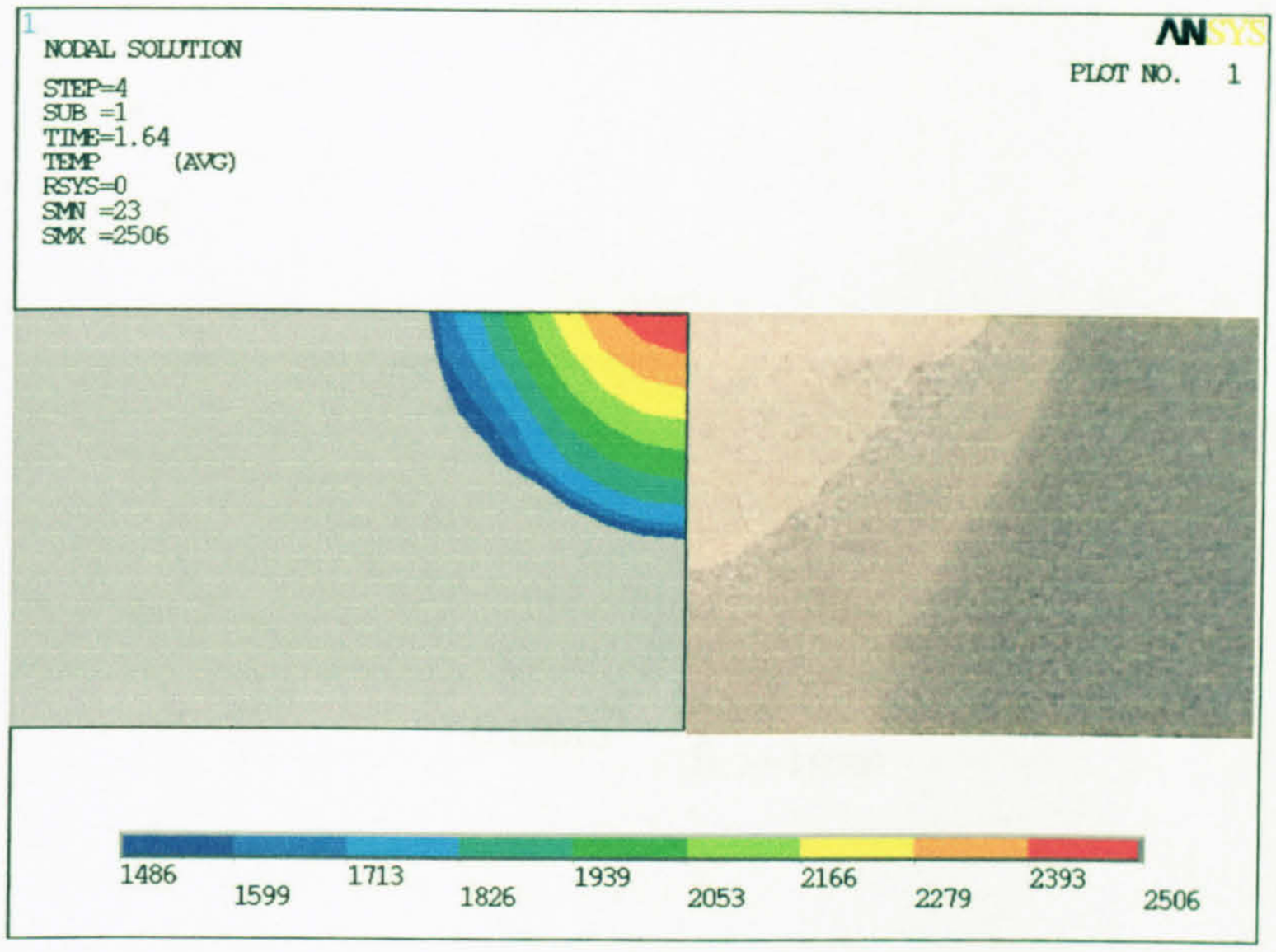

Figure 6.23

Simulated weld depth of model 5C

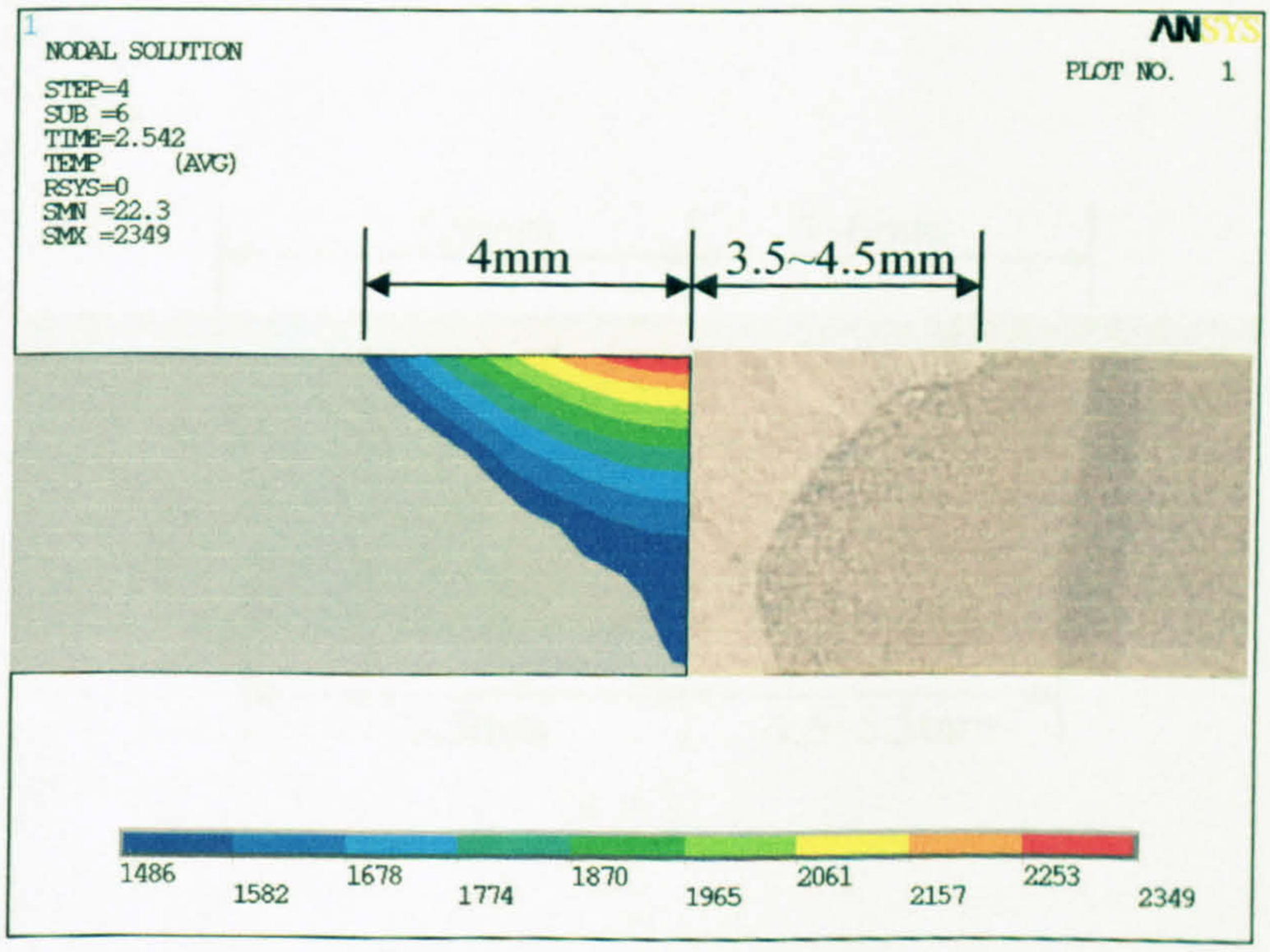

Figure 6.24

Simulated top weld widths of model 1C

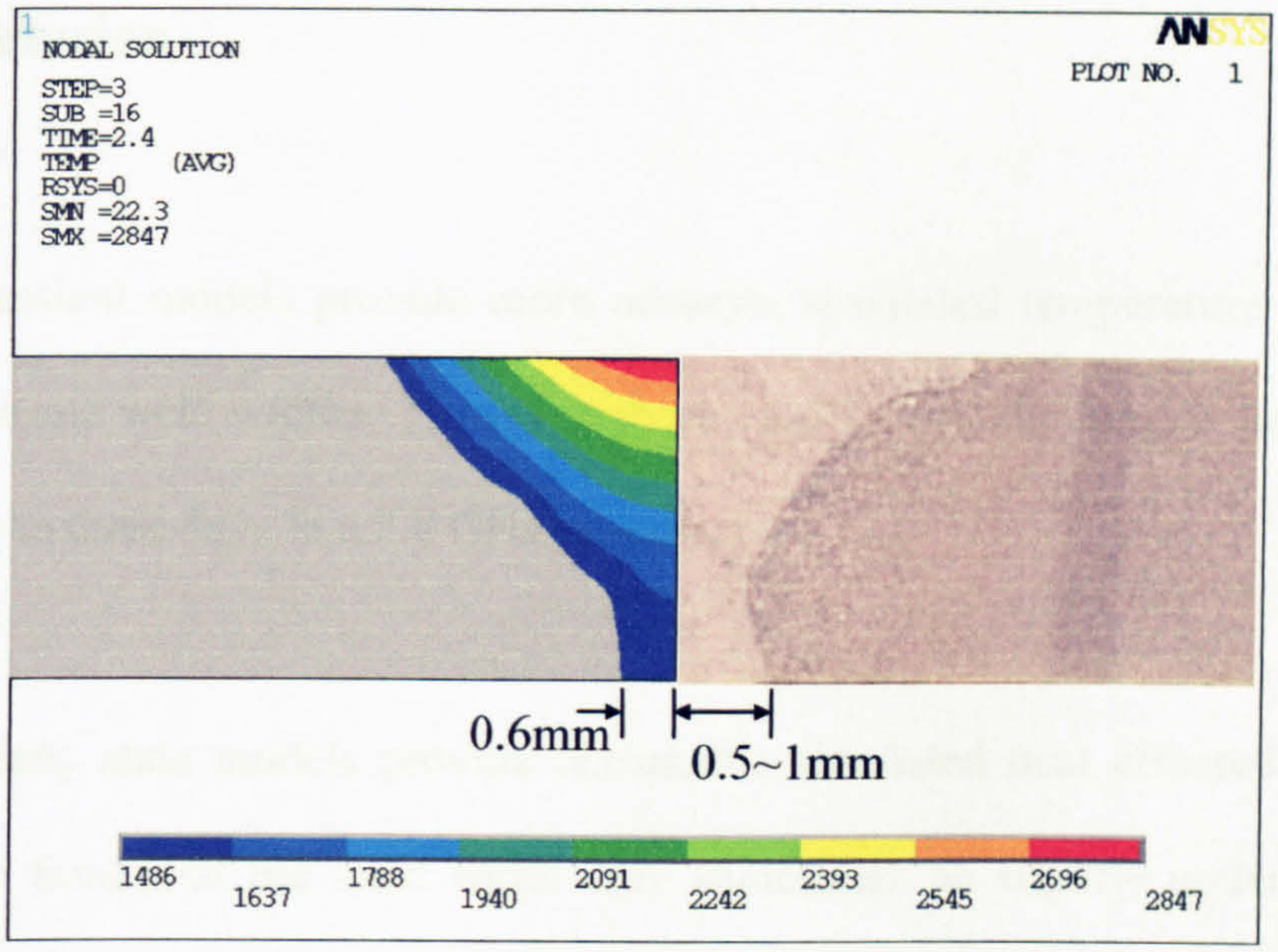

Figure 6.25

Simulated bottom weld widths of model 1C

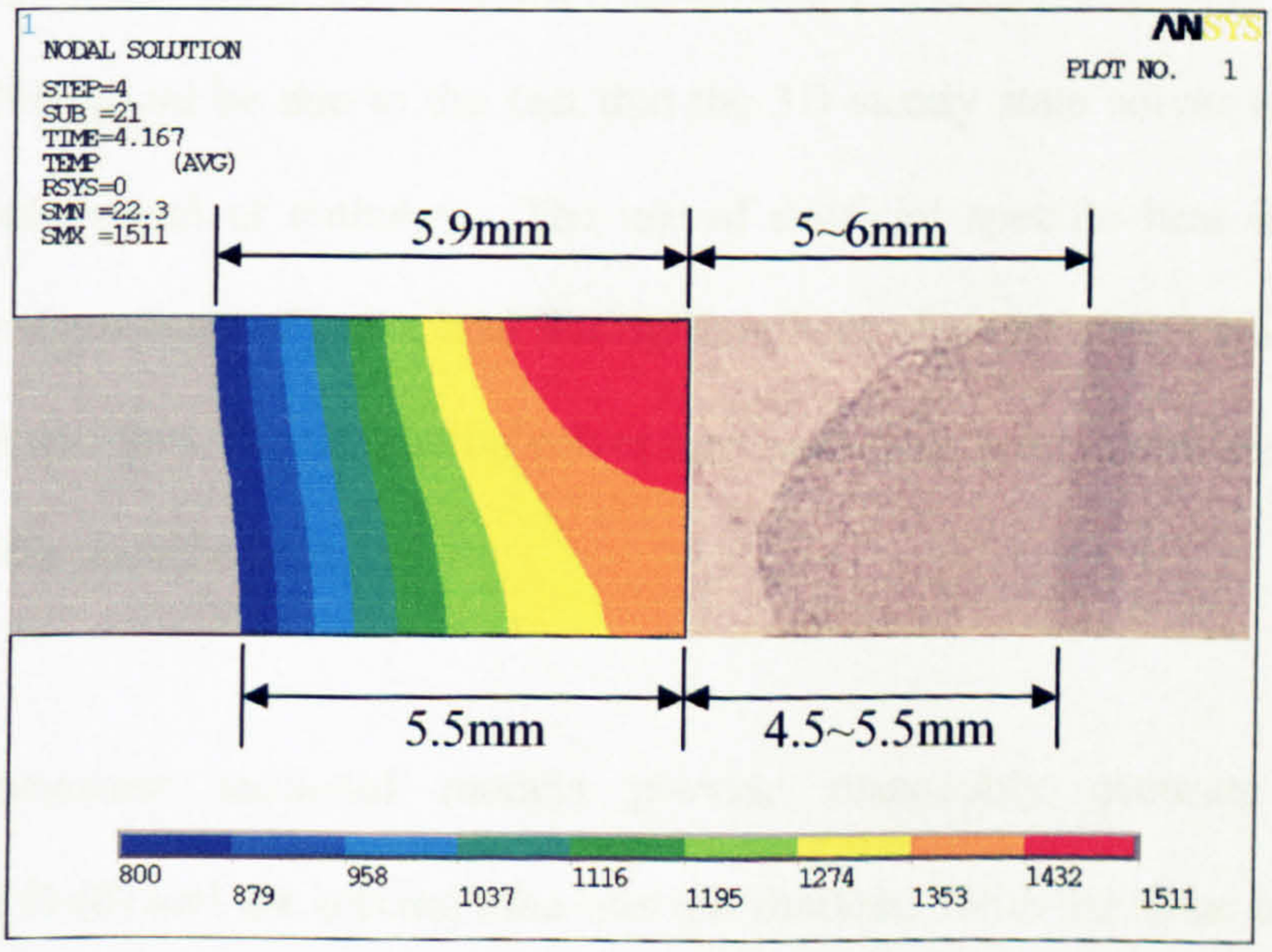

Figure 6.26

Simulated heat affected zone of model 1C

6.8 Conclusion

The 3D transient models provide more accurate simulated temperature fields, heat affect zones and weld widths. However, these models took the longest time to solve, around two to three days in a 2.8 GHz processor.

The 3D steady state models provide reasonable simulated heat affected zones and temperature fields but the weld width may sometimes be slightly under predicted. The converted temperature histories are limited by the length of the model. However, the maximum temperature of weld pool may at times be lower than expected. The problem took 2 to 3 hours to solve using the same computer. The solutions of these steady state models occasionally fluctuated during the solving process. This could be due to the fact that the 3D steady state solver can only use specific heat instead of enthalpy. The use of artificial specific heat is needed to account for the release of latent heat during the phase changes over a small range of temperature and thus, the simulation solver may sometime miss capturing the sudden changes of the specific heat.

The 2D transient sectional models provide reasonably accurate simulated temperature fields and the solving time was the shortest. With the same computer, it took only around 5 minutes to solve. However, sometimes the simulated weld width was wider than the experimental measurement, the peak temperatures at locations near or within the heat affected zone were higher than the measured values and the maximum temperature of the weld pool was sometimes even higher than the boiling

point (3000°C) of impure steel. This probably was because the heat flow in the welding direction was neglected in the 2D transient sectional models. This resulted in more heat flow in the direction normal to the weld path and consequently the simulation results were higher than the measured results. However, the simulated temperature history at locations away from heat affected zone was in good agreement with the experimental temperature history.

Experience suggests that the 2D transient sectional models may provide a better cooling temperature history than the 3D steady state models. This is because the 2D transient sectional model is permitted to use enthalpy for simulation.

Chapter 7 – Discussion

7.1 Introduction

Various vital input parameters have been used in the previous computer modelling, namely the heat input efficiency factor, the radius of the Gaussian heat source, the temperature of the molten filler droplet and the value of the enhancement conductivity to simulate the weld pool stirring motion. These parameters were obtained by trial and error in the process of trying to match the simulated results with the experimental values. It is important to study the effects of slight variation of these parameters on the predicted results. The surface emissivity is another important parameter that takes into account the surface radiation heat loss from the plate during welding process. The emissivity values were taken from [38] for the computer simulations. However, these values are sometimes not easy to obtain and may differ from one book to another. Therefore, it is necessary to study the effects of using different values of emissivity on the computed results.

The investigation of these parameters is presented in Section 7.2. It should be noted that the models in these sections were computed according to welding parameters of experiment 4 – 'V' weld-prep 3 mm thick plate using the 3D transient model. This was chosen because model 4A was found to be very sensitive to small changes in the input parameters that result in significant changes of the computed results.

In addition, some important observations on the cooling rate history are described in Section 7.3.

7.2 Effect of slight variation of input parameter

7.2.1 Effect of heat input efficiency factor

The heat input efficiency factor of 0.87 has been used for the computer simulation of Model 4A in Chapter 6. In order to see the sensitivity of heat input efficiency factor, two further heat input efficiency factors of 0.85 and 0.89 were used while keeping all other parameters unchanged.

Table 7.2.1 presents a summary of these computed results. The unreasonable computed values which are considered to be out of reasonable range are highlighted in yellow. The values in table 7.2.1 have been plotted in graphical form and shown in Figure 7.2.1a. It can be seen that, as the heat input efficiency factor increases, the size of the computed top and bottom weld width, the peak temperature of the weld pool and the computed top and bottom surface peak temperatures increase.

The computed weld pool peak temperature of the model with heat input efficiency factor 0.85 was slightly lower than the experimental stationary weld pool peak temperature over the range of 1950°C to 2708°C [18]. The computed bottom surface peak temperature with heat input efficiency factor 0.89 was slightly higher than the

experimental results. Figure 7.2.1b compares the temperature histories of points at T1 and B1 for various heat input efficiency factors where T1 is located at the upper face of the plate and B1 is located at the lower face of the plate, both within the heat affected zone. This plot shows that the model with higher heat input efficiency factor cools down at a higher cooling path and vice versa. Overall, slight variation of heat input efficiency factor has little significant effect on the computed results but has a bigger effect on the cooling paths of the temperature histories.

Table 7.2.1

The computed results summary of various heat input efficiency factors

Heat input efficiency factor	**0.85**	**0.87**	**0.89**
Top weld width (mm)	5.7	5.8	6
Bottom weld width (mm)	1.2	1.2	1.4
Weld pool peak temperature (^{o}C)	1898	1905	1918
T1/T2 peak temperature (^{o}C)	865.6	889.5	907.8
B1/B2 peak temperature (^{o}C)	811	834.3	854.5

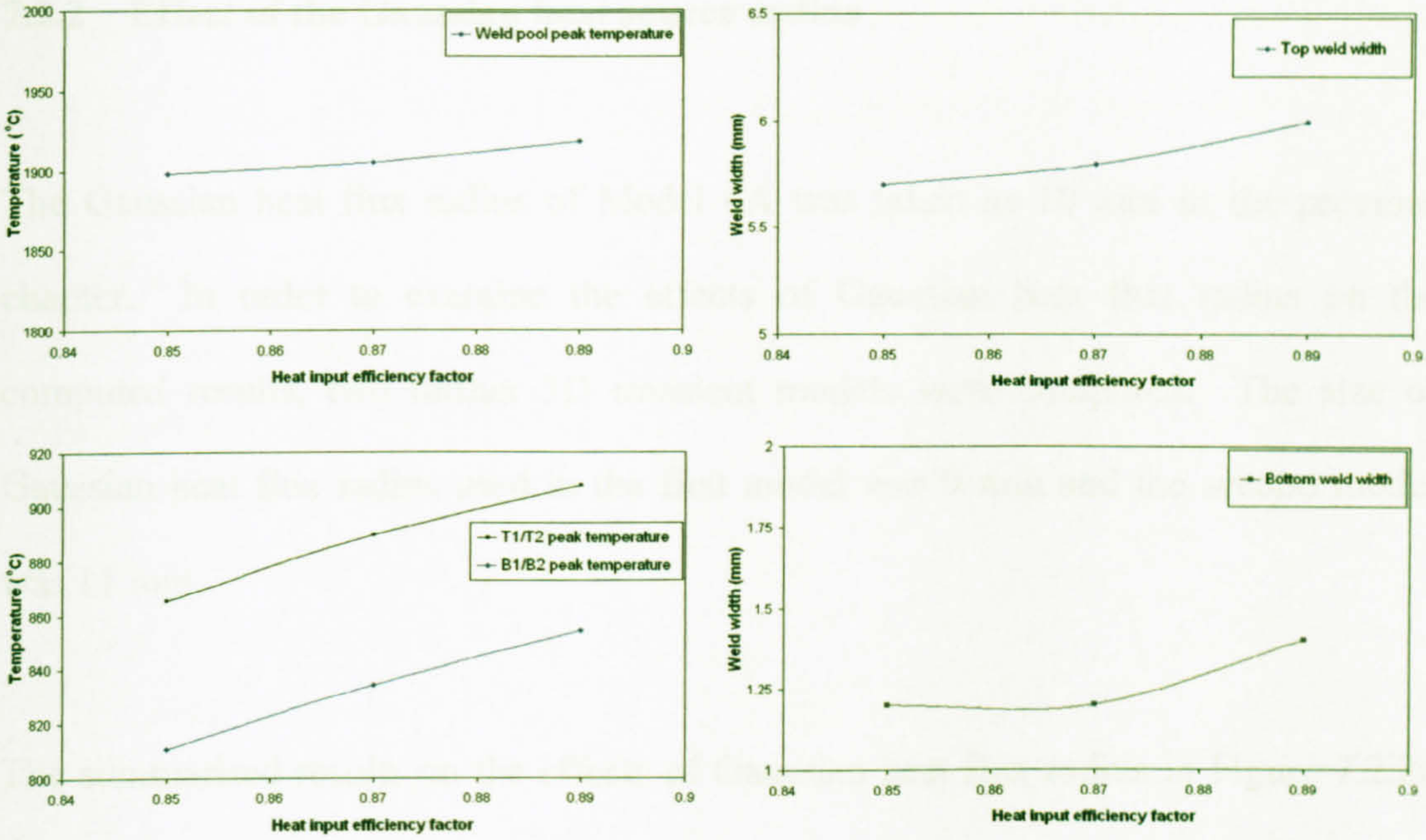

Figure 7.2.1a

The computed results summary of various heat input efficiency factors

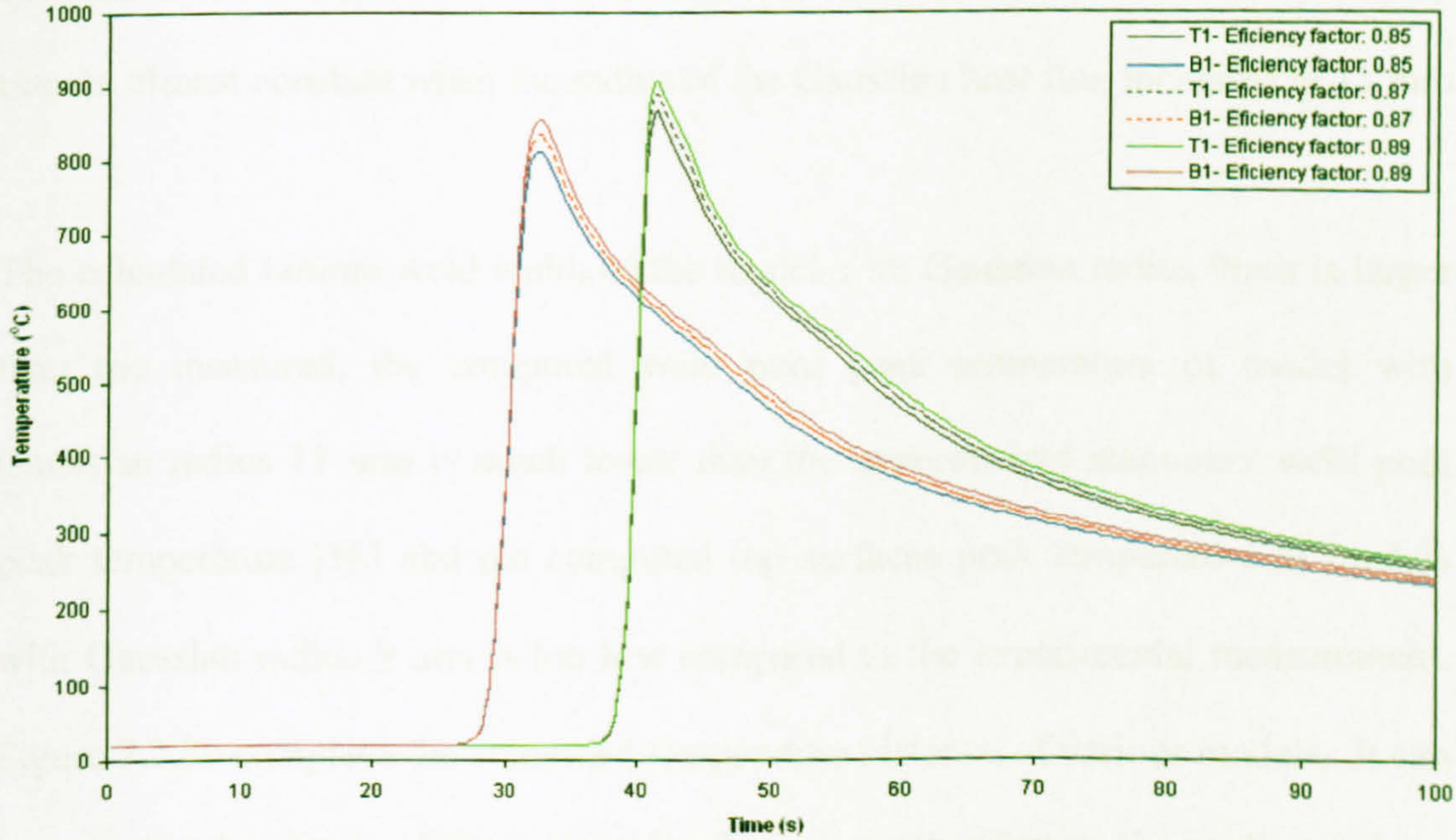

Figure 7.2.1b

Comparison of temperature histories

7.2.2 Effect of the Gaussian heat source radius

The Gaussian heat flux radius of Model 4A was taken as 10 mm in the previous chapter. In order to examine the effects of Gaussian heat flux radius on the computed results, two further 3D transient models were computed. The size of Gaussian heat flux radius used in the first model was 9 mm and the second model was 11 mm.

The summarised results on the effects of Gaussian heat flux radius in Figure 7.2.2a and table 7.2.2 show that peak temperature of the weld pool and the computed top and bottom weld widths decrease as the Gaussian heat flux radius increases. In addition, they show that the predicted top and bottom surface peak temperatures increase as the radius of the Gaussian heat flux increases from 9 to 10 mm but they remain almost constant when the radius of the Gaussian heat flux increases to 11 mm.

The calculated bottom weld width of the model with Gaussian radius 9mm is larger than the measured, the computed weld pool peak temperature of model with Gaussian radius 11 mm is much lower than the experimental stationary weld pool peak temperature [18] and the computed top surfaces peak temperature of models with Gaussian radius 9 mm is too low compared to the experimental measurement. Figure 7.2.2b compares the computed temperature histories of various models. It can be seen that the change of Gaussian radius has not much effect on the cooling path.

On the whole, the size of the Gaussian heat flux radius has a strong influence on the bottom weld width, top surface peak temperature and weld pool peak temperature.

Table 7.2.2

The computed results summary of various sizes of Gaussian heat flux radius

Gaussian heat flux Radius (mm)	**9**	**10**	**11**
Top weld width (mm)	6	5.8	5.4
Bottom weld width (mm)	2.4	1.2	1
Weld pool peak temperature (°C)	1966	1905	1861
T1/T2 peak temperature (°C)	860.9	889.5	888.6
B1/B2 peak temperature (°C)	842.2	834.3	833.1

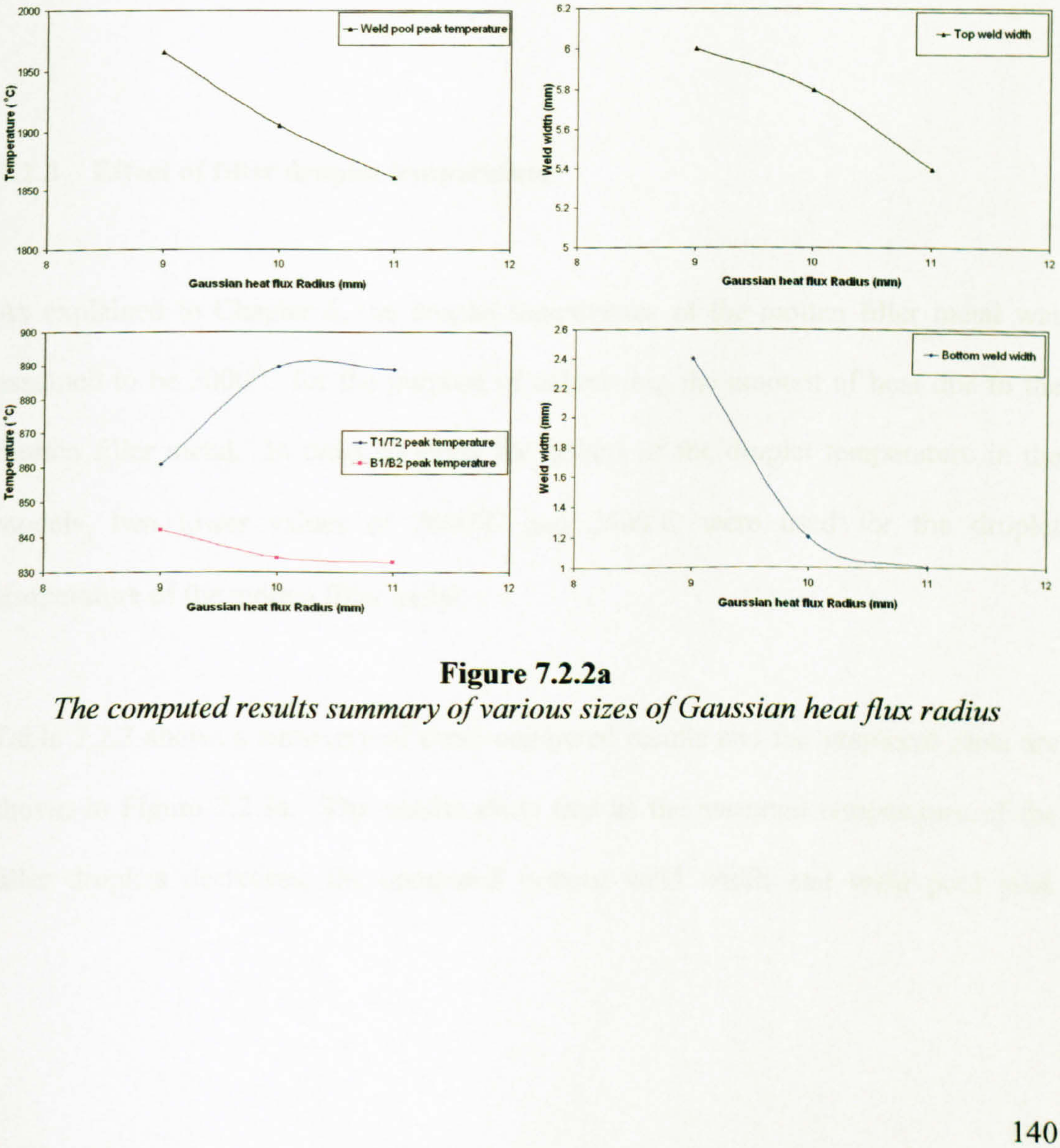

Figure 7.2.2a

The computed results summary of various sizes of Gaussian heat flux radius

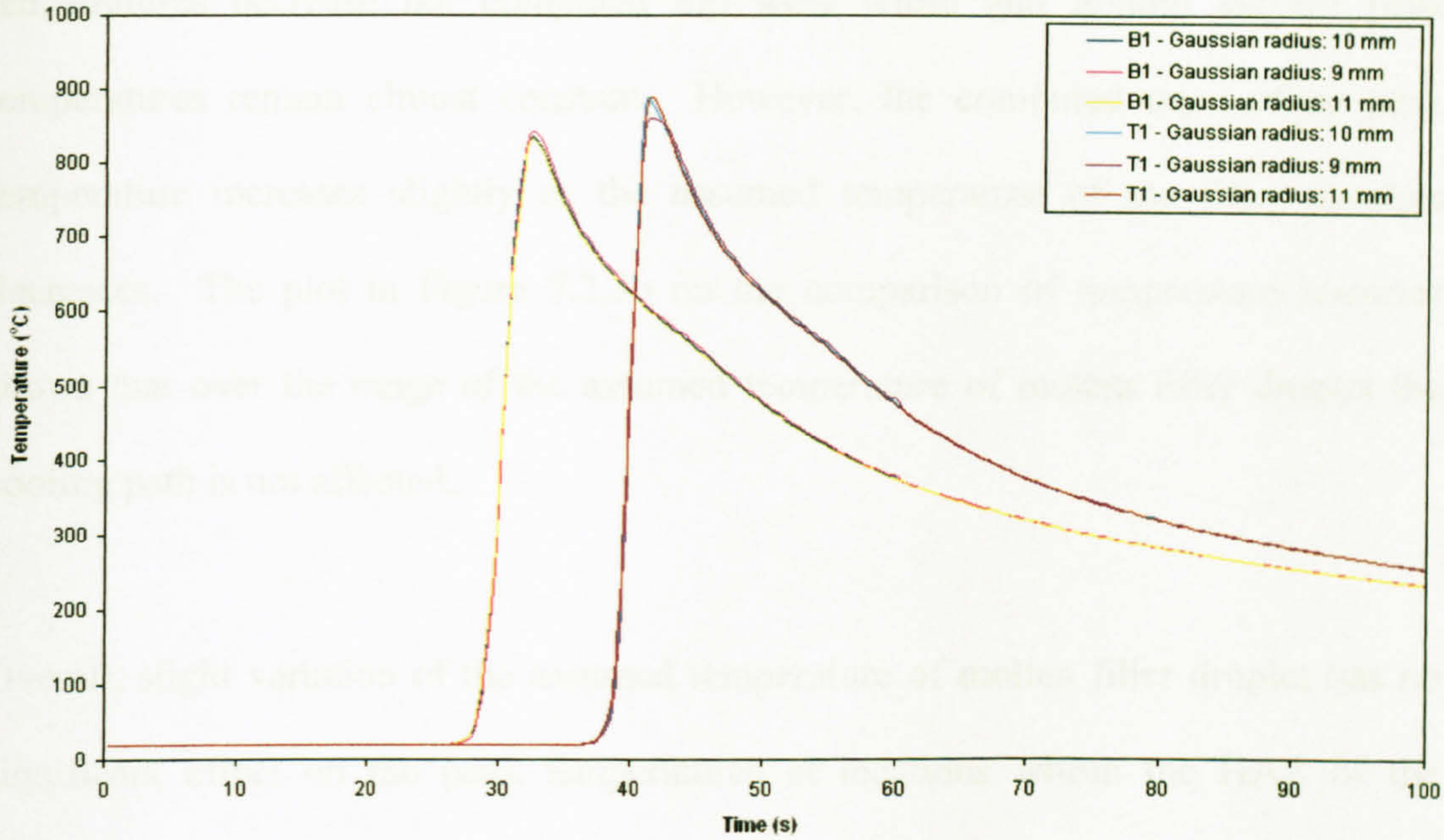

Figure 7.2.2b

Comparison of temperature histories

7.2.3 Effect of filler droplet temperature

As explained in Chapter 6, the droplet temperature of the molten filler metal was assumed to be 3000°C for the purpose of calculating the amount of heat due to the molten filler metal. In order to study the effects of the droplet temperature in the models, two lower values of 2800°C and 2600°C were used for the droplet temperature of the molten filler metal.

Table 7.2.3 shows a summary of these computed results and the graphical plots are shown in Figure 7.2.3a. The results show that as the assumed temperature of the filler droplets decreases, the computed bottom weld width and weld pool peak

temperatures decrease but computed top weld width and bottom surface peak temperatures remain almost constant. However, the computed top surface peak temperature increases slightly as the assumed temperature of the filler droplets decreases. The plot in Figure 7.2.3b on the comparison of temperature histories shows that over the range of the assumed temperature of molten filler droplet the cooling path is not affected.

Overall, slight variation of the assumed temperature of molten filler droplet has no significant effect on the peak temperatures at locations within the HAZ of the welding plate but it has a slight influence on the weld pool peak temperature.

Table 7.2.3

The computed results summary of assumed molten filler droplets temperature

Molten filler droplet temperature (^{o}C)	**3000**	**2800**	**2600**
Top weld width (mm)	5.8	5.8	5.8
Bottom weld width (mm)	1.2	1.1	1.1
Weld pool peak temperature (^{o}C)	1905	1901	1886
T1/T2 peak temperature (^{o}C)	889.5	891	896.5
B1/B2 peak temperature (^{o}C)	834.3	834.6	835.1

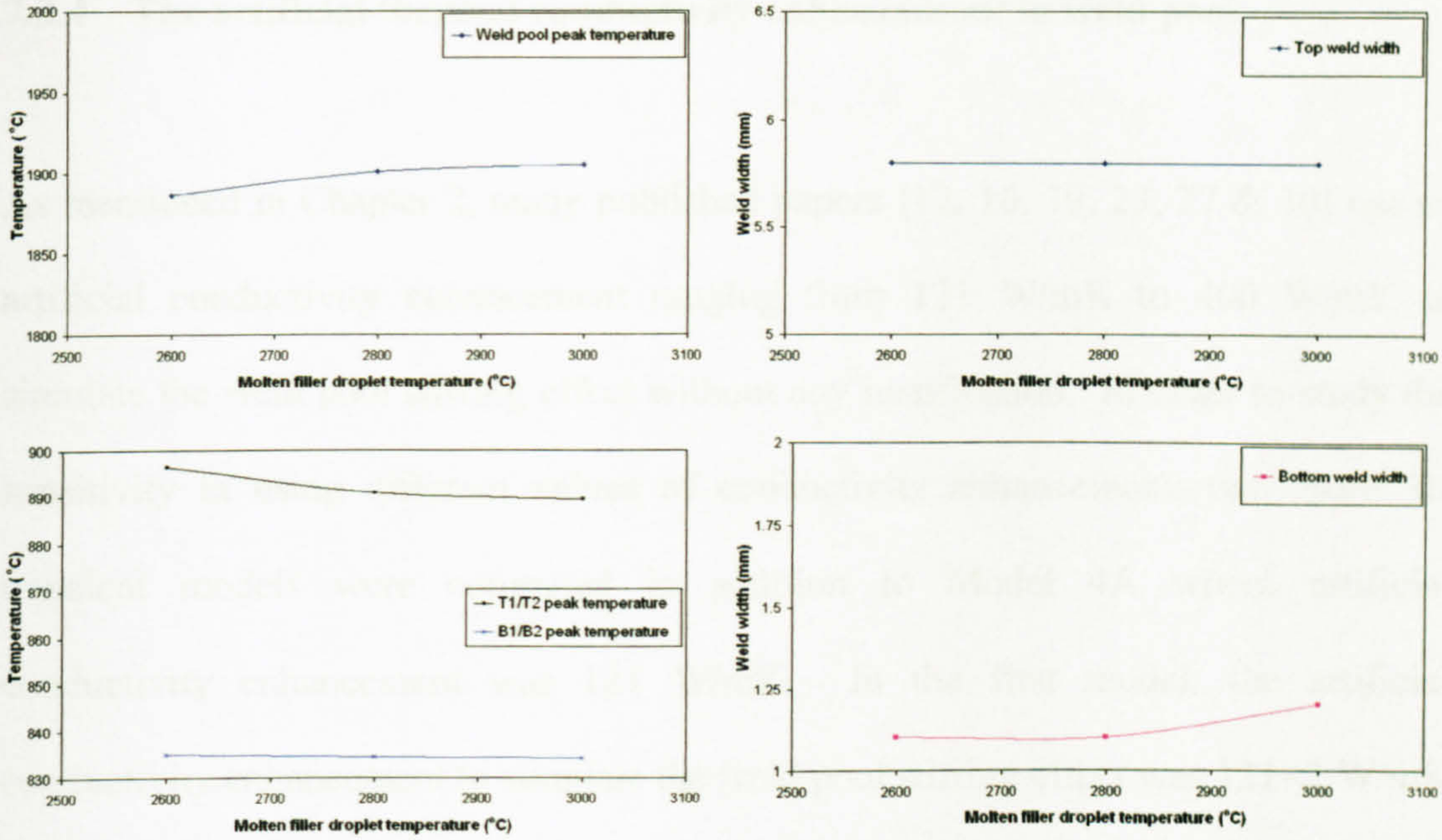

Figure 7.2.3a

The computed results summary of assumed molten filler droplets temperature

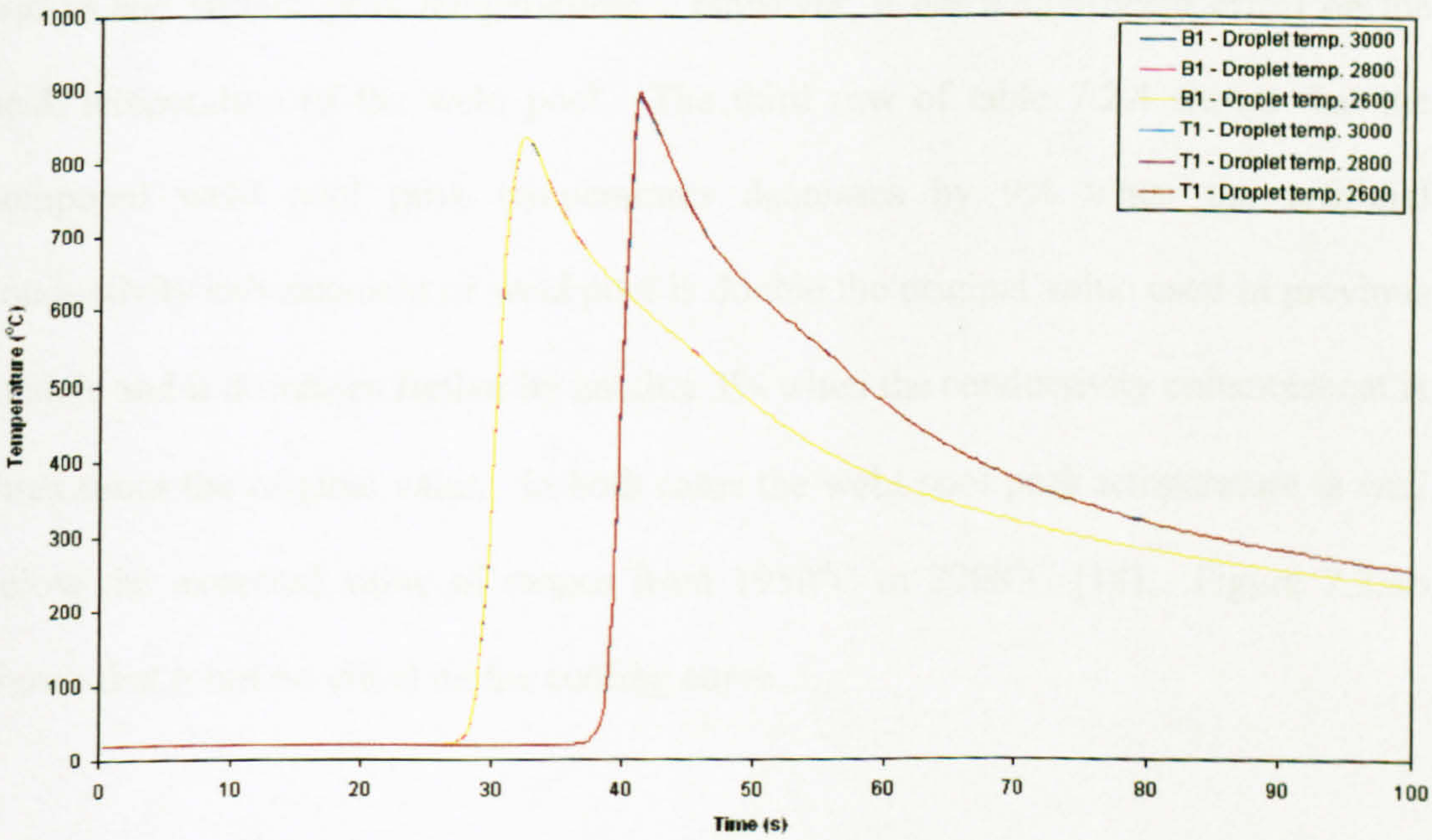

Figure 7.2.3b

Comparison of temperature histories

7.2.4 The artificial thermal conductivity enhancement in weld pool

As mentioned in Chapter 2, many published papers [12, 16, 19, 23, 27 & 30] use an artificial conductivity enhancement ranging from 121 W/mK to 400 W/mK to simulate the weld pool stirring effect without any justification. In order to study the sensitivity in using different values of conductivity enhancement, two more 3D transient models were computed in addition to Model 4A where artificial conductivity enhancement was 121 W/mK. In the first model, the artificial conductivity enhancement to simulate the weld pool stirring effect was 121×2 W/mK and 121×3 W/mK in the second one.

Table 7.2.4 and Figure 7.2.4a present the result summary of these computations. Both the table and Figure show that the change of artificial conductivity enhancement of weld pool has very mild effect on the computed top and bottom weld widths and surface peak temperatures. However, it has a significant effect on the peak temperature of the weld pool. The third row of table 7.2.4 shows that the computed weld pool peak temperatures decreases by 9% when the artificial conductivity enhancement of weld pool is double the original value used in previous models and it decreases further by another 3% when the conductivity enhancement is three times the original value. In both cases the weld pool peak temperature is well below the expected value of ranges from 1950°C to 2708°C [18]. Figure 7.2.4b shows that it has no effect on the cooling curve.

Overall, the value of artificial conductivity enhancement of weld pool is seen to have an influence on the peak temperature of the computed weld pool only.

Table 7.2.4

The computed results summary of the various values of conductivity enhancement

Thermal conductivity in weld pool (W/m K)	**121**	**121 × 2**	**121 × 3**
Top weld width (mm)	5.8	5.7	5.7
Bottom weld width (mm)	1.2	1.2	1.4
Weld pool peak temperature (°C)	1905	1737	1676
T1/T2 peak temperature (°C)	889.5	889.6	890
B1/B2 peak temperature (°C)	834.3	836.7	838.6

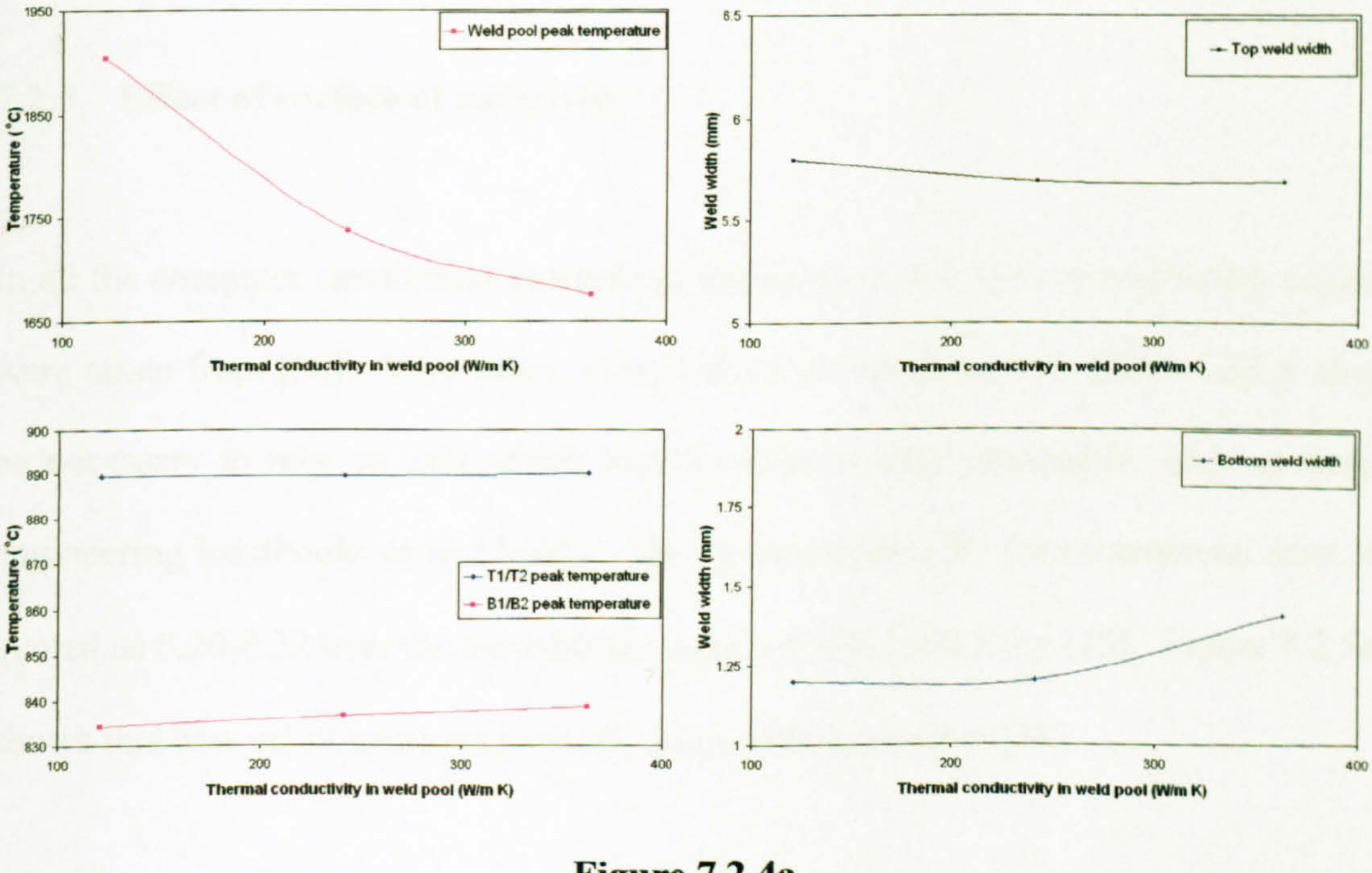

Figure 7.2.4a

The computed results summary of the various values of conductivity enhancement

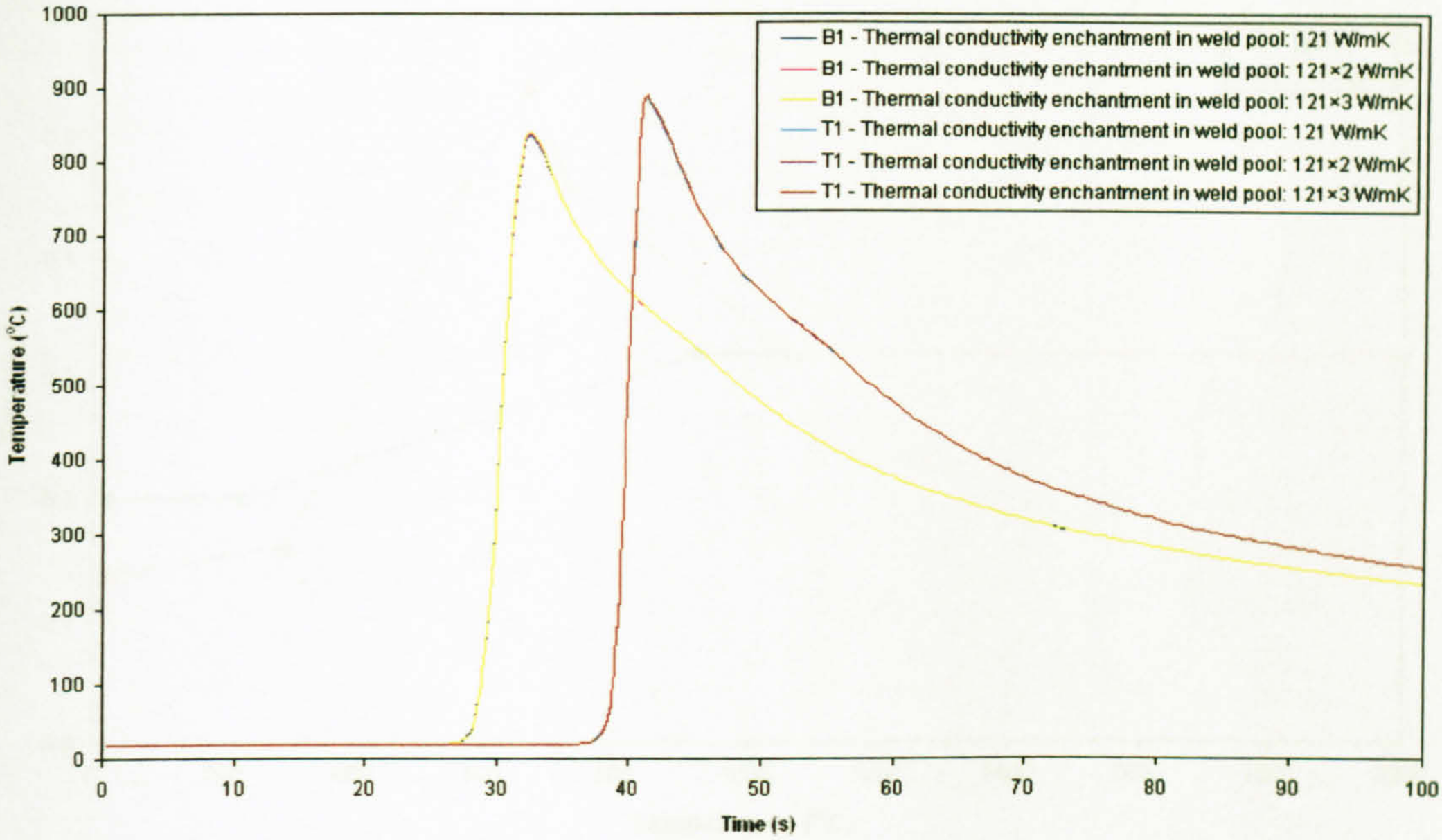

Figure 7.2.4b

Comparison of temperature histories

7.2.5 Effect of surface of emissivity

In all the computer simulations carried out in this work, the surface emissivity values were taken from [38]. Very often, these values are not always available and it may be necessary to rely on data which may be more readily obtainable, such as from engineering handbooks or text books. The surface emissivity for commercial steel is quoted as 0.20-0.32 over the temperature range of 300-1200 K by [45]. Figure 7.2.5a shows this new set of emissivity values along with those from [38].

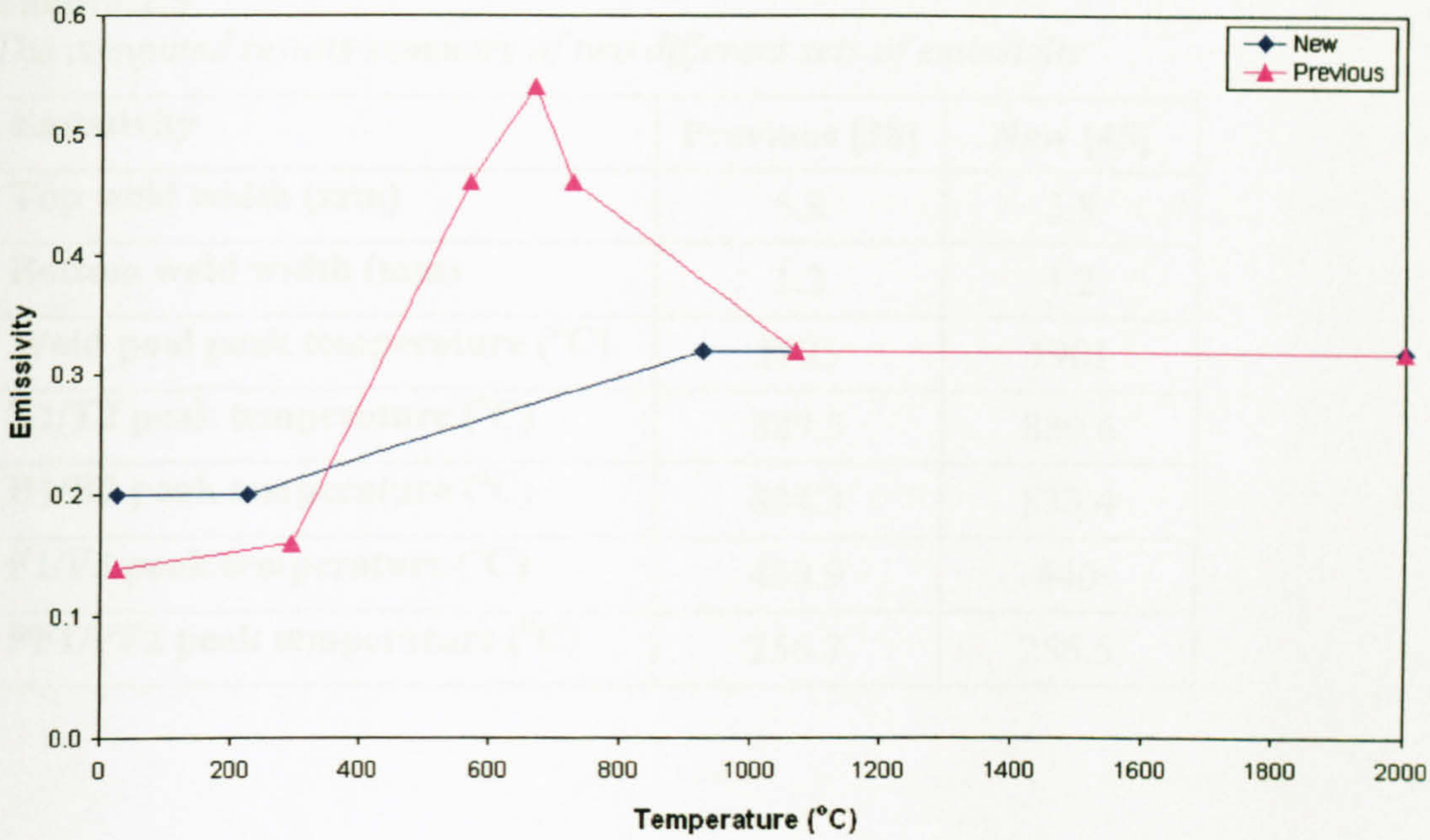

Figure 7.2.5a

The two set of emissivity values

The effects of using these two sets of emissivity values are given in Table 7.2.5. It can be seen that, the two sets of results are almost identical. The only obvious difference is the weld pool peak temperature where the result of the new set is slightly lower than the previous.

Figure 7.2.5b compares the temperature histories of using two different set of emissivity values. The comparison shows that these values of emissivity have negligible influence on the cooling path.

On the whole, slight variation of the emissivity values has almost no effect on the results except it has only a very slight influence on the weld pool peak temperature.

Table 7.2.5

The computed results summary of two different sets of emissivity

Emissivity	Previous [38]	New [45]
Top weld width (mm)	5.8	5.8
Bottom weld width (mm)	1.2	1.2
Weld pool peak temperature (^{o}C)	1905	1901
T1/T2 peak temperature (^{o}C)	889.5	889.6
B1/B2 peak temperature (^{o}C)	834.3	833.4
F1/F2 peak temperature (^{o}C)	439.9	440
FF1/FF2 peak temperature (^{o}C)	256.7	256.5

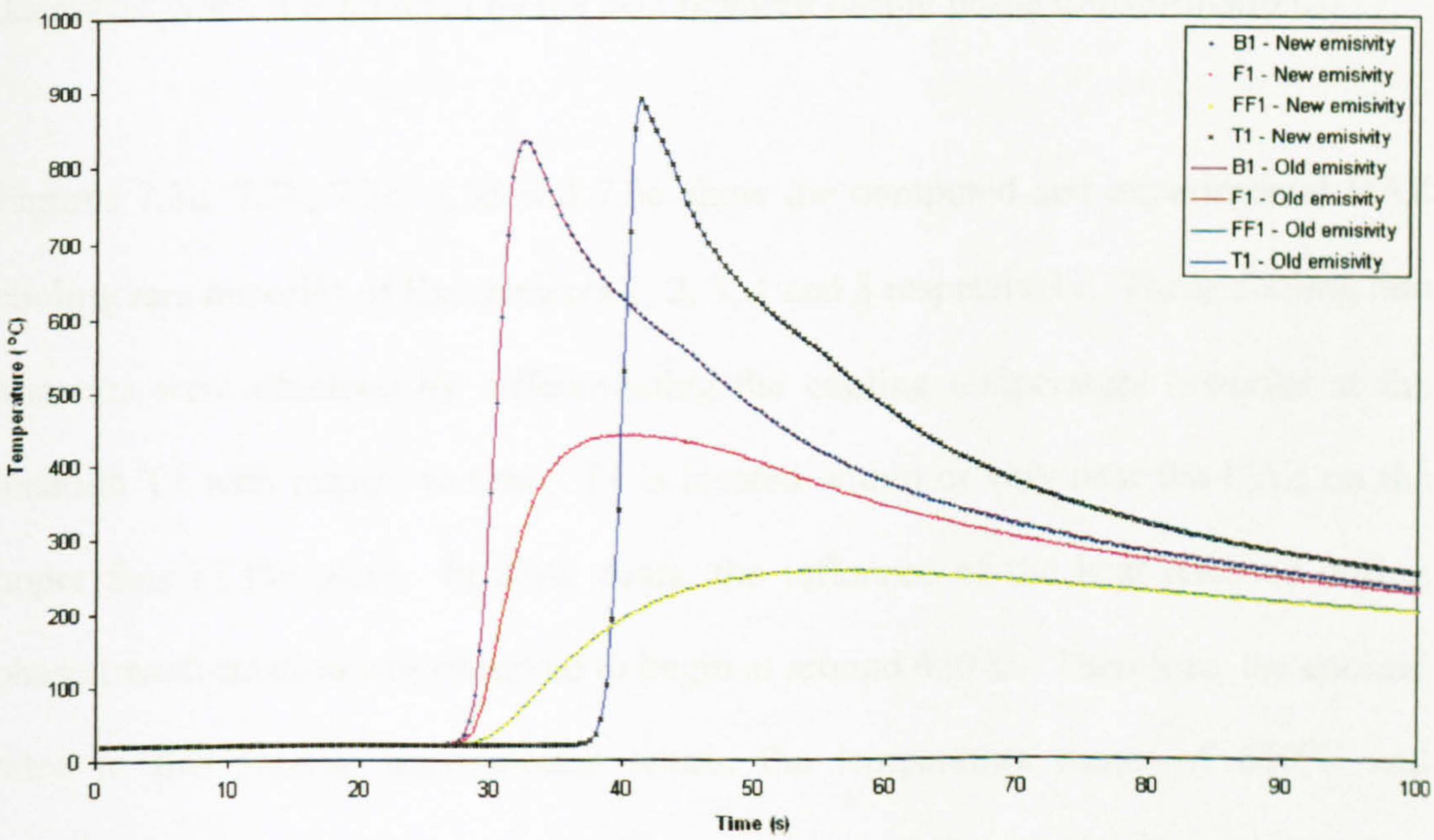

Figure 7.2.5b

Comparison of temperature histories

7.3 Comparison of experimental and computed cooling rates

As noted in Chapter 1, the same techniques of modelling the temperature history of the weldments can be used to study weld microstructure formation, grain structure of the weld and hardness of the weld. The cooling rate of the weldment is the main factor to be considered in these studies. Therefore, it is necessary to verify the computed cooling rate with the experimental cooling rate. It should also be noted that for steel, there are phase transformations during the solidification of liquid metal and when austenite transforms to ferrite in the solid phase. The cooling rate usually decreases when it is affected by the heat released during phase transformation.

Figures 7.3a, 7.3b, 7.3c, 7.3d and 7.3e show the computed and experimental HAZ cooling rate histories of Experiments 1, 2, 3, 4 and 5 respectively. These cooling rate histories were obtained by differentiating the cooling temperature histories at the location T1 with respect to time. T1 is located within or very near the HAZ on the upper face of the plate. In these cases, the influence of the heat released during phase transformation was observed to begin at around 650°C. Therefore, the cooling rates in this section were plotted within the temperature range of 650°C and ~300°C/~250°C. The cooling rate of Experiment 1 and Experiment 4 are observed to be almost identical. Experiment 3 is seen to have the lowest cooling rate. The cooling rate of Experiment 5 is found to be the highest.

The experimental cooling rate curve of Experimental 4 in Figures 7.3d is observed to be lower than all the computed cooling rate curves in the first ten seconds. This

happened because Experiment 4 (3mm thick plate) was purposely carried out with a large amount of overflow filler-metal but the computer model did not take this extra material into account. This overflowed filler-metal released additional latent heat during the phase transformation and thus reduced the cooling rate further in the first ten seconds. However, in normal circumstances such as in Experiments 1, 2, 3 and 5, the slightly overflowed filler-metal is seen to be not affecting the cooling rates as shown in Figures 7.3a, 7.3b, 7.3c and 7.3e. On the whole, all the computed cooling rate curves agree reasonably well with the experimental cooling rate curves. However, the 2D transient sectional model is found to be the best for simulating the cooling rate among them because there were few fluctuations in the cooling rate curves and the model can be easily used to compute longer cooling rate histories by prolonging the time for cooling.

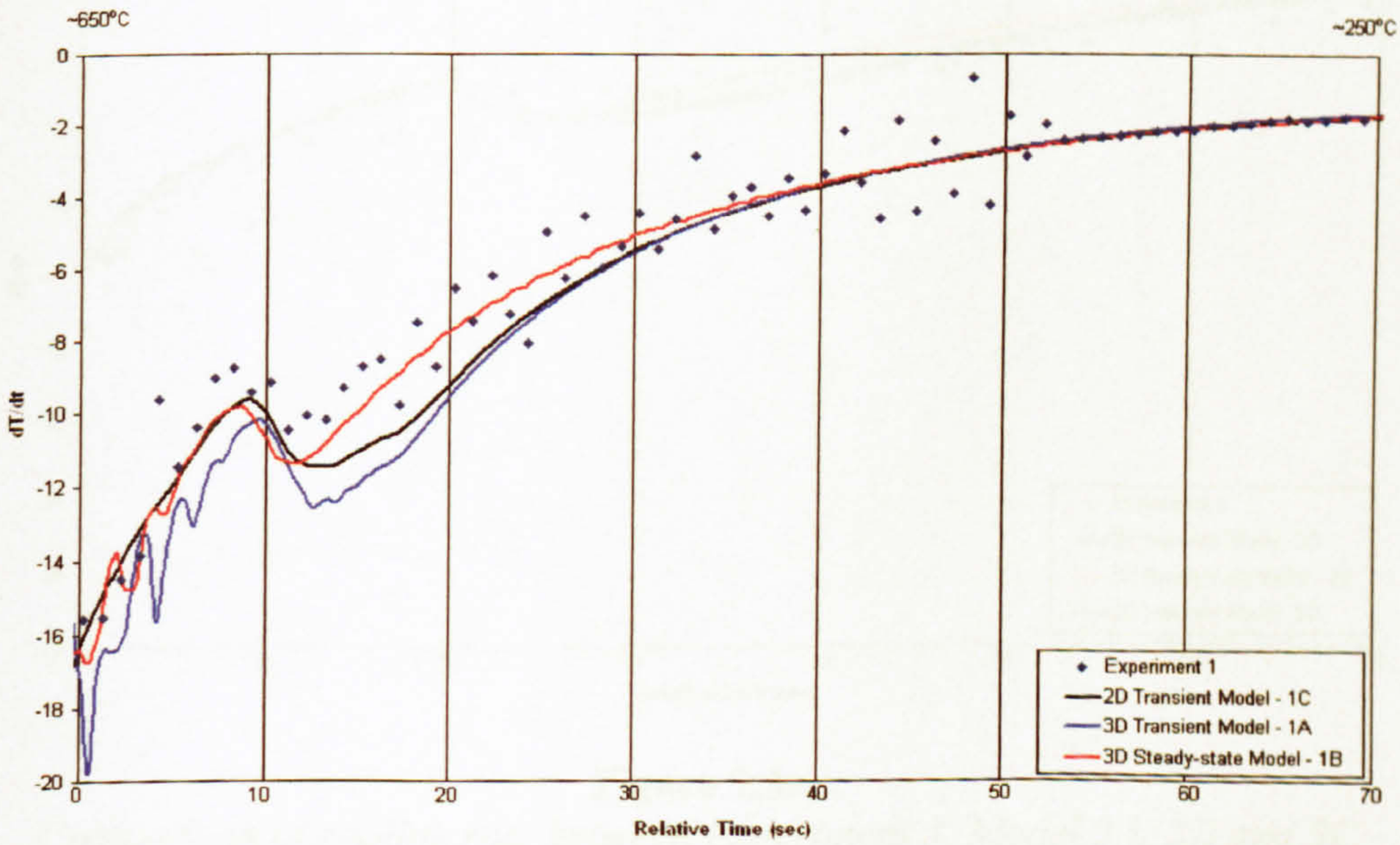

Figure 7.3a

Comparison of cooling rate between Experiment 1, Model 1A, 1B and 1C

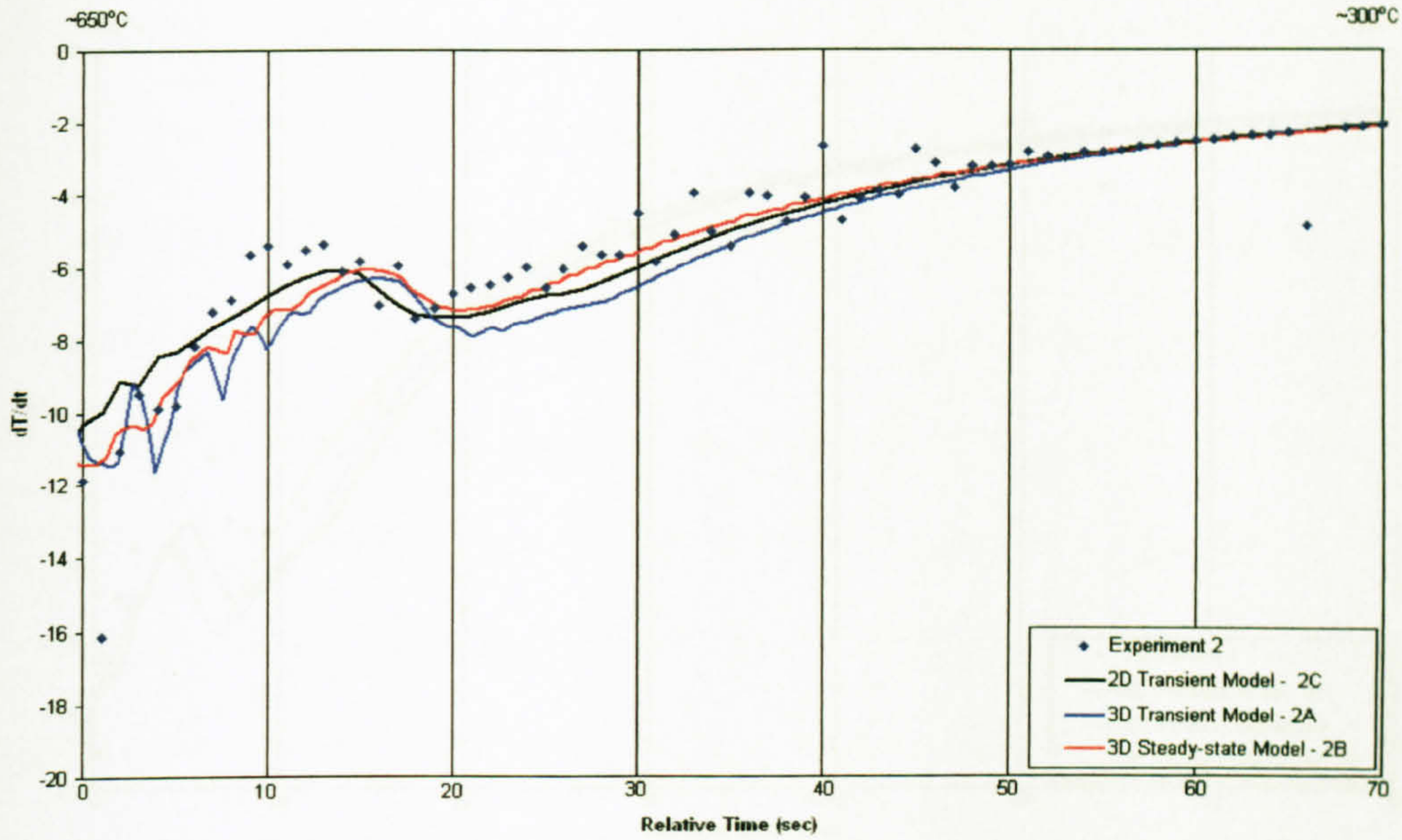

Figure 7.3b

Comparison of cooling rate between Experiment 2, Model 2A, 2B and 2C

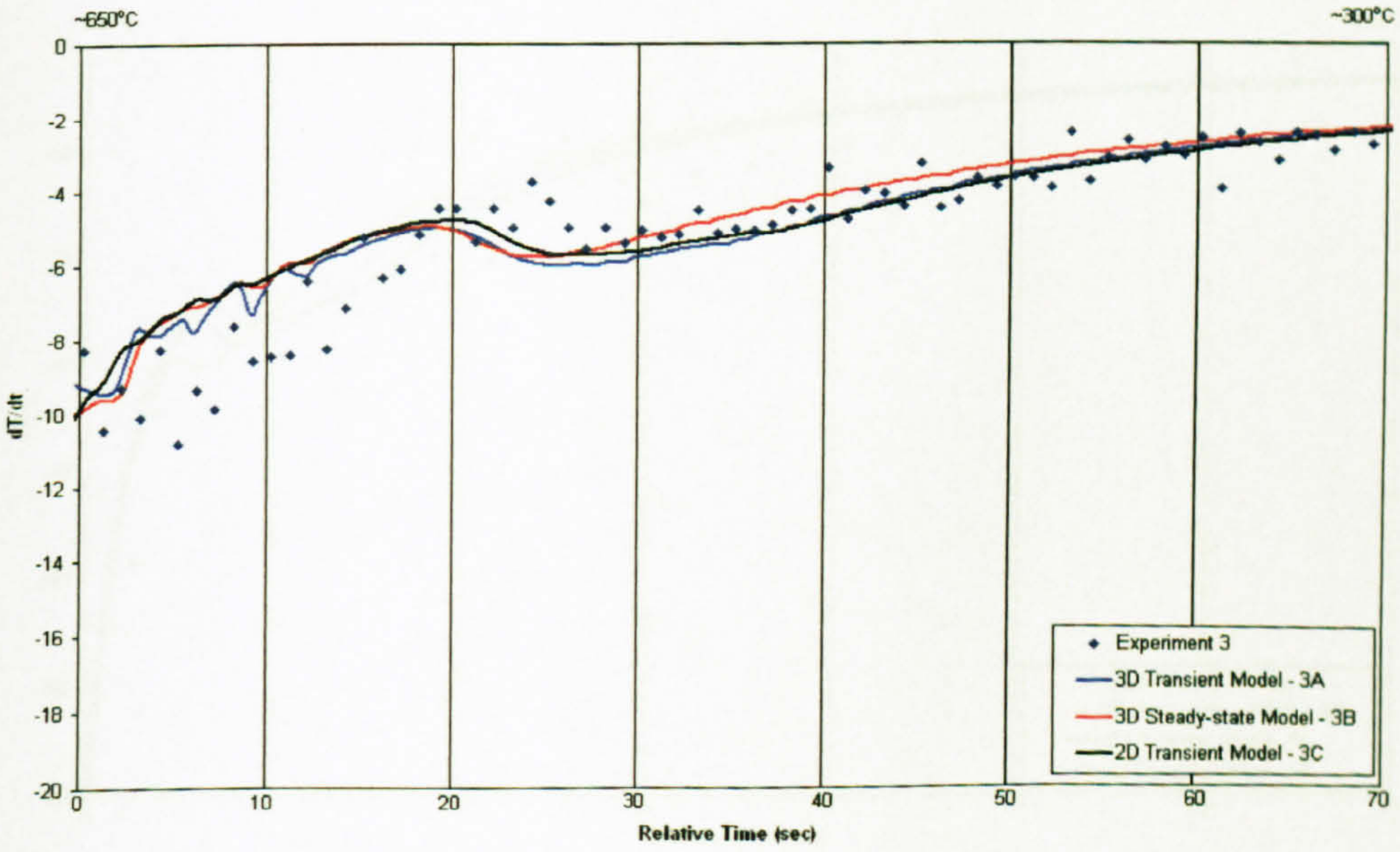

Figure 7.3c

Comparison of cooling rate between Experiment 3, Model 3A, 3B and 3C

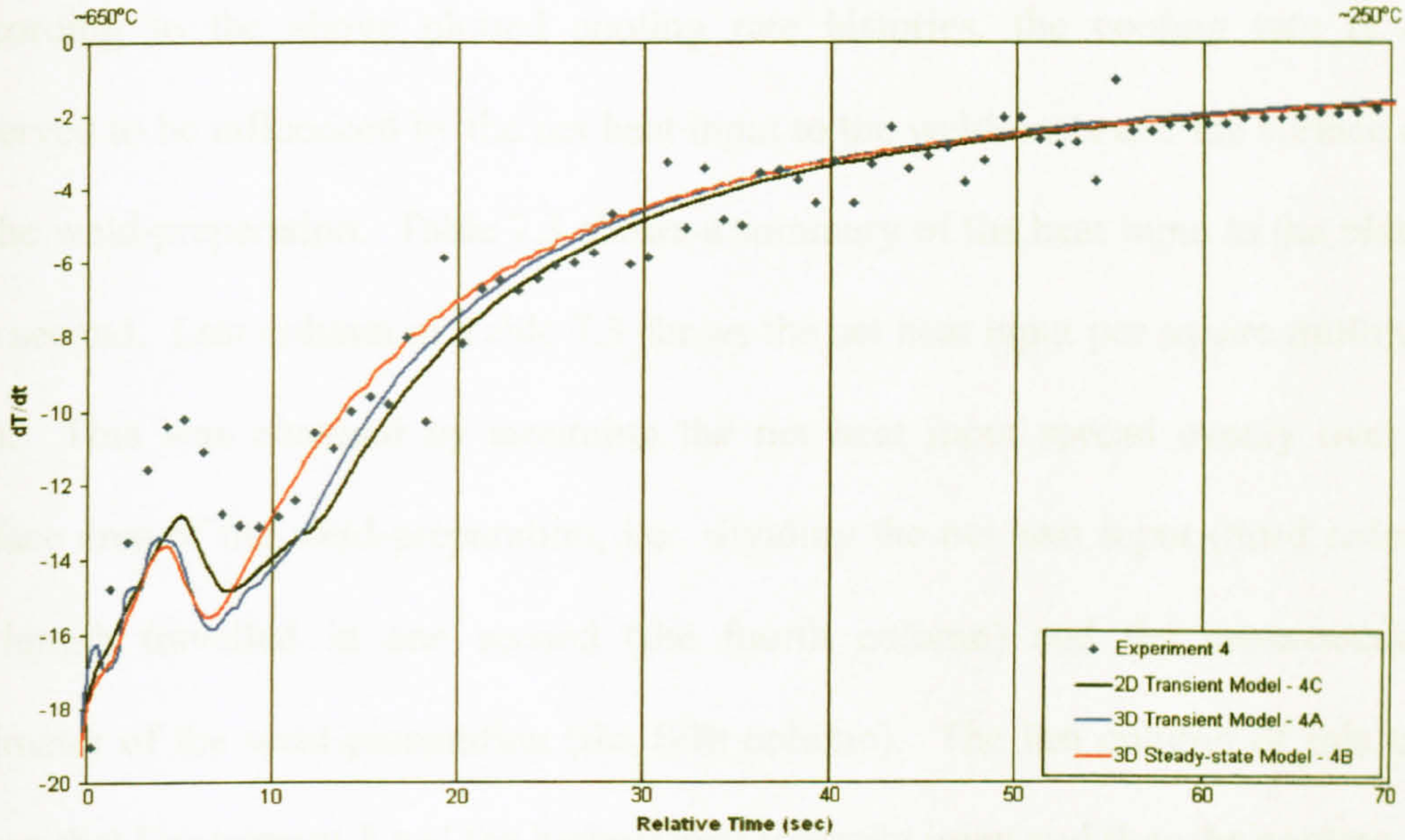

Figure 7.3d

Comparison of cooling rate between Experiment 4, Model 4A, 4B and 4C

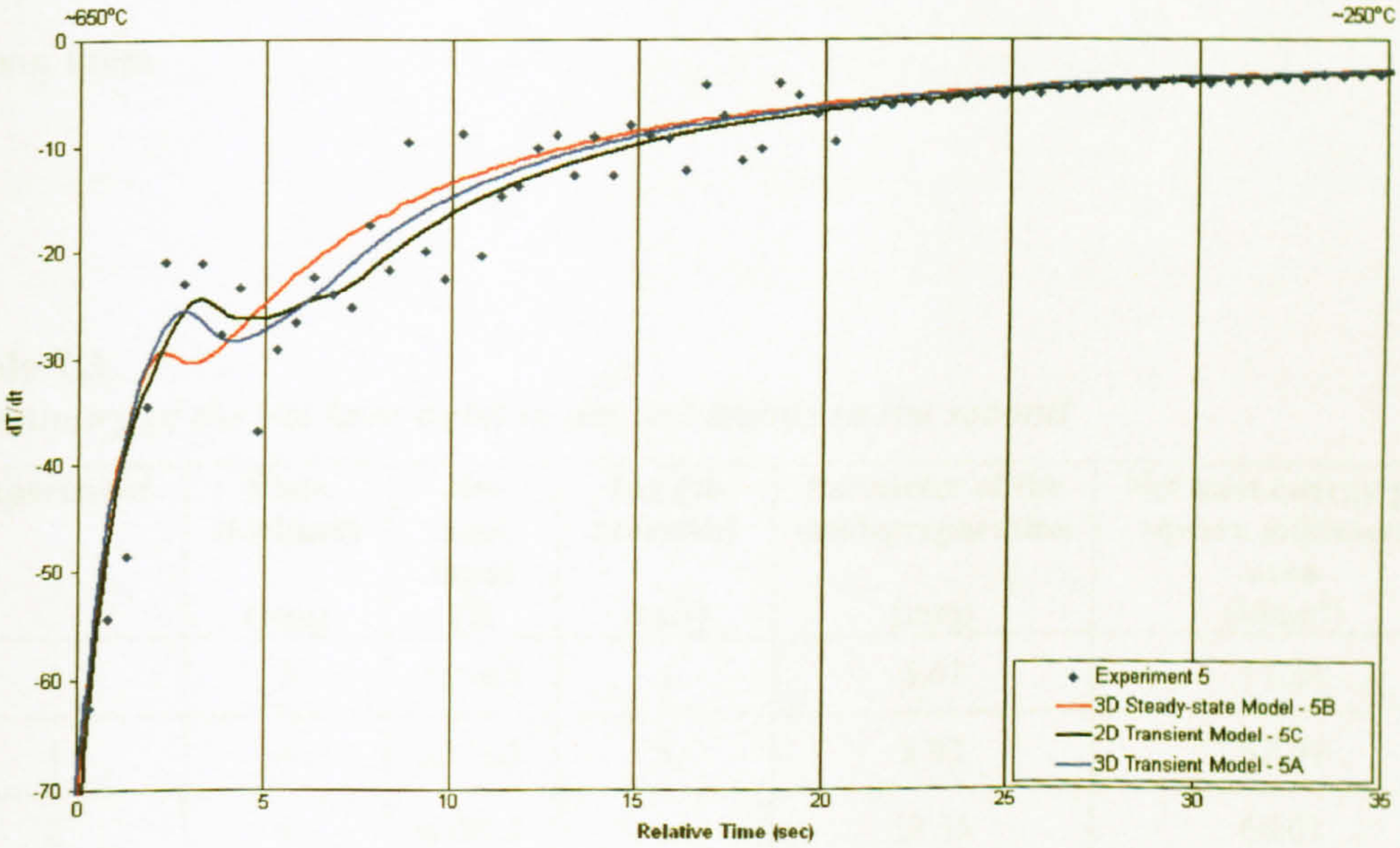

Figure 7.3e

Comparison of cooling rate between Experiment 5, Model 5A, 5B and 5C

According to the above plotted cooling rate histories, the cooling rate is also observed to be influenced by the net heat input to the weldments and the surface area of the weld-preparation. Table 7.3 shows a summary of the heat input to the plate in one second. Last column of Table 7.3 shows the net heat input per square millimetre area. This was obtained by assuming the net heat input spread evenly over the surface area of the weld-preparation, i.e. dividing the net heat input (third column) by length travelled in one second (the fourth column) and the cross-sectional perimeter of the weld-preparation (the fifth column). The last column of this table shows that Experiment 3 had the highest heat intensity input and thus the cooling rate was lowest among them. The heat intensity input of Experiment 1 and Experiment 4 were almost identical and therefore their cooling rates were almost identical as well. Experiment 5 had the lowest heat flux input and thus its cooling rate was the highest among them.

Table 7.3
A summary of the net heat input to the weldments in the second

Experiment	Plate thickness (mm)	Net heat input (J)	Length travelled (mm)	Perimeter of the weld-preparation (mm)	Net heat energy per square millimetre area (J/mm^2)
4	3	1696.5	5	6.62	51.26
1	4	2323.2	5	8.93	52.04
2	6	4471.7	5	13.55	66.01
3	8	4607.2	3.33	18.17	76.15
5	6	2136	5	9.42	45.33

7.4 Conclusion

The comparisons in section 7.2.1 show that the heat input efficiency factor has only a slight influence on the computed surface peak temperatures and the weld widths. In addition, it shows that small variations in the heat input efficiency factor have almost no effect on the modelled weld pool peak temperatures. However, it has a great influence on the computed cooling curves. The model with higher heat input efficiency factor produces higher cooling curve and vice versa. In fact, matching the experimental and computed cooling curves provides a good way of obtaining the appropriate efficiency factor for the simulation.

The analysis in section 7.2.2 shows that the radius of the Gaussian heat flux has a significant effect on the computed bottom weld width, the weld pool peak temperature and the top surface peak temperature at locations very near to or within the HAZ of the welding plate. If the radius of the heat flux is too small, the heat source becomes very concentrated and results in better penetration. This can cause the bottom weld width to be too wide and the computed weld pool peak temperature to be too high. The low heat input on the top surface at regions around the HAZ of the welding plate due to the use small heat flux radius can cause the computed top surface peak temperatures to be too low. If the radius of the heat flux is too large the intensity of the heat source becomes too weak. This may cause the computed weld pool peak temperature to be too low.

In section 7.2.3, it was shown that the exact molten droplet temperature used for calculating the amount of heat due to the filler metal is not very significant. If the droplet temperature is too low it can only cause the computed weld pool peak temperature to become too low. Apart from that, the computed top and bottom weld width, and the computed top and bottom surface peak temperatures at locations very near to or within the HAZ of the welding plate are not significantly affected by the value of the droplet temperature used. Experience suggests that 2800°C to 3000°C is a possible range for the temperature of the molten filler droplet.

The analysis on the use of artificial conductivity enhancement to simulate the weld pool stirring effect in section 7.2.4 shows that even large variation of artificial conductivity from 121 W/mK to 121×3 W/mK is not very critical. The computed weld pool peak temperature can only become too low if the value of artificial conductivity is too high. Otherwise, variations of this value do not have any serious effects on the other results.

The results in Section 7.2.5 shows that slight variation of the emissivity values have almost no effect on the computed results.

The cooling rate is observed to be influenced by the net heat input to the weldments and the surface area of the weld-preparation. By assuming the net heat input to be spread evenly over the surface area of the weld-preparation, surfaces with higher heat flux will result in lower cooling rate and vice versa. In general, all the computed cooling rate curves agree reasonably well with the experimental cooling rate curves.

The 2D transient sectional model has been observed to be the best among them in computing cooling rates histories.

In summary, slight variations of the molten droplet temperature, the conductivity enhancement of the weld pool and the emissivity have little significant effects on the simulation results. The sensitivity studies show that the effect of the heat input efficiency factor is mainly on the cooling curve and if the Gaussian radius is too small the top surface peak temperature can become too low.

Chapter 8 – Conclusions and Recommendations

Experimental work on temperature measurement has been successfully carried out to provide data for the purposes of validating the computer models. The recorded temperature histories of five welding experiments were considered to be sufficiently accurate for use in verifying the computer models.

A simple computational technique that applied uniform heat generation across the thickness was tested in 3D transient, 3D steady state, and 2D transient sectional models to simulate the temperature history or distribution. This technique was shown to be capable of predicting the temperature field remote from the heat affected zone correctly in the region where the temperature is almost uniform across the thickness.

Finally, a new computational technique to simulate the temperature history or distribution near the heat source as well as away from the heat source was developed. This technique took into consideration the surface heating due to the welding arc and the heat energy in the weld-preparation to evaluate the heat source for the use of finite element modelling. This new technique has been applied to 3D transient, 3D steady state and 2D transient sectional models and was verified by the measured temperature histories of the five actual welding experiments.

On the whole, the 3D transient models provide more accurate simulated temperature fields, heat affected zones and weld widths. However, these models took the longest time to solve, around 2 to 3 days on a 2.8GHz processor. In addition, the 3D

transient model is the most versatile way of simulating the temperature field during welding. It also includes the end effect of the temperature field during welding. Therefore, this technique is best used for studying the end effects of weldments that may result in cracking or out-of-plane distortion. It also can be used for general 3D weldments and appendages.

The simulated weld widths and heat affected zones of 3D steady state models were slightly less accurate than those predicted by the 3D transient models. However, these models took only 2 to 3 hours for the solution using the same computer. It should be noted that the solutions of these steady state models occasionally fluctuated during the solving process due to the use of specific heat instead of enthalpy to account for the release of latent heat during the phase changes.

The 2D transient sectional models provide reasonably accurate simulated temperature fields and the solution time was the shortest among them. With the same computer, it took only around 5 minutes for the calculation. However, the predicted maximum temperature of the weld pool can be higher than the boiling point (3000°C) of impure steel. Otherwise, the simulated temperature histories of the 2D transient sectional models were better than the simulated results of 3D steady state models. In addition the 2D transient sectional model was observed to be the best among them for computing cooling rate histories.

The present study is limited to the range of the experimental results that presented in Chapter 3. These experiments were done via gas metal arc welding process at a low

speed (5 mm/s) on butt jointing steel plates. The thickness of the plates was limited to the range of 3 mm to 8 mm for practical reasons. The simulation models were validated based on these limited range of thickness and speed of weld. Therefore, it is recommended to make further investigation on the use of present technique for different types of weld joint, material, welding process and higher welding speed.

Appendix A – Results of 3D transient Models

A.1 Model 1A – 4mm thick welding plate with a "V" weld-prep

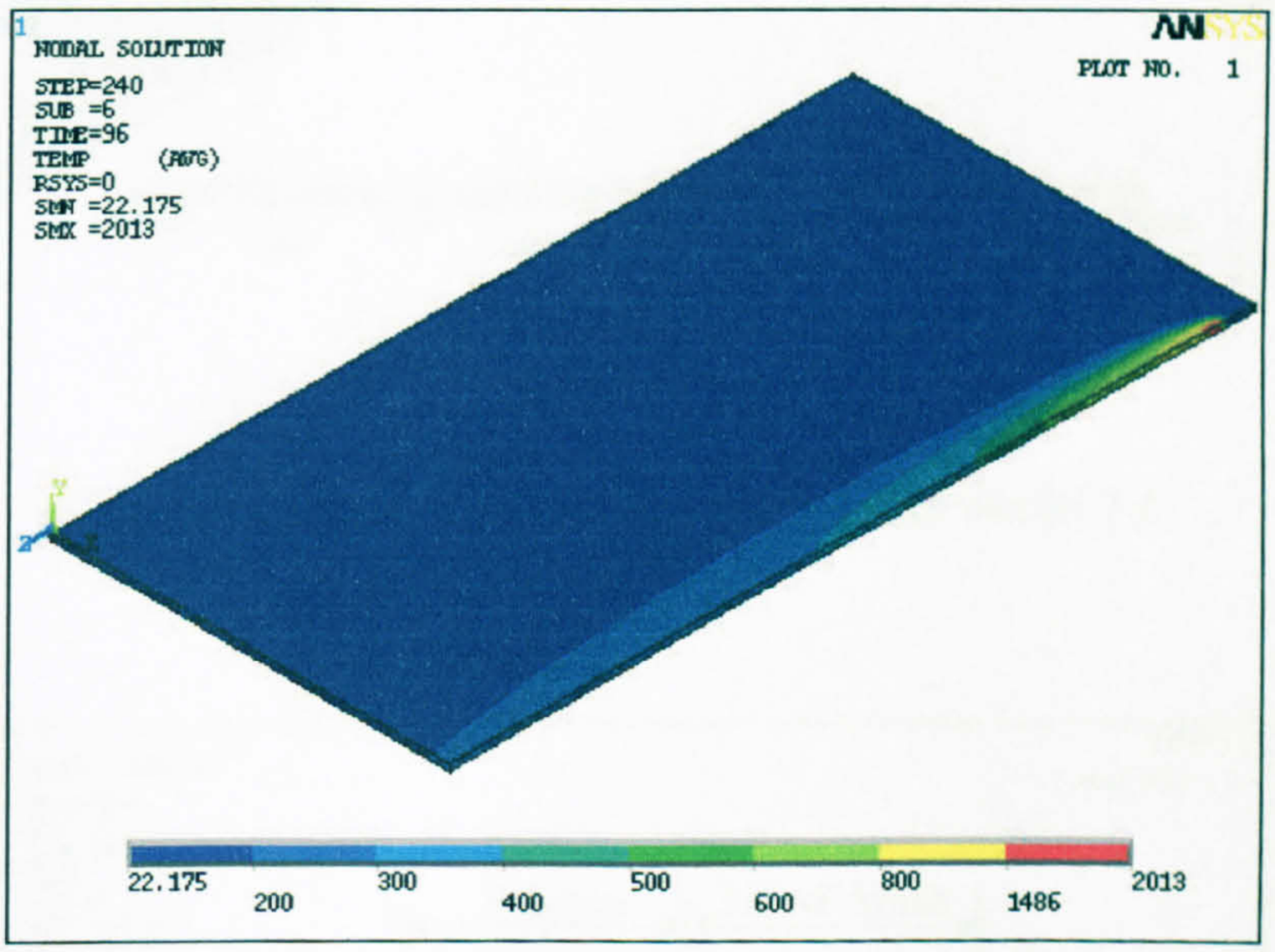

Figure 1A-O

Temperature contour at 96 seconds of model 1A

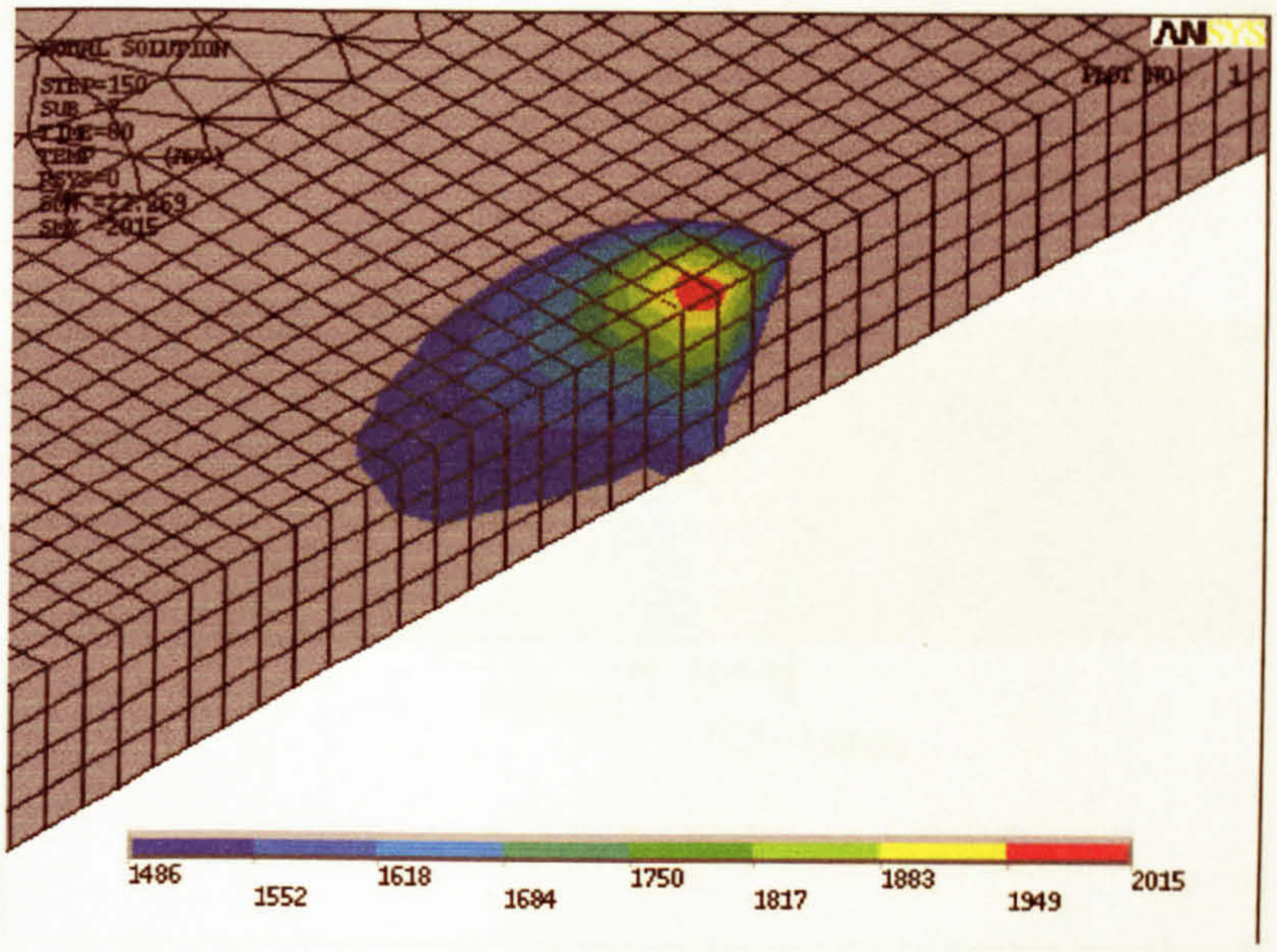

Figure 1A-P

Temperature contour of the weld pool of model 1A

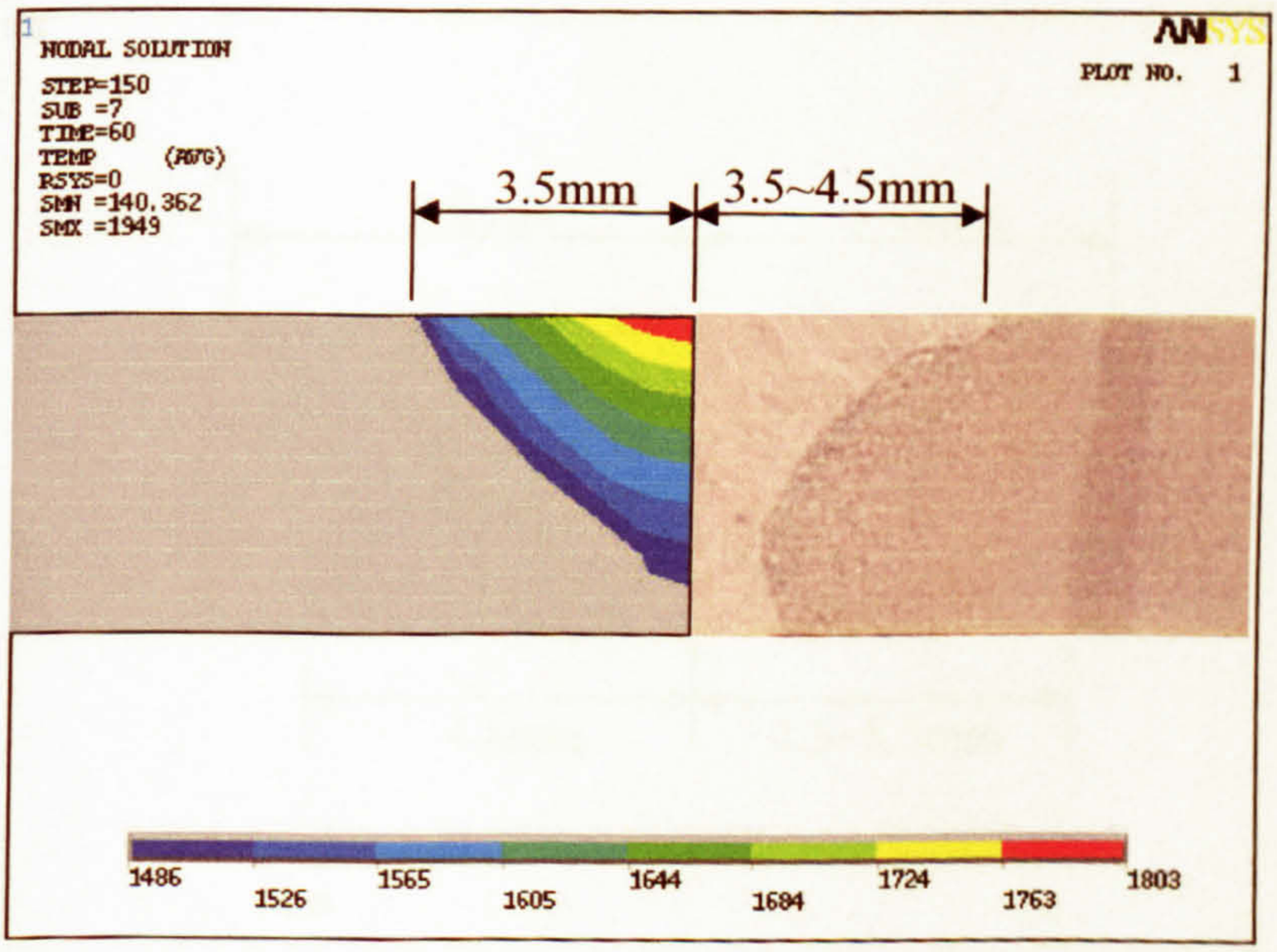

Figure 1A-TW

Simulated top weld width of model 1A

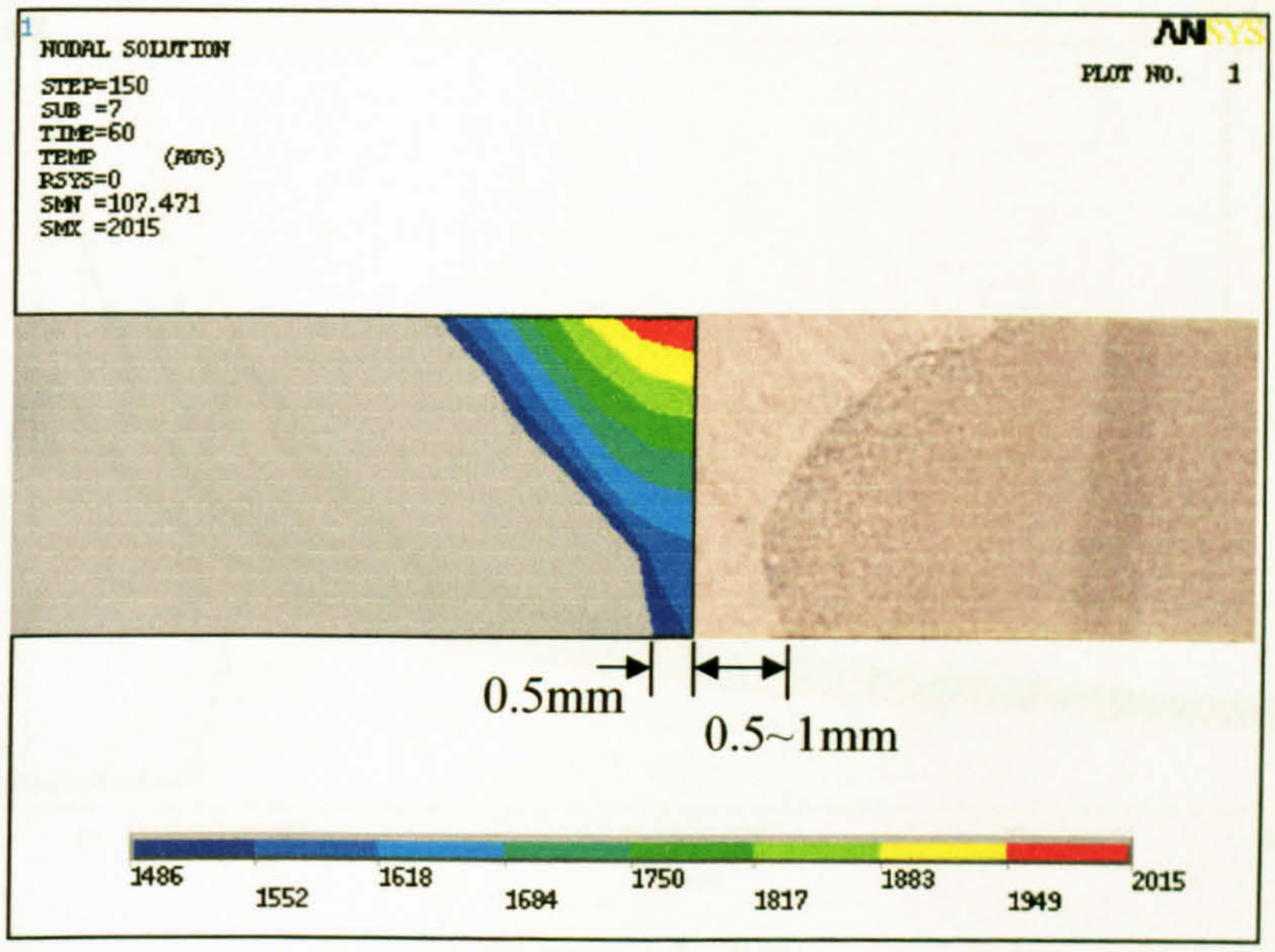

Figure 1A-BW

Simulated bottom weld width of model 1A

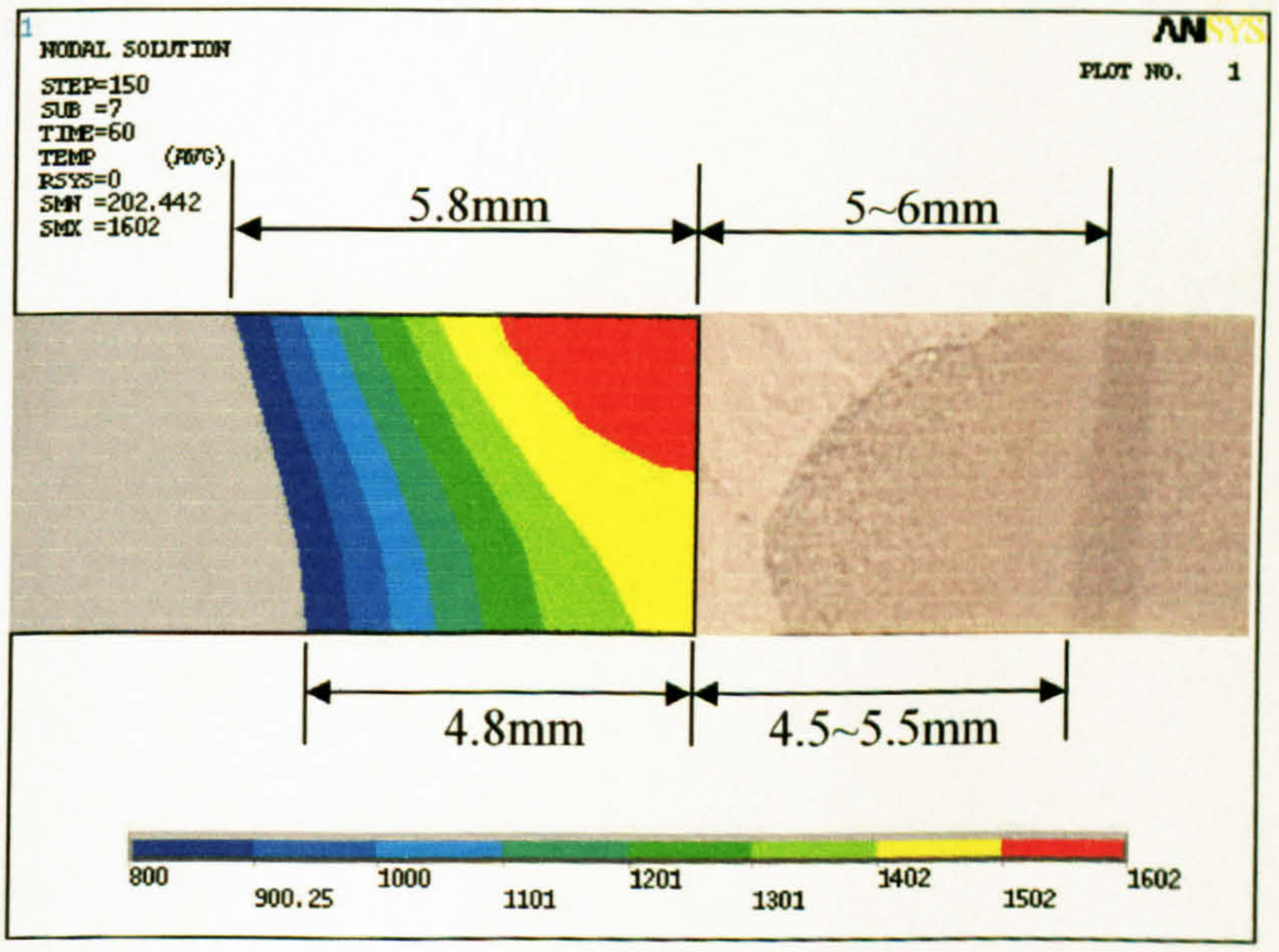

Figure 1A-H

Simulated heat affected zone of model 1A

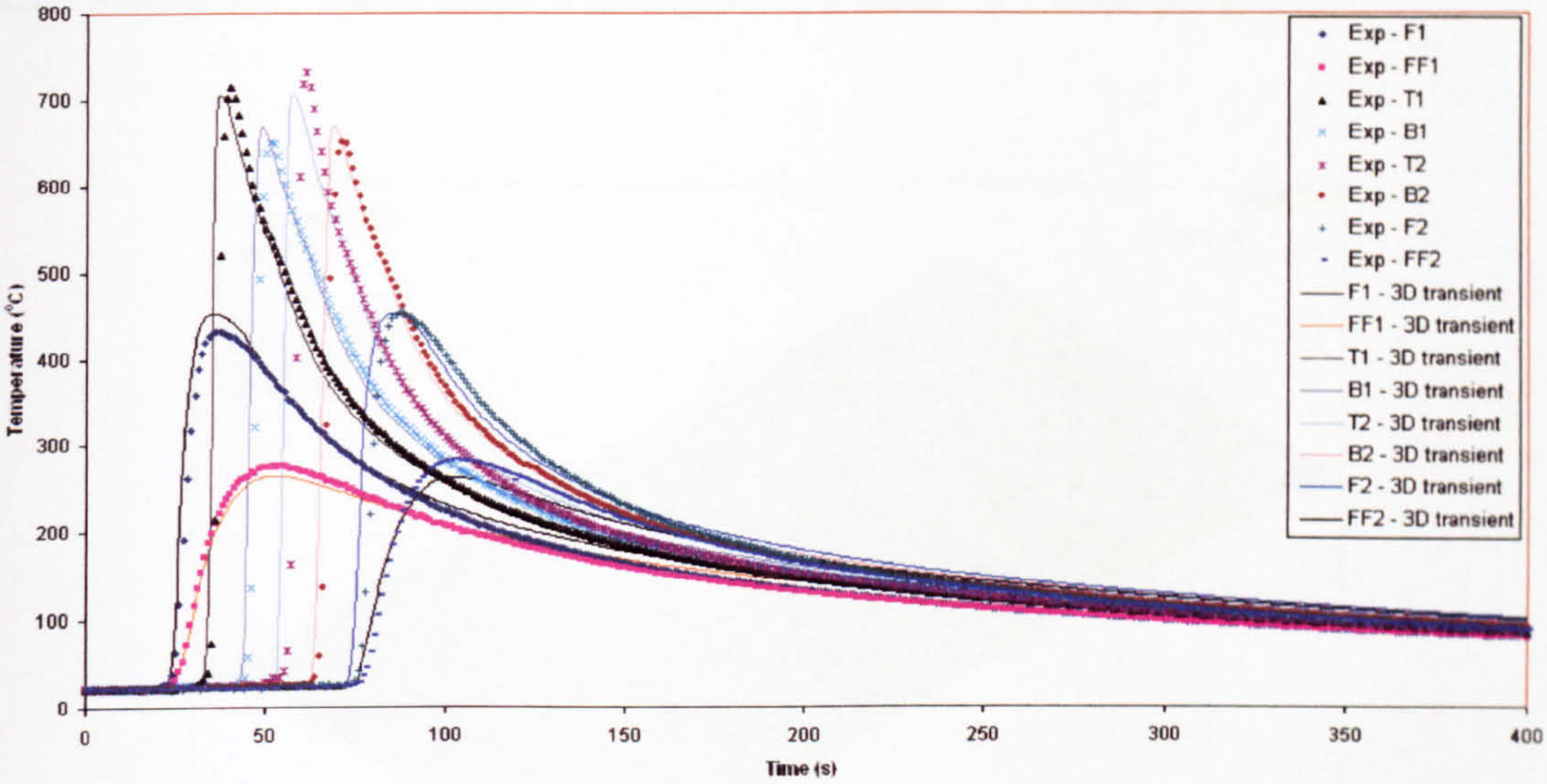

Figure 1A-TH

Comparison of the simulation with the measured temperature histories of model 1A

A.2 Model 2A – 6mm thick welding plate with a "V" weld-prep

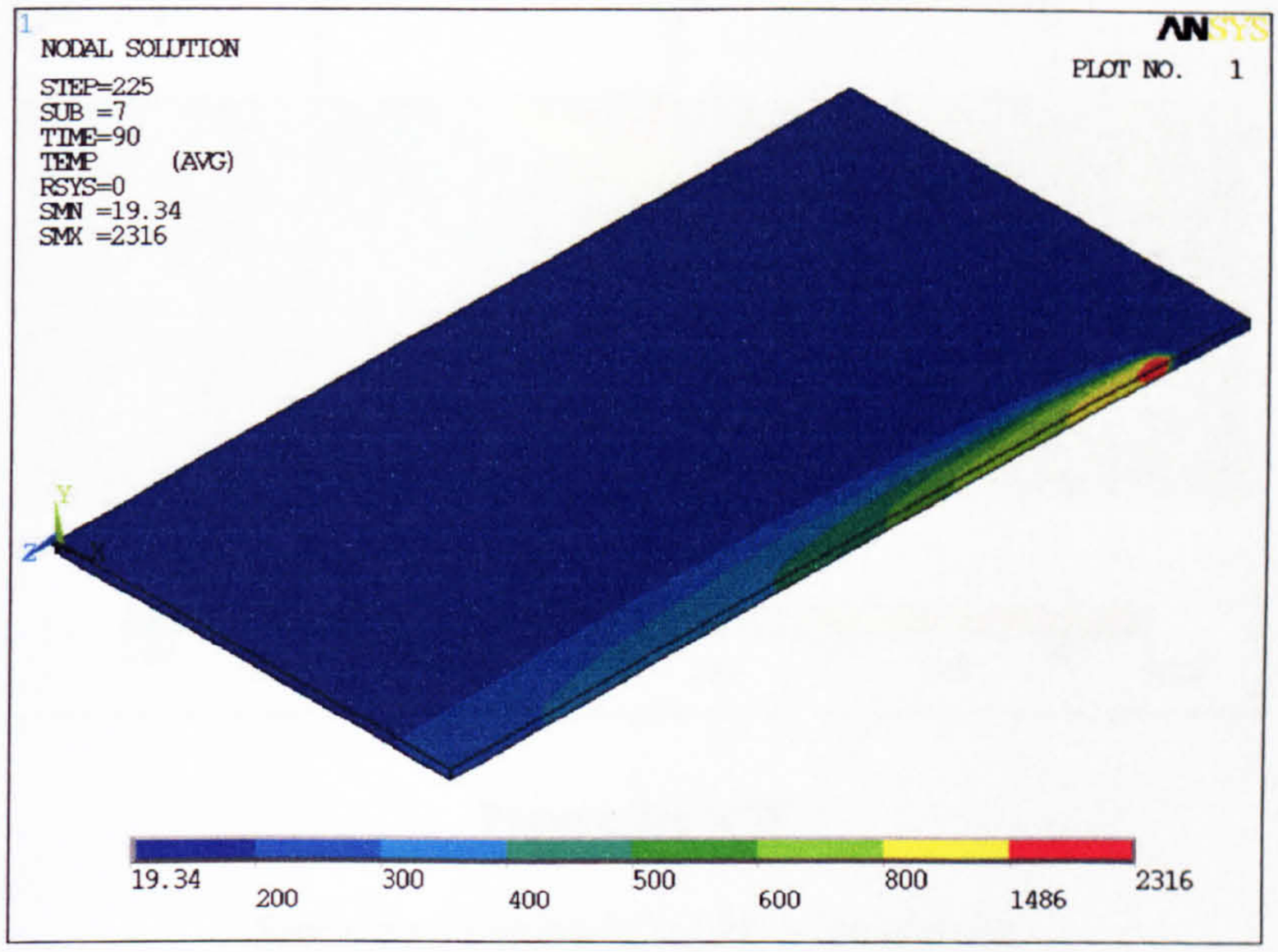

Figure 2A-O

Temperature contour at 90 seconds of model 2A

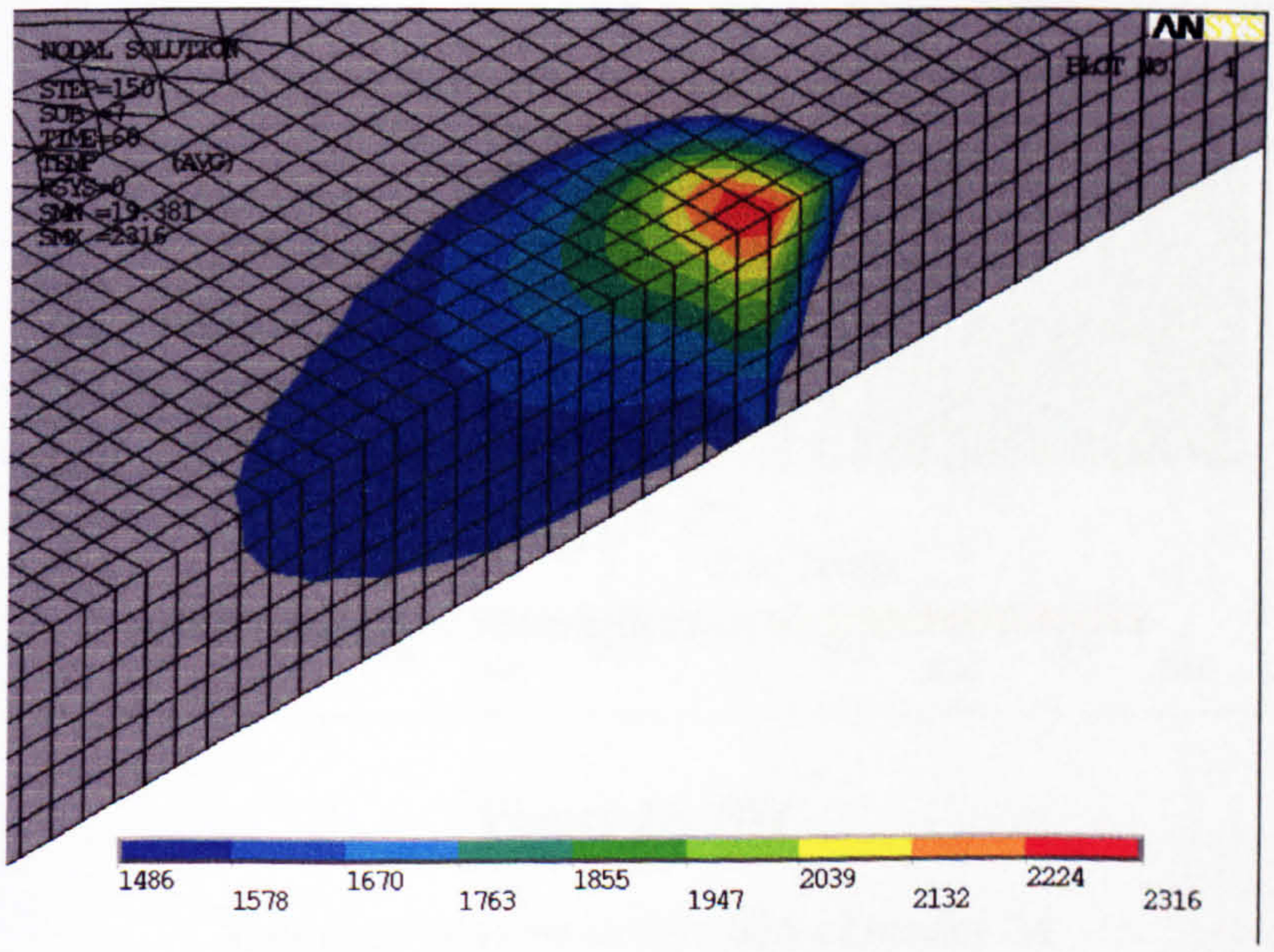

Figure 2A-P

Temperature contour of the weld pool of model 2A

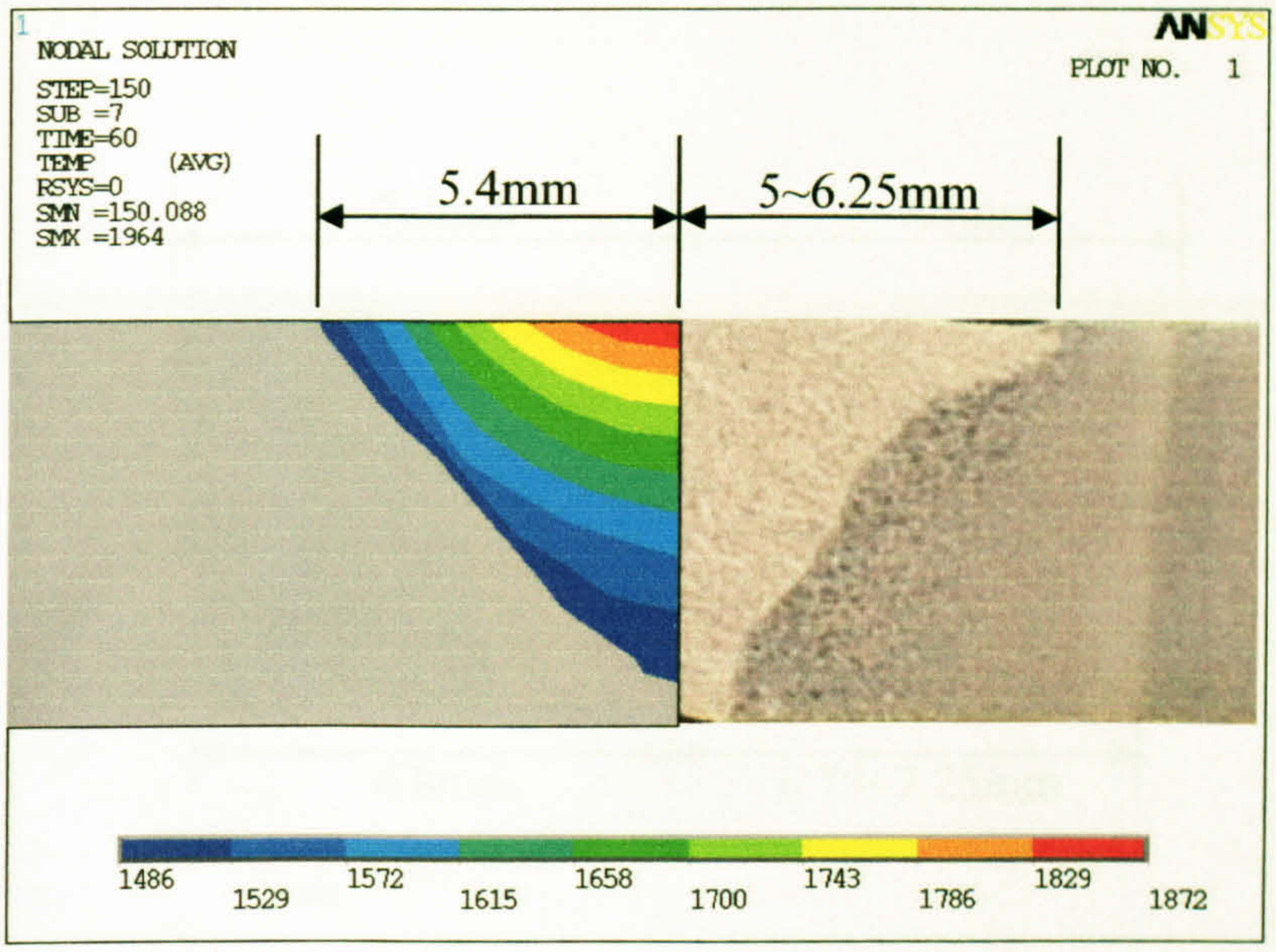

Figure 2A-TW

Simulated top weld width of model 2A

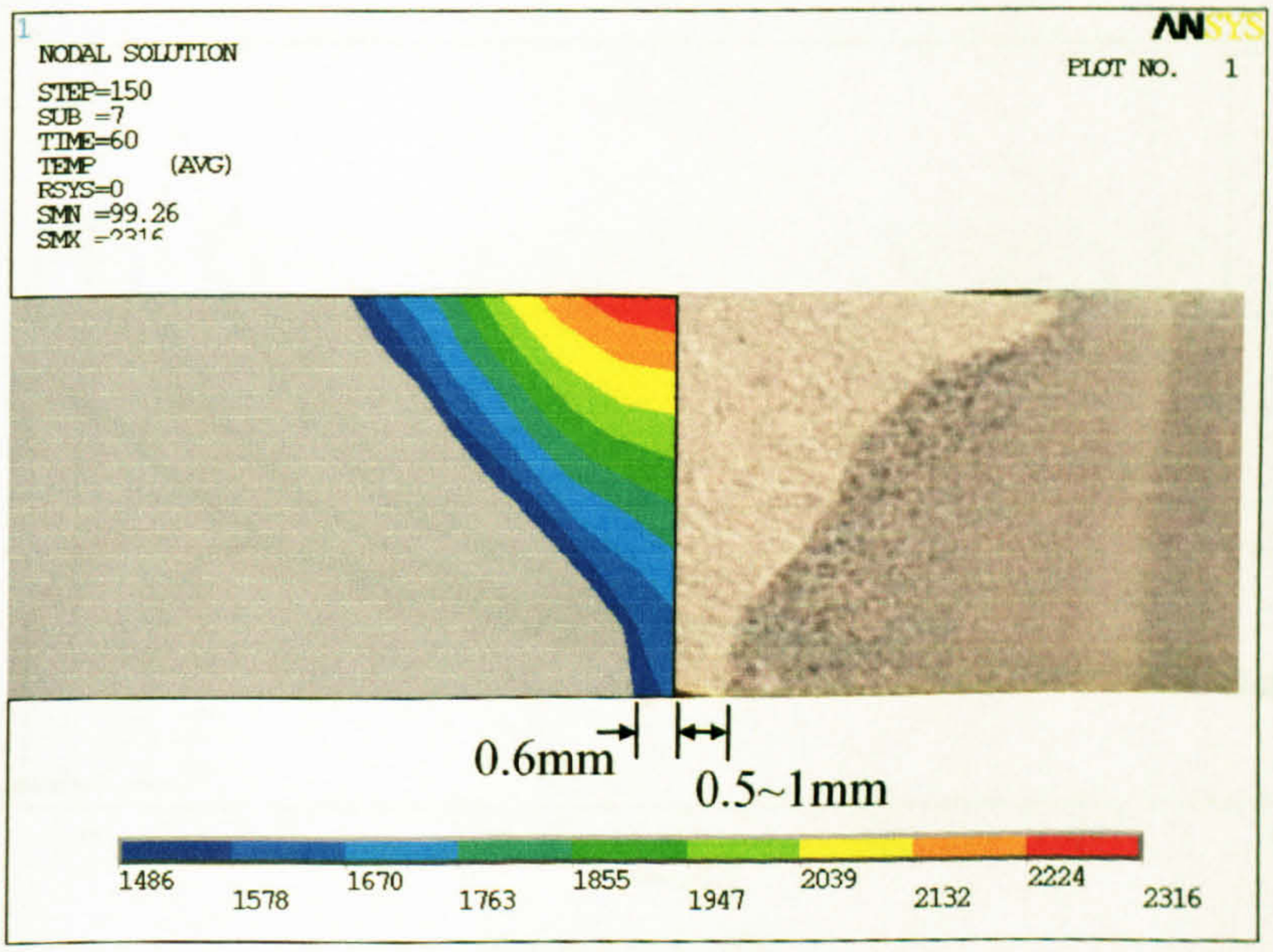

Figure 2A-BW

Simulated bottom weld width of model 2A

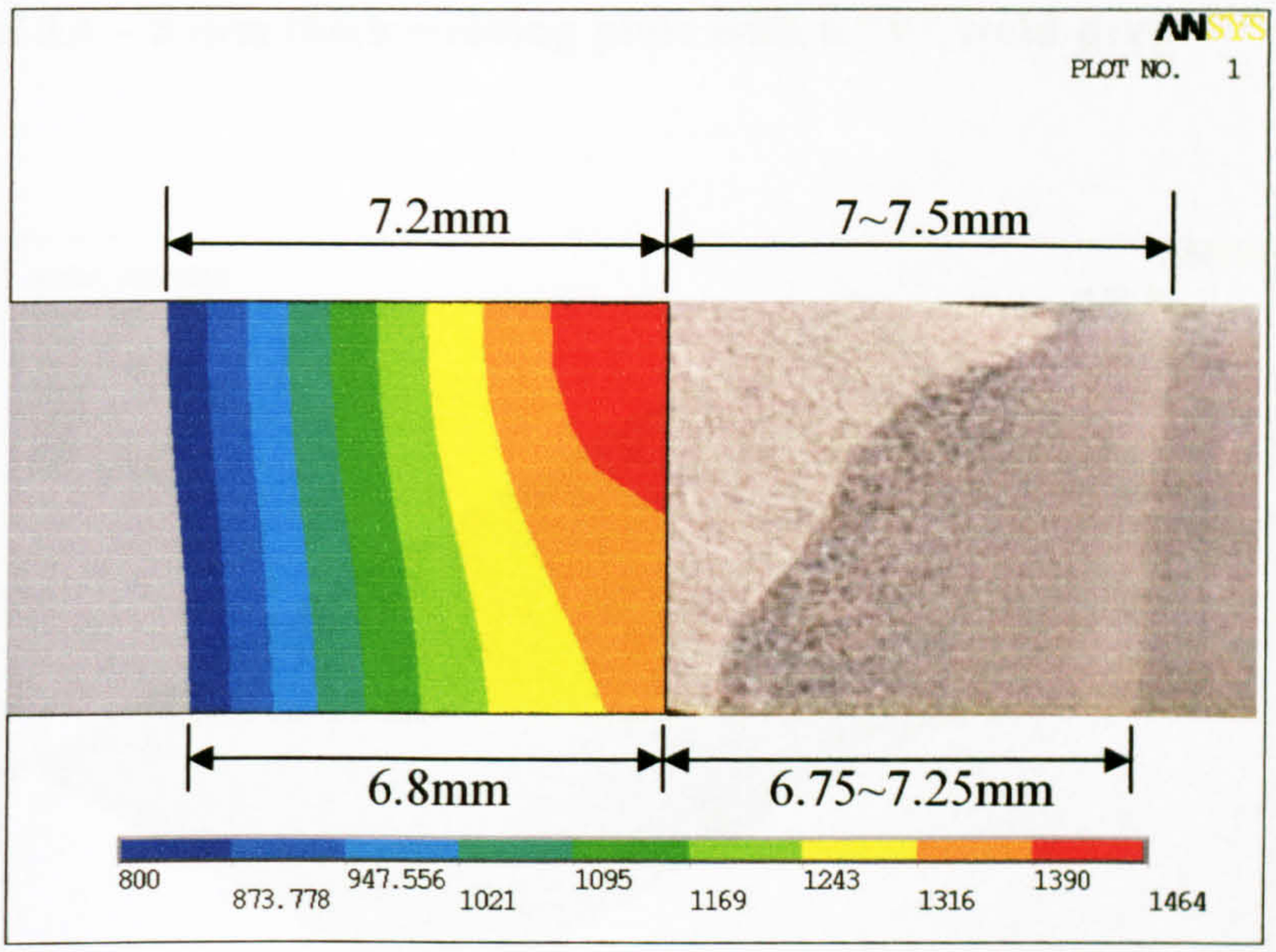

Figure 2A-H

Simulated heat affected zone of model 2A

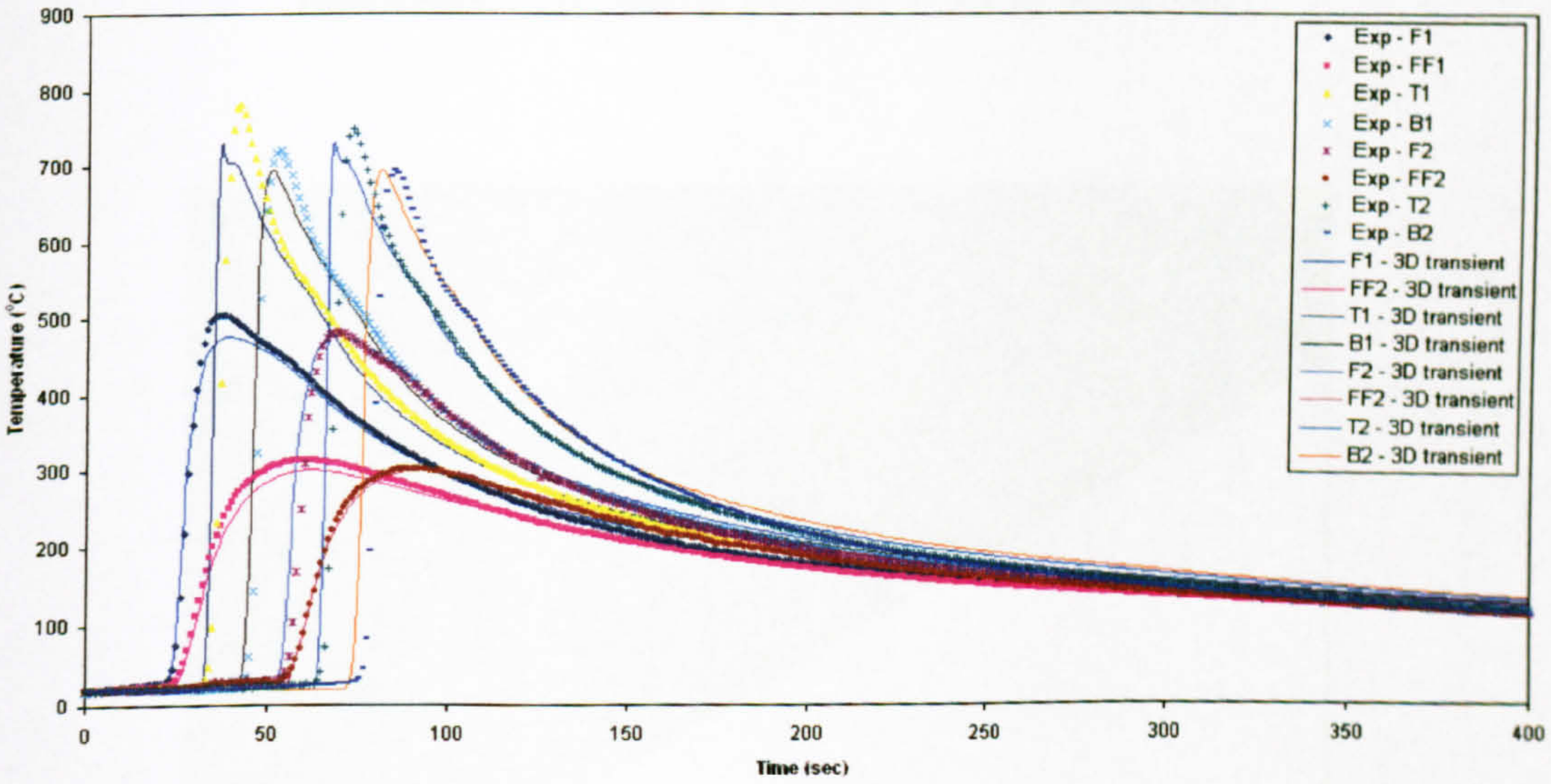

Figure 2A-TH

Comparison of the simulation with the measured temperature histories of model 2A

A.3 Model 3A – 8 mm thick welding plate with a "V" weld-prep

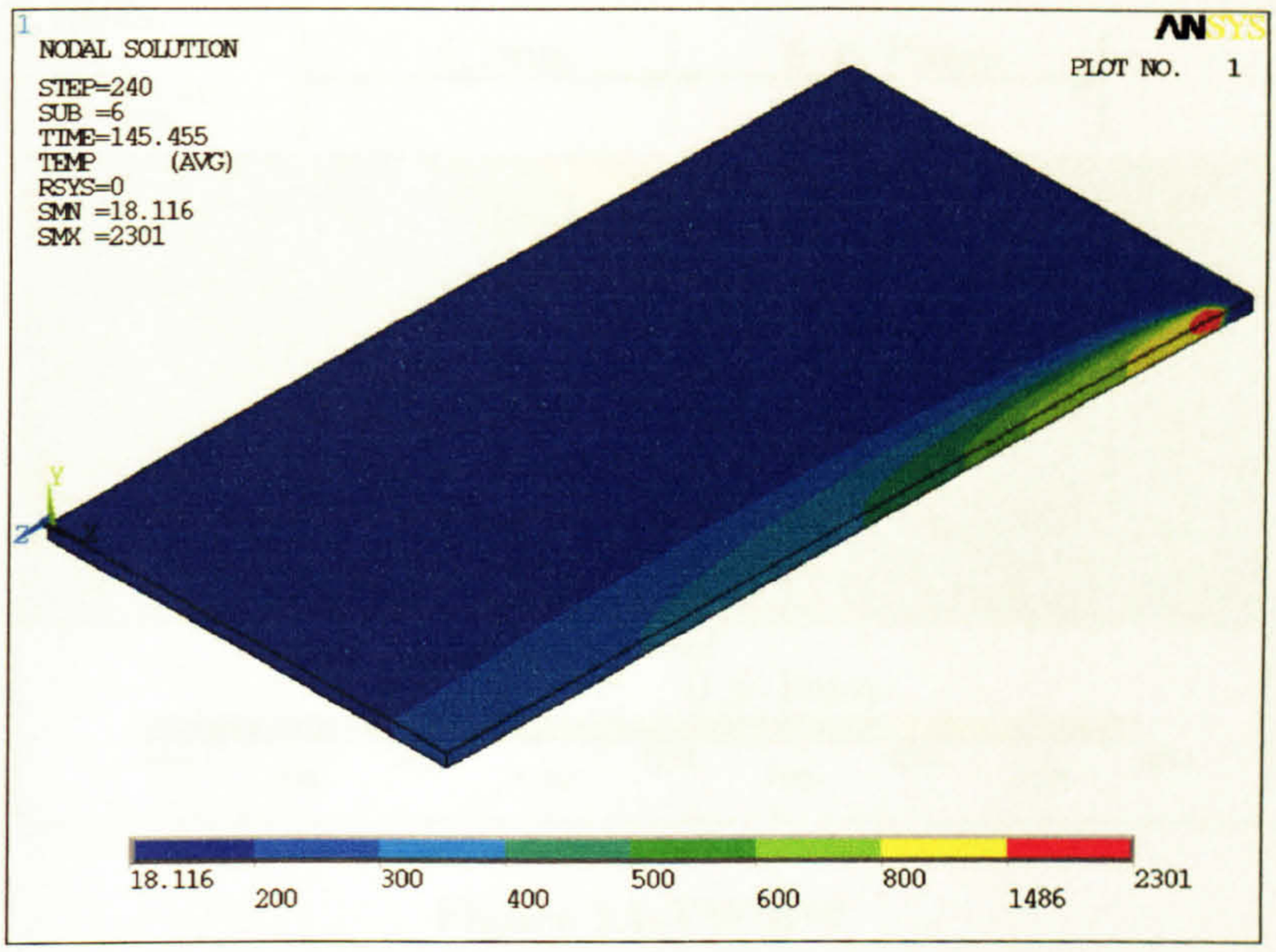

Figure 3A-O

Temperature contour at 145.5 seconds of model 3A

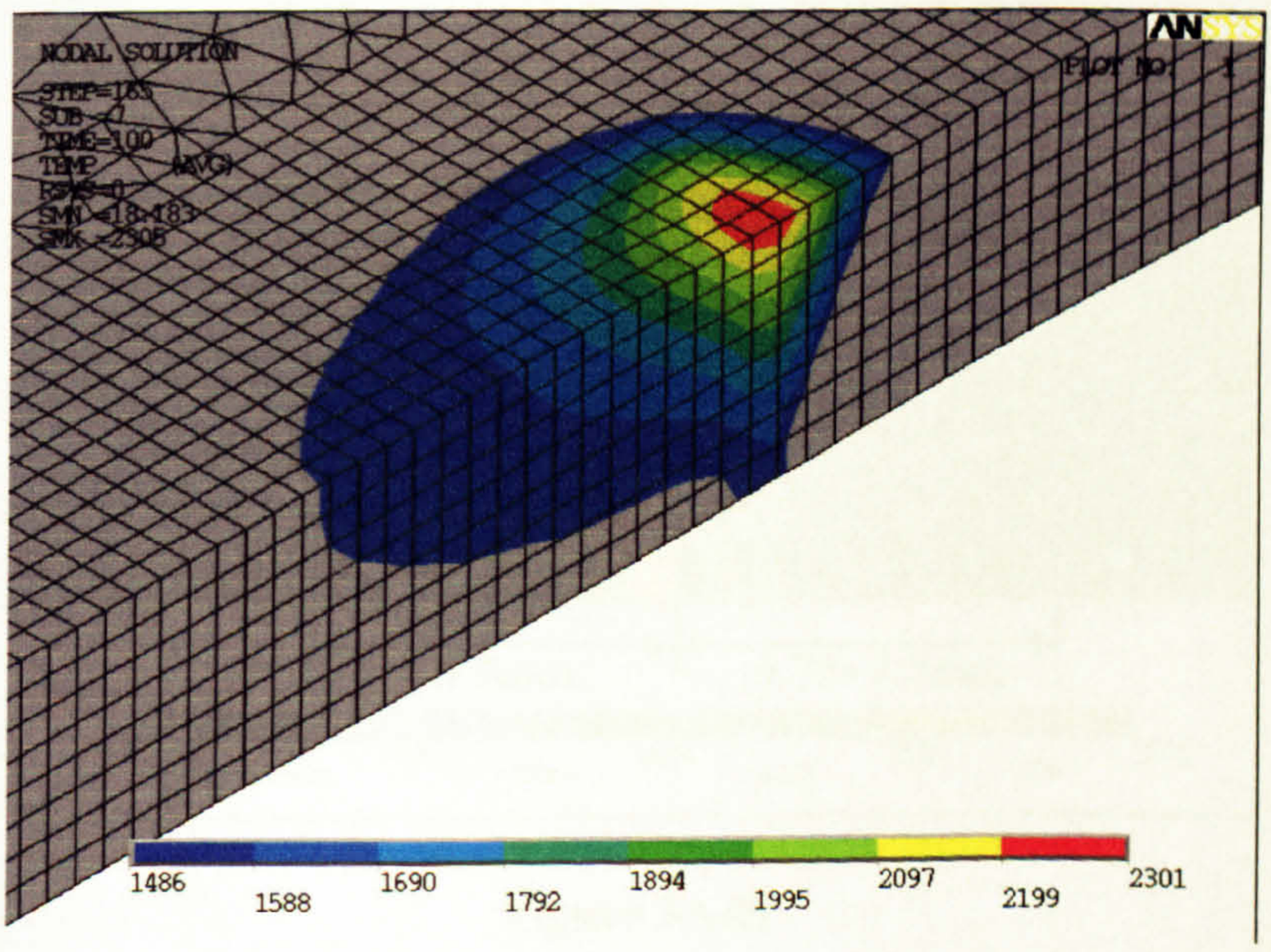

Figure 3A-P

Temperature contour of the weld pool of model 3A

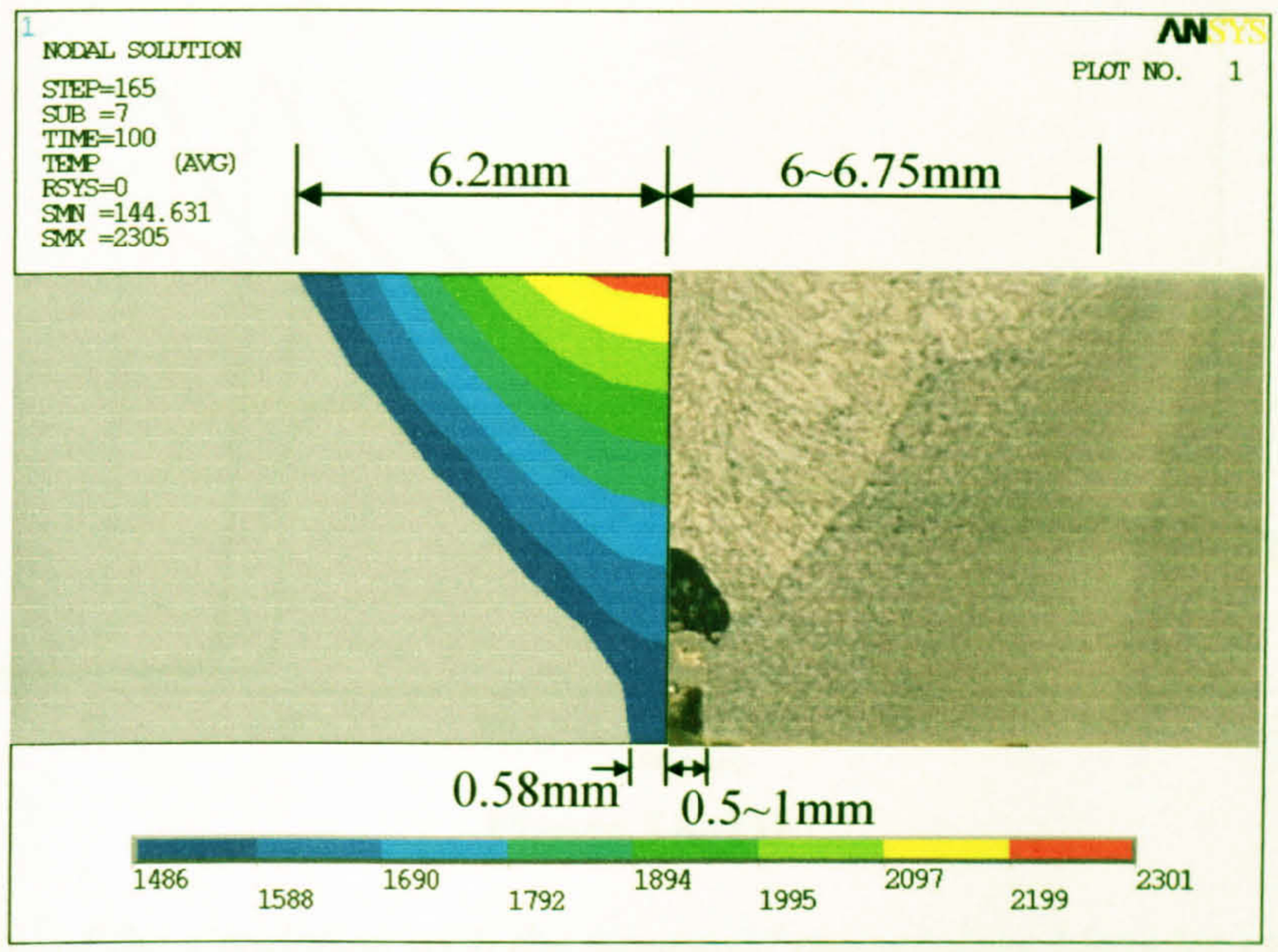

Figure 3A-TW/BW

Simulated top weld width and bottom weld width of model 3A

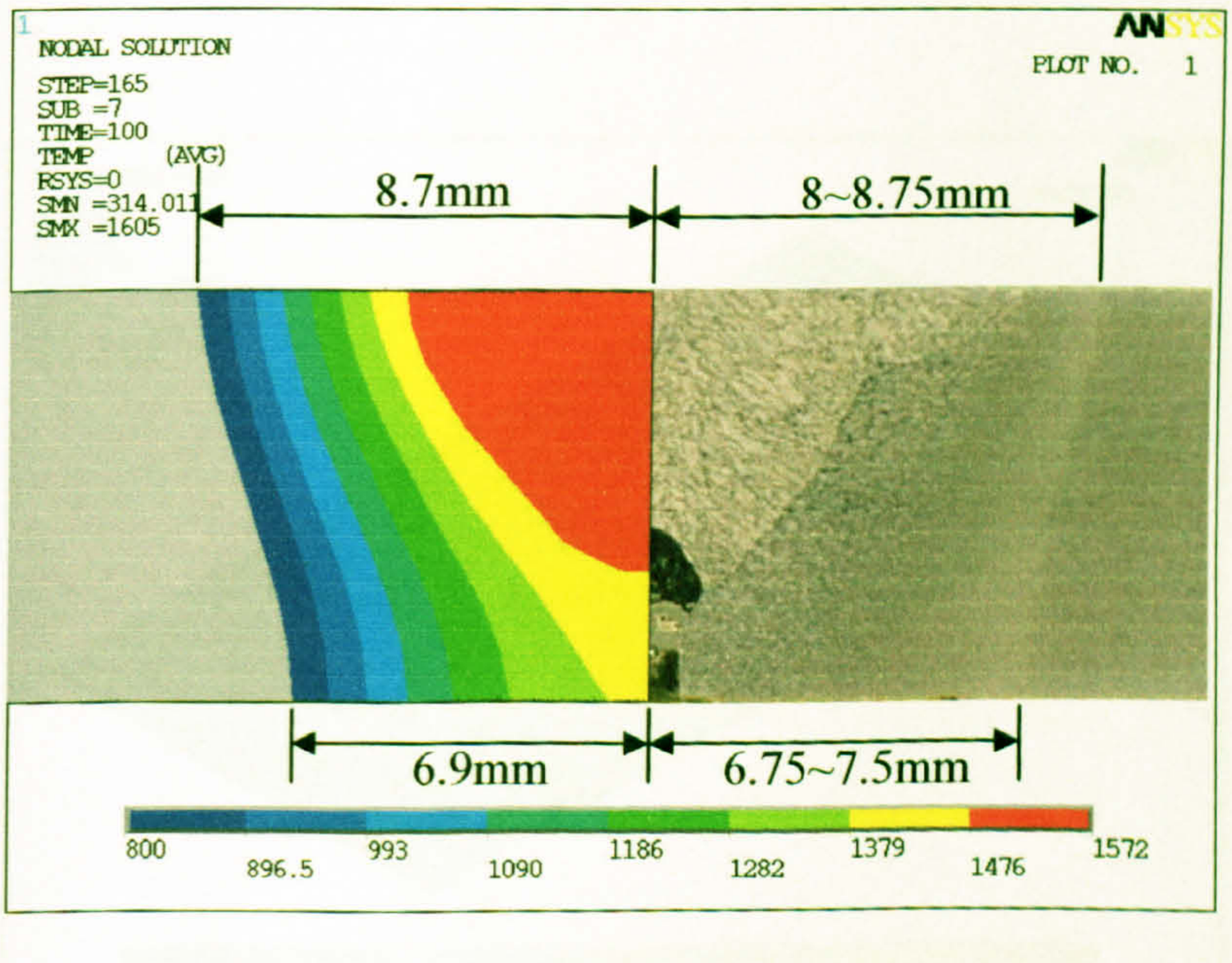

Figure 3A-H

Simulated heat affected zone of model 3A

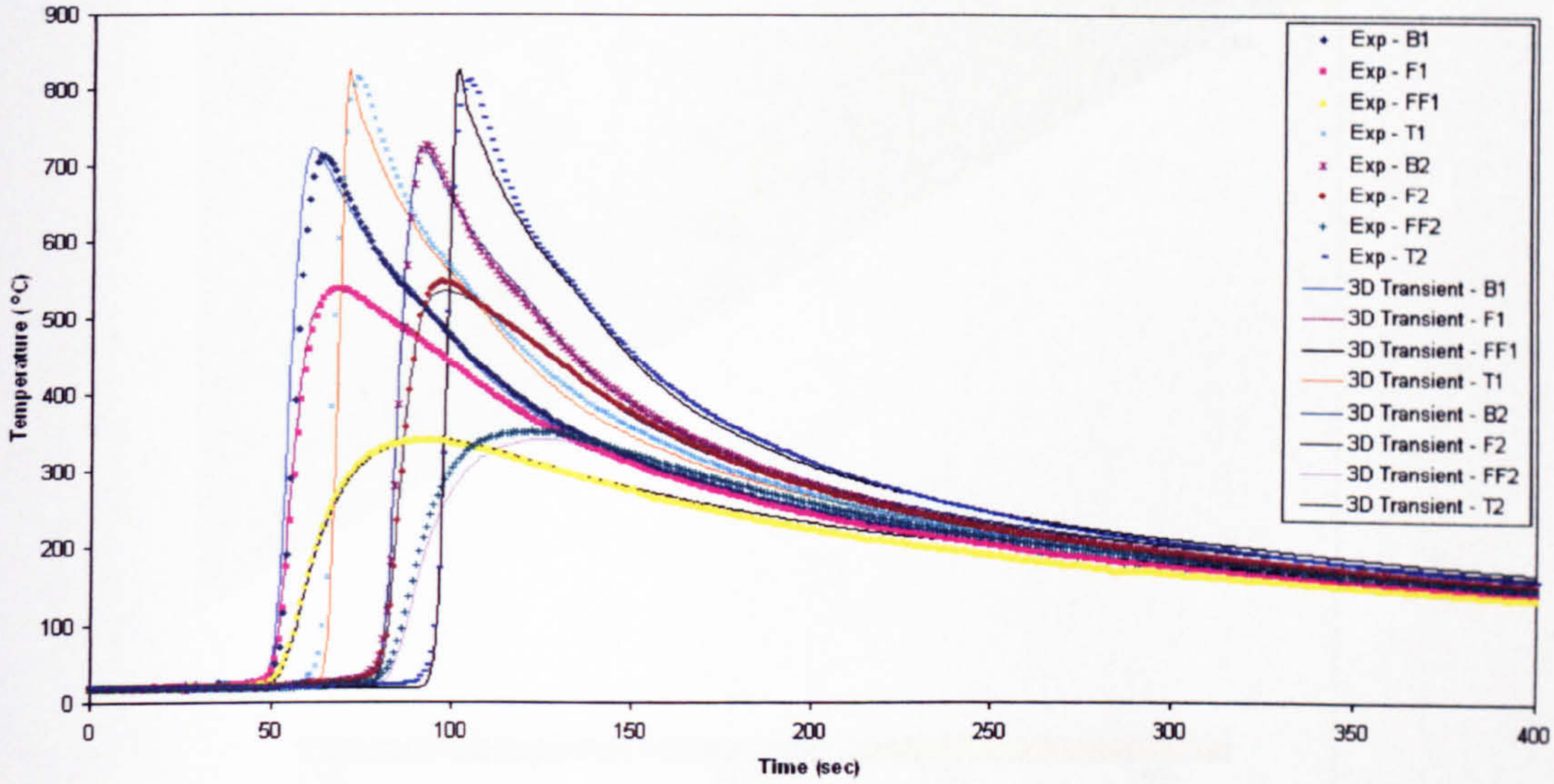

Figure 3A-TH

Comparison of the simulation with the measured temperature histories of model 3A

A.4 Model 4A – 3 mm thick welding plate with a "V" weld-prep

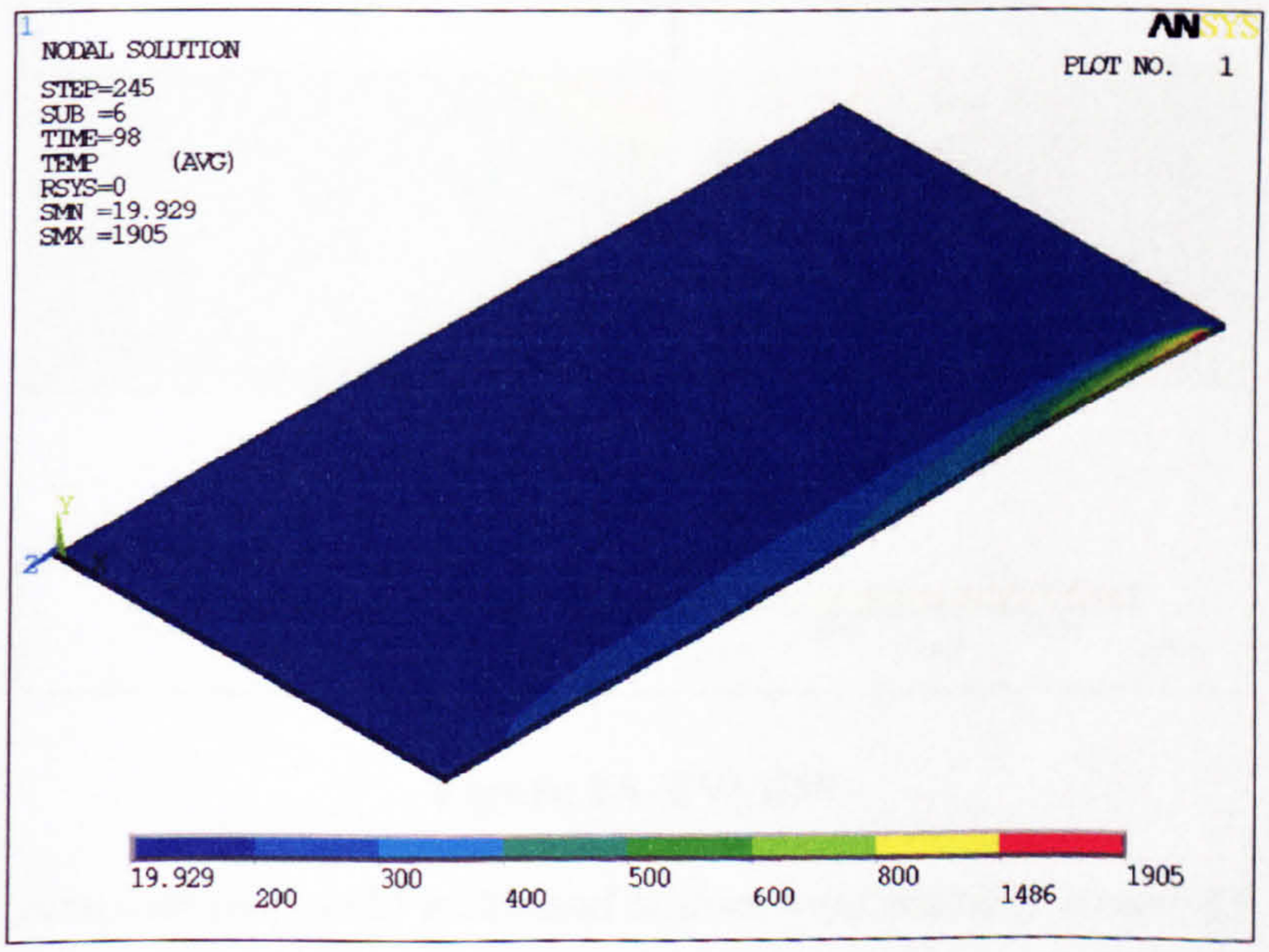

Figure 4A-O

Temperature contour at 98 seconds of model 4A

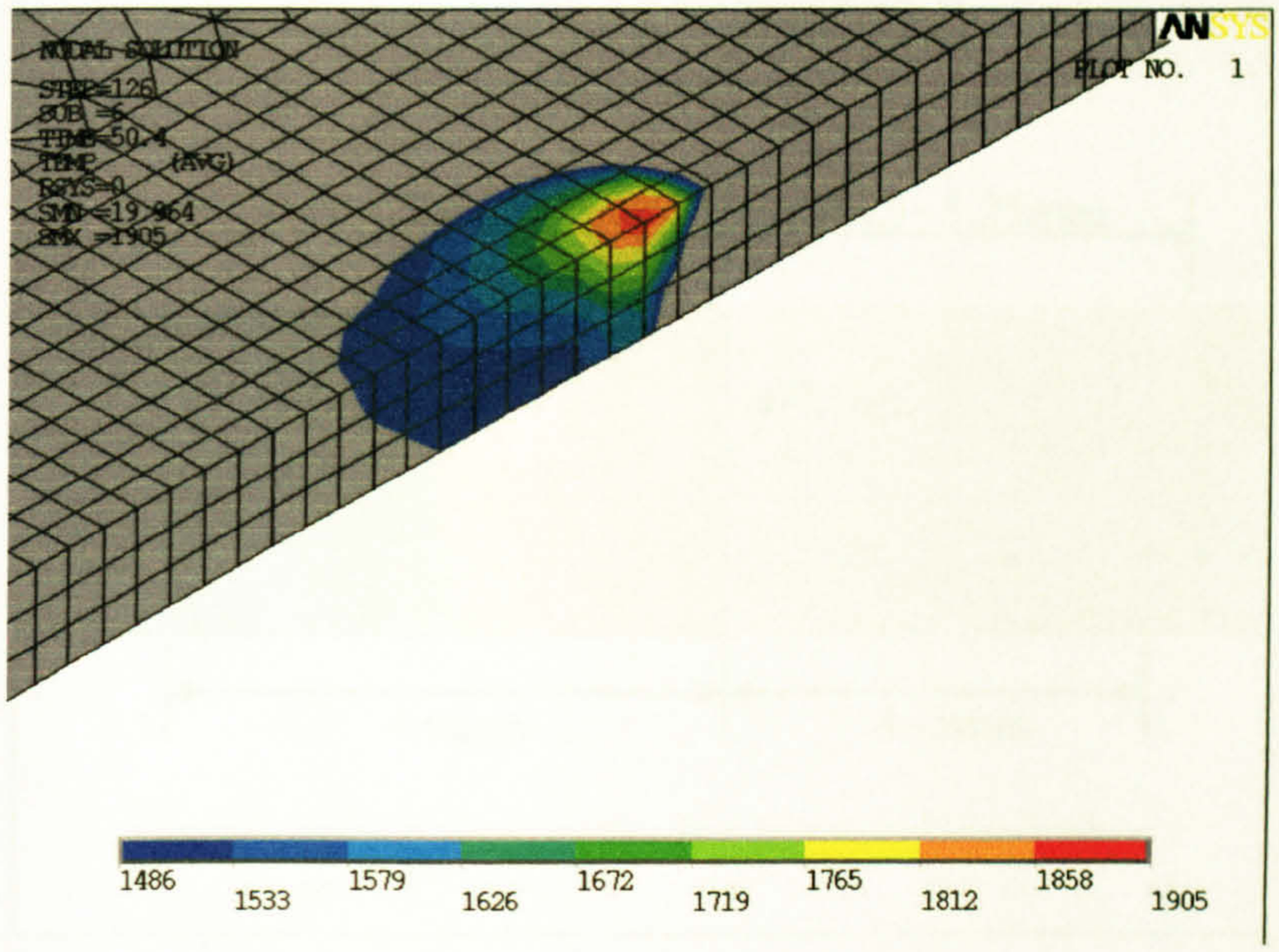

Figure 4A-P

Temperature contour of the weld pool of model 4A

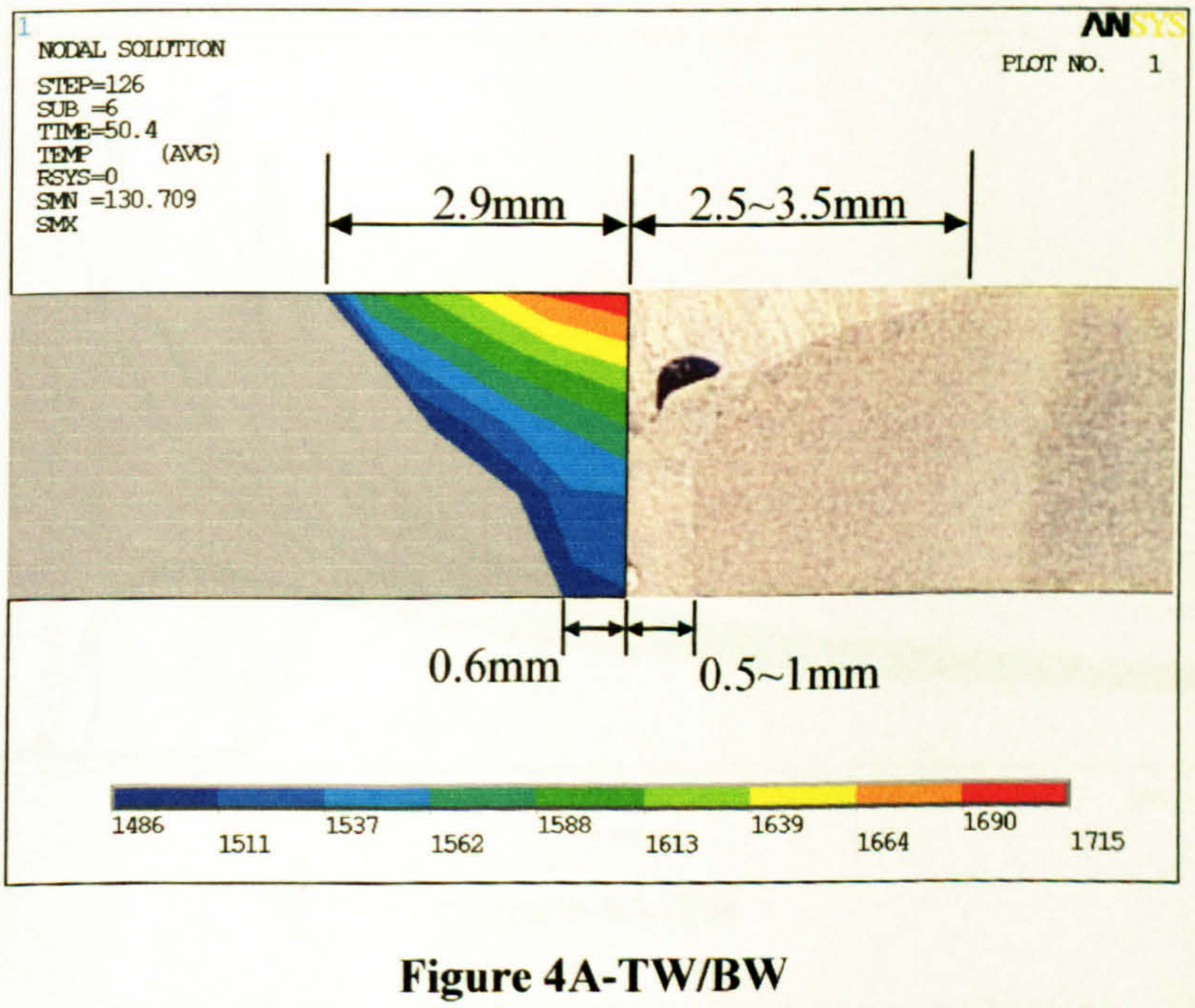

Figure 4A-TW/BW

Simulated top weld width and bottom weld width of model 4A

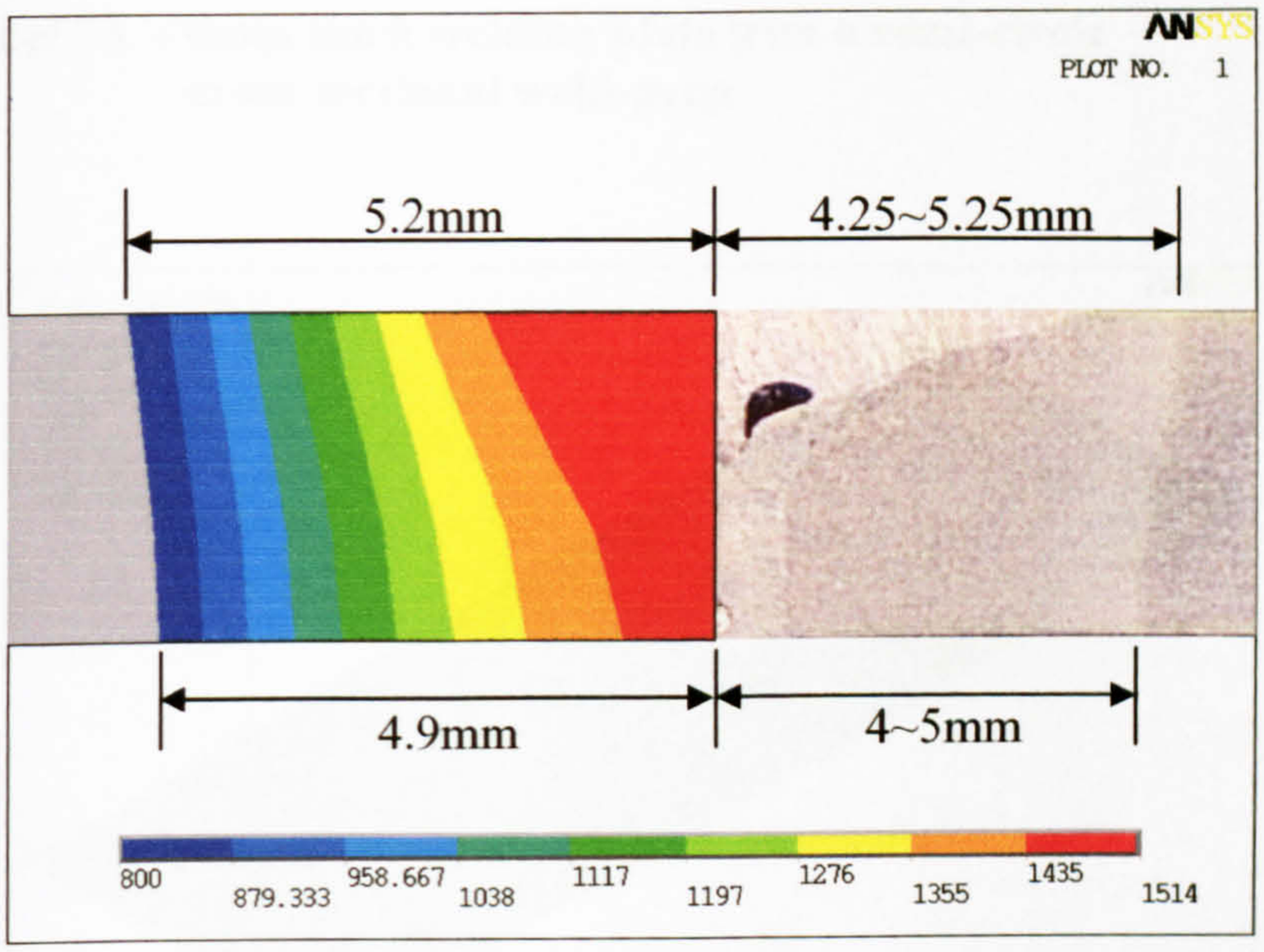

Figure 4A-H

Simulated heat affected zone of model 4A

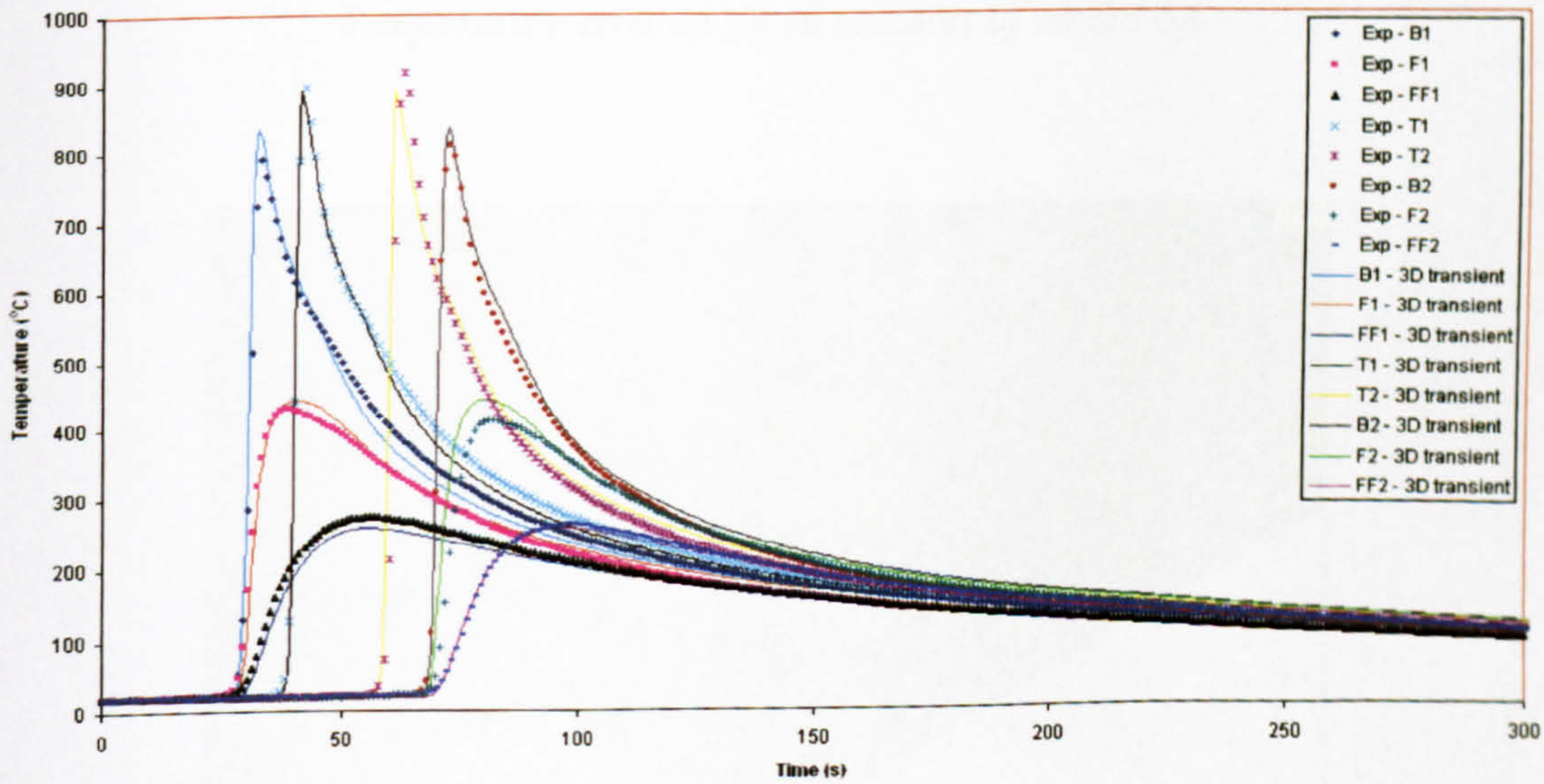

Figure 4A-TH

Comparison of the simulation with the measured temperature histories of model 4A

A.5 Model 5A – 6mm thick welding plate with a semi-circle cross-sectional weld-prep

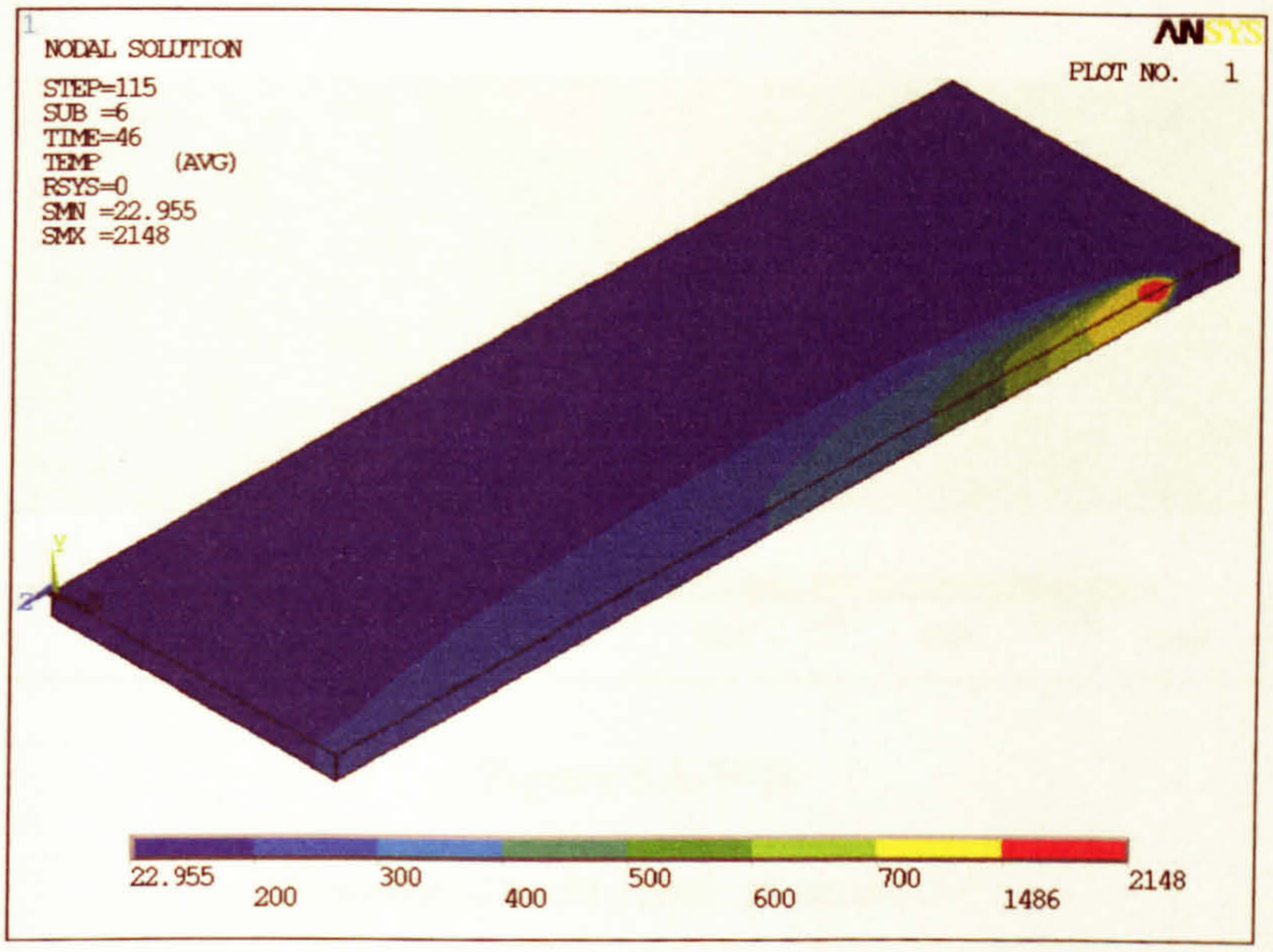

Figure 5A-O

Temperature contour at 46 seconds of model 5A

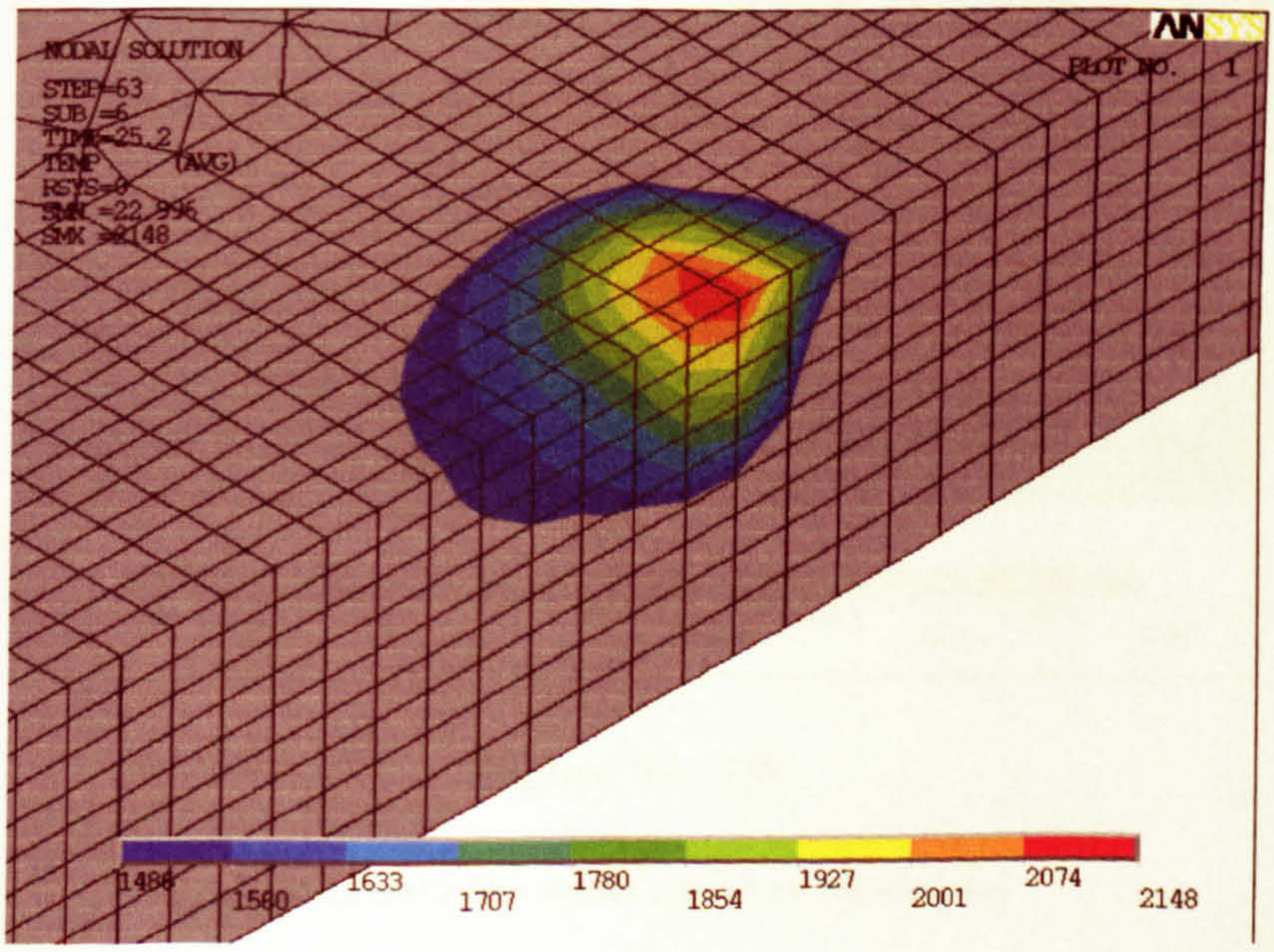

Figure 5A-P

Temperature contour of the weld pool of model 5A

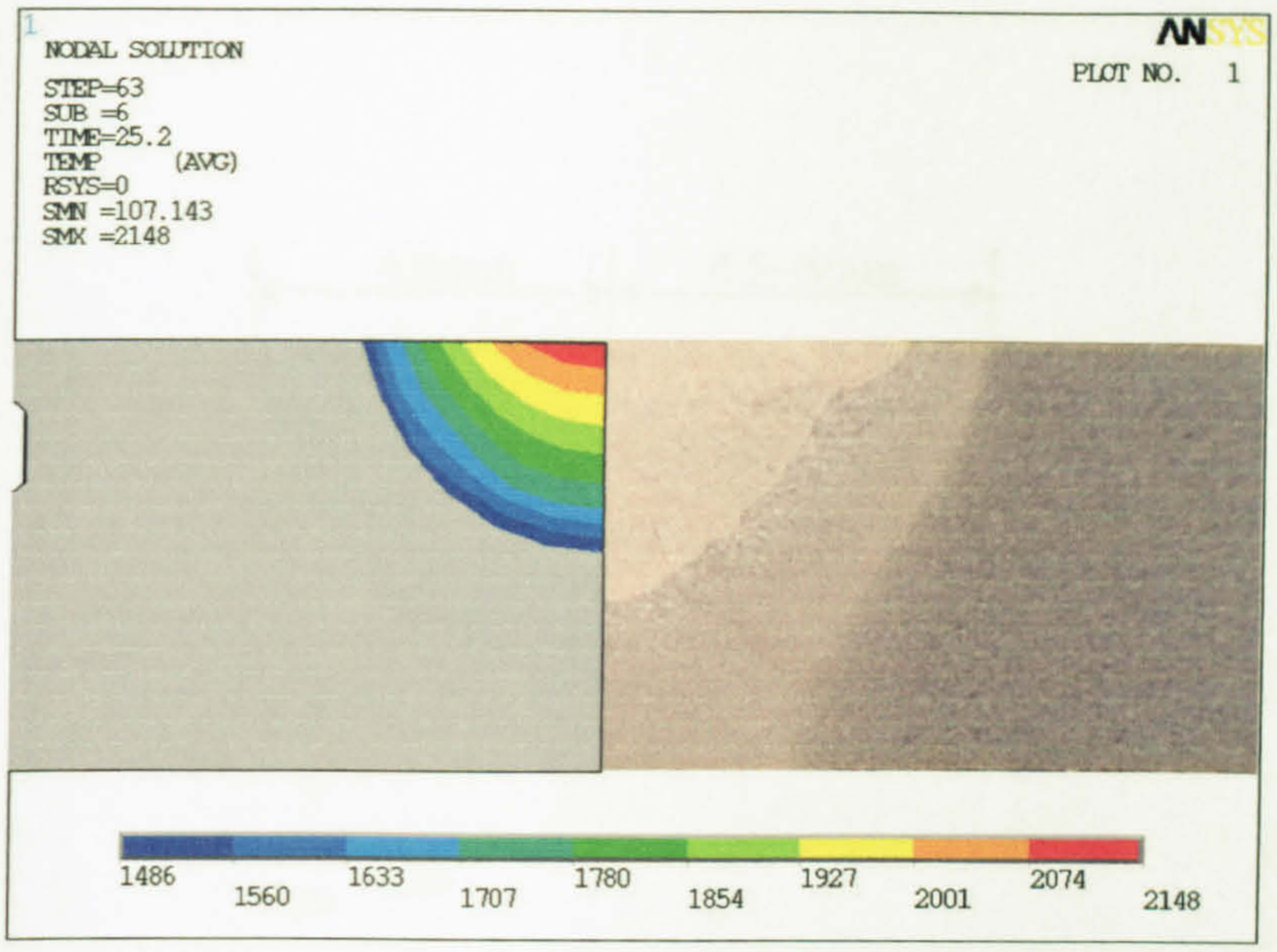

Figure 5A-WD

Simulated weld depth of model 5A

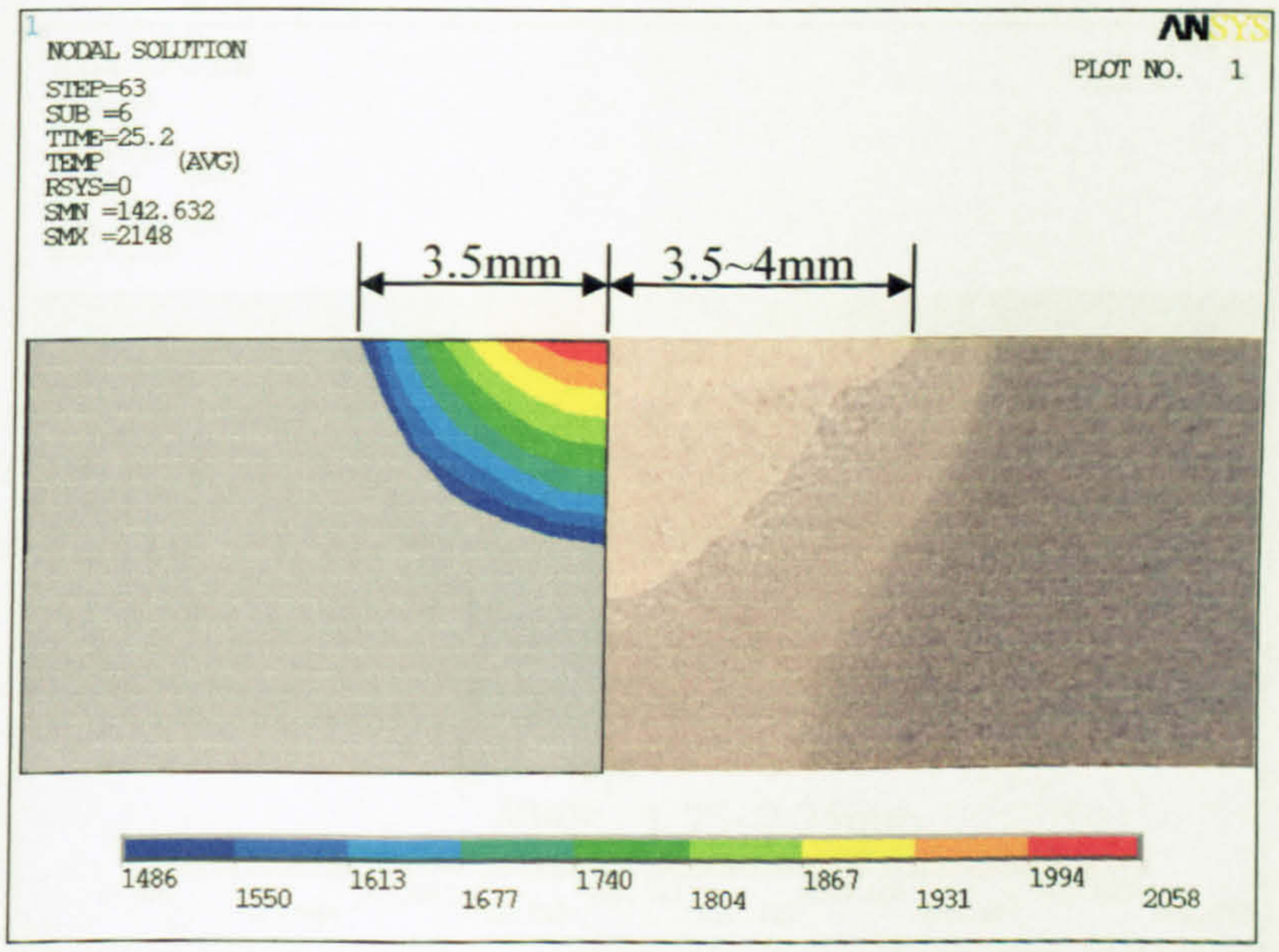

Figure 5A-TW

Simulated top weld width of model 5A

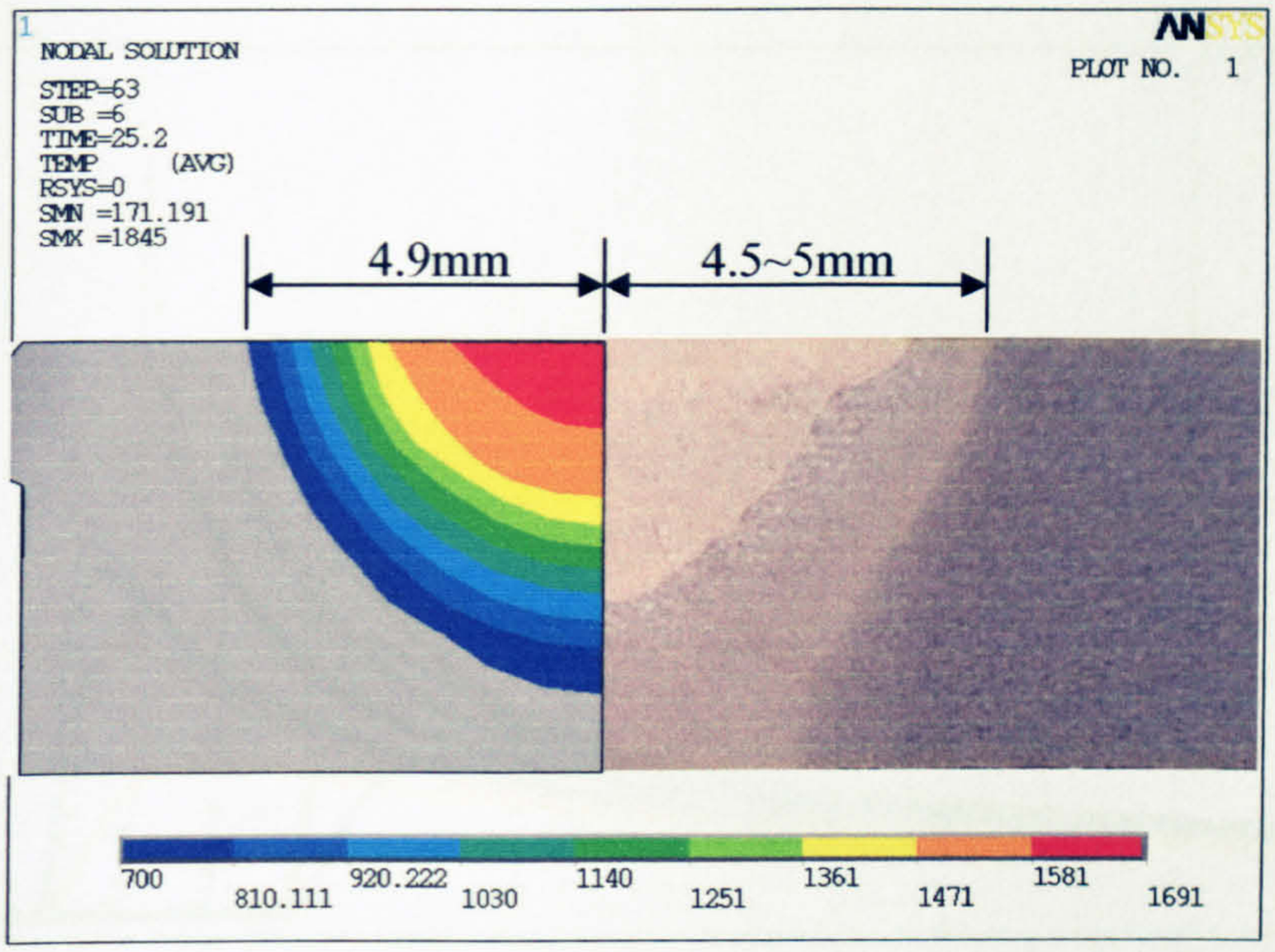

Figure 5A-HT

Simulated top heat affected zone of model 5A

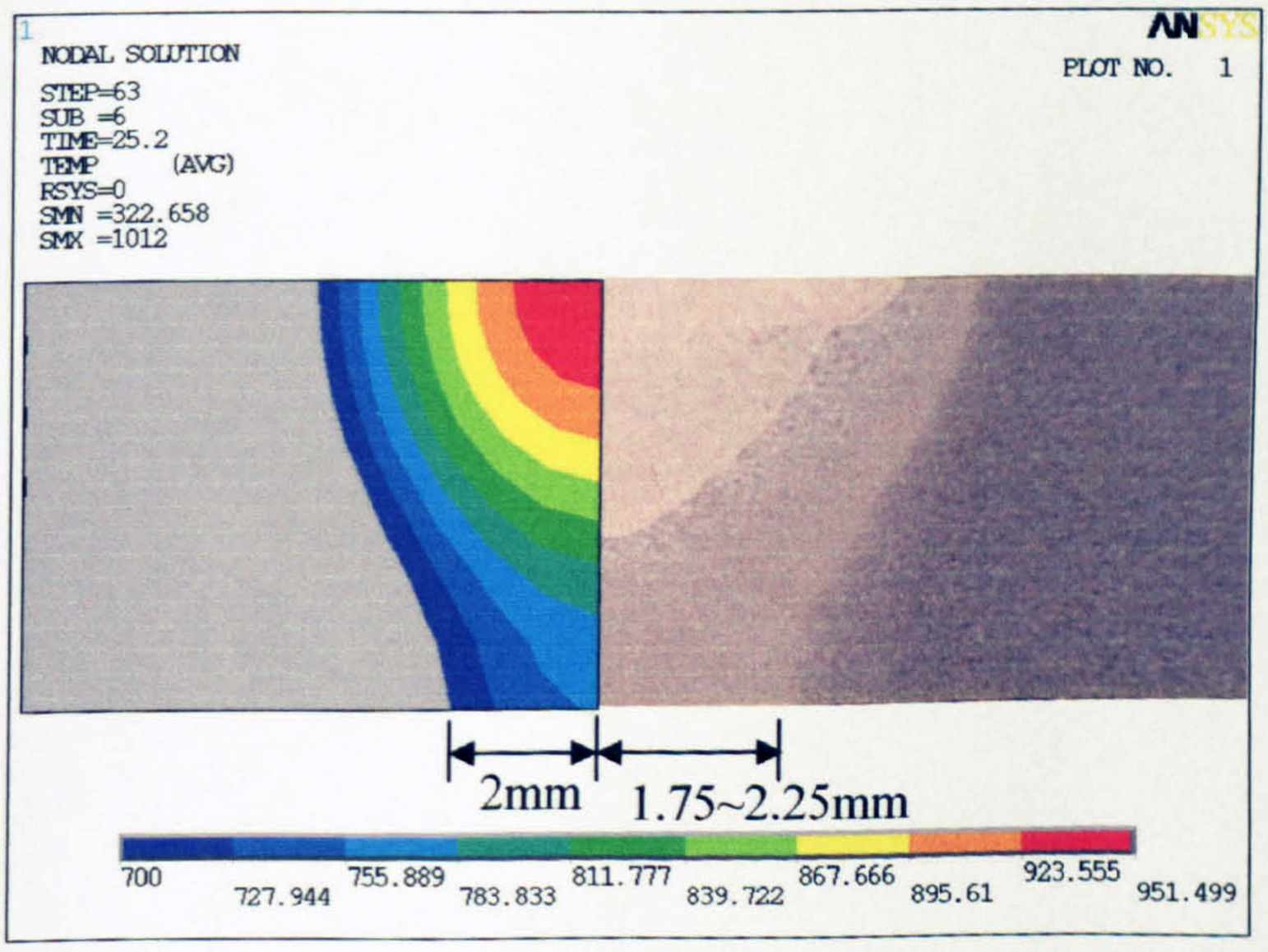

Figure 5A-HB

Simulated bottom heat affected zone of model 5A

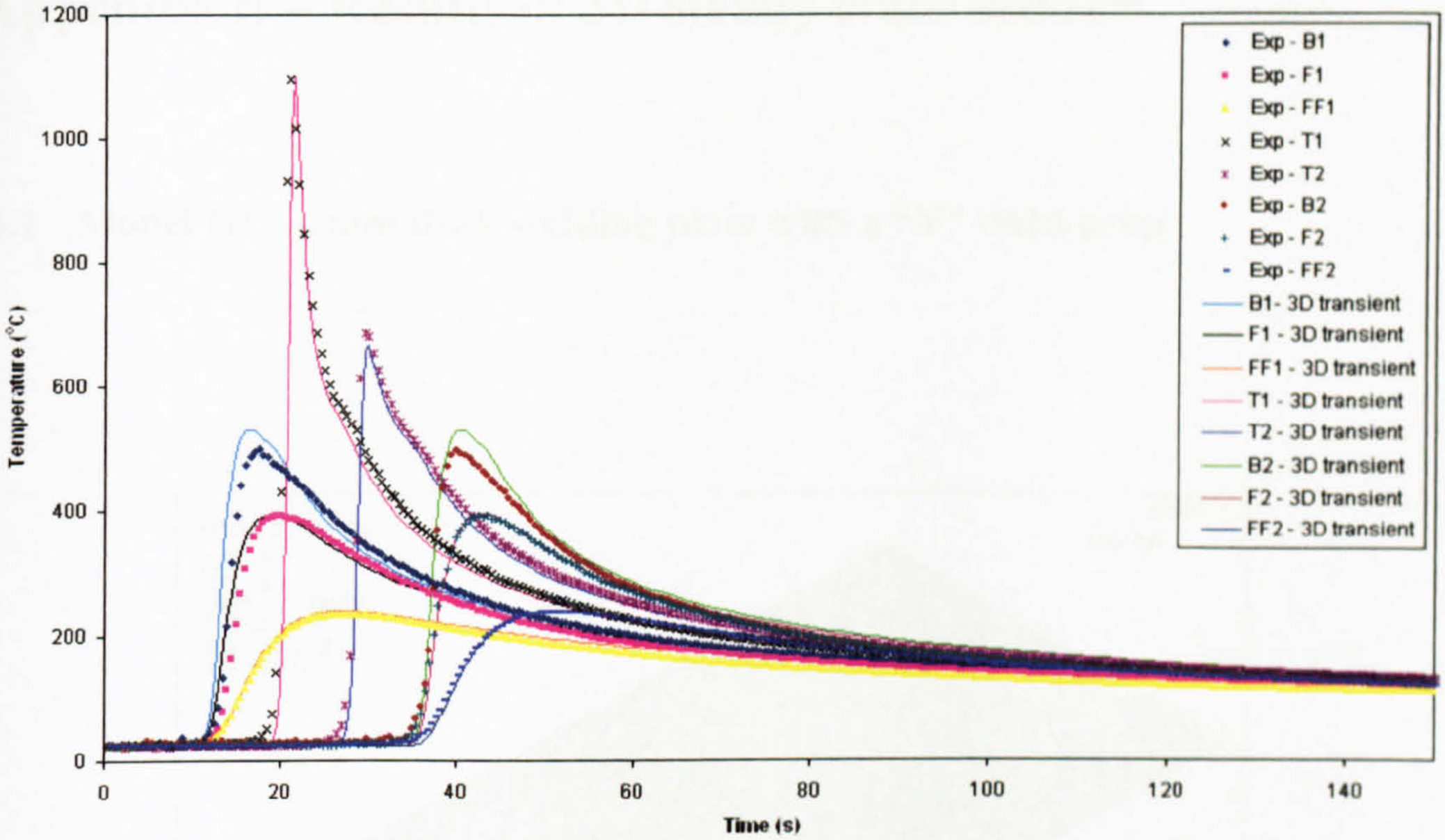

Figure 5A-TH

Comparison of the simulation with the measured temperature histories of model 5A

Appendix B – Results of 3D steady state Models

B.1 Model 1B – 4 mm thick welding plate with a "V" weld-prep

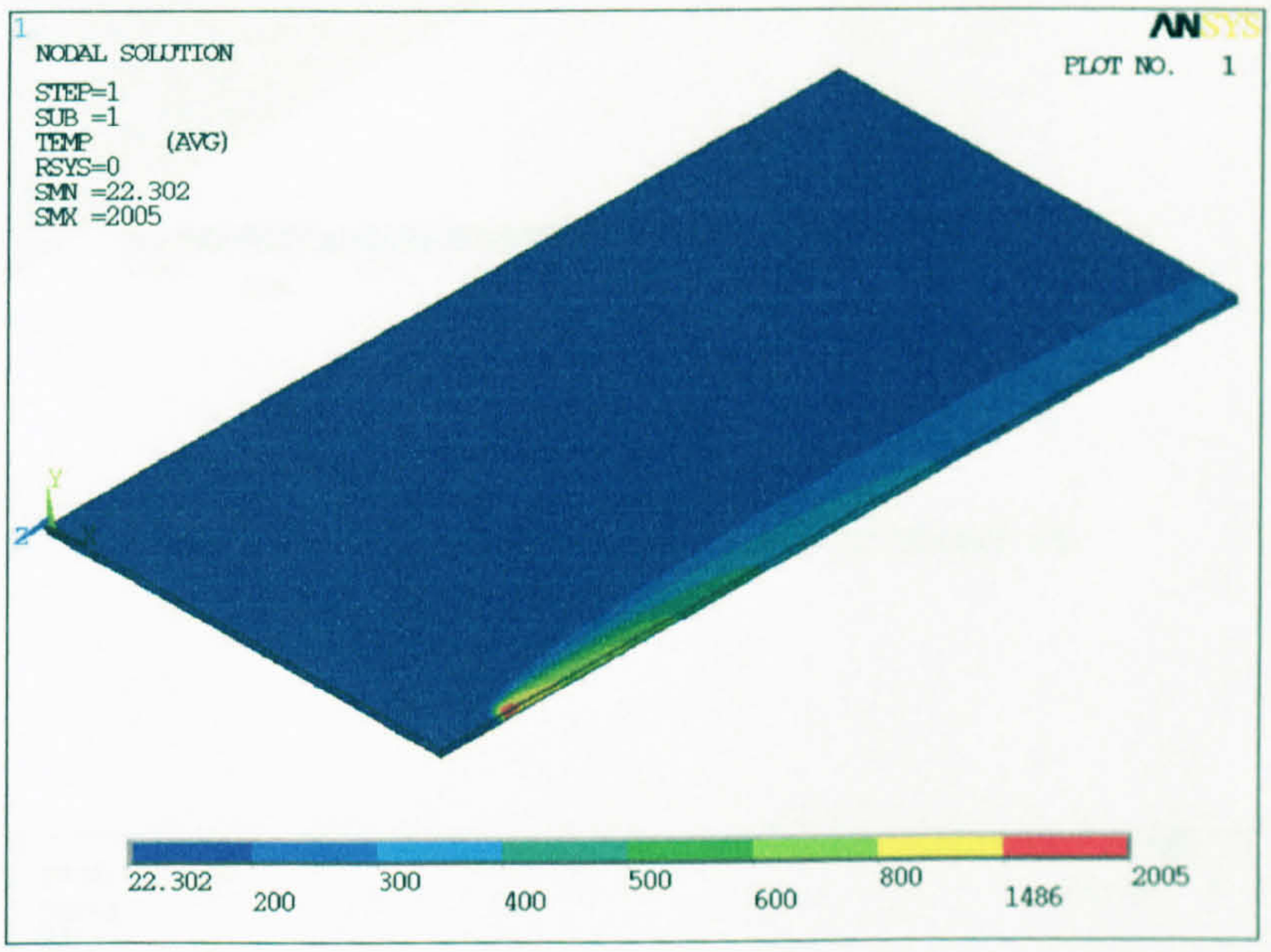

Figure 1B-O

Temperature contour of model 1B

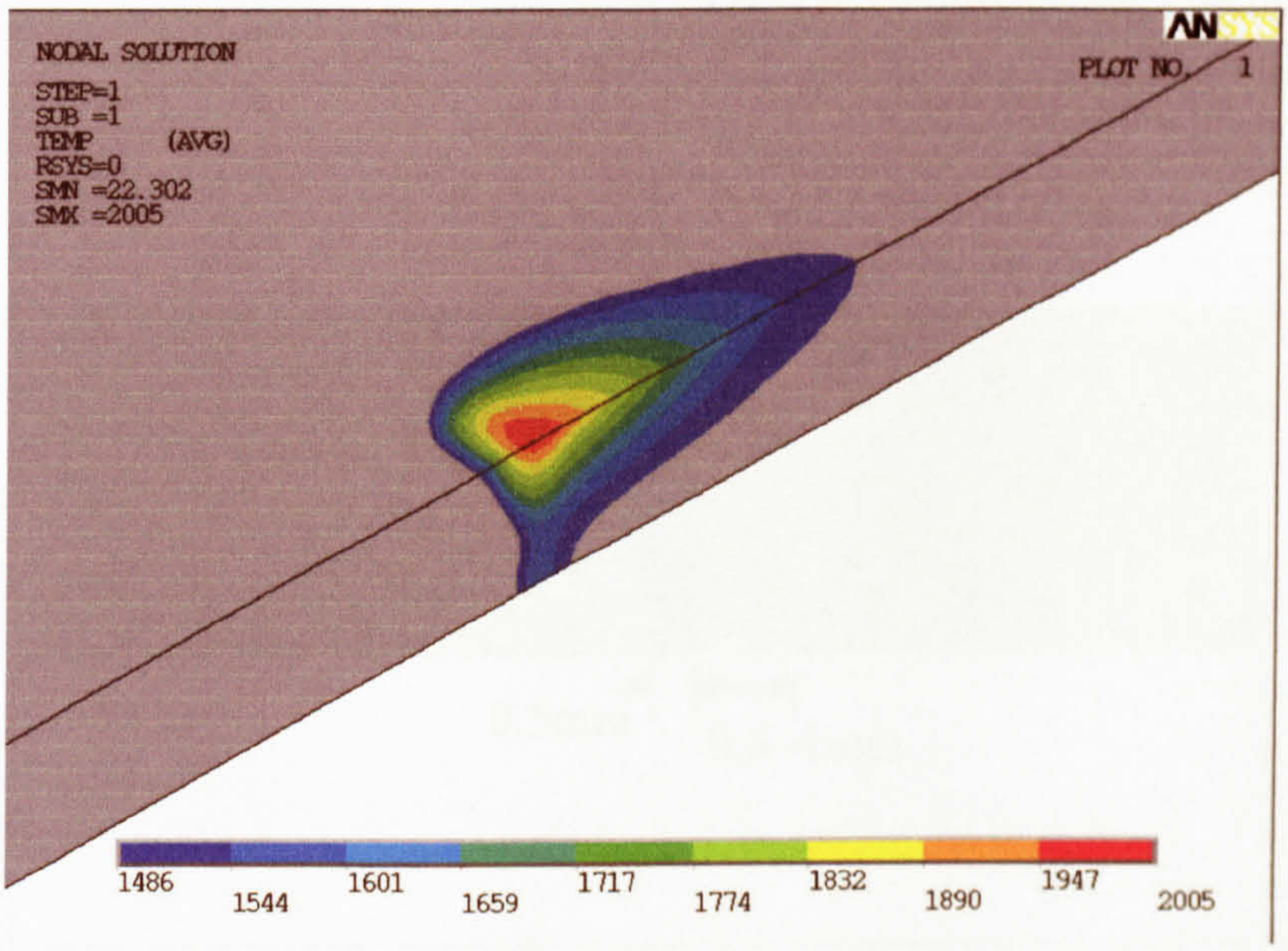

Figure 1B-P

Weld pool temperature contour of model 1B

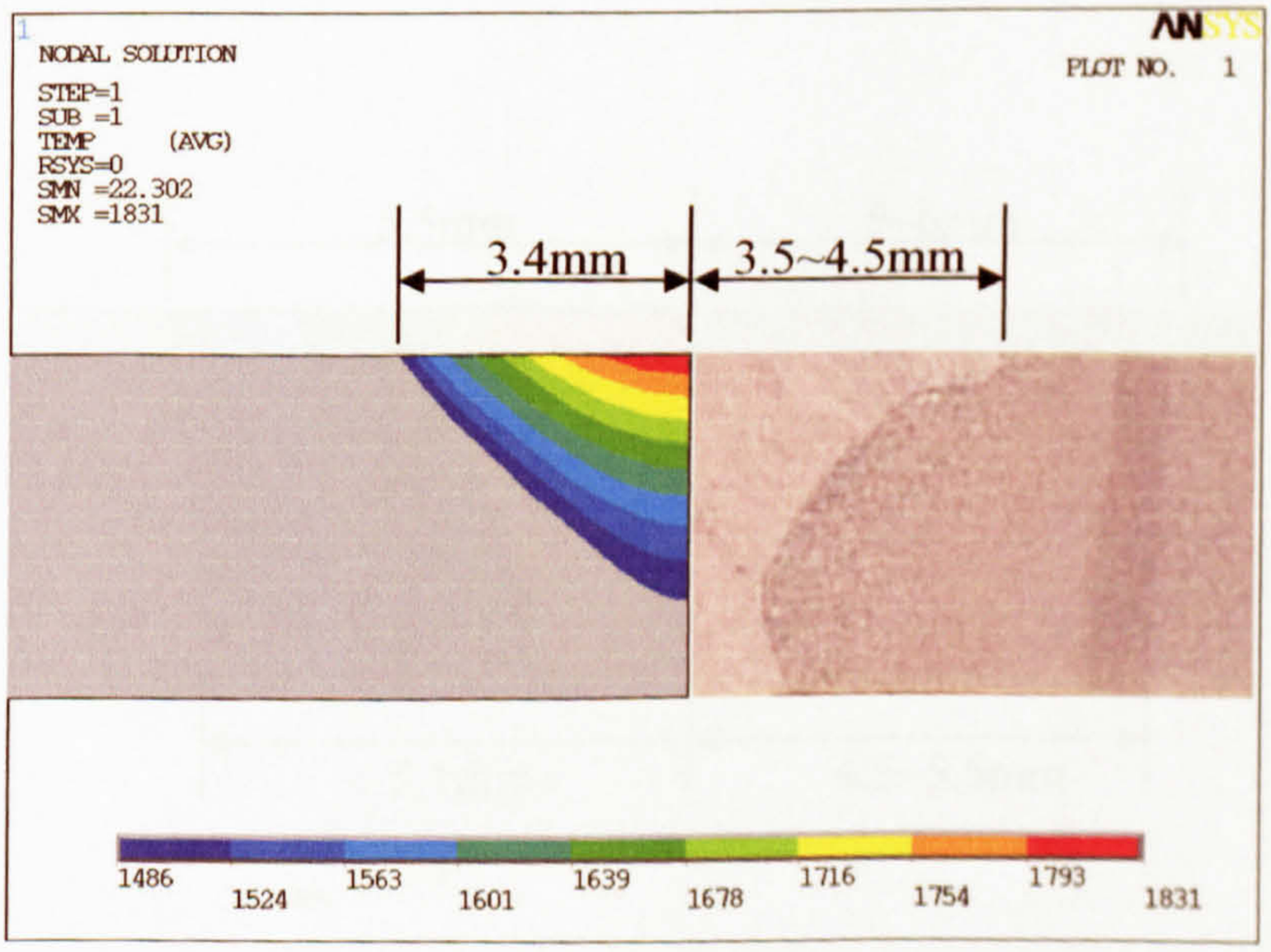

Figure 1B-TW

Simulated top weld width of model 1B

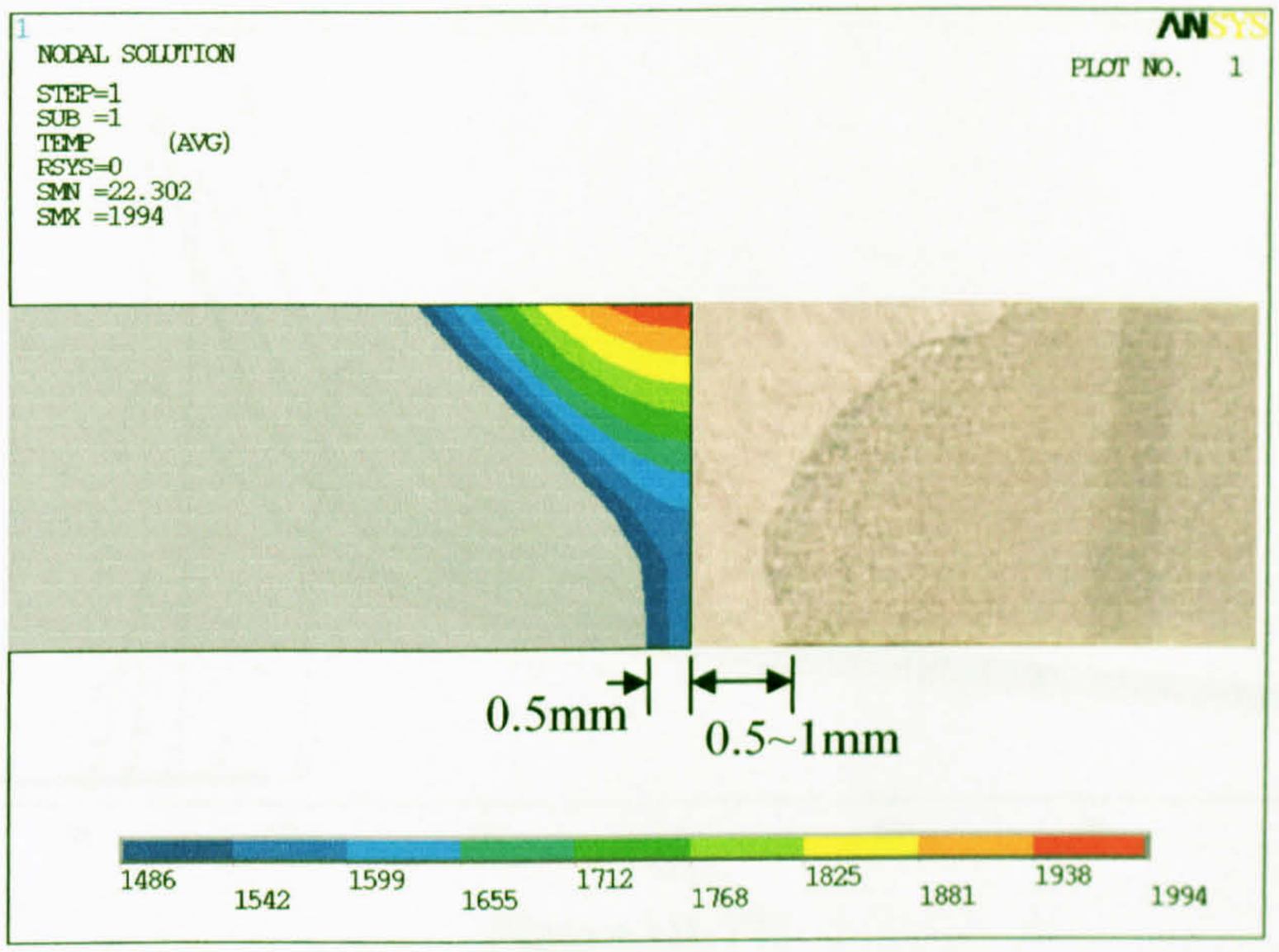

Figure 1B-BW

Simulated bottom weld width of model 1B

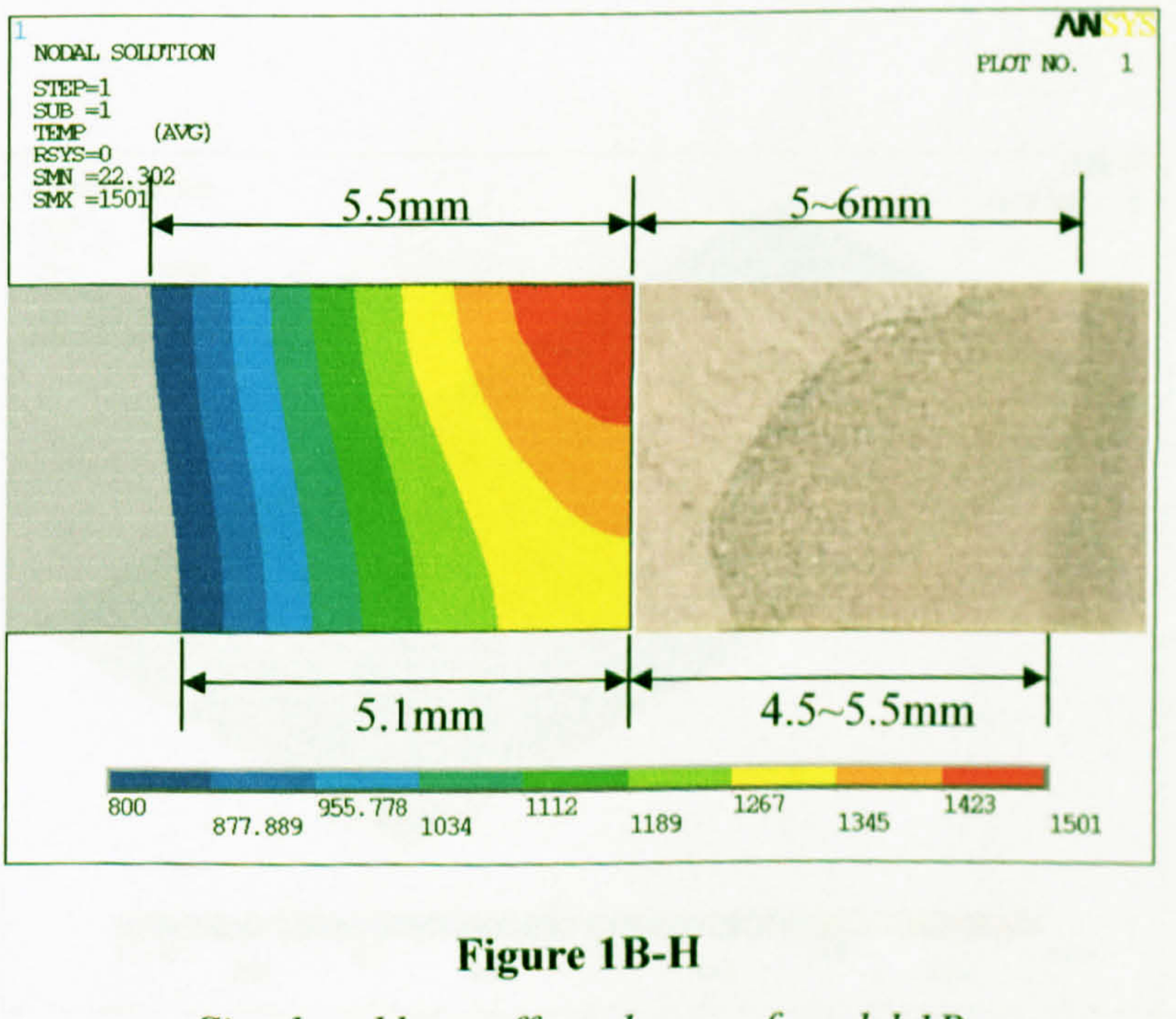

Figure 1B-H

Simulated heat affected zone of model 1B

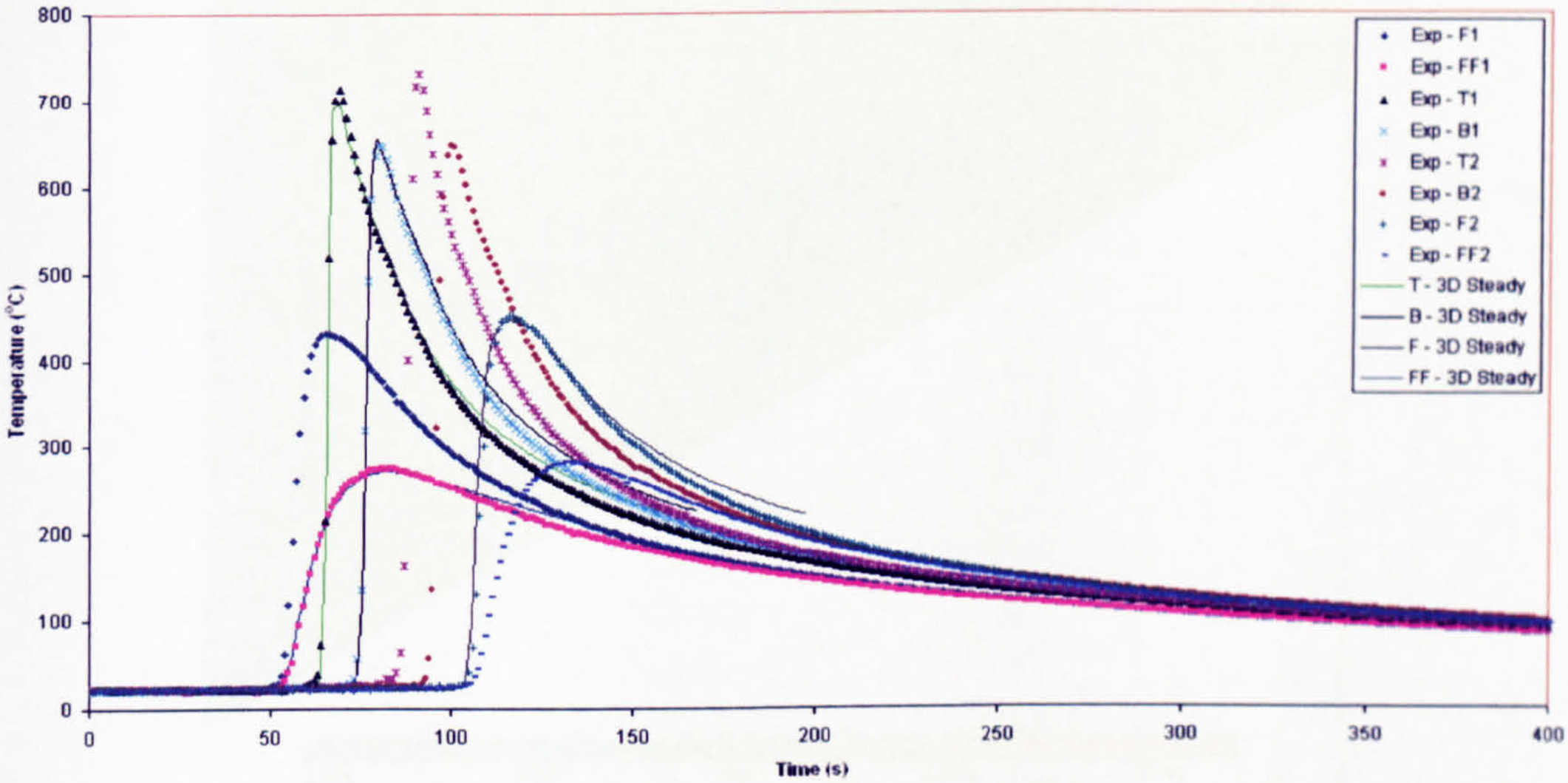

Figure 1B-TH

Comparison of the converted simulation with the measured temperature histories of model 1B

B.2 Model 2B – 6 mm thick welding plate with a "V" weld-prep

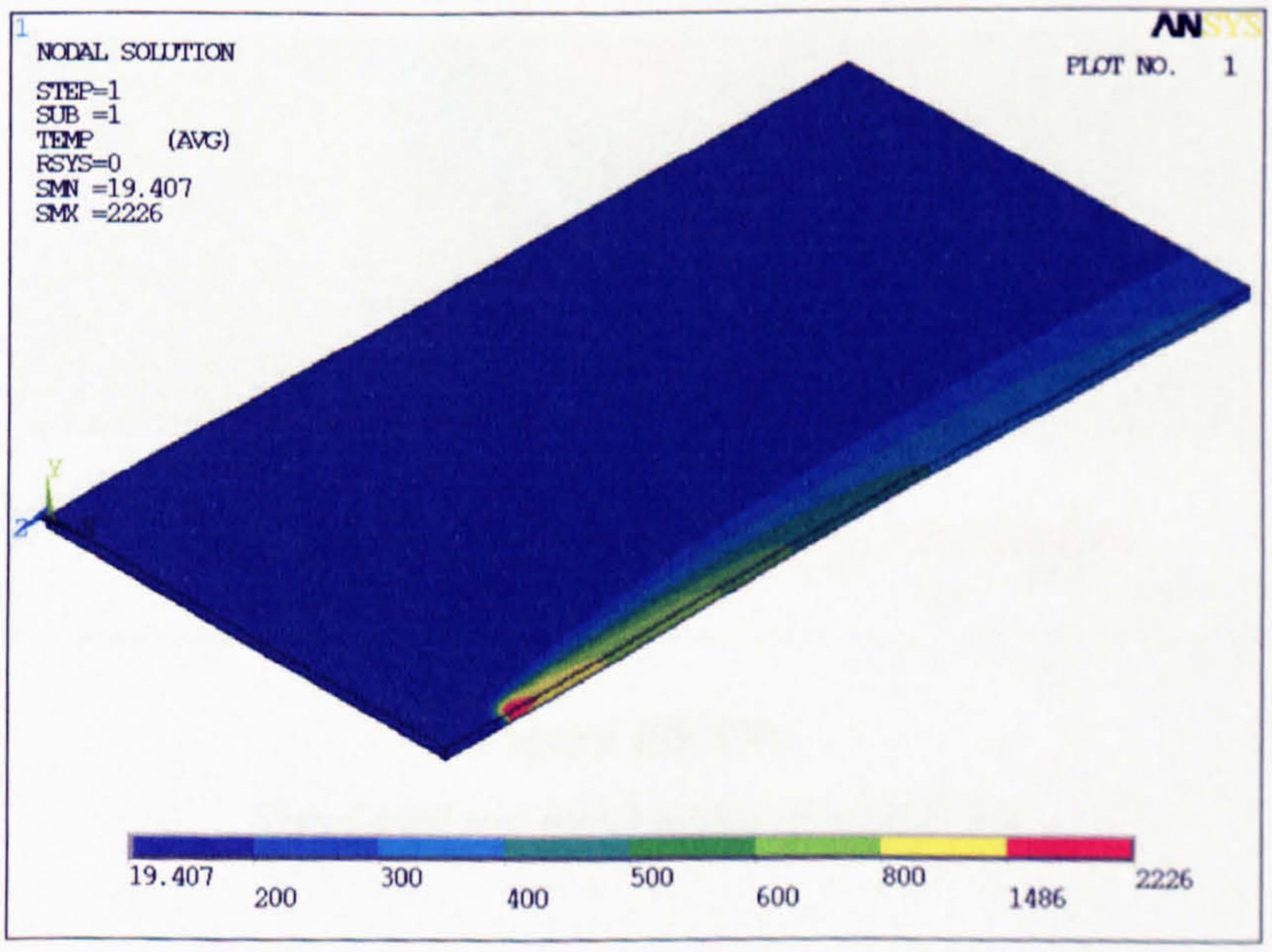

Figure 2B-O

Temperature contour of model 2B

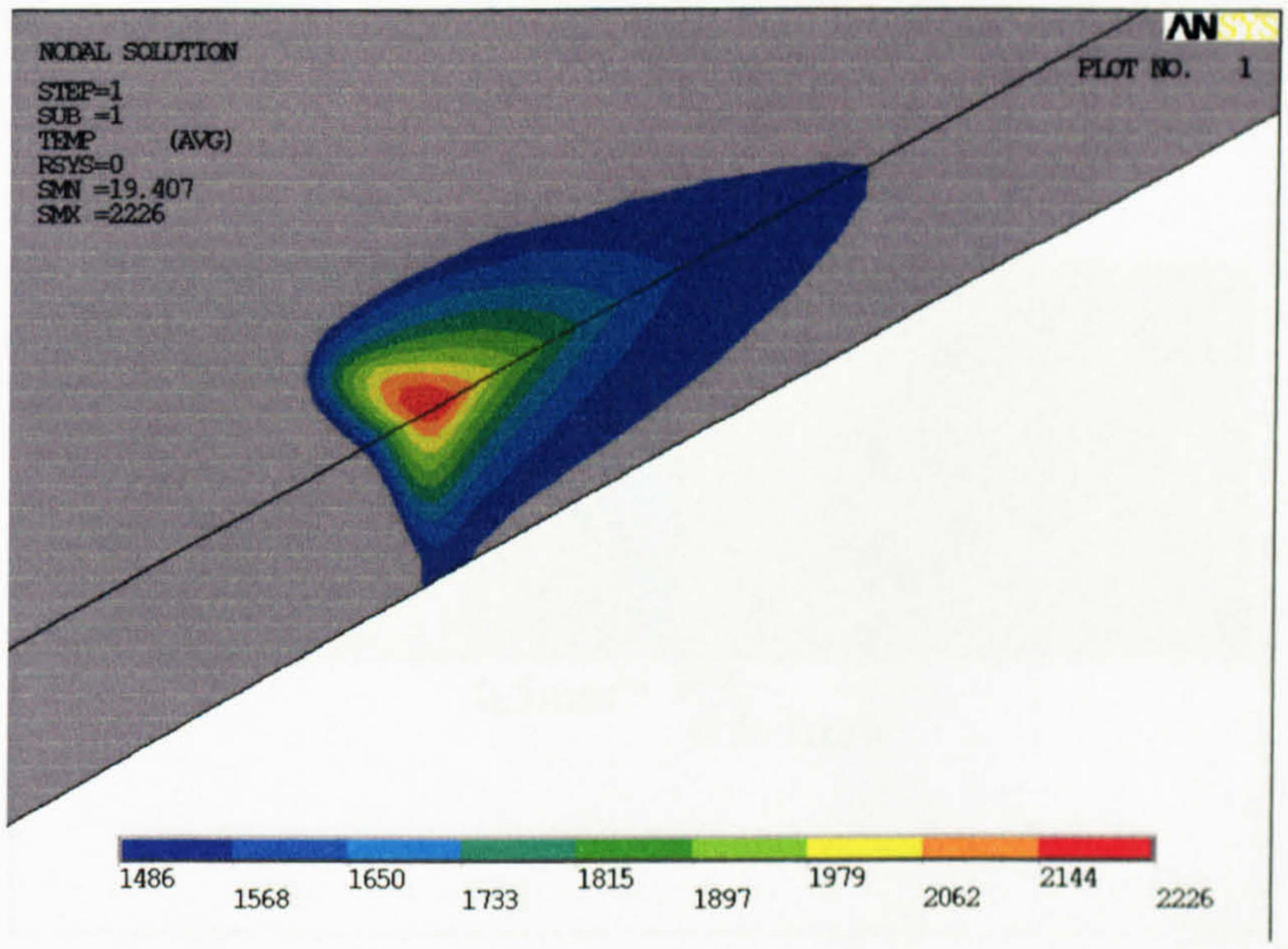

Figure 2B-P

Weld pool temperature contour of model 2B

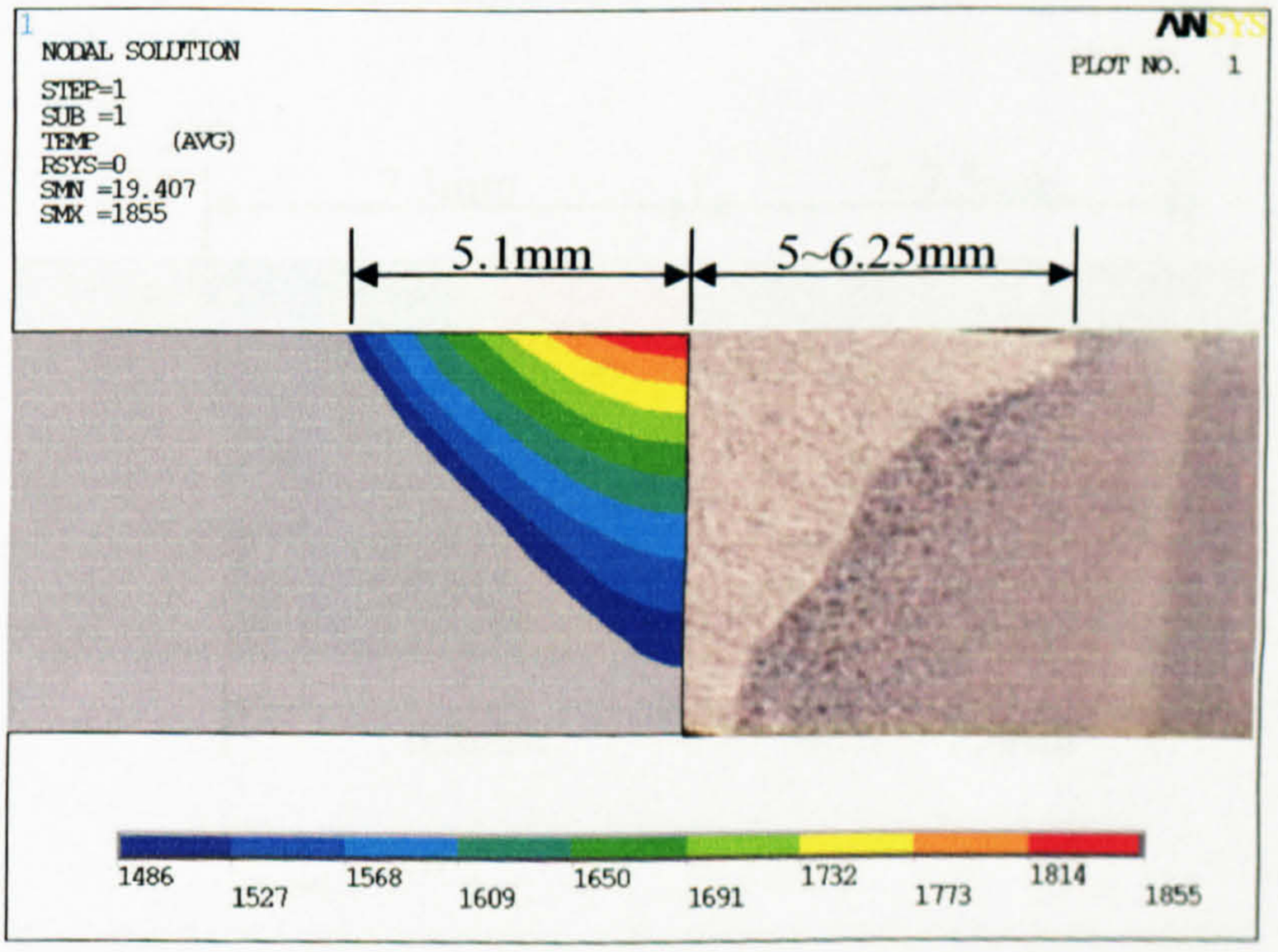

Figure 2B-TW

Simulated top weld width of model 2B

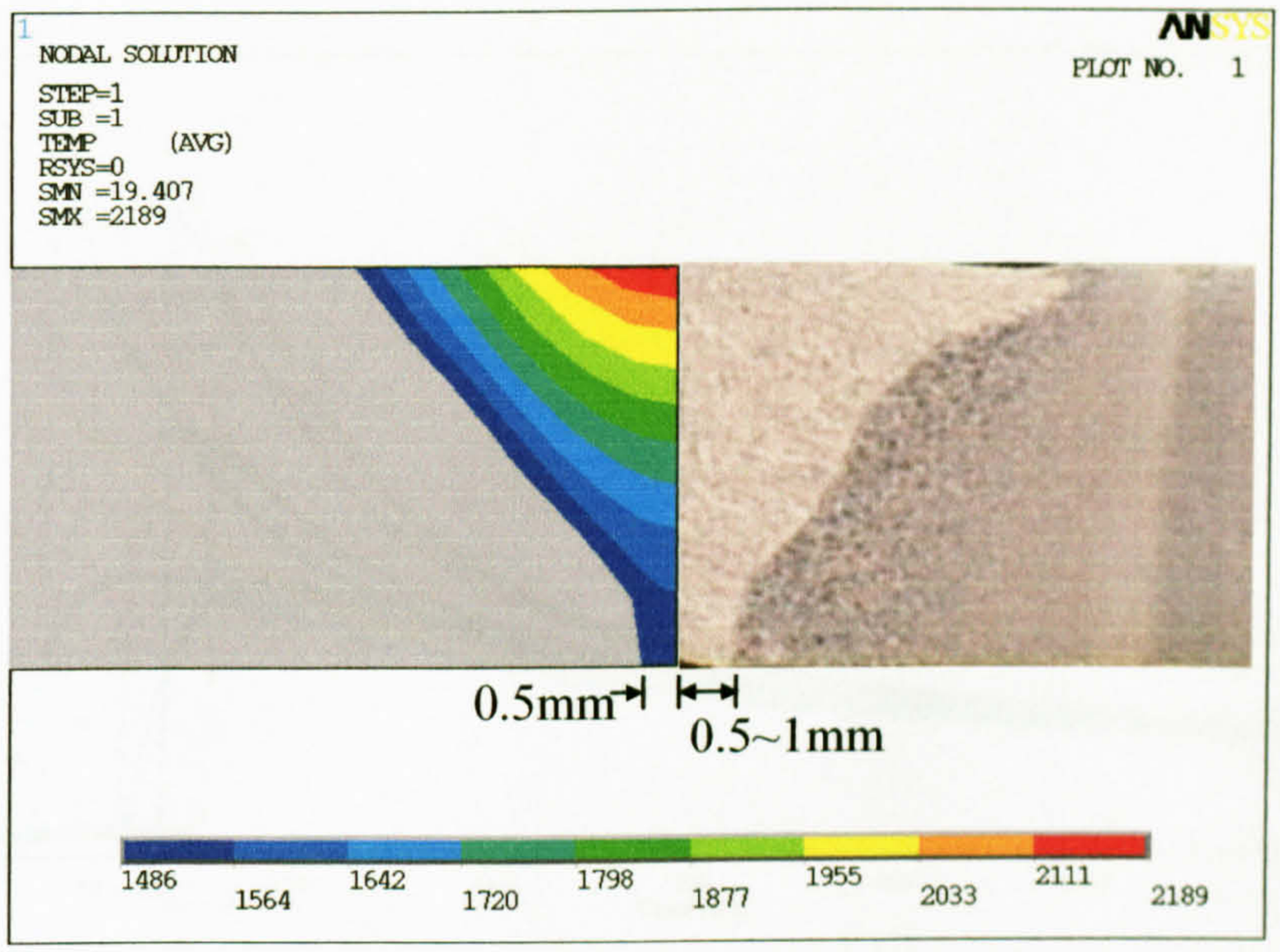

Figure 2B-BW

Simulated bottom weld width of model 2B

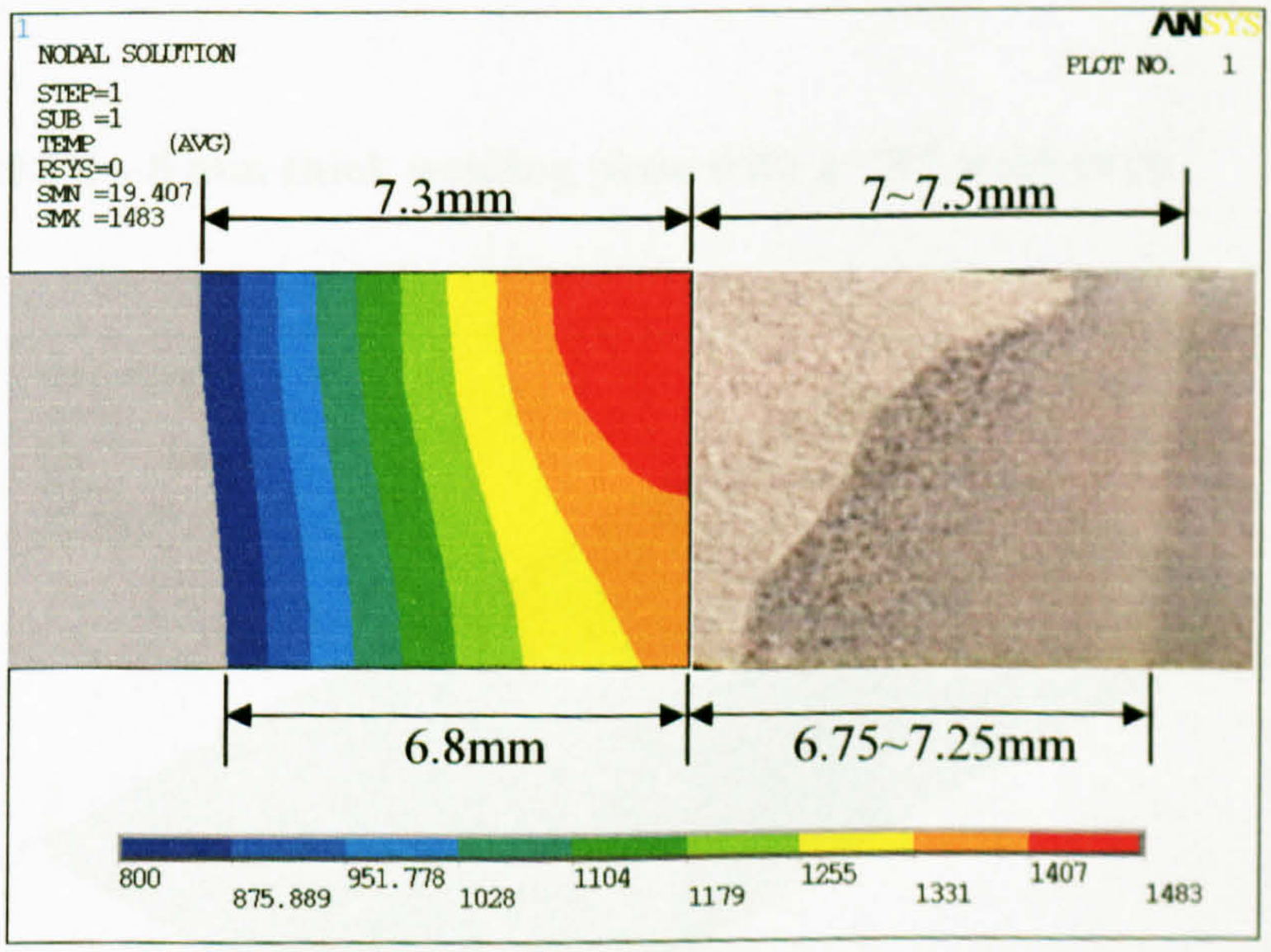

Figure 2B-H

Simulated heat affected zone of model 2B

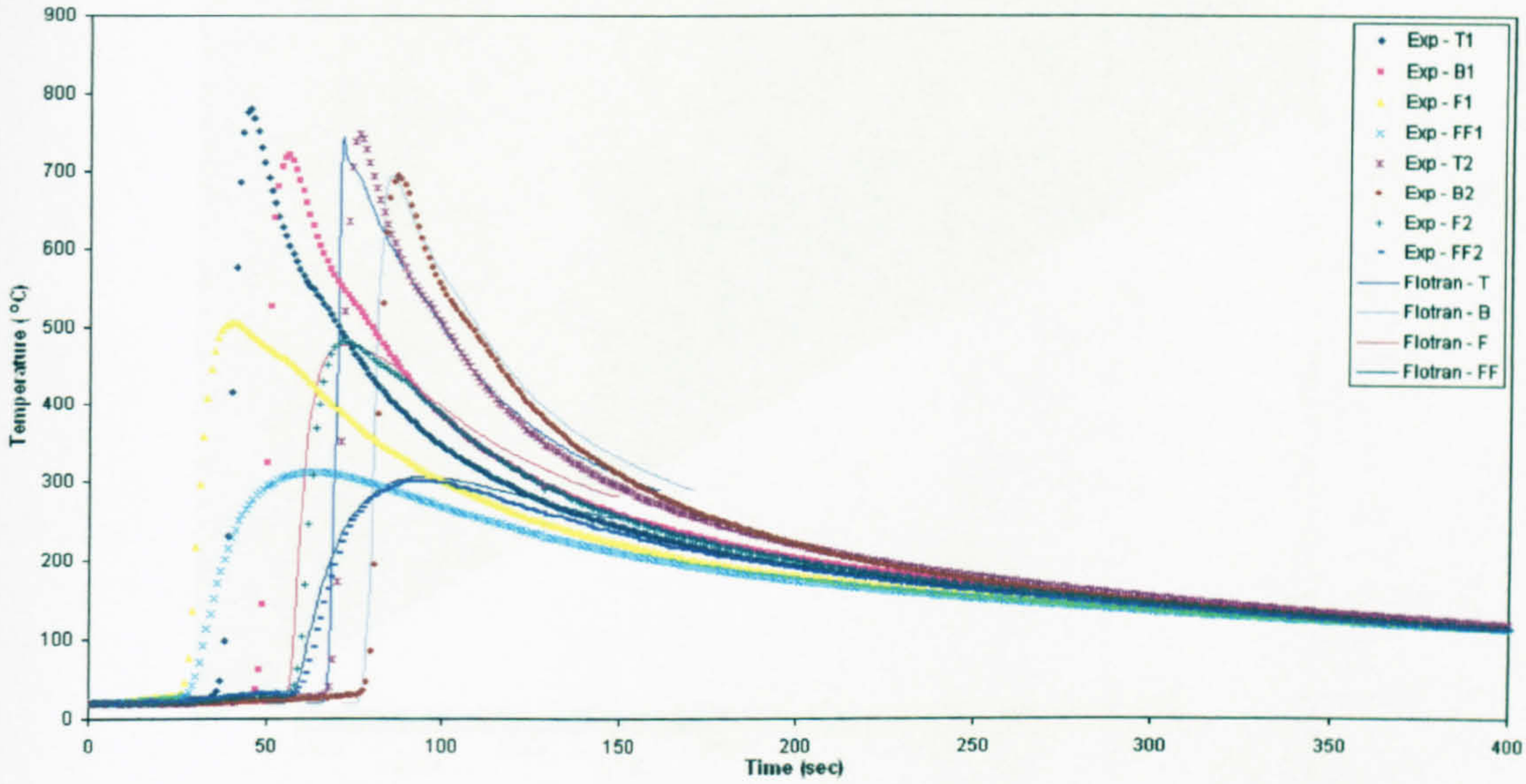

Figure 2B-TH

Comparison of the converted simulation with the measured temperature histories of model 2B

B.3 Model 3B – 8 mm thick welding plate with a "V" weld-prep

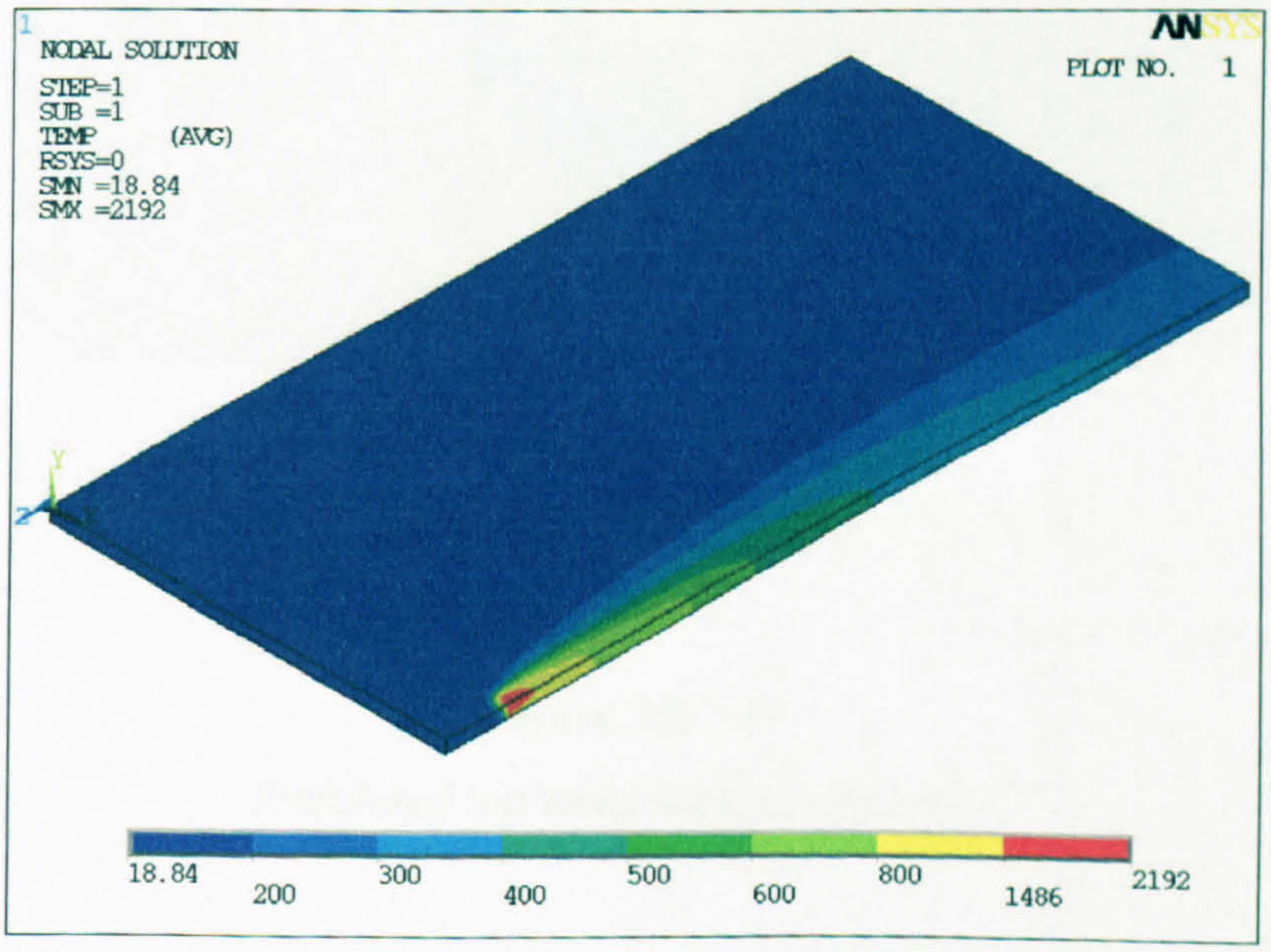

Figure 3B-O

Temperature contour of model 3B

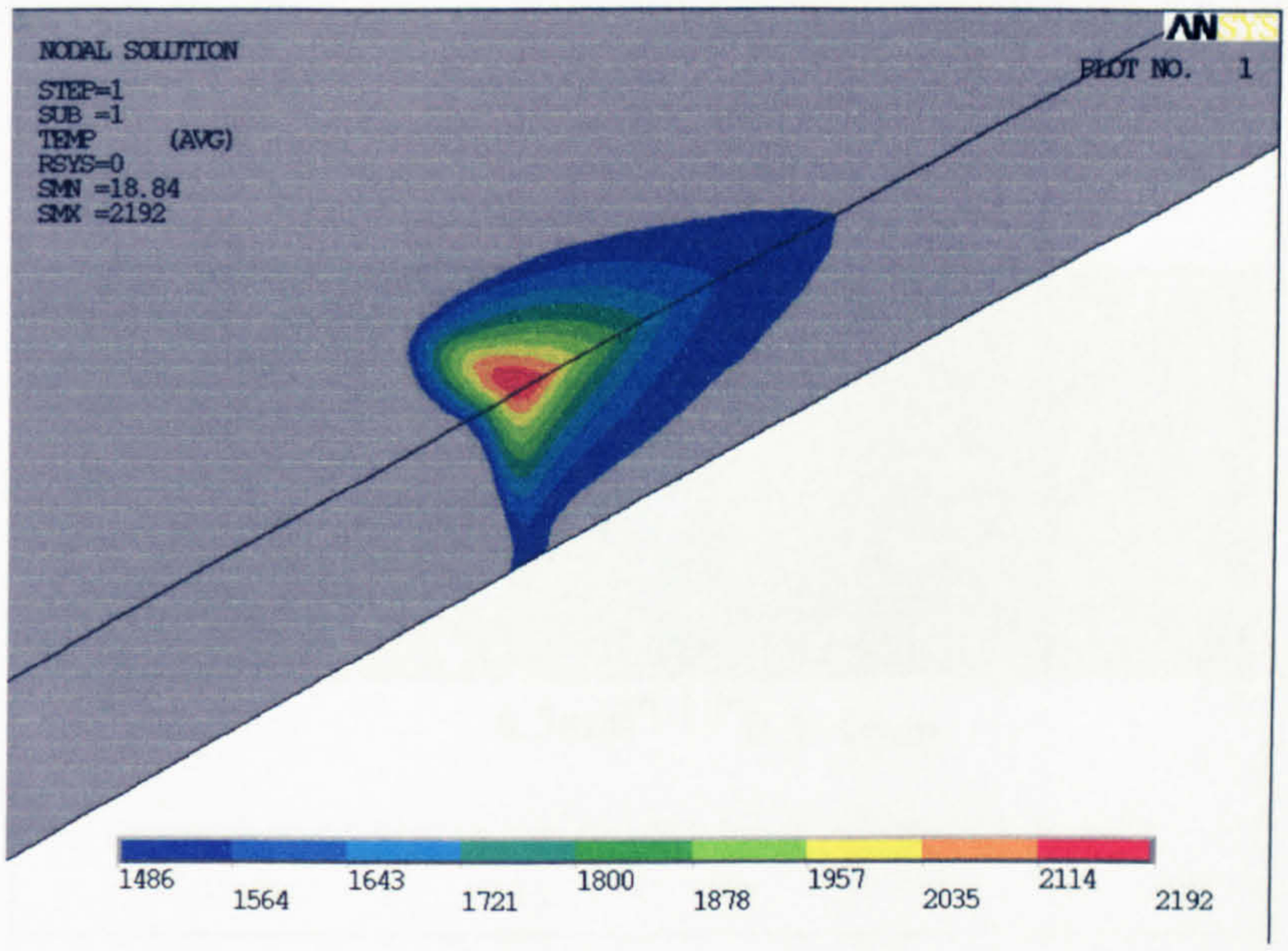

Figure 3B-P

Weld pool temperature contour of model 3B

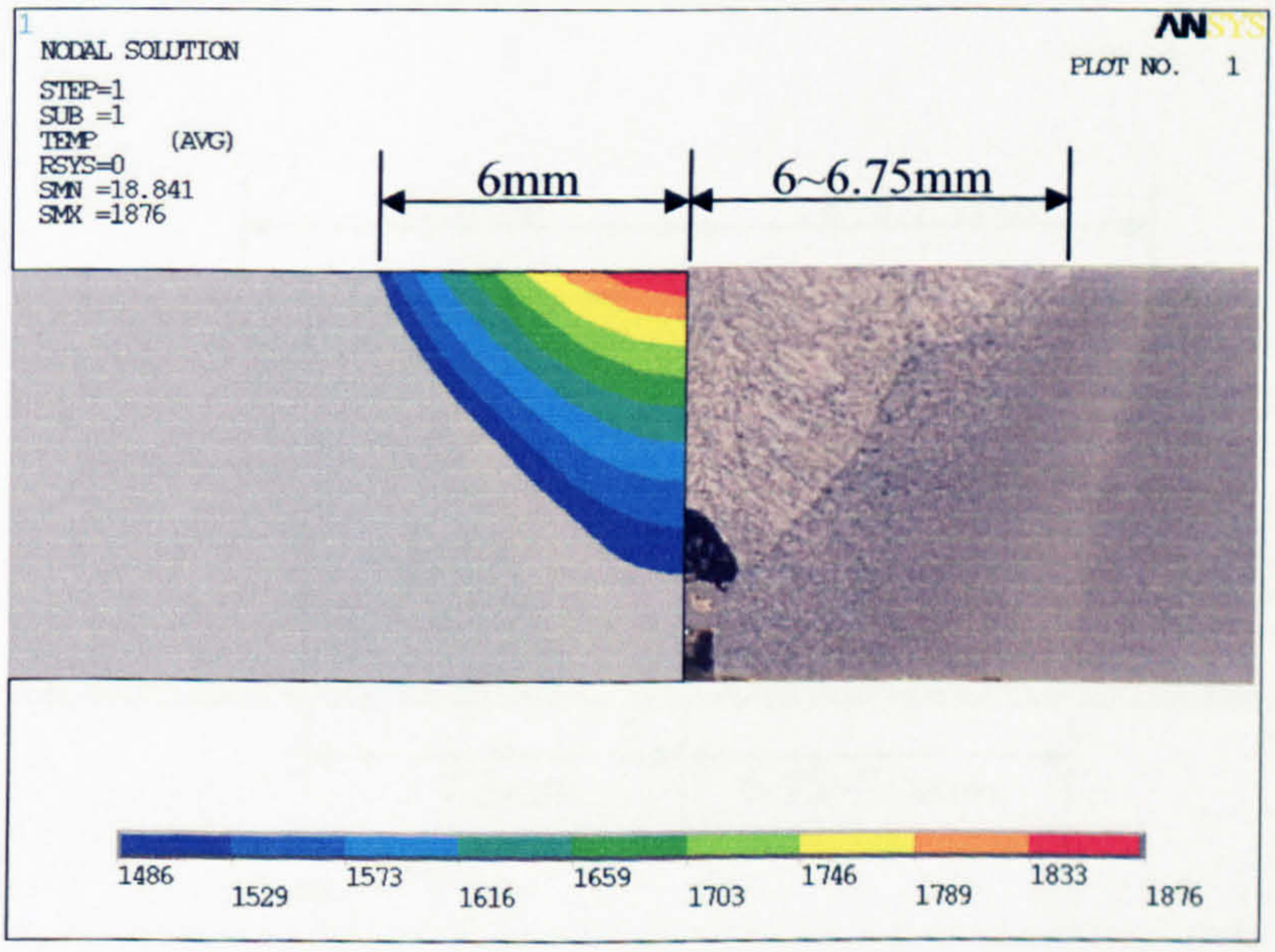

Figure 3B-TW

Simulated top weld width of model 3B

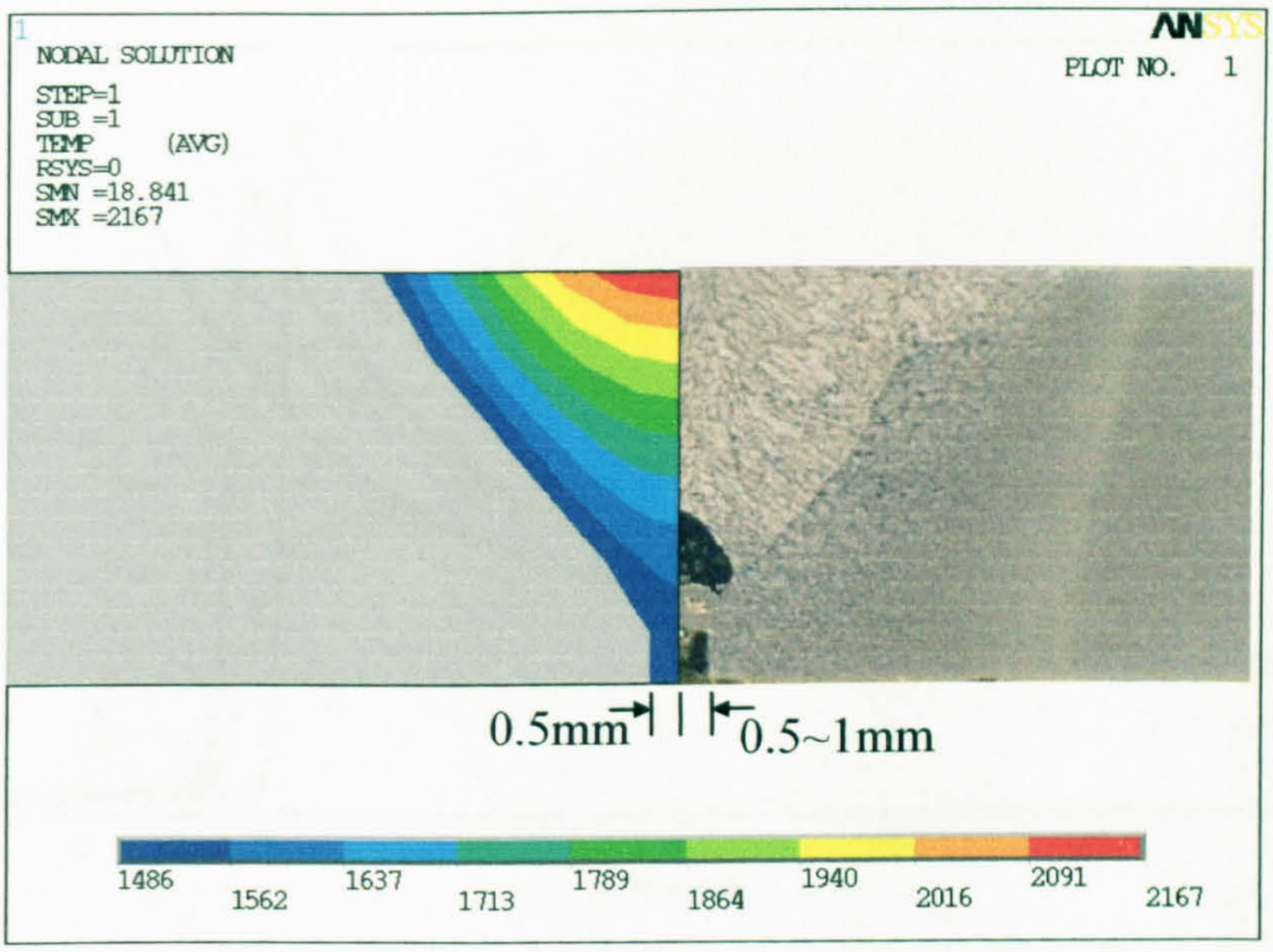

Figure 3B-BW

Simulated bottom weld width of model 3B

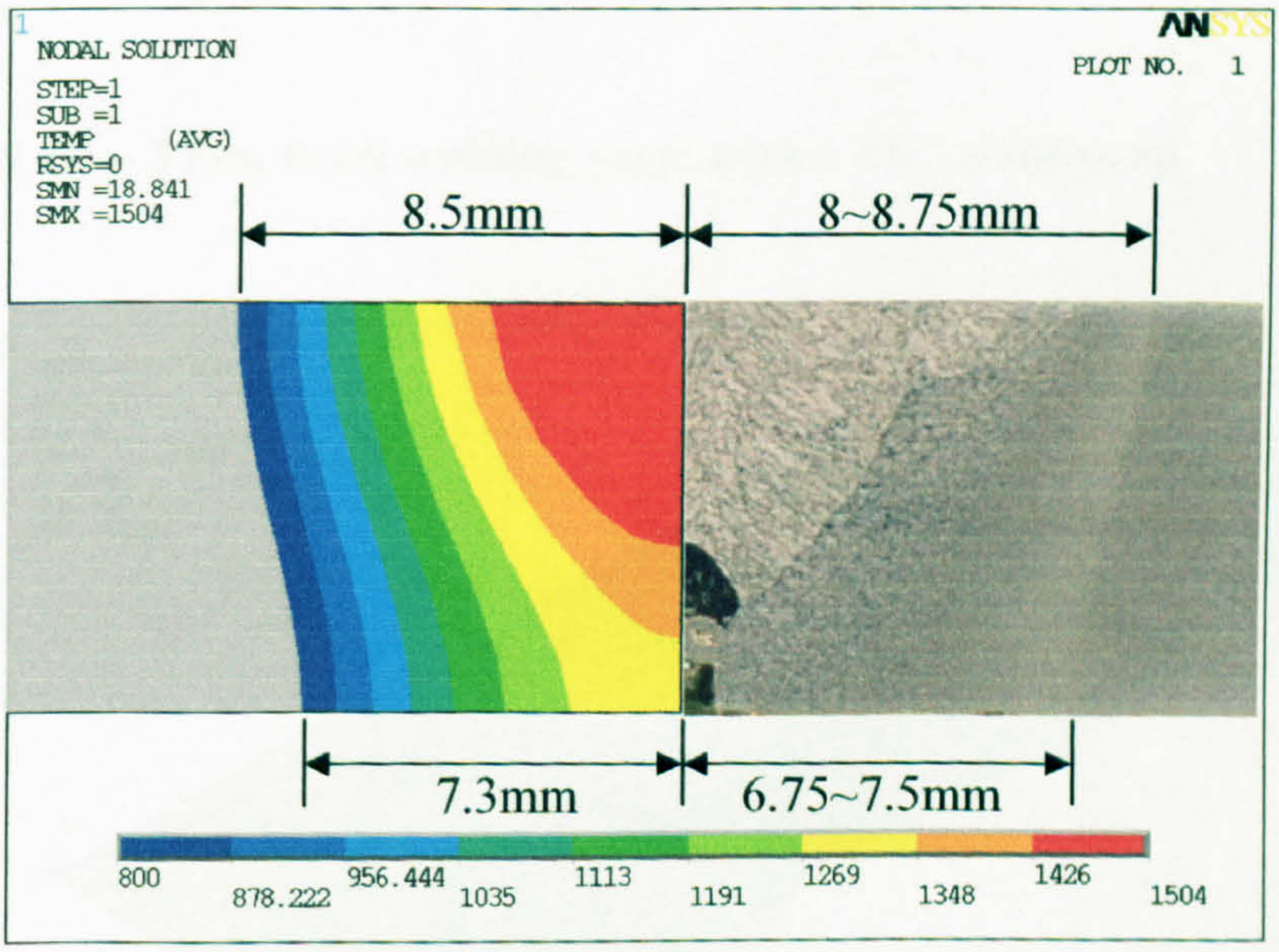

Figure 3B-H

Simulated heat affected zone of model 3B

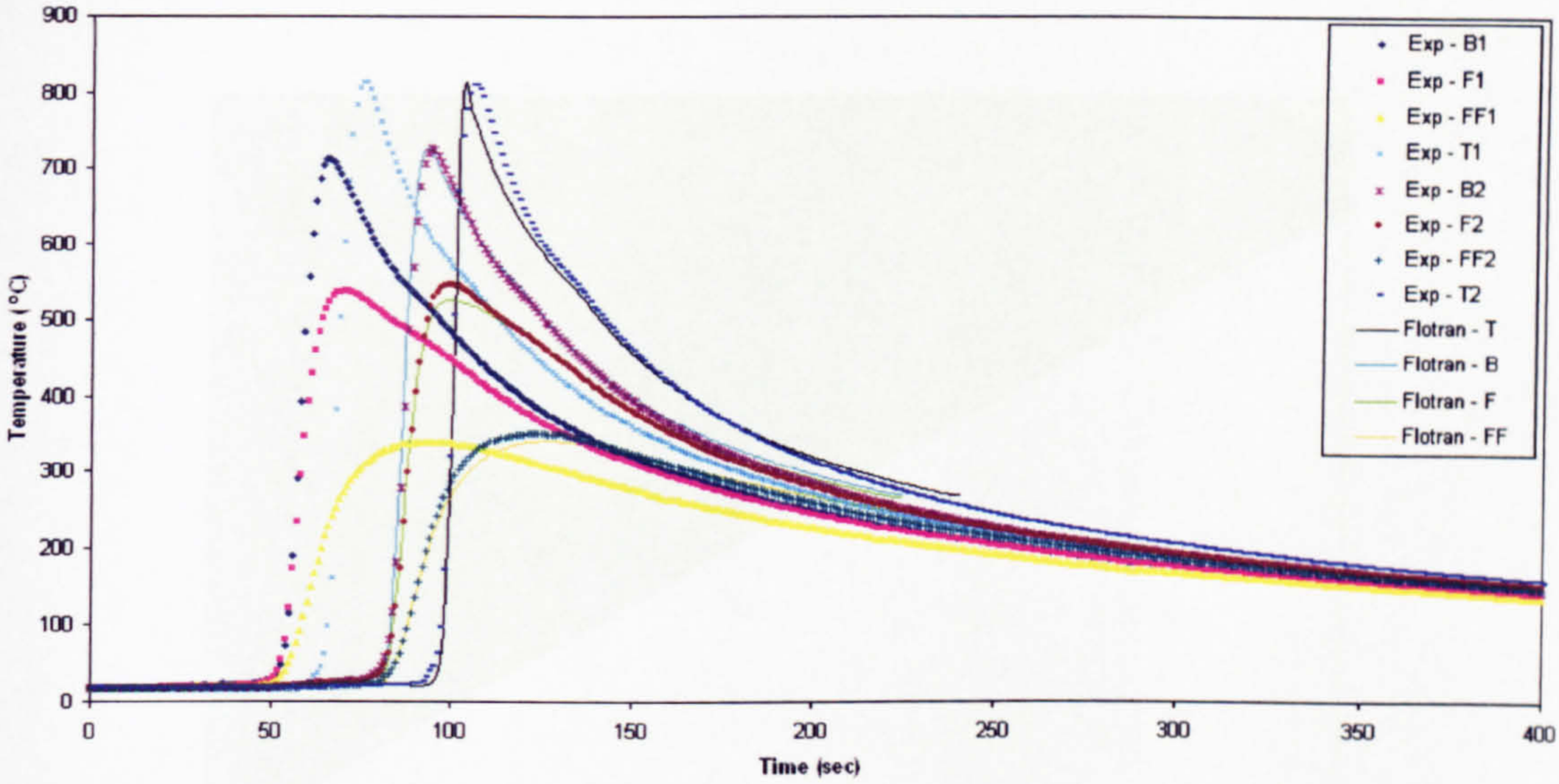

Figure 3B-TH

Comparison of the converted simulation with the measured temperature histories of model 3B

B.4 Model 4B – 3 mm thick welding plate with a "V" weld-prep

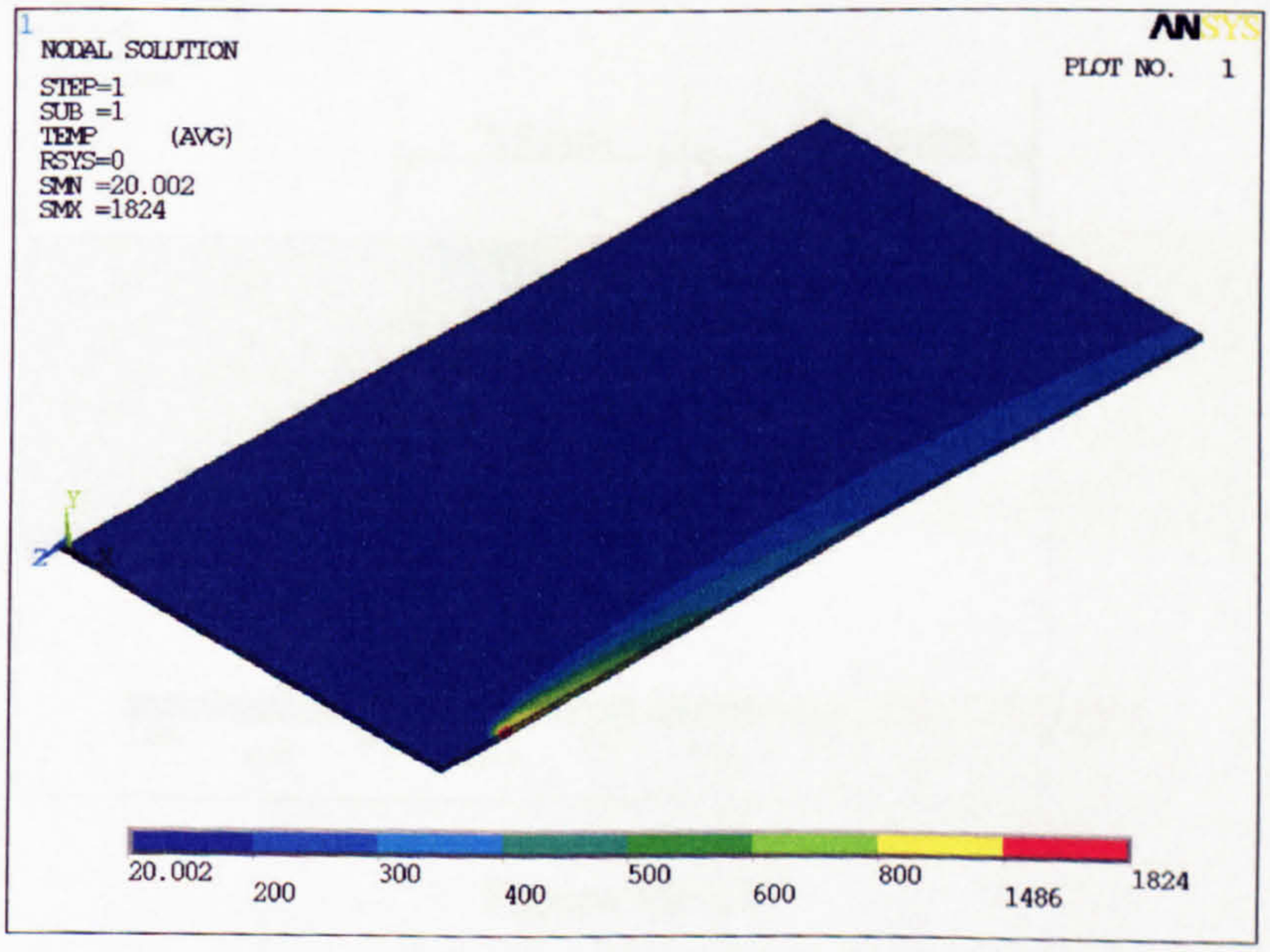

Figure 4B-O

Temperature contour of model 4B

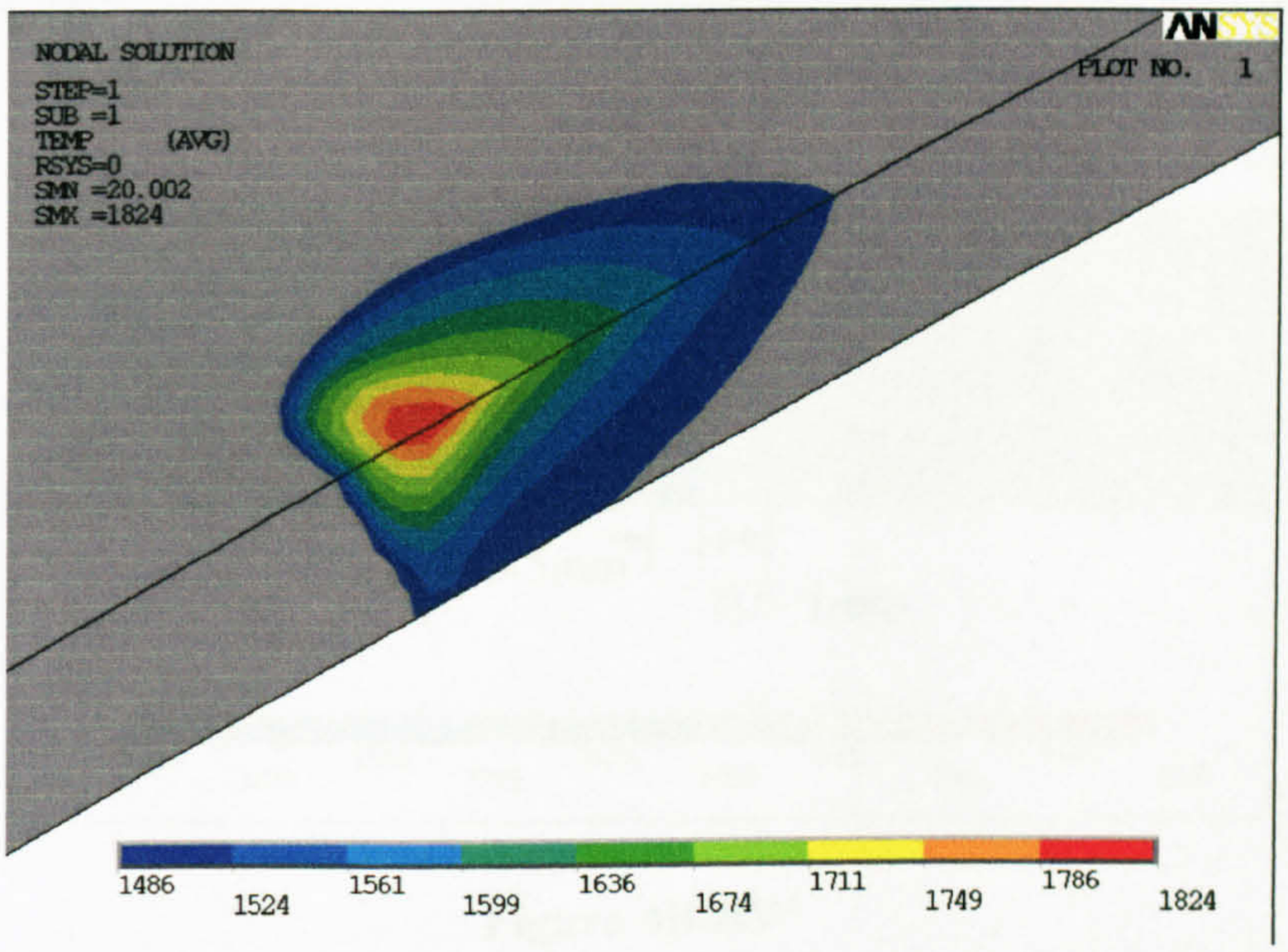

Figure 4B-P

Weld pool temperature contour of model 4B

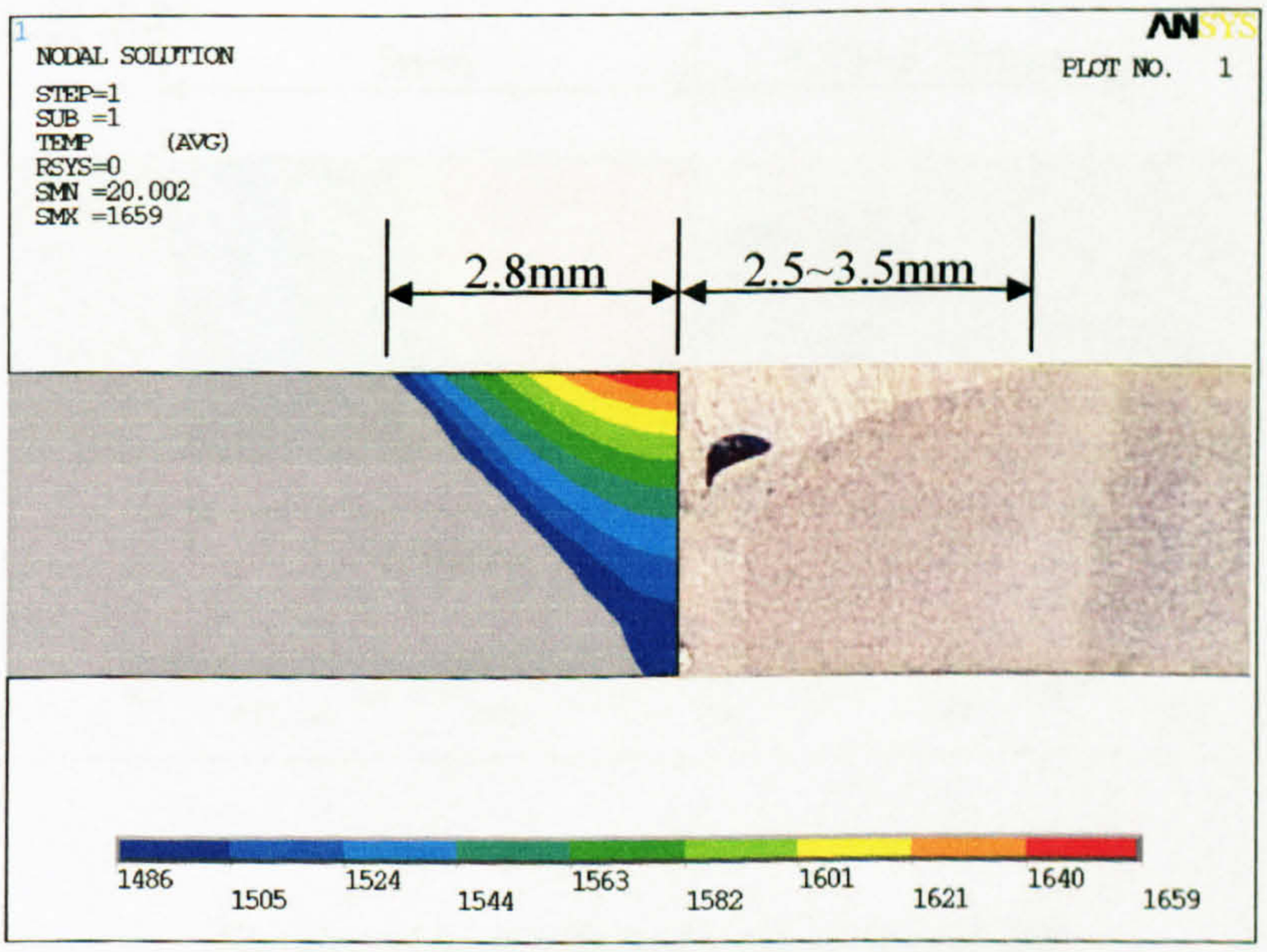

Figure 4B-TW

Simulated top weld width of model 4B

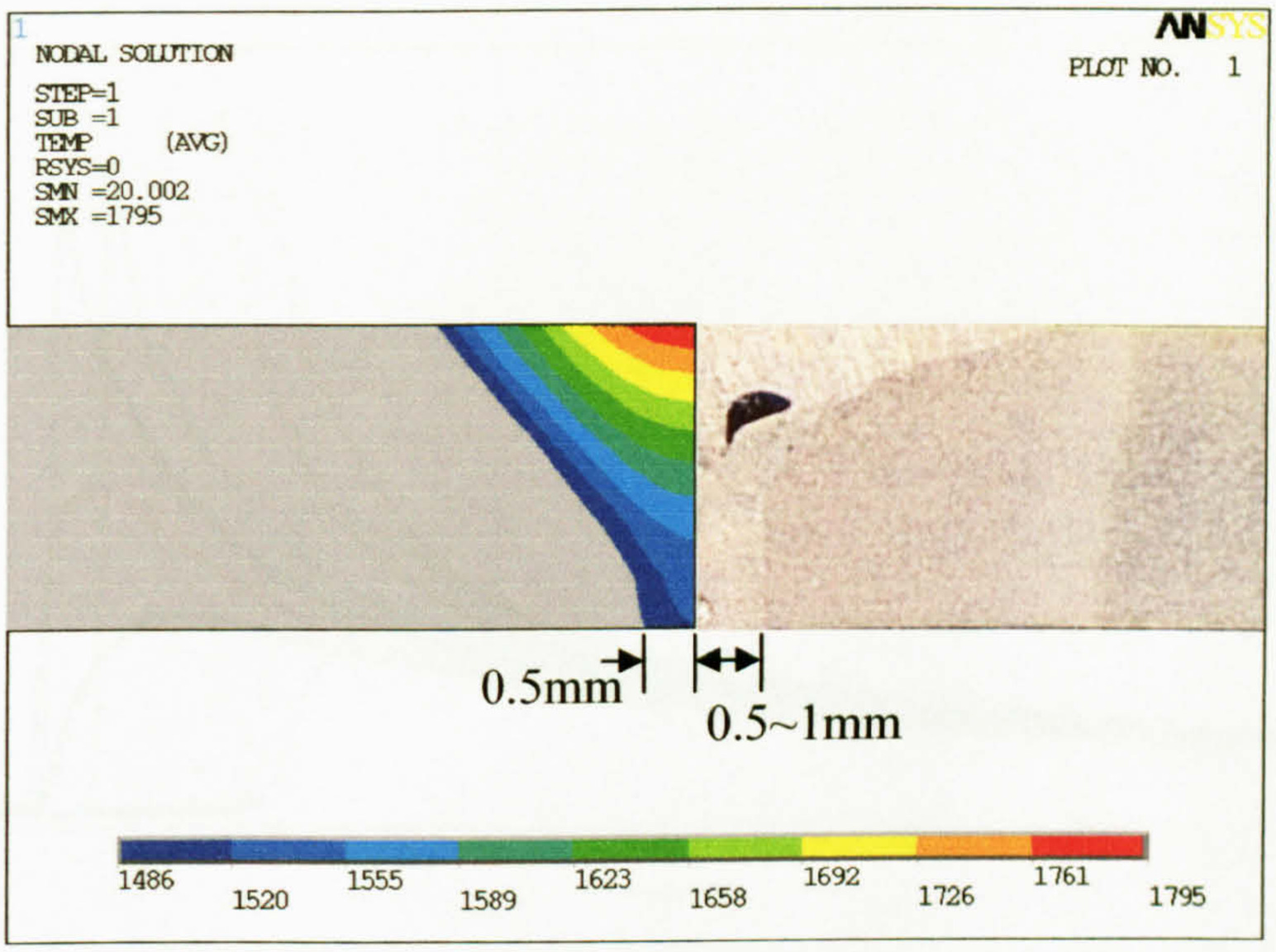

Figure 4B-BW

Simulated bottom weld width of model 4B

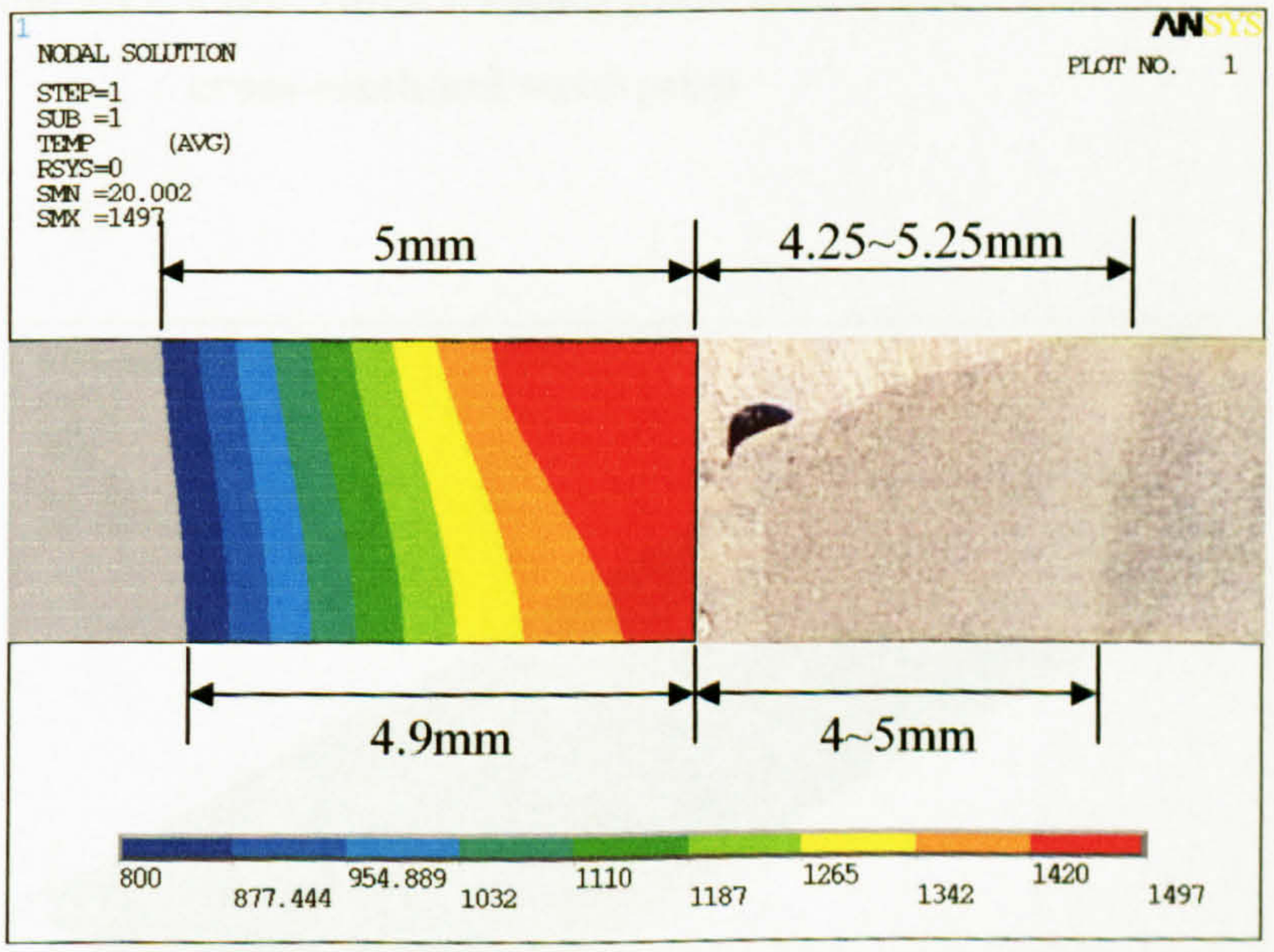

Figure 4B-H

Simulated heat affected zone of model 4B

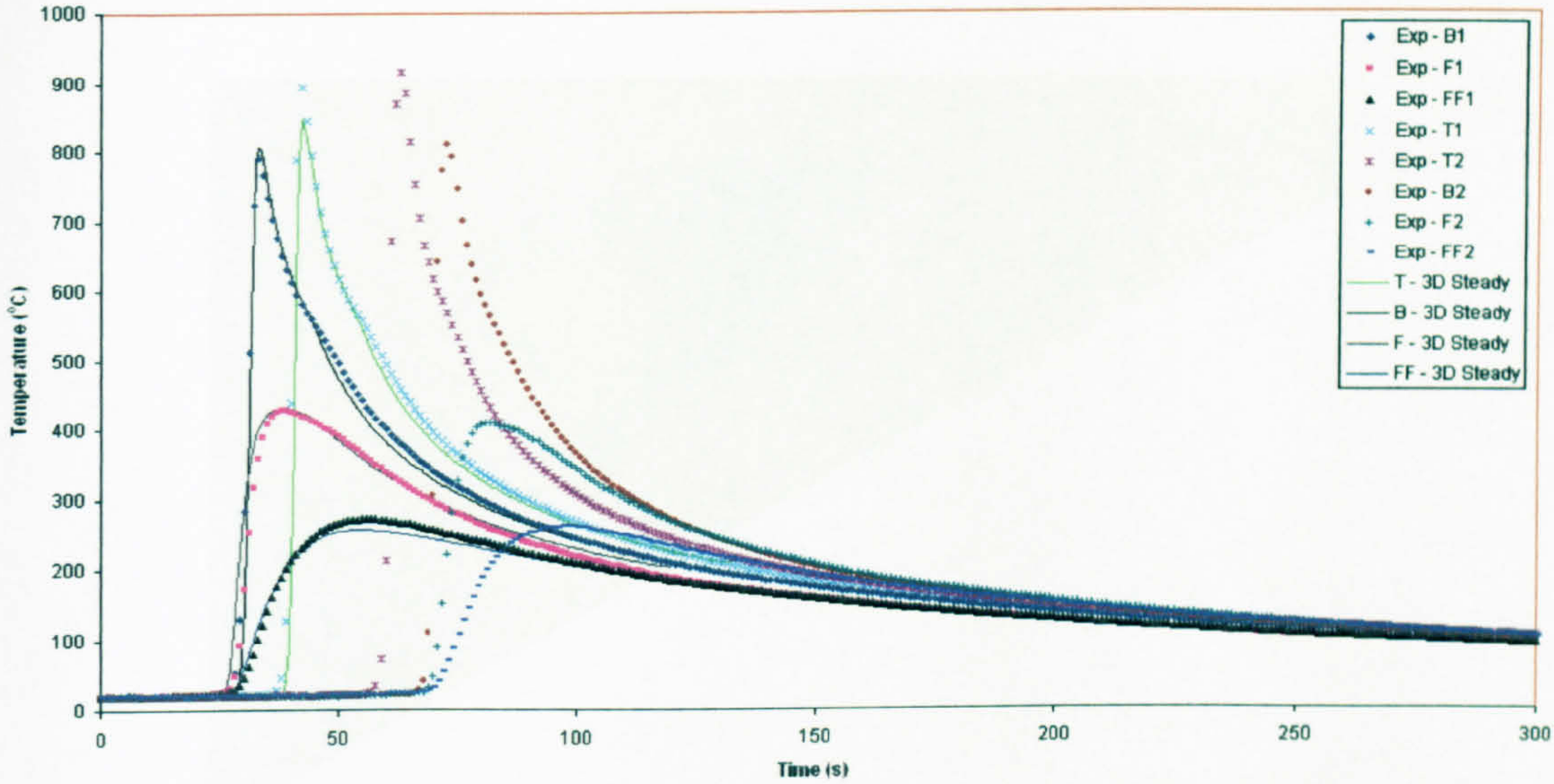

Figure 4B-TH

Comparison of the converted simulation with the measured temperature histories of model 4B

B.5 Model 5B – 6 mm thick welding plate with a semi-circle cross-sectional weld-prep

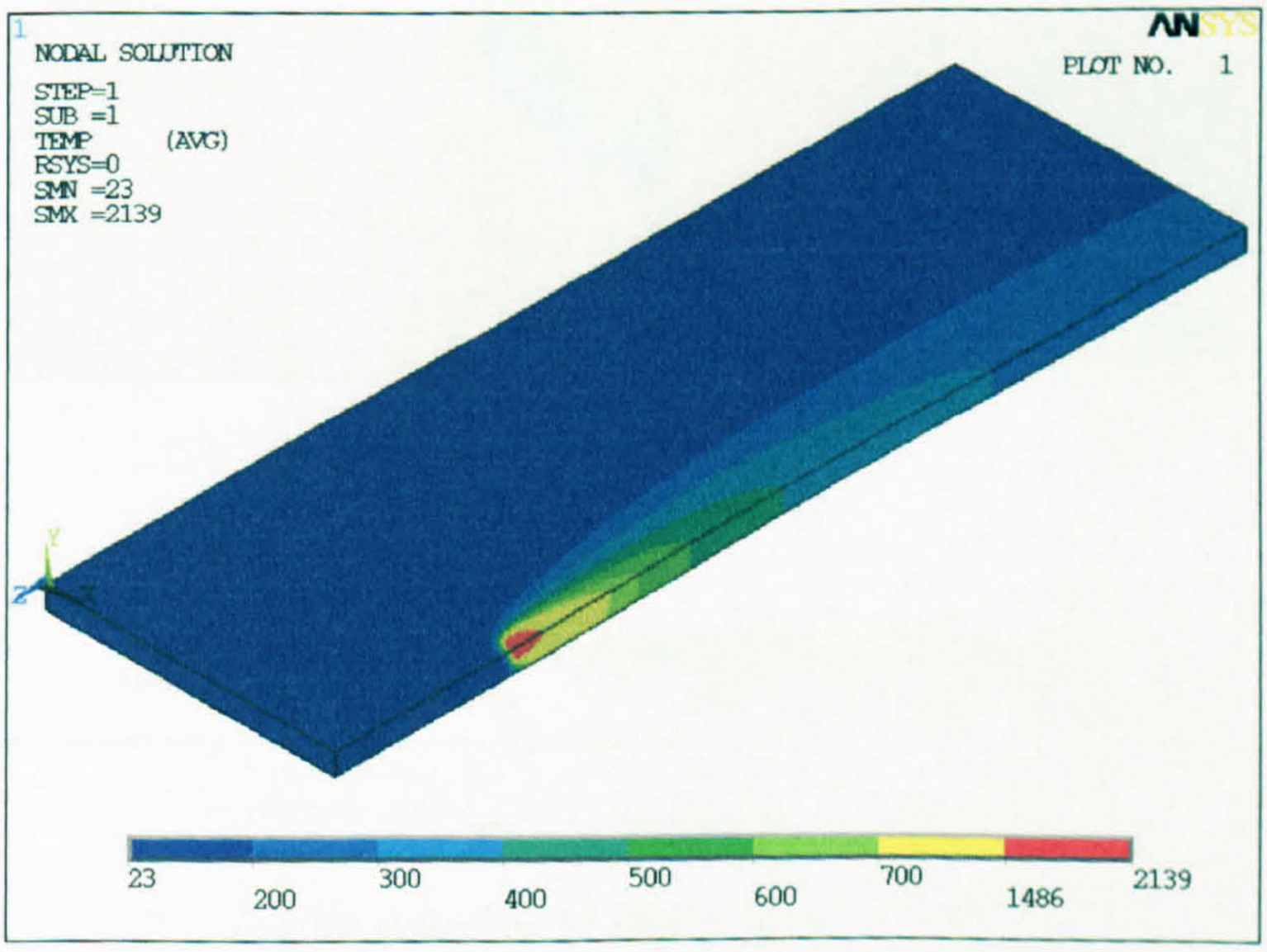

Figure 5B-O

Temperature contour of model 5B

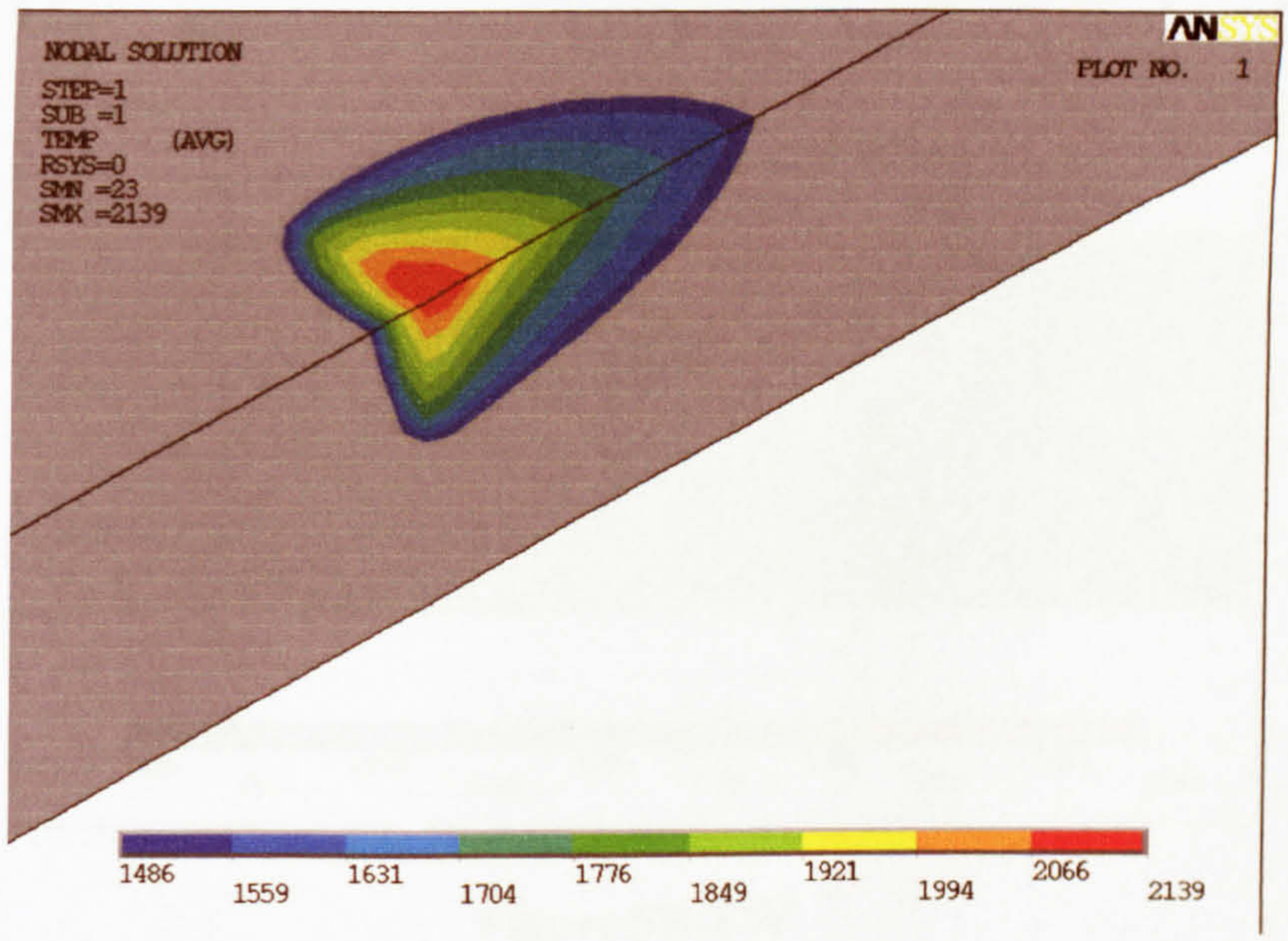

Figure 5B-P

Weld pool temperature contour of model 5B

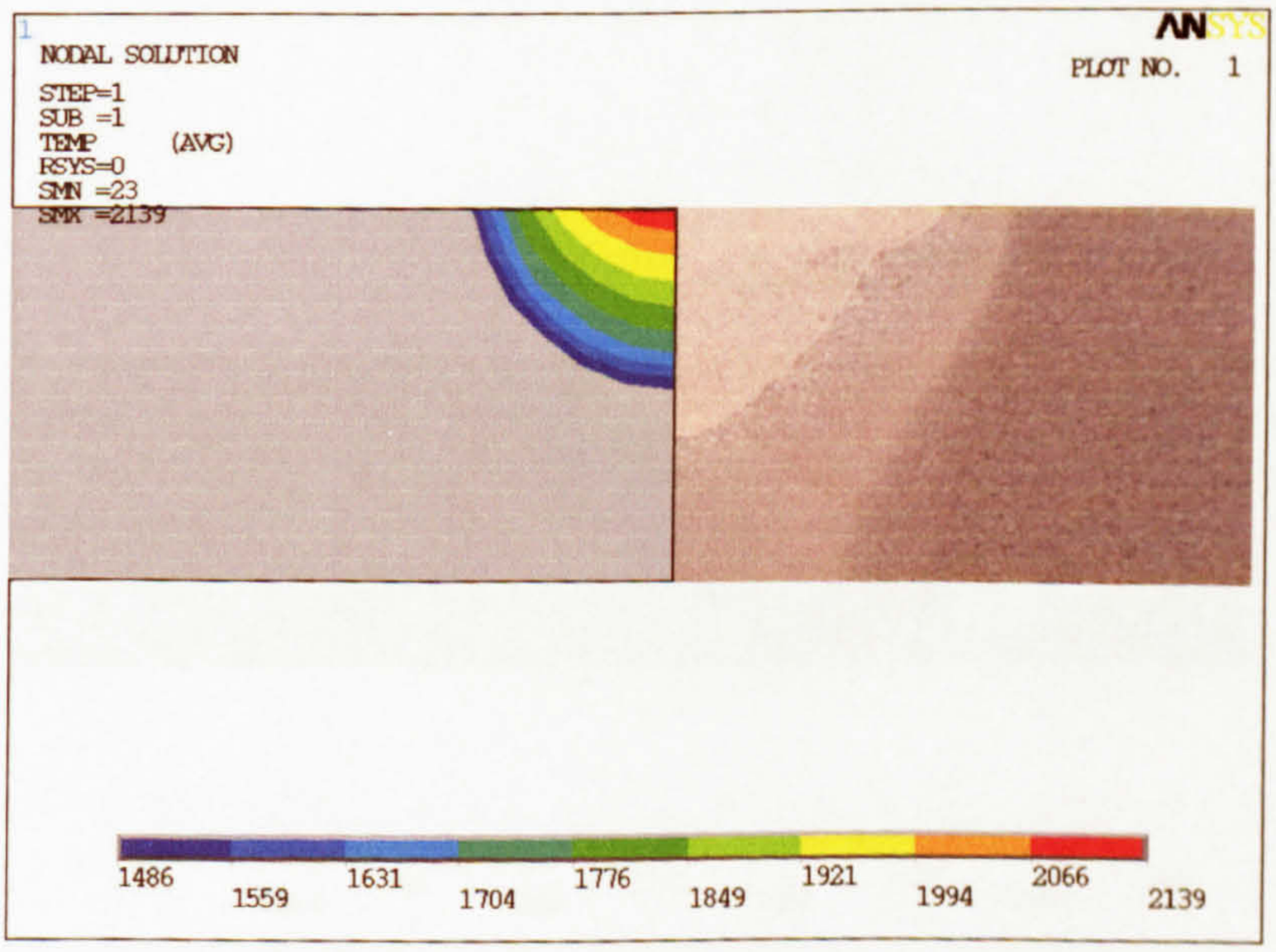

Figure 5B-WD

Simulated weld depth of model 5B

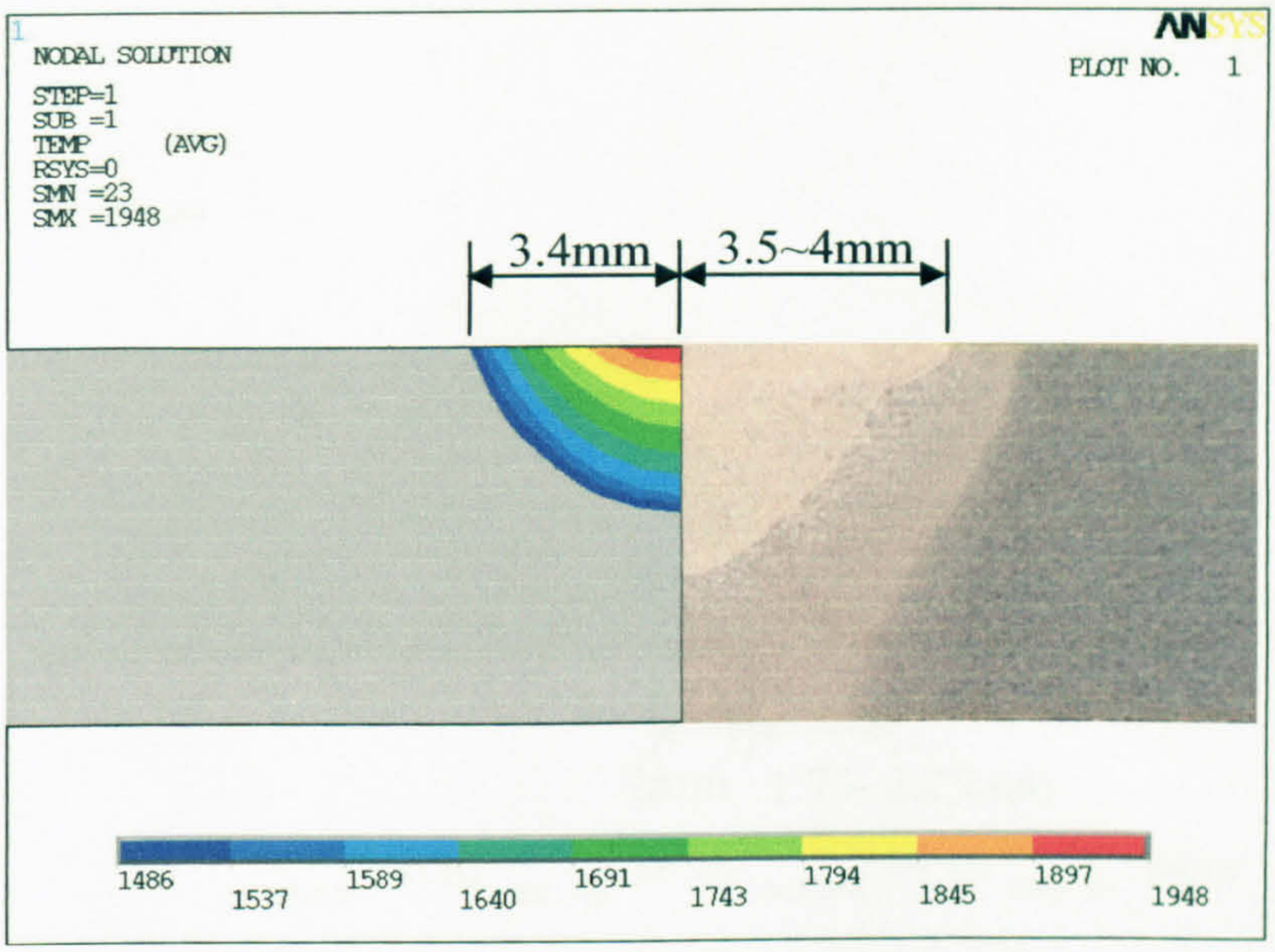

Figure 5B-TW

Simulated top weld width of model 5B

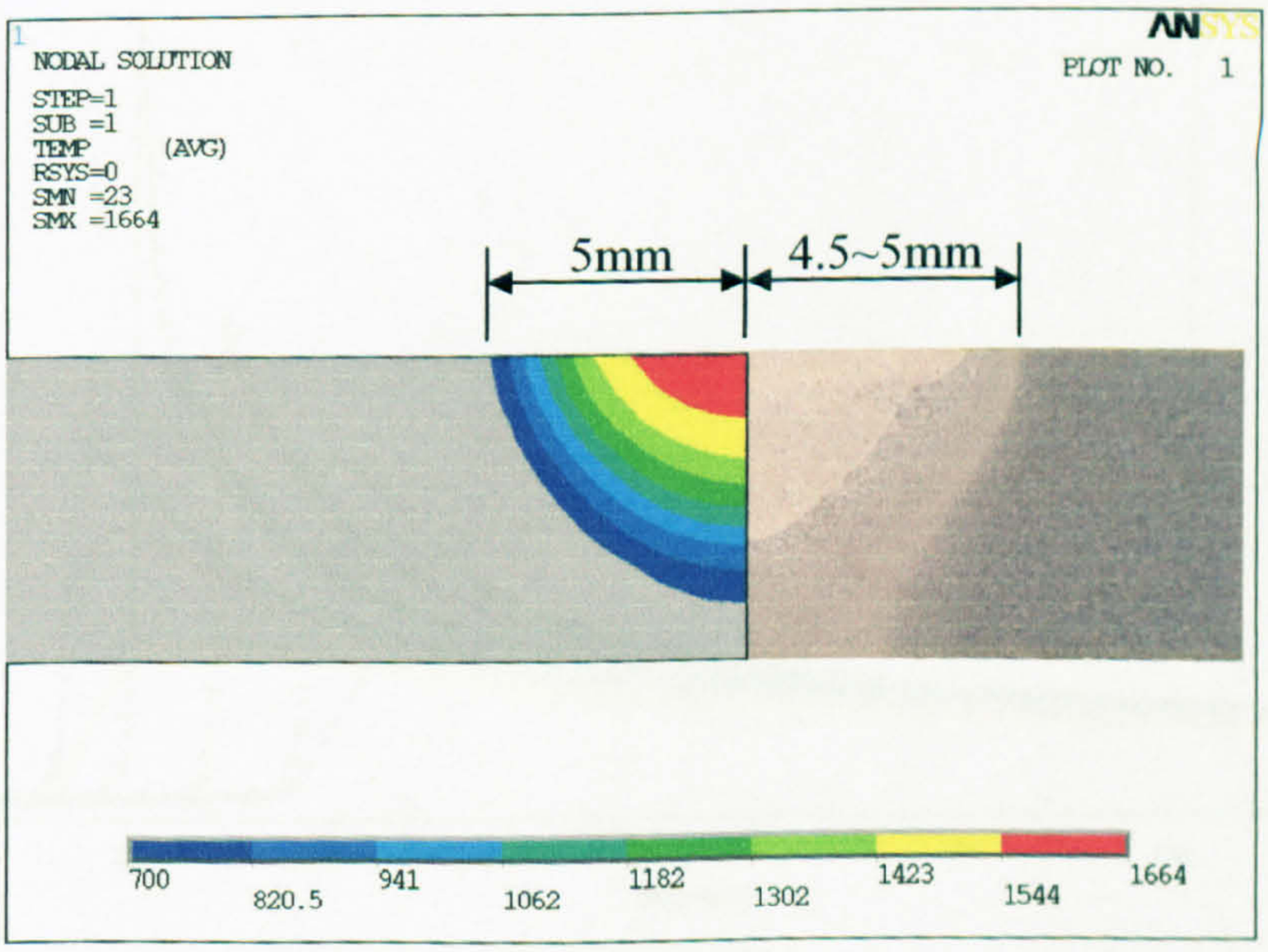

Figure 5B-HT

Simulated top heat affected zone of model 5B

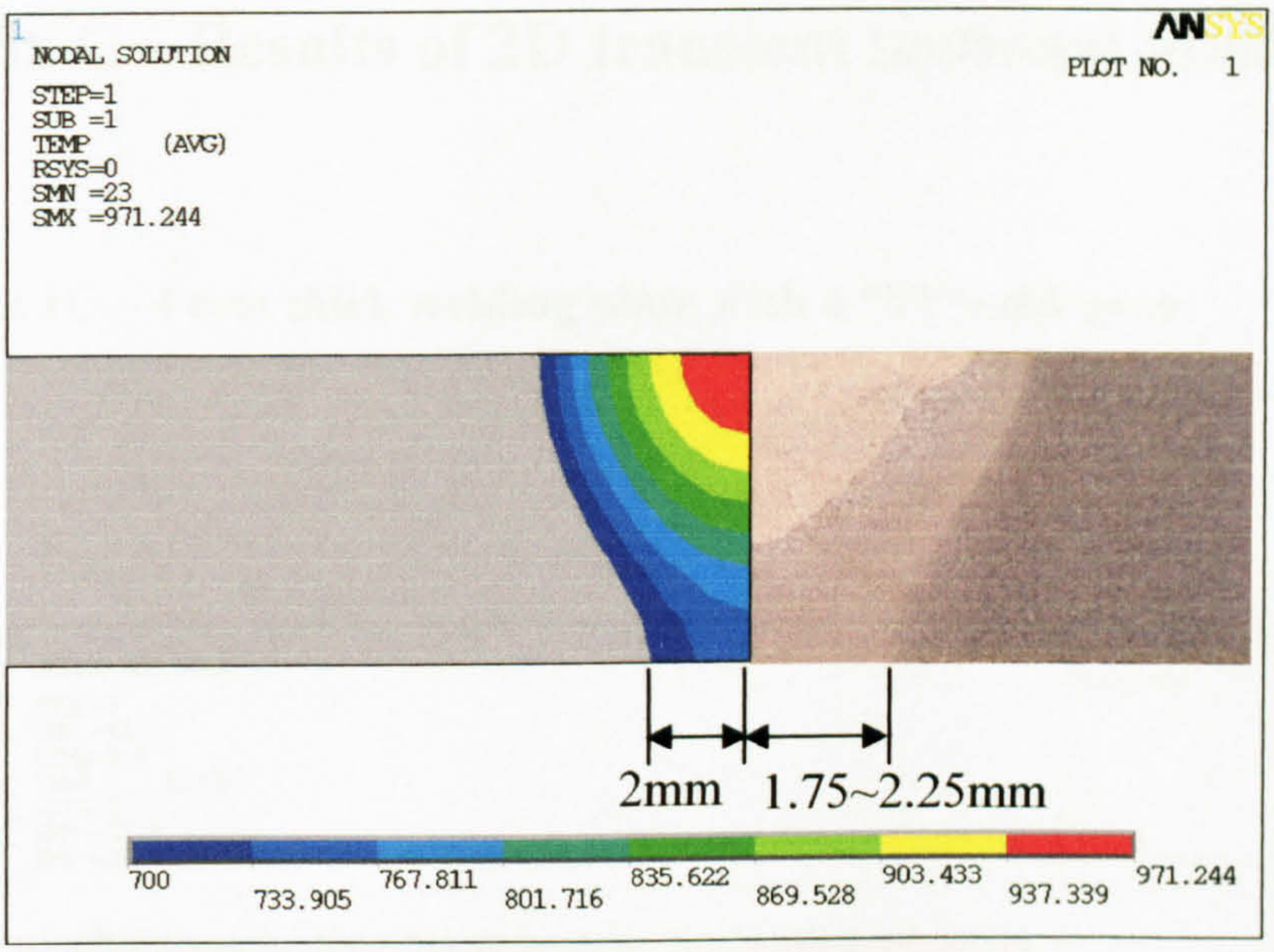

Figure 5B-HB

Simulated bottom heat affected zone of model 5B

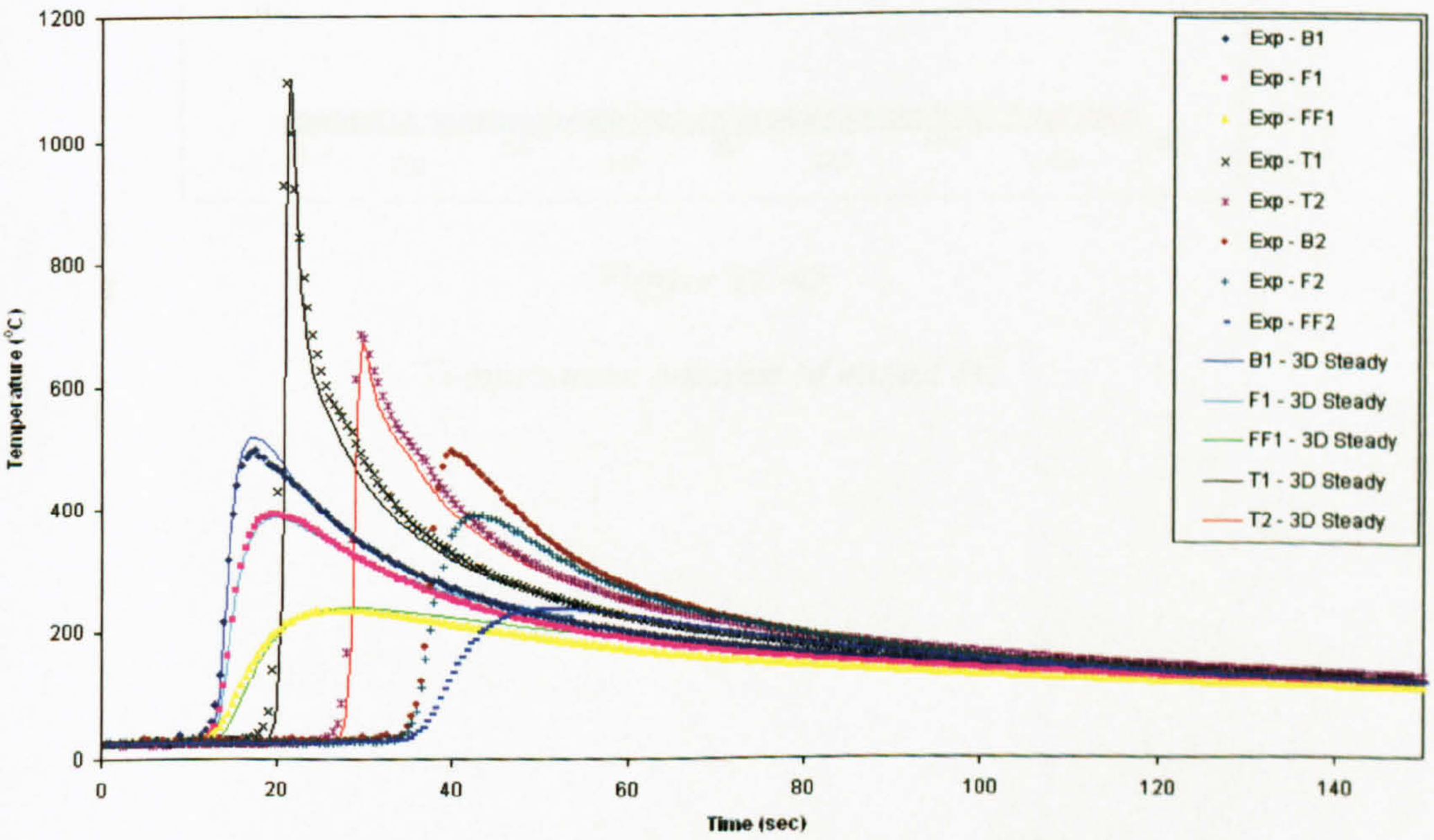

Figure 5B-TH

Comparison of the converted simulation with the measured temperature histories of model 5B

Appendix C – Results of 2D transient sectional Models

C.1 Model 1C – 4 mm thick welding plate with a "V" weld-prep

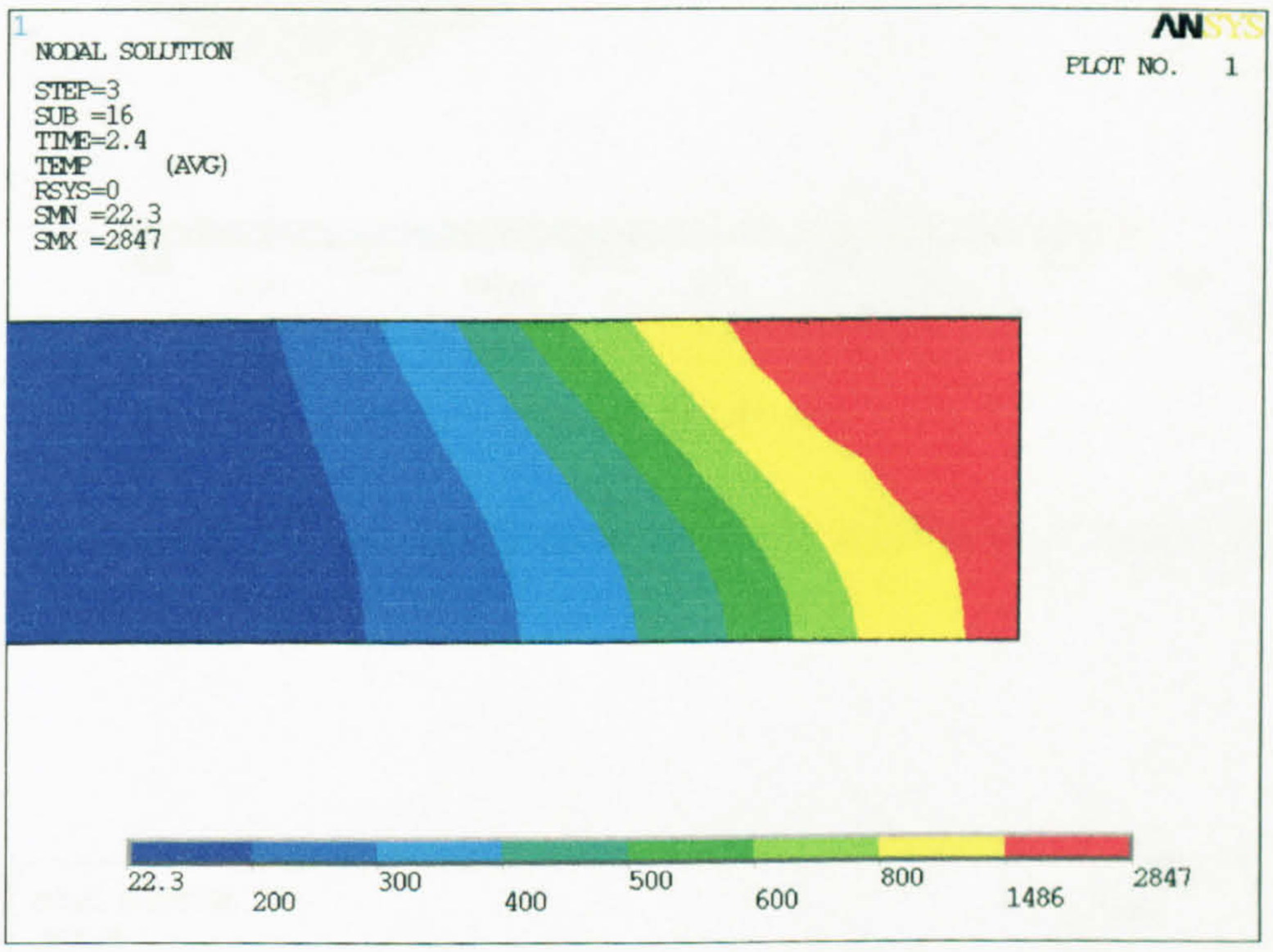

Figure 1C-O

Temperature contour of model 1C

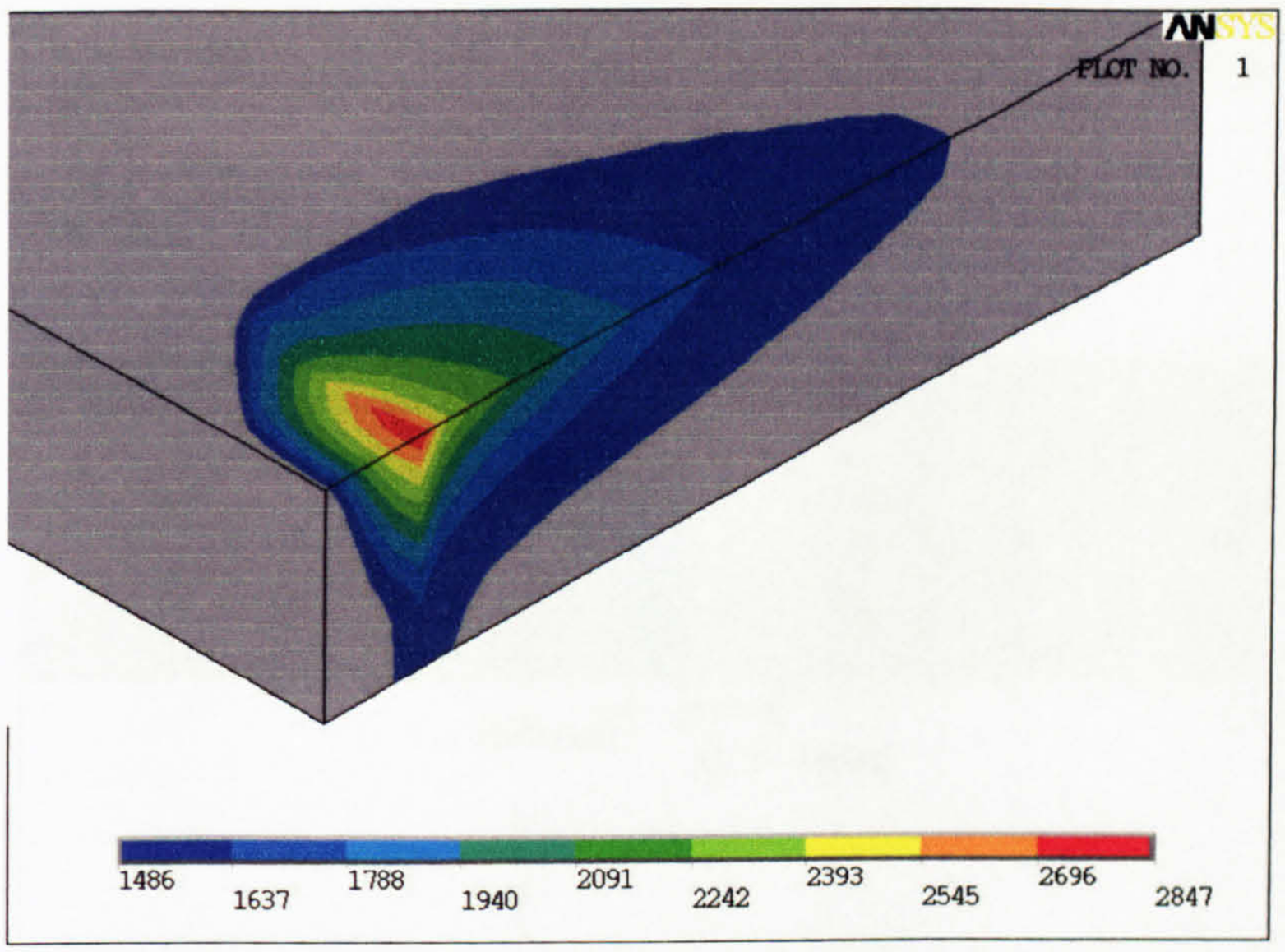

Figure 1C-P

The converted temperature contour of the weld pool of model 1C

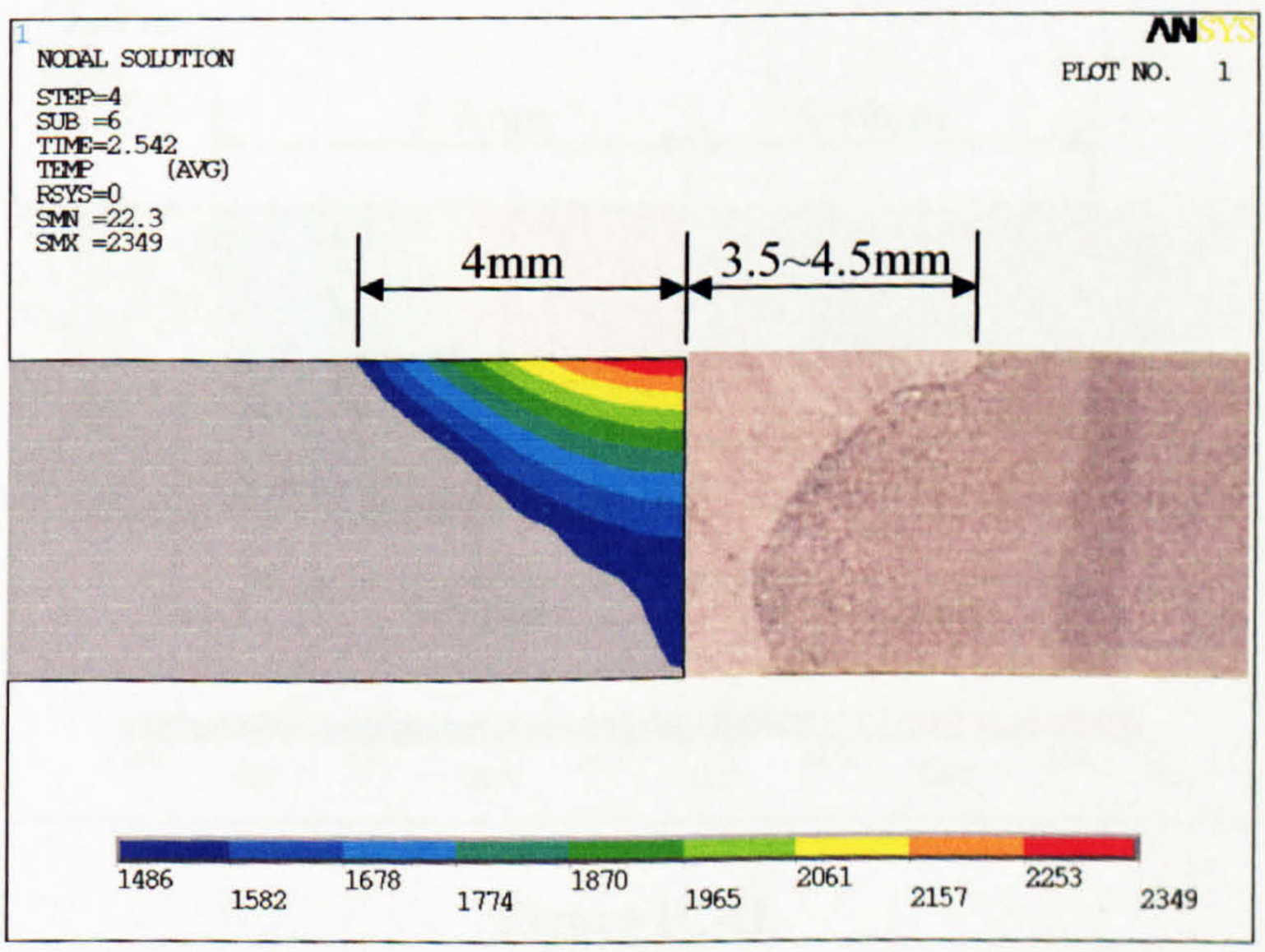

Figure 1C-TW

Simulated top weld widths of model 1C

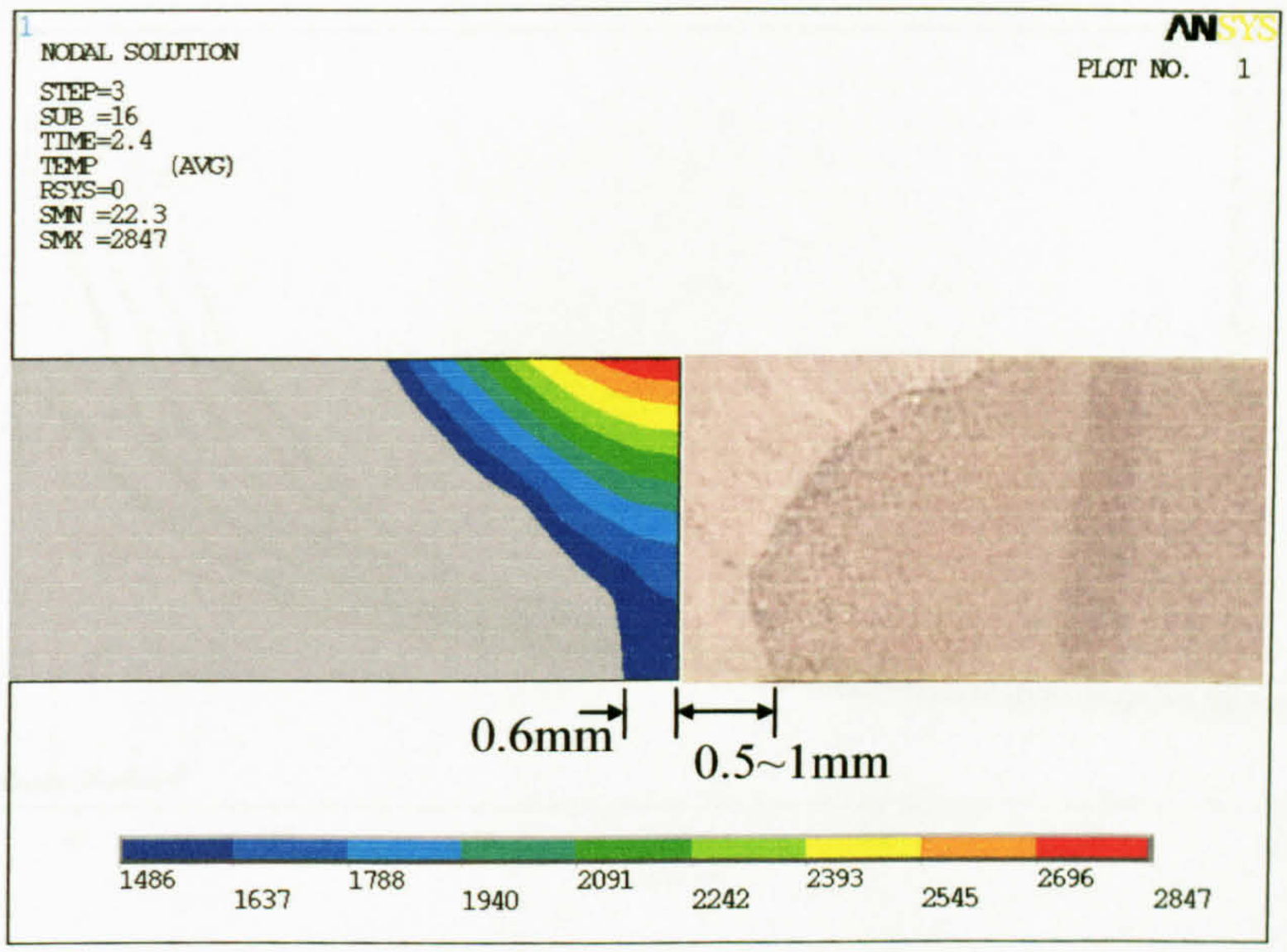

Figure 1C-BW

Simulated bottom weld widths of model 1C

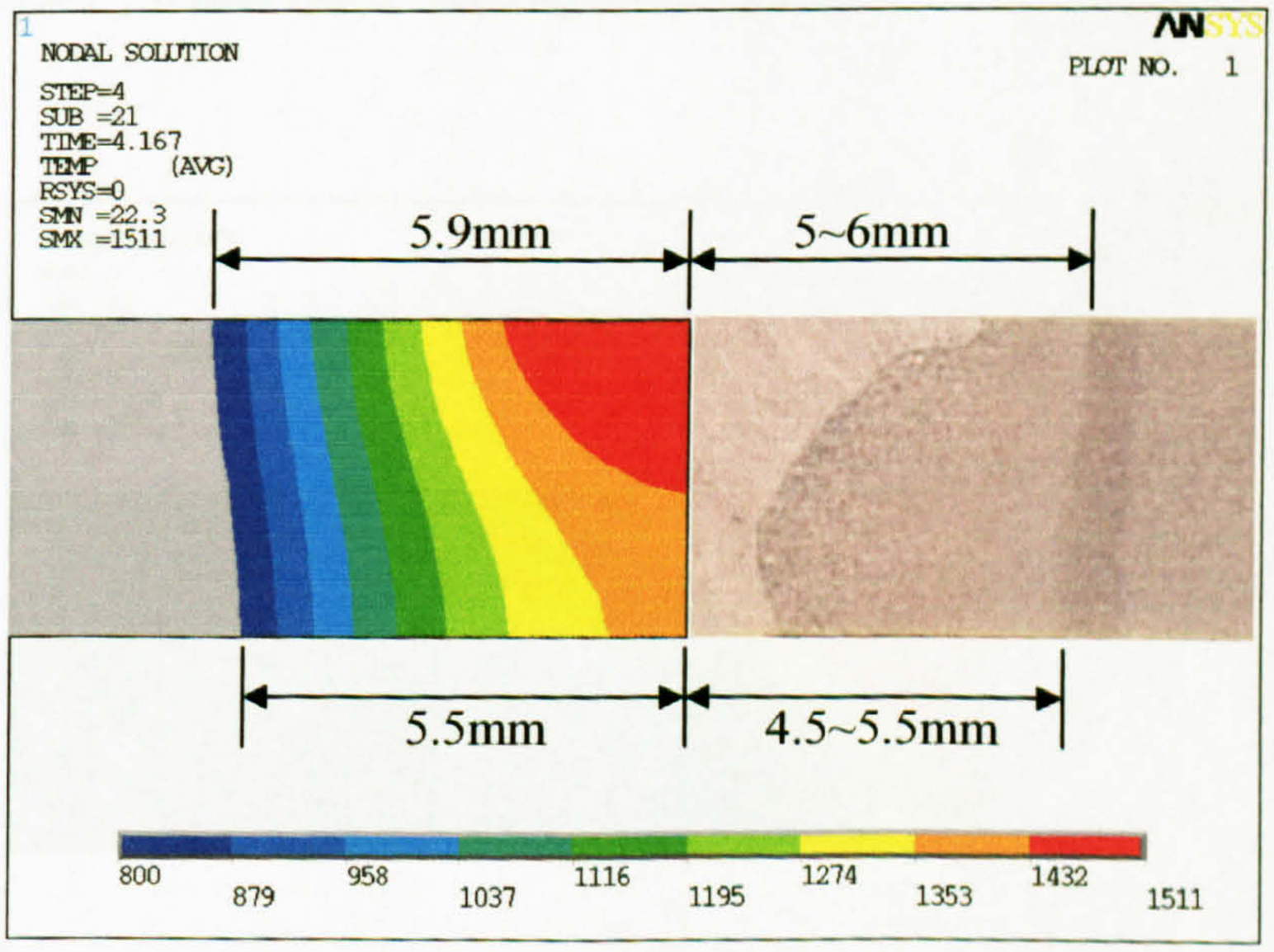

Figure 1C-H

Simulated heat affected zone of model 1C

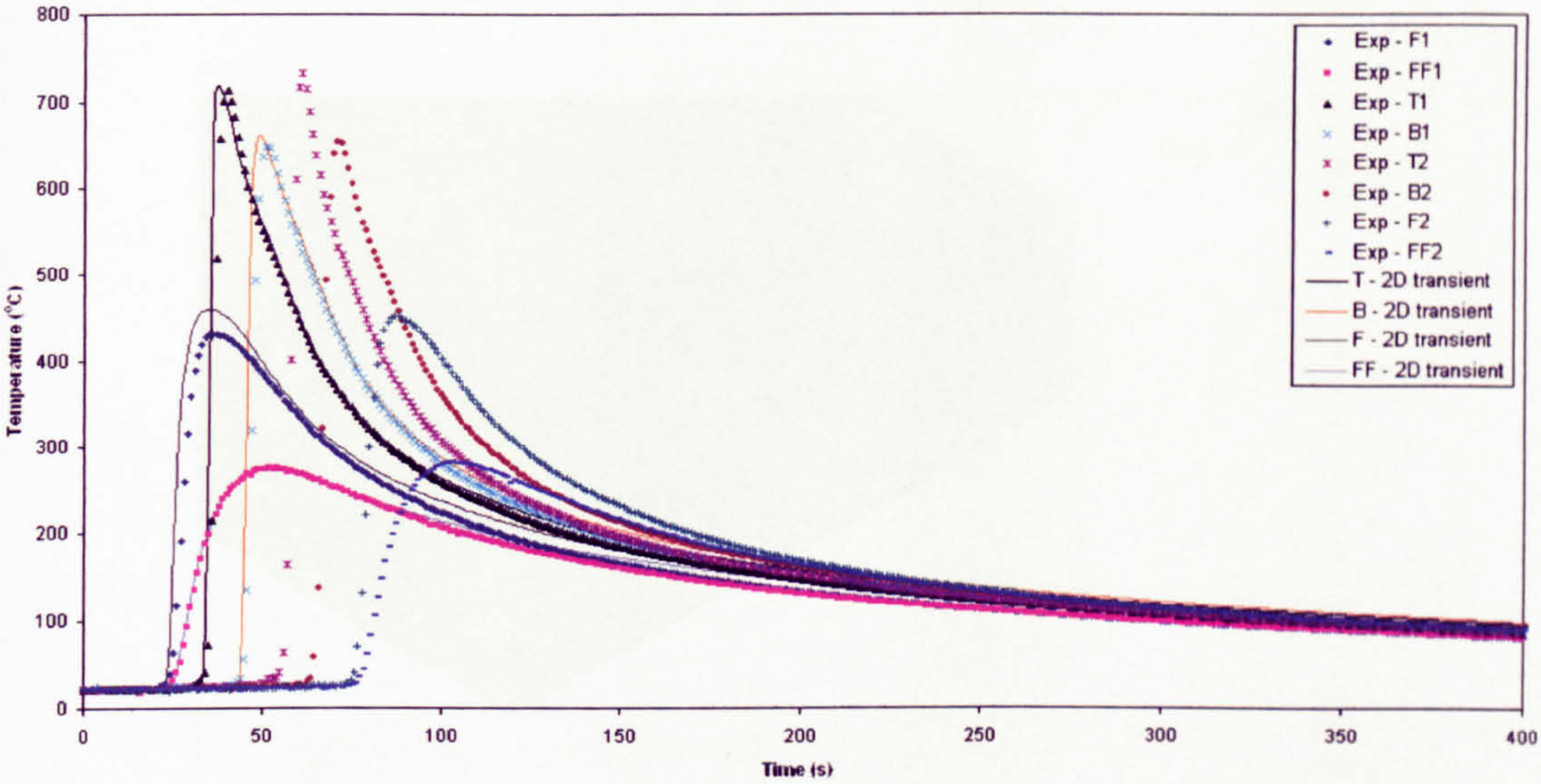

Figure 1C-TH

Comparison of the simulation temperature histories of model 1C with the measured

C.2 Model 2C – 6 mm thick welding plate with a "V" weld-prep

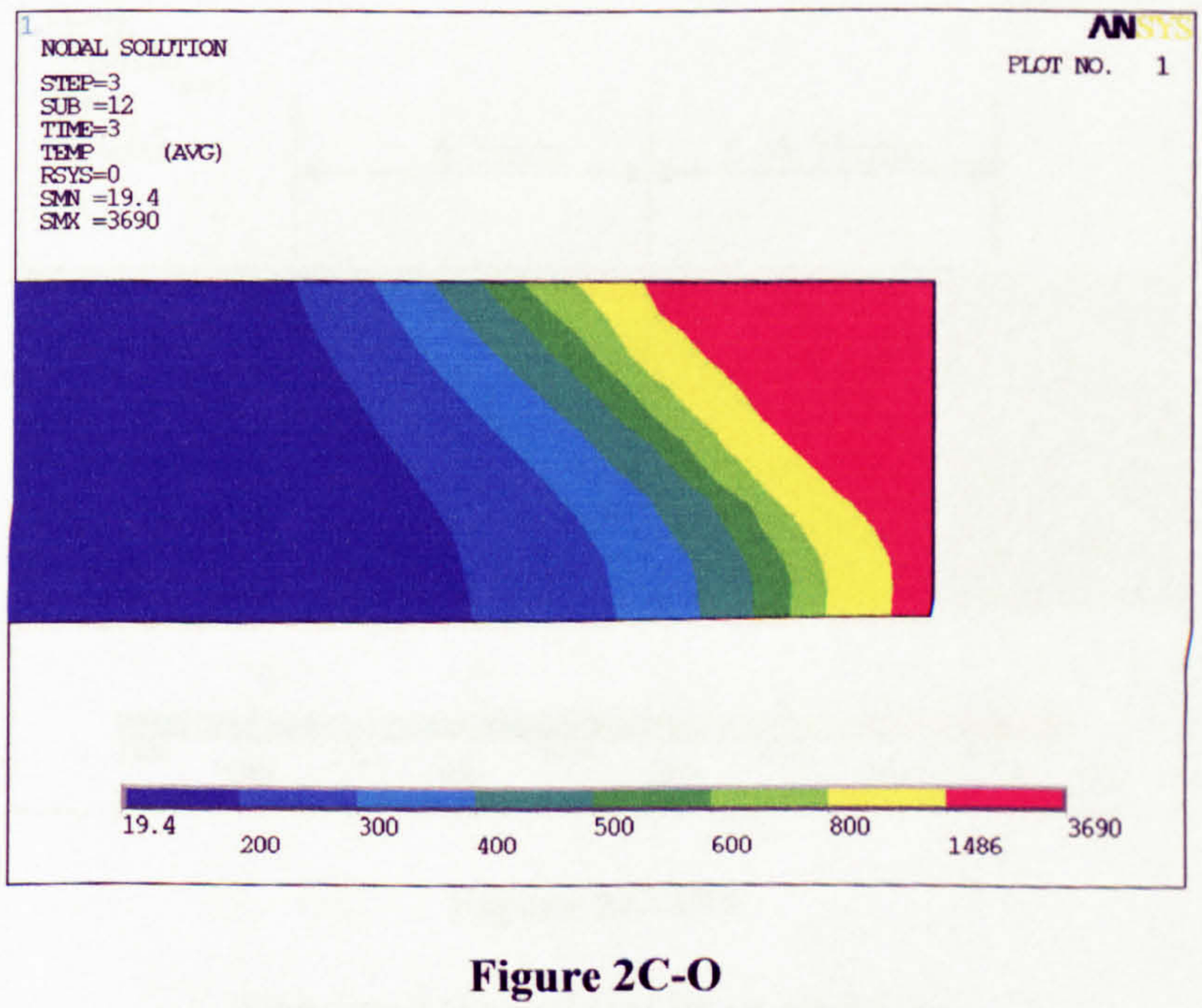

Figure 2C-O

Temperature contour of model 2C

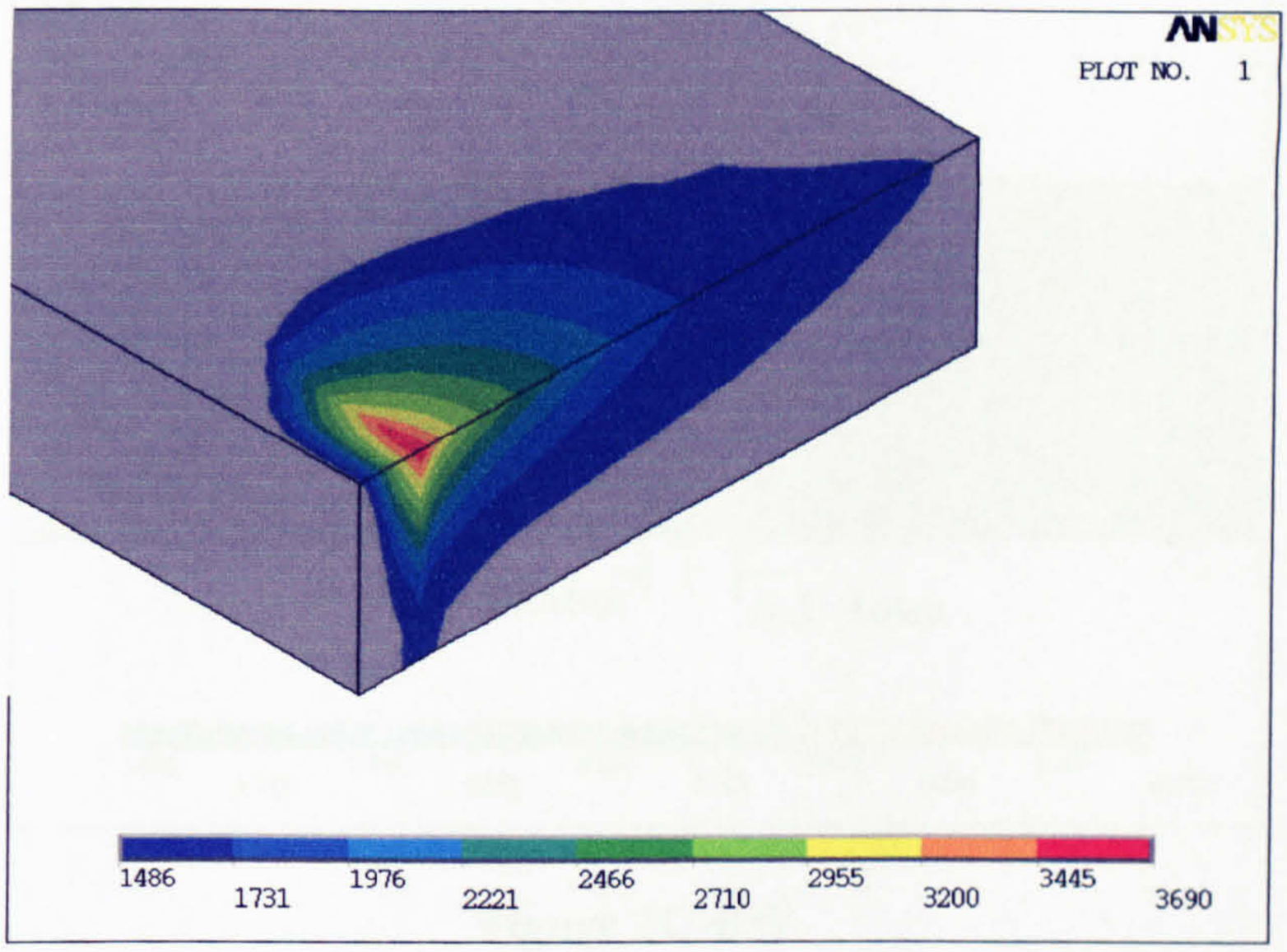

Figure 2C-P

The converted temperature contour of the weld pool of model 2C

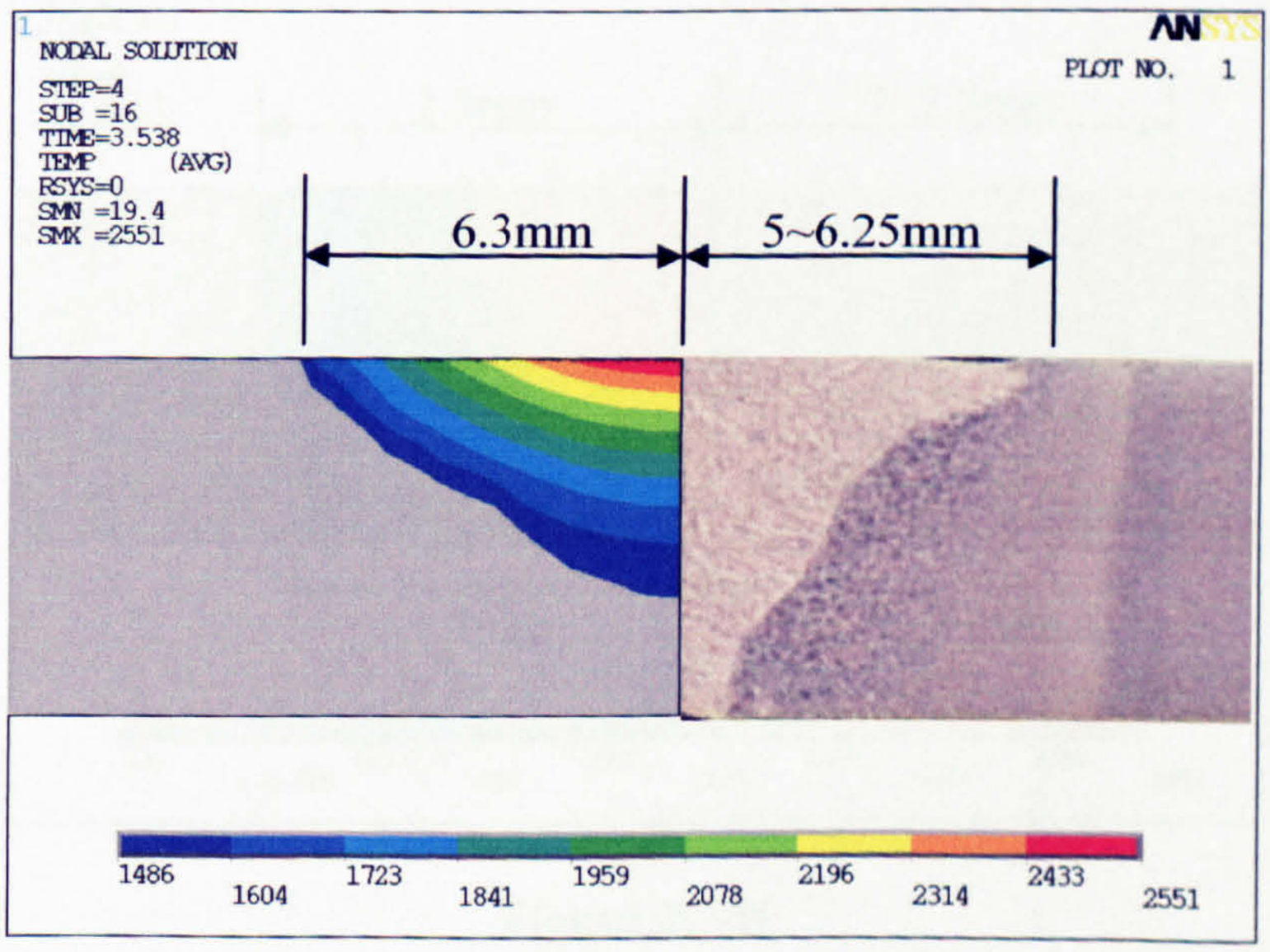

Figure 2C-TW

Simulated top weld width of model 2C

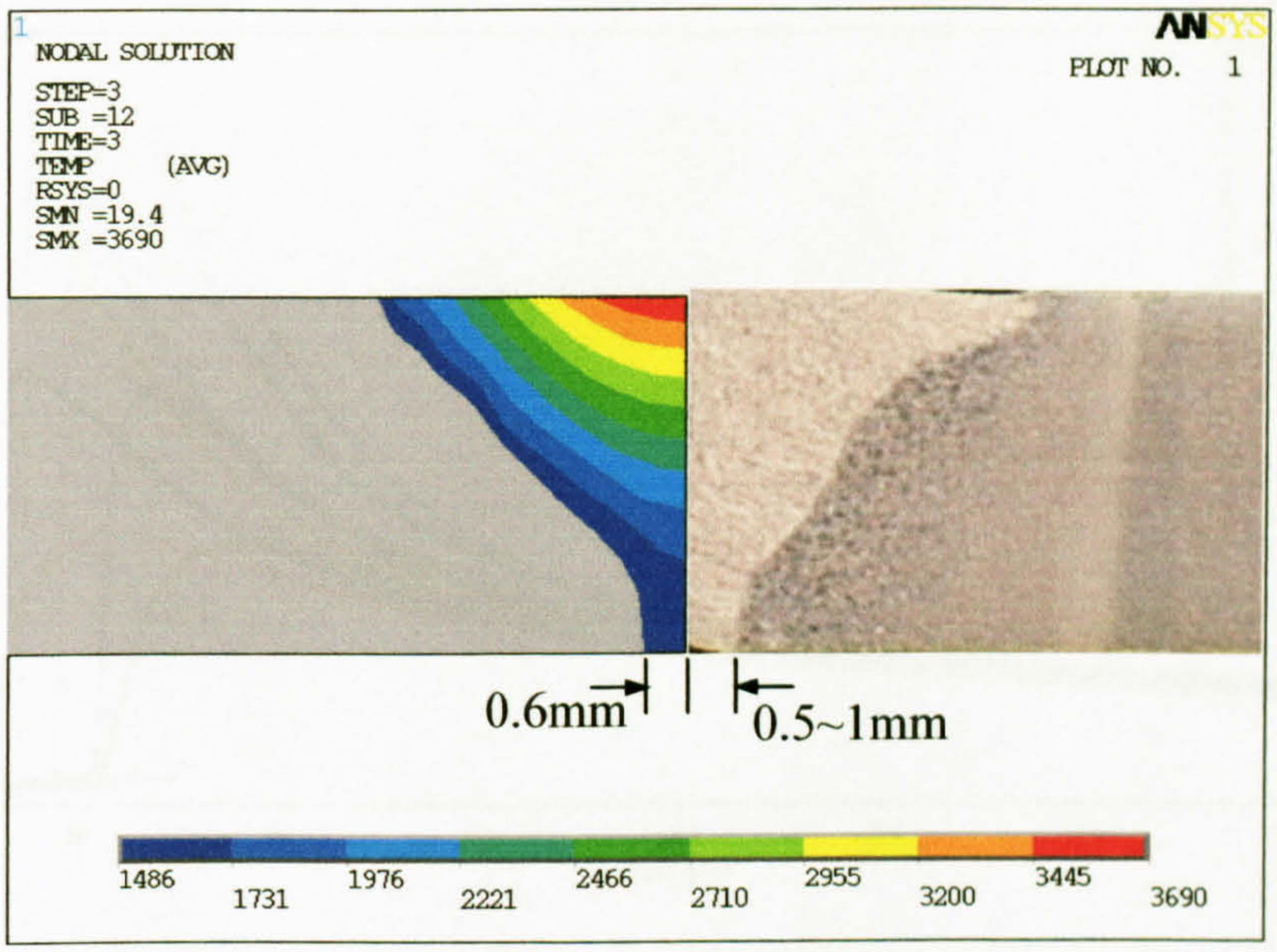

Figure 2C-BW

Simulated bottom weld width of model 2C

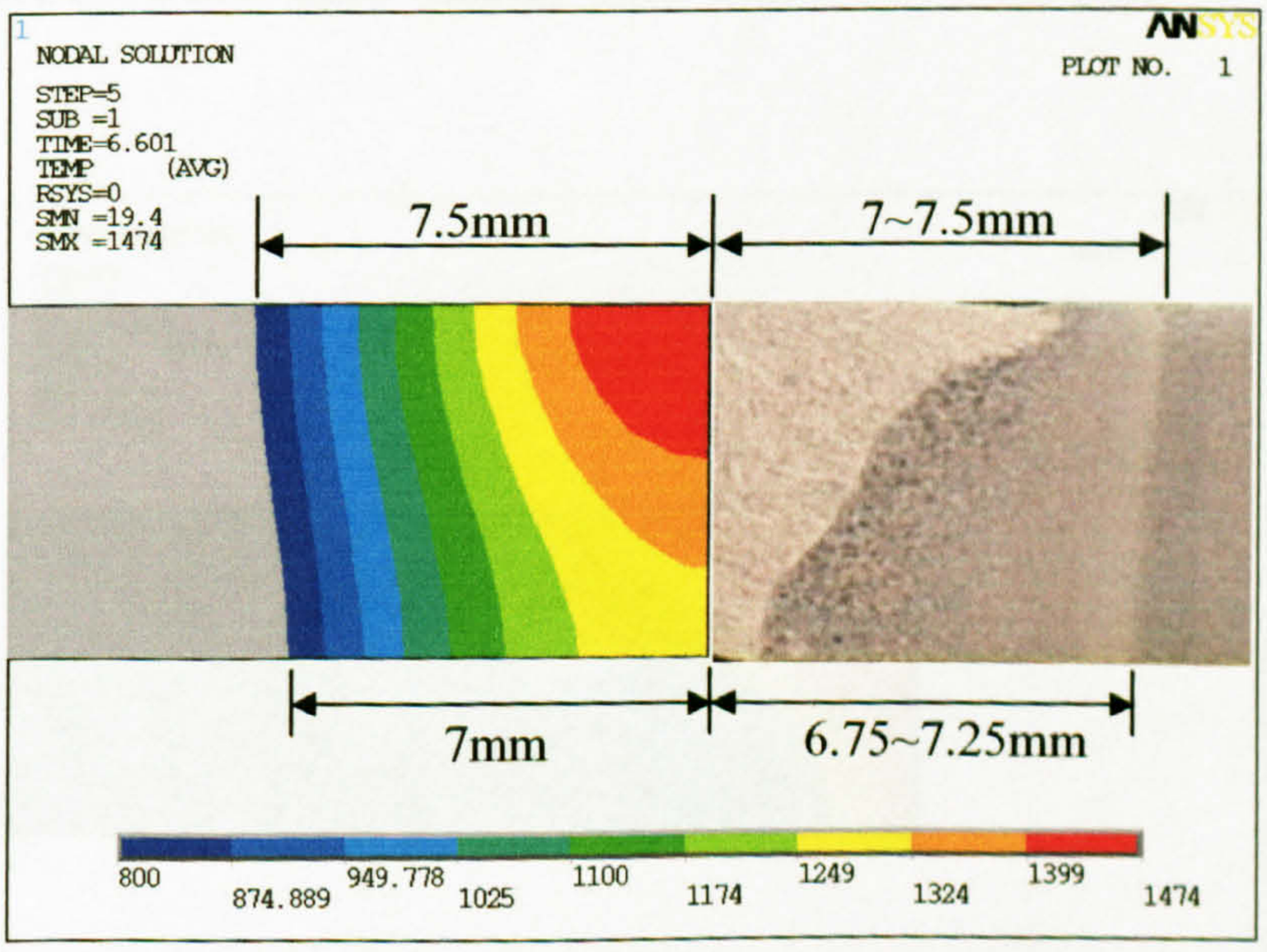

Figure 2C-H

Simulated heat affected zone of model 2C

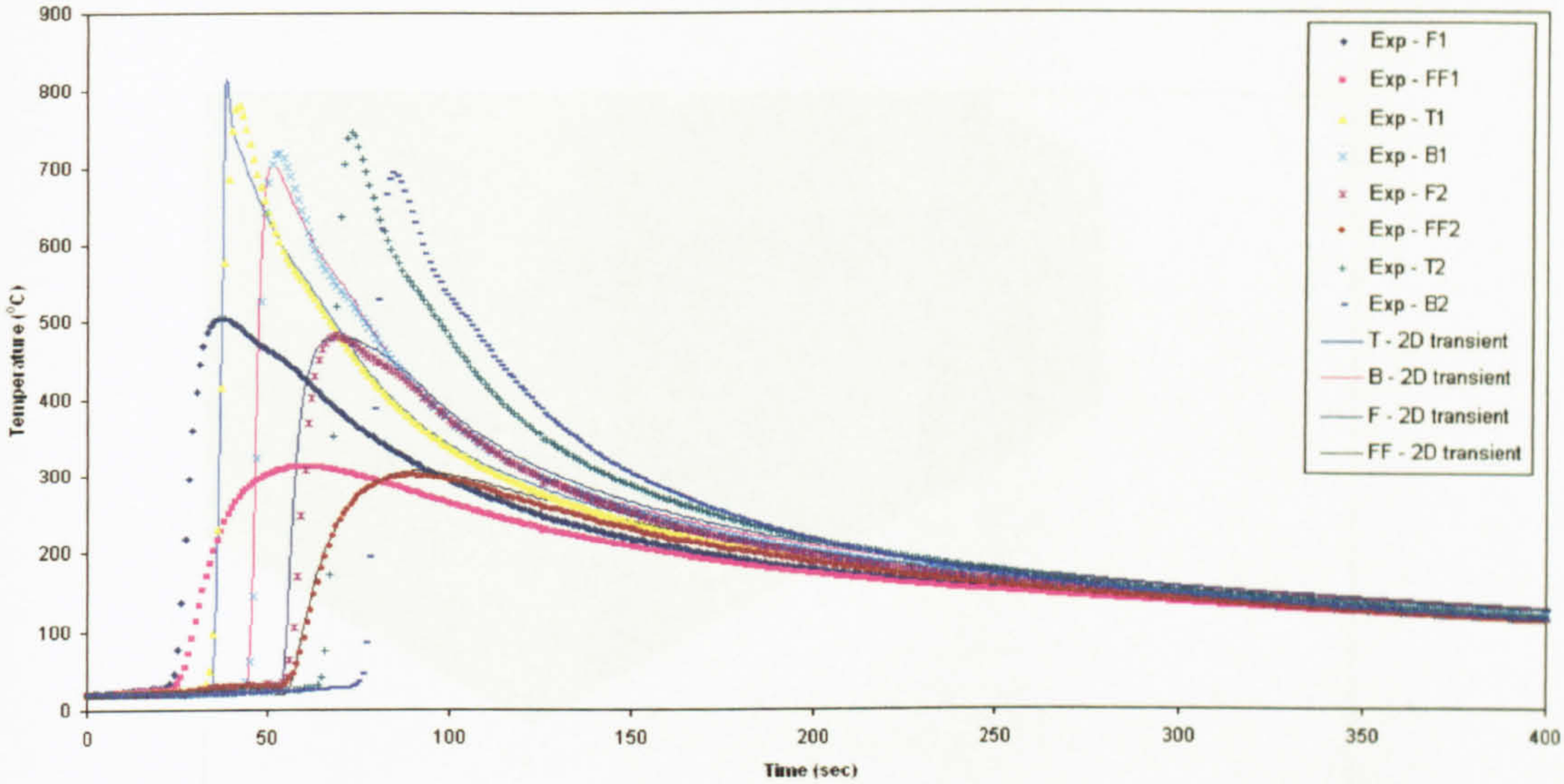

Figure 2C-TH

Comparison of the simulation temperature histories of model 2C with the measured

C.3 Model 3C – 8 mm thick welding plate with a "V" weld-prep

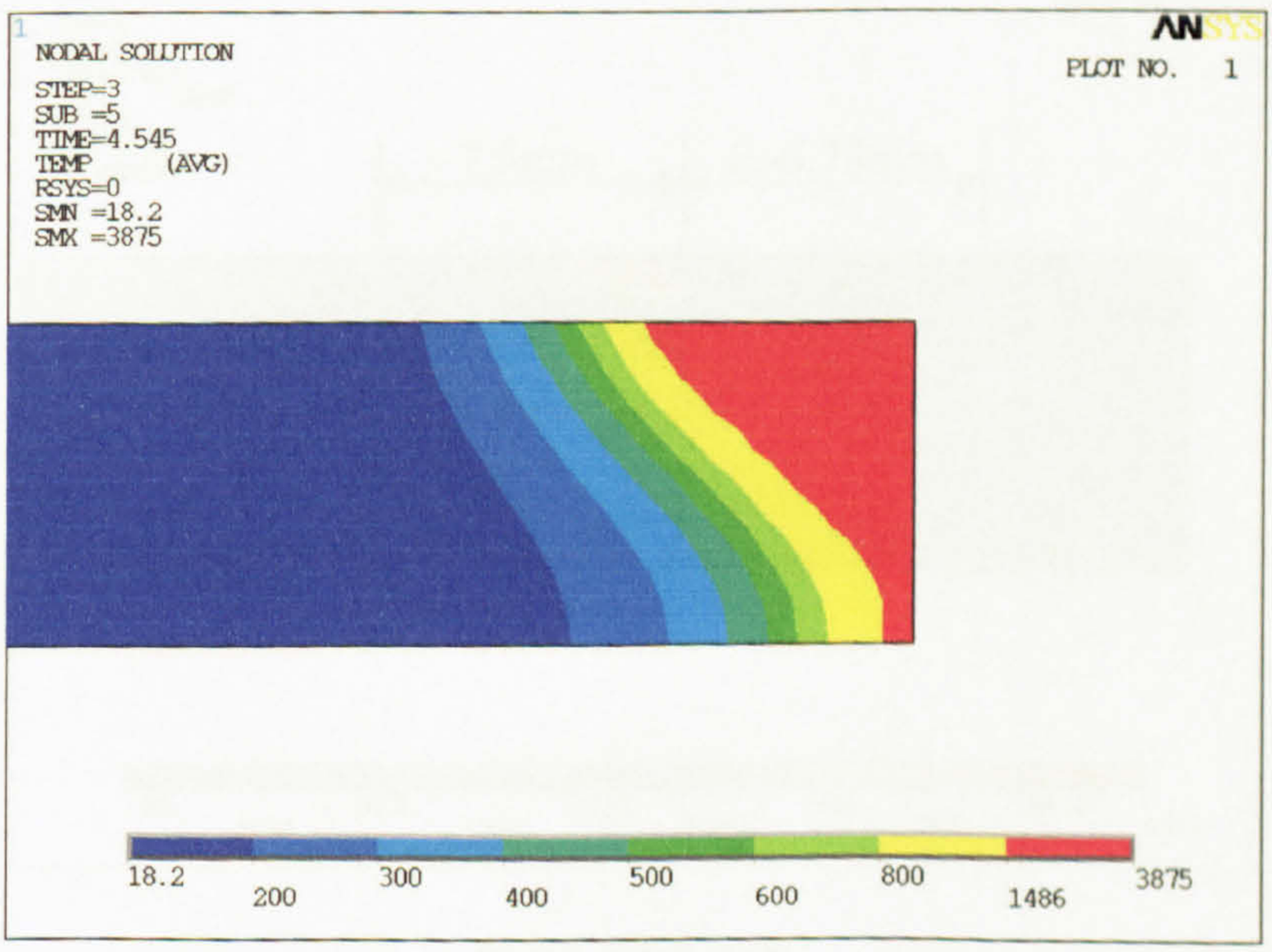

Figure 3C-O

Temperature contour of model 3C

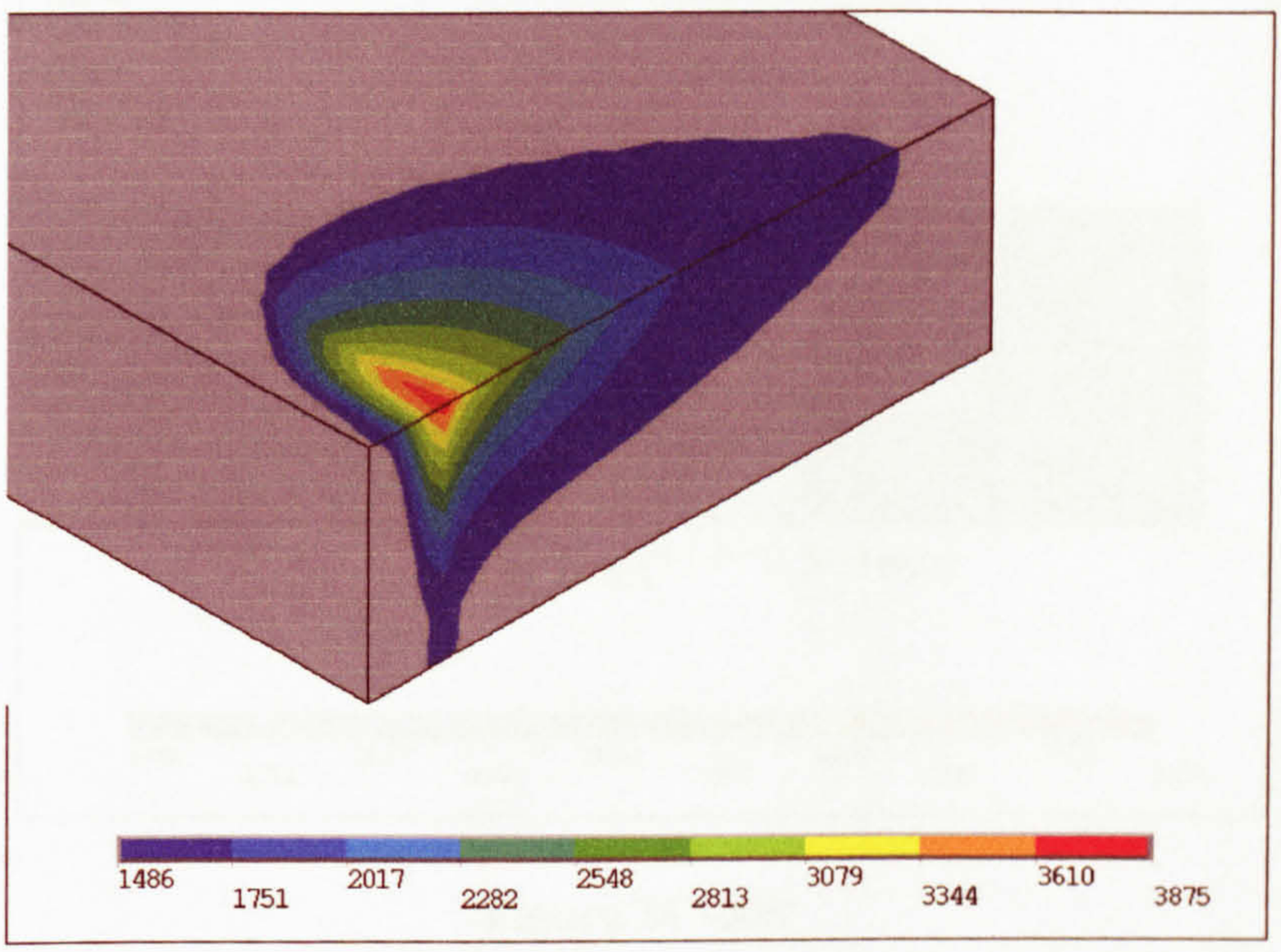

Figure 3C-P

The converted temperature contour of the weld pool of model 3C

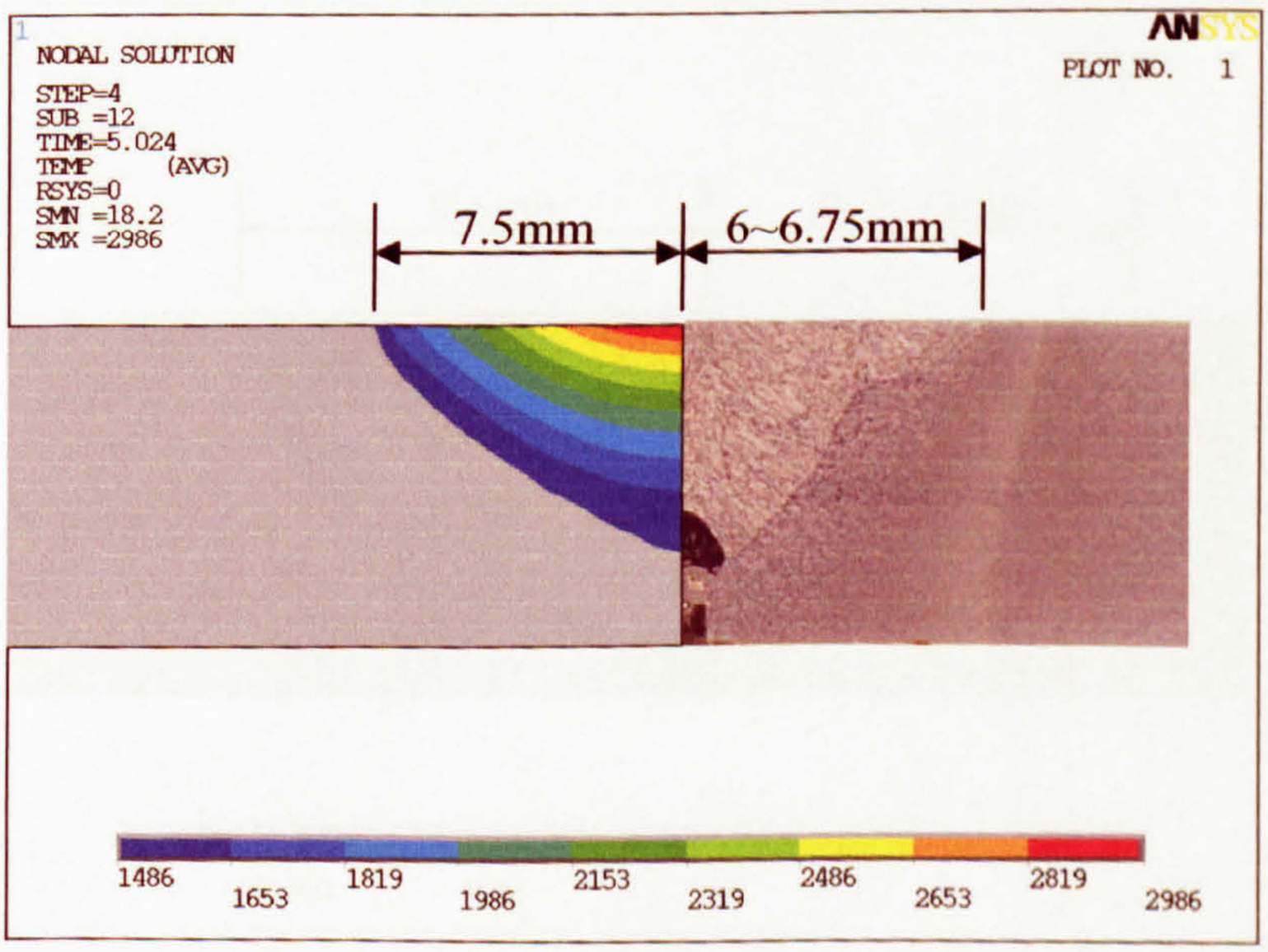

Figure 3C-TW

Simulated top weld width of model 3C

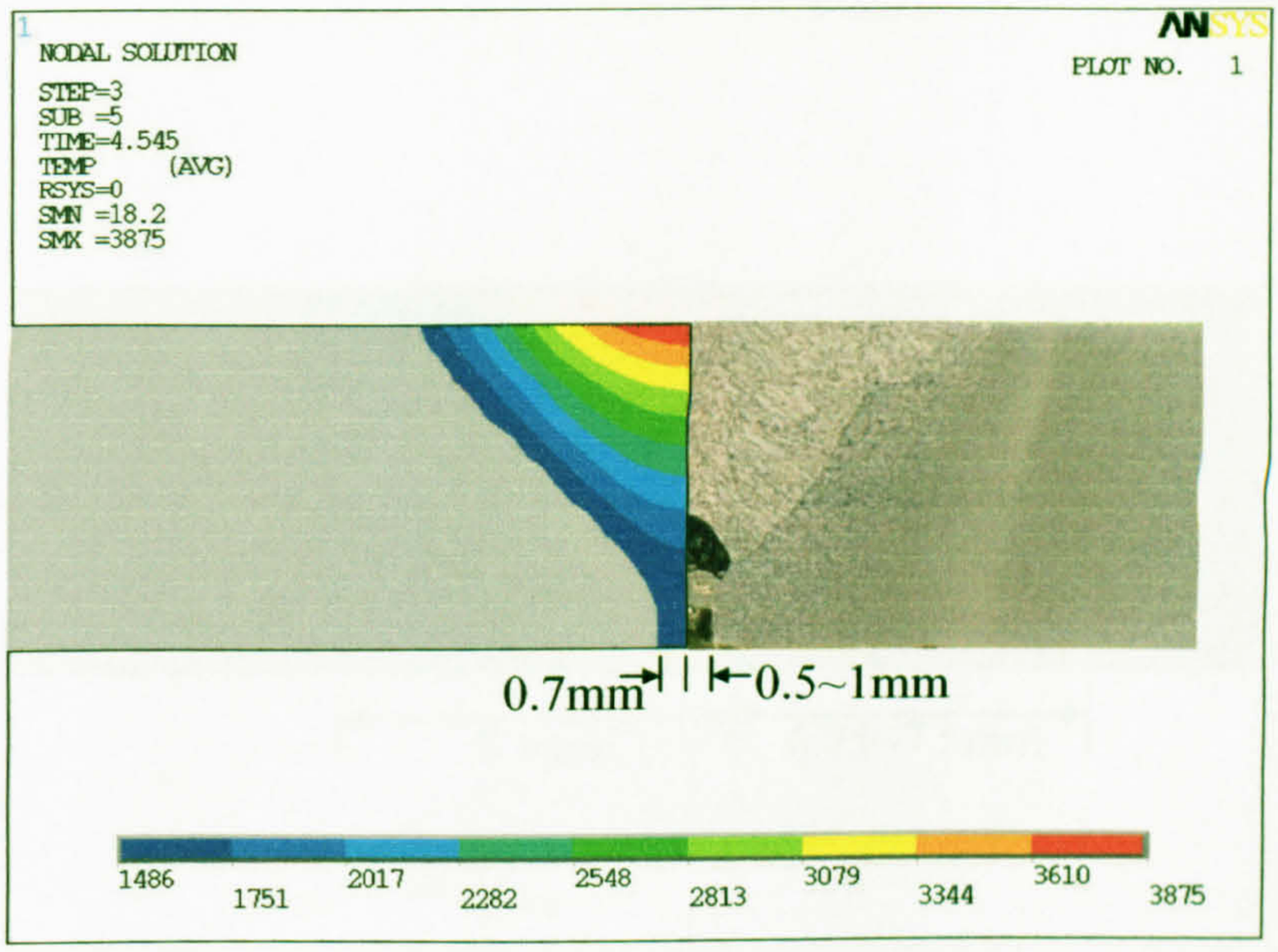

Figure 3C-BW

Simulated bottom weld width of model 3C

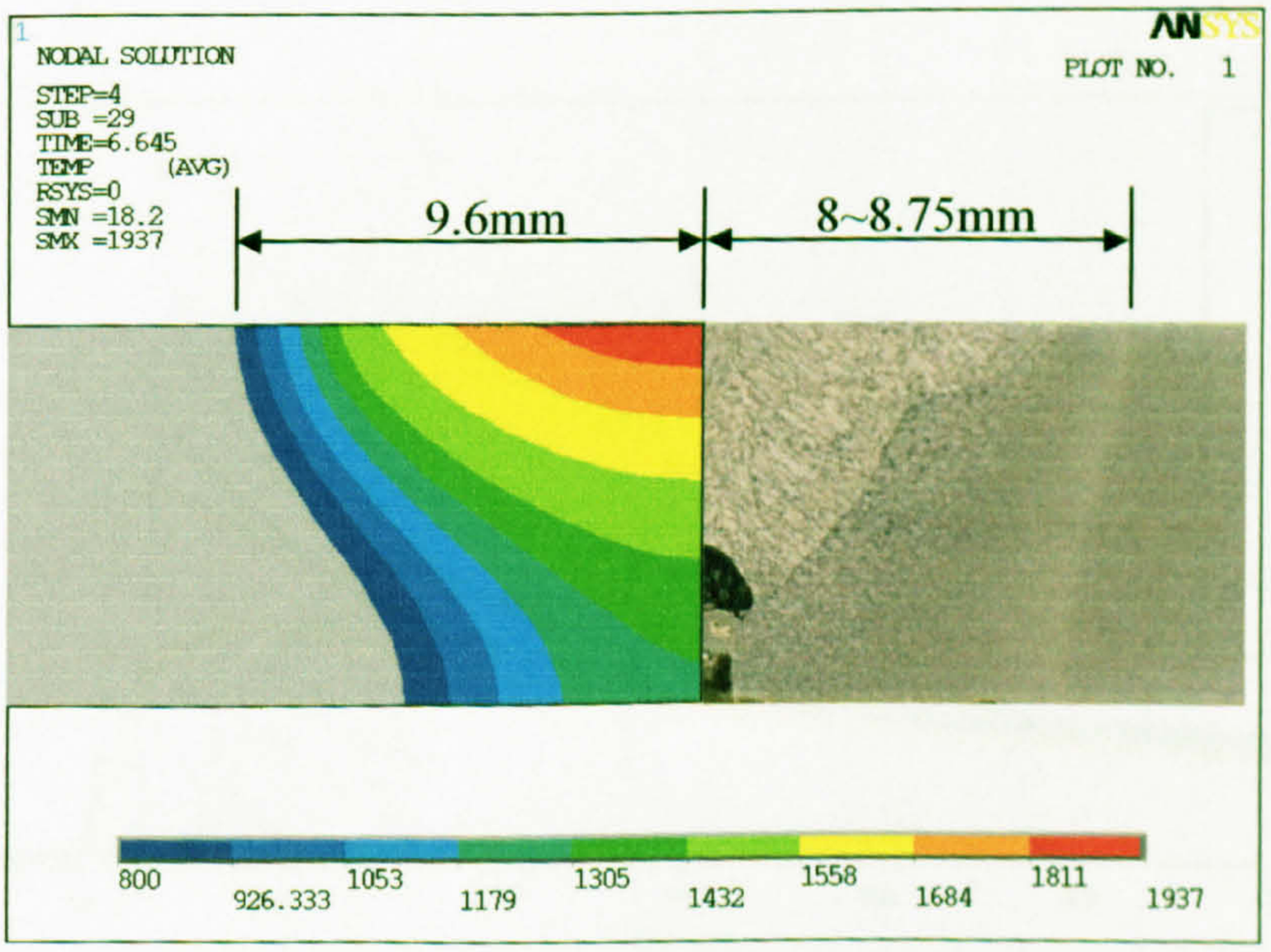

Figure 3C-HT

Simulated top heat affected zone of model 3C

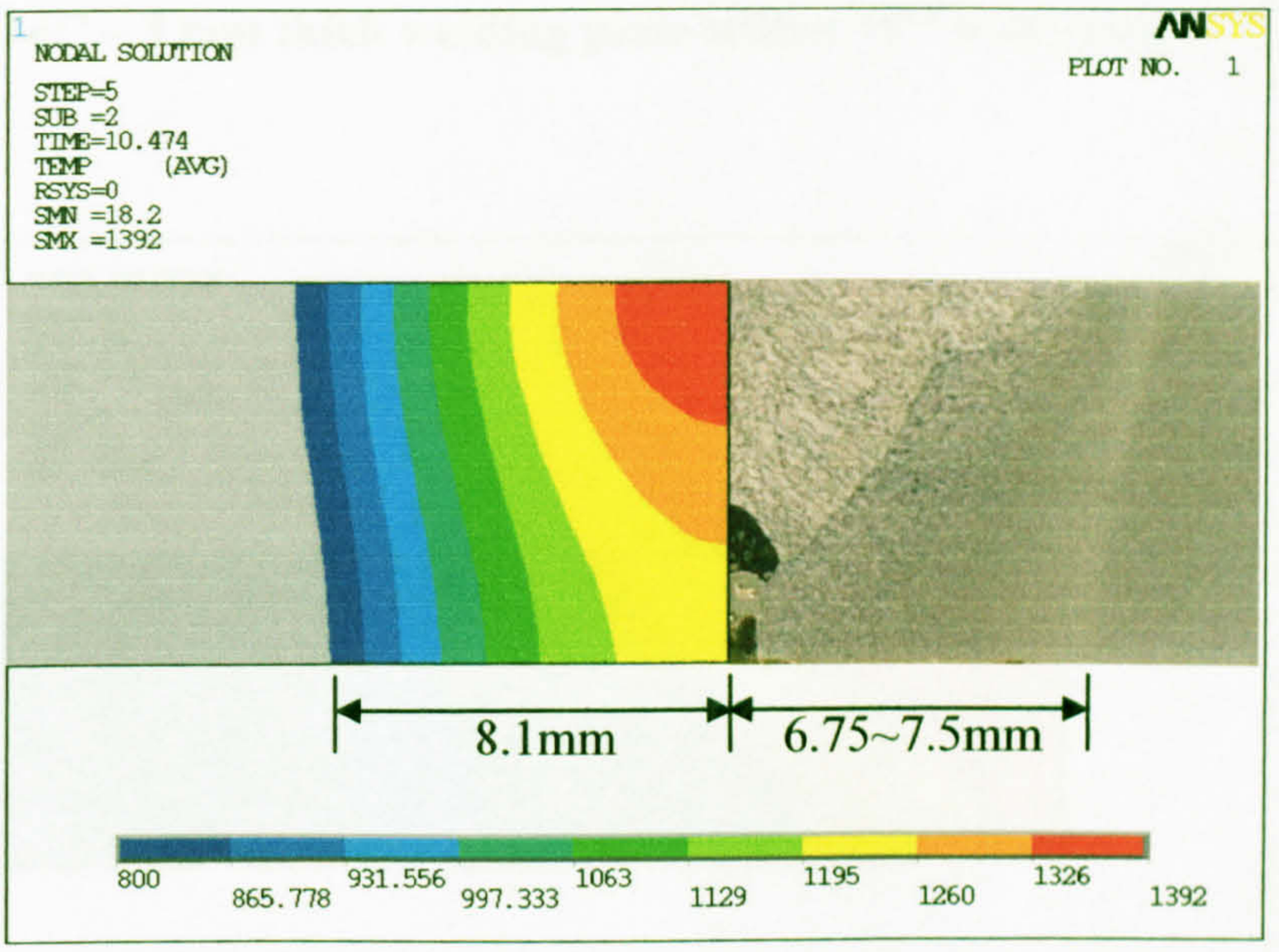

Figure 3C-HB

Simulated bottom heat affected zone of model 3C

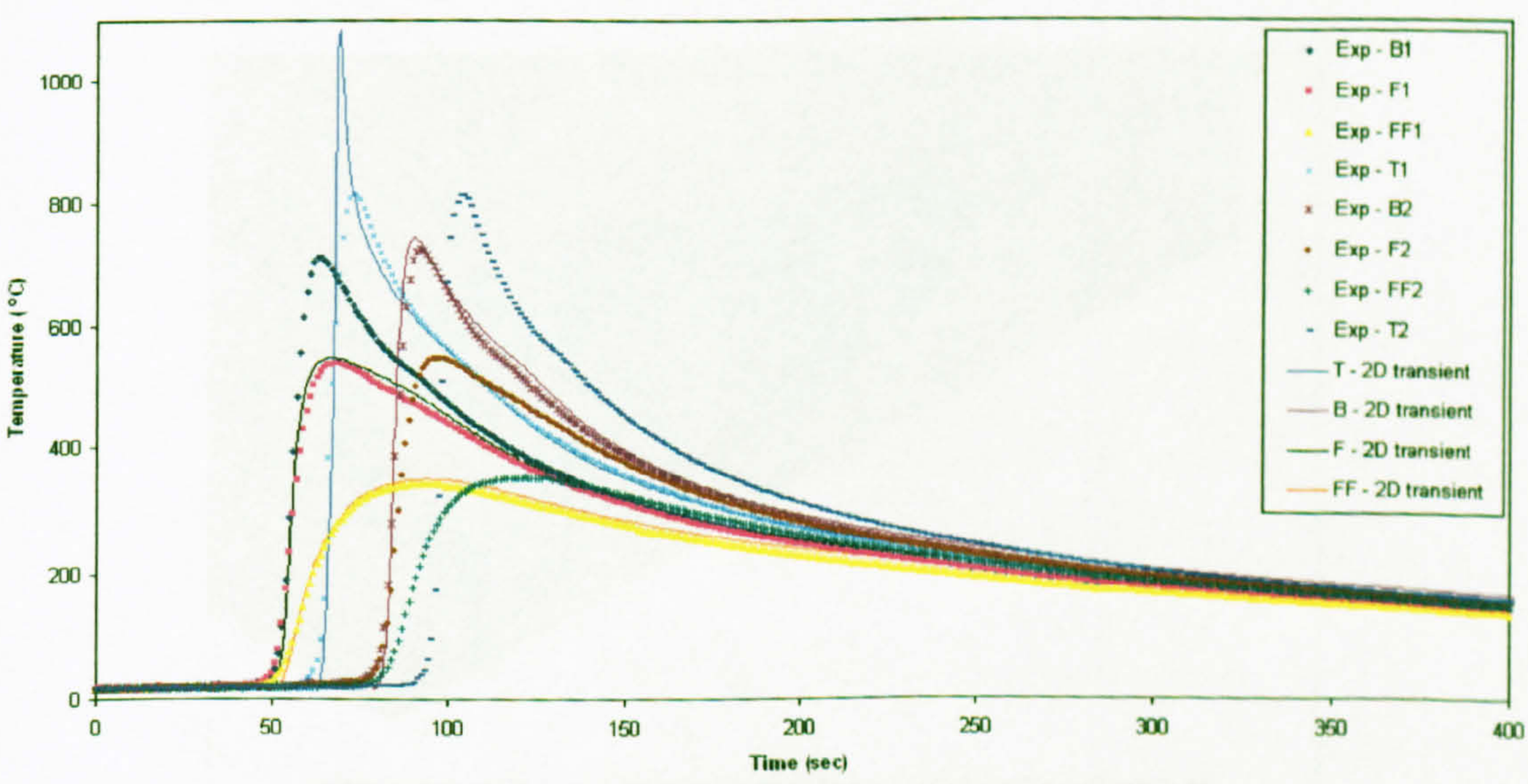

Figure 3C-TH

Comparison of the simulation temperature histories of model 3C with the measured

C.4 Model 4C – 3 mm thick welding plate with a "V" weld-prep

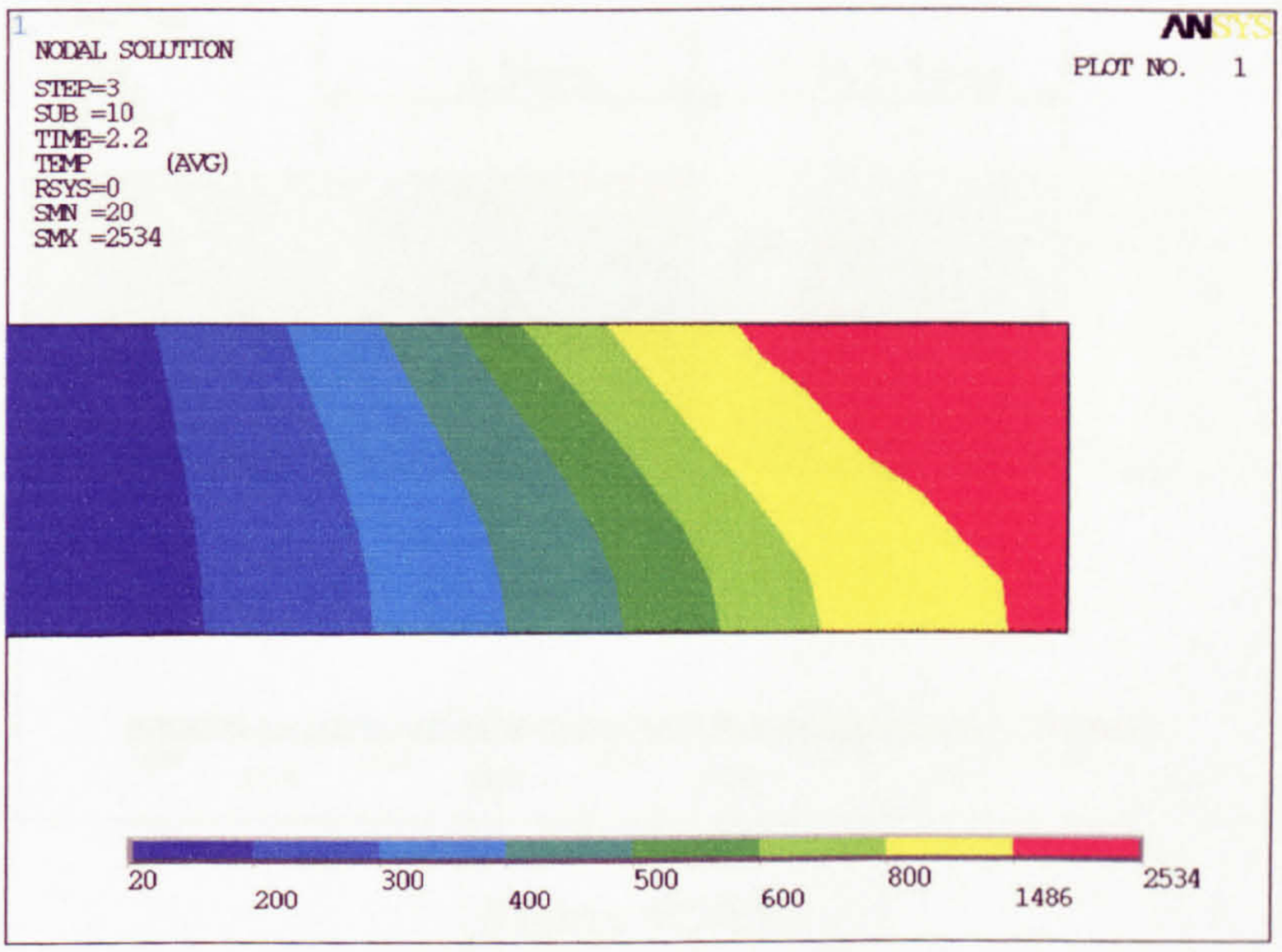

Figure 4C-O

Temperature contour of model 4C

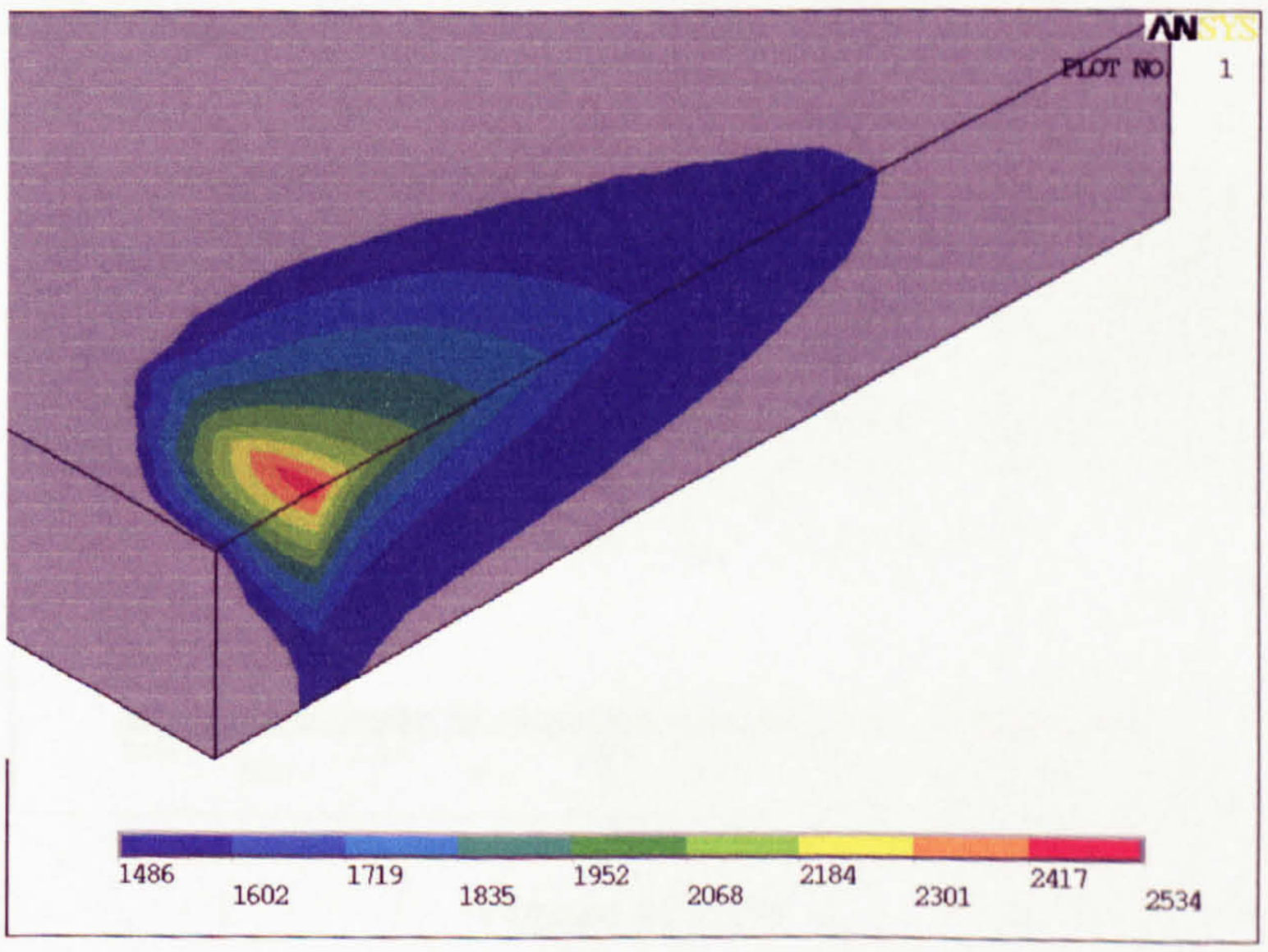

Figure 4C-P

The converted temperature contour of the weld pool of model 4C

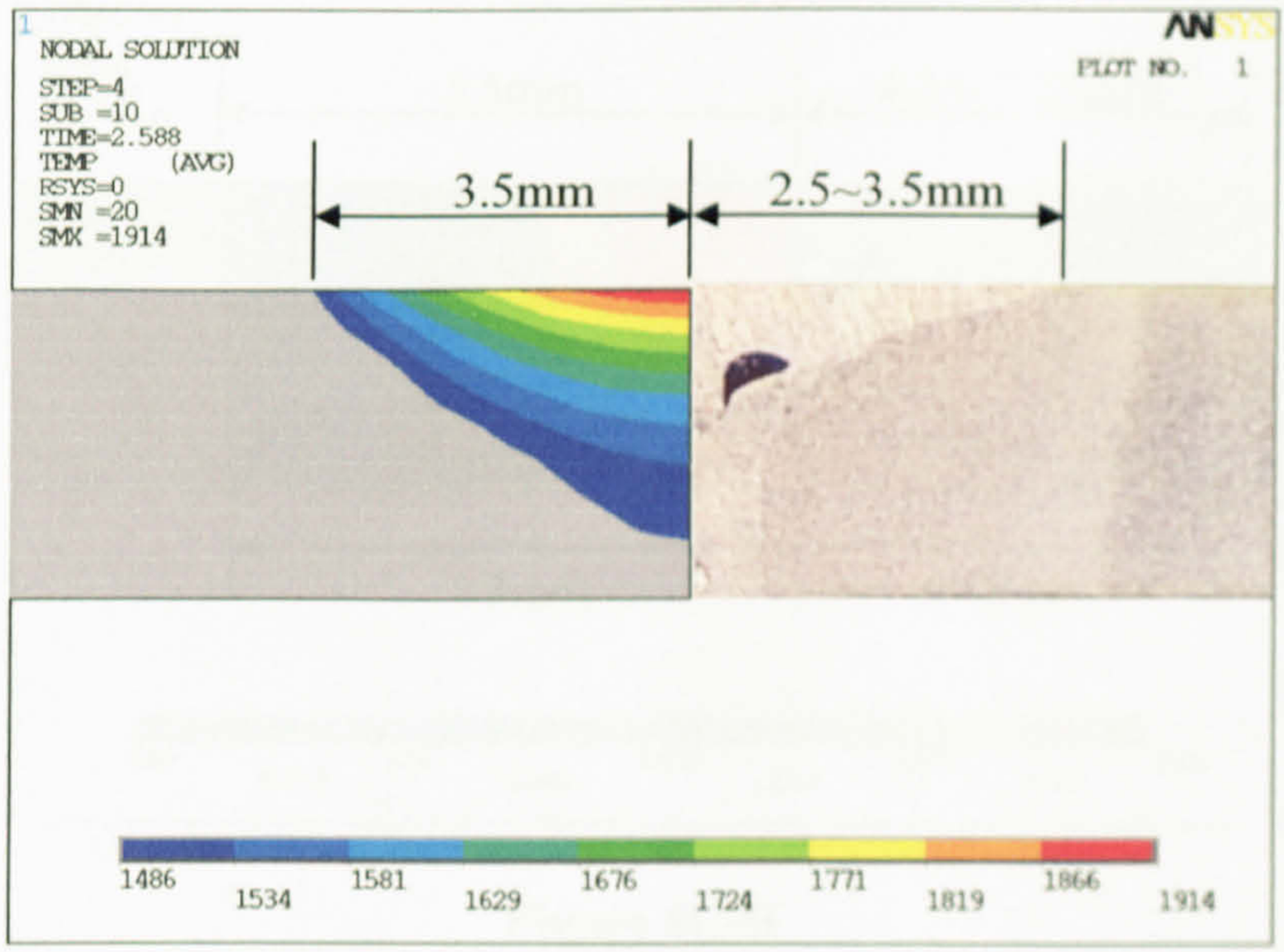

Figure 4C-TW

Simulated top weld width of model 4C

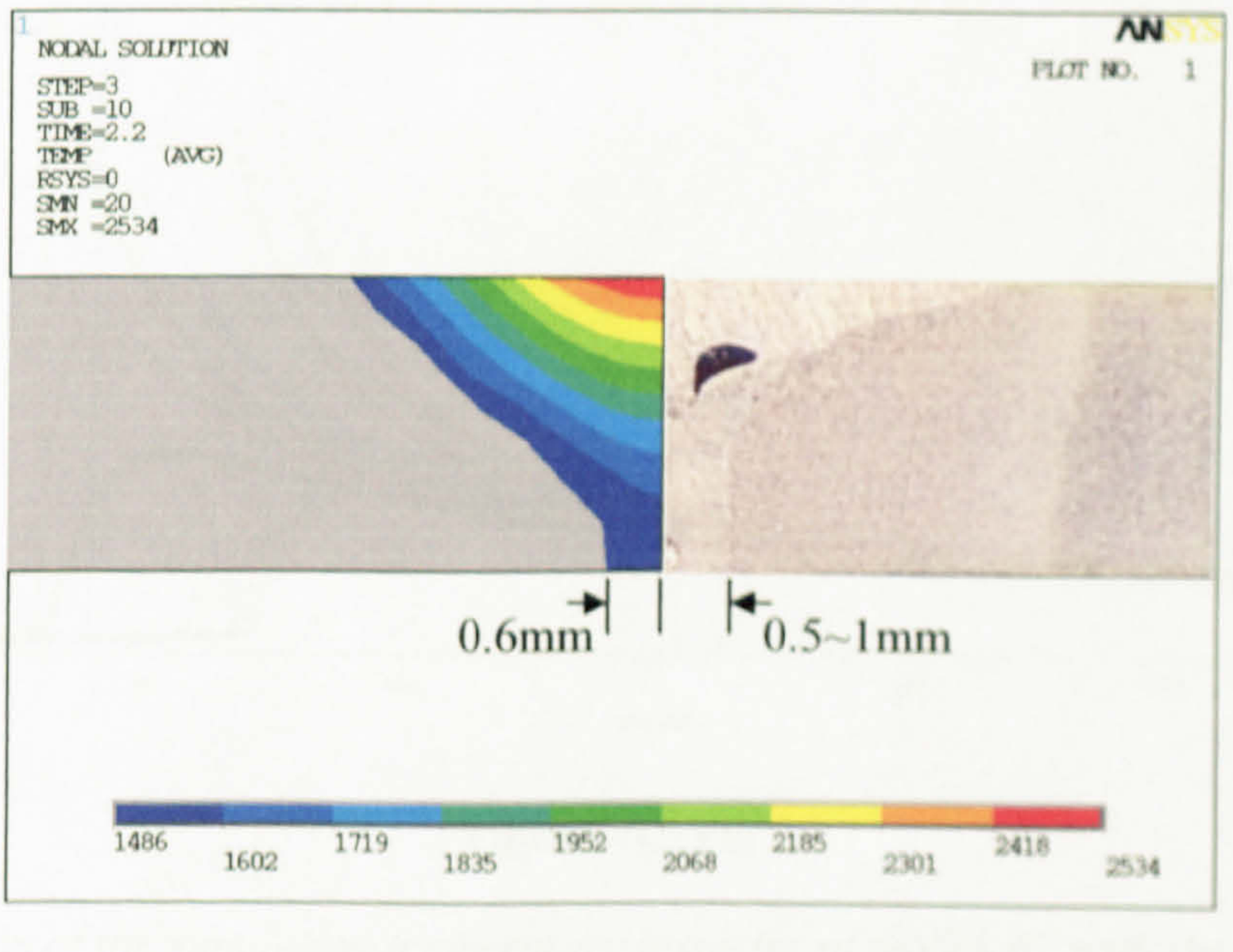

Figure 4C-BW

Simulated bottom weld width of model 4C

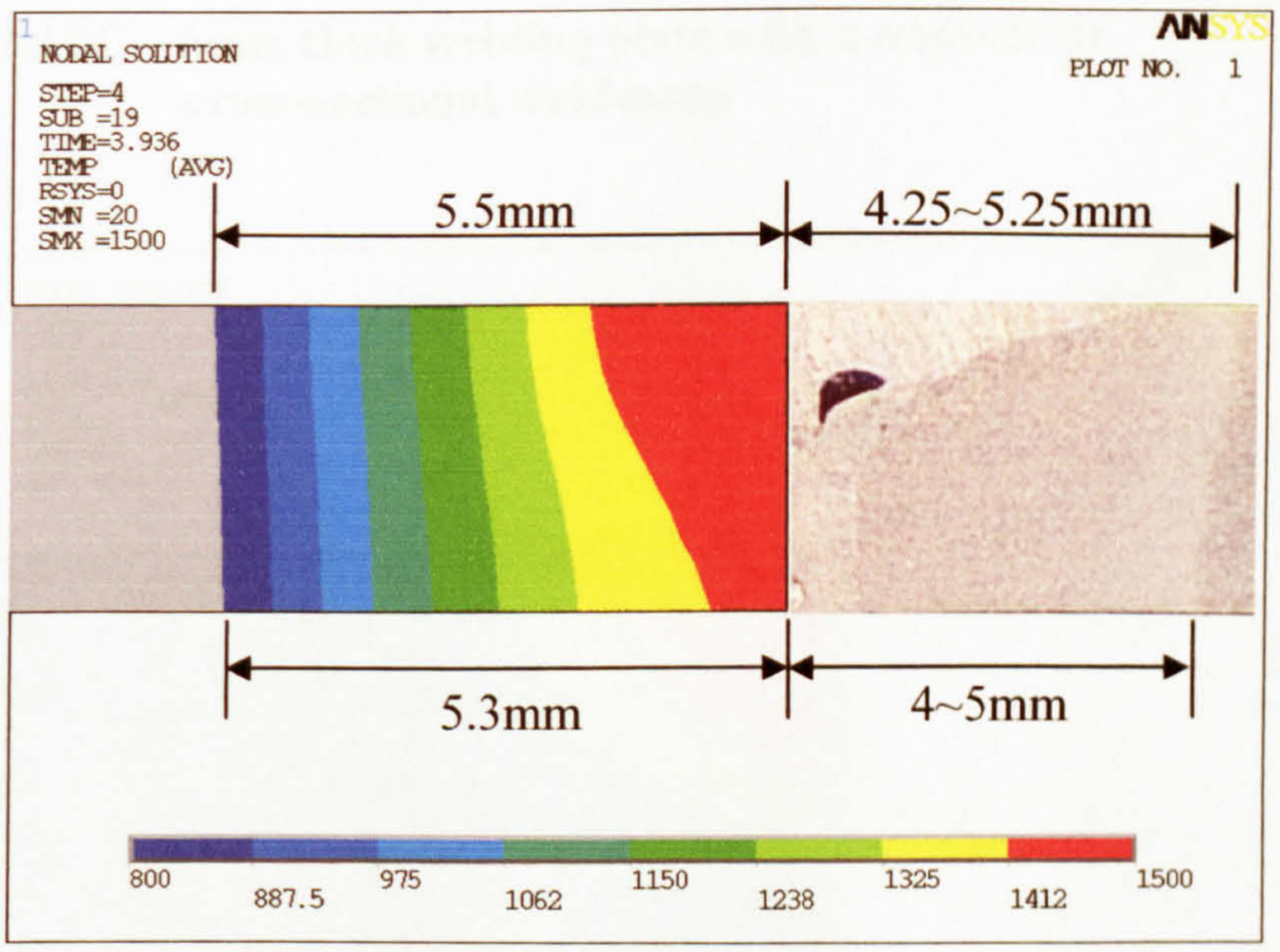

Figure 4C-H

Simulated heat affected zone of model 4C

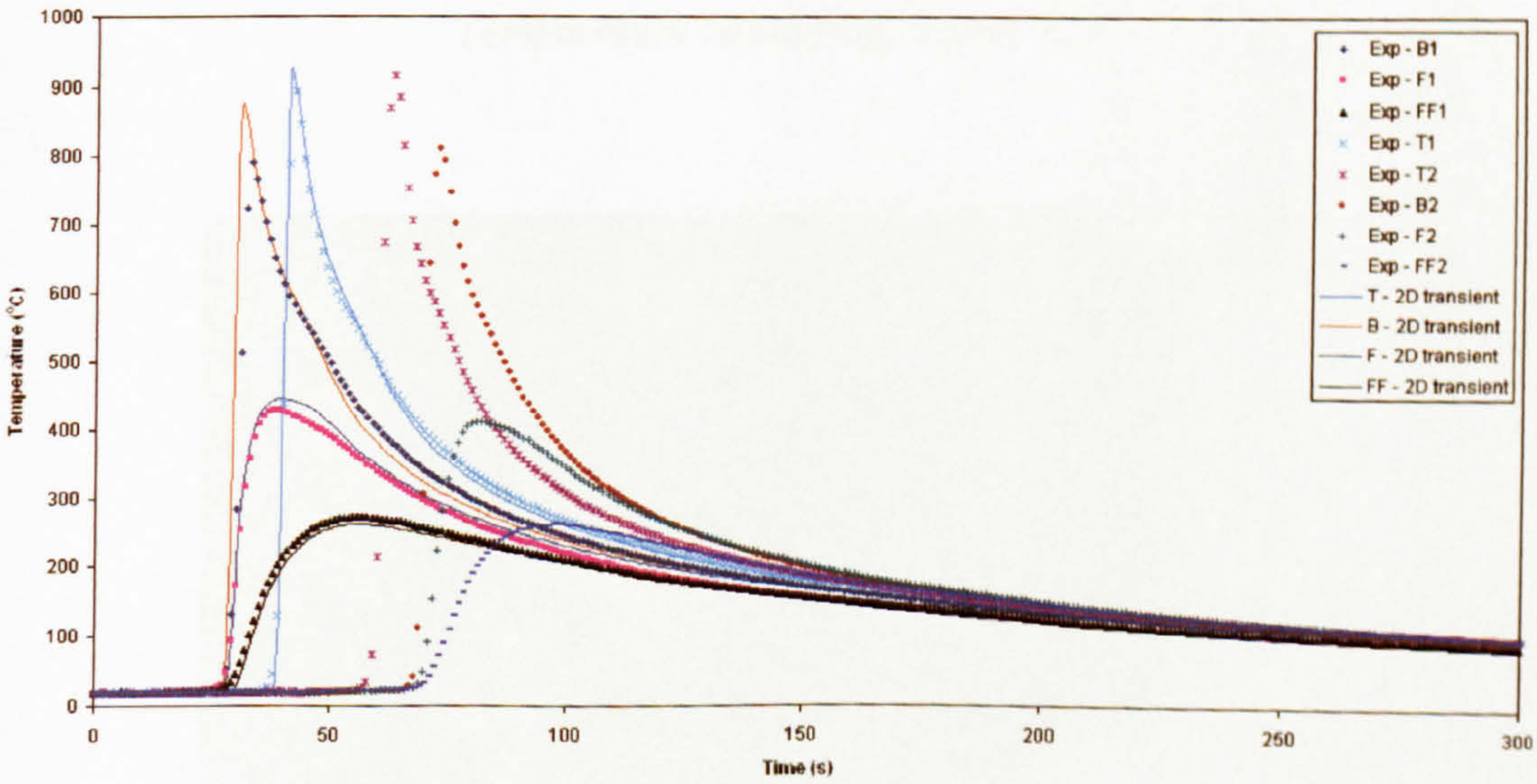

Figure 4C-TH

Comparison of the simulation temperature histories of model 4C with the measured

C.5 Model 5C – 6mm thick welding plate with a semi-circle cross-sectional weld-prep

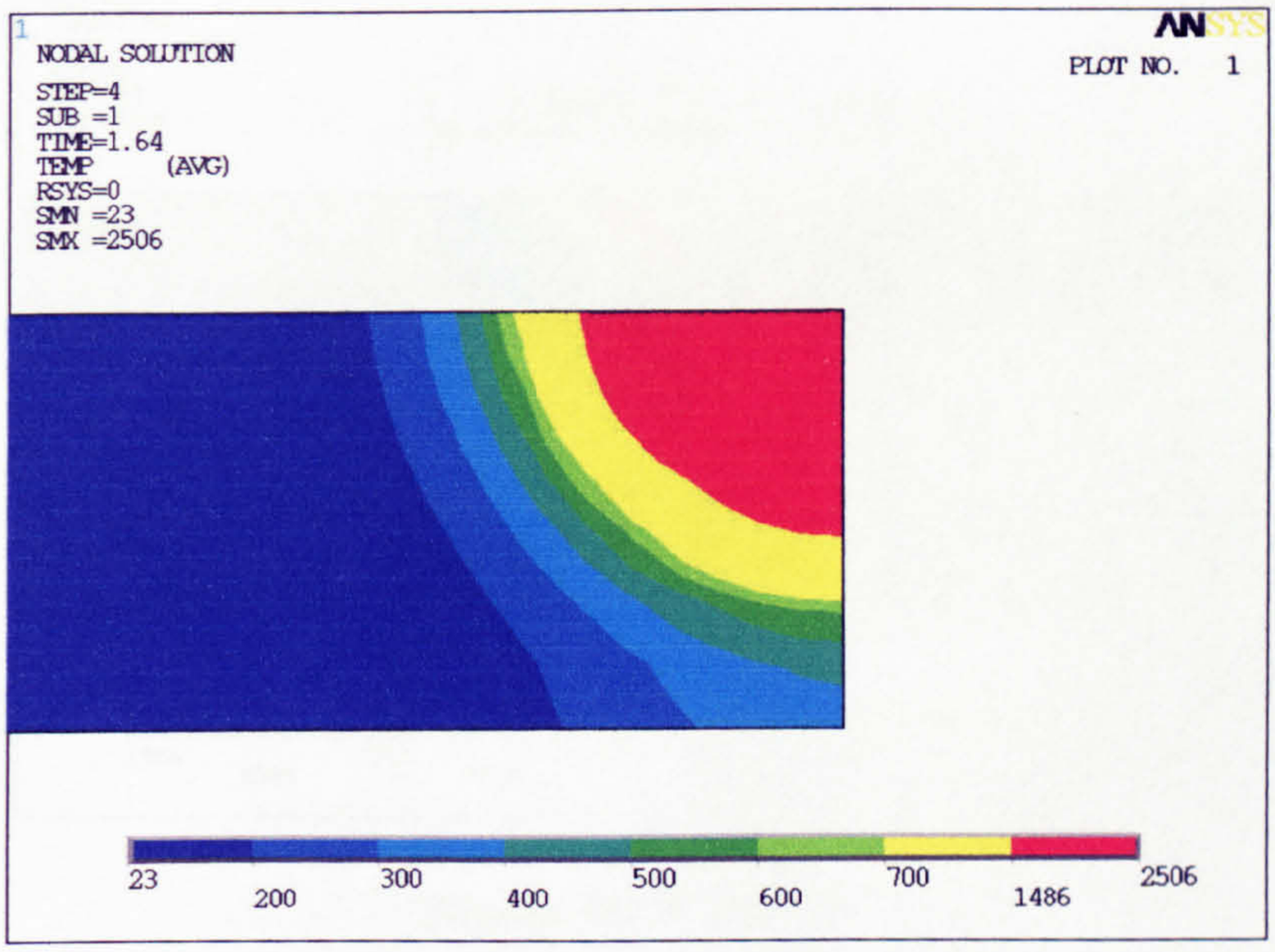

Figure 5C-O

Temperature contour of model 5C

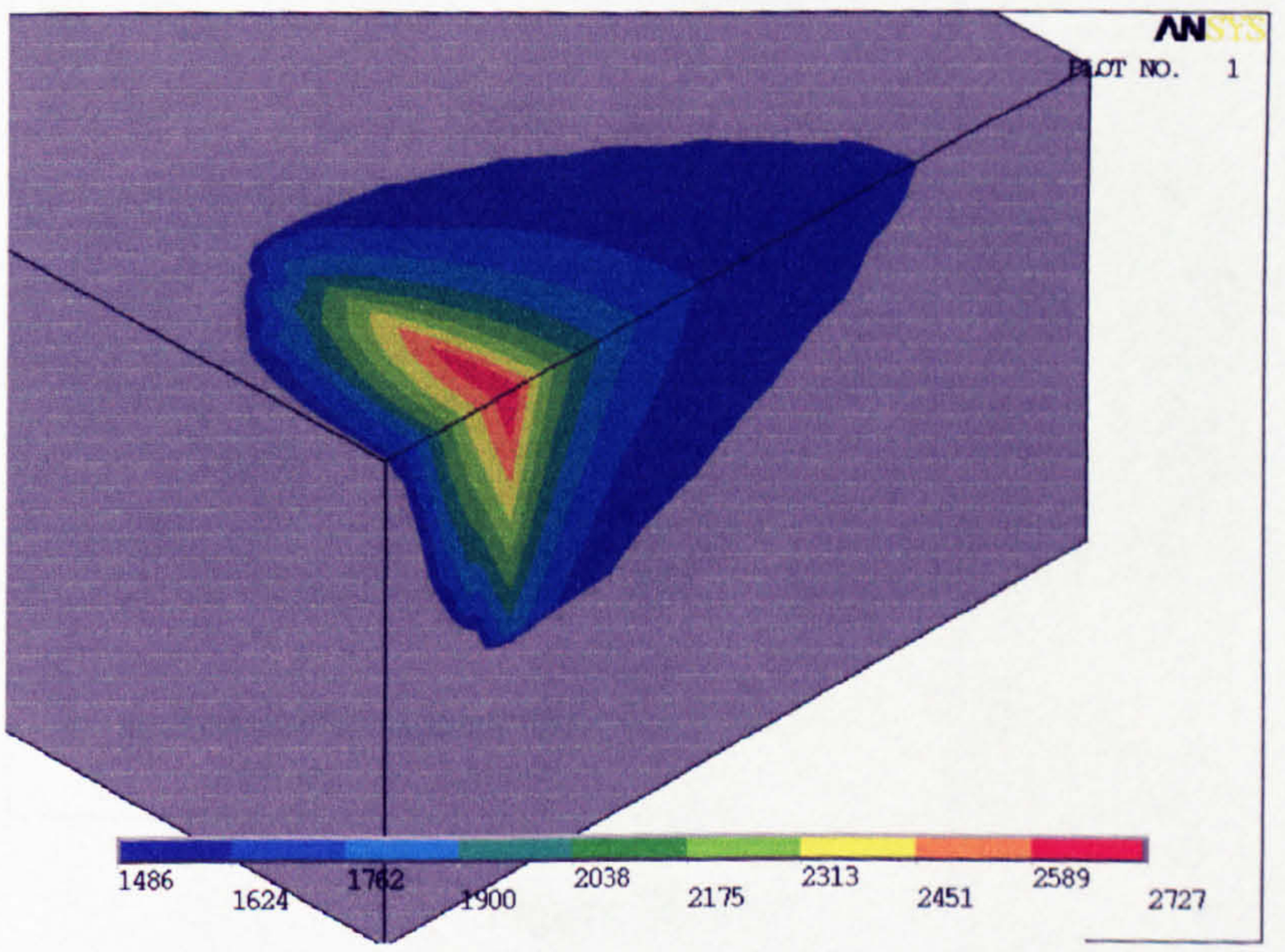

Figure 5C-P

The converted temperature contour of the weld pool of model 5C

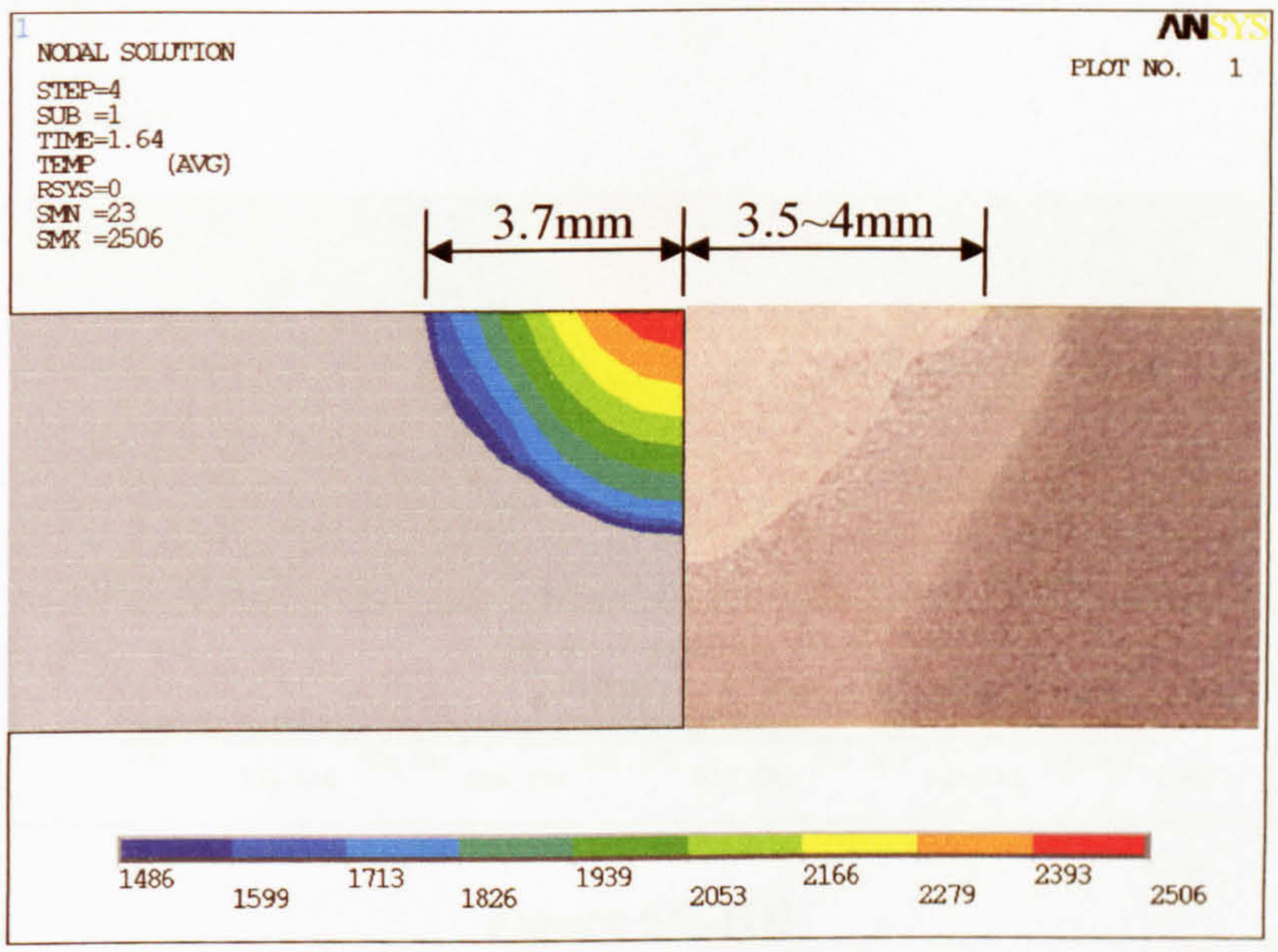

Figure 5C-TW/WD

Simulated top weld width and weld depth of model 5C

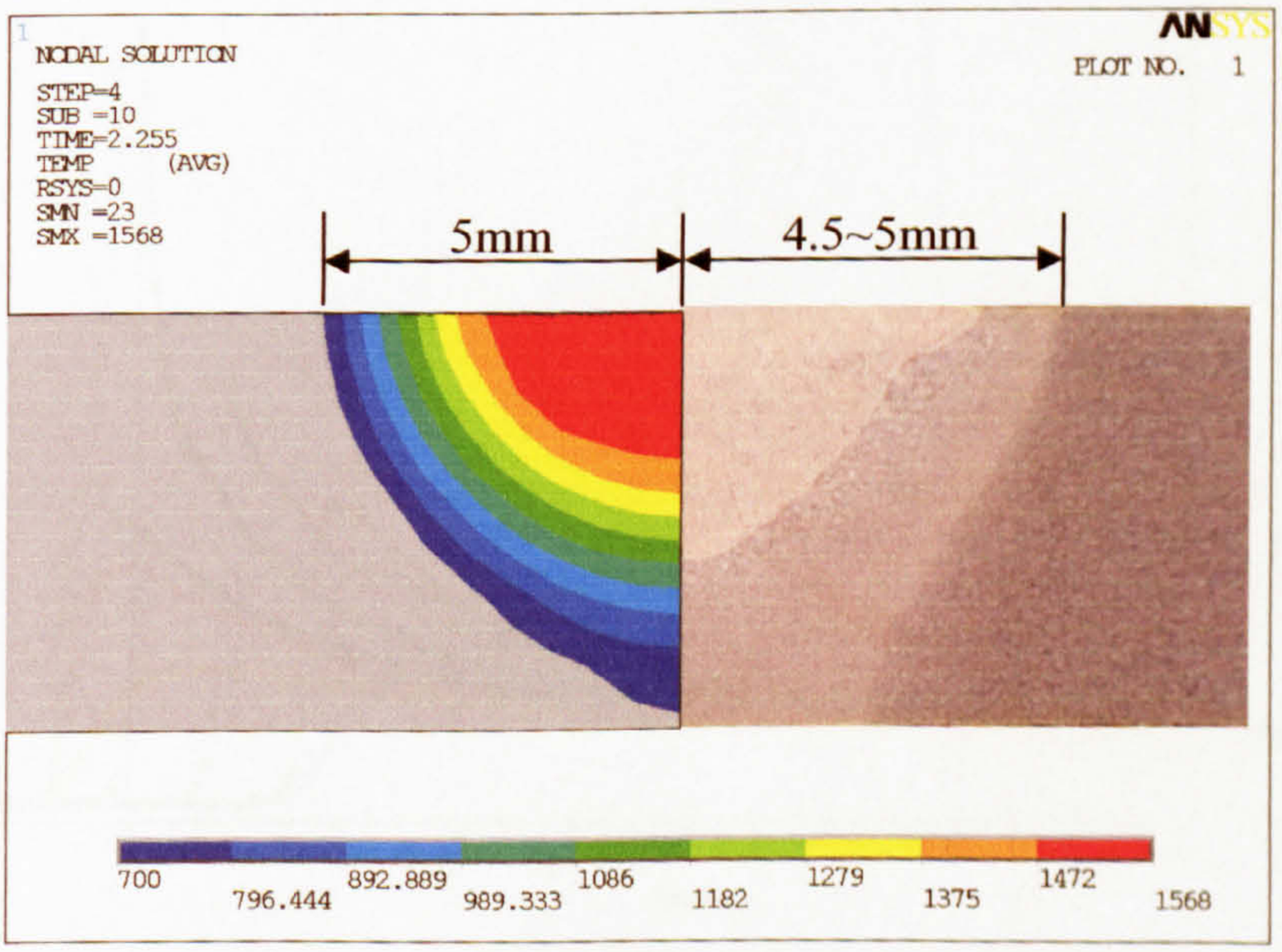

Figure 5C-HT

Simulated top heat affected zone of model 5C

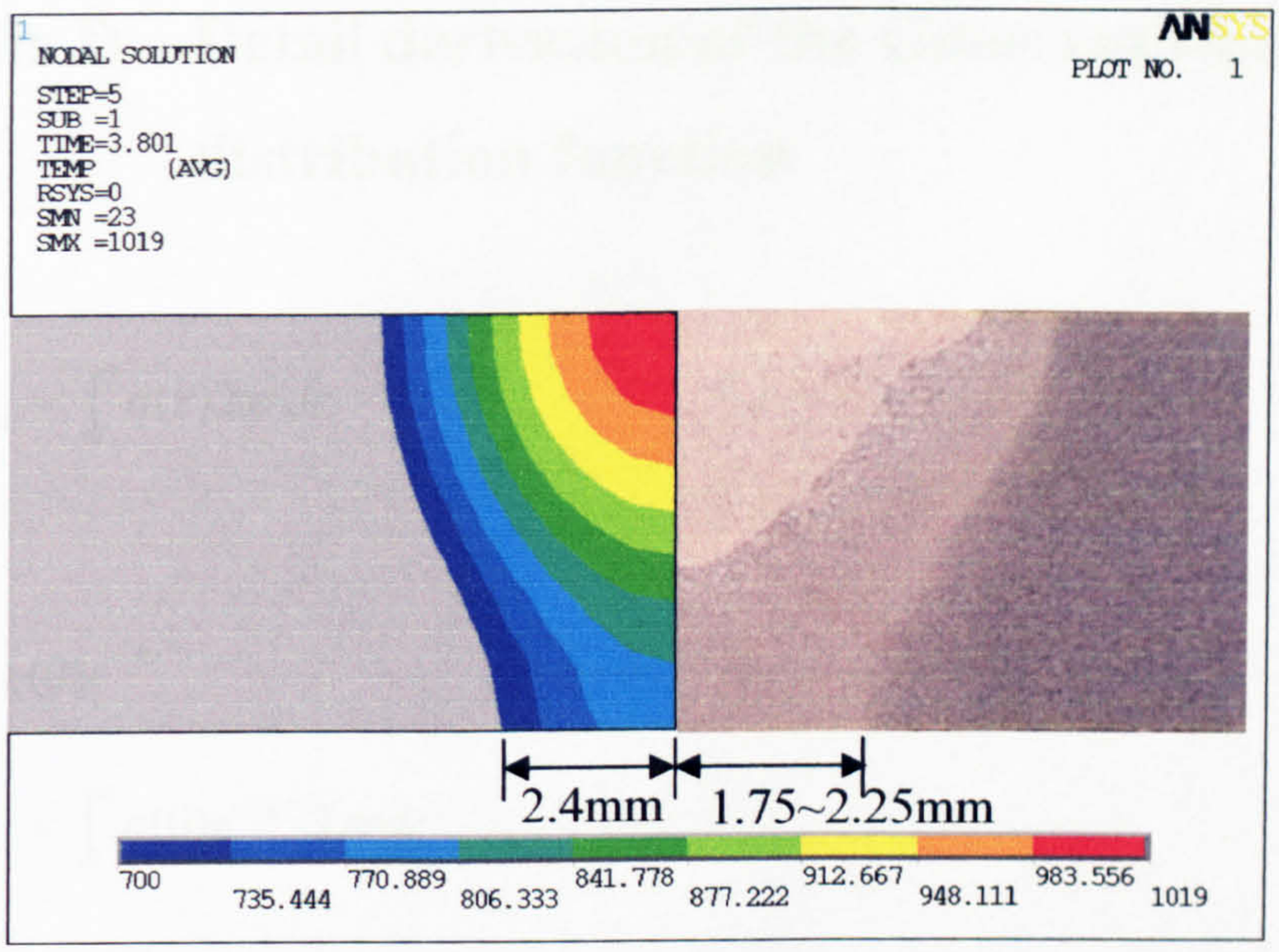

Figure 5C-HB

Simulated bottom heat affected zone of model 5C

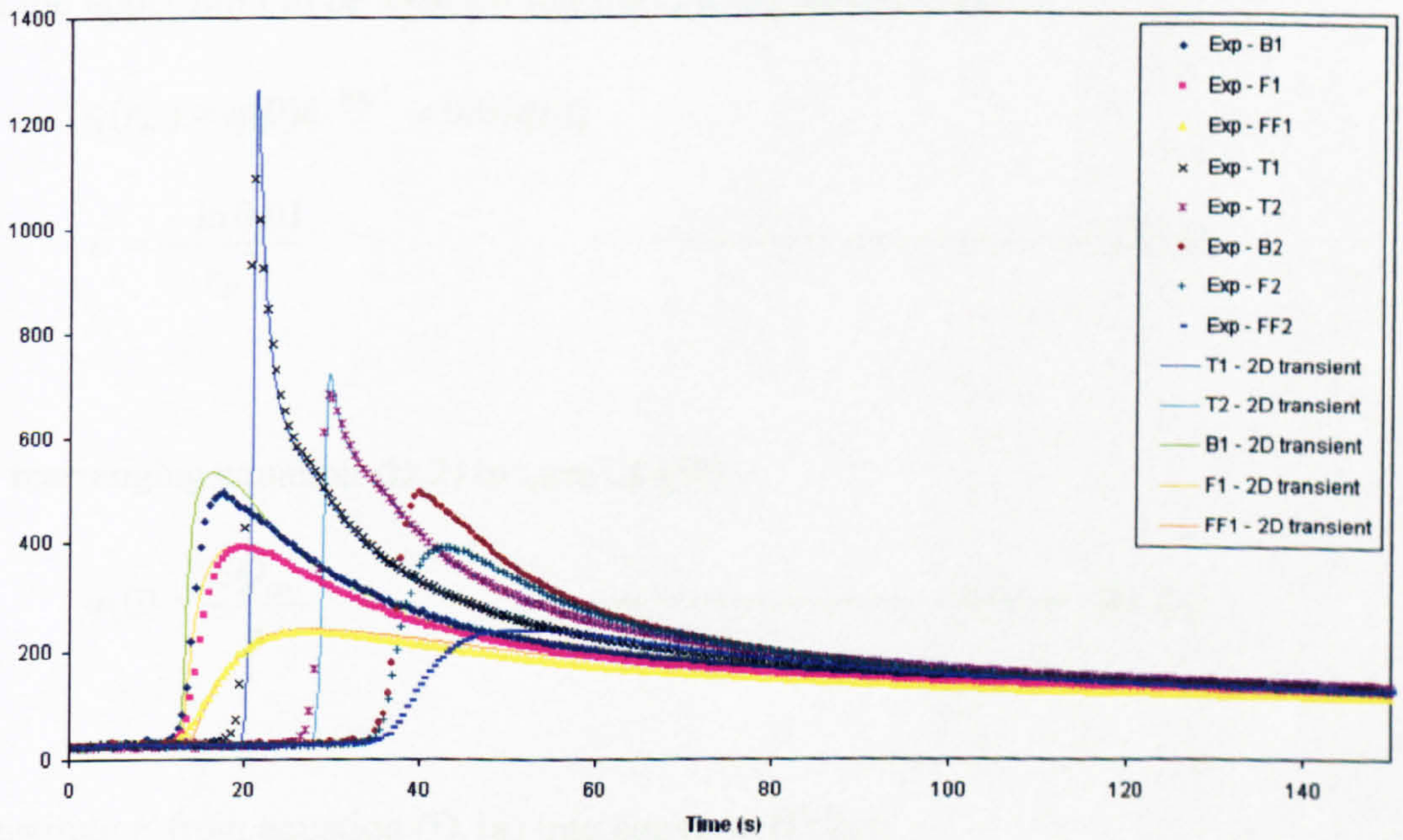

Figure 5C-TH

Comparison of the simulation temperature histories of model 5C with the measured

Appendix D – Detail derivation of the Gaussian heat flux distribution function

$$Q_{arc} = \int_0^\infty q(r) 2\pi r dr$$

Let $q(r) = q(0)e^{-Er^2}$ ---------- (D.1)

$$Q_{arc} = \int_0^\infty q(0)e^{-Er^2} 2\pi r dr$$

$$Q_{arc} = \frac{q(0)\pi}{E} \quad \text{---------- (D.2)}$$

where E is the unknown constant

Let the upper limit to be 99% for finding E using equation (D.1):

$$q(r_H) = q(0)e^{-Er_H^2} = 0.01q(0)$$

$$E = \frac{-\ln 0.01}{r_H^2} \quad \text{---------- (D.1a)}$$

By rearranging equation (D.2) in term of $q(0)$:

$$q(0) = \frac{EQ_{arc}}{\pi} \quad \text{---------- (D.2a)}$$

Substitute E from equation (D.1a) into equation (D.2a):

$$q(0) = \frac{-\ln 0.01 \times Q_{arc}}{\pi r_H^2} \quad \text{---------- (D.2b)}$$

Substitute $q(0)$ from equation (D.2b) into equation (D.1):

$$q(r) = \frac{-\ln 0.01 \times Q_{arc}}{\pi r_H^{\,2}} e^{\frac{\ln 0.01}{r_H^{\,2}} r^2}$$

where Q_{arc} is the amount of heat due to welding arc, $q(r)$ is the heat flux distribution as a function of radius; r_H is the radius of the heat source and r is the variable radius ranging from 0 to r_H.

Appendix E – Converting the temperature distribution of a 3D steady state model to a temperature history

Figure E.1 shows the temperature distribution in reverse direction of welding of the steady state model presented in Chapter 5. The left hand datum position on the plate is arbitrary but the point chosen is such that at ambient temperature. Figure E.2 shows the experimental temperature histories of the centre row of thermocouples: Row B (see Figure 5.1 in Chapter 5) is 0.1 m from the starting edge of weld. These figures appear similar although in Figure E.1, temperature is plotted against distance while in Figure E.2 temperature is plotted against time.

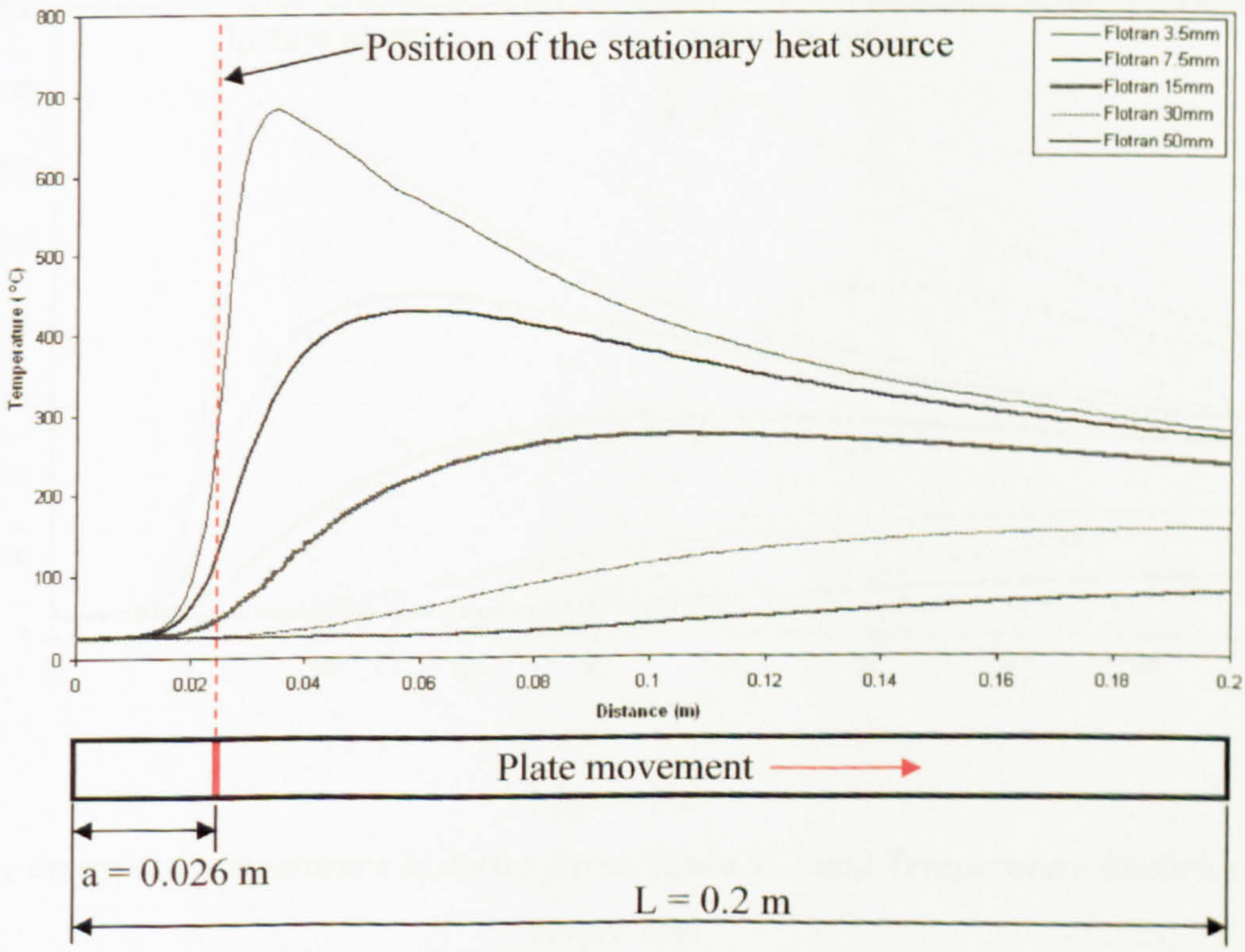

Figure E.1

Temperature distribution in reverse direction of weld

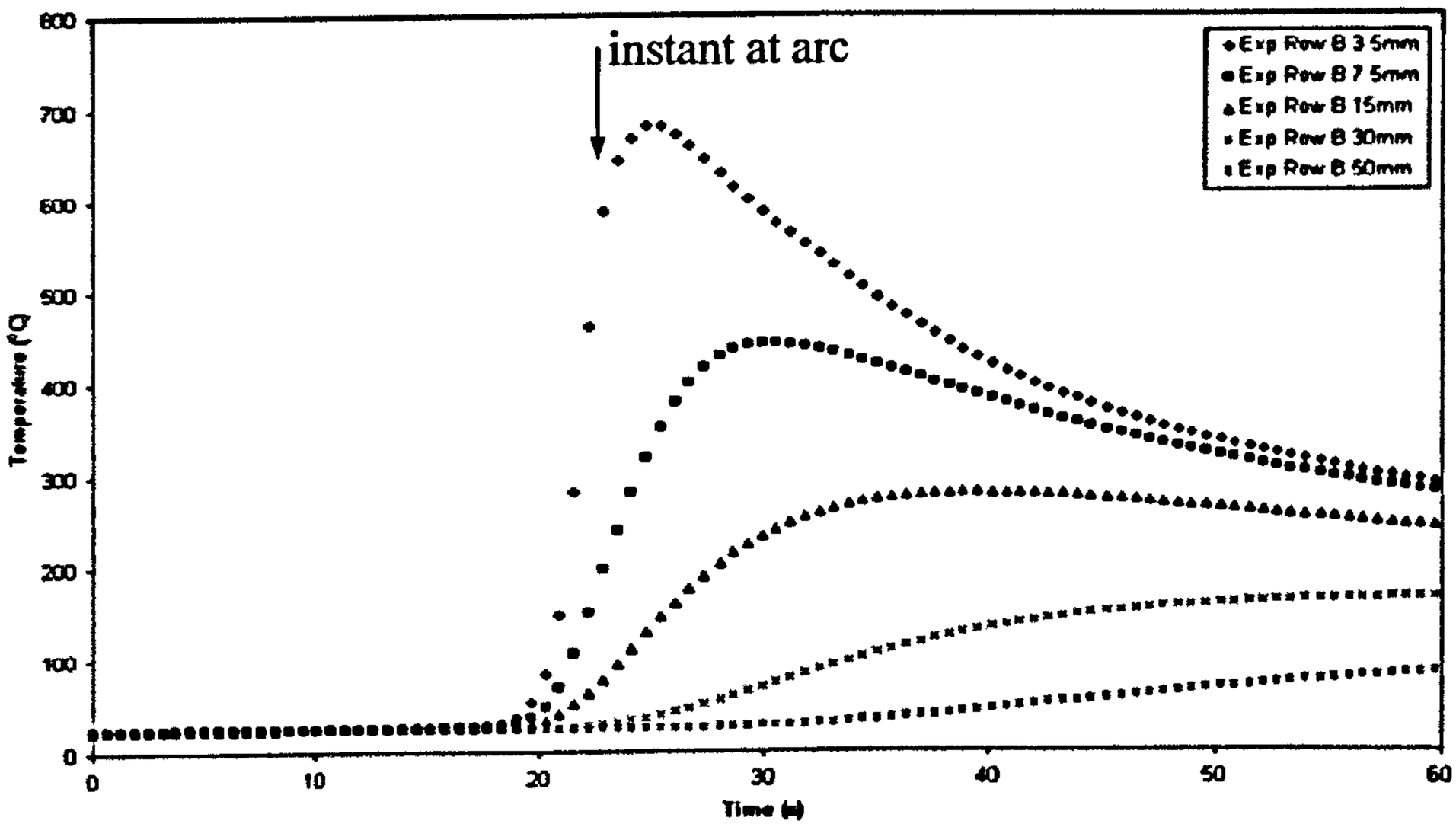

Figure E.2

The experimental temperature histories of centre row

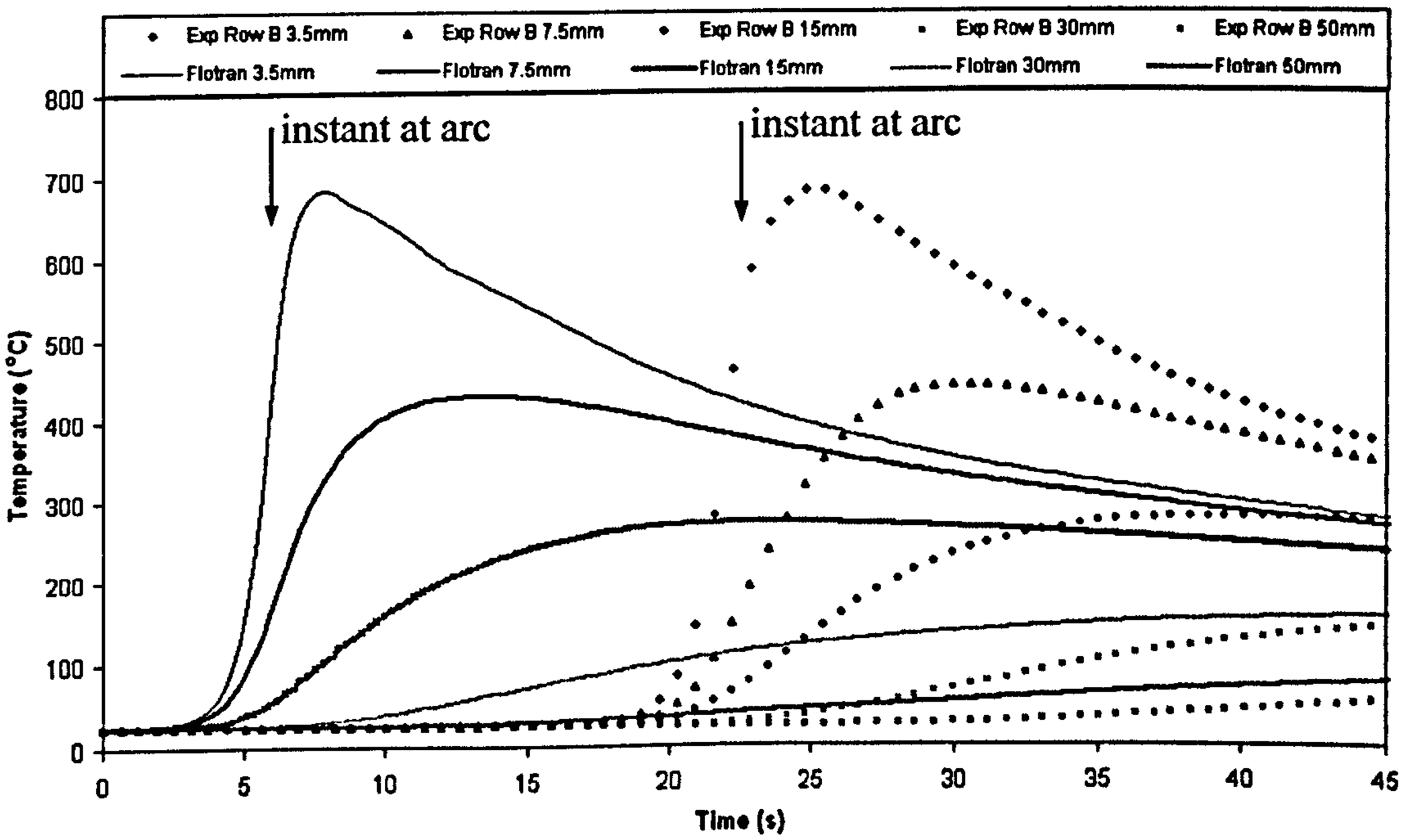

Figure E.3

The converted temperature histories from Figure E.1 and Temperature histories of centre row

The conversion of distance to time uses the relationship speed = distance / time where the welding speed is $4.\dot{4}$ mm/s. The plot of converted temperature histories from Figure E.1 is shown in Figure E.3 and the position of stationary heat source in Figure E.1 is now become at the time of instant arc. Figure E.3 also shows the experimental temperature histories of the centre row of thermocouples.

The time shift needed to align the two sets of data is given by

$$ts = \frac{b - a}{u}$$

where 'a' is the instant arc position of the converted temperature histories to be as shown in Figure E.4, 'b' is the instant arc position of the experimental temperature histories as shown in Figure E.5, 'u' is the welding speed and 'ts' is the amount of time shift needed to align the two sets of data.

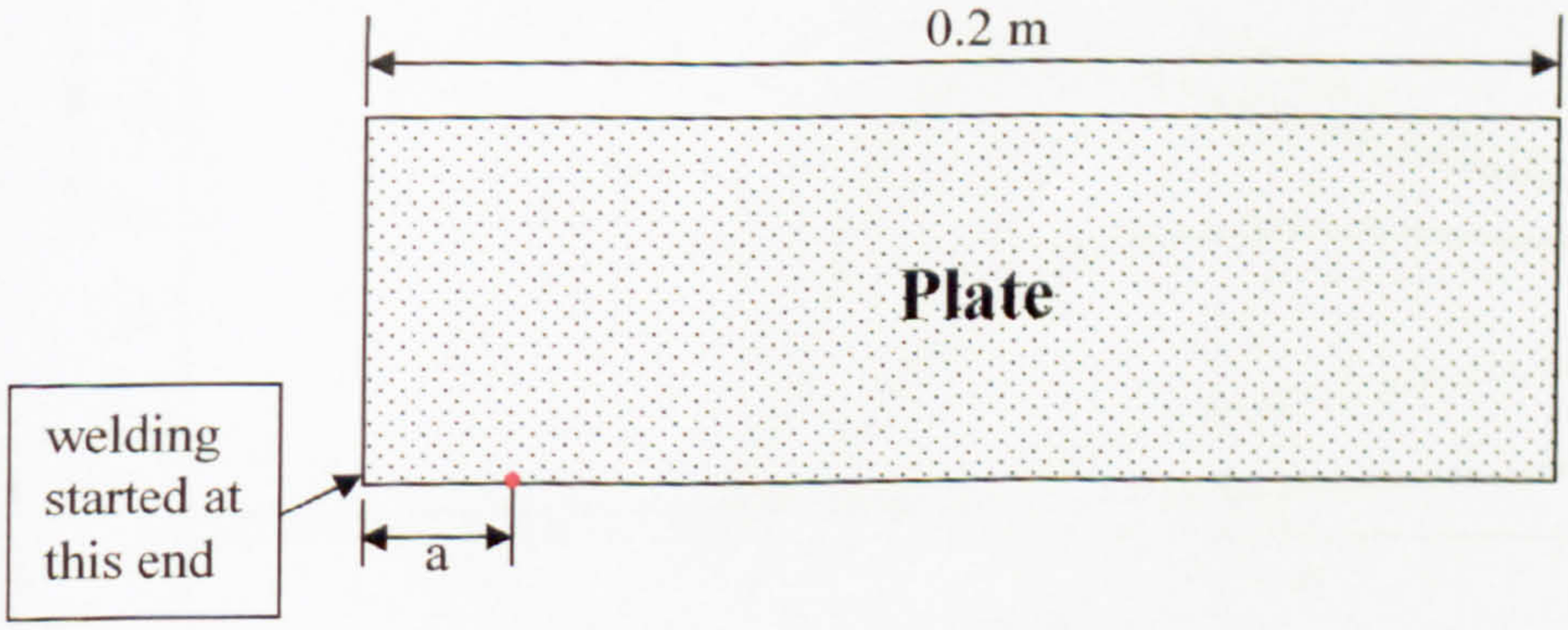

Figure E.4

The instant arc position of the converted temperature histories in Figure E.3

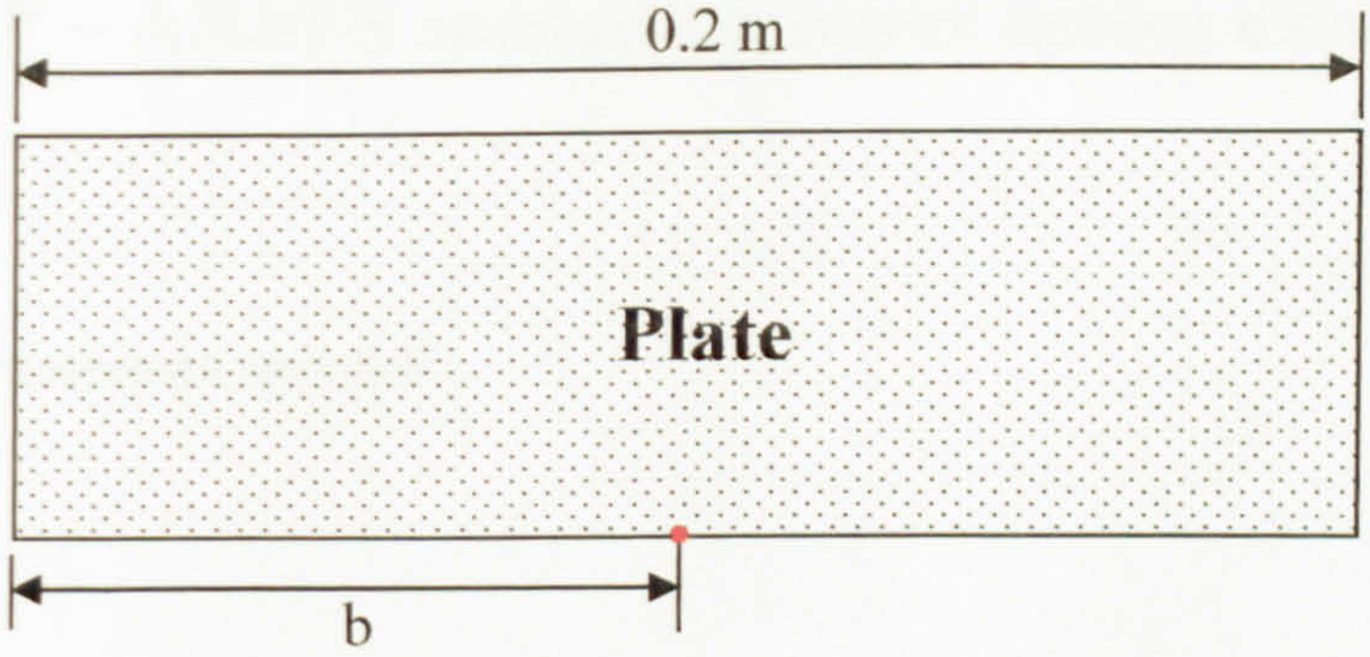

Figure E.5

The instant arc position of the experimental temperature histories in Figure E.3

For example: a = 0.026 m, b = 0.1 m and u = 0.00444 m/s

$$\therefore ts = \frac{0.1 - 0.026}{0.00444} = \underline{16.594\ s}$$

Figure E.6 shows a plot of converted temperature histories of the steady state model that aligns well with the experimentally measured temperature history after shifting.

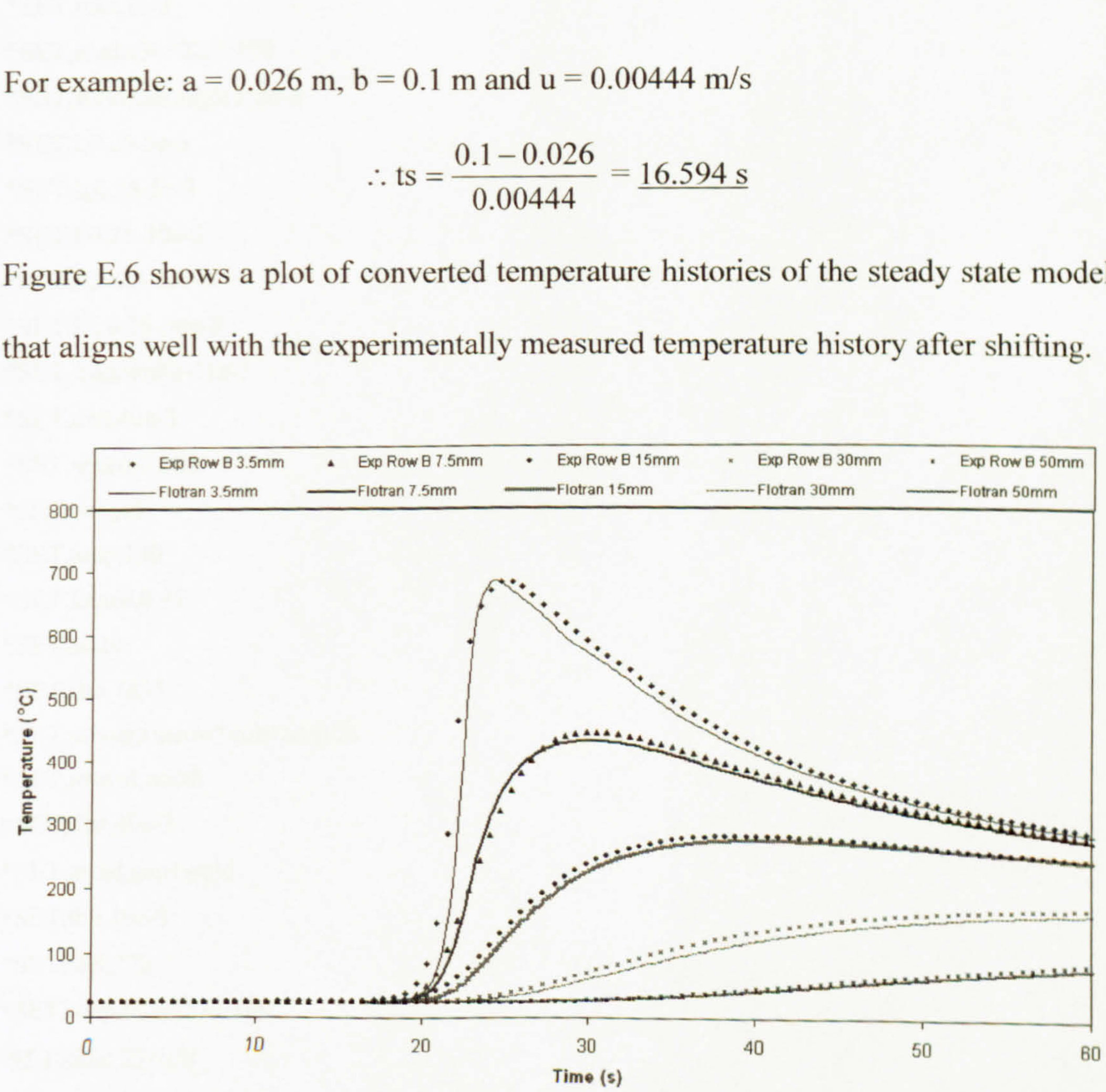

Figure *E.6*

Comparison between converted temperature histories of the steady state model and experimentally measured (centre row)

Appendix F – ANSYS modelling input listing examples

F.1 3D Transient model

```
/prep7
*SET,length,0.5
*SET,gap,1e-3/2
*SET,width,0.25+gap
*SET,thk,3e-3
*SET,root,1e-3
*SET,angle,30*22/7/180
*SET,weld,tan(angle)*2e-3
*SET,t,0.25-5e-3
*SET,b,0.25-5e-3
*SET,f,0.25-10e-3
*SET,ff,0.25-20e-3
*SET,fff,0.25-50e-3
*SET,frad,width-11e-3
*SET,dist,40e-3
*SET,speed,0.005
*SET,volt,15
*SET,amp,130
*SET,factor,0.87
*SET,ta,20
*SET,rho,7833
*SET,power,(factor*volt*amp/2)
*SET,totwid,width
*SET,dist,40e-3
*SET,arrad,gap+weld
*SET,tbb,10e-3
*SET,toff,273
*SET,topp,factor*73/100
*SET,sidet,22/100
*SET,sideb,5/100
*dim,cnvtop,table,10,,,temp
*SET,cnvtop(1,1) , 10.84,10.88,11.32,11.76,13.24,33.72,47.06,46.86,66.23,239.83
*SET,cnvtop(1,0) , 298-toff,302-toff,352-toff,402-toff,568.4-toff,842-toff,942-toff,1000-toff,
```

1342-toff,2273-toff

*dim,cnvbot,table,10,,,temp

*SET,cnvbot(1,1) , 5.84,5.88,6.32,6.76,8.24,28.72,42.06,41.86,61.23,234.83

*SET,cnvbot(1,0) , 298-toff,302-toff,352-toff,402-toff,568.4-toff,842-toff,942-toff,1000-toff,

1342-toff,2273-toff

*dim,cnvside,table,10,,,temp

*SET,cnvside(1,1) , 12.84,12.88,13.32,13.76,15.24,35.72,49.06,48.86,68.23,241.83

*SET,cnvside(1,0) , 298-toff,302-toff,352-toff,402-toff,568.4-toff,842-toff,942-toff,1000-toff,

1342-toff,2273-toff

MPTEMP,1,0,150,400,600,800,1485

MPDATA,KXX,1,1,52,49.8,42.7,35.6,25.9,32.4

MPTEMP,7,1487,1700,4000

MPDATA,KXX,1,7,121,121,121

mptemp,1,0,500,620.6,672,715.5,800

mpdata,enth,1,1,0,2444929954,3194264706,4018176471,4366816176,4983856178

mptemp,7,862,1461,1511,2000,4000

mpdata,enth,1,7,5336301471,8331301471,10431301471,12876301471,22875909271

mp,dens,1,rho

k,1,t

k,2,b,-thk

k,3,f

k,4,f,-thk

k,5,width

k,6,width,-thk

k,7,ff,

k,8,ff,-thk

k,9,fff

k,10,fff,-thk

k,12,t,-thk+root

k,14,f,-thk+root

k,16,width,-thk+root

k,18,ff,-thk/2

k,20,fff,-thk/2

k,21,width-weld-gap,

k,22,width-gap,-thk

k,23,width-gap,-thk+root

a,21,5,16,23

a,23,16,6,22

a,1,21,23,12

a,12,23,22,2

a,3,1,12,14

a,7,3,14,4,8,7

a,14,12,2,4

a,8,7,9,10

LESIZE,10,,,2

LESIZE,2,1e-3

LESIZE,11,1e-3

LESIZE,9,1e-3

LESIZE,1,1e-3

LESIZE,8,1e-3

LESIZE,12,,,1

LESIZE,7,,,1

LESIZE,5,,,1

LESIZE,3,,,1

LESIZE,6,,,1

LESIZE,4,,,3

et,1,70

et,2,55

mat,2

amesh,1,4

LESIZE,20,,,5

LESIZE,14,,,5

LESIZE,13,,,5

LESIZE,21,,,5

LESIZE,15,,,2

LESIZE,17,,,1

amesh,7

amesh,5

LESIZE,16, , ,4

LESIZE,18, , ,4

LESIZE,19, , ,1

k,15,fff,0,-length

l,9,15

LESIZE,24,1e-3

allsel

VDRAG,all,,,,,,24

LESIZE,52,5e-3

LESIZE,56,5e-3

```
allsel
aclear,all
eplot
mat,1
EMODIF,all
etdel,2
mat,1
mshape,1,3d
vmesh,6
LESIZE,63,20e-3
LESIZE,62,20e-3
LESIZE,60,20e-3
LESIZE,22, , ,1
LESIZE,61, , ,1
LESIZE,21, , ,5,2
LESIZE,23, , ,5,1/2
LESIZE,59, , ,5,2
LESIZE,63, , ,5,1/2
vmesh,all
k,36
l,9,36
LESIZE,64, , ,6,
asel,s,loc,x,0.2
VDRAG,all,,,,,,64
vclear,9
LESIZE,72,40e-3,,,
LESIZE,68,40e-3,,,
LESIZE,66,25e-3,,,1.9
LESIZE,67,25e-3,,,1.9
LESIZE,71,25e-3,,,1.9
LESIZE,69,25e-3,,,1.9
vmesh,all
allsel
nummrg,all
KEYOPT,1,2,1
vsum
*get,vtop,volu,1,volu
*get,vbot,volu,2,volu
*SET,vtope,vtop/250
```

*SET,vbote,vbot/250

tref,ta

tunif,ta

*SET,ldsteps,251

*SET,elleng,2e-3

*SET,eltime,elleng/speed

save

finish

/solu

antype,trans

deltim,0.4/5,0.4/10,0.4

autots,on

kbc,1

nropt,full

timint,on

tintp

LNSRCH,on

eqslv,ICCG

*do,i,1,ldsteps,1

*SET,newtime,i*eltime

time,newtime

*SET,zpos,(i-1)*elleng-0.01

*dim,sflux_,table,9,9,,x,z

*SET,sflux_(1,0),0.2405,0.24175,0.243,0.24425,0.2455,0.24675,0.248,0.24925,0.2505

*SET,sflux_(0,9),-zpos-0,2858.45*topp,8411.64*topp,21435.34*topp,47302.10*topp,90392.09*topp,
149582.37*topp,214353.42*topp,265999.26*topp,285844.88*topp

*SET,sflux_(0,8),-zpos-0.00125,8411.64*topp,24753.15*topp,63078.36*topp,139197.18*topp,
265999.26*topp,440180.12*topp,630783.64*topp,782763.24*topp,841163.51*topp

*SET,sflux_(0,7),-zpos-0.0025,21435.34*topp,63078.36*topp,160742.39*topp, 354715.71*topp,
677845.04*topp,1121709.56*topp,1607423.91*topp,1994713.02*topp,2143534.23*topp

*SET,sflux_(0,6),-zpos-0.00375,47302.10*topp,139197.18*topp,354715.71*topp,782763.24*topp,
1495823.75*topp,2475314.71*topp,3547157.10*topp,4401801.19*topp,4730210.01*topp

*SET,sflux_(0,5),-zpos-0.005,90392.09*topp,265999.26*topp,677845.04*topp,1495823.75*topp,
2858448.84*topp,4730210.01*topp,6778450.41*topp,8411635.07*topp,9039208.90*topp

*SET,sflux_(0,4),-zpos-0.00625,149582.37*topp,440180.12*topp,1121709.56*topp,
2475314.71*topp,4730210.01*topp,7827632.42*topp,11217095.65*topp,13919717.55*topp,
14958237.45*topp

*SET,sflux_(0,3),-zpos-0.0075,214353.42*topp,630783.64*topp,1607423.91*topp,3547157.10*topp,
6778450.41*topp,11217095.65*topp,16074239.06*topp,19947130.23*topp,21435342.30*topp

*SET,sflux_(0,2),-zpos-0.00875,265999.26*topp,782763.24*topp,1994713.02*topp,
4401801.19*topp,8411635.07*topp,13919717.55*topp,19947130.23*topp,24753147.12*topp,
26599925.67*topp
*SET,sflux_(0,1),-zpos-0.01,285844.88*topp,841163.51*topp,2143534.23*topp,4730210.01*topp,
9039208.90*topp,14958237.45*topp,21435342.30*topp,26599925.67*topp,28584488.36*topp
*dim,sfluxa_,table,9,9,,x,z
*SET,sfluxa_(1,0),0.2405,0.24175,0.243,0.24425,0.2455,0.24675,0.248,0.24925,0.2505
*SET,sfluxa_(0,9),-zpos-0.01,285844.88*topp,841163.51*topp,2143534.23*topp,4730210.01*topp,
9039208.90*topp,14958237.45*topp,21435342.30*topp,26599925.67*topp,28584488.36*topp
*SET,sfluxa_(0,8),-zpos-.01125,265999.26*topp,782763.24*topp,1994713.02*topp,
4401801.19*topp,8411635.07*topp,13919717.55*topp,19947130.23*topp,24753147.12*topp,
26599925.67*topp
*SET,sfluxa_(0,7),-zpos-0.0125,214353.42*topp,630783.64*topp,1607423.91*topp,
3547157.10*topp,6778450.41*topp,11217095.65*topp,16074239.06*topp,19947130.23*topp,
21435342.30*topp
*SET,sfluxa_(0,6),-zpos-.01375,149582.37*topp,440180.12*topp,1121709.56*topp,
2475314.71*topp,4730210.01*topp,7827632.42*topp,11217095.65*topp,13919717.55*topp,1495823
7.45*topp
*SET,sfluxa_(0,5),-zpos-0.015,90392.09*topp,265999.26*topp,677845.04*topp,1495823.75*topp,
2858448.84*topp,4730210.01*topp,6778450.41*topp,8411635.07*topp,9039208.90*topp
*SET,sfluxa_(0,4),-zpos-0.01625,47302.10*topp,139197.18*topp,354715.71*topp,782763.24*topp,
1495823.75*topp,2475314.71*topp,3547157.10*topp,4401801.19*topp,4730210.01*topp
*SET,sfluxa_(0,3),-zpos-0.0175,21435.34*topp,63078.36*topp,160742.39*topp,354715.71*topp,
677845.04*topp,1121709.56*topp,1607423.91*topp,1994713.02*topp,2143534.23*topp
*SET,sfluxa_(0,2),-zpos-0.01875,8411.64*topp,24753.15*topp,63078.36*topp,139197.18*topp,
265999.26*topp,440180.12*topp,630783.64*topp,782763.24*topp,841163.51*topp
*SET,sfluxa_(0,1),-zpos-0.02,2858.45*topp,8411.64*topp,21435.34*topp,47302.10*topp,
90392.09*topp,149582.37*topp,214353.42*topp,265999.26*topp,285844.88*topp
outres,nsol,last
allsel
nsel,s,ext
nsel,r,loc,y,0
nsel,r,loc,x,frad,totwid
nsel,r,loc,z,-zpos-0,-zpos-0.02
nsel,inve
nsel,r,loc,y,0
sf,all,conv,%cnvtop%,ta
allsel
nsel,s,ext

```
nsel,r,loc,y,-thk
sf,all,conv,%cnvbot%,ta
allsel
asel,s,ext
asel,u,loc,x,totwid
asel,u,loc,y,0
asel,u,loc,y,-thk
nsla,,1
sf,all,conv,%cnvside%,ta
allsel
nsel,s,ext
nsel,r,loc,y,0
nsel,r,loc,x,frad,totwid
nsel,r,loc,z,-zpos-0,-zpos-0.01
sf,all,hflux,%sflux_%
allsel
nsel,s,ext
nsel,r,loc,y,0
nsel,r,loc,x,frad,totwid
nsel,r,loc,z,-zpos-0.01,-zpos-0.02
sf,all,hflux,%sfluxa_%
allsel
 VSEL,s,loc,x,width-weld-gap,width
 VSEL,r,loc,y,0,-thk+root
 nslv,,1
 nsel,r,loc,z,-zpos-0.01+1e-3,-zpos-0.01-1e-3
 esln,,1
 bfe,all,hgen,,power/vtope*sidet
 allsel
 VSEL,s,loc,x,width-weld-gap,width
 VSEL,r,loc,y,-thk+root,-thk
nslv,,1
nsel,r,loc,z,-zpos-0.01+1e-3,-zpos-0.01-1e-3
esln,,1
 bfe,all,hgen,,power/vbote*sideb
 allsel
 solve
 allsel
 bfedele,all,hgen
```

```
sfdele,all,conv
sfdele,all,hflux
*DEL,,PRM_
*enddo
deltim,1,1e-5,1
time,400
outres,nsol,all
allsel
bfedele,all,hgen
sfdel,all,hflux
asel,s,loc,y,0
nsla,,1
sf,all,conv,%cnvtop%,ta
allsel
asel,s,loc,y,-thk
nsla,,1
sf,all,conv,%cnvbot%,ta
alls
asel,s,loc,x,0
asel,a,loc,z,0
asel,a,loc,z,-length
nsla,,1
sf,all,conv,%cnvside%,ta
allsel
solve
```

F.2 3D Steady state model

```
/prep7
*SET,length,0.5
*SET,gap,1e-3/2
*SET,width,0.25+gap
*SET,thk,3e-3
*SET,root,1e-3
*SET,angle,30*22/7/180
*SET,weld,tan(angle)*2e-3
*SET,tb,width-6e-3
*SET,f,width-11e-3
```

```
*SET,ff,width-22e-3-gap
*SET,dist,40e-3
*SET,speed,0.005
*SET,volt,15
*SET,amp,130
*SET,factor,0.87
*SET,ta,20
*SET,rho,7833
*SET,power,(factor*volt*amp/2)
*SET,totwid,width
*SET,dist,40e-3
*SET,arrad,2e-3
*SET,tbb,10e-3
*SET,toff,273
*SET,topp,factor*72/100
*SET,side,28/100
*SET,zpos,dist-tbb
*dim,sflux,table,9,9,,x,z
*SET,sflux(1,0),0.2405,0.24175,0.243,0.24425,0.2455,0.24675,0.248,0.24925,0.2505
*SET,sflux(0,9),-zpos-0,2858.45*topp,8411.64*topp,21435.34*topp,47302.10*topp,90392.09*topp,
149582.37*topp,214353.42*topp,265999.26*topp,285844.88*topp
*SET,sflux(0,8),-zpos-0.00125,8411.64*topp,24753.15*topp,63078.36*topp,139197.18*topp,
265999.26*topp,440180.12*topp,630783.64*topp,782763.24*topp,841163.51*topp
*SET,sflux(0,7),-zpos-0.0025,21435.34*topp,63078.36*topp,160742.39*topp,354715.71*topp,
677845.04*topp,1121709.56*topp,1607423.91*topp,1994713.02*topp,2143534.23*topp
*SET,sflux(0,6),-zpos-0.00375,47302.10*topp,139197.18*topp,354715.71*topp,782763.24*topp,
1495823.75*topp,2475314.71*topp,3547157.10*topp,4401801.19*topp,4730210.01*topp
*SET,sflux(0,5),-zpos-0.005,90392.09*topp,265999.26*topp,677845.04*topp,1495823.75*topp,
2858448.84*topp,4730210.01*topp,6778450.41*topp,8411635.07*topp,9039208.90*topp
*SET,sflux(0,4),-zpos-0.00625,149582.37*topp,440180.12*topp,1121709.56*topp,2475314.71*topp,
4730210.01*topp,7827632.42*topp,11217095.65*topp,13919717.55*topp,14958237.45*topp
*SET,sflux(0,3),-zpos-0.0075,214353.42*topp,630783.64*topp,1607423.91*topp,3547157.10*topp,
6778450.41*topp,11217095.65*topp,16074239.06*topp,19947130.23*topp,21435342.30*topp
*SET,sflux(0,2),-zpos-0.00875,265999.26*topp,782763.24*topp,1994713.02*topp,4401801.19*topp,
8411635.07*topp,13919717.55*topp,19947130.23*topp,24753147.12*topp,26599925.67*topp
*SET,sflux(0,1),-zpos-0.01,285844.88*topp,841163.51*topp,2143534.23*topp,4730210.01*topp,
9039208.90*topp,14958237.45*topp,21435342.30*topp,26599925.67*topp,28584488.36*topp
*dim,sfluxa,table,9,9,,x,z
*SET,sfluxa(1,0),0.2405,0.24175,0.243,0.24425,0.2455,0.24675,0.248,0.24925,0.2505
```

*SET,sfluxa(0,9),-zpos-0.01,285844.88*topp,841163.51*topp,2143534.23*topp,4730210.01*topp,
9039208.90*topp,14958237.45*topp,21435342.30*topp,26599925.67*topp,28584488.36*topp
*SET,sfluxa(0,8),-zpos-0.01125,265999.26*topp,782763.24*topp,1994713.02*topp,
4401801.19*topp,8411635.07*topp,13919717.55*topp,19947130.23*topp,24753147.12*topp,
26599925.67*topp
*SET,sfluxa(0,7),-zpos-0.0125,214353.42*topp,630783.64*topp,1607423.91*topp,3547157.10*topp,
6778450.41*topp,11217095.65*topp,16074239.06*topp,19947130.23*topp,21435342.30*topp
*SET,sfluxa(0,6),-zpos-0.01375,149582.37*topp,440180.12*topp,1121709.56*topp,
2475314.71*topp,4730210.01*topp,7827632.42*topp,11217095.65*topp,13919717.55*topp,
14958237.45*topp
*SET,sfluxa(0,5),-zpos-0.015,90392.09*topp,265999.26*topp,677845.04*topp,1495823.75*topp,
2858448.84*topp,4730210.01*topp,6778450.41*topp,8411635.07*topp,9039208.90*topp
*SET,sfluxa(0,4),-zpos-0.01625,47302.10*topp,139197.18*topp,354715.71*topp,782763.24*topp,
1495823.75*topp,2475314.71*topp,3547157.10*topp,4401801.19*topp,4730210.01*topp
*SET,sfluxa(0,3),-zpos-0.0175,21435.34*topp,63078.36*topp,160742.39*topp,354715.71*topp,
677845.04*topp,1121709.56*topp,1607423.91*topp,1994713.02*topp,2143534.23*topp
*SET,sfluxa(0,2),-zpos-0.01875,8411.64*topp,24753.15*topp,63078.36*topp,139197.18*topp,
265999.26*topp,440180.12*topp,630783.64*topp,782763.24*topp,841163.51*topp
*SET,sfluxa(0,1),-zpos-0.02,2858.45*topp,8411.64*topp,21435.34*topp,47302.10*topp,
90392.09*topp,149582.37*topp,214353.42*topp,265999.26*topp,285844.88*topp
*dim,cnvtop,table,10,,,temp
*SET,cnvtop(1,1) , 10.84,10.88,11.32,11.76,13.24,33.72,47.06,46.86,66.23,239.83
*SET,cnvtop(1,0) , 298-toff,302-toff,352-toff,402-toff,568.4-toff,842-toff,942-toff,1000-toff,
1342-toff,2273-toff
*dim,cnvbot,table,10,,,temp
*SET,cnvbot(1,1) , 5.84,5.88,6.32,6.76,8.24,28.72,42.06,41.86,61.23,234.83
*SET,cnvbot(1,0) , 298-toff,302-toff,352-toff,402-toff,568.4-toff,842-toff,942-toff,1000-toff,
1342-toff,2273-toff
*dim,cnvside,table,10,,,temp
*SET,cnvside(1,1) , 12.84,12.88,13.32,13.76,15.24,35.72,49.06,48.86,68.23,241.83
*SET,cnvside(1,0) , 298-toff,302-toff,352-toff,402-toff,568.4-toff,842-toff,942-toff,1000-toff,
1342-toff,2273-toff
MPTEMP,1,0,150,400,600,800,1485
MPDATA,KXX,1,1,52,49.8,42.7,35.6,25.9,32.4
MPTEMP,7,1487,3000
MPDATA,KXX,1,7,121,121
MPTEMP,1,18.2,620,621,672,673,715
MPDATA,C,1,1,550,826.07,2046.4,2046.4,1023.15,1023.15
MPTEMP,7,862,1460,1462,1510,1512,5000

```
MPDATA,C,1,7,638.3,638.3,5361.9,5361.9,638.3,638.3
mp,dens,1,rho
k,1,tb
k,2,tb,-thk
k,3,f
k,4,f,-thk
k,5,width
k,6,width,-thk
k,7,ff,
k,8,ff,-thk
k,9,0
k,10,0,-thk
k,12,tb,-thk+root
k,14,f,-thk+root
k,16,width,-thk+root
k,18,ff,-thk+root
k,20,0,-thk+root
k,21,0.25-weld,
k,22,0.25,-thk
k,23,0.25,-thk+root
a,21,5,16,23
a,23,16,6,22
a,1,21,23,12
a,12,23,22,2
a,3,1,12,14
a,18,14,4,8
a,7,3,14,18
a,14,12,2,4
a,9,20,18,7
a,18,8,10,20
LESIZE,1, , ,4
LESIZE,3, , ,4
LESIZE,6, , ,4
LESIZE,8, , ,7
LESIZE,9, , ,9,2
LESIZE,11, , ,9,2
LESIZE,13, , ,4
LESIZE,14, , ,4
LESIZE,22, , ,4
```

```
LESIZE,16, , ,6,1/2
LESIZE,18, , ,6,2
LESIZE,20, , ,6,1/2
LESIZE,25, , ,30,5
LESIZE,26, , ,30,5
LESIZE,24, , ,30,1/5
LESIZE,2, , ,4
LESIZE,4, , ,4
LESIZE,10, , ,4
LESIZE,15, , ,4
LESIZE,21, , ,4
LESIZE,23, , ,4
et,1,142
k,81,,,-dist+tbb
k,91,,,-dist+arrad/2
k,92,,,-dist-arrad/2
k,93,,,-dist-tbb
k,101,,,-length
l,9,81,15,1/3
l,81,91,15
l,91,92,4
l,92,93,15
l,93,101,100,10
vdra,all,,,,,,28,29,30,31,32
allsel
esize,,2
vmesh,all
vsum
*get,vt,volu,21,volu
*get,vb,volu,22,volu
*SET,vW,vt+vb
eplot
FINISH
/SOL
FLDATA,solu,flow,f
FLDATA,solu,temp,t
FLDATA7,PROT,VISC,CONSTANT
FLDATA8,NOMI,VISC,1e6
FLDATA7,PROT,DENS,CONSTANT
```

```
FLDATA8,NOMI,DENS,rho,
FLDATA7,PROT,COND,table
FLDATA,VARY,COND,TRUE
FLDATA7,PROT,SPHT,table
FLDATA,VARY,SPHT,TRUE
FLDATA,relx,temp,0.8
FLDATA,relx,COND,0.8
FLDATA,relx,spht,0.8
FLDATA33,ADVM,temp,supg
FLDATA34,MIR,temp,0.1
FLDATA,OUTP,COND,TRUE
FLDATA,OUTP,SPHT,TRUE
FLDATA,iter,exec,770
FLDATA2,ITER,appe,10
FLDATA,meth,temp,6
FLDATA,meth,vx,0
FLDATA,meth,vy,0
FLDATA,meth,ENKE,0
FLDATA,meth,ENDS,0
FLDATA14,TEMP,NOMI,ta
allsel
asel,s,ext
nsla,,1
d,all,ENKE,-1
d,all,vz,-speed
allsel
asel,s,loc,z,0
nsla,,1
d,all,temp,ta
allsel
asel,s,loc,y,0
nsla,,1
sf,all,conv,%cnvtop%,ta
allsel
asel,s,loc,y,-thk
nsla,,1
sf,all,conv,%cnvbot%,ta
allsel
asel,s,loc,x,0
```

```
asel,a,loc,z,0
asel,a,loc,z,-length
nsla,,1
sf,all,conv,%cnvside%,ta
allsel
VSEL,s,,,21,22
eslv
bfe,all,hgen,,power/vW*side
allsel
nsel,s,loc,y,0
nsel,r,loc,x,width-tbb,width
nsel,r,loc,z,-zpos-0,-zpos-0.01
sfdel,all,conv
sf,all,hflux,%sflux%
nsel,s,loc,y,0
nsel,r,loc,x,width-tbb,width
nsel,r,loc,z,-zpos-0.01,-zpos-0.02
sfdel,all,conv
sf,all,hflux,%sfluxa%
allsel
csys,0
ic,all,vz,-speed
ic,all,vx,0
ic,all,vy,0
IC,ALL,TEMP,TA
solve
```

F.3 2D Transient sectional model

```
/prep7
*SET,length,0.5
*SET,gap,1e-3/2
*SET,width,0.25+gap
*SET,thk,3e-3
*SET,root,1e-3
*SET,angle,30*22/7/180
*SET,weld,tan(angle)*2e-3
```

```
*SET,tbb,0.25-4.5e-3
*SET,tb,0.25-4.5e-3
*SET,f,0.25-10e-3
*SET,ff,0.25-20e-3
*SET,dist,40e-3
*SET,speed,0.005
*SET,volt,15
*SET,amp,130
*SET,factor,0.87
*SET,ta,20
*SET,rho,7833
*SET,power,(factor*volt*amp/2)
*SET,totwid,width
*SET,dist,40e-3
*SET,arrad,2e-3
*SET,Q,power/speed
*SET,tt,2e-3/speed
*SET,mpower,Q/tt
*SET,topp,72/100*factor
*SET,side1,23/100
*SET,side2,5/100
*SET,t1,0.01/speed-1e-3/speed
*SET,t2,0.01/speed
*SET,t3,0.01/speed+1e-3/speed
*SET,t4,0.02/speed
*SET,toff,273
*dim,cnvtop,table,10,,,temp
*SET,cnvtop(1,1) , 10.84,10.88,11.32,11.76,13.24,33.72,47.06,46.86,66.23,239.83
*SET,cnvtop(1,0) , 298-toff,302-toff,352-toff,402-toff,568.4-toff,842-toff,942-toff,1000-toff,
1342-toff,2273-toff
*dim,cnvbot,table,10,,,temp
*SET,cnvbot(1,1) , 5.84,5.88,6.32,6.76,8.24,28.72,42.06,41.86,61.23,234.83
*SET,cnvbot(1,0) , 298-toff,302-toff,352-toff,402-toff,568.4-toff,842-toff,942-toff,1000-toff,
1342-toff,2273-toff
*dim,cnvside,table,10,,,temp
*SET,cnvside(1,1) , 12.84,12.88,13.32,13.76,15.24,35.72,49.06,48.86,68.23,241.83
*SET,cnvside(1,0) , 298-toff,302-toff,352-toff,402-toff,568.4-toff,842-toff,942-toff,1000-toff,
1342-toff,2273-toff
*dim,sflux_,table,9,9,,x,time
```

*SET,sflux_(1,0),0.2405,0.24175,0.243,0.24425,0.2455,0.24675,0.248,0.24925,0.2505
*SET,sflux_(0,1),0/speed,2858.45*topp,8411.64*topp,21435.34*topp,47302.10*topp,90392.09*topp,
149582.37*topp,214353.42*topp,265999.26*topp,285844.88*topp
*SET,sflux_(0,2),0.00125/speed,8411.64*topp,24753.15*topp,63078.36*topp,139197.18*topp,
265999.26*topp,440180.12*topp,630783.64*topp,782763.24*topp,841163.51*topp
*SET,sflux_(0,3),0.0025/speed,21435.34*topp,63078.36*topp,160742.39*topp,354715.71*topp,
677845.04*topp,1121709.56*topp,1607423.91*topp,1994713.02*topp,2143534.23*topp
*SET,sflux_(0,4),0.00375/speed,47302.10*topp,139197.18*topp,354715.71*topp,782763.24*topp,
1495823.75*topp,2475314.71*topp,3547157.10*topp,4401801.19*topp,4730210.01*topp
*SET,sflux_(0,5),0.005/speed,90392.09*topp,265999.26*topp,677845.04*topp,1495823.75*topp,
2858448.84*topp,4730210.01*topp,6778450.41*topp,8411635.07*topp,9039208.90*topp
*SET,sflux_(0,6),0.00625/speed,149582.37*topp,440180.12*topp,1121709.56*topp,
2475314.71*topp,4730210.01*topp,7827632.42*topp,11217095.65*topp,13919717.55*topp,
14958237.45*topp
*SET,sflux_(0,7),0.0075/speed,214353.42*topp,630783.64*topp,1607423.91*topp,3547157.10*topp,
6778450.41*topp,11217095.65*topp,16074239.06*topp,19947130.23*topp,21435342.30*topp
*SET,sflux_(0,8),0.00875/speed,265999.26*topp,782763.24*topp,1994713.02*topp,
4401801.19*topp,8411635.07*topp,13919717.55*topp,19947130.23*topp,24753147.12*topp,
26599925.67*topp
*SET,sflux_(0,9),0.01/speed,285844.88*topp,841163.51*topp,2143534.23*topp,4730210.01*topp,
9039208.90*topp,14958237.45*topp,21435342.30*topp,26599925.67*topp,28584488.36*topp
*dim,sfluxa_,table,9,9,,x,time
*SET,sfluxa_(1,0),0.2405,0.24175,0.243,0.24425,0.2455,0.24675,0.248,0.24925,0.2505
*SET,sfluxa_(0,1),0.01/speed,285844.88*topp,841163.51*topp,2143534.23*topp,4730210.01*topp,
9039208.90*topp,14958237.45*topp,21435342.30*topp,26599925.67*topp,28584488.36*topp
*SET,sfluxa_(0,2),0.01125/speed,265999.26*topp,782763.24*topp,1994713.02*topp,
4401801.19*topp,8411635.07*topp,13919717.55*topp,19947130.23*topp,24753147.12*topp,
26599925.67*topp
*SET,sfluxa_(0,3),0.0125/speed,214353.42*topp,630783.64*topp,1607423.91*topp,
3547157.10*topp,6778450.41*topp,11217095.65*topp,16074239.06*topp,19947130.23*topp,
21435342.30*topp
*SET,sfluxa_(0,4),0.01375/speed,149582.37*topp,440180.12*topp,1121709.56*topp,
2475314.71*topp,4730210.01*topp,7827632.42*topp,11217095.65*topp,13919717.55*topp,
14958237.45*topp
*SET,sfluxa_(0,5),0.015/speed,90392.09*topp,265999.26*topp,677845.04*topp,1495823.75*topp,
2858448.84*topp,4730210.01*topp,6778450.41*topp,8411635.07*topp,9039208.90*topp
*SET,sfluxa_(0,6),0.01625/speed,47302.10*topp,139197.18*topp,354715.71*topp,782763.24*topp,
1495823.75*topp,2475314.71*topp,3547157.10*topp,4401801.19*topp,4730210.01*topp
*SET,sfluxa_(0,7),0.0175/speed,21435.34*topp,63078.36*topp,160742.39*topp,354715.71*topp,

677845.04*topp,1121709.56*topp,1607423.91*topp,1994713.02*topp,2143534.23*topp

*SET,sfluxa_(0,8),0.01875/speed,8411.64*topp,24753.15*topp,63078.36*topp,139197.18*topp,

265999.26*topp,440180.12*topp,630783.64*topp,782763.24*topp,841163.51*topp

*SET,sfluxa_(0,9),0.02/speed,2858.45*topp,8411.64*topp,21435.34*topp,47302.10*topp,

90392.09*topp,149582.37*topp,214353.42*topp,265999.26*topp,285844.88*topp

MPTEMP,1,0,150,400,600,800,1485

MPDATA,KXX,1,1,52,49.8,42.7,35.6,25.9,32.4

MPDATA,Kyy,1,1,52,49.8,42.7,35.6,25.9,32.4

MPTEMP,7,1487,4000

MPDATA,KXX,1,7,121,121

MPDATA,Kyy,1,7,32.4,32.4

mptemp,1,0,500,620.6,672,715.5,800

mpdata,enth,1,1,0,2444929954,3194264706,4018176471,4366816176,4983856178

mptemp,7,862,1461,1511,2000,4000

mpdata,enth,1,7,5336301471,8331301471,10431301471,12876301471,22875909271

mp,dens,1,rho

*SET,totwid,width

k,1,tbb

k,2,tb,-thk

k,3,f

k,4,f,-thk

k,5,width

k,6,width,-thk

k,7,ff,

k,8,ff,-thk

k,9,0

k,10,0,-thk

k,12,tb,-thk+root

k,14,f,-thk+root

k,16,width,-thk+root

k,18,ff,-thk+root

k,20,0,-thk+root

k,21,width-weld-gap,

k,22,width-gap,-thk

k,23,width-gap,-thk+root

a,21,5,16,23

a,23,16,6,22

a,1,21,23,12

a,12,23,22,2

```
a,3,1,12,14
a,18,14,4,8
a,7,3,14,18
a,14,12,2,4
a,9,20,18,7
a,18,8,10,20
LESIZE,1,1e-3/2
LESIZE,3,, ,3
LESIZE,6,, ,3
LESIZE,8,1e-3/2
LESIZE,9,1e-3/2
LESIZE,11,1e-3/2
LESIZE,13,1e-3/2
LESIZE,14,1e-3/2
LESIZE,22,1e-3/2
LESIZE,16,1e-3
LESIZE,18,1e-3
LESIZE,20,1e-3
LESIZE,25, , ,40,10
LESIZE,26, , ,40,10
LESIZE,24, , ,40,1/10
LESIZE,2,1e-3/2
LESIZE,4, , ,6
LESIZE,10,1e-3/2
LESIZE,15,,,4
LESIZE,21,,,2
LESIZE,23,,,2
LESIZE,5,,,2
LESIZE,7,,,2
LESIZE,12,,,2
LESIZE,17,,,2
LESIZE,19,,,1
LESIZE,27,,,1
et,1,55
nummrg,all
amesh,all
keyopt,1,1,1
asum
*get,area1,area,1,area
```

```
*get,area2,area,2,area
eplot
allsel
tref,ta
tunif,ta
FINISH
/SOL
antype,trans
deltim,0.01,0.001,0.2
autots,on
kbc,1
nropt,full
timint,on
tintp
LNSRCH,on
time,t1
outres,nsol,all
allsel
nsel,s,loc,y,0
nsel,u,loc,x,totwid-10e-3,totwid
sf,all,conv,%cnvtop%,ta
allsel
nsel,s,loc,y,-thk
sf,all,conv,%cnvbot%,ta
allsel
nsel,s,loc,x,0
sf,all,conv,%cnvside%,ta
allsel
nsel,s,loc,y,0
nsel,r,loc,x,totwid-10e-3,totwid
sf,all,hflux,%sflux_%
allsel
solve
time,t2
allsel
ASEL,s,,,1
esla
bfe,all,hgen,,mpower/area1*side1
allsel
```

```
ASEL,s,,,2
esla
bfe,all,hgen,,mpower/area2*side2
allsel
solve
time,t3
allsel
nsel,s,loc,y,0
nsel,r,loc,x,totwid-10e-3,totwid
sf,all,hflux,%sfluxa_%
allsel
solve
time,t4
allsel
bfedel,all,hgen
allsel
solve
deltim,1,0.01,1
time,405
outres,nsol,all
allsel
sfdel,all,hflux
sfdel,all,conv
allsel
nsel,s,loc,y,0
sf,all,conv,%cnvtop%,ta
allsel
nsel,s,loc,y,-thk
sf,all,conv,%cnvbot%,ta
allsel
nsel,s,loc,x,0
sf,all,conv,%cnvside%,ta
allsel
solve
```

Appendix G – Bibliography

1) Harold A. Wilson, *On Convection of heat*, Proceedings of the Cambridge Philosophical Society, 1904, Vol. XII, pp. 406-423, The University Press

2) Daniel Rosenthal, *Mathematical Theory of Heat Distribution During Welding and Cutting*, Welding Research Supplement, 1941, Vol. 20, pp. 220s-234s

3) E. M. Mahla, M. C. Rowland, C. A. Shook and G. E. Doan, *Heat Flow in Arc Welding*, Welding Research Supplement, 1941, Vol. 20, pp. 459s-468s

4) A. A. Wells, *Heat Flow in Welding*, Welding Research Supplement, 1952, Vol. 31, pp. 265s-267s

5) R.L. Apps and D. R. Milner, *Heat Flow in Argon-Arc Welding*, British Welding Journal, 1955, Vol. 34, pp. 475-485

6) Clyde M. Adams, JR, *Cooling Rates and Peak Temperatures in fusion welding*, Welding Research Supplement, 1958, Vol. 37, pp.210s.215s

7) J. M. Barry, Zvi Paley and M. Adams, JR, *Heat Conduction from Moving Arcs in Welding*, Welding Research Supplement, 1963, Vol. 42, pp. 97s-104s.

8) N. Christensen, V. de L. Davies and K. Gjermundsen, *Distribution of Temperatures in Arc Welding*, British Welding Journal, 1965, Vol. 12, pp. 54-75

9) V. Pavelic, R. Tanbakuchi, O. A. Uyehara and P. S. Myers, *Experimental and Computed Temperature Histories in Gas Tungsten-Arc Welding of Thin Plates,* Welding Research Supplement, 1969, Vol. 48, pp. 295-305

10) E. Friedman, *Thermo-mechanical Analysis of the welding process using the Finite Element Method,* Journal of Pressure Vessel Technology, Transactions of the ASME, 1975, pp. 206-213

11) Z. Paley and P.D. Hibbert, *Computation of Temperatures in Actual Weld Designs,* Welding Research Supplement, 1975, Vol.54, pp. 385s-392s

12) G.W. Krutz and L.J.Segerlind, *Finite Element Analysis of Welded Structures,* Welding Research Supplement, 1978, Vol. 57, pp. 211s-216s

13) T. W. Eagar and N. S. Tsai, *Temperature Fields Produced by travelling Distribution Heat Sources*, Welding Research Supplement, 1983, Vol. 62, pp. 346s-355s

14) K. Easterling, *Introduction to the Physical Metallurgy of Welding*, 1983, pp.18.38, London Butterworths.

15) John Goldak, Aditya Chakravart and Malcolm Bibby, *A New Finite Element Model for Welding Heat Sources,* Metallurgical Transaction B Vol. 15B, 1984, pp. 299-305

16) J. E. Moore, M. J. Bibby, J. A. Goldak and S. Santyr, *A comparison of the point source and finite element schemes for computing weld cooling*, in Nippes, E.F. and Ball, D.J. (Eds.): *Welding Research: The State of the Art*, Chap. 1, Metals Park, Ohio 1985

17) P. Tekriwal and J. Mazumder, *Finite Element Analysis of Three-Dimensional Transient Heat Transfer in GMA welding,* Welding Research Supplement, 1988, Vol. 67, pp. 150s-156s

18) H. G. Krans, *Experimental Measurement of Stationary SS 304, SS 316 L and 8630 GTA Weld Pool Surface Temperatures*, Welding Research Supplement, 1989, Vol. 68, pp. 269s-279s

19) E. Pardo and D.C. Weckman, *Prediction of Weld Pool and Reinforcement Dimensions of GMA Welds Using a Finite-Element Model,* Metallurgical transactions B, Vol. 20B, 1989, pp. 937-947

20) Adrian Bejan, *Heat Transfer*, pp.171-184, John Wiley & Sons, Inc. 1993

21) T. Kasuya and N. Yurioka, *Prediction of Welding Thermal History by a Comprehensive Solution*, Welding Research Supplement, 1993, Vol. 72, pp. 107s-115s

22) V. Kamala and . A. Goldak, *Error Due to Two Dimensional Approximation in Heat Transfer Analysis of Welds,* Welding Research Supplement, 1993, Vol. 72, pp. 440s-446s

23) R. M. Dighde, L. L. Meekisho, D. G. Atteridge and W. E. Wood, *Simulation of Welding Heat Transfer in Tekken Weldability Tests using the ANSYS program*, ANSYS® 1994: Conf. Proc. May 2-6, Pittsburgh, PA, vol. 1, pp. 3.41-3.53, The Pittsburgh Hilton & Towers, Swanson Analysis Systems, Inc.

24) J. M. DuPONT and A. R. MARDER. *Thermal Efficiency of Arc Welding Processes*, British Welding Journal, 1995, vol.74, (12), pp. 406s-416s

25) Margarita Baera, Plamen Baev and Alexander Kaplan, *An analysis of the heat transfer from a moving elliptical cylinder*, Journal of Physics D: Apply Physic 30, 1997, pp.1190-1196

26) M. A. Wahab, M. J. Painter, M. H. Davies, *The prediction of the temperature distribution and weld pool geometry in the gas metal arc welding process,* Journal of Materials Processing Technology 77, 1998, pp. 233-239

27) S. Murugan, P. V. Kumar, T. P. S. Gill, B. Raj, and M. S. C. Bose, *Numerical modelling and experimental determination of temperature distribution during manual metal arc welding,* Science and Technology of Welding and Joining, 1999, Vol. 4, No. 6, pp. 357-364

28) N.T. Ngnyen, A. Ohta, K. Matsuoka, N. Suzuki and Y. Maeda, *Analytical solutions for Transient Temperature of Semi-infinite Body Subjected to 3D Moving Heat Sources*, Welding Research Supplement, 1999, Vol.78, pp. 265s-274s

29) S.H. Kang and H. S. Chol, *Analytical solution for transient temperature distribution in gas tungsten arc welding with consideration of filler wire*, Proc. Instn. Mech. Engrs., 1999, Vol. 213, Part B, pp.199-811

30) E. A. Bonifaz, *Finite Element Analysis of Heat Flow in Single-Pass Arc Welds,* Welding Research Supplement, 2000, Vol. 79, pp. 121s-125s

31) Annedi Achuta Reddy, Bimalendu Guha and D. R. G. Achar, *Finite Element Modeling of Three-Dimensional Transient Heat Transfer in Stainless Steel (304) Pulsed GTA Weldments,* Numerical Heat Transfer, 2002, Part A, Vol. 41, pp. 41-64

32) C. S. Wu and J. Q. Gas, *Analysis of the heat flux distribution at the mode of a TIG welding arc*, Computational Materials Science 24, 2002, pp.323-327

33) WANG Yu, ZHAO Haiyan, WU Su, ZHANG Jianqiang and LIU Dianbing, *Shape parameter determination of double ellipsoidal heat source model in numerical simulation of high-energy beam welding,* Transactions of the China Welding Institution, 2003, Vol. 24, No. 2, pp. 67-70

34) Clarence E. Jackson and Arthur E. Shrubsall, *Control of the Penetration and Melting Ratio with Welding Technique*, Welding Research Supplement, 1953, Vol. 32, pp. 172s-178s

35) C.K. Lee, J, Candy and C.P.H. Tan, *Measurement and finite element analysis of temperature distribution in arc welding process*, International Journal of Computer Applications in Technology, 2004, Vol. 21, No.4, pp. 171-177

36) Ø. Grong, *Metallurgical Modelling of Welding*, The Institute of Materials, 1994, pp. 1-115

37) J.R. Lloyd and W.R. Moran, *Natural Convection Adjacent to Horizontal Surfaces of Various Platforms*, 1974, ASME Paper 74-WA/HT-66

38) R.D. Pehlke, A. Jeyarajan and H. Wada, *Summary of Thermal Properties for Casting Alloys and Mould Materials*, National Science Foundation,1982

39) J.M. Woolman and R.A. Mottram, *The Mechanical and Physical Properties of the British Standard En Steel*, 1964-66 (B.S. 970-1995) Vol. 1, En 1 to En 20

40) The direction of the ASM Handbook Committee *Metals Handbook Comprehensive Index*, Metals Park, Ohio, 1986

41) T. Iida and R.I.L Guthrie, *Physical Properties of Liquid Metals*, Oxford Science, 1988

42) The British Iron and Steel Research Association, *Physical Constants of Some Commercial Steels at Elevated Temperatures*, 1953

43) K. Easterling, *Introduction to the Physical Metallurgy of Welding*, Butterworths, London, 1983, pp. 18-38

44) X. Chen, M. Becker and L. Meekisho, *Welding analysis in moving coordinates*, in Cerjak, H. (Ed.): Mathematical Modelling of Weld Phenomena 4, IOM Communications, 1998, pp.396-410

45) Y.A Cengel, R.H. Turner, *Fundamentals of Thermal-Fluid Sciences*, McGraw-Hill, International Edition, 2001, pp. 970